# CHARACTERIZING AND ENGINEERING THE METAL CONTACT INTERFACE IN 1D AND 2D CHALCOGENIDE SYSTEMS

by

Christopher M. Smyth

THE UNIVERSITY OF TEXAS AT DALLAS

EST. 1969

APPROVED BY SUPERVISORY COMMITTEE:

Robert M. Wallace, Co-Chair

Christopher L. Hinkle, Co-Chair

Luigi Colombo

Massimo V. Fischetti

Chadwin D. Young

To my parents, sister, brother-in-law, and best friend

# CHARACTERIZING AND ENGINEERING THE METAL CONTACT INTERFACE IN 1D AND 2D CHALCOGENIDE SYSTEMS

by

CHRISTOPHER M. SMYTH, BS

DISSERTATION

Presented to the Faculty of

The University of Texas at Dallas

in Partial Fulfillment

of the Requirements

for the Degree of

DOCTOR OF PHILOSOPHY IN

MATERIALS SCIENCE AND ENGINEERING

THE UNIVERSITY OF TEXAS AT DALLAS

December 2018

# ACKNOWLEDGMENTS

I would like to thank Professors Robert M. Wallace and Christopher L. Hinkle for giving me a chance to prove my worth in a PhD program. They have instilled in me a passion for research I will carry into my future endeavors. Their creativity and intuition has been a refreshing and inspiring perspective. The incredibly high standard they hold their students to cultivates excellence and I am proud to be a product of their advisement. I would also like to thank my dissertation committee, Dr. Luigi Colombo, Dr. Chadwin Young, and Dr. Massimo Fischetti, for their invaluable guidance and encouragement throughout this arduous journey.

I would like to give special thanks to Dr. Lee A. Walsh currently a postdoctoral fellow at Tyndall National Institute) for his patience, his perspectives on scientific and practical subjects, and his constant support. He continues to be a role model for me in all areas of life. I am forever greatful for the wealth of knowledge I have gained from him and look forward to future collaboration and friendship. My thanks also goes to Dr. Stephen McDonnell and Dr. Rafik Addou for providing daily guidance and for showing me how to effectively lead, teach, and inspire. My thanks also goes out to past and present Wallace group members, Dr. Angelica Azcatl, Dr. Hui Zhu, Dr. Xiaoye Qin, Ms. Ava Khosravi, and Mr. Christopher Cormier, for their patience, enlightening discussions, and comraderie. Without them, my research would not have been possible.

I would also like to extend my gratitude to Dr. Paul Hurley, Dr. Greg Hughes, Dr. Michael Schmidt, Dr. Brendan Sheehan, Dr. Karim Cherkaoui, Mr. Gioele Mirabelli, (Tyndall National Institute) and Mr. Connor McGeough (Dublin City University) for their warm hospitality and generous dedication of time and resources to make my stay in Ireland for the NSF UNITE collaboration trip so culturally and scientifically enriching. Thank you for making those three weeks some of the best I've had in graduate school and for the fruitful collaboration over the course of the UNITE program.

I would like to thank other current and previous scientists and students from the department (Mr. Adam Barton, Mr. Pavel Bolshakov, Ms. Joy Lee, Mr. Arul Ravichandran, and Mr. Yasiel Cabrera, Dr. Antonio Lucero, Dr. Lanxia Cheng, Dr. Guanyu Zhou, Dr. Massimo Catalano, Dr. Guanyu Zhou, Dr. Ruoyu Yue, Mr. Luhua Wang, and Mr. Peng Zhao) for their valuable contributions to this work and, most importantly, their friendship. I also thank members of our technical staff, Mr. Tommy Bennett, and Mr. Dave Stimson, for their hard work and patience in the lab solving any problems needed to keep the systems up and running; our research would not be possible without them and it has been a pleasure working with and getting to know them.

Finally and most importantly, thank you to my parents, Jessie, Amanda, and Billy for all of the strength, words of encouragement, love, and laughs they have provided throughout this challenging phase of life. They are everything.

This work was supported in part by NSF Award No. 1407765 under the US/Ireland UNITE collaboration and by the Semiconductor Research Corporation (SRC) as the 1) LEAST and 2) NEWLIMITS Centers and NIST through award number 70NANB17H041.

October 2018

# CHARACTERIZING AND ENGINEERING THE METAL CONTACT INTERFACE IN 1D AND 2D CHALCOGENIDE SYSTEMS

Christopher M. Smyth, PhD
The University of Texas at Dallas, 2018

Supervising Professors: Robert M. Wallace, Co-Chair
Christopher L. Hinkle, Co-Chair

The layered ransition metal dichalcogenides (TMDs) exhibit unique phase- and thickness-dependent electronic, photonic, and magnetic properties intriguing for future device technologies. Historically, contact engineering in silicon devices has relied on a detailed understanding of the relationships between contact chemistry, phase, and resistance. However, similar relationships in metal–TMD systems are not yet understood and high contact resistance critically limits TMD device performance. This dissertation employs a variety of materials characterization techniques, such as *in–situ* photoelectron spectroscopies, Raman spectroscopy, and scanning probe microscopy, to study the metal–TMD and metal–Te interface chemistries, structures, and band alignments as a function of pre-metallization, *in-situ* metallization, and post-metallization processing conditions. The band alignments of similarly processed Schottky diodes and field-effect transistors are extracted analytically and corroborated with chemical and structural changes during processing. Process recommendations for consistent, high-performance contacts to $MoS_2$ and $WSe_2$ are provided.

## TABLE OF CONTENTS

# LIST OF FIGURES

# LIST OF TABLES

# CHAPTER 1

# INTRODUCTION

## 1.1 Two-Dimensional Chalcogenide Materials for Next-Generation Electronics

Two-dimensional (2D) materials have been used for tribological applications for decades. The isolation of single carbon atom thick sheets of graphene by mechanical exfoliation in 2004 and the subsequent discovery of its extraordinary electronic properties[1,2] spawned a 2D materials revolution. Around the same time graphene was first isolated, field-effect transistors (FETs) based on transition metal dichalcogenides (TMDs) were demonstrated for the first time illuminating the potential utility of TMDs in next generation electronics.[3] The family of interesting new 2D materials quickly expanded to include black phosphorous (BP) and hexagonal boron nitride (hBN).[4,5] The diverse selection of allotrope-dependent novel properties make 2D materials intriguing for next generation technologies in a wide variety of applications. The extremely high mobility demonstrated in graphene devices ($10^5$ $\mathrm{cm^2/V\ s}$) is ideal for fast switching and high on current ($I_{\mathrm{ON}}$) required in radio frequency transistors.

However, the absence of a band gap in graphene results in poor $I_{\mathrm{ON}}/I_{\mathrm{OFF}}$ ratios rendering graphene unusable in mainstream logic applications. TMDs and BP exhibit moderate mobilities and high $I_{\mathrm{ON}}/I_{\mathrm{OFF}}$ ratios making them ideal alternatives to graphene in future low power dissipation logic devices such as meta- oxide-semiconductor field-effect transistors (MOSFETs),[6] tunnel field effect transistors (TFETs),[7] diodes,[8] thermoelectrics,[9] and memory storage devices.[10] The performance of $MoS_2$ in transistor structures has been most widely studied of all the 2D materials to date. Impressive mobilities as high as 34,000 $\mathrm{cm^2/V\ s}$ at 2 K, room temperature mobilities of almost 500 $\mathrm{cm^2/V\ s}$, $I_{\mathrm{ON}}$ in the order of mA/mm, $I_{\mathrm{ON}}/I_{\mathrm{OFF}}$ ratios in the order of $10^8$, and steep switching near the thermal limit have been demonstrated.[11-13] Although the mobility and $I_{\mathrm{ON}}$ are slightly degraded (200 $\mathrm{cm}^2$/V s and ~800 nA) in the single layer limit of $MoS_2$ FETs,[6] the relative immunity to short channel effects and carrier confinement within each dangling bond-free 2D sheet is promising for beyond-silicon electronics.

Despite the impressive device operation demonstrated in TMD devices to date, mobility still falls short of expectations. Non-idealities in all areas of the TMD device structure, including intrinsic and extrinsic (neutral or charged) impurities, substrate roughness, charged defects within the substrate and gate dielectrics, crystal quality, selective-area growth, and high contact resistance ($R_{\mathrm{c}}$), must be remedied before dramatic performance improvements can be realized.

The range of band gaps exhibited by the semiconducting TMDs and BP (0.3-2.2 eV) have been leveraged in novel optoelectronic and photonic applications. The low band gaps of bulk $MoTe_2$ (1.0 eV) and BP (0.3-1.0 eV) are ideal for future photonics and optoelectronics devices operating in the visible to near-infrared wavelengths. Potentially groundbreaking silicon waveguides with integrated photodetector and light source based on graphene, $MoTe_2$, and BP have recently been demonstrated at operating frequencies in the GHz range, pulse widths down to sub-100 fs, and across wavelength ranges from the visible to the mid-infrared.[14-17]

More recently, the novel magnetic properties of the Mo, W, Cr, Ni, Sc, and Mn based TMDs have been theorized and, in some cases, demonstrated. The giant spin orbit splitting that occurs in the valence band of the Mo and W based TMDs facilitates locked spin and valley degrees of freedom that can be exploited in high-efficiency memory devices and circularly polarized photonics.[18,19] The favorable electron-photon interactions, extremely long-lived electron-hole pair lifetimes, and spin valley diffusion lengths in TMD heterostructures are essential for charge current-free devices with low power consumption and high-efficiency photovoltaics.[19,20]

The theoretical dangling bond-free surface, ultra-thin body, and high carrier mobility of the semiconducting TMDs are projected to solve many issues encountered in the extreme scaling limits of silicon-based electronics. Scaling the body thickness ($T_{body}$) of silicon-on-insulator MOSFETs below 10 nm invokes serious mobility degradation and enhanced subthreshold voltage according to a $T_{body}^{6}$ dependency, which has been shown to result from surface roughness.[22] The dangling bond-free van der Waals (vdW) surface and sub-nanometer $T_{body}$ of TMDs make them ideal candidates as the channel material in next generation MOSFET technology as the unique physical properties circumvent the issues encountered with ultra-thin body silicon. The decay length of the channel potential, or $\lambda$ as defined in Equation 1.1,

$$\lambda = \sqrt{\frac{\epsilon_{ch}}{2\epsilon_{ox}}\left(1 + \frac{\epsilon_{ox} t_{ch}}{4\epsilon_{ch} t_{ox}}\right) t_{ch} t_{ox}}$$

Equation 1.1

where $\varepsilon_{ch}$ ($\varepsilon_{ox}$) and $t_{ch}$ ($t_{ox}$) are the permittivity and thickness of the channel (oxide), respectively, encountered in highly scaled conventional MOSFET technology can be alleviated by decreasing the channel thickness.[23] The theoretical absence of dangling bonds on the TMD vdW surface can circumvent the $T_{body}^{6}$ degradation effect associated with surface roughness and theoretically will result in higher electric fields in the channel and $I_{ON}$.

Another fundamental bottleneck limiting the continued scaling of conventional silicon MOSFET technology is the thermodynamic limit of the gate voltage ($V_G$) required to turn the device from off to on, or the subthreshold slope (*SS*) as defined in Equation 1.2[7]

$$SS = \left(1 + \frac{C_d}{C_{ox}}\right) ln10 \frac{kT}{q}$$

Equation 1.2

where $C_d$ and $C_{ox}$ are the depletion and oxide capacitances, respectively, and $kT/q$ is the thermal voltage. Reducing the power dissipation in conjunction with channel length scaling requires simultaneous lowering of the supply and threshold voltages, which causes an exponential increase in the leakage current (i.e., power dissipation). The negative relationship between reduced channel length and increased leakage current can be circumvented by designing the device to operate based on tunneling current, which permits *SS* scaling below the 60 mV/dec thermodynamic limit. TMD-based TFETs have been demonstrated with the negative differential resistance characteristic of band-to-band tunneling[23] and impressive 31 mV/dec switching in an $MoS_2$/Ge heterostructure,[24] which highlights the utility and feasibility of designing device operation based on tunneling for future low power electronics.

## 1.2 Properties of Two-Dimensional Materials

TMDs are a broad family of layered materials with the chemical formula $MX_2$ where M is a transition metal from Groups 4-10 on the periodic table and X is one of the three chalcogen atoms S, Se, or Te. Other 2D materials exist where M is Ga, In, or Sn. Ga and In chalcogenides exhibit a layered rhombohedral crystal structure, while Sn monochalcogenides exhibit a structure analogous with hBN and Sn dichalcogenides exhibit a 2H structure (Figure 1.2d). The Mo- and W-based TMDs exhibit both semiconducting and semimetallic electronic properties (Figure 1.1), depending on the phase, and are the focus of the work in this dissertation. In general, a single TMD layer described by the $MX_2$ formula is ~0.7 Å thick and consists of a central layer of metal atoms covalently bound to layers of chalcogen atoms above and below (Figures 1.2 a-c). The upper and lower surfaces of the chalcogen atom sheets are theoretically free of dangling bonds, which results in vdW bonding between each 2D sheet in the multi-layer form. The low energy vdW bonds holding each sheet together are easily broken and can be exploited to easily isolate individual TMD sheets from bulk crystals. The 2H (1H in a single layer) phase is physically characterized by a trigonal prismatic unit cell in which each metal atom is coordinated by six chalcogen atoms and is associated with semiconducting electronic behavior.[25] The semiconducting TMDs with stable 2H structure at room temperature include $MoS_2$, $MoSe_2$, $MoTe_2$, $WS_2$, and $WSe_2$. The 1T and $1T_d$ phases are isostructural with small asymmetric differences and are characterized by a rhombohedral structure in which each metal atom is octahedrally coordinated. The semimetal $WTe_2$ is stable in the $1T_d$ phase at room temperature. The transition metal *d*-orbital filling largely dictates the most stable crystal structure of each TMD. Only 43 meV is required to induce a 2H to 1T phase transition in $MoTe_2$, which can be exploited for novel catalytic applications and high performance homojunction contacts (discussed in greater detail later).[26] The 2H to 1T phase transition in other TMDs has been achieved using lithium intercalation,[27,28] but requires roughly 10× the energy to induce the transition than in $MoTe_2$. Each TMD exhibits characteristic Raman shifts according to the number of layers (single layer to multi layer, typically 5-8) and the phase present in the crystal.[29,30]

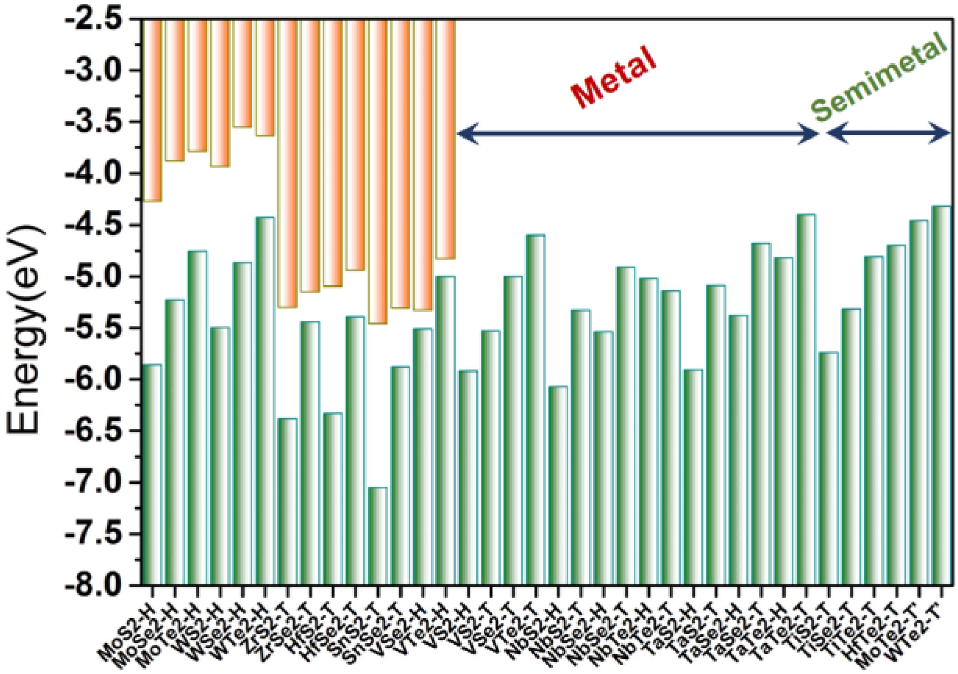

Figure 1.1. Band structure and alignment between monolayer semiconducting, metallic, and semimetallic TMDs.[31] © IOP Publishing. Reproduced with permission. All rights reserved.

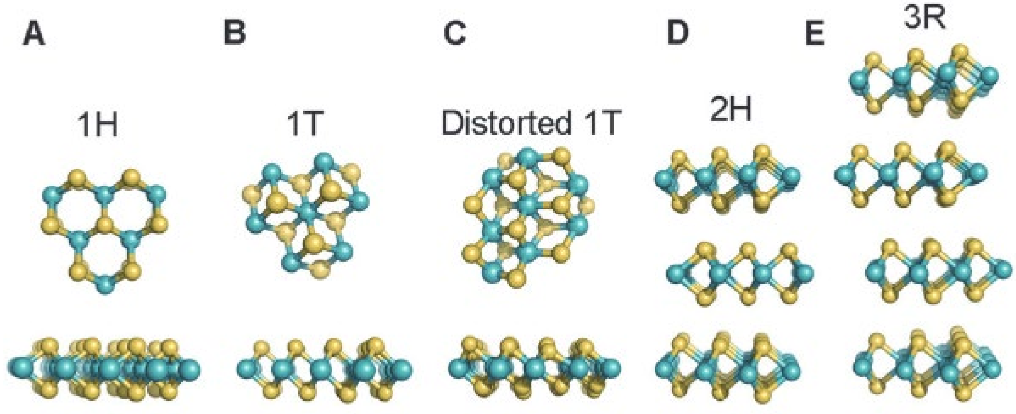

Figure 1.2. The various phases exhibited by transition metal dichalcogenide materials, which include the a) 1H, b) 1T, c) $1T_d$, d) 2H, and e) 3R plases. Adapted from Ref. 25 with permission from The Royal Society of Chemistry.

Early research efforts focused on TMDs involved bulk geological crystals mined from the ground or bulk crystals synthesized by chemical vapor transport (CVT). Impurity concentrations in the order of $10^{19}$ $cm^{-3}$ are routinely found in geological TMDs from the uncontrolled growth environment[32,33] and in CVT TMDs from the halogens most often employed as transport agents,[34,35] which cause spatially non-uniform doping and highly variable electronic and photonic properties. More recently, the push to integrate TMDs into commercial electronics has necessitated a much higher material quality, thereby driving a diversification of the TMD synthesis techniques and a dramatic improvement in defect and layer number control. Crude exfoliation techniques using mechanical peeling (Scotch® tape, polymethyl methacrylate) and solution processing (N-Methyl-2-pyrrolidone, n-butyl lithium)[36,37] produce many TMD flakes with a broad size and thickness distribution. Moderate layer number and grain size control is achieved using pulsed laser deposition or atomic layer deposition.[38,39] Large μm scale, few layer grains can be achieved with molecular beam epitaxy.[40] The largest single crystal films and greatest layer number control has been achieved using chemical vapor deposition (CVD), yielding fully coalesced single layer and bilayer TMD films on 4" wafers ideal for commercial integration.[41] However, the metal-organic and chalcogen precursors most often employed and the inability to aerially control nucleation in a CVD process often lead to impurities and high densities of grain boundaries in TMD films that degrade the intrinsic mobility and must be mitigated for future commercial applications. Synthesizing the highest quality TMDs to date has typically been accomplished using high growth temperatures (> 500 °C), which must be lowered in order to successfully integrate TMDs in a back end of line process. In this work, bulk TMD crystals with both geological and synthetic origins from commercial vendors are mechanically exfoliated unless otherwise noted.

## 1.3 Tellurium Overview

Historically, Te has been used in high-efficiency infrared absorber and detector materials,[42,43] solar cells,[44] and thin film transistors for radiation detection.[45] Recently, Te has been recognized as a potential high performance semiconductor material for next generation electronics and novel device physics. Te naturally forms helical chains of two-fold coordinated Te atoms that exhibit intra-chain three-fold screw axis symmetry and inter-chain vdW bonding. It is also theoretically predicted to form stable 2D rhombohedral (α-Te), tetragonal (β-Te) and trigonal prismatic (γ-Te) allotropes. Te exhibits a thickness dependent electronic structure with a 0.33 eV direct band gap in the bulk form that increases to a 0.92 eV indirect band gap in a 2D monolayer (e.g., the α-Te and β-Te phases),[46-48] providing band gap tuneability between semimetallic graphene and the TMDs.

The extraordinary room temperature hole mobility (~700 $cm^2/V\ s$), 3-4× smaller electron and hole effective masses than 2H-$MoS_2$,[46] and remarkable crystal quality demonstrated at growth temperatures ≤ 120 °C on a diverse array of substrates (single crystal, amorphous, polymer)[49,50] make Te an ideal material for seamless integration of high performance, low power transistors in a back end of line process. High mobility Te transistors and photodetectors based on solution synthesized crystals have been demonstrated, but low temperature molecular beam epitaxy offers the most promising route to commercial integration of Te provided a growth templating scheme is engineered. Te has also emerged as a potential topological material for defect-tolerant electronics and spintronics due to the strong spin-orbit interactions,[51] Weyl nodes in the valence band,[52] and topological surface states it exhibits.[48] Te-based transistors reported to date have predominantly exhibited p-type conduction, which is largely due to the high work function Pd contacts most commonly employed.[50-52] In fact, electrons transporting both parallel and perpendicular to the 1D Te chains are ligher than holes in bulk Te[53] indicating an electron mobility comparable with (and perhaps superior to) the reported hole mobilities[50-52] should be achievable in the bulk form. Therefore, low electron Schottky barrier height (SBH) metal contacts are essential to realizing n-type Te devices.

## 1.4 Metal-Semiconductor Contacts

Continued geometric scaling in semiconductor device technology has required simultaneous improvements in critical component performance to realize reduced switching speed and power dissipation for enhanced computing power. To enhance the circuitry speed, parasitic capacitance and series resistance, which includes contact resistance, should be minimized to reduce the RC (resistance-capacitance) time delay and increase the clock frequency. Many properties are required for high performance contacts compatible with state of the art electronic circuitry, which include a low contact resistivity and good chemical stability to channel materials, satisfactory thermal and mechanical properties with reference to channel materials, satisfactory morphological thermal stability, compatibility with standard processing technology, and do not induce detrimental contamination that will affect device performance. Before we explore past and present contact technology in conventional electronic circuits, we will first discuss the physics of forming a metal-semiconductor contact and limitations to reducing the resistance of the 3D metal-semiconductor junction.

When a metal is brought into contact with a semiconductor, charge transfer occurs due to differences in chemical potential often resulting in band bending in the semiconductor (Figure 1.3a).

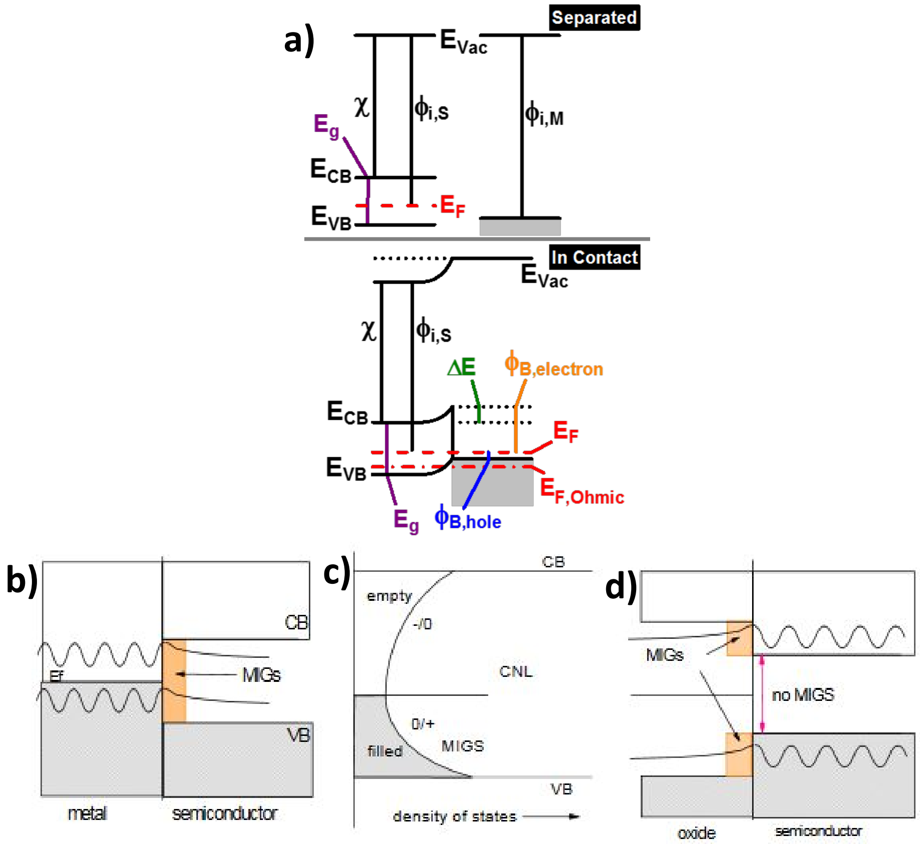

Figure 1.3. a) Schematic representation of band bending and corresponding core level binding energy shifts that can occur when metal and semiconductor are brought into intimate contact. b) Metal induced gap state (MIGS) decay into semiconductor band gap. c) Branch point between empty and filled surface states representing the charge neutrality level of the semiconductor. d) Absence of MIGS when the band gaps of the semiconductor and contacting material overlap. © 2009 IEEE

This is a gross underestimation of the complex nature of charge neutralization due to a large number of variables which contribute to the equilibrium Fermi level ($E_F$) at a metal–semiconductor junction. The Schottky-Mott rule[54] offers the most basic model of SBH formation and quantifies the SBH as the difference between the metal work function and the electron affinity of the semiconductor.

Quantifying the amount of charge transferred across a metal–semiconductor interface is nearly impossible to predict as all contributions to the resulting semiconductor surface states must be accounted for. Charge neutrality must be maintained between the surface and bulk of the semiconductor. Surface structure (i.e., dangling bonds) and defects result in surface localized energy bands that can be quite different from that of the bulk. Equilibrium formed between *all* surface localized states, not only those within the vicinity of the band gap, represents the CNL, which can also be considered as the surface $E_F$ (Figure 1.3c). When a metal is brought into contact with a semiconductor, bulk metal Bloch states decay into the semiconductor, which convolutes surface states. Metal Bloch states decaying into the semiconductor are also known as metal induced gap states (MIGS, Figure 1.1.1b), which are often invoked to explain $E_F$ pinning in metal–semiconductor systems.[55,56]

Local variations in density of states (DoS) at the semiconductor surface, which can originate from defect sites or dopant atoms on the order of $10^{13}$ cm$^{-2}$, can alter the local SBH by a magnitude closely related to the energy of the defect state/dopant relative to the semiconductor band edges. It is important to note the surface $E_F$ is often pinned at the defect level in the semiconductor energy gap, with defect levels deep in the gap exhibiting a more significant pinning effect.[57-59]

Strong $E_F$ pinning and correspondingly poor contact performance has been circumvented in Si-based devices by an assortment of strategies which include but are not limited to: ion implantation-facilitated degenerate doping in the contact region adjacent the channel,[60] low resistance transition metal silicide contacts,[61,62] and metal–insulator–Si contact structures. These strategies have been successfully extended to Ge[63,64] and III–V materials.[62,65] Chalcogen-based solution treatments have been widely employed in attempts to simultaneously remove native surface oxides and passivate dangling bonds. Although an $(NH_4)_2S_x$ solution provides a self-limiting oxide etch and corresponding surface state passivation,[65,66] its ability to reduce $R_c$ diminishes with increased semiconductor doping density as it only locally dopes the metal–semiconductor interface.[67]

In the case of silicide (i.e., transition metal–silicon alloy) contacts, significant time and effort has been invested in determining intermetallic phases which are both low resistance and stable under the typical thermal budget required for device fabrication. Silicides replaced degenerately doped polycrystalline silicon decades ago as superior contact materials due to their low contact resistivity, thermal stability, and ability to form the source, drain, and gate interconnects in one processing step.[68,69] Initial development of low resistance $TiSi_2$ and $CoSi_2$ contacts stemmed from the relationships between the chemistry and structure of each phase and the associated contact resistance.[70] NiSi contacts have since replaced $TiSi_2$ and $CoSi_2$ electrodes due to its superior resistance, thermal stability, and volume change at formation compared to $TiSi_2$ or $CoSi_2$. Similarly, Ni, Co, and Ti ternary alloys were developed for low resistance contacts to SiGe based on a detailed understanding of the thermodynamics, kinetics, and process-chemistry-structure relationships in these systems.[71-73]

It was estimated in the 2015 international technology roadmap for semiconductors (ITRS) that series resistance degrades the contact resistance by 40% more from that of the ideal case. The requirements for low contact resistance will become increasingly stringent as the pitch width and interconnect geometry, other sources of parasitic resistance in a logic circuit, are scaled. Strict thermal budgets accompany extreme device scaling (i.e., sub 10 nm nodes) to preserve physical and electronic strutures,[74] which has been temporarily remedied through heterogeneous epitaxy, wafer bonding, or thermal expansion mismatch engineering. Significant reduction in contact resistance to 3D semiconductors has recently been realized by incorporating novel 2D materials, such as hBN and graphene, at the metal contact interface resulting in record low contact resistivities near the 1.3 nΩ cm$^2$ theoretical limit.[75]

Theoretical calculations indicate the lower limit of contact resistivity ($\rho_c^{LL}$) is weakly dependent upon the valley degeneracy, band anisotropy, and higher energy bands. According to Equation 1.3,[76]

$$\rho_c^{LL} = \frac{h}{4q^2}\frac{m_{DOS}^{3D}}{m_{DOM}^{3D}}\frac{4}{\left(3\sqrt{\pi}n^{3D}\right)^{\frac{2}{3}}}$$

Equation 1.3

where $h$ is Planck's constant, $q$ is the electron charge, $m_{DOS}^{3D}$ and $m_{DOM}^{3D}$ are the DoS effective mass and distribution of modes effective mass, respectively, and $n^{3D}$ is the carrier density, the $\rho_c^{LL}$ is nearly independent of the semiconductor and depends most on the carrier density in the channel. Nonidealities, such as metal-semiconductor interface roughnes, contact oxidation, and phase stability, increase the contact resistivity and must be mitigated to achieve continued improvements. Generally, interface roughness causes scattering and reduces contact resistivity. But in some cases, contact resistivity can be reduced by increasing the interface roughness. Take for instance Al contacts to Si. The growth of AlSi grains results in a rough interface with Si but reduces the contact resistivity by enhancing the local field around AlSi protrusions.

## 1.5 Contacts to Transition Metal Dichalcogenides and Te: Current Technology, Challenges, and Research Motivation

Despite the novel properties and exciting applications of TMDs, the $R_c$ to semiconducting TMDs remains at least an order of magnitude higher than that achieved in more mature, 3D semiconductor devices (Figure 1.4). Parasitic $R_c$ continues to plague performance enhancement and device scaling, preventing researchers from benchmarking intrinsic TMD properties in some cases. The $R_c$ discrepancy is largely due to the reduced carrier density and DoS in a 2D semiconductor compared to that in a 3D semiconductor.

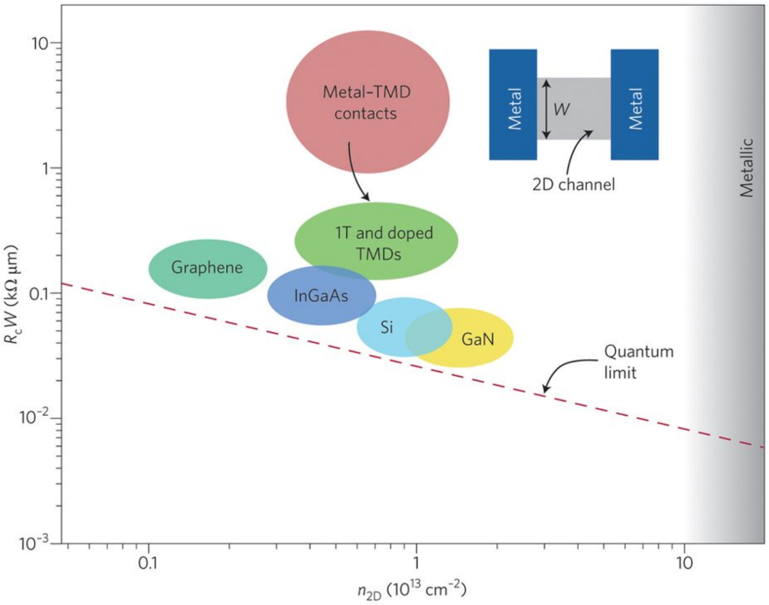

Figure 1.4. Contact resistances for various semiconductor materials against the quantum limits for crystalline materials. Reprinted by permission from Springer Nature (Jena, D.; Banerjee, K.; Xing, G. H. 2D Crystal Semiconductors: Intimate Contacts., Nature Materials, 2014, 13, 1076-1078.) Copyright 2014.

The carrier injection across the 3D metal-2D semiconductor junction is fundamentally different from the current injection across a 3D metal–3D semiconductor junction. There is no provision for band bending in the vertical direction in a single TMD layer below a bulk metal, so carriers are injected in a cascade of mechanisms: 1) vertically downward into the TMD underneath the metal, 2) horizontally through the electronically modified TMD film in direct contact with the metal, and 3) across the barrier from the electronically altered section of TMD underneath the metal into the uncontacted TMD channel. Such a cascaded barrier injection mechanism can be modeled as a series combination of two diodes and a resistor at the source end (Figure 1.5). Assuming a zero thermal barrier and ballistic transport in the $MoS_2$ underneath the bulk metal and using the Landauer quantum transport formalism, the $R_c$ limit of a 2D semiconductor–3D metal junction is calculated to be roughly 50 Ω μm at $n^{2D} = 10^{13}$ cm$^{-2}$ and increases by roughly a factor of 10 when the $n^{2D}$ is reduced to $10^{11}$ cm$^{-2}$.[77] The lower $R_c$ limit between bulk metals and 2D materials depends slightly less on $n^{2D}$ (to the power -1/2) than the relationship between the lower limit in 3D semiconductors and $n^{3D}$ (to the power -2/3).[76] The assumption that the carrier transport in the TMD under the metal is ballistic has been made using gross oversimplifications of the metal–TMD interface (Figure 1.6). Theoretical models do not take into account the effects of organic residues, impurities, defects, or metal–TMD reaction products at the metal–TMD interface on the electrostatics of the junction, the carrier injection mechanism, the SBH, or the conductivity of the interfacing TMD. These properties play critical roles in the properties of 3D metal–3D semiconductor junctions and are therefore likely to play an even more significant role in the 2D semiconductor limit. The transistor architecture (i.e., back-gated versus top-gated) also significantly affects $R_c$. In back-gated devices, $n^{2D}$ in the TMD underneath the bulk metal contact is a function of $V_G$, which leads to a deceivingly low $R_c$ compared with the top gated structure, which is more representative of a commercial device architecture.[78]

In stark contrast with theory, both geological and synthetic TMDs are inherently defective. Chalcogen vacancies (most stable) and a number of different elemental impurities are the most common defects.[32,33] Much of the work in this dissertation demonstrates covalent metal–TMD interfaces (i.e., reactive) are the norm rather than the exception in the majority of such systems, with high inherent defect density a likely contributor to their reactive nature.[33,79] Wavefunction overlap and therefore charge transfer between the metal and the TMD can vary significantly at

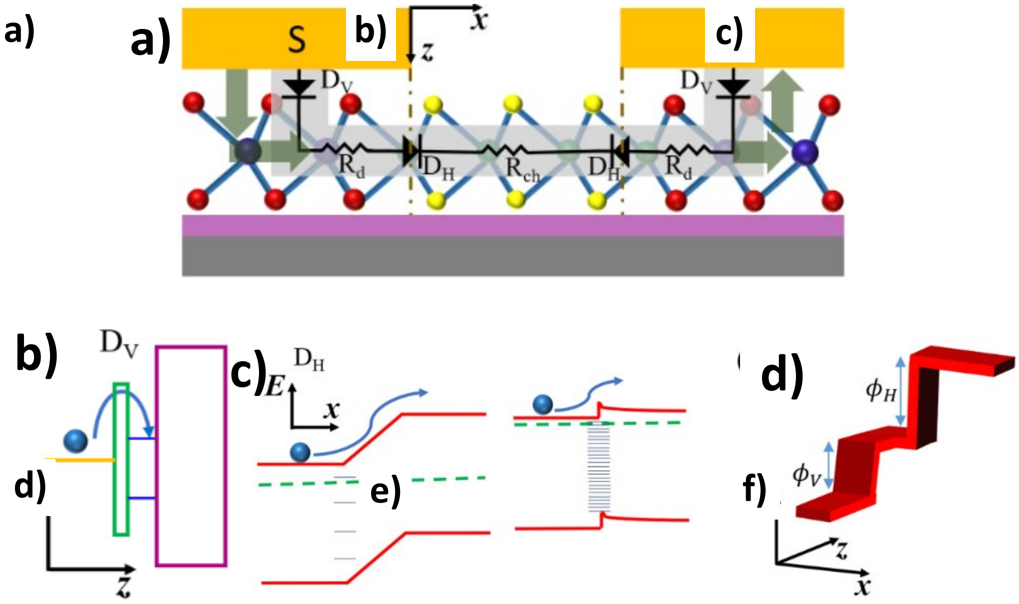

Figure 1.5. a) Schematic diagram showing possible carrier injection processes from metal to single layer $MoS_2$. b) The origin of the vertical diode between the metal and the $MoS_2$ through a tunneling gap. c) Two possible origins of potential barriers in a van der Waals metal-TMD contact and d) a schematic diagram depicting them. https://doi.org/10.1103/PhysRevB.96.205423 Copyright American Physical Society 2017.

defect sites on the TMD, which can enhance charge injection locally by serving as low SBH, low resistivity regions. The work in this dissertation also shows the interface chemistry varies significantly with deposition chamber ambient (UHV versus HV). Defects can dominate $R_c$ due to the corresponding spatially varying $E_F$ (as much as 0.8 eV and 0.5 eV in the cases of $MoS_2$ and $WSe_2$, respectively) and significant local DoS variation corresponding with regions of low or high conductivity relative to the surrounding TMD.[33]

Significant sample quality variation and likely the formation of interfacial reaction products have contributed to discrepancies between theoretical and experimentally derived contact performance. For example, Kang et al. predicts covalent bonding and “Ohmic interfaces” between $WSe_2$ and Pd, W, and Ti.[80] However, experimentally determined n-type and ambipolar transport in $WSe_2$

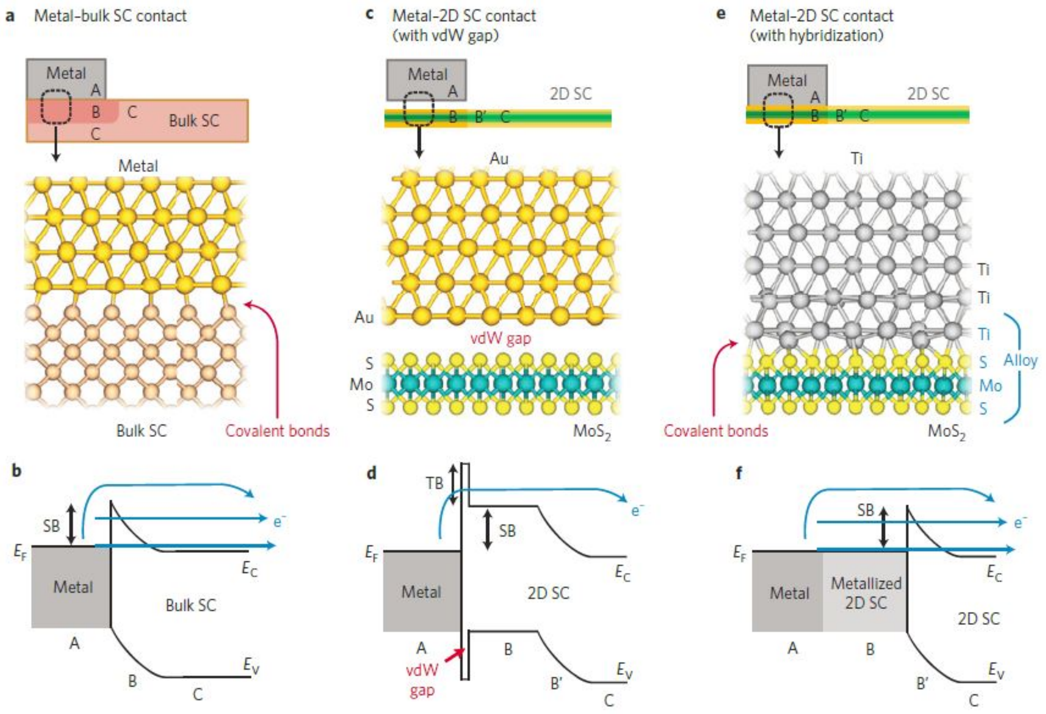

Figure 1.6. Theoretical a) metal-bulk semiconductor and b,c) metal-TMD interface structures with d-f) the corresponding band alignment. Reprinted by permission from Springer: Nature Materials (Allain, A.; Kang, J.; Banerjee, K.; Kis, A. Electrical Contacts to Two-Dimensional Semiconductors., Nature Materials, 2015, 14, 1195-1204.) Copyright 2015.

FETs employing In and Ti as contact materials, respectively, disagree with density functional theory regarding analogous device architectures.[80-82] In some cases, for example for Ti contacts deposited on $MoS_2$ under HV conditions, an unexpected electron SBH (0.05 eV)[83] can be explained by considering the electrostatics associated with a completely oxidized Ti contact.[79] The critical relationships between silicide chemistry, structure, and performance necessitate a similar understanding in metal contact–TMD systems. It is possible that the interface chemistry can be exploited to reduce $R_c$, similar to silicide contacts in Si devices.

Ion beam irradiation has been successfully employed to reduce $R_c$ to $WSe_2$.[84,85] The mechanism behind the reduced $R_c$ is not clear and could be a convolution of the increased interface roughness, a dramatic increase in defects that enhance carrier injection, and enhanced reactivity between the contact metal and the damaged TMD.

The low dimensionality of TMDs typically employed in devices prevents adaptation of traditional doping strategies (e.g., ion implantation) successfully employed in bulk semiconductor systems for reduced $R_c$. Molecular doping via chemisorption (benzyl viologen, $NO^-$),[86,87] physisorption ($K^+$),[82] and ionic liquid gating[88] has provided up to $10^5$ reduction in $R_c$ due to degenerate doping. However, doping density achieved by these techniques is not stable over time and therefore more robust doping strategies are necessary for commercial viability. Covalent nitrogen doping in $MoS_2$ has recently been demonstrated for the first time[89] and represents perhaps the most promising avenue for stable TMD doping. In addition the 2D nature of TMDs provides a less explored, yet unique opportunity for electrostatic channel doping and $E_F$ shift in the contact region by exploiting fixed charges in the substrate, which can be tuned with choice of substrate material.[90]

Similar to TMD-specific doping schemes, $(NH_4)_2S_x$ treatment for surface passivation and reduced $R_c$ has only recently been attempted on TMDs, specifically $MoS_2$. Employing an $(NH_4)_2S_x$ treatment to $MoS_2$ prior to metallization resulted in ~2× increase in field effect mobility and ~10× decrease in $R_c$.[91] However, the same treatment also enhanced $E_F$ pinning. Improved contact performance likely resulted from surface doping similar to that observed in $(NH_4)_2S_x$-treated Si.[67] $E_F$ pinning can theoretically be prevented by separating the metal and semiconductor enough to prevent substantial metal wavefunction overlap with semiconductor surface states. Similar to the MIS contact scheme successfully employed between 3D metal contacts and 3D semiconductors, metal–insulator–TMD contact structures have been successfully employed to ‘depin’ the $E_F$ and have resulted in substantial reduction in $\rho_c$ and the SBH for both n-type[92-94] and p-type[95] conduction. However, the best $\rho_c$ achieved in TMD-based devices employing an insulating interlayer at the contact interface (~$10^{-5}$ $\Omega$ $cm^{-2}$)[93] is far from that achieved in conventional devices with an analogous structure. Other interlayer materials, such as graphene[96] or metallic TMDs,[97] have also been proposed. However, epitaxial growth techniques must mature further to permit controlled growth of such heterostructures.

A popular strategy to overcome the enhanced tunneling resistance due to the theoretical vdW gap between metals and TMDs is to access the abundance of dangling bonds at the TMD edge rather than contacting the vdW surface. However, genuine heterogeneous 2D–2D edge contacts have proven elusive largely due to metastable and inhomogeneous heterostructure formation. This issue has been circumvented by exploiting the metallic 1T’ phase of $MoS_2$[98] and $MoTe_2$[99] for homogeneous Ohmic edge contacts with the lowest $R_c$ (0.2 kΩ μm) in a TMD-based device to date. Nonetheless, record low $R_c$ in TMD–based devices remains at least an order of magnitude greater than that achieved in conventional devices (0.01 kΩ μm).

All studies on Te transistor performance have reported hole dominant conduction, but the electron and hole effective masses in helical-Te are comparable. This suggests Te electron transistors can be fabricated, possibly through contact engineering. There have only been a few studies investigating contacts to Te to date, which indicate strong $E_F$ pinning occurs near the valence band edge of Te. In addition, the effects of the native Te surface oxide on the metal contact band alignement and performance are not yet known. Crystalline $TeO_2$ is a wide gap semiconductor, which suggests the native surface oxide could be engineered to depin the $E_F$ at the metal contact interface. It is reasonable to expect the pre-metallization surface chemistry and post-metallization interface chemistry will significantly affect the contact performance and, perhaps more importantly, polarity, similar to 3D metal–3D semiconductor systems. Therefore, a more detailed understanding of the interface chemistry and the role of the surface oxide on $E_F$ pinning in contact metal–Te systems is needed.

## 1.6 Dissertation Outline

The discrepancy between contact performance in mature silicide technologies and underdeveloped contacts to TMDs is unacceptable. Continued engineering of silicide contacts has enabled unabated Moore's law scaling and has been achieved via a detailed understanding of the relationships between contact metal, silicide chemistry and structure, and processing conditions. The purpose of this research is to establish analogous relationships in contact metal–TMD systems by corroborating detailed metal–TMD interface chemistry and structural analysis with contact performance as a function of controlled processing conditions. Much of the experiments are carried out *in–situ* in a UHV cluster tool to exclude the perturbative effects of ambient factors and thereby establish an accurate picture of metal–TMD interfaces in analogous device structures. Mo- and W-based TMDs and helical-Te are the materials investigated and discussed throughout this work.

In Chapters 3 and 5, the interface chemistry, surface morphology, and band alignment between contact metals (Au, Ir, Cr, and Sc) and TMDs (Chapter 3: $MoS_2$, $MoSe_2$, $MoTe_2$; Chapter 5: $WS_2$, $WSe_2$, and $WTe_2$) are investigated as a function of the deposition chamber ambient. In general, Au forms a vdW interface with all sulfides and selenides investigated, but reacts with the tellurides. Intermetallic reaction products are detected at all other metal–TMD interfaces regardless of the deposition chamber ambient. The more reactive contact metals Ti and Sc completely oxidize *in–*

*situ*, which likely plays a significant role in unexpected performance of analogous contacts reported to date. None of the metal–TMD systems obey the Schottky-Mott rule. In general, the $E_F$ is pinned in the upper half of the sulfide band gap and in the lower half of the selenide band gap. The research highlights the highly reactive nature of metal–TMD interfaces and relates the chemistry with the band alignment.

The work in Chapter 4 considers the effects of photoresist residue on the band alignment, interface chemistry, and performance of Ti contacts to $MoS_2$. An $O_2$ plasma treatment is employed to clean photoresist residue from the $MoS_2$ surface and enhance Ti contact performance. The cleaning effect of the $O_2$ plasma is clear in AFM images obtained after lithography and subsequent plasma treatment. The $O_2$ plasma provides a dual benefit of removing organic residue and functionalizing the $MoS_2$ surface, which facilitates the formation of a low resistance $TiO_x/Ti_xS_y$ contact to $MoS_2$. This work demonstrates a successful process to simultaneously clean the $MoS_2$ surface of organic residue and form low resistance $TiO_x$ contacts to $MoS_2$. In addition, this work highlights the need to understand the effects of organic residue on contacts to TMDs.

In Chapters 6 and 7, the effects of post metallization annealing conditions on the interface chemistry and structure, band alignment, and performance of Pd and Sc contacts to $WSe_2$ are established to determine ideal processing conditions for the consistent, high-performance contacts. The lowest contact resistance occurs when a 60 minute post metallization anneal at 400 °C in forming gas (FG; 90% $N_2$, 10% $H_2$) is performed. In contrast, the work in Chapter 7 demonstrates the highest performance $WSe_2$ transistors with Sc contacts are achieved without post-metallization processing by depositing the Sc contacts in UHV at room temperature. The dramatic change in interface chemistry significantly degrades the device performance regardless of the annealing environment (UHV or FG). STM and STS show the unexpectedly high electron SBH between Sc and $WSe_2$ is caused by the enhanced density of states in the gap below the $E_F$ around Sc atoms in the $WSe_2$ lattice. The opposing trends in Pd and Sc contact performance with annealing highlights the significant role contact chemistry plays on performance, similar with silicide technologies.

In Chapter 8, the interface chemistry and band alignment between the Pd contact and Te films are studied as a function of the Te surface oxide thickness. Pd reacts with Te to form $PdTe_x$ regardless of the $TeO_x$ thickness. For the first time, the surface $TeO_x$ is completely removed by employing an atomic hydrogen treatment. The $E_F$ is pinned in the Te conduction band when the surface oxide is removed before metallization. In contrast, the $E_F$ is depinned when Pd is deposited on the oxidized Te films. This work demonstrates the utility of an atomic hydrogen treatment to clean the surface oxide from Te and shows the native surface oxide offers a promising route to controllable contact polarity in Te devices.

## 1.7 References

(1) Novoselov, K. S.; Geim, A. K.; Morozov, S. V.; Jiang, S.; Karsnelson, M. I.; Grigorieva, I. V.; Dubonos, S. V.; Firson, A. A. Two-Dimensional Gas of Massless Dirac Fermions in Graphene, *Nature*, **2005**, *438*, 197-200.

(2) Kim, K.; Choi, J.-Y.; Kim, T.; Cho, S.-H.; Chung, H.-J. A Role for Graphene in Silicon-based Semiconductor Devices. *Nature*, **2011**, *479*, 338-344.

(3) Podzorov, V.; Gershenson, M. E.; Kloc, C.; Zeis, R.; Bucher, E. High-Mobility Field-Effect Transistors based on Transition Metal Dichalcogenides. *Appl. Phys. Lett.*, **2004**, *84*, 3301.

(4) Dean, C. R.; Young, A. F.; Meric, I.; Lee, C.; Wang, L.; Sorgenfrei, S.; Watanabe, K.; Taniguchi, T.; Kim, P.; Shepard, K. L.; Hone, J. Boron Nitride Substrates for High-Quality Graphene Electronics. *Nature Nanotechnol.*, **2010**, *5*, 722-726.

(5) Liu, H.; Neal, A. T.; Zhu, Z.; Luo, Z.; Xu, X.; Tomanek, D.; Ye, P. D. Phosphorene: An Unexplored 2D Semiconductor with a High Hole Mobility. *ACS Nano*, **2014**, *8* (4), 4033-4041.

(6) Radisavljevic, B.; Radenovic, A.; Brivio, J.; Giacometti, V.; Kis, A. Single-Layer $MoS_2$ Transistors. *Nature Nanotechnol.*, **2011**, *6*, 147-150.

(7) Ionescu, A. M.; Riel, H. Tunnel Field-Effect Transistors as Energy-Efficient Electronic Switches. *Nature*, **2011**, *479*, 329-337.

(8) Rivera, P.; Schailbley, J. R.; Jones, A. M.; Ross, J. S.; Wu, S.; Aivazian, G.; Klement, P.; Seyler, K.; Clark, G.; Ghimire, N. J.; Yan, J.; Mandrus, D. G.; Yao, W.; Xu, X. Observation of Long-Lived Interlayer Excitons in Monolayer $MoSe_2$-$WSe_2$ Heterostructures. *Nat. Commun.*, **2015**, *6*, 6242.

(9) Ma, J.; Chen, Y.; Han, Z.; Li, W. Strong Anisotropic Thermal Conductivity of Monolayer $WTe_2$. *2D Mater.*, **2016**, *3*, 045010.

(10) Li, Y.; Duerloo, K.-A. N.; Wauson, K.; Reed, E. J. Structural Semiconductor-to-Semimetal Phase Transition in Two-Dimensional Materials Induced by Electrostatic Gating. *Nat. Commun*., **2016**, *7*, 10671.

(11) Baugher, B. W. H.; Churchill, H. O. H.; Yang, Y.; Jarillo-Herrero, P. Intrinsic Electronic Transport Properties of High-Quality Monolayer and Bilayer $MoS_2$. *Nano Lett.*, **2013**, *13*, 4212-4216

(12) Bao, W.; Cai, X.; Kim, D.; Sridhara, K.; Fuhrer, M. S. High Mobility Ambipolar $MoS_2$ Field-Effect Transistors: Substrate and Dielectric Effects. *Appl. Phys. Lett.*, **2013**, *102*, 042104.

(13) Cui, X.; Lee, G.-H.; Kim, Y. D.; Arefe, G.; Huang, P. Y.; Lee, C.-H.; Chenet, D. A.; Zhang, X.; Wang, L.; Ye, F.; Pizzocchero, F.; Jessen, B. S.; Watanabe, K.; Taniguchi, T.; Muller, D. A.; Low, T.; Kim, P.; Hone, J. Multi-Terminal Transport Measurements of $MoS_2$ using a van der Waals Heterostructure Device Platform. *Nat. Nanotechnol.*, **2015**, *10*, 534-540.

(14) Bie, Y.-Q.; Grosso, G.; Heuck, M.; Furchi, M. M.; Cao, Y.; Zheng, J.; Bunandar, D.; Navarro-Moratalla, E.; Zhou, L.; Efetov, D. K.; Taniguchi, T.; Watanabe, K.; Kong, J.; Englund, D.; Jarillo-Herrero, P. A $MoTe_2$-based Light-Emitting Diode and photodetector for Silicon Photonic Integrated Circuits. *Nature Nanotechnol.*, **2017**, *12*, 1124-1129.

(15) Martinez, A.; Sun, Z. Nanotube and Graphene Saturable Absorbers for Fibre Lasers. *Nature Photonics*, **2013**, *7*, 842-845.

(16) Luo, Z.; Wu, D.; Xu, B.; Xu, H.; Cai, Z.; Peng, J.; Weng, J.; Xi, S.; Zhu, C.; Wang, F.; Sun, Z.; Zhang, H. Two-Dimensional Material-based Saturable Absorbers: Towards Compact Visible-Wavelength all-Fiber Pulsed Lasers. *Nanoscale*, **2016**, *8*, 1066-1072.

(17) Martinez, A.; Yamashita, S. 10 GHz Fundamental Mode Fiber Laser Using a Graphene Saturable Absorber. *Appl. Phys. Lett.*, **2012**, *101*, 041118.

(18) Ye, Y.; Xiao, J.; Wang, H.; Ye, Z.; Zhu, H.; Zhao, M.; Wang, Y.; Zhao, J.; Yin, X.; Zhang, X. Electrical Generation and Control of the Valley Carriers in a Monolayer Transition Metal Dichalcogenide. *Nature Nanotechnol.*, **2016**, *11*, 598-602.

(19) Manchon, A.; Koo, H. C.; Nitta, J.; Frolov, S. M.; Duine, R. A. New Perspectives for Rashba Spin-Orbit Coupling. *Nature Mater.*, **2015**, *14*, 871-882.

(20) Jin, C.; Kim, J.; Utama, M. I. B.; Regan, E. C.; Kleemann, H.; Cai, H.; Shen, Y.; Shinner, M. J.; Sengupta, A.; Watanabe, K.; Taniguchi, T.; Tongay, S.; Zettl, A.; Wang, F. Imaging of Pure Spin-Valley Diffusion Current in $WS_2$-$WSe_2$ Heterostructures. *Science*, **2018**, *360*, 893-896.

(21) Britnell, L.; Ribeiro, R. M.; Eckmann, A.; Jalil, R.; Belle, B. D.; Mishchenko, A.; Kim, Y.-J.; Gorbachev, R. V.; Georgiou, T.; Morozov, S. V.; Grigorenko, A. N.; Geim, A. K.; Casiraghi, C.; Neto, A. H. C.; Novoselov, K. S. Strong Light-Matter Interactions in heterostructures of Atomically Thin Films. *Science*, **2013**, *340*, 1311-1314.

(22) Low, T.; Li, M.-F.; Samudra, G.; Yeo, Y.-C.; Zhu, C.; Chin, A.; Kwong, D.-L. Modeling Study of the Impact of Surface Roughness on Silicon and Germanium UTB MOSFETs. *IEEE Trans. Electron Devices,* **2005**, *52* (11), 2430-2439.

(23) Roy, T.; Tosun, M.; Cao, X.; Fang, H.; Lien, D.-H.; Zhao, P.; Chen, Y.-Z.; Chueh, Y.-L.; Guo, J.; Javey, A. Dual-Gated $MoS_2$/$WSe_2$ van der Waals Tunnel Diodes and Transistors. *ACS Nano*, **2015**, *9* (2), 2071-2079.

(24) Sarkar, D.; Xie, X.; Liu, W.; Cao, W.; Kang, J.; Gong, Y.; Kraemer, S.; Ajayan, P. M.; Banerjee, K. A Subthermionic Tunnel Field-Effect Transistor with an Atomically Thin Channel. *Nature*, **2015**, *526*, 91-95.

(25) Voiry, D.; Mohite, A.; Chhowalla, M. Phase Engineering of Transition Metal Dichalcogenides. *Chem. Soc. Rev.*, **2015**, *44*, 2702.

(26) Duerloo, K.-A. N.; Li, Y.; Reed, E. J. Structural Phase Transitions in Two-Dimensional Mo- and W-Dichalcogenide Monolayers. *Nature Commun.*, **2014**, *5*, 4214.

(27) Voiry, D.; Yamaguchi, H.; Li, J.; Silva, R.; Alves, D. C. B.; Fujita, T.; Chen, M.; Asefa, T.; Shenoy, V. B.; Eda, G.; Chhowalla, M. Enhanced Catalytic Activity in Strained Chemically Exfoliated $WS_2$ Nanosheets for Hydrogen Evolution. *Nature Mater.*, **2013**, *12*, 850-855.

(28) Py, M. A.; Haering, R. R. Structural Destabilization Induced by Lithium Intercalation in $MoS_2$ and Related Compounds. *Can. J. Phys.*, **1983**, *61*, 76.

(29) O'Brien, M.; McEvoy, N.; Hanlon, D.; Hallam, T.; Coleman, J. N.; Duesberg, G. S. Mapping of Low-Frequency Raman Modes in CVD-Grown Transition Metal Dichalcogenides: Layer Number, Stacking Orientation and Resonant Effects. *Sci. Rep.* **2016**, *6*, 19476.

(30) Rhodes, D.; Chenet, D. A.; Janicek, B. E.; Nyby, C.; Lin, Y.; Jin, W.; Edelberg, D.; Mannebach, E.; Finney, N.; Antony, A.; Schiros, T.; Klarr, T.; Mazzoni, A.; Chin, M.; Chiu, Y.-c.; Zheng, W.; Zhang, Q. R.; Ernst, F.; Dadap, J. I.; Tong, X.; Ma, J.; Lou, R.; Wang, S.; Qian, T.; Ding, H.; Osgood Jr., R. M.; Paley, D. W.; Lindenberg, A. M.; Huang, P. Y.; Pasupathy, A. N.; Dubey, M.; Hone, J.; Balicas, L. Engineering the Structural and Electronic Phases of $MoTe_2$ through W Substitution. *Nano Lett.*, **2018**, *17*, 1616-1622.

(31) Zhang, C.; Gong, C.; Nie, Y.; Min, K.-A.; Liang, C.; Oh, Y. J.; Zhang, H.; Wang, W.; Hong, S.; Colombo, L.; Wallace, R. M.; Cho, K. Systematic Study of Electronic Structure and Band Alignment of Monolayer Transition Metal Dichalcogenides in van der Waals Heterostructures. *2D Mater.*, **2017**, *4*, 015026.

(32) Addou, R.; McDonnell, S.; Barrera, D.; Guo, Z.; Azcatl, A.; Wang, J.; Zhu, H.; Hinkle, C. L.; Quevedo-Lopez, M.; Alshareef, H. N., et al. Impurities and Electronic Property Variations of Natural $MoS_2$ Crystal Surfaces. *ACS Nano* **2015**, *9*, 9124-9133.

(33) McDonnell, S.; Addou, R.; Buie, C.; Wallace, R. M.; Hinkle, C. L. Defect Dominated Doping and Contact Resistance in $MoS_2$. *ACS Nano* **2014**, *8*, 2880-2888.

(34) Ovchinnikov, D.; Allain, A.; Huang, Y.-S.; Dumcenco, D.; Kis, A. Electrical Transport Properties of Single-Layer $WS_2$. *ACS Nano*, **2014**, *8* (8), 8174-8181.

(35) Pisoni, A.; Jacimovic, J.; Barišić, O. S.; Walter, A.; Náfrádi, B.; Bugnon, P.; Magrez, A.; Berger, H.; Revay, Z.; Forró, L. The Role of Transport Agents in $MoS_2$ Single Crystals. *J. Phys. Chem. C*, **2015**, *119* (8), 3918-3922.

(36) Voiry, D.; Yamaguchi, H.; Li, J.; Silva, R.; Alves, D. C. B.; Fujita, T.; Chen, M.; Asefa, T.; Shenoy, V. B.; Eda, G.; Chhowalla, M. Enhanced Catalytic Activity in Strained Chemically Exfoliated $WS_2$ Nanosheets for Hydrogen Evolution. *Nature Mater.*, **2013**, *12*, 850-855.

(37) Coleman, J. N.; Lotya, M.; O'Neill, A.; Bergin, S. D.; King, P. J.; Khan, U.; Young, K.; Gaucher, A.; De, S.; Smith, R. J.; Shvets, I. V.; Arora, S. K.; Stanton, G.; Kim, H.-Y.; Lee, K.; Kim, G. T.; Duesberg, G. S.; Hallam, T.; Boland, J. J.; Wang, J. J.; Donegan, J. F.; Grunlan, J. C.; Moriarty, G.; Shmeliov, A.; Nicholls, R. J.; Perkins, J. M.; Grieveson, E. M.; Theuwissen, K.; McComb, D. W.; Nellist, P. D.; Nicolosi, V. Two-Dimensional Nanosheets Produced by Liquid Exfoliation of Layered Materials. *Science*, **2011**, *331*, 568-571.

(38) Serna, M. I.; Yoo, S. H.; Moreno, S.; Xi, Y.; Oviedo, J. P.; Choi, H.; Alshareed, H. N.; Kim, M. J.; Minary-Jolandan, M.; Quevedo-Lopez, M. A. Large-Area Deposition of $MoS_2$ by Pulsed Laser Deposition with In Situ Thickness Control. *ACS Nano*, **2016**, *10* (6), 6054-6061.

(39) Hao, W.; Marichy, C.; Journey, C. Atomic Layer Deposition of Stable 2D Materials. *2D Mater.*, **2018**, in press https://doi.org/10.1088/2053-1583/aad94f.

(40) Yue, R.; Nie, Y.; Walsh, L. A.; Addou, R.; Liang, C.; Lu, N.; Barton, A. T.; Zhu, H.; Che, Z.; Barrera, D.; Cheng, L.; Cha, P.-R.; Chabal, Y. J.; Hsu, J. W. P.; Kim, J.; Kim, M. J.; Colombo, L.; Wallace, R. M.; Cho, K.; Hinkle, C. L. Nucleation and Growth of $WSe_2$: Enabling Large Grain Transition Metal Dichalcogenides. *2D Mater.*, **2017**, *4*, 045019.

(41) Kang, K.; Xie, S.; Huang, L.; Han, Y.; Huang, P. Y.; Mak, K. F.; Kim, C.-J.; Muller, D.; Park, J. High-Mobility Three-Atom-Thick Semiconducting Films with Wafer-Scale Homogeneity. *Nature*, **2015**, *520*, 656-660.

(42) Brazis, R.; Nausewicz, D. Far-Infrared Photon Absorption by Photons in ZnTe Crystals. *Opt. Mater.*, **2008**, *30* (5), 789-791.

(43) Chen, M. C.; List, R. S.; Chandra, D.; Bevan, M. J.; Colombo, L.; Shaake, H. F. Key Performance-Limiting Defects in P-on-N HgCdTe LPE Heterojunction Infrared Photodiodes. *J. Electron. Mater.*, **1996**, *25* (8), 1375-1382.

(44) Gur, I.; Fromer, N. A.; Geier, M. L.; Alivisatos, P. Air-Stable All-Inorganic Nanocrystal Solar Cells Processed from Solution. *Science*, **2005**, *310*, 462-465.

(45) Murphey, J. W.; Smith, L.; Calkins, J.; Kunnen, G. R.; Mejia, I.; Cantley, K. D.; Chapman, R. A.; Sastre-Hernandez, J.; Mendoza-Perez, R.; Contreras-Puente, G.; Allee, D. R.; Quevedo-Lopez, M.; Gnade, B. Thin Film Cadmium Telluride Charged Particle Sensors for Large Area Neutron Detectors. *Appl. Phys. Lett.*, **2014**, *105*, 112107.

(46) Zhu, Z.; Cai, X.; Yi, S.; Chen, J.; Dai, Y.; Niu, C.; Guo, Z.; Xie, M.; Liu, F.; Cho, J.-H.; Jia, Y.; Zhang, Z. Multivalency-Driven Formation of Te-Based Monolayer Materials: A Combined First-Principles and Experimental Study. *Phys. Rev. Lett.*, **2017**, *119*, 106101.

(47) Huang, X.; Guan, J.; Lin, Z.; Liu, B.; Xing, S.; Wang, W.; Guo, J. Epitaxial Growth and Band Structure of Te Film on Graphene. *Nano Lett.*, **2017**, *17*, 4619-4623.

(48) Liu, Y.; Wu, W.; Goddard, W. A. Tellurium: Fast Electrical and Atomic Transport along the Weak Interaction Direction. *J. Am. Chem. Soc.*, **2018**, *140*, 550-553.

(49) Zhou, G.; Addou, R.; Wang, Q.; Honari, S.; Cormier, C. R.; Cheng, L.; Yue, R.; Smyth, C. M.; Laturia, A.; Kim, J.; Vandenberghe, W. G.; Kim, M. J.; Wallace, R. M.; Hinkle, C. L. High-Mobility Helical Tellurium Field-Effect Transistors Enabled by Transfer-Free, Low-Temperature Direct Growth. *Adv. Mater.*, **2018**, *30* (36), 1803109.

(50) Wang, Y.; Qiu, G.; Wang, R.; Huang, S.; Wang, Q.; Liu, Y.; Du, Y.; Goddard, W. A.; Kim, M. J.; Xu, X.; Ye, P. D.; Wu, W. Field-Effect Transistors made from Solution-Grown Two-Dimensional Tellurene. *Nature Electronics*, **2018**, *1*, 228-236.

(51) Qui, G.; Wang, Y.; Nie, Y.; Zheng, Y.; Cho, K.; Wu, W.; Ye, P. D. Quantum Transport and Band Structure Evolution under High Magnetic Field in Few-Layer Tellurene. *Nano Lett.*, **2018**, *18*, 5760-5767.

(52) Hirayama, M.; Okugawa, R.; Ishibashi, S.; Murakami, S.; Miyake, T. Weyl Node and Spin Texture in Trigonal Tellurium and Selenium. *Phys. Rev. Lett.*, **2011**, *114*, 206401.

(53) Peng, H.; Kioussis, N. Elemental Tellurium as a Chiral p-Type Thermoelectric Material. *Phys. Rev. B*, **2014**, *89*, 195206.

(54) Schottky, W. *Z. Phys.* **1939**, *113*, 367.

(55) Dandrea, R. G.; Duke, C. B. Calculation of the Schottky Barrier Height at the Al/GaAs(001) Heterojunction: Effect of Interfacial Atomic Relaxations. *J. Vac. Sci. Technol. A*, **1993**, *11* (4), 848-853.

(56) Tung, R. T. Recent Advances in Schottky barrier Concepts. *Mater. Sci. Eng. Rep.,* **2001**, *35*, 1-138.

(57) Poindexter, E. H.; Gerardi, G. J.; Rueckel, M.-E.; Caplan, P. J. Electronic Traps and $P_b$ Centers at the $Si/SiO_2$ Interface: Band-Gap Energy Distribution. *J. Appl. Phys.*, **1984**, *56* (10), 2844-2849.

(58) Broqvist, P.; Alkauskas, A.; Pasquarello, A. Defect Levels of Dangling Bonds in Silicon and Germanium Through Hybrid Functionals. *Phys. Rev. B*, **2008**, *78*, 075203.

(59) Dimoulas, A.; Tsipas, P.; Sotiropoulos, A.; Evangelou, E. K. Fermi-Level Pinning and Charge Neutrality Level in Germanium. *Appl. Phys. Lett.*, **2006**, *89*, 252110.

(60) Chang, C. Y.; Fang, Y. K.; Sze, S. M. Specific Contact Resistance of Metal–Semicnoductor Barriers. *Solid-State Electronics*, **1971**, *14*, 541-550.

(61) Tung, R. T. The Physics and Chemistry of the Schottky Barrier Height. *Appl. Phys. Rev.*, **2014**, *1*, 011304.

(62) Monch, W. On Metal–Semiconductor Surface Barriers. *Surf. Sci.*, **1970**, *21* (2), 443-446.

(63) Yamane, K.; Hamaya, K.; Ando, Y.; Enomoto, Y.; Yamamoto, K.; Sadoh, T.; Miyao, M. Effect of Atomically Controlled Interfaces on Fermi-Level Pinning at Metal/Ge Interfaces. *Appl. Phys. Lett.*, **2010**, *96*, 162104.

(63) Lee, J. S.; Bishop, S. R.; Kaufman-Osborn, T.; Chagarov, E.; Kummel, A. C. Monolayer Passivation of Ge(100) Surface via Nitridation and Oxidation. *ECS Trans.*, **2010**, *33* (6). 447-454.

(64) Abraham, M.; Yu, S.-Y.; Choi, W. H.; Lee, T. P. Very Low Resistance Alloyed Ni-Based Ohmic Contacts to InP-Capped and Uncapped $n^+$-$In_{0.53}Ga_{0.47}As$. *J. Appl. Phys.*, **2014**, *116*, 164506.

(65) Tsai, C.-D.; Lee, C.-T. Passivation Mechanism Analysis of Sulfur-Passivated InGaP Surfaces Using X-ray Photoelectron Spectroscopy. *J. Appl. Phys.*, **2000**, *87* (9), 4230-4233.

(66) Suyatin, D. B.; Thelander, C.; Bjork, M. T.; Maximov, I. Samuelson, L. Sulfur Passivation for Ohmic Contact Formation to InAs Nanowires. *Nanotechnology*, **2007**, *18*, 105307.

(67) Chan, J.; Martinez, N. Y.; Fitzgerald, J. J. D.; Walker, A. V.; Chapman, R. A.; Riley, D.; Jain, A.; Hinkle, C. L.; Vogel, E. M. Extraction of Correct Schottky Barrier Height of Sulfur Implanted NiSi/n-Si Junctions: Junction Doping Rather than Barrier Height Lowering. *Appl. Phys. Lett.*, **2011**, *99*, 012114.

(68) Zhang, S.-L.; Smith, U. Self-Aligned Silicides for Ohmic Contacts in Complementary Metal-Oxide-Semiconductor Technology: $TiSi_2$, $CoSi_2$, and NiSi. *J. Vac. Sci. Technol. A*, **2004**, *22*, 1361.

(69) Zhang, S.-L.; Ostling, M. Metal Silicides in CMOS Technology: Past, Present, and Future Trends. *Critical Reviews in Solid State and Materials Science*, **2010**, *28* (1), 100-129.

(70) Massalski, T. B. Binary Alloy Phase Diagrams, American Society for Metals, Metal Park, Ohio, 1986.

(71) Ma, Z.; Xiao, H. Z.; Allen, L. H.; Park, B. J. Manipulation of the Ti/Si Reaction Paths by Introducing an Amorphous Ge Interlayer. *Appl. Phys. Lett.*, **1994**, *65*, 561.

(72) Wang, Z.; Chen, Y. L.; Ying, H.; Nemanich, R. J.; Sayers, D. E. Phase Formations in Co/Si and Co/$Si_{1-x}Ge_x$ by Solid Phase Reactions. *Mat. Red. Soc. Symp. Proc.*, **1994**, *320*, 397.

(73) Lin, C. Y.; Chen, W. J.; Lai, C. H.; Chin, A.; Liu, J. Formation of Ni Gemona-silicide on Single Crystalline $Si_{0.3}Ge_{0.7}$/Si. *IEEE Electron Device Lett.*, **2002**, EDL-23, 464.

(74) Motayed, A.; Bonevich, J. E.; Krylyuk, S.; Davydov, A. V.; Aluri, G.; Rao, M. Correlation between the Performance and Microsctucture of Ti/A;/Ti/Au Ohmic Contacts to p-Type Silicon Nanowires. *Nanotechnol.*, **2011**, *22*, 075206.

(75) Lee, M.-H.; Cho, Y.; Byun, K.-E.; Shin, K. W.; Nam, S.-G.; Kim, C.; Kim, H.; Han, S.-A.; Kim, S.-W.; Shin, H.-J.; Park, S. Two-Dimensional Materials Inserted at the Metal/Semiconductor Interface: Attractive Candidates for Semiconductor Device Contacts. *Nano Lett.*, **2018**, *18*, 4878-4884.

(76) Maassen, J.; Jeong, C.; Baraskar, A.; Rodwell, M.; Lundstrom, M. Full Band Calculations of the Intrinsic Lower Limit of Contact Resistivity. *Appl. Phys. Lett.*, **2013**, *102*, 111605.

(77) Somvanshi, D.; Kallatt, S.; Venkatesh, C.; Nair, S.; Gupta, G.; Anthony, J. K.; Karmakar, D.; Majumdar, K. Nature of Carrier Injection in Metal/2D-Semiconductor Interface and its Implications for the Limits of Contact Resistance. *Phys. Rev. B*, **2017**, *96*, 205423.

(78) Yuan, H.; Cheng, G.; Yu, S.; Walker, A. R. H.; Richter, C. A.; Pan, M.; Li, Q. Field Effects of Current Crowding in Metal-$MoS_2$ Contacts. *Appl. Phys. Lett.*, **2016**, *108*, 103505.

(79) McDonnell, S.; Smyth, C.; Hinkle, C. L.; Wallace, R. M. $MoS_2$-Ti Contact Interface Reactions. *ACS Appl. Mat. Interf.* **2016**, *8*, 8289-8294.

(80) Kang, J.; Liu, W.; Sarkar, D.; Jena, D.; Banerjee, K. Computational Study of Metal Contacts to Monolayer Transition Metal Dichalcogenide Semiconductors. *Phys. Rev. X* **2014**, *4*, 031005.

(81) Liu, W.; Kang, J.; Sarkar, D.; Khatami, Y.; Jena, D.; Banerjee, K. Role of Metal Contacts in Designing High-Performance Monolayer n-Type $WSe_2$ Field Effect Transistors. *Nano Lett.* **2013**, *13*, 1983-1990.

(82) Fang, H.; Chuang, S.; Chang, T. C.; Takei, K.; Takahashi, T.; Javey, A. High-Performance Single Layered $WSe_2$ p-FETs with Chemically Doped Contacts. *Nano Lett.* **2012**, *12*, 3788-3792.

(83) Das, S.; Chen, H. Y.; Penumatcha, A. V.; Appenzeller, J. High Performance Multilayer $MoS_2$ Transistors with Scandium Contacts. *Nano Lett.* **2013**, *13*, 100-105.

(84) Kim, D.; Du, H.; Kim, T.; Shin, S.; Kim, S.; Song, M.; Lee, C.; Lee, J.; Cheong, H.; Seo, D. H.; Seo, S. The Enhanced Low Resistance Contacts and Boosted Mobility in Two-Dimensional p-Type $WSe_2$ Transistors through $Ar^+$ Ion-Beam Generated Surface Defects. *AIP Adv.*, **2016**, *6*, 105307.

(85) Stanford, M. G.; Pudasaini, P. R.; Gallmeier, E. T.; Cross, N.; Liang, L.; Oyedele, A.; Duscher, G.; Mahjouri-Samani, M.; Wang, K.; Xiao, K.; Geohegan, D. B.; Belianinov, A.; Sumpter, B. G.; Rack, P. D. High Conduction Hopping Behavior Induced in Transition Metal Dichalcogenides by Percolating Defect Networks: Toward Atomically Thin Circuits. *Adv. Funct. Mater.*, **2017**, *27*, 1702829.

(86) Zhao, P.; Kiriya, D.; Azcatl, A.; Zhang, C.; Tosun, M.; Liu, Y.-S.; Hettick, M.; Kang, J. S.; McDonnell, S.; KC, S.; Guo, J.; Cho, K.; Wallace, R. M.; Javey, A. Air Stable p–Doping of $WSe_2$ by Covalent Functionalization. *ACS Nano*, **2014**, *8* (10), 10808-10814.

(87) Kiriya, D.; Tosun, M.; Zhao, P.; Kang, J. S.; Javey, A. Air-Stable Surface Charge Transfer Doping of $MoS_2$ by Benzyl Viologen. *J. Am. Chem. Soc.*, **2014**, *136*, 7853-7856.

(88) Kim, C.; Moon, I.; Lee, D.; Choi, M. S.; Ahmed, F.; Nam, S.; Cho, Y.; Shin, H.-J.; Park, S.; Yoo, W. J. Fermi Level Pinning at Electrical Metal Contacts of Monolayer Molybdenum Dichalcogenides. *ACS Nano*, **2017**, *11* (2), 1588-1596.

(89) Azcatl, A.; Qin, X.; Prakash, A.; Zhang, C.; Cheng, L.; Wang, Q.; Lu, N.; Kim, M. J.; Kim, J.; Cho, K.; Addou, R.; Hinkle, C. L.; Appenzeller, J.; Wallace, R. M. Covalent Nitrogen Doping and Compressive Strain in $MoS_2$ by Remote $N_2$ Plasma Exposure. *Nano Lett.*, **2016**, *16*, 5437-5443.

(90) Joo, M.-K.; Moon, B. H.; Ji, H.; Han, G. H.; Kim, H.; Lee, G.; Lim, S. C.; Suh, D.; Lee, Y. H. Electron Excess Doping and Effective Schottky Barrier Reduction on the $MoS_2$/h-BN Heterostructure. *Nano Lett.*, **2016**, *16*, 6383-6389.

(91) Bhattacharjee, S.; Ganapathi, K. L.; Nath, D. N.; Bhat, N. Surface State Engineering of Metal/$MoS_2$ Contacts Using Sulfur Treatment for Reduced Contact Resistance and Variability. *IEEE Trans. Electron Dev.*, **2016**, *63* (6), 2556-2562.

(92) Lee, S.; Tang, A.; Aloni, S.; Philip Wong, H.-S. Statistical Study on the Schottky Barrier Reduction of Tunneling Contacts to CVD Synthesized $MoS_2$. *Nano Lett.*, **2016**, *16*, 276-281.

(93) Kaushik, N.; Karmakar, D.; Nipane, A.; Karande, S.; Lodha, S. Interfacial n-Doping Using an Ultrathin $TiO_2$ Layer for Contact Resistance Reduction in $MoS_2$. *ACS Appl. Mater. Interfaces*, **2016**, *8*, 256-263.

(94) Chen, J.-R.; Odenthal, P. M.; Swartz, A. G.; Floyd, G. C.; Wen, H.; Luo, K. Y.; Kawakami, R. K. Control of Schottky Barriers in Single Layer $MoS_2$ Transistors with Ferromagnetic Contacts. *Nano Lett.*, **2013**, *13*, 3106-3110.

(95) Yamamoto, M., Nakahara, S., Ueno, K., Tsukagoshi, K. Self-Limiting Oxides on $WSe_2$ as Controlled Surface Acceptors and Low-Resistance Hole Contacts. *Nano Lett.*, **2016**, *16* (4), 2720-2727.

(96) Liu, Y.; Wu, H.; Cheng, H.-C.; Yang, S.; Zhu, E.; He, Q.; Ding, M.; Li, D.; Guo, J.; Weiss, N. O.; Huang, Y.; Duan, X. Toward Barrier Free Contacts to Molybdenum Disulfide Using Graphene Electrodes. *Nano Lett.*, **2015**, *15*, 3030-3034.

(97) Liu, Y.; Stradins, P.; Wei, S.-H. Van der Waals Metal-Semiconductor Junction: Weak Fermi Level Pinning Enables Effective Tuning of Schottky Barrier. *Sci. Adv.*, **2016**, *2*, e1600069.

(98) Cho, S.; Kim, S.; Kim, J. H.; Zhao, J.; Seok, J.; Keum, D. H.; Baik, J.; Choe, D.-H.; Chang, K. J.; Suenaga, K.; Kim, S. W.; Lee, Y. H.; Yang, H. Phase patterning for Ohmic Homojunction Contact in $MoTe_2$. *Science*, **2015**, *349* (6248), 625-628.

(99) Kappera, R.; Voiry, D.; Yalcin, S. E.; Branch, B.; Gupta, G.; Mohite, A. D.; Chhowalla, M. Phase-Engineered Low-Resistance Contacts for Ultrathin $MoS_2$ Transistors. *Nature Materials*, **2014**, *13*, 1128-1134.

# CHAPTER 2

# EXPERIMENTAL METHODS

## 2.1 *In-Situ* UHV Cluster Tools

The surface and interface science-based research discussed below, both completed and proposed, will be performed within two ultra-high vacuum cluster tools (UHV, base pressure $< 1 \times 10^{-9}$ mbar) designed and built by Omicron Scientific (Figure 2.1).

Figure 2.1a displays the larger of the two cluster tools equipped with X-ray photoelectron spectroscopy (XPS), low energy ion scattering spectroscopy (LEIS), ultraviolet photoelectron spectroscopy (UPS), low energy electron diffraction (LEED), molecular beam epitaxy (MBE), physical vapor deposition (PVD: e-beam and sputter deposition), ultraviolet lamp, reflection high energy electron diffraction (RHEED), and plasma enhanced atomic layer deposition (PEALD).[1] The seven chambers which house these tools are interconnected via a central backbone also held under UHV to permit sample transfer between chambers without breaking vacuum. The second, smaller cluster tool displayed in Figure 2.1b is equipped with LEED, PVD (thermal evaporation), XPS, UPS, and dual capability atomic force microscope/variable temperature scanning tunneling microscope (AFM/STM) contained in two interconnected chambers under UHV conditions.[2]

### 2.1.1 Photoelectron Spectroscopy

*X-ray Photoelectron Spectroscopy*

XPS is a well-established, non-destructive characterization technique that is primarily employed thoroughout this work to qualitatively and quantitatively identify sample chemistry, structure, and electronic band alignment. Diverse chemical analysis can be achieved with XPS; elements present in concentrations of roughly 0.1 at.% or more can be detected, the bonding environment around

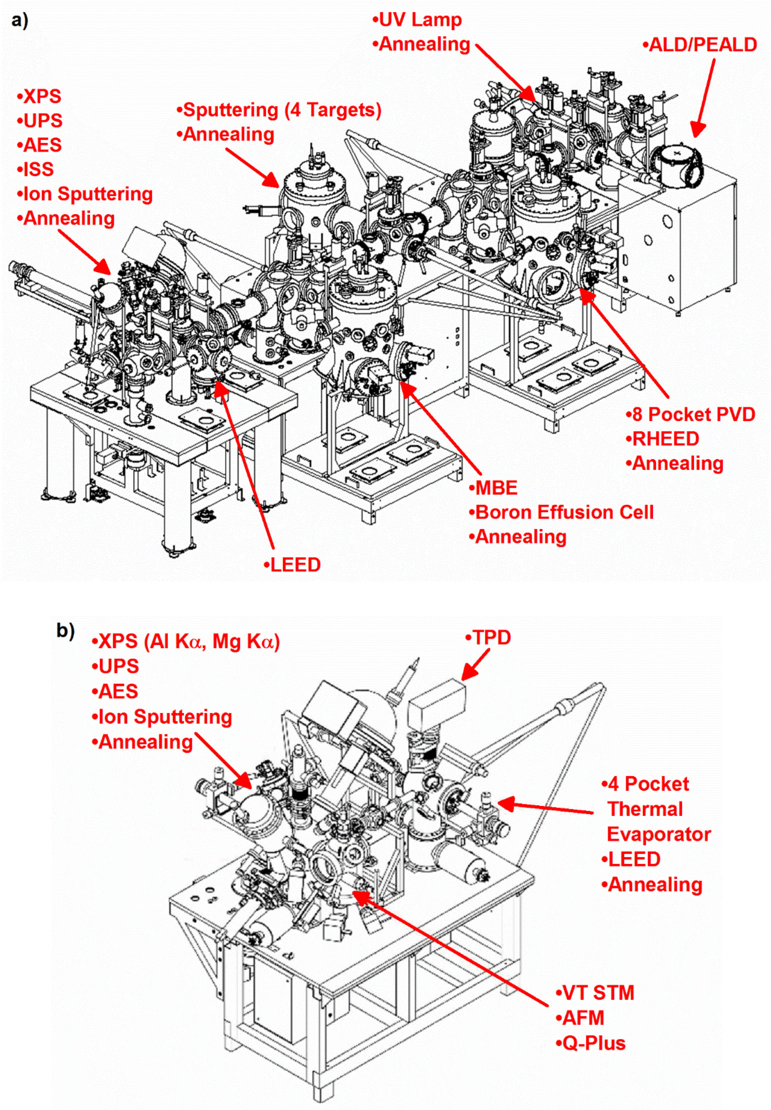

Figure 2.1. a) 7 chamber and b) 2 chamber *in-situ* cluster tools, with major synthesis, processing, and characterization capabilities listed, which are located in the Wallace labs at the University of Texas at Dallas.

each element can be determined from the oxidation states detected in associated core levels, and the stoichiometry of individual compounds can be determined from the integrated intensities of associated chemical states. Both UHV cluster tools employed in this work are equipped with monochromated XPS instruments from Physical Electronics (USA), which include high energy resolution spectrometers (~50 meV) and reasonable spatial resolution (~500 $\mu m^2$ and 640 $\mu m^2$ associated with the instruments in Figure 2.1a, and 2.1b, respectively). In XPS, the kinetic energy (*KE*) of core level photoelectrons ejected from a sample irradiated with a monochromated beam of photons (typically X-rays) of energy $h\nu$ is measured (Figure 2.2a). In this work Al $K\alpha^1$ X-ray photons ($h\nu$ = 1486.7 eV) are employed and photoelectron *KE* is measured with an Omicron EA125 hemispherical electrostatic analyzer using a pass energy of 15 eV and an acceptance angle of 8°. The Al $K\alpha^2$ X-ray emission line is filtered from the incident beam by an Omicron XM1000 X-ray monochromator. An elastic energy exchange typically occurs between the incident photon and ejected photoelectron resulting in characteristic energy conservation that defines the resulting *KE* of the ejected photoelectron according to Equation 2.1,[3]

$$BE = h\nu - KE - \varphi_{sp}$$

Equation 2.1

where *BE* is the photoelectron binding energy and $\varphi_{sp}$ is the work function of the spectrometer. The $\varphi_{sp}$ is calibrated according to the standard procedure defined in ASTM E2108.[4] Electrical contact is made between the spectrometer and the sample, which causes their Fermi levels ($E_F$) to align (Figure 2.2b). However, a photoelectron entering the spectrometer feels a potential equal to the work function difference between the spectrometer and the sample, which must be accounted for by subtracting it from the *BE*.

The photoelectron from each core level of each element exhibits a characteristic *BE* allowing for easy element identification, which is evident from the unique features in the survey spectra from four different compounds shown in Figure 2.3a. The chemical environment of an atom manifests as a characteristic *BE* shift of a magnitude that depends on the Coulombic interaction with the

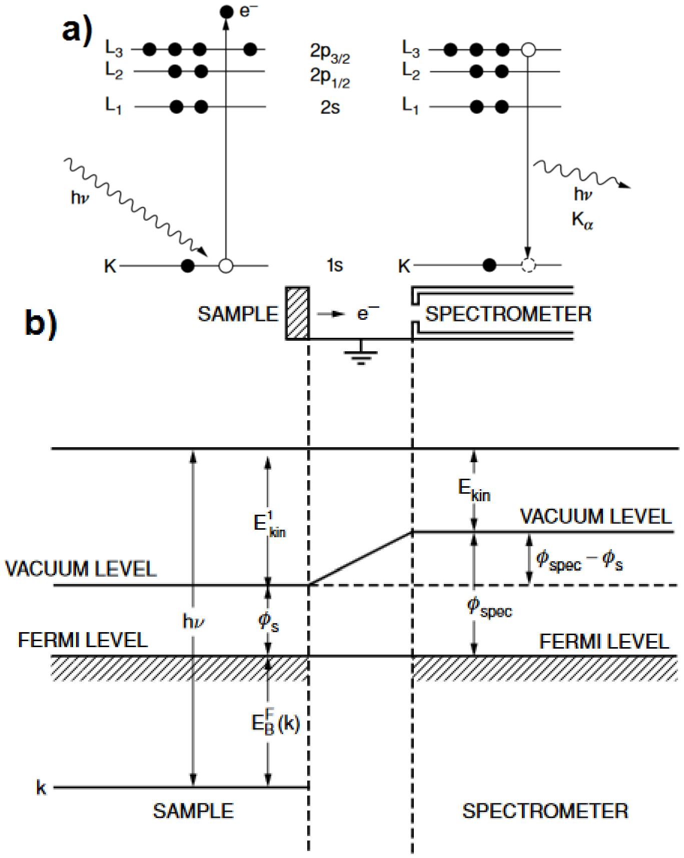

Figure 2.2. Energy band schematics of the a) X-ray photon and photoelectron emission processes and b) the vacuum level alignment between the sample and the spectrometer via electrical continuity. Figures a) and b) are reprinted with permission from Ref. 3 Copyright (2007) Springer Science + Buisness Media, Inc.[5]

surrounding atoms. Chemical states of metallic compounds (e.g., $WTe_2$, Figure 2.3b) exhibit negligible *BE* shifts from the elemental constituents, while chemical states from ionic compounds exhibit significant *BE* shifts from the elemental constituents (e.g., $WS_2$, $WSe_2$). The more ionic the bond and the larger the electronegativity difference between two atoms, the larger the *BE* shift from the *BE* of the corresponding neutral element, which is evident by the increasing W $4f_{7/2}$ *BE* shift from W–Se to W–S to W–O bonds (Figure 2.3b). The core levels are labeled by $nl_j$, where $n$ is the principle quantum number, $l$ is the orbital quantum number ($l$ = 0, 1, 2, 3,…; alternatively $l$ = $s$, $p$, $d$, $f$,…), and $j$ is the total angular momentum ($|l + s|$, where $s$ represents the spin +½/-½).[5]

The *p*, *d*, *f*, etc. core levels in which $l \neq 0$ split into two peaks ($j_+ = l + s$, $j_- = l - s$) with an integrated intensity ratio of $(2j_+ + 1)/(2j_- + 1)$. The peak separation, or spin orbit splitting, depends on the core level and is generally constant in each core level as is observed in the W 4*f* core level from different compounds (Figure 2.3b). In some cases, the spin orbit splitting of a particular core level can vary from compound to compound (e.g., Ti–Ti versus Ti–O chemical states in the Ti 2*p* core level).[6] A chemical state *BE* shift can also manifest from defects and impurities,[7] which may or may not require more sensitive characterization techniques to detect (e.g., STM, secondary ion mass spectroscopy (SIMS)). Bringing the substrate into contact with another material, often by deposition, can induce a core level *BE* shift due to $E_F$ alignment, such as the W 4*f* shift to lower *BE* induced by depositing an Au film (red spectrum, Figure 2.3b). Core level spectra are deconvolved with the peak fitting software AAnalyzer.[4]

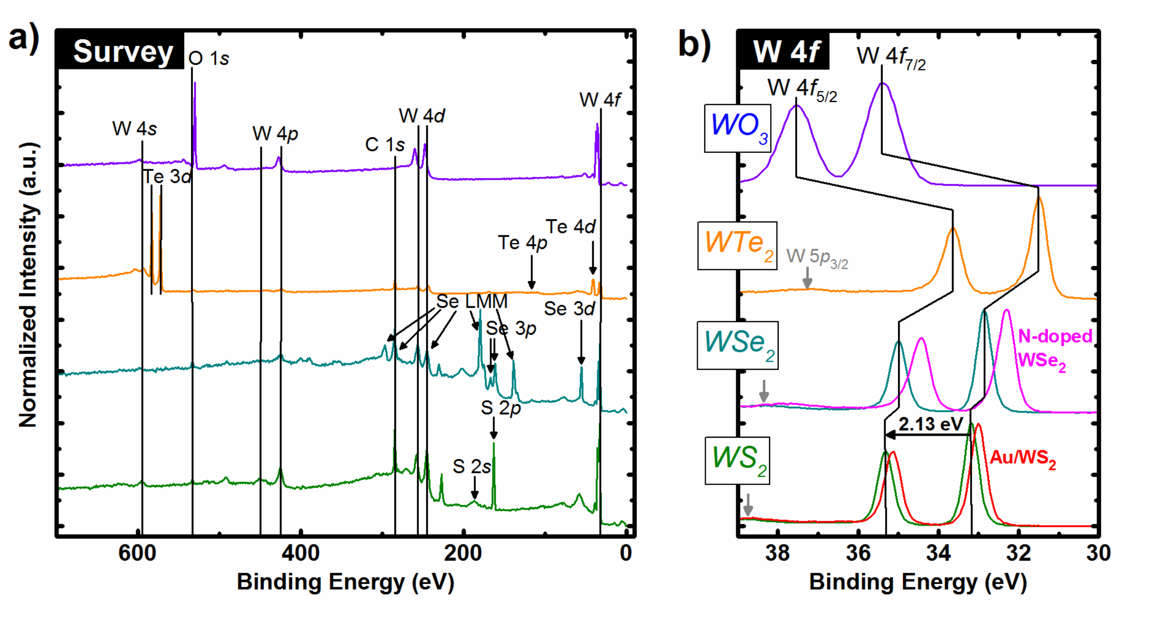

Figure 2.3. a) Survey and b) W 4*f* core level spectra obtained from bulk WS$_2$, 2 nm Au/WS$_2$, WSe$_2$, N doped WSe$_2$, WTe$_2$, and WO$_3$ deposited by reactive sputter.

The $E_F$ relative the valence band edge is defined by the intercept of a best fit line of the linear region in the low $BE$ tail of the valence band spectrum with the background noise level of the spectrum. The energy difference between core levels and the valence band edge remains constant excluding compositional or electronic perturbations (Figure 2.4). The band alignment relative to the vacuum level is determined by measuring the work function of the sample via the secondary electron cutoff. Photoelectrons can be ejected from the secondary electron cutoff by negatively biasing the sample to lower the binding energy within the Al Kα[1] energy. Therefore, the initial band alignment of a semiconductor is indicated by the valence band edge and secondary electron cutoff (Figure 2.4), provided the band gap is known. Core level shifts to lower or higher $BE$ detected during subsequent material deposition or surface treatment are associated with equivalent $E_F$ shifts towards the valence band and conduction band, respectively. This technique is useful to determine the Schottky barrier height (*SBH*) in a metal–semiconductor heterostructure, as is done throughout this work, and to determine the band alignment in a semiconductor heterostructure.

Other important quantative can be determined with XPS including the thickness of an overlayer and the composition of a sample. Approximately 95% of all emitted photoelectrons escape from within 5-10 nm of the sample surface (depending on the atomic origin of the photoelectron), or $3\lambda$, where $\lambda$ represents the inelastic mean free path ($\lambda$) unique to the attenuating material and the $KE$ of the ejected photoelectron. The $\lambda$ of an ejected photoelectron is dependent upon its $KE$ and the density of the material(s) through which it travels.[3] It can be estimated in inorganic compounds via Equation 2.2,[8]

$$\lambda = 538KE^{-2} + 0.41(aKE)^{1/2}$$

Equation 2.2

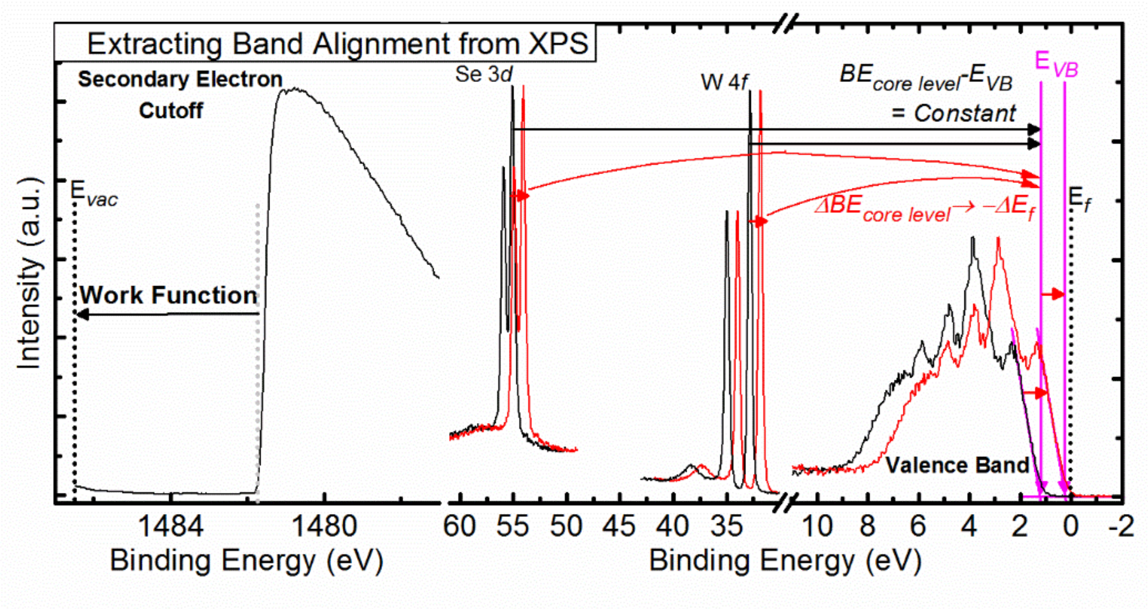

Figure 2.4. Secondary electron cutoff, Se 3*d*, W 4*f*, and valence band spectra showing the relationship between the secondary electron cutoff and the work function, the constant energy difference between each core level and the valence band edge, and the relationship between a $E_F$ shift and core level shift.

where $a$ represents the monolayer thickness (½ lattice constant) of the material through which the photoelectron travels. The intensity of an element $i$ at a depth from the sample surface is represented by Equation 2.3

$$dI_i = S(E)F\Delta\Omega n_{\mathrm{i}}\frac{d\sigma_x}{d\Omega}\exp\left(\frac{t}{\lambda_i cos\theta}\right)$$

Equation 2.3

where $S(E)$ is a function related to the analyzer transmission function, the probed area, and the detector efficiency, $F$ is the incident flux of X-rays, $\Delta\Omega$ is the acceptance angle of the analyzer, $n_{\mathrm{i}}$ is the density of the element $i$ in the film of interest, $(d\sigma_x/d\Omega)$ is the photoionization cross section, and $\theta$ is the angle between the detector and the sample surface normal. This equation indicates that the intensity of a core level far from the surface will increase with increasing $\theta$, while the intensity of core levels from surface localized elements will increase relative to more bulk-like elements will increase with decreasing $\theta$. If the attenuating overlayer $i$ is uniformly deposited onto a substrate $j$, the intensity of photoelectrons originating from element $i$ are defined by Equation 2.4[9]

$$I_{\mathrm{i}} = S(E)F\Delta\Omega n_{\mathrm{i}}\left(\frac{d\sigma_x}{d\Omega}\right)_{\mathrm{i}}\lambda_{\mathrm{i}}\left[1-\exp\left(-\frac{t}{\lambda_{\mathrm{i}}cos\theta}\right)\right] = I_{\mathrm{i}}^{\infty}\left[1-\exp\left(-\frac{t}{\lambda_{\mathrm{i}}cos\theta}\right)\right]$$

Equation 2.4

where $I_{\mathrm{i}}^{\infty}$ represents the core level intensity from the $i$ element of an infinitely thick overlayer.

The intensity of photoelectrons originating from the substrate element(s) $j$ are defined similarly according to Equation 2.5[9]

$$I_{\mathrm{j}} = S(E)F\Delta\Omega n_{\mathrm{j}}\left(\frac{d\sigma_x}{d\Omega}\right)_{\mathrm{j}}\lambda_{\mathrm{j}}\left[1-\exp\left(-\frac{t}{\lambda_{\mathrm{j}}cos\theta}\right)\right] = I_{\mathrm{j}}^{0}\left[1-\exp\left(-\frac{t}{\lambda_{\mathrm{j}}cos\theta}\right)\right]$$

Equation 2.5

where $I_{\mathrm{j}}^{0}$ represents the core level intensity from the $j$ element of a bare, bulk substrate. Provided reference spectra from the bare, bulk substrate and infinitely thick overlayer, the (finite) thickness of the overlayer can be determined using Equations 2.4 and 2.5.

The chemical composition of a sample can be determined according to atomic sensitivity factors, which are related to the $S(E)\Delta\Omega(d\sigma_x/d\Omega)\lambda$ term. Sensitivity factors are often normalized to the F 1*s* core level, which is assigned a relative sensitivity factor (*RSF*) of 1.[10] The *RSF*s employed throughout this work are supplied by the spectrometer manufacturer. The integrated intensity of a core level is divided by the appropriate *RSF* according to Equation 2.6.

$$X_{\mathrm{i}} = \frac{I_{\mathrm{i}}}{RSF_{\mathrm{i}}} \Big/ \Sigma\left(\frac{I_{\mathrm{n}}}{RSF_{\mathrm{n}}}\right)$$

Equation 2.6

*Ultraviolet Photoelectron Spectroscopy (UPS)*

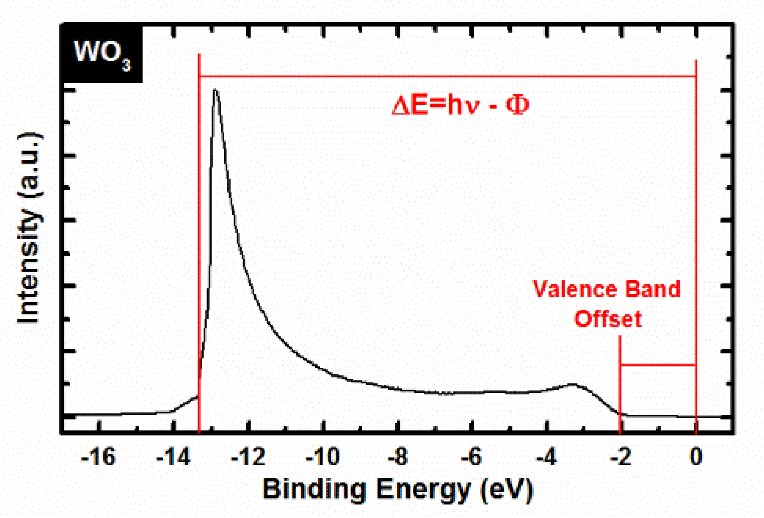

Figure 2.5. Ultraviolet photoelectron spectrum obtained via He lamp ($h\nu_{HeI}$=21.2 eV) from a reactively sputtered, amorphous $WO_3$ film. A -9.82 V bias was applied to the sample to access the secondary electron cutoff.

UPS operates under similar physical principles as XPS, however incident photons originate from the HeI emission line (*hv* = 21.2 eV) via He discharge lamp with much narrower energy distribution and greater flux than the Al Kα[1] source in XPS. UPS is highly surface sensitive due to the extremely low *KE* of incident photons and is employed to determine important electronic properties such as the work function and ionization energy. Detailed analysis of the valence band structure (e.g., orbital hybridization) is facilitated by the narrow line width of the HeI ultraviolet photon line and the energy dependence of core level intensities at low excitation energies. However, certain core level information that would appear in XPS may not appear in UPS because certain transitions in the Brillouin zone are forbidden by the momentum conservation selection rule.[11] The work function is determined by subtracting the difference in the low and high *BE* onsets from the energy of incident HeI photons (Figure 2.5).

### 2.1.2 Physical Vapor Deposition (PVD)

PVD encompasses a broad range of line-of-sight deposition techniques, specifically electron beam (e-beam) deposition and sputter deposition in the case of this work.

*Electron Beam Deposition.* E-beam deposition operates under a pressure of $< 1 \times 10^{-5}$ mbar and employs a beam of high energy electrons (9 keV in this work) impinging upon the surface of a bulk target material to evaporate or eject atoms and/or multi-atom clusters towards a substrate. The target temperature increases with electron flux until either evaporation or sublimation, depending upon the material, becomes thermodynamically favorable. This occurs at a temperature less than the ambient pressure melting temperature due to substantially higher equilibrium vapor pressure under high vacuum (HV) and, even more so, UHV conditions. Liberated atoms or atomic clusters travel in a straight line from the target until reaching another surface (e.g., the sample) where condensation is likely due to comparably low surface temperature. A suite of materials (Table 2.1) were deposited on transition metal dichalcogenides (TMDs) via e-beam deposition in this work. Generally, vapor pressures measured during deposition under UHV conditions were $\sim 1 \times 10^{-8}$ mbar, while under HV conditions were $\sim 2 \times 10^{-6}$ mbar. The applied current varied depending on the temperature required to achieve an equilibrium vapor pressure on the order of those listed above as well as the thermal conductivity of the target material (Table 2.1). The target flux depends upon the equilibrium vapor pressure as well as the thermal conductivity of the target material.

Table 2.1. Evaporation temperature of various metals according to vacuum conditions as well as their respective thermal conductivities.[12,13]

| | | **Ir** | **Au** | **Pd** | **Ti** | **Cr** | **Sc** | **Si** |
|---|---|---|---|---|---|---|---|---|
| **T(° C)** | $10^{-8}$ torr | 1850 | 807 | 842 | 1067 | 837 | 714 | 992 |
| | $10^{-6}$ torr | 2080 | 947 | 992 | 1235 | 977 | 837 | 1447 |
| **κ (J/mol-K)** | | 25.10 | 25.42 | 25.98 | 25.02 | 23.35 | 25.52 | 20.00 |

It is believed that the damage arises from X-rays generated as the electron beam strikes the metal source in the evaporator crucible. These X-rays are thought to create defects within the bulk substrate or near the surface of a thick gate oxide. In this study, it is possible that characteristic X-rays are generated as the e-beam impacts the source metal. In this study, damage to the TMD substrate (i.e., bond scission, defect generation) is considered instead. The deposition rates employed here, on the order of $10^{-3}$ Å/s, are approximately three orders of magnitude lower than those commonly employed in studies investigating electron beam-induced radiation damage in metal-oxide-semiconductor structures ~1 Å/s).[14,15] Therefore, we anticipate the X-ray flux produced during e-beam deposition in this study to be orders of magnitude lower than the X-ray flux produced in other studies employing deposition rates much higher than what is used here. $MoS_2$ is considered as a representative TMD in which e-beam induced X-ray damage could manifest during metallization. The most energetic characteristic X-ray which can be generated by the four metals employed in this study (Sc, Cr, Ir, and Au) exhibit penetration depths into $MoS_2$ that are orders of magnitude greater than the sampling depth of XPS. Assuming $MoS_2$ exhibits a $\rho = 5.06$ g/cm$^3$,[16] we calculate the $K\alpha^1$ X-ray line of Sc and Cr and $K\beta^1$ X-ray line of Ir and Au to exhibit penetration depths of 10.9, 22.1, 5867.5, and 7102.8 μm, respectively, into $MoS_2$. The penetration depths of the same X-ray lines from Au, Ir, Cr, and Sc into the higher density TMD $WSe_2$ ($\rho = 9.32$ g/cm$^3$)[17] are within the same order of magnitude, respectively. The sampling depth of XPS is roughly 10 nm. Therefore, e-beam induced radiation damage inflicted upon the TMDs during metal position does not affect the surface chemistry of any samples fabricated in this work. We note that additional chemical states at lower binding energy in the Mo 3*d* core level spectrum and higher binding energy in the S 2*p* core level spectrum characteristic of $He^+$ ion induced damage in $MoS_2$ are not observed here.[18] Symmetric broadening of both Mo 3*d* and S 2*p* doublet peaks could also manifest as a result of radiation damage, however this is not observed either. Furthermore, it may be difficult to distinguish between preexisting defects in $MoS_2$ and e-beam radiation-induced defects via electrical measurements given the inherently defective nature of geological and synthetic $MoS_2$.

There is an astounding difference in Langmuir (*L*), or amount of time it takes to completely cover a surface with adsorbate molecules (~$10^{15}$ atoms/cm$^2$), assuming a sticking coefficient of 1, under a given pressure, between $1 \times 10^{-6}$ mbar and $1 \times 10^{-9}$ mbar. *L* is a function of total surface exposure to a gas fluence and depends on the total gas flux perpendicular to the direction of a single surface over a period of time (Equation 2.7).

$$L = \int J_N dt$$

Equation 2.7

where $J_N$ represents the flux of gas molecules in the direction of a single surface.

$J_N$ depends on the pressure ($p$), temperature ($T$), and molecular mass ($m$) of the gas impinging on the surface of interest according to Equation 2.8.

$$J_N = p\sqrt{\frac{1}{2\pi kTm}}$$

Equation 2.8

According to this model, complete surface coverage occurs in one second under a pressure of $1 \times 10^{-6}$ mbar corresponding with 1 $L$. However, under a pressure of $1 \times 10^{-9}$ mbar, 1 $L$ of air exposure requires $10^4$ seconds. This demonstrates the significant difference in substrate surface conditions between metallization under HV conditions and UHV conditions.

The $\lambda$ of a gas molecule typically found in HV (e.g., $H_2$, He, $N_2$, CO, $H_2O$) is ~50 m in HV and ~50 km in UHV according to the kinetic theory of gases (Equation 2.9)[19]

$$\lambda = \frac{kT}{\sqrt{2}\pi p d_m^2}$$

Equation 2.9

($d_m$ = diameter of the gas molecule), which are much larger than the metal source to substrate distance in the e-beam reactors employed throughout this work (~0.5 m). Here, a gas molecule with diameter ~$2 \times 10^{-10}$ m, $T = 298$ K, and pressures of $5 \times 10^{-6}$ mbar (HV) and $2 \times 10^{-9}$ mbar (UHV) are considered. In addition, the collision frequencies in HV and UHV are roughly 10 $s^{-1}$ and 0.01 $s^{-1}$, respectively. The rapid gas impingement rate, extremely high $\lambda$, and negligible collision rate in HV indicate a reaction between a metal atom ejected from the source and a background gas molecule will occur on the substrate rather than in transit. The kinetic theory of gases assumes sticking coefficients equal to unity for all constituents within a system, which is unrealistic considering the sticking coefficient depends on a number of factors (e.g., surface morphology, chemistry). Calculating accurate sticking coefficients involves detailed modeling and substantial computing power[20] and are therefore outside the scope of this work. Therein lies the utility of studying the corresponding difference in metal–TMD interface chemistry as a function of reactor base pressure as has been done here.

*QCM.* A quartz crystal microbalance (QCM) was employed to determine the deposition rate of various metals, providing reliable thickness control within a few Å of the desired film thickness. A QCM consists of a thin quartz disk with electrodes on both sides and operates based on the dependence of the quartz oscillation frequency on the deposited mass.[21] The quartz crystal is typically cut along a specific orientation to ensure the acoustic waves travel perpendicular to the crystal surface. If the deposited mass exceeds ~2% of the mass of the quartz crystal, the linear relationship between the deposited mass and the frequency change becomes nonlinear and the crystal must be replaced. The QCM was properly calibrated according to the tooling factor (*TF*), which is unique to the deposition tool, according to the target material (density and Z-factor, Table 2.2) and target-sample distance by the relationship defined in Equation 2.10.

$$TF_{Actual} = TF_{Approximate} \times \frac{Th_{Actual}}{Th_{QCM}}$$

Equation 2.10

Table 2.2. Density and Z-factors of relevant materials evaporated in this work.

| Metal | Au | Cr | Ir | Sc | Ti | Pd | Si |
|---|---|---|---|---|---|---|---|
| **Density ($g/cm^3$)** | 19.3 | 7.2 | 22.4 | 3.0 | 4.5 | 12.0 | 2.3 |
| **Z-factor** | 0.38 | 0.31 | 0.13 | 0.91 | 0.63 | 0.36 | 0.71 |

A ~100 nm film should be deposited for accurate extraction. The approximate tooling factor ($TF_{Approximate}$) is either a previously determined $TF$ or, if unknown, an estimate. AFM and profilometry are most commonly employed to determine the actual deposited thickness ($Th_{Actual}$). The procedure can be performed more than once to maximize accuracy.

*Sputter Deposition.* Sputtering generally operates under low vacuum conditions ($1 \times 10^{-3}$ -$1 \times 10^{-1}$ mbar) and offers much poorer control over the deposited film thickness (i.e., generally employed for > 10 nm films). A carrier gas (e.g., Ar, $N_2$, $O_2$, or a mixture) flows through the deposition chamber where a plasma is ignited by applying a large bias to the target material. Ionized gas molecules with large *KE* impinge upon the target ejecting multi-atom clusters towards the sample surface where they are deposited. Deposition rate can be tuned and variants of the target material can be deposited, such as oxide or nitride analogs, by changing the gas composition and flow rate accordingly. In this work, sputtering is performed using a 600 W, confocal radio frequency sputter magnetron source and a mass flow controller for stable gas injection throughout the deposition.[22] Specific parameters employed in sputtering processes are provided in the associated chapters.

## 2.2 *Ex–situ* Tools

### 2.2.1 Raman Spectroscopy

Molecular vibrational modes exhibit quantized allowed energies (and therefore frequencies) via simple harmonic vibration through the relationship expressed in Equation 2.11

$$E_{vib} = h\upsilon_{vib}\left(\upsilon + \frac{1}{2}\right), \upsilon = 0, 1, 2, \ldots$$

Equation 2.11

where $E_{vib}$, $v_{vib}$, $v$, and $h$ represent the vibrational energy, vibrational frequency (typically $6 \times 10^{12}$-$1.2 \times 10^{14}$ Hz), vibrational quantum number, and Planck's constant, respectively.[23] Long range lattice vibrations are typically excited within a low wavenumber range between 20 and 300 cm$^{-1}$, however the detectable range is most often limited by the laser employed (He-Ne in the case of this work) in the spectrometer. Raman spectroscopy is enabled by inelastic scattering of single-frequency incident photons, with Stokes scattering (excited vibrational mode relaxes to energy level greater than initial state) dominating detectable vibrational modes (Figure 2.6).

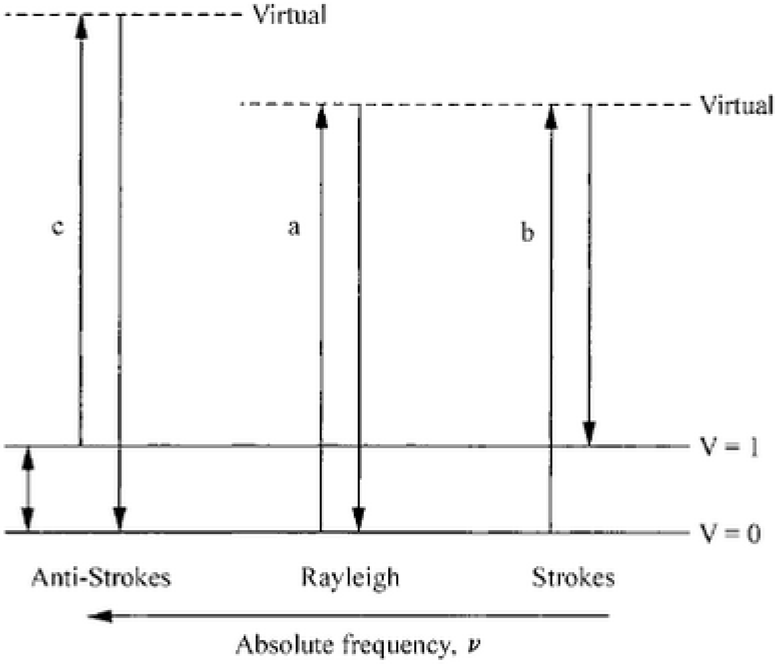

Figure 2.6. Frequency transition diagram of the basic elastic (Rayleigh) and inelastic (Stokes, Anti-Stokes) scattering processes. Adapted from Ref. 23. Copyright (2013) John Wiley and Sons.

Optical phonon modes (~10$^{14}$ Hz), e.g., in plane ($E^1_{2g}$) and out of plane ($A_{1g}$) Raman modes, are typically employed in phonon-based characterization of 2D materials in their mono- and few-layer forms as these modes often exhibit characteristic red (blue) shifted $E^1_{2g}$ ($A_{1g}$) peaks. Acoustic (~10$^{12}$ Hz) phonon modes can be employed in analogous characterization of materials which do not exhibit systematic layer number dependent shifts in optical modes. Raman spectroscopy is employed in this work to determine the previously unexplored characteristic red shift with layer number of the 2nd order longitudinal acoustic (2LA(M)) mode of $WSe_2$ from one to five layer structures.

It is also important to note Raman spectroscopy, which is typically assumed to be nondestructive, can impart significant damage upon TMDs.[24] In addition, degree of structural damage can differ significantly with metal–chalcogen pair. It is therefore of great interest to study the structural damage imparted upon TMDs as a function of laser power density, acquisition time, and number of sweeps. Analogous work is performed here on $WSe_2$. An Invia Confocal Renishaw microscope with laser wavelength of 532 nm and power densities from 0.49-3.32 mW/$\mu m^2$ are employed in this work.

### 2.2.2 Scanning Probe Microscopy

*Scanning Tunneling Microscopy*

STM provides the unique ability to directly study the structural and electronic properties of a surface with extremely high spatial resolution. Imaging and spectroscopy require an atomically sharp probe tip, usually W prepared by etching in KOH, and a sample with enough surface states to facilitate tunneling from the probe. A bias is applied to the tip, typically between -2 and 2 V in this work. It is then lowered to the surface until the wavefunction of the tip overlaps with that of the surface and the tunneling probability becomes non-negligible. A ‘constant current’ mode is typically employed for imaging in which the z-coordinate of the tip is constantly adjusted by software-modulated piezoelectric actuation as the tip is rastered across the surface to maintain constant tunneling current. Therefore, images obtained via STM represent a convolution of both the topographical and electronic surface structure.

In addition, scanning tunneling spectroscopy (STS) can provide the greatest detail regarding local density of surface states. The total *I(V)* from electrons tunneling into and out of the sample for applied voltage greater than zero is given by Equation 2.12[25]

$$I(V) \propto \int_{0}^{eV} \rho_s(E)\rho_t(E-eV)T(z,E,V_t)dE$$

Equation 2.12

where $\rho_t(E)$, $\rho_s(E\text{-}eV)$ and *T(E,V)* represent the local densities of states (DoS) of the tip and sample, respectively, and tunneling transmission coefficient between surface and tip. The Wentzel-Kramers-Brillouin (WKB) approximation is commonly employed to model the tunneling transmission probability $T(z,E,V_t)$ according to Equation 2.13

$$T(z,E,V_t) = \exp\left(-z(r)\sqrt{\frac{4m}{\hbar}(\varphi_s + \varphi_t + eV - 2E)}\right)$$

Equation 2.13

where *z(r)* represents the tip-to-sample distance and the work function difference between the sample ($\varphi_s$) and tip ($\varphi_t$). The local DoS conveyed in an image are also tip bias-dependent; unoccupied surface states are represented under positive tip bias while a negative tip bias yields image contrast corresponding with occupied surface states. In this work, spectroscopic data is obtained experimentally from a single location by holding the tip position constant while performing a voltage sweep and measuring current. However, $T(z,E,V_t)$ decreases exponentially with increasing tip-to-sample distance (Equation 2.13) and any variation from location to location at which spectra are obtained can distort spectral features potentially leading to misinterpretation of I-V or *dI/dV* (conductivity) curves. However, normalizing the conductivity (*dI*(*V*)/*dV*/(*I/V*)) significantly reduces the dependence on tip–surface separation and applied bias. The normalized conductivity takes the form

$$\frac{\frac{dI(V)}{dV}}{\frac{I}{V}} = \frac{\rho_s(eV)\rho_t(0) + A(V)}{B(V)}$$

Equation 2.14

where *A(V)* and *B(V)* slowly vary with voltage.[25]

STM and STS are employed in this work to study the nucleation and growth mechanisms as well as the surface electronic structure throughout stepwise Pd deposition and *in-situ* post metallization annealing.

*Atomic Force Microscopy*

In contrast with STM, AFM employs direct surface contact via oscillating cantilever probe (e.g., tapping mode) to determine surface structure with resolution on the order of a few nm. A Veeco Dimension 3100 V Atomic Probe Microscope[26] was employed prior to and following metal deposition on TMDs to investigate initial surface structure and deposited film morphology.

### 2.2.3 Scanning Transmission Electron Microscopy Sample Preparation: Focused Ion Beam Milling

The scanning tunneling electron microscopy (STEM) lamella discussed in Chapters 6 and 7 are fabricated in a focused ion beam (FIB) microscope (FEI Nova 200 Dual Beam) equipped with a Zyvex F100 nano-manipulation stage. 700 nm $SiO_2$/1 μm Pt are deposited by e-beam (5 kV, 1.6 nA) followed by an additional 2-3 μm Pt by ion beam (~1 μm at 20 kV, 0.081 nA then ~1 μm at 30 kV, 0.100 nA). The lamella is isolated by milling material around three sides of the deposited $SiO_2$/Pt structure via ion beam (30 kV, 5 nA). The Zyvex manipulator is inserted and bonded to the lamella via Pt (e-beam, 30 kV, 0.050 nA). The final cut is performed (ion beam, 30 kV, 0.050 nA) to release the lamella from the substrate and the manipulator is retracted with the lamella attached. An ~11 μm × ~20 μm rectangle is milled (ion beam, 30 kV, 7 nA) from the end of a pin on the Cu grid. The manipulator/lamella is inserted and the bottom corners of the lamella are bonded (e-beam Pt, 30 kV, 0.500 nA) to the top corners of the milled rectangle in the Cu grid. The manipulator is detached from the lamella via ion beam (30 kV, 1 nA). The lamella is thinned using increasingly delicate parameters (1st: 30 kV, 0.500 nA; 2nd: 20 kV, 0.037 nA) until the thickness of the lamella is < 80 nm. A final beam shower is performed (5 kV, 0.029 nA) to clean any residue materials (Ga, Cu, C) from the milling process. STEM images were obtained from the lamella within three days of milling.

### 2.2.4 Device Fabrication

*Schottky Diode Structure*

Schottky diodes are fabricated in the work described in Chapters 6 and 7 for temperature dependent *I-V* measurements. The bulk TMD is exfoliated and placed exfoliated side up on a 4” stainless steel sample holder. A shadow mask with arrays of circular openings ranging in diameter from 10-200 μm (Appendix B) is placed over top of the exfoliated TMD and fixed to the sample holder via washers and screws. The plate is loaded into the UHV cluster tool (Figure 2.1) and contact metals are deposited to thicknesses specified in associated chapters. Metal sources are outgassed, deposition rates are determined, and metals are deposited using the same steps outlined in Appendixes A and B. Post-metallization anneals were performed and the relevant details are provided in the respective chapters because they are important to the discussion. At least five diodes with diameters of 200 µm and 50 µm each were fabricated in all relevant experiments to ensure statistically significant data sets were obtained.

*Field Effect Transistors*

The following process description applies to back-gated transistors discussed in Chapters 4, 6, and 7. A 27 nm $Al_2O_3$ film is deposited on a p++ Si wafer with a native oxide for back gate isolation using atomic layer deposition (ALD, 250 °C). After depositing an Al backside contact on the opposite side of the wafer, the wafer is annealed at 400 °C in FG (90% $N_2$, 10% $H_2$) to reduce charge traps within the back gate $Al_2O_3$. TMD flakes are exfoliated using a scotch tape method, transferred to the $Al_2O_3$, and few layer flakes are isolated using optical contrast. Source and drain regions are patterned via conventional photolithography (negative resist, AZ nLOF 2020).[27] Pre-metallization treatments and/or contact metallization follow lithographic patterning and the pertinent details are discussed in the respective chapters as the deposition conditions and metals are important for the discussion. In the work described in Chapters 6 and 7, post-metallization anneals are performed in succession at 200 °C, 300 °C, and 400 °C in UHV or FG (90% $N_2$, 10% $H_2$) for one hour each. At least 10 devices are fabricated using each unique combination of metallization and post-metallization anneals (see relevant chapters for details) to ensure the conclusions derived are statistically significant.

### 2.2.5 Electrical Characterization

*Schottky Diode*

*I-V* measurements are performed on a Kiethley 4200 Semiconductor Characterization System in a Cascade Probe Station. Temperature dependent *I-V* measurements are obtained under a constant $N_2$ gas flow at -20 °C, 0 °C, 25 °C, 50 °C, 70 °C, 90 °C, 110 °C, and 130 °C in the same probe station using a Temptronic ThermoChuck TP03000 Thermal Inducing Vacuum Platform (-50 °C to 130 °C) to control the sample temperature. *I-V* measurements are obtained at least 15 minutes after the chuck reached a new temperature setpoint to allow the system to equilibrate. The top pad is probed as the source contact and the chuck is the drain contact. The bulk TMD crystals were typically > 0.5 $\mathrm{cm}^2$, which is larger than the top contact by a factor of ~$10^3$. Therefore, the back contact between the TMD and the chuck is considered to be Ohmic compared with the top contact. *I-V* measurements are obtained by sweeping from 0 to 2 V and 0 to -2 V using a voltage step of ±0.01 V to avoide hysteresis effects. At least five diodes with diameters of 200 μm and 50 μm each are measured in all relevant experiments to ensure statistically significant datasets are obtained.

*C-V* measurements are obtained from the same Schottky diodes in parallel with the *I-V* measurements using an HP 4284 LCR meter in parallel capacitance mode. The LCR meter is interfaced with the Kiethley 4200 to enable measurement control via the Kiethley 4200 interface. *C-V* measurements are obtained at 3-5 frequencies between 100 kHz and 1 MHz using a hysteresis sweep from -7 V to 3 V bias, an oscillation amplitude of 50 mV, and a voltage step of 0.1 V.

*Field Effect Transistors*

Electrical measurements were obtained in air at room temperature immediately following metallization and in succession with the post-metallization anneals using a Kiethley 4200 Semiconductor Characterization System in a Cascade Probe Station. $I_{\mathrm{DS}}$-$V_{\mathrm{DS}}$ measurements are obtained at a drain bias of 0.5 V, while the gate bias range is dependent upon the threshold voltage ($V_{\mathrm{T}}$) of the transistor due to significant $V_{\mathrm{T}}$ shifts manifesting from the post-metallization processing. All $I_{DS}$-$V_{GS}$ measurements include separate forward sweep (-7 V to 7 V), reverse sweep (7 V to -7 V), hysteresis sweep, and gate leakage measurements.

## 2.3 References

(1) Wallace, R. M. In *Physics and Technology of High-K Gate Dielectrics 6*; Kar, S.; Landheer, D.; Houssa, M.; Misra, D.; VanElshocht, S.; Iwai, H.; The Electrochemical Society: Pennington, NJ, 2008; Ch. 6, pp 255-271.

(2) Wallace, R. M. In–Situ Studies on 2D Materials. *ECS Trans*. **2014**, *64*, 109–116.

(3) Ratner, B. D.; Castner, D. G. Electron Spectroscopy for Chemical Analysis. In Surface Analysis– The Principal Techniques 2nd Edition; Vickerman, J. C.; Gilmore, I. S., Eds.; VCH: United Kingdom, **2013**; pp 47-99.

(4) Herrera-Gomez, A.; Hegedus, A.; Meissner, P. L. Chemical Depth Profile of Ultrathin Nitrided $SiO_2$ Films. *Appl. Phys. Lett.*, **2002**, *81*, 1014–1016.

(5) Alfold, T. L.; Feldman, L. C.; Mayer, J. W. Fundamentals of Nanoscale Film Analysis; Springer US, 2007, 199-213.

(6) McDonnell, S.; Smyth, C.; Hinkle, C. L.; Wallace, R. M. $MoS_2$-Titanium Contact Interface Reactions. *ACS Appl. Mater. Interfaces*, **2016**, *8* (12), 8289-8294.

(7) McDonnell, S.; Addou, R.; Buie, C.; Wallace, R. M.; Hinkle, C. L. Defect Dominated Doping and Contact Resistance in $MoS_2$. *ACS Nano* **2014**, *8*, 2880-2888.

(8) Seah, M. P.; Dench, W. A. Quantitative Electron Spectroscopy of Surfaces: A Standard Data Base for Electron Inelastic Mean Free Paths in Solids. *Surf. Interface Anal.*, **1979**, *1* (1), 2-11.

(9) Jablonski, A.; Zemek, J. Overlayer Thickness Determination by XPS Using the Multiline Approach. *Surf. Interface Anal.* **2009**, *41*, 193-204.

(10) Wagner, C. D.; Raymond, R. H.; Gale, L. H. Empirical Atomic Sensitivity Factors for Quantitative Analysis by Electron Spectroscopy for Chemical Analysis. *Surf. Interface Anal.* **1981**, *3*, 211–225.

(11) Hufner, S. Photoelectron Spectroscopy: Principles and Applications; Springer, US, 2003, 14-20.

(12) Thin film reference data, Oxford Vacuum Science Ltd, 2018; http://www.oxford-vacuum.com/background/thin_film/reference_data.pdf.

(13) Powell, R. W.; Ho, C. Y.; Liley, P. E. Thermal Conductivity of Selected Materials. National Standard Reference Data Series-National Bureau of Standards-8, Category 5-Thermodynamic and Transport Properties, 1966.

(14) Chen, C-H.; Hu, E. L.; Schoenfeld, W. V.; Petroff, P. M. Metallization-Induced Damage in III-V Semiconductors. *J. Vac. Sci. Technol. B.* **1998**, *16*, 3354-3358.

(15) Burek, G. J.; Hwang, Y.; Carter, A. D.; Chobpattana, V.; Law, J. J. M.; Mitchell, W. J.; Thibeault, B.; Stemmer, S.; Rodwell, M. J. W. Influence of Gate Metallization Processes on the Electrical Characteristics of High-κ/$In_{0.53}Ga_{0.47}As$ Interfaces. *J. Vac. Sci. Technol. B.* **2011**, *29*, 040603.

(16) Properties of Inorganic Materials. In *CRC Handbook of Chemistry and Physics 70th Edition*; Weast, R. C.; Lide, D. R.; Astle, M. J.; Beyer, W. H.; CRC Press Inc.: Boca Raton, FL, 1989-1990.

(17) Agarwal, M. K.; Wani, P. A. Growth Conditions and Crystal Structure Parameters of Layer Compounds in the Series $Mo_{1-x}W_xSe_2$. *Materials Research Bulletin*, **1979**, *14* (6), 825-830.

(18) Addou, R.; McDonnell, S.; Barrera, D.; Guo, Z.; Azcatl, A.; Wang, J.; Zhu, H.; Hinkle, C. L.; Quevedo-Lopez, M.; Alshareef, H. N., et al. Impurities and Electronic Property Variations of Natural $MoS_2$ Crystal Surfaces. *ACS Nano* **2015**, *9*, 9124-9133.

(19) Christian Edelmann, Vakuumphysik, Spektrum Akademischer Verlag, Heidelberg/Berlin 1988, p. 38.

(20) Yue, R.; Nie, Y.; Walsh, L. A.; Addou, R.; Liang, C.; Lu, N.; Barton, A. T.; Zhu, H.; Che, Z.; Barrera, D.; Cheng, L.; Cha, P.-R.; Chabal, Y. J.; Hsu, J. W. P.; Kim, J.; Kim, M. J.; Colombo, L.; Wallace, R. M.; Cho, K.; Hinkle, C. L. Nucleation and Growth of WSe2: Enabling Large Grain Transition Metal Dichalcogenides. *2D Materials*, **2017**, *4*, 045019.

(21) Vashist, S. K.; Vashist, P. Recent Advances in Quartz Crystal Microbalance-Based Sensors. *J. Sensors*, **2011**, 571405.

(22) Wallace, R. M. In-Situ Studies of Interfacial Bonding of High-k Dielectrics for CMOS Beyond 22nm. *ECS Trans.* **2008**, *16* (5), 255-271.

(23) Vibrational Spectroscopy for Molecular Analysis in "Materials Characterization", Leng, Y., Wiley–VCH Verlag GmbH & Co., Germany, **2013**.

(24) Khac, B. C. T.; Jeon, K.-J.; Choi, S. T.; Kim, Y. S.; DelRio, F. W.; Chun, K.-H. Laser-Induced Particle Adsorption on Atomically Thin $MoS_2$. *ACS Appl. Mater. Interfaces*. **2016**, *8* (5), 2974-2984.

(25) Yu, E. T. Cross-Sectional Scanning Tunneling Microscopy, *Chem. Rev.* **1997**, *97*, 1017–1044.

(26) University of Texas at Dallas Cleanroom http://www.utdallas.edu/research/cleanroom/ (Accessed March 25, 2016).

(27) Introduction to DNQ-Novolac Resists - Henderson Research Group https://sites.google.com/site/hendersonresearchgroup/helpful-primers-introductions/intro-to-dnq-novolac-resists. (Accessed October 3, 2018)

# CHAPTER 3

# EFFECTS OF DEPOSITION CONDITIONS ON THE INTERFACE CHEMISTRY BETWEEN CONTACT METALS AND MOLYBDENUM CHALCOGENIDES

Authors – Christopher M. Smyth[†], Rafik Addou[†], Stephen McDonnell[‡],

Christopher L. Hinkle[†], and Robert M. Wallace[†]

[†]The Department of Materials Science and Engineering, RL10
The University of Texas at Dallas
800 West Campbell Road
Richardson, Texas, 75080, USA

[‡]The Department of Materials Science and Engineering
University of Virginia
Charlottesville, Virginia, 22904, USA

## 3.1 Preface

Thin films of contact metals, specifically Au, Ir, Cr, and Sc, are deposited on exfoliated, bulk $MoS_2$, $MoSe_2$, and $MoTe_2$ using electron beam (e-beam) deposition under two different reactor base pressures to determine the interface chemistry between contact metals and transition metal dichalcogenides (TMDs) and its dependence on the reactor ambient. The high work function metal Au does not react with $MoS_2$ or $MoSe_2$ but does react with $MoTe_2$, regardless of reactor ambient. In contrast, interfacial reactions between Mo-based TMDs and another high work function metal, Ir, are observed when it is deposited under both high vacuum (HV, $\sim 1 \times 10^{-6}$ mbar) and ultra-high vacuum (UHV, $\sim 1 \times 10^{-9}$ mbar). The TMD near the interface is completely reduced by interfacial reactions with low work function (high chemical potential) metals (Cr, Sc). In addition, Sc is rapidly oxidized on the TMD surface, whereas Cr is only partially oxidized when deposited under HV conditions. This indicates that deposition chamber ambient can affect the contact metal chemistry in addition to the chemistry present at the contact metal-TMD interface. Furthermore, the band alignment between Au, Ir, and Sc and the Mo-based TMDs deviates significantly from the Schottky-Mott rule. In contrast, the Cr–TMD band alignments loosely obey the Schottky Mott rule resulting in a near midgap Fermi level, which is detrimental for contact performance. These results elucidate the true chemistry of some contact metal–TMD interfaces and its dependence on the deposition ambient, and highlight the need to consider the chemical states present at the interface and their impact on contact resistance with Mo-based TMDs.

The content of this chapter is reproduced in part with permission from the Journal of Physical Chemistry C from (Contact Metal-$MoS_2$ Interface Reactions and Potential Implications on $MoS_2$-Based Device Performance. Journal of Physical Chemistry C. **2016**, 120 (27), 14719-14729).

Copyright (2016) American Chemical Society. In this work, the experiments were inspired by Dr. S. McDonnell (while he was still working at UTD) and performed by myself. Dr. R. Addou and the other coauthors provided valuable inputs throughout the process of preparing the manuscript.

## 3.2 Introduction

Recently, a number of new device architectures have been proposed and explored to support the scaling of current Si-based field effect transistor (FET) technologies. FETs based on 2D materials, which may rely on mono- or few-layer transition metal dichalcogenides (TMDs) as a channel material, show much promise in lower power consumption applications compared to existing Si-based semiconductor devices.[1-4] For example, $MoS_2$- and $MoSe_2$ based devices with impressive subthreshold swing approaching 60 mV/dec,[5] $I_{ON}/I_{OFF}$ ratio in the order of $10^{10}$, and room temperature electron and hole mobilities of 470 and 480 $cm^2/V\ s$, respectively, have been demonstrated.[4,6] $MoTe_2$ is perhaps the most intriguing semiconductor of the three Mo-based TMDs due to its moderate band gap [~1.0 eV (bulk) to 1.2 eV (single layer)], which facilitates low power device operation and is promising for optoelectronic applications in the infrared wavelengths.[7] However, substantial statistical variations in performance are observed when a suitable device population is studied, even for devices processed in the same laboratory with the same property extraction methods.[8] These properties indicate significant improvement in device performance is possible, while also highlighting aspects which need to be engineered further to improve device performance. In particular, the fundamental understanding of contact resistance behavior on TMDs is lacking and truly Ohmic contacts have not yet been achieved. When the channel material is on the order of a few atoms thick, the quality of contacts, quantified by contact resistance, must be such that key properties like drain current, photoresponse, and mobility are limited not by the quality of the contacts, but by the intrinsic properties of materials used in the device architecture. Metal contacts should ideally be Ohmic and have low resistance, as high parasitic contact resistance has been identified as a critical limiting factor to TMD-based device performance, similar to Si-based devices, and must be mitigated.[9-15]

A number of different metals have been explored for use as contacts in TMD-based devices, via both density functional theory (DFT) calculations and experimentation, with mixed results and typically under the assumption of pristine metal–TMD interfaces.[5,15-17] Das et al. reported that Sc and Ti, with respective work functions of 3.5 and 4.1 eV, form extremely low electron Schottky barrier heights (*SBH*) of 0.03 and 0.05 eV, respectively, to $MoS_2$.[14] Even high work function metals such as Au (5.1 eV)[18] and Pd (5.6 eV),[18] form abnormally low electron *SBH*s compared to the barrier expected from considering the alignment of the $MoS_2$ band structure with the work functions of these metals. Significant Fermi level ($E_F$) pinning has also been reported between a number of contact metals and $MoTe_2$.[19] DFT calculations suggest various states are formed in the band gap of Mo-based TMDs due to contact metal–chalcogen interactions at the interface[7,20] and intrinsic defects,[21-23] which have been observed in high aerial density in both geological and synthetic Mo-based TMDs.[24] Even low concentrations of defects have a significant impact on the contact metal–TMD junction current due to parallel conduction through defects and the contact metal.[25] These phenomena have been proposed as potential mechanisms by which $E_F$ pinning occurs between contact metal and TMDs.[20,21,26]

The interface between contact metal and $MoS_2$, $MoSe_2$, and $MoTe_2$ has thus far proved more difficult to engineer in TMD-based devices than analogous interfaces in traditional Si-based devices. Interfacial treatments employed on Si to mitigate contact resistance, such as substitutional doping, are not always applicable on TMDs due to potential negative impacts of such treatments.[10] Moreover, many metallization processes include an "adhesion layer" such as Cr in some contact structures, and do not carefully consider the implications that reactions between the contact metal and channel can have on the performance of devices employing an atomically thin channel.

There are many factors involved in determining the nature of a metal–TMD interface, including the difference between metal work function and TMD electron affinity as described by the Schottky-Mott model and the wavefunction overlap character (electronegativity) between valence orbitals of the contact metal, chalcogen, and Mo. Previous work has sought to predict the chemical and electrical nature of metal-semiconductor interfaces using various combinations of these properties.[12,14,27,28] Moreover, McDonnell et al. has also demonstrated the deposition chamber ambient can have significant implications in determining the resulting chemistry of electron beam deposited Ti contacts as well as the nature of the interface formed between Ti and $MoS_2$.[29] Important details of the *in-situ* contact metal deposition conditions, such as chamber pressure, are typically omitted from reports of TMD-based transistor performance evaluations. A typical device fabrication process will include electron-beam evaporation of contact metal(s) in a HV chamber at an unspecified pressure, with subsequent air exposure for an unreported amount of time.

It is also noted that various forms of intrinsic defects, such as sulfur vacancies, structural defects, and impurities, present at the contact metal-TMD interface strongly impact the electrical behavior.[25] Significant impurity concentrations are also detected in both geological and synthetic $MoS_2$ $MoSe_2$, and $MoTe_2$ crystals.[23,30,31] Therefore, one cannot assume that an abrupt contact–TMD interface will translate to lower contact resistance or even an Ohmic contact. The presence of dangling bonds at defect sites on the often-assumed 'inert' van der Waals (vdW) surface of Mo-based TMDs will alter the thermodynamics involved in determining the chemical nature of the contact metal–TMD interface. Typically, DFT models of such interfaces only consider pristine TMD layers, which is far from reality and neglect the potential for interfacial reactions to consume material beyond surface chalcogen in an Mo-based TMD.[5,6,16,17] Models which consider a more realistic contact metal–TMD interface, including defects in the TMD and the availability of oxidizing gas species at the interface depending on deposition ambient, in tandem with careful experimental design are needed to determine the ideal contact material and deposition ambient for Ohmic contacts on TMDs.

To elucidate and understand the chemistry of such contact interfaces, the effects of the deposition chamber ambient, i.e., background pressure conditions, on the interface chemistry between exfoliated, bulk $MoS_2$, $MoSe_2$, and $MoTe_2$ and contact metals are explored, specifically Au, Ir, Cr, and Sc, with work functions ranging between 3.5 and 5.3 eV.[14,18,19] The interface between thin metal films deposited under two separate reactor base pressures is characterized using X-ray photoelectron spectroscopy (XPS) to analyze the interface chemistry. The band alignment formed between the contact metals and the TMDs are extracted from the XPS measurements and trends are discussed in relation to interface chemistry commonalities across metal–TMD systems. Speculation is given regarding the potential effects of reactor ambient on contact resistance based on the band alignments.

## 3.3 Experimental Methods

*Sample Preparation and Characterization Prior to Metal Deposition*

Bulk geological $MoS_2$ used here was purchased from WARD's Science.[32] Bulk synthetic $MoSe_2$ and $MoTe_2$ used here were purchased from HQ Graphene.[33] For each respective metal deposition, bulk $MoS_2$, $MoSe_2$, and $MoTe_2$ crystals were mounted to a silicon wafer via conductive carbon tape. Identical steps were carried out for each separate metal deposition with a common chamber base pressure of ~$1 \times 10^{-6}$ mbar used for depositions under HV conditions and ~$1 \times 10^{-9}$ mbar used for depositions under UHV conditions. All samples were initially cleaned via mechanical exfoliation using Scotch Magic® tape immediately prior to any spectroscopic analysis or metal deposition. Samples used for metal depositions under UHV conditions were characterized with XPS in their "as-exfoliated" condition prior to any metal deposition, while samples used for depositions under HV conditions (see below) were not. The surfaces of as-exfoliated samples used for deposition under HV conditions are assumed to be chemically congruent with those characterized prior to deposition under UHV conditions.

*Metal Deposition and Subsequent Characterization*

The procedures employed in this work to outgas Au, Ir, Cr, and Sc sources, determine metal deposition rates, deposit metals onto the TMDs, and transfer samples throughout the experiments were identical to all other e-beam metal depositions performed *in–situ* in UHV and *ex–situ* in HV throughout the work described in this dissertation. Detailed outlines of these procedures are provided in Appendix A.

All samples originated from the same $MoS_2$, $MoSe_2$, and $MoTe_2$ crystals, but individual pieces were sliced from these crystals and exfoliated for each respective metal deposition.

The procedure employed in this work to prepare and characterize Au, Ir, Cr, and Sc metal reference films is the same throughout this dissertation and is therefore described in detail in Appendix B. An Mo source was not available in the UHV cluster tool to obtain reference spectra from metallic Mo. Therefore a bulk, polycrystalline Mo sample was employed to establish the metallic Mo reference spectra. Special care was taken to ensure a clean Mo surface prior to obtaining the reference spectra. The detailed cleaning and characterization procedures are applied in this work and also in the work discussed in Chapter 4 and are described in detail in Appendix B.

The targeted thickness of all metal films was 1.5 nm, at a deposition rate ranging from 0.3 nm/min to 0.6 nm/min to permit XPS detection of any interfacial reaction products that might form between metal and $MoS_2$. The deposition rates are determined differently for depositions under UHV compared with depositions under HV because the deposition chamber under UHV is configured such that the quartz crystal monitor (QCM) cannot be used to monitor the total deposited film thickness during deposition whereas this is possible in the cleanroom deposition tool. Instead, the deposition rate and corresponding electron beam current must be determined prior to deposition under UHV.

### *X-ray Photoelectron Spectroscopy and Spectra Analysis*

XPS on all sample surfaces was carried out using a monochromated Al Kα source and an Omicron EA125 hemispherical analyzer with resolution of ±0.05 eV. The analyzer acceptance angle of 8°, takeoff angles of 45° and 37° (angle resolved XPS or ARXPS), and pass energy of 15 eV were utilized in this study. The takeoff angle represents the angle formed between the detector and sample surface. The analyzer was calibrated using sputter cleaned Au, Cu, and Ag foils, as is outlined in the ASTM E2108.[34] Spectra were deconvolved using the curve fitting software AAnalyzer and the stoichiometry calculation method is addressed in the Appendix.[35]

Figure A.1 graphically displays the experimental procedure broken down step by step.

### *Atomic Force Microscopy*

AFM images were obtained *ex–situ* from bare Mo-based TMDs immediately following exfoliation and again after metal deposition and XPS interrogation using a Veeco Model 3100 Dimension V Atomic Probe Microscope in non-contact tapping mode in the cleanroom facility.[36] WSxM software[37] was employed to process images, obtain line profiles, and determine RMS roughness values reported here.

## 3.4 Results and Discussion

Both experimentally derived[38] and theoretically predicted[39] thermodynamic data, such as the $\Delta G^\circ_f$'s of various compounds at metal–$MoS_2$ interfaces, are used as a tool to predict interfacial bond formation. All $\Delta G^\circ_f$ values are reported per chalcogen or oxygen atom.[40] All electronegativity comparisons are reported according to the Pauling electronegativity scale. Metal–$MoS_2$ interfaces exhibiting reaction products in related XPS spectra will be described as "covalent" interfaces. Interfaces which do not exhibit any additional chemical states besides the metallic contact metal and bulk Mo and chalcogen states in $MoS_2$, $MoSe_2$, or $MoTe_2$ will be described as "vdW" interfaces.

### 3.4.1 Au

*MoS₂*

Reactions between $MoS_2$ and Au are not favorable as the Gibbs free energy of formation of $Au_2S$ ($\Delta G^\circ_{f,Au2S}$ = -58.1 kJ/mol)[41] is positive relative to that of $MoS_2$ ($\Delta G^\circ_{f,MoS2}$ = -118.0 kJ/mol).[38,41,42] Figure 3.1a shows the Mo and S core levels obtained from exfoliated $MoS_2$ and subsequent Au deposition under UHV and HV conditions.

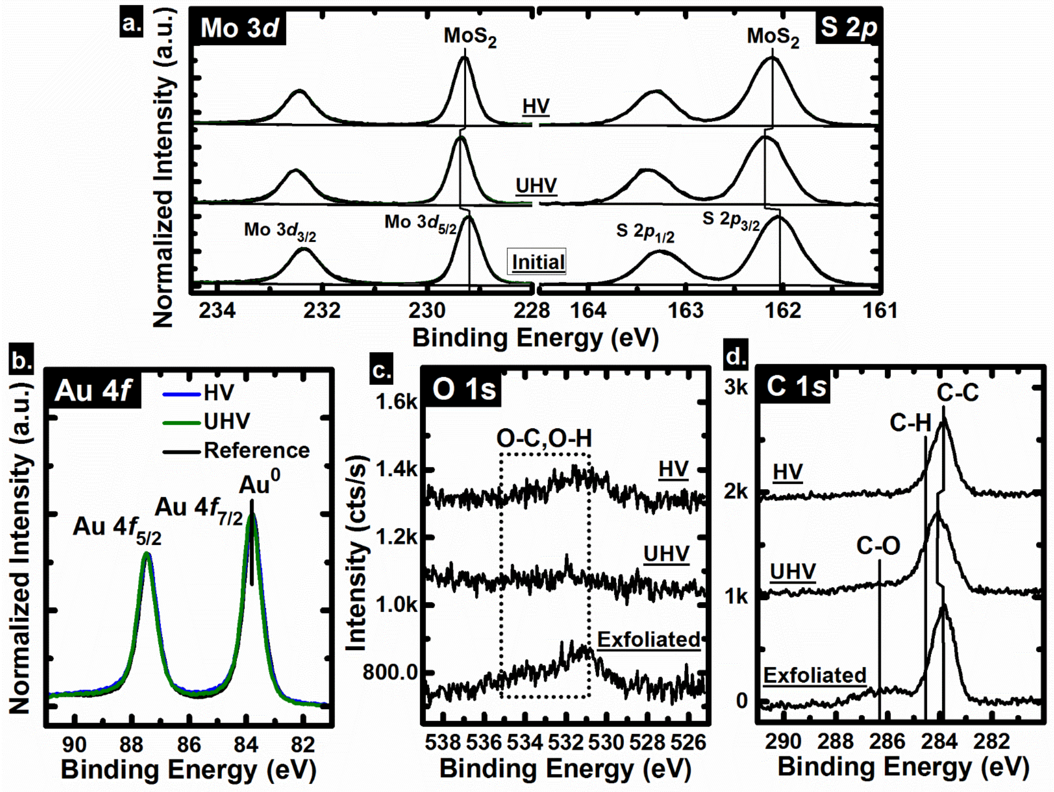

Figure 3.1. a) Mo 3*d*, S 2*s*, S 2*p*, b) Au 4*f*, c) O 1*s*, and d) C 1*s* core level spectra obtained from bulk $MoS_2$ after exfoliation and subsequent Au deposition in UHV (*in–situ*) or HV (*ex–situ*). The spectra in a) and b) are normalized to the Mo $3d_{5/2}$, S $2p_{3/2}$, and Au $4f_{7/2}$ core levels, respectively.

No additional chemical states arise following Au deposition under either UHV or HV conditions in any of the Mo 3*d*, S 2*p*, O 1*s* (Figure 3.1c), or C 1*s* (Figure 3.1d) core level spectra. Therefore, Au forms a vdW interface with $MoS_2$. Previous experiments have demonstrated secondary electrons and X-ray radiation generated during e-beam gate metal deposition can inflict damage on the gate oxide and semiconductor channel in metal-oxide-semiconductor (MOS) structures.[43-46] In this study, it is possible that characteristic X-rays are generated as the electron beam impacts the source metal. Our study does not involve any thick oxide layers, therefore damage to the $MoS_2$ substrate would be more likely (i.e., bond scission, defect generation). However, the deposition rates employed here, on the order of $10^{-3}$ Å/s, are approximately three orders of magnitude lower than those commonly employed in studies investigating e-beam-induced radiation damage in MOS structures, on the order of 1 Å/s.[45,46] Therefore, we anticipate the X-ray flux produced during e-beam deposition in this study to be orders of magnitude lower than the X-ray flux produced in other studies employing deposition rates much higher than what is used here. In addition, the most energetic characteristic X-ray which can be generated by the four metals employed in this study (Sc, Cr, Ir, and Au) exhibit penetration depths into $MoS_2$ orders of magnitude greater than the sampling depth of XPS. Assuming $MoS_2$ has a density of 5.06 g/cm$^3$,[47] we calculate the K$\alpha_1$ X-ray line of Sc and Cr and K$\beta_1$ X-ray line of Ir and Au to exhibit penetration depths of 10.9, 22.1, 5867.5, and 7102.8 μm, respectively, into $MoS_2$. The sampling depth of XPS is on the order of 10 nm. Therefore, e-beam induced radiation damage inflicted upon $MoS_2$ during metal deposition in this study should not affect the chemistry of $MoS_2$ within the vicinity of the sample surface.

Figure 3.1b shows normalized Au 4*f* core level spectra obtained following Au deposition overlapping with that obtained from a reference Au film (see Appendix B for details on preparing the Au reference film) in order to establish the detection of chemical states. These spectra exhibit a "tail" intensity structure toward high binding energy (*BE*), which is typically attributed to core-hole screening effects.[48,49] The absence of chemical states other than metallic Au in the Au 4*f* spectra confirms the vdW nature of the Au–$MoS_2$ interface. Au has a 5*s* valence shell, which translates to a weak interaction with $MoS_2$ due to insignificant wavefunction overlap between Au in the contact material and Mo in the top most $MoS_2$ layer.[27] Appreciable charge transfer therefore does not occur across the Au–$MoS_2$ interface, resulting in the formation of a vdW gap between Au and $MoS_2$.

Adventitious species including hydroxyl (O–H), carboxyl (C–O), hydrocarbon (C–H), and adventitious carbon (C–C) are detected on $MoS_2$ prior to Au deposition and likely originate from briefly exposing the sample to air between exfoliation and loading into the cluster tool (Figure 3.1c,d). Gold oxide and gold carbide species formed as a result of reactions between Au and the adventitious species are below the limit of XPS detection, which is expected considering Au–O bond formation is endothermic ($\Delta G^{\circ}_{f,Au2O3}$ = 26.6 kJ/mol).[38,50] The stable $Au_2C_2$ compound has been reported previously, but was synthesized in solution and was highly unstable.[51] It is therefore reasonable to assume Au–C bond formation at RT is endothermic. However, the effects of adventitious species on contact performance in cases where the contact metal forms a vdW interface with the TMD, as is observed in other metal–TMD systems discussed later, should not be ignored. For example, Pd, which forms a vdW interface with $WSe_2$ at room temperature, undergoes an exothermic reaction to form Pd–C when deposited on graphene.[52]

Although a Au contact does not interact chemically with $MoS_2$, it does impact electronic properties. A *BE* shift of the $Mo^{4+}$ and $S^{2-}$ states by the same value sans any changes in the line shape of either core level is characteristic of band bending in a semiconductor in contact with a metal.[12,13] The *BE*s of the Mo 3*d* and chalcogen core levels obtained from all Mo-based TMDs

Table 3.1. Binding energies of chemical states detected in Mo $3d_{5/2}$, S $2p_{3/2}$, Se $3d_{5/2}$, and Te $3d_{5/2}$ core level spectra after exfoliation and subsequent metal deposition in UHV or HV.

| Metals | TMD | Core Level | Exfoliated (UHV) | UHV | HV |
|---|---|---|---|---|---|
| Au | $MoS_2$ | Mo $3d_{5/2}$ | 229.20 ($MoS_2$) | 229.35 ($MoS_2$) | 229.29 ($MoS_2$) |
| | | S $2p_{3/2}$ | 162.04 ($MoS_2$) | 162.17 ($MoS_2$) | 162.11 ($MoS_2$) |
| | $MoSe_2$ | Mo $3d_{5/2}$ | 229.16 ($MoSe_2$) | 228.95 ($MoSe_2$) | 229.08 ($MoSe_2$) |
| | | Se $3d_{5/2}$ | 54.71 ($MoSe_2$) | 54.52 ($MoSe_2$) | 54.64 ($MoSe_2$) |
| | $MoTe_2$ | Mo $3d_{5/2}$ | 228.53 ($MoTe_2$) | 228.30 ($MoTe_2$) | 228.38 ($MoTe_2$)<br>231.99 ($MoO_x$) |
| | | Te $3d_{5/2}$ | 573.21 ($MoTe_2$)<br>575.78 ($TeO_2$) | 572.70 ($AuTe_x$)<br>573.04 ($MoTe_2$)<br>575.51 ($TeO_2$) | 572.60 ($AuTe_x$)<br>573.06 ($MoTe_2$)<br>575.65 ($TeO_2$) |
| Ir | $MoS_2$ | Mo $3d_{5/2}$ | 229.28 ($MoS_2$) | 228.61 ($MoS_x$)<br>229.07 ($MoS_2$) | 228.31 ($MoS_x$)<br>228.84 ($MoS_2$) |
| | | S $2p_{3/2}$ | 162.11 ($MoS_2$) | 161.91 ($MoS_2$)<br>162.54 ($MoS_x$, $IrS_x$) | 161.65 ($MoS_2$)<br>162.30 ($MoS_x$, $IrS_x$) |
| | $MoSe_2$ | Mo $3d_{5/2}$ | 229.21 ($MoSe_2$) | 228.35 ($Mo_xIr_ySe_z$)<br>228.72 ($MoSe_2$) | 228.29 ($Mo_xIr_ySe_z$)<br>228.78 ($MoSe_2$)<br>232.42 ($MoO_x$) |
| | | Se $3d_{5/2}$ | 54.77 ($MoSe_2$) | 54.26 ($Mo_xIr_ySe_z$)<br>54.45 ($MoSe_2$) | 54.36 ($Mo_xIr_ySe_z$)<br>54.51 ($MoSe_2$) |
| | $MoTe_2$ | Mo $3d_{5/2}$ | 228.52 ($MoTe_2$)<br>232.52 ($MoO_x$) | 228.15 ($Mo_xIr_yTe_x$)<br>228.28 ($MoTe_2$) | 228.31 ($Mo_xIr_yTe_z$)<br>228.44 ($MoTe_2$)<br>231.73 ($MoO_x$) |
| | | Te $3d_{5/2}$ | 573.19 ($MoTe_2$)<br>576.04 ($TeO_2$) | 572.97 ($MoTe_2$)<br>573.25 ($Mo_xIr_yTe_z$) | 573.18 ($MoTe_2$)<br>573.92 ($Mo_xIr_yTe_z$)<br>575.66 ($TeO_2$) |
| Cr | $MoS_2$ | Mo $3d_{5/2}$ | 229.04 ($MoS_2$) | 227.86 ($Mo^0$)<br>229.23 ($MoS_2$) | 227.81 ($Mo^0$)<br>229.39 ($MoS_2$) |
| | | S $2p_{3/2}$ | 161.86 ($MoS_2$) | 161.44 ($CrS_x$)<br>162.05 ($MoS_2$) | 161.60 ($CrS_x$)<br>162.20 ($MoS_2$) |
| | $MoSe_2$ | Mo $3d_{5/2}$ | 229.18 ($MoSe_2$) | 227.61 ($Mo^0$)<br>228.75 ($MoSe_2$) | 227.82 ($Mo^0$)<br>228.98 ($MoSe_2$) |
| | | Se $3d_{5/2}$ | 54.72 ($MoSe_2$) | 54.20 ($CrSe_c$)<br>54.30 ($MoSe_2$) | 54.32 ($CrSe_x$)<br>54.52 ($MoSe_2$) |
| | $MoTe_2$ | Mo $3d_{5/2}$ | 228.47 ($MoTe_2$) | 227.64 ($Mo^0$)<br>228.30 ($MoTe_2$) | 227.75 ($Mo^0$)<br>228.27 ($MoTe_2$) |
| | | Te $3d_{5/2}$ | 573.16 ($MoTe_2$)<br>575.80 ($TeO_2$) | 572.78 ($CrTe_x$)<br>573.00 ($MoTe_2$) | 572.61 ($CrTe_x$)<br>572.94 ($MoTe_2$) |
| Sc | $MoS_2$ | Mo $3d_{5/2}$ | 229.32 ($MoS_2$) | 227.88 ($Mo^0$)<br>229.33 ($MoS_2$) | 228.59 ($MoO_x$)<br>229.04 ($MoS_2$)<br>229.65 ($MoO_xS_y$) |
| | | S $2p_{3/2}$ | 162.14 ($MoS_2$) | 162.00 ($ScS_x$)<br>162.16 ($MoS_2$) | 161.89 ($MoS_2$)<br>162.49 ($MoO_xS_y$) |
| | $MoSe_2$ | Mo $3d_{5/2}$ | 229.17 ($MoSe_2$) | 227.69 ($Mo^0$)<br>229.00 ($MoSe_2$) | 229.10 ($MoSe_2$) |
| | | Se $3d_{5/2}$ | 54.71 ($MoSe_2$) | 54.52 ($MoSe_2$)<br>54.80 ($ScSe_x$) | 54.20 ($MoSe_2$) |
| | $MoTe_2$ | Mo $3d_{5/2}$ | 228.53 ($MoTe_2$) | 227.72 ($Mo^0$)<br>228.53 ($MoTe_2$) | 227.60 ($Mo^0$)<br>228.21 ($MoTe_2$)<br>232.40 ($MoO_x$) |
| | | Te $3d_{5/2}$ | 573.22 ($MoTe_2$)<br>576.19 ($TeO_2$) | 572.86 ($ScTe_x$)<br>573.20 ($MoTe_2$) | 572.86 ($MoTe_2$)<br>576.41 ($TeO_2$) |

after exfoliation and subsequent metal deposition in UHV and HV conditions are presented in Table 3.1. The probed region on the exfoliated $MoS_2$ sample used for Au deposition under UHV conditions exhibits a S:Mo ratio of 1.8:1, which remains constant after Au deposition. The *BE*s of both the Mo 3*d* and S 2*p* core levels as well as the stoichiometry reported here are consistent with previous results correlating XPS-indicated sulfur-deficient $MoS_2$ with associated regions exhibiting n-type behavior.[25,30]

*$MoSe_2$*

Reactions between Au and $MoSe_2$ are not thermodynamically favorable considering the $\Delta G°_{f,AuSe}$ (-33.0 kJ/mol) is far more positive than the $\Delta G°_{f,MoSe2}$ (-98.2 kJ/mol) $MoSe_2$.[53] Any reaction products that form during Au deposition on $MoSe_2$ are below the limit of XPS detection (Figure 3.2a), indicating Au forms a vdW interface with $MoSe_2$. The bulk $MoSe_2$ chemical states exhibit a 0.21 eV shift to lower *BE*, which is consistent with upward band bending induced by the high work function of Au (5.1 eV) relative to the $E_F$ (relative to the vacuum level) of $MoSe_2$. Weak orbital overlap between the Au *s*-orbitals, Mo *d*-orbitals, and Se *p*-orbitals in the valence of Au and $MoSe_2$ has been predicted[54] and corroborates the vdW Au–$MoSe_2$ interface detected in this work.

The Au 4*f* core level is detected 0.25 eV and 0.30 eV higher than that of the Au reference film after depositing Au in UHV and HV (Figure 3.2b), which is attributed to the volmer weber (VW)-like growth of Au on $MoSe_2$ (Figure 3.2b). Metal nanoparticles can exhibit significantly different ionization potentials from their bulk counterpart and therefore different core level *BE*s.[55] In addition, the full width at half maximum (*FWHM*) of the Au $4f_{7/2}$ core level detected after deposition in UHV and HV (0.73 eV) is in good agreement with that of the Au reference (0.74 eV) and therefore indicates only Au–Au bonds are detectable by XPS in the films deposited on $MoSe_2$. Adventitious species are detected on the exfoliated $MoSe_2$ surface in the corresponding O 1*s* and C 1*s* core level spectra in the form of hydroxyl (O–H), hydrocarbon (C–H), and $sp^3$ carbon (C–C) species (Figure 3.2c,d). Similar to the Au–$MoS_2$ system, reactions between adventitious species and Au are below the limit of XPS detection in the Au–$MoSe_2$ system.

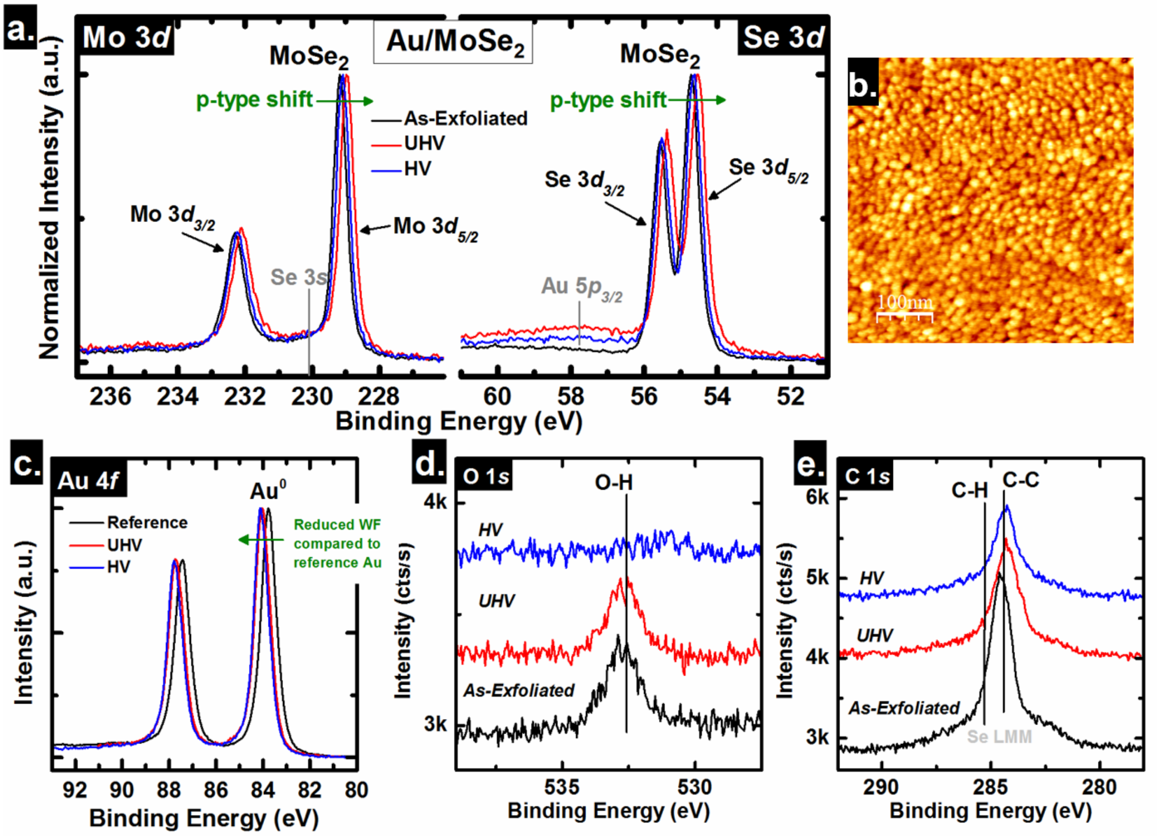

Figure 3.2. a) Mo 3*d*, Se 3*s*, Se 3*d*, Au 5$p_{3/2}$ c) Au 4*f*, d) O 1*s*, and e) C 1*s* core level spectra obtained from bulk $MoSe_2$ after exfoliation and subsequent Au deposition in UHV (*in–situ*) and HV (*ex–situ*). b) 500 × 500 nm AFM image obtained *ex–situ* after ~1 nm Au deposition on $MoSe_2$.

### *$MoTe_2$*

Reactions between Au and $MoTe_2$ have been ruled out in a previous XPS study, in which the hemispherical analyzer employed exhibited a resolution of 0.9 eV.[56] The spectrometer employed in XPS measurements performed here has a resolution of 0.05 eV and is therefore capable of detecting minute changes in the line shape of $MoTe_2$ core levels that could indicate the formation of reaction products.

After exfoliation, a Te:Mo ratio of 2.77 is detected from the $MoTe_2$ crystal indicating a Te-rich chemistry, which is commonly observed in $MoTe_2$ grown by chemical vapor transport (CVT).[23,57] This ratio is calculated using the integrated intensities of the $MoTe_2$ chemical states in the Te $3d_{5/2}$ and Mo 3*d* core levels corrected with the appropriate atomic sensitivity factors.[58] The Te $3d_{5/2}$ core level is more surface sensitive than the Te 4*d* core level at much lower *BE* and therefore may yield a higher Te:Mo ratio than that calculated with the Te 4*d* intensity. It is possible that excess Te accumulates near the surface of the bulk $MoTe_2$ during the cooling stage of the CVT growth process, which could also explain the Te excess detected in this work. However, previous work performed in the Wallace lab has commonly found excess Te in bulk $MoTe_2$ crystals (grown by CVT) after many exfoliations,[57] which indicates interstitial or intercalated Te is energetically favorable in $MoTe_2$.[23] A high *BE* chemical state is detected at 575.78 eV in addition to the $MoTe_2$ chemical state in the Te $3d_{5/2}$ core level indicating the presence of $TeO_2$ on the exfoliated surface. Te oxidation is likely exacerbated by the excess Te within the XPS sampling depth of the $MoTe_2$ surface considering $MoTe_2$ with a low surface defect density and a smaller concentration of excess Te is quite resistant to oxidation.[57] After depositing ~1 nm Au in either UHV or HV, additional chemical states are detected at 572.70 eV and 227.88 eV (low *BE* relative to the $MoTe_2$ chemical states) in the Te $3d_{5/2}$ and Mo $3d$ core levels indicating the formation of $AuTe_x$ and a Mo-based metallic species, respectively (Figure 3.3a). Reactions between Au and Te are exothermic ($\Delta G°_{f,AuTe2} = -65.0$ kJ/mol)[59] and therefore rationalizes reactions between Au and the excess Te in the $MoTe_2$ crystals employed in this work. The $AuTe_x$ chemical state exhibits a lower *BE* than the $MoTe_2$ chemical state in the Te $3d_{5/2}$ core level because the Au-Te electronegativity difference (0.59)[60] is less than that of Mo-Te (0.71).[60] Therefore, the $AuTe_x$ chemical state in the Te core levels will exhibit a *BE* closer to elemental Te than the $MoTe_2$ chemical state. The persistence of $TeO_2$ throughout the Au depositions is expected considering the endothermicity of the Au-O reaction and the sizeable bond dissociation energy (*BDE*) of Te–O (391.0 kJ/mol).[40] The low *BE* chemical state in the Mo $3d$ core level spectra obtained after Au deposition agrees with that of a Mo reference sample, indicating a metallic Mo-based species. A recent study found transition metal atoms that are deposited post-growth on Mo-based TMDs readily diffuse to interstitial sites near the $MoTe_2$ surface, leading to metallic inversion domain boundaries.[61] It is possible that some of the deposited Au behaves analogously in this work, resulting in local charge transfer around diffused Au and therefore the metallic Mo chemical state.

The Au exhibits VW-like growth on $MoTe_2$ (Figure 3.3b) and, similar to the Au–$MoSe_2$ system, the corresponding Au $4f$ core level is detected ~0.25 eV higher than the Au reference. A second chemical state is detected at 84.83 eV and 84.98 eV in the Au $4f$ core levels obtained after Au is deposited on $MoTe_2$ in UHV and HV, respectively, corresponding with the $AuTe_x$ intermetallic.

Adventitious species are detected on the $MoTe_2$ surface after exfoliation in the form of hydroxyls, hydrocarbons, and adventitious carbon (Figures 3.3 d, e). The presence of $TeO_2$ is corroborated by the chemical state detected below 531.0 eV after exfoliation and subsequent Au depositions, which is consistent with chalcogen-oxygen bonding. After Au deposition in UHV, the O 1*s* core level attenuates as expected. However, the $TeO_2$ chemical state intensity in the O 1*s* core level spectrum after Au deposition in HV is comparable with that detected on exfoliated $MoTe_2$, which suggests $MoTe_2$ oxidation occurs during Au deposition in HV as a result of the abundant supply of residual gases in the elastomer-sealed deposition tool, the Te-rich chemistry of the $MoTe_2$ and the relative instability of $MoTe_2$ compared with $MoS_2$ or $MoSe_2$ (see Section 3.5 for more details). Nonetheless, Au does not react with adventitious species on the $MoTe_2$ surface in agreement with the Au–$MoS_2$ and Au–$MoSe_2$ systems discussed above.

The vdW Au–$MoS_2$ and Au–$MoSe_2$ interfaces detected in this work are consistent with previous calculations.[10,12,16,17,54] In contrast with a previous study that ruled out Au–$MoTe_2$ reactions, the $AuTe_x$ intermetallic is detected at the Au–$MoTe_2$ interface in this work and its formation is thermodynamically favorable. One may expect the Au–TMD interface formed under UHV conditions to have fewer impurities than that formed under HV conditions, even for TMDs after exfoliation and prior to metal deposition.[15] Assuming ideal gas behavior, it is well known that approximately one monolayer of gas molecules will impact a surface each second in a chamber under a pressure of $10^{-6}$ mbar, whereas the same process should take approximately $10^3$ seconds under a pressure of $10^{-9}$ mbar.[62] Considering all depositions occurred at a rate less than 0.01 nm/s, it is quite obvious that there is a continuous supply of gas species at the surface throughout deposition in HV. In UHV, only a fraction of a monolayer of gas molecules will interact with $MoS_2$ *in–situ* throughout the entire experiment. Moreover, the relatively high flux of residual gas species present in HV would also be expected to enable interfacial reactions at much higher metal deposition rates as well. Therefore, the presence of adventitious organics at the metal–TMD

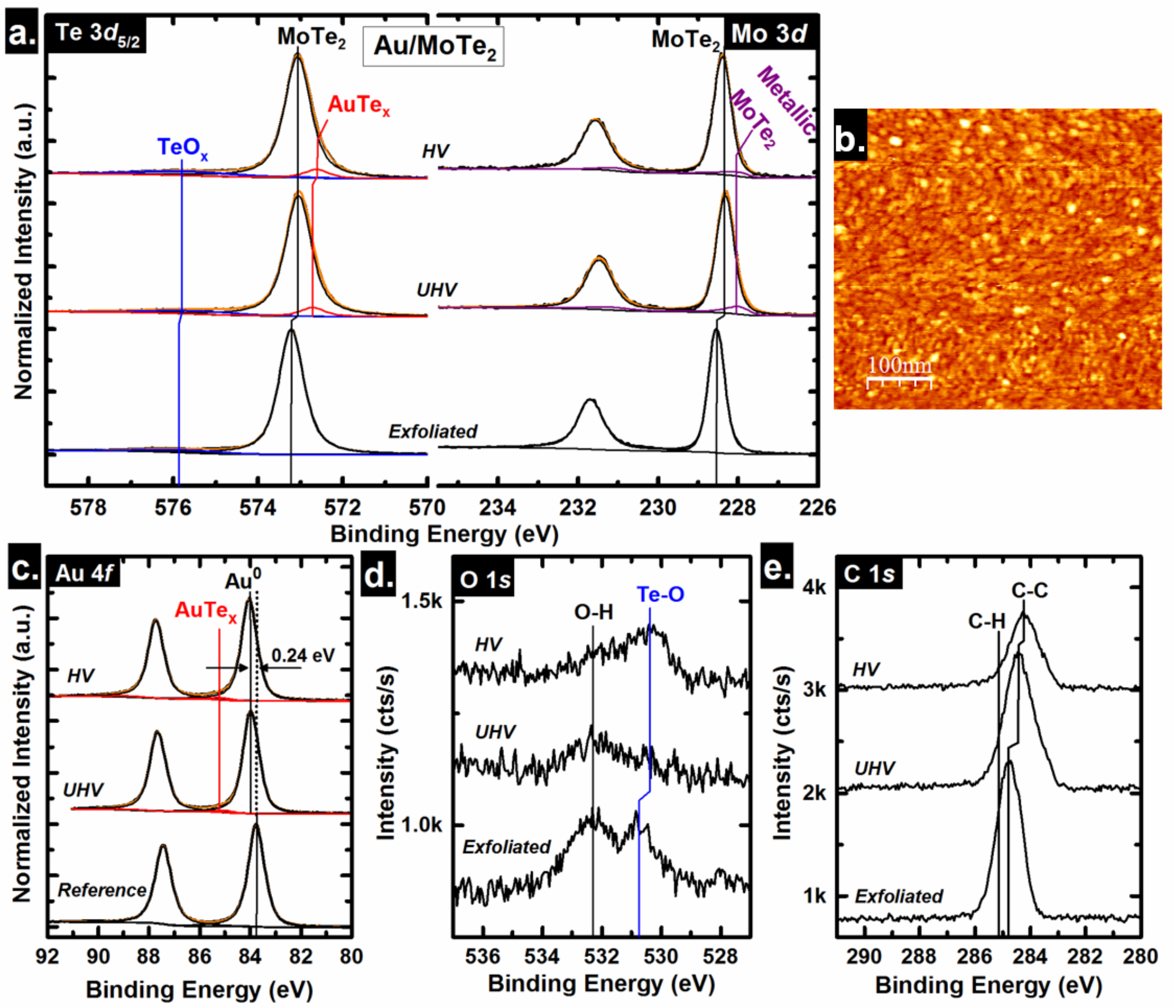

Figure 3.3. a) Te 3$d_{5/2}$, Mo 3*d*, c) Au 4*f*, d) O 1*s*, and e) C 1*s* core level spectra obtained from bulk $MoTe_2$ after exfoliation and subsequent Au deposition in UHV (*in–situ*) and HV (*ex–situ*). b) 500 nm$^2$ AFM image obtained *ex–situ* after ~1 nm Au deposition on $MoTe_2$.

interface should be expected and necessitates further investigation of their effects on contact performance. In other experiments discussed in Chapter 7, more reactive contact metals bond with adventitious species on TMD surfaces. The presence of metal carbide and metal oxide species at the contact–TMD interface can affect the contact performance significantly and will be addressed in detail in Chapters 4 and 7.

### 3.4.2 Ir

*MoS₂*

Polycrystalline Ir, with a work function of 5.3 eV, has been widely described as a noble metal due to its high work function and filled 4*f* valence shell.[63,64] The $\Delta G^\circ_{f,IrS2}$ and $\Delta G^\circ_{f,Ir2S3}$ (-66.0 and -73.6 kJ/mol, respectively),[65] suggest that a covalent Ir–$MoS_2$ interface is not thermodynamically favorable as these values are positive relative to that of $MoS_2$. One might therefore expect Ir, like Au, to form a vdW interface with $MoS_2$. Figure 3.4 presents the results from Ir deposition on bulk $MoS_2$ in UHV and HV.

Interestingly, reaction products are detected at the Ir–$MoS_2$ interface according to the chemical states in addition to those of bulk $MoS_2$ that appear in the Mo 3*d* and S 2*p* core level spectra after Ir deposition in UHV and HV (Figure 3.4a). $IrS_x$ forms from Ir reduction of $MoS_2$ in both UHV and HV (Figures 3.4a, c). The chemical state detected at high BE in the S 2*p* core level spectra obtained after Ir deposition exhibits a *FWHM* comparable with that of the bulk $MoS_2$ chemical state. This suggests one single reaction product forms from the reactions between Ir and $MoS_2$ rather than two separate $IrS_x$ and $MoS_x$ species as is labeled in Figure 3.4a. The formation of a ternary Ir-based intermetallic in the Ir–$MoS_2$ system is chemically congruent with other Ir–TMD systems and will be discussed in greater detail at the end of this Section.

The S 2*p* core level attenuates less than the Mo 3*d* core level after depositing a uniform Ir film (Figure 3.4b). This implies that sulfur diffusion occurs into the deposited Ir film, and is further evidence for the formation of Ir–S bonds. The use of the term "diffusion" could imply that bonding does not occur between Ir and sulfur as sulfur moves up into the Ir film, however the detection of Ir–S bonding in the Ir 4*f* and S 2*p* core level spectra after Ir deposition in both UHV and HV

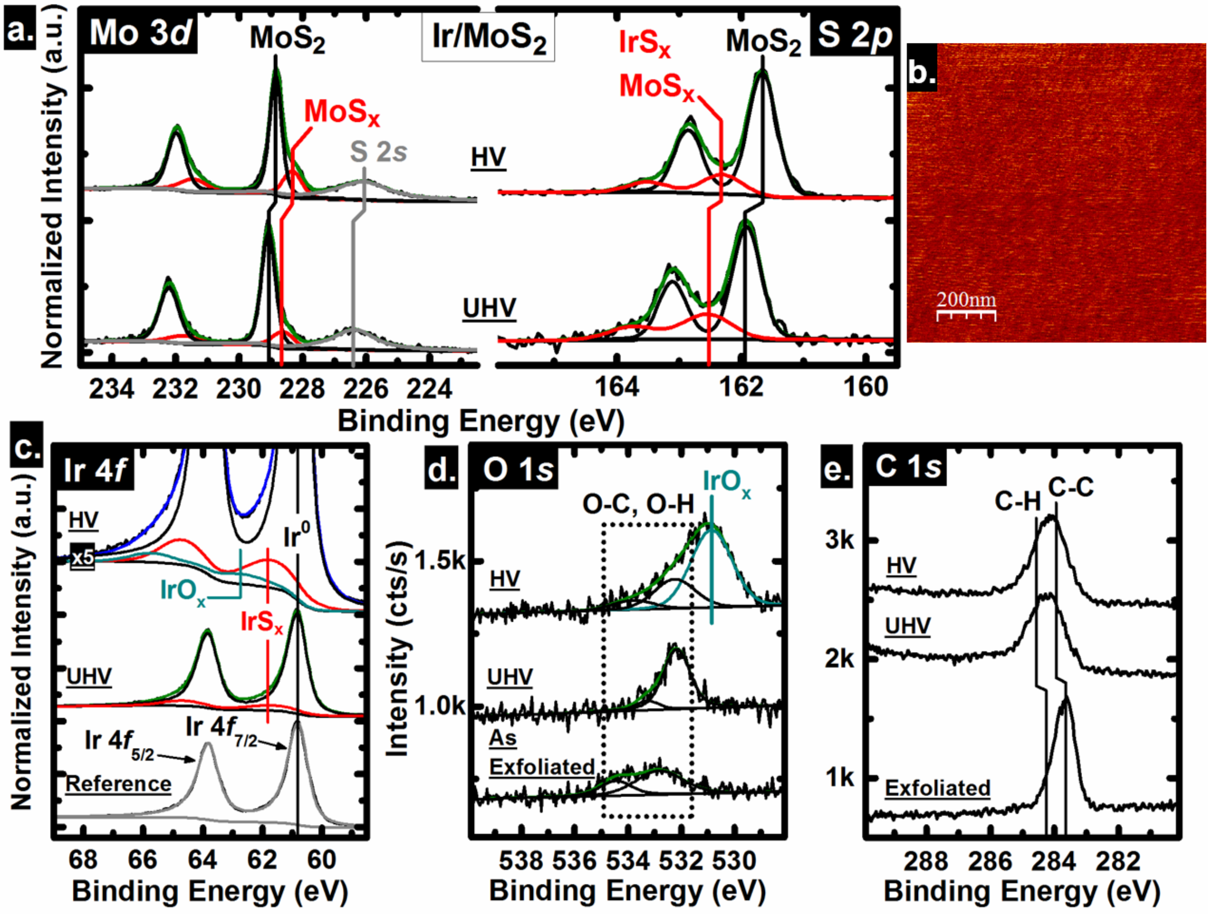

Figure 3.4. a) Mo 3*d*, S 2s, S 2*p*, c) Ir 4*f*, d) O 1*s*, and e) C 1*s* core level spectra obtained from bulk $MoS_2$ after exfoliation and subsequent ~1 nm Ir deposition in UHV (*in–situ*) or HV (*ex–situ*). The spectra in a) and c) are normalized to the Mo $3d_{5/2}$, S $2p_{3/2}$, and Ir $4f_{7/2}$ core levels, respectively. The intensity of the 'HV' spectrum in c) is multiplied by 5 to ensure the doublet corresponding to $IrO_x$ is clearly visible. b) 1 × 1 μm AFM image obtained after depositing ~1 nm Ir on $MoS_2$ in UHV showing the atomically flat surface.

indicates that such bonding is detected as a final reaction product. Elemental sulfur (S–S bonding) has been reported with a *BE* of ~164.0 eV.[66] There are no chemical states detected near this binding energy in the S 2*p* core level spectra following Ir deposition under either UHV or HV conditions that would suggest the presence of S–S bonding.

Observation of reactions between Ir and $MoS_2$, despite the unfavorable thermodynamics of the system, suggests that an additional kinetic reaction mechanism is necessary to reduce the formation energy of Ir–S bonds. DFT modeling indicates wavefunction modulation can result in significant charge displacement in both the metal and $MoS_2$ in the vicinity of the metal–$MoS_2$ interface, even for a noble, high work function metal.[20] Charge redistribution across an interface which involves a high work function metal and defect free $MoS_2$ is presumably not substantial enough to favor interfacial reactions due to metal wavefunction screening by sulfur atoms. Of course, exfoliated $MoS_2$ has a significant defect density with defects exhibiting a range of possible morphologies from single sulfur vacancies[38,66] to clusters of sulfur vacancies up to ~5 nm in diameter.[31] Near these defects, substantial charge transfer between Ir and $MoS_2$ through Mo–Ir *d*-orbital overlap could shift the $\Delta G^{\circ}_{f,IrxSy}$ more negative than that of $MoS_2$, promoting reactions. $MoS_2$ reduction would result in chemical states exhibiting unique BEs compared to the bulk Mo 3*d* and S 2*p* states, which are represented by the high *BE* state in the Mo 3*d* core level and the low *BE* state in the S 2*p* core level spectra in Figure 3.4a. A similar effect is not observed in the Au–$MoS_2$ system due to the *s*-orbital valence of Au. Wavefunction overlap arguments for enhanced favorability of Ir reactions with $MoS_2$ raises the question as to why Au and Ir differ in the nature of the interfaces each forms with $MoS_2$ despite considering both as noble metals. Interactions between *s*-orbital metals, such as Au, and $MoS_2$ are weak, whereas *d*-orbital metals, such as Ir, interact quite strongly with $MoS_2$ as Mo also has a *d*-orbital valence shell. The enhanced interaction between Ir and $MoS_2$ contrasts with that between Au and $MoS_2$ and is quantified by DFT calculations, which predict the equilibrium metal–$MoS_2$ interfacial gap to be 0.29 nm between Au and $MoS_2$ and 0.24 nm between Ir and $MoS_2$, which is indicative of a stronger orbital interaction.[14] This argument rationalizes the reactions observed between Ir and $MoS_2$ and the contrasting vdW interface formed between Au and $MoS_2$.

Figure 3.4c displays the normalized Ir 4*f* spectra obtained from a reference Ir film and from Ir deposited on $MoS_2$ in UHV and HV. Metallic Ir, which is detected at 60.76 eV, is the dominant species in the deposited film and the associated chemical state exhibits a typical high *BE* "tail" characteristic of core-hole screening effects.[48] This is in good agreement with the previously reported *BE* of an evaporated Ir film of 60.75 eV.[67] The additional state in both the UHV and HV Ir 4*f* core level spectra in Figure 3.4c at 61.65 eV is attributed to the formation of $IrS_x$-based intermetallic. Electronegativity arguments suggest the bond character of $IrS_x$, and therefore the binding energy of the sulfur state in the $IrS_x$-based intermetallic, will be quite similar to that of the sulfur state in $MoS_x$. The high binding energy doublet found in both S 2*p* core level spectra in Figure 3.4a are attributed to both Ir–S and Mo–S (reduced $MoS_2$) bonds, which constitute the ternary Ir-based intermetallic. A third state is detected in the Ir 4*f* core level at 62.69 eV after depositing Ir *ex–situ* in HV. This is due in part to both *ex-situ* air exposure induced surface oxidation of Ir and also *in-situ* oxidation as Ir is deposited in HV at $10^{-6}$ mbar.

This assignment is supported by a state detected at 530.84 eV in the O 1*s* core level spectrum after Ir deposition in HV (Figure 3.4d), which is consistent with a transition metal oxide.[68] In contrast, there are no states detected below 531.0 eV in the O 1*s* core level spectrum after depositing ~1 nm Ir in UHV, illustrating the absence of a detectable metal-oxygen bond formation. Ir oxidation is exothermic in the presence of atmospheric gases ($\Delta G^{\circ}_{f,IrO2}$ = -137.0 kJ/mol).[65] It is likely that the Ir–O reaction is self-limiting, considering the majority of the deposited metallic Ir film is preserved after deposition in HV. Further work is required to confirm the mechanism proposed above as the driving force for a covalent Ir–$MoS_2$ interface, but nonetheless reactions are in fact detected regardless of deposition chamber ambient.

Carbon in the form of C–C and C–H species is detected on the $MoS_2$ surface after exfoliation and Ir deposition in UHV due to the brief air exposure. However, no chemical states are detected in any of the C 1*s*, Mo 3*d*, S 2*p*, or Ir 4*f* core level spectra that would indicate the formation of reaction products involving carbon.

### *$MoSe_2$*

The formation energy of iridium selenide is not known. However, the fugacity of Se required for iridium selenide formation from the elemental constituents is higher than that of $MoSe_2$ and therefore the endothermicity of the Ir–Se reaction can be inferred.[59] The Mo 3*d* core level obtained from $MoSe_2$ after exfoliation is convoluted by the Se 3*s* core level. One chemical state is detected in each of the Mo 3*d* and Se 3*d* core level spectra corresponding with bulk $MoSe_2$ (Figure 3.5a). Significant concentrations of defects are expected on the surface of CVT $MoSe_2$ crystals according to a recent STM study.[22] However, the close fit of the Mo 3*d* and Se 3*d* core level spectra achieved with a single chemical state in each case indicates the defect densities in the $MoSe_2$ crystals employed in this work are below the limit of XPS detection. After depositing ~1 nm Ir on $MoSe_2$ in UHV and HV, an additional chemical state is detected at low (high) *BE* in the Mo 3*d* (Se 3*d*) core level spectrum indicating the formation of a ternary $Mo_xIr_ySe_z$ species as a result of reactions between Ir and $MoSe_2$. It is also possible that two separate $IrSe_x$ and $MoSe_x$ reaction products form, which would result in two unique chemical states at high *BE* from the bulk $MoSe_2$ chemical state in the Se 3*d* core level spectrum. $MoSe_x$, which would as Ir scavenges Se from the $MoSe_2$, should exhibit a chemical state closer to elemental Se (e.g., at higher *BE*) than $MoSe_2$ in the Se 3*d* core level. The most common stable allotropes of iridium selenide ($IrSe_2$, $Ir_2Se_3$)[59] would both exhibit chemical states in the Se 3*d* core level closer to elemental Se (e.g., higher *BE*) than the $MoSe_2$. The smaller electronegativity difference between Se and Ir (0.95) compared with Se and Mo (1.18) suggests the Se–Ir bond is more covalent than the Se–Mo bond, which would manifest as a smaller *BE* offset of the $Se^{2-}$ chemical state in $IrSe_2$ than that in $MoSe_2$.[60] Therefore, the broad chemical state detected at high *BE* in the Se 3*d* core level could represent a convolution of $IrSe_x$ and $MoSe_x$ chemical states, however it is not reasonable to arbitrarily distinguish between the two without more detailed characterization of the bonding environment at the Ir–$MoSe_2$ interface (e.g., studying the X-ray absorption fine structure). A small concentration of $MoO_x$ is detected after *ex–situ* Ir deposition in HV, which is indicated by the low intensity chemical state detected in the corresponding Mo 3*d* core level. $MoO_x$ formation in air is a highly exothermic process and therefore should be expected in this work considering the ~1 nm metal films employed could contain pinholes through which adventitious species can access the reaction products for additional reactions. In addition, the reactions presumably involve interdiffusion that could promote partial oxidation of the reactants products.

The Ir 4*f* core level spectra obtained after depositing Ir on $MoSe_2$ in UHV and HV are dominated by a doublet with high *BE* tail and a *BE* that is consistent with metallic Ir (Figure 3.5b). An additional chemical state is detected at 61.62 eV and 61.69 eV after deposition in UHV and HV, respectively, corresponding with the $Mo_xIr_ySe_z$ chemical state. After depositing Ir *ex–situ* in HV, $IrO_x$ is also detected in the corresponding Ir 4*f* core level spectrum at 63.45 eV.

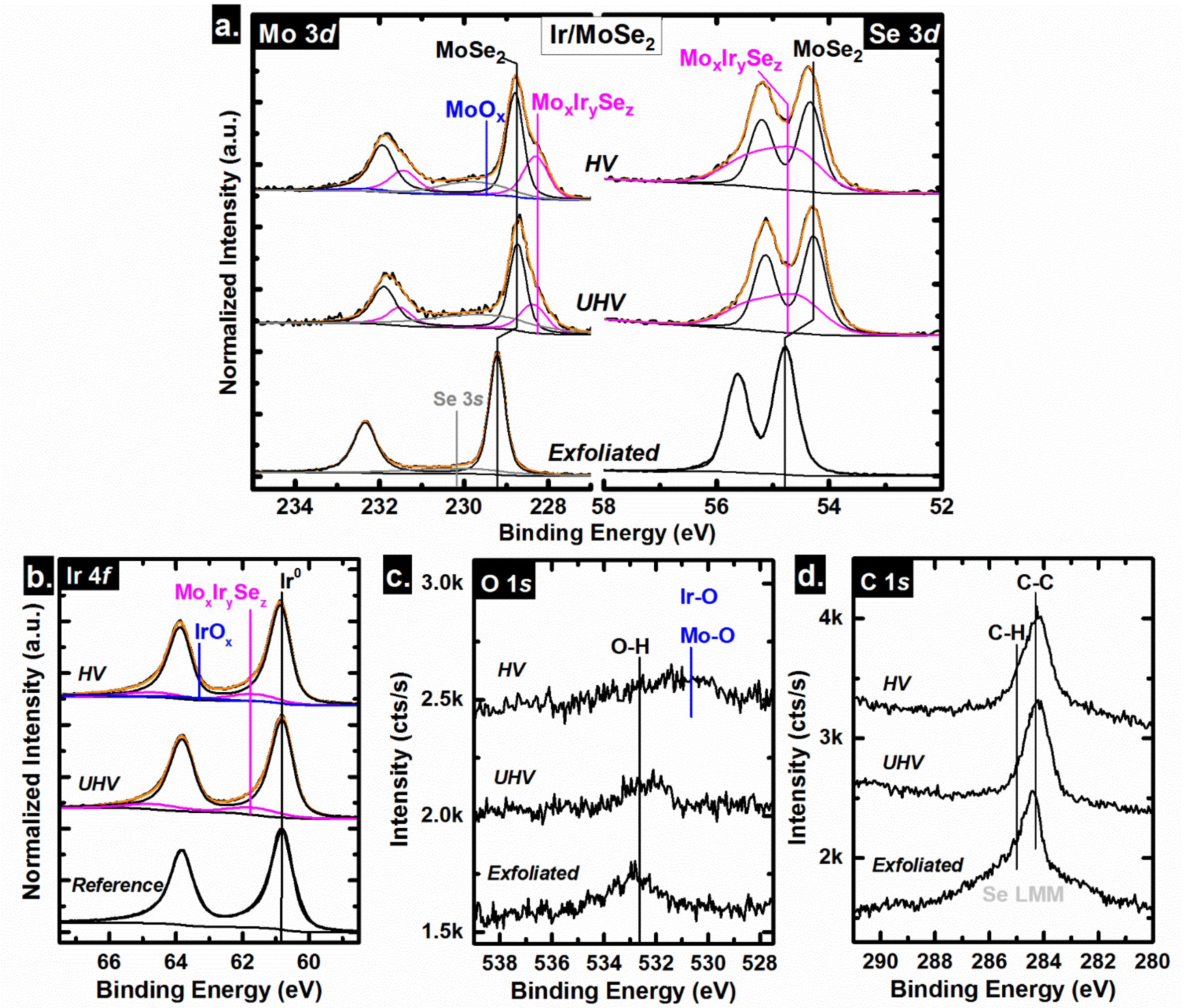

Figure 3.5. a) Mo 3*d*, Se 3*s*, Se 3*d*, b) Ir 4*f*, c) O 1*s*, and d) C 1*s* core level spectra obtained from bulk $MoSe_2$ after exfoliation and subsequent ~1 nm Ir deposition in UHV (*in–situ*) and HV (*ex–situ*).

Similar to the Ir–$MoS_2$ system, Ir does not react with the oxygen or carbon based adventitious species on the $MoSe_2$ surface, which is indicated by an absence of iridium carbide or iridium oxide chemical states in the O 1*s* or C 1*s* core level spectra obtained *in–situ* after depositing Ir in UHV (Figure 3.5c,d). However, a feature is detected in the O 1*s* core level at ~530.5 eV, which is presumably a convolution of the $MoO_x$ and $IrO_x$ chemical states and corroborates the formation of transition metal oxide species during Ir deposition in HV and/or during the *ex–situ* transfer from the elastomer-sealed deposition tool to the UHV cluster tool.

*MoTe$_2$*

Before depositing Ir in UHV, the exfoliated MoTe$_2$ crystal exhibits a Te:Mo ratio of 2.86, which is slightly higher than that detected before Au deposition in UHV. A higher Te concentration and therefore a more defective MoTe$_2$ sample (within the XPS sampling depth) promotes surface oxidation in air. In addition to the bulk MoTe$_2$ chemical states, TeO$_2$ and MoO$_x$ chemical states are detected after exfoliating the MoTe$_2$ in the corresponding Te 3$d_{5/2}$ and Mo 3$d$ core levels (Figure 3.6a). After depositing ~1 nm Ir in UHV, additional chemical states are detected in the Te 3$d_{5/2}$ and Mo 3$d$ core level spectra at high BE and low BE from the bulk MoTe$_2$ chemical states, respectively, indicating the formation of a Mo$_x$Ir$_y$Te$_z$ intermetallic. In addition, the MoTe$_2$ chemical states shift 0.24 eV to lower *BE* corresponding with a $E_F$ shift of equal magnitude towards the valence band edge and therefore downward band bending (see Section 3.5 for further discussion). After depositing Ir *ex–situ* in HV, analogous Mo$_x$Ir$_y$Te$_z$ chemical states are detected in the Te 3$d_{5/2}$ and Mo 3$d$ core level spectra. However, the intensity of the intermetallic state in the Te 3$d_{5/2}$ core level is roughly half the intensity of the same state detected after Ir deposition in UHV. The significant decrease in Te concentration in the Mo$_x$Ir$_y$Te$_z$ intermetallic formed in HV is likely facilitated by the highly exothermic reaction between Te and O to form TeO$_2$, which is detected at high BE in the corresponding Te 3$d_{5/2}$ spectrum. A small concentration of MoO$_x$ is also detected in the Mo 3$d$ core level obtained after Ir deposition in HV.

The chemical states detected in the Ir 4*f* core level spectra after depositing Ir on $MoTe_2$ in UHV and HV are analogous to the corresponding spectra obtained in the Ir–$MoS_2$ and Ir–$MoSe_2$ systems and will therefore not be discussed in detail.

Unlike the exfoliated $MoS_2$ and $MoSe_2$ crystals, C–O and C=O bonds are detected on the exfoliated $MoTe_2$ prior to depositing Ir in UHV (Figures 3.6 c, d). To study the interface chemistry as a function of deposition chamber base pressure, metals were deposited on a number of TMD crystals fixed to the same plate by carbon tape (see Appendix A for details). The exfoliated surface area of the $MoTe_2$ crystal employed in this work is significantly smaller than the $MoS_2$ or $MoSe_2$ crystals. It is therefore likely that the C–O and C=O bonds are detected in small concentrations from the carbon tape fixing the $MoTe_2$ to the plate for analysis. In addition, features are detected below 531.0 eV in the O 1*s* spectrum obtained from the exfoliated $MoTe_2$, which corroborate the presence of $MoO_x$ and $TeO_x$ on the initial surface. Reactions between Ir and the preexisting $MoTe_2$ surface oxides are not thermodynamically or kinetically favorable. After depositing Ir in HV, the low *BE* feature in the corresponding O 1*s* spectrum is roughly 4× the intensity of the analogous metal oxide chemical states in the O 1*s* spectra obtained after Ir deposition on $MoS_2$ and $MoSe_2$ in HV, which corroborates the relative instability of the $Mo_xIr_yTe_z$ intermetallic in the presence of oxidizing gases.

Mo and Te oxidation detected after *ex–situ* Ir deposition in HV suggests the $Mo_xIr_yTe_z$ intermetallic is less stable than the analogous intermetallic species that form at the Ir–$MoS_2$ and Ir–$MoSe_2$ interfaces. In the Ir–$MoTe_2$ system, the $Mo_xIr_yTe_z$ chemical state is detected at a higher *BE* from the bulk $MoTe_2$ chemical state in the Te $3d_{5/2}$ core level spectrum (i.e., farther from the expected *BE* of elemental Te than the bulk $MoTe_2$ state), which contrasts the intermetallic chemical

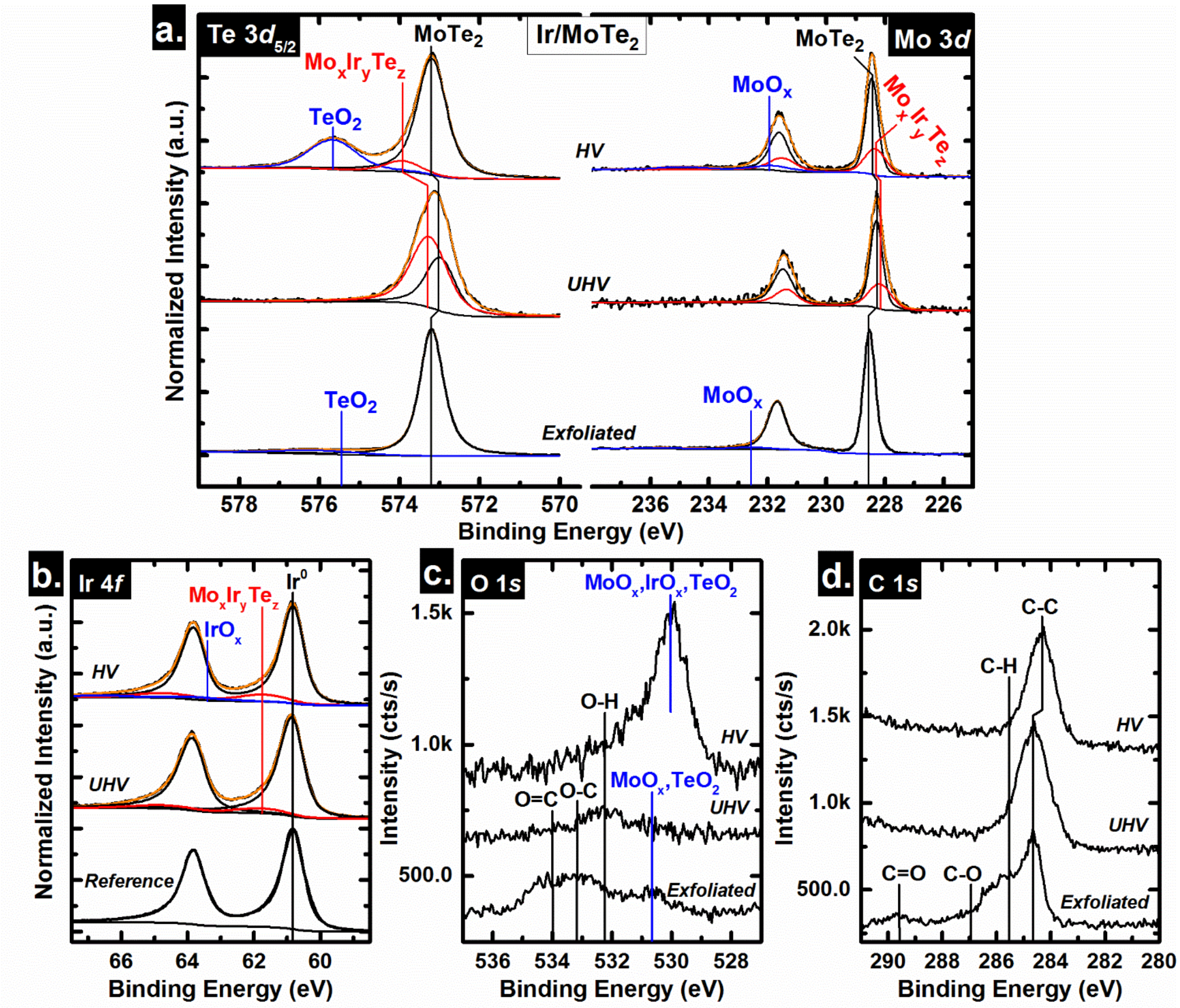

Figure 3.6. a) Te $3d_{5/2}$, Mo 3*d*, b) Ir 4*f*, c) O 1*s*, and d) C 1*s* core level spectra obtained from bulk $MoTe_2$ after exfoliation and subsequent ~1 nm Ir deposition in UHV (*in–situ*) and HV (*ex–situ*).

state in the chalcogen core levels detected after Ir deposition on $MoS_2$ and $MoSe_2$. The higher density of Te *p*-orbitals involved in bonding with transition metals could lead to a greater degree of charge transfer with Ir as a result of the observed reactions compared with the charge transfer that occurs in Ir–S or Ir–Se bonding.[69] This Ir–chalcogen charge transfer trend would explain the increased oxidation state of the $Mo_xIr_yTe_z$ intermetallic relative to the $MoTe_2$ state in the Te $3d_{5/2}$ spectrum observed here.

### 3.4.3 Cr

*$MoS_2$*

The interface chemistry between chromium, often employed as an "adhesion layer" in metal contacts to semiconductors, and TMDs is of particular interest. In the context of 2D devices, one notes that the atomic layer thickness of such semiconductors presents a very significant departure from the typical metal-(bulk) semiconductor contacts. Figure 3.7 shows the XPS spectra obtained after depositing Cr on $MoS_2$ in UHV and HV exhibiting the formation of interfacial reaction products, specifically the reduction of $MoS_2$ to form $CrS_x$ and metallic Mo.

In the Mo 3*d* core level spectra shown in Figure 3.7a, the presence of an additional state exhibiting an asymmetric line shape is found at 227.86 eV and 227.81 eV following Cr deposition under UHV and HV, respectively. These binding energies are in agreement with that previously reported of evaporated Mo films and the Mo reference prepared in this work.[68,70]

$CrS_x$ formation is evidenced by the additional states detected at low *BE* (blue peaks) appearing in the respective S 2*p* core level spectral envelope following Cr deposition under UHV and HV (Figure 3.7a). When Cr is deposited onto $MoS_2$, Cr–S bond formation is thermodynamically more favorable than the persistence of Mo–S bonds considering the $\Delta G^\circ_{f,MoS2}$ is significantly more positive relative to the $\Delta G^\circ_{f,Cr2S3}$ (-148.2 kJ/mol).[71] The electronegativity difference between Cr and S, which is more than twice that between Mo and S, is also consistent with the chemical shift assigned to $CrS_x$. Because Cr is significantly less electronegative than Mo, $CrS_x$ has a more ionic bond character resulting in the binding energy of the $S^{2-}$ state in $CrS_x$ appearing lower than that of $S^{2-}$ in $MoS_2$. Interestingly, the new state appearing in each respective S 2*p* core level and Mo 3*d* core level in Figure 3.7a exhibit virtually the same *BE* shift from the bulk $Mo^{4+}$ and $S^{2-}$ states of

‘$MoS_2$’ in each spectra. This suggests that the reaction products formed at the Cr–$MoS_2$ interface are chemically congruent, regardless of reactor base pressure. The reactions reported here are in agreement with previous observation of reactions when Cr is deposited on $MoS_2$ under UHV conditions.[13]

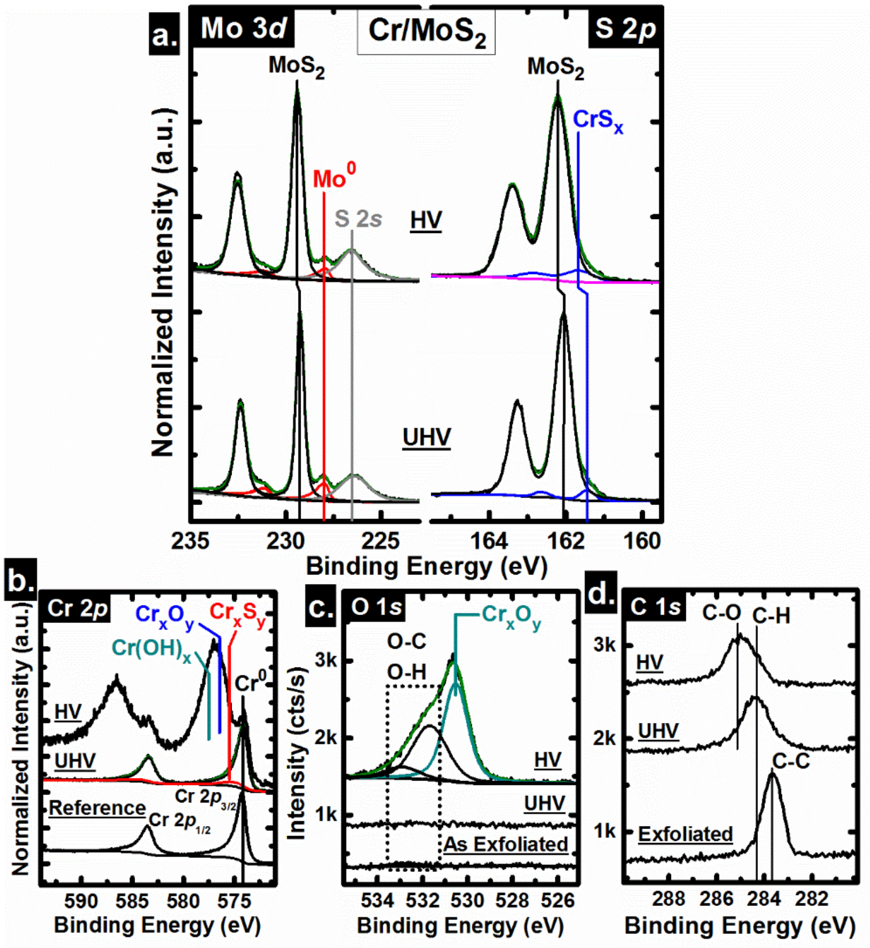

Figure 3.7. a) Mo 3*d*, S 2*s*, S 2*p*, b) Cr 2*p*, c) O 1*s*, and d) C 1*s* core level spectra obtained from bulk $MoS_2$ after exfoliation and subsequent ~1 nm Cr deposition in UHV (*in–situ*) or HV (*ex–situ*). The high BE feature in in Cr 2*p* core level is convoluted by multiplet meaks from the $Cr^{3+}$ oxidation state, but are not labeled here for convenience.

The Cr 2*p* core level spectra in Figure 3.7b clearly shows that Cr films deposited under different base pressures exhibit pronounced differences in their chemical constituents. The Cr 2*p* core level spectrum obtained after depositing Cr in UHV is dominated by the presence of metallic Cr, which is indicated by the high degree of asymmetry of the doublet peaks, consistent with core-hole screening effects.[45] In addition to metallic Cr, a small shoulder appears at higher *BE* corresponding with the $CrS_x$ intermetallic formed at the Cr–$MoS_2$ interface. When Cr is deposited under HV conditions, a small concentration of metallic Cr is detected at 573.76 eV, but the Cr 2*p* core level spectrum is dominated by an extremely broad doublet centered around 576.80 eV in the Cr $2p_{3/2}$ core level. This broad doublet is a convolution of chromium oxide, chromium hydroxide, multiplet peaks associated with the $Cr^{3+}$ oxidation state,[68] and a relatively low intensity $CrS_x$ chemical state.[72] It is difficult to deconvolve individual chemical states from the broad doublet detected in the HV Cr 2*p* core level spectrum (see Chapter 5 for a detailed deconvolution). However, the identity of individual states within the broad feature can be inferred. The lower *BE* state in the HV S 2*p* core level represented by the blue doublet (Figure 3.7a) indicates the presence of $CrS_x$ and the intense peak centered around 530.50 eV in the HV O 1*s* core level indicates the formation of a significant concentration of transition metal oxide and hydroxide species (Figure 3.7c).

A small concentration of adventitious oxygen is detected on exfoliated $MoS_2$ near the limit of detection according to the chemical state at 532.80 eV in the corresponding O 1*s* spectrum (Figure 3.7c). In contrast, the *BE* of the state in the HV O 1*s* core level spectrum at 530.64 eV confirms the presence of a high concentration of chromium oxide, which is in agreement with thermodynamically favorable metallic chromium oxidation in air. The $\Delta G°_{f,Cr2O3}$ and $\Delta G°_{f,Cr3O4}$ (-352.6 and -382.8 kJ/mol, respectively)[71] are far more negative than the $\Delta G°_f$ of any sulfide species detected in the Cr–$MoS_2$ system. Such states are consistent with oxygen “gettering” from the deposition environment, as well as any adventitious surface contamination. The high concentration of states corresponding to O–C and O–H bonds in the HV O 1*s* core level are therefore due in part from the presence of these species in appreciable concentration in the background gas in HV and also from the air exposure during transfer from the elastomer-sealed deposition tool to the analysis chamber.

Recently, McDonnell et al.[29] demonstrated that Ti preferentially oxidizes *in-situ* when deposited via e-beam on $MoS_2$ in a HV environment (typical of fabrication tool vacuum conditions) instead of reacting with the substrate. It is therefore reasonable to assume that $Cr_xO_y$ also forms *in-situ* when Cr is deposited under HV conditions regardless of deposition rate (see Chapters 4 and 7 for concrete evidence of *in–situ* oxidation of early transition metals during deposition in HV).[73] Despite the highly exothermic formation of $Cr_xO_y$, a small concentration of metallic Cr is preserved at the Cr–$MoS_2$ interface formed in HV. In contrast, there are no states detected in the UHV O 1*s* core level spectrum below a *BE* of 531 eV (Figure 3.7c), indicating the Cr–O bonds that may form in UHV are below the XPS detection limit. Thus, the deposition ambient plays an important role in the chemical nature of the contact interface, and is expected to impact the electronic properties. Furthermore, Schottky barriers in $MoS_2$ based devices fabricated in typical cleanroom deposition tools with a Cr adhesion layer at the contact-$MoS_2$ interface have likely been extracted without considering the true chemistry at the interface, evidenced by the significant concentration of chromium oxide detected in the Cr film deposited on $MoS_2$ under HV conditions. Carbon present as C–C and C–H is detected on the surface of exfoliated $MoS_2$ as a result of air exposure after exfoliation and also after depositing Cr in both UHV and HV. No chemical states which would suggest the formation of reaction products involving carbon are detected in any of the related core level spectra (C 1*s*, Mo 3*d*, S 2*p*, Cr 2*p*). However, chromium carbide formation from elemental Cr(*s*) and C(*s*) is an exothermic process ($\Delta G^{\circ}_{f,Cr3C2}$ = -10.1 kJ/mol)[74] and therefore the presence of Cr–C bonds at the Cr contact interface cannot be confidently ruled out. Another low work function metal, Ti, reacts with carbonaceous photoresist residues on the $MoS_2$ surface left behind from the lithographic patterning process in a typical FET fabrication flow (see Chapter 4, Appendix D), which suggests Cr may also react with carbonaceous species. Further experimentation is needed to determine conditions under which reactions between Cr and organics will readily occur on the $MoS_2$ surface.

### *MoSe₂*

The formation of chromium selenide as a result of reactions between Cr and $MoSe_2$ is thermodynamically favorable considering the $\Delta G^{\circ}_{f,MoSe2}$ (-98.2 kJ/mol)[53] is more positive than the $\Delta G^{\circ}_{f,Cr2Se3}$ (-175.1 kJ/mol).[75] Cr completely reduces the $MoSe_2$ at the interface to form metallic Mo and $CrSe_x$ during deposition in either UHV or HV (Figure 3.8a), which is chemically congruent to the Cr–$MoS_2$ interface detected in this work.

The chemical states detected in the Cr 2*p*, O 1*s*, and C 1*s* core level spectra after Cr deposition on $MoSe_2$ in UHV and HV are also chemically congruent with those detected in the Cr–$MoS_2$ system discussed above. Therefore, the corresponding spectra are displayed in Figures 3.8 b-d but will not be discussed further.

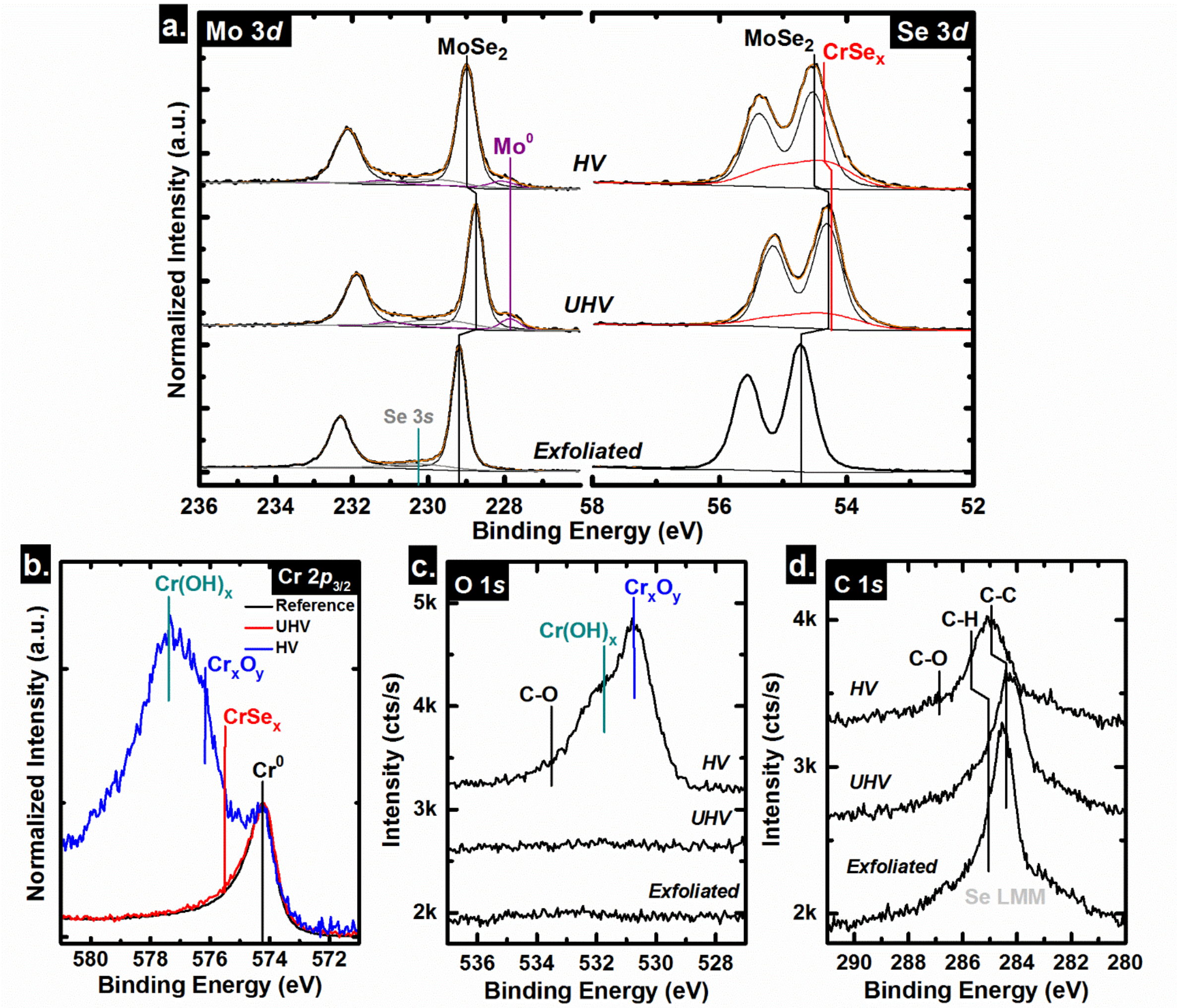

Figure 3.8. a) Mo 3*d*, Se 3*s*, Se 3*d*, b) Cr 2$p_{3/2}$, c) O 1*s*, and d) C 1*s* core level spectra obtained from bulk MoSe$_2$ after exfoliation and subsequent ~1 nm Cr deposition in UHV (*in–situ*) and HV (*ex–situ*).The Cr 2$p_{3/2}$ spectra in b) are normalized to the low binding energy metallic Cr chemical state, Cr$^0$.

### *MoTe$_2$*

Reactions between Cr and crystalline, stoichiometric 2H-MoTe$_2$ are slightly endothermic considering the $\Delta G°_{f,CrTe1.029}$ (-70.3 kJ/mol)[76] is slightly more positive than the $\Delta G°_{f,MoTe2}$ (-77.9 kJ/mol).[77] The free energies of formation of chromium telluride compounds with other, potentially more stable stoichiometries are not known for comparison. It is therefore possible that the formation of a more stable chromium telluride compound (e.g., Cr$_2$Te$_3$) could be thermodynamically favorable compared with the persistence of $MoTe_2$ when in contact with Cr. Nonetheless, the reaction between elemental Cr(*s*) and Te(*s*) is exothermic. The Te:Mo ration detected after exfoliating the $MoTe_2$ is ~2.8. Therefore, the formation of $CrTe_x$ at the Cr–$MoTe_2$ interface is thermodynamically favorable due to the Te excess available for the exothermic reaction with Cr. $TeO_2$ is detected at high *BE* in the Te $3d_{5/2}$ core level after exfoliation, which is expected considering the Te excess detected in the $MoTe_2$. Additional chemical states are detected at low *BE* in the Te $3d_{5/2}$ and Mo 3*d* core level spectra obtained after depositing Cr in UHV and HV indicating significant reactions occur between Cr and $MoTe_2$ regardless of deposition chamber base pressure (Figure 3.9a). The additional chemical state in the Mo 3*d* spectra obtained after depositing Cr in UHV and HV exhibits an asymmetric line shape with high *BE* tail (characteristic of a metallic species) and a *BE* close to that expected of metallic Mo. Therefore, Cr not only reacts with the excess Te in $MoTe_2$ but also completely reduces the $MoTe_2$ near the interface to form metallic Mo and $CrTe_x$. The low BE state detected in the corresponding Te $3d_{5/2}$ spectra exhibits a BE near that of elemental Te, which indicates the $CrTe_x$ is a metallic species. Chromium telluride is known to exhibit metallic behavior and exhibits permanent magnetic anisotropy that could be useful in future memory technology.[78] In addition, the metallic behavior of the $CrTe_x$ reaction product at the Cr–$MoTe_2$ interface may benefit carrier injection and more efficiently preserve the spin state of injected carriers, which is commonly an inefficient process.[79]

The Te $3d_{5/2}$ core level is convoluted by the Cr $2p_{3/2}$ core level at high *BE*. The Cr $2p_{3/2}$ core level obtained from a Cr reference film is normalized and displayed on top of the Te $3d_{5/2}$ spectrum obtained after exfoliating $MoTe_2$ for comparison. The spectra displayed in the left panel of Figure 3.9a obtained after depositing Cr in UHV and HV are normalized to the Te $3d_{5/2}$ core level. The

Cr $2p_{3/2}$ core level spectrum obtained after depositing Cr in UHV is convoluted by the metallic Cr and $CrTe_x$ chemical states, but these are not individually resolvable as they exhibit similar *BE*s due to the shared metallic behavior. It is likely that Cr scavenges oxygen from $TeO_2$ on the $MoTe_2$ surface as it is deposited in UHV, but any Cr–O bonds that form *in–situ* are below the XPS detection limit. This is reasonable considering the initial concentration of oxygen on the $MoTe_2$ surface is also near the limit of detection and the corresponding chemical state intensities are attenuated by the deposited Cr film. Cr readily oxidizes when deposited in HV according to the appearance of a large feature at high *BE* in the corresponding Cr $2p_{3/2}$ spectrum. Cr oxidation is more thermodynamically favorable than the formation of the most stable tellurium or molybdenum oxides ($\Delta G^{\circ}_{f,TeO2}$ = -161.0 kJ/mol, $\Delta G^{\circ}_{f,MoO3}$ = -167.0 kJ/mol)[41,80] which rationalizes the absence of Mo–O or Te–O bonds after depositing Cr *ex–situ* in HV. This suggests the native chromium oxide that forms in air is a good oxygen diffusion barrier that otherwise could result in oxidation of the underlying reaction products or $MoTe_2$.

The presence of $TeO_2$ on the exfoliated $MoTe_2$ surface is corroborated by the chemical state detected at ~530.6 eV in the corresponding O 1*s* spectrum (Figure 3.9b). Cr may scavenge oxygen from the $TeO_2$ during Cr deposition in UHV, but the Cr–O and Te–O chemical states cannot be rigorously distinguished from each other in the corresponding O 1*s* core level spectrum considering the O 1*s* chemical state associated with both species is expected between 530 and 531 eV. A significant concentration of $Cr_xO_y$ and $Cr(OH)_x$ are detected after Cr is deposited in HV. Oxidation could occur both *in–situ* during deposition in HV and *ex–situ* during transfer from the elastomer-sealed deposition tool to the UHV cluster tool. Evidence will be provided in Chapters 4 and 7 that confirms the rapid oxidation of early transition metals *in–situ* during deposition in HV

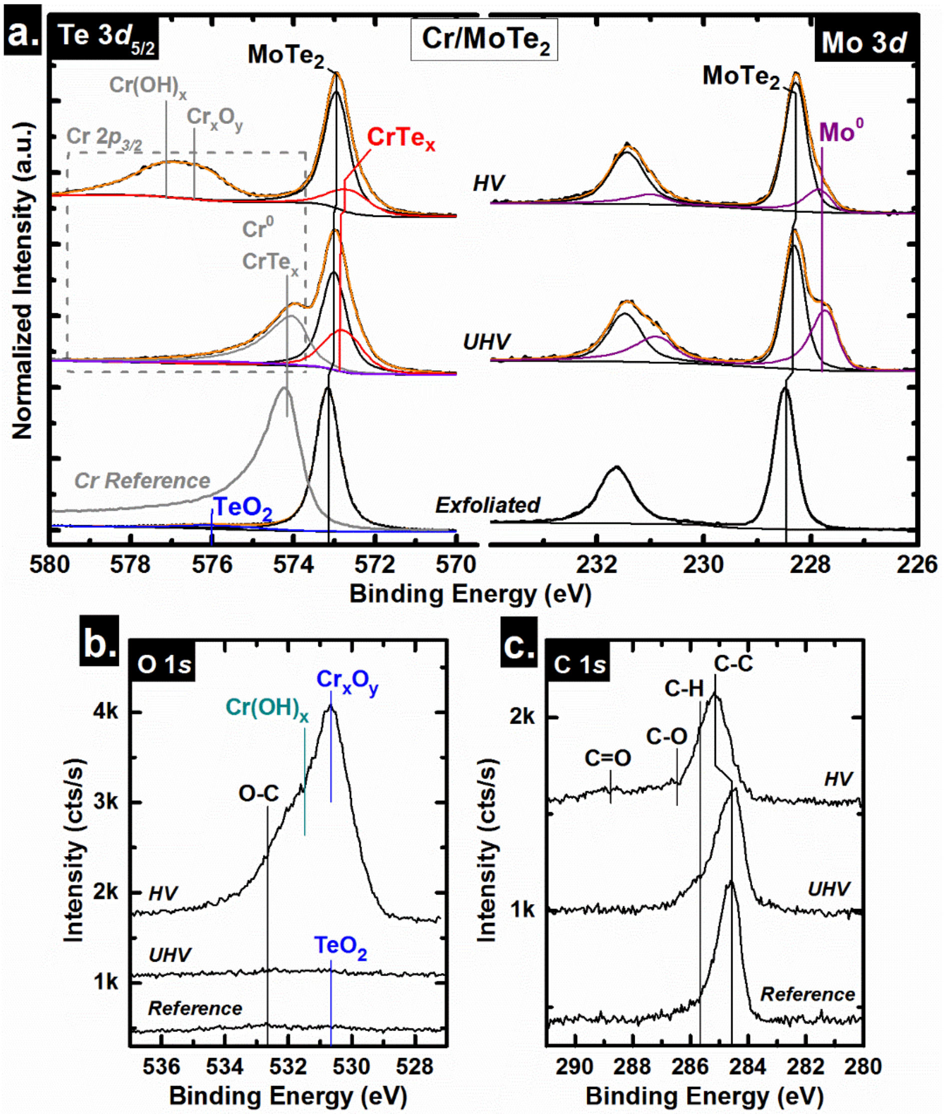

Figure 3.9. a) Cr 2$p_{3/2}$, Te 3$d_{5/2}$, Mo 3$d$, b) O 1$s$, and c) C 1$s$ core level spectra obtained from bulk MoTe$_2$ after exfoliation and subsequent ~1 nm Cr deposition in UHV (*in–situ*) and HV (*ex–situ*).The spectra in the left panel of a) are normalized to the Te 3$d_{5/2}$ core level.

conditions. Therefore, a significant concentration of chromium oxide in the form of Cr–O and Cr–OH bonds should be expected in a Cr contact and the effects of such species on the contact performance should not be ignored.

Adventitious species are detected on the exfoliated $MoTe_2$ before Cr deposition (Figure 3.9 c,d). Any reaction products that form from reactions between Cr and the adventitious species are below the XPS detection limit, which is analogous to the chemistry observed in the Cr–$MoS_2$ and Cr–$MoSe_2$ systems after exfoliation and subsequent Cr deposition in UHV. Therefore, the adventitious species in the Cr–$MoTe_2$ system will not be discussed further.

DFT calculations predicting covalent bonding between certain early transition metals (e.g., Cr, Sc, Ti) and Mo-based TMDs ($MoS_2$, $MoSe_2$)[20,81] only consider a small number of atoms in their interface models due to computational constraints, thus neglecting to consider the effects that long range lattice mismatch induced stress can have on the initial chemistry of such metal films. Cr is known to initially grow as clusters on Si(111),[8] despite forming reaction products with the substrate. AFM images obtained from $MoS_2$, $MoSe_2$, and $MoTe_2$ crystals after depositing ~1 nm Cr in HV show clear pinholes in the Cr films despite readily bonding with the substrate (Figure 3.10). A few-nm thick Cr film, commonly used as an adhesion layer for other contact metals, could have implications regarding the contact resistance of analogous contacts on TMDs in cases where the film is incomplete, as is observed on all Mo-based TMDs investigated here. Contacts that employ an ‘adhesion layer’ must be carefully designed and, more importantly, fabricated to ensure the true interface structure and chemistry yields the desired contact electrostatics.

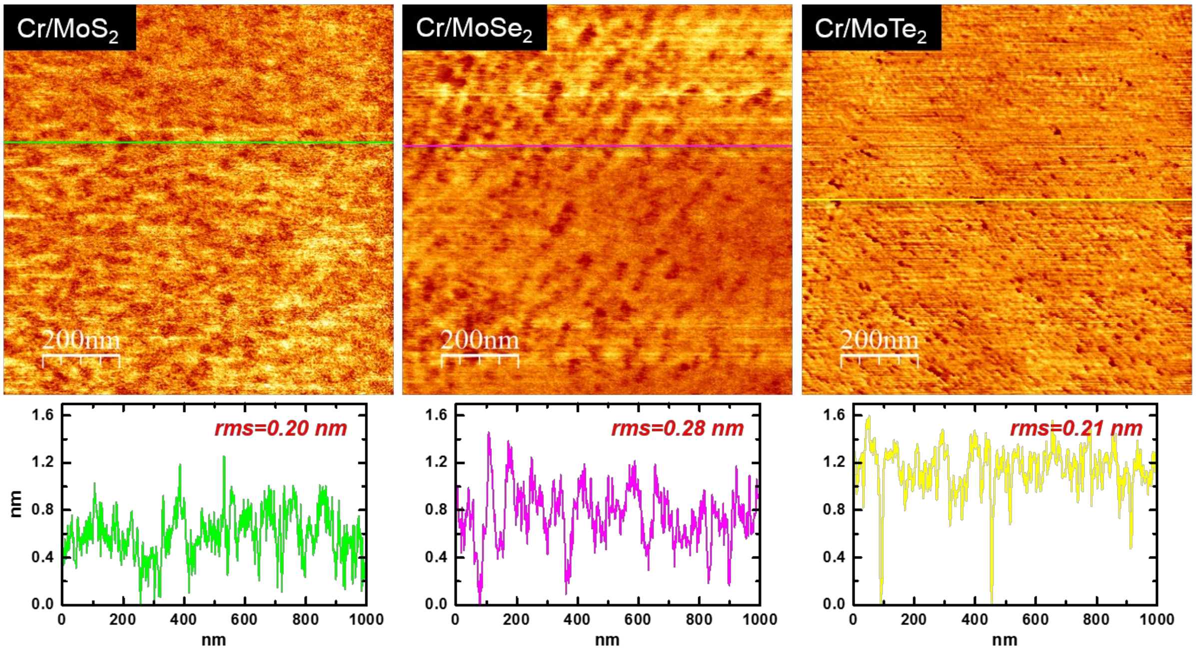

Figure 3.10. 1 μm$^2$ AFM images and associated line profiles (below) obtained *ex–situ* from bulk $MoS_2$, $MoSe_2$, and $MoTe_2$ crystals after depositing ~1 nm Cr in HV.

### 3.4.4 Sc

*MoS₂*

Figure 3.11 presents the XPS spectra obtained after depositing ~1 nm Sc on $MoS_2$ in UHV and HV.

Metallic Mo and $ScS_x$ are detected in the Mo 3*d* and S 2*p* core level spectra following Sc deposition under UHV conditions in addition to bulk $MoS_2$ chemical states (Figure 3.11a). These new states correspond with the formation of metallic Mo as a result of reactions between Sc and S to form $ScS_x$. $\Delta G°_{f,MoS2}$ is much more positive relative to $\Delta G°_{f,ScS}$ (-343.0 kJ/mol),[41] which indicates the formation of $ScS_x$ is thermodynamically favored over the persistence of $MoS_2$. The difference in electronegativity between Sc and S (1.22)[60] is much greater than that between Mo and S (0.42),[60] which is consistent with the chemical shift shown in Figure 3.11a.

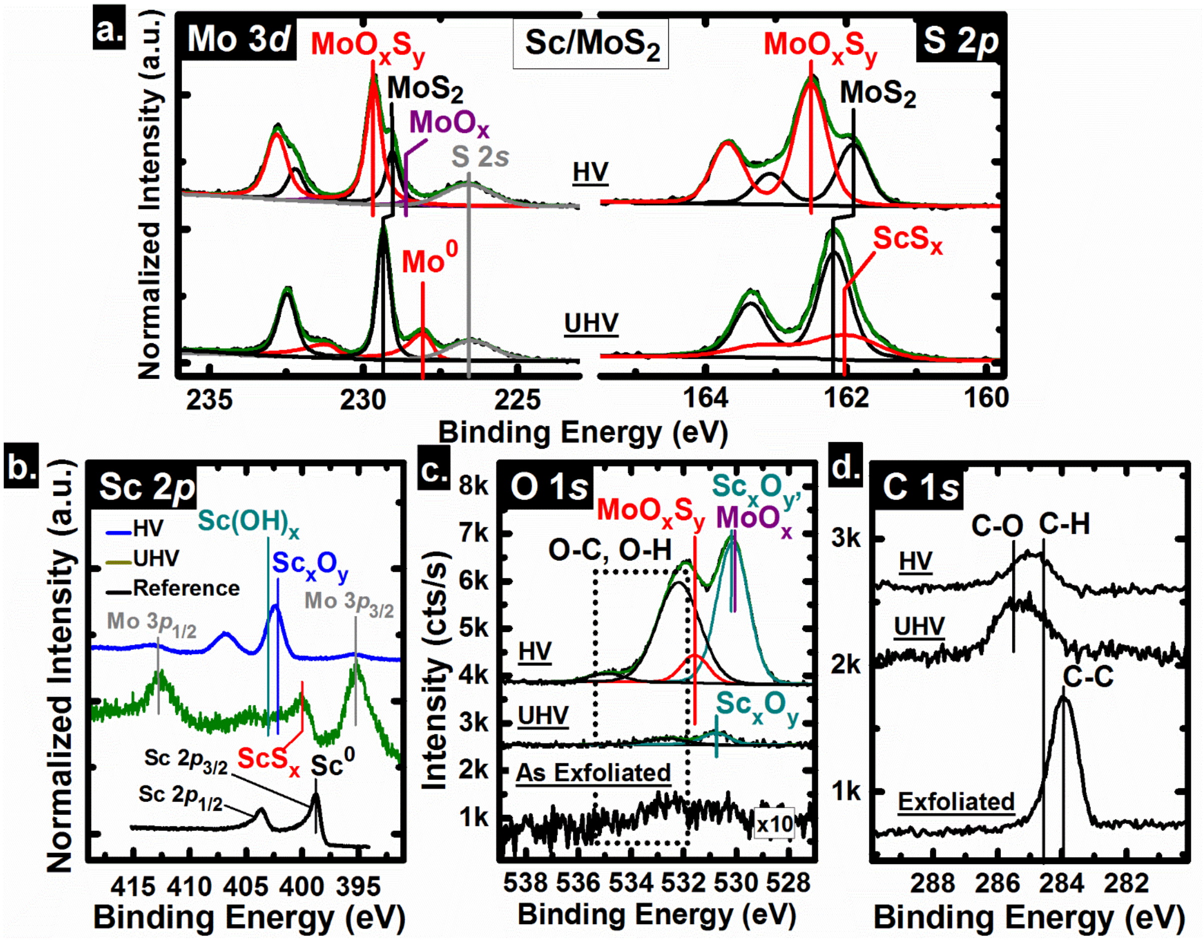

Figure 3.11. a) Mo 3*d*, S 2*s*, S 2*p*, b) Sc 2*p*, c) O 1*s*, and d) C 1*s* core level spectra obtained from bulk $MoS_2$ after exfoliation and subsequent Sc deposition in UHV (*in–situ*) or HV (*ex–situ*). The Sc spectra in b) are normalized to the Sc $2p_{3/2}$ core level. The lower resolution of the Sc 2*p* core level spectra obtained following Sc deposition under UHV conditions compared to the other two Sc 2*p* core level spectra shown in this figure is addressed in the text.

The *BE* of the state in the Mo 3*d* core level spectrum detected at 227.88 eV is in agreement with that obtained from a bulk Mo sample prepared for reference in this study and is therefore attributed to metallic Mo.

The chemistry of the Sc–$MoS_2$ interface differs depending on the deposition chamber ambient. Three separate chemical states are found in the Mo 3*d* core level spectrum following deposition under HV conditions, while only two are found in the corresponding S 2*p* core level spectrum

(Figure 3.11a). The state detected in the Mo 3*d* core level spectrum at a *BE* of 229.04 eV and the low *BE* state in the S 2*p* core level spectrum found at 161.89 eV originate from bulk $MoS_2$. The 67.18 eV separation between these two chemical states matches the separation of similar chemical states detected in the Mo 3*d* and S 2*p* core level spectra obtained from exfoliated $MoS_2$ in this study. The states at high *BE* in both the Mo 3*d* and S 2*p* core level spectra found at 229.65 and 162.49 eV, corresponding with the Mo $3d_{5/2}$ and S $2p_{3/2}$ core levels, respectively, indicate the formation of a molybdenum oxysulfide species at the interface formed between Sc and $MoS_2$. Both the *BE*s and *BE* separation of 67.10 eV of these chemical states are in agreement with those previously reported for amorphous $MoO_xS_y$ films where x=y=1.6.[82]

The low binding energy state in the Mo 3*d* core level spectrum in Figure 3.11a obtained following Sc deposition under HV conditions suggests a small concentration of $MoO_x$ is present. The pristine basal plane of $MoS_2$ may be inert, however structural defects and step edges can act as reactive sites. Previous studies on the various surface oxides of Mo report $Mo^{6+}$ and $Mo^{4+}$ in $MoO_3$ and $MoO_2$ with *BE*s of 232.4 and 230.0 eV, respectively.[68,70] The position of the low *BE* state (228.59 eV) is between the expected *BE*s of the $Mo^{3+}$ ($Mo_2O_3$) and $Mo^{2+}$ (MoO) oxidation states based on the proximity of this state to the expected *BE*s of $Mo^{4+}$ and metallic Mo (227.8 eV), respectively.[68,70]

Figure 3.11b shows the Sc 2*p* core level spectra obtained from a reference Sc film as well as $MoS_2$ following Sc deposition under UHV and HV conditions. A single state, which exhibits core-hole screening effects,[48] is found in the spectrum obtained from the reference sample (black spectra) corresponding to metallic Sc. The Sc 2*p* core level spectrum obtained following Sc deposition under UHV conditions contains significantly more noise than the other two spectra in Figure 3.11b.

Similar to Ti, Sc is susceptible to oxidation even under UHV conditions. As a result, the interface chemistry between Sc and $MoS_2$ as well as the chemistry of the Sc film are metastable *in-situ*. Therefore, the UHV Sc 2*p* spectrum was obtained using fewer sweeps compared with the other two Sc 2*p* spectra in Figure 3.11b to ensure the true chemical states present at the Sc–$MoS_2$ interface formed under UHV conditions were observed, hence the higher noise level in the green spectrum. Multiple states in the Sc 2*p* core level are detected following deposition under UHV conditions, corresponding to $ScS_x$ and a surprisingly large concentration of $Sc_xO_y$ considering that the deposition was performed under UHV conditions. Formation of a significant amount of oxygen-deficient $Sc_2O_3$ (O:Sc ~1.3:1) is evidence for the high potential for metallic Sc to be oxidized through a gettering reaction process. A single chemical state is detected in the Sc 2*p* core level following Sc deposition under HV (Figure 3.11b). The presence of a broad shake-up satellite feature shifted approximately 11 eV to higher *BE* from the Sc $2p_{3/2}$ core level serves as confirmation that this state is in fact indicative solely of scandium oxide. Neither scandium sulfides nor any scandium alloys (i.e., Sc–Mo) produce this satellite feature or any satellite features nearby that could be confused with that produced by $Sc_xO_y$.[83] Although Sc completely oxidizes when deposited under HV conditions similar to Ti (see Chapter 4),[29] new chemical states arise in the Mo 3*d* and S 2*p* core level spectra following Sc deposition under HV conditions.

Figure 3.11c presents the O 1*s* core level spectra obtained from exfoliated $MoS_2$ and also from Sc deposited on $MoS_2$ under UHV and HV conditions. There is a small concentration of adventitious oxygen detected on the surface of exfoliated $MoS_2$. This concentration is on the same order of magnitude of adventitious oxygen detected on the other exfoliated samples, however the intensity of the O 1*s* core level spectrum obtained from exfoliated $MoS_2$ displayed in Figure 3.11c has been multiplied by 10 for clarity. Following deposition under UHV conditions, adventitious oxygen is detected as indicated by the state at 532.60 eV in addition to a state at 530.74 eV corresponding with $Sc_xO_y$. It is likely that Sc scavenges oxygen from preexisting adventitious species on the $MoS_2$ surface and also from the background gases in the cluster tool considering the highly reactive nature of Sc. Following Sc deposition under HV, adventitious oxygen is present in the forms of O-C and O-H species in much higher concentrations than that observed following deposition under UHV conditions. The intense state at 530.13 eV is indicative of a completely oxidized Sc film. The state in the O 1*s* core level spectrum corresponding to $Sc_xO_y$ is shifted to lower *BE* following deposition under HV conditions relative to a similar state detected following deposition under UHV conditions. This is a result of a greater oxygen deficiency in $Sc_xO_y$ formed under UHV conditions compared with $Sc_xO_y$ formed under HV conditions, where oxygen is readily available. The *BE* of the Sc state in $Sc_xO_y$ is found higher than that of the Sc state in $ScS_x$, which is consistent with the greater difference in electronegativity between Sc and O (2.08)[60] compared with that between Sc and S.

The state in the O 1*s* core level spectrum obtained from Sc deposition under HV conditions (Figure 3.11c) detected at a *BE* of 531.57 eV falls within the expected range of *BE*s for oxygen states in metal oxysulfide species.[68,82] The formation of a molybdenum oxysulfide species with stoichiometry $MoO_{1.6}S_{1.6}$ would involve reduction of the $S^{2-}$ state in $MoS_2$ and resulting presence of a higher BE state in the S 2*p* core level spectrum. It would also involve oxidation of the $Mo^{4+}$ state in $MoS_2$ resulting in the formation of a $Mo^{x+}$ state (x=5) found at higher *BE* from the $Mo^{4+}$ state in $MoS_2$. Both of these chemical states are observed in the Mo 3*d* and S 2*p* core level spectra obtained following Sc deposition under HV conditions, which indicates it is likely that a $MoO_xS_y$

species has indeed formed. The stoichiometry of $MoO_xS_y$ detected in this study calculated from the corresponding states in the Mo 3*d*, S 2*p*, and O 1*s* core level spectra is found to be 1.6:1.6:1 (O:S:Mo), which is in agreement with that reported by Benoist et al. for a thin $MoO_xS_y$ film.[82] It is reasonable to assume the $MoO_{1.6}S_{1.6}$ species has formed at the interface between Sc and $MoS_2$ when considering the attenuation of corresponding states detected in the Mo 3*d*, S 2*p*, and O 1*s* core level spectra with photoelectron takeoff angle. Figure 3.12 displays the normalized Mo 3*d*, S 2*p*, O 1*s*, and Sc 2*p* core level spectra obtained at photoelectron takeoff angles of 45° and 37° with the sample surface following Sc deposition on $MoS_2$ in HV. Surface sensitivity of XPS measurements increases with decreased takeoff angle. Compositional information with depth from the surface can be obtained by measuring XPS spectra at multiple takeoff angles. Spectra obtained at different angles are overlaid for direct comparison of the intensities of all detected chemical states to determine where various chemical states exist in reference to the sample surface. The intensity of bulk $MoS_2$ states detected in the Mo 3*d* and S 2*p* core level spectra decrease relative to the states corresponding with $MoO_{1.6}S_{1.6}$ in both core levels as the takeoff angle decreases from 45° to 37° (Figure 3.12a). This indicates that the high binding energy states in the Mo 3*d* and S 2*p* core level spectra corresponding with $MoO_{1.6}S_{1.6}$, resides closer to the sample surface than bulk $MoS_2$ and is most likely in contact with the overlying $Sc_xO_y$ film. Decreased intensity of only one state in the O 1*s* core level spectrum (Figure 3.12b) with decreased takeoff angle indicates that this particular state resides deeper than other oxygen chemical states, which include those in $Sc_xO_y$ and adventitious oxygen species (O–C,

O–H). This is further indication that there is a $MoO_{1.6}S_{1.6}$ species that has formed farther from the surface than $Sc_xO_y$ or adventitious oxygen species, i.e., at the $Sc_xO_y$–$MoS_2$ interface. The Sc 2*p* core level spectra (Figure 3.12c) overlap regardless of take-off angle, indicating that the Sc film is localized to the surface of the sample. The feature centered around ~418 eV denoted by "**" corresponds with the loss feature unique to scandium oxide found ~11 eV from the Sc $2p_{3/2}$ core level.[83]

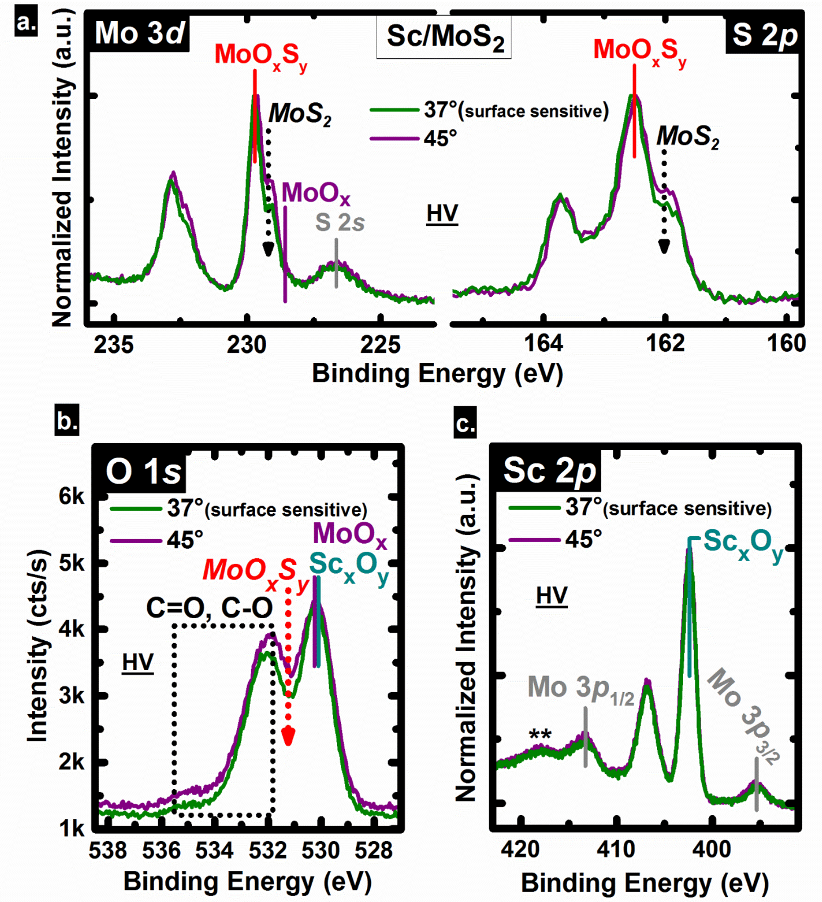

Figure 3.12. Comparison of the normalized and overlaid a) Mo 3*d* and S 2*p*, b) O 1*s*, and c) Sc 2*p* core level spectra obtained from Sc deposited on $MoS_2$ in HV with takeoff angles of 45° and 37°.

Carbon present as C-C and C-H is detected on the surface of exfoliated $MoS_2$ as a result of air exposure after exfoliation (Figure 3.11d). No chemical states are detected in any of the Sc 2*p*, Mo 3*d*, S 2*p*, or C 1*s* core level spectra following Sc deposition under either UHV or HV conditions which would suggest the formation of reaction products involving carbon. However, similar with the Cr–TMD interfaces discussed in the previous Section, reactions between Sc and adventitious carbon cannot be definitively ruled out. In fact, evidence is provided in Chapter 9 that indicates reactions do occur between Sc and organic surface residues on the TMD surface, but are not detectable in the early stages of Sc deposition. Therefore, it is likely that Sc reacts with adsorbates on the $MoS_2$ surface, but the Sc–C bond concentration is below the limit of XPS detection in this case. Scandium carbide is also below the limit of detection after depositing Sc on $MoSe_2$ and $MoTe_2$ (see below for relevant spectra).

*$MoSe_2$*

Reactions between Sc and $MoSe_2$ are more exothermic than the Sc–$MoS_2$ reaction considering $MoS_2$ is more thermodynamically stable than $MoSe_2$. Figure 3.13 shows the Mo 3*d*, Se 3*d*, Sc 2*p*, O 1*s*, and C 1*s* core level spectra obtained after depositing ~1 nm Sc on $MoSe_2$ in UHV and HV. Additional chemical states are detected in the Mo 3*d* and Se 3*d* core level spectra, which indicate the formation of metallic Mo and $ScSe_x$ as a result of reactions between Sc and $MoSe_2$. An additional chemical state is detected in the Mo 3*d* core level near the *BE* of metallic Mo that exhibits an asymmetric shape consistent with core-hole screening effects therefore indicating the presence of metallic Mo. The high *BE* chemical state detected in the corresponding Se 3*d* core level indicates the formation of $ScSe_x$ as Sc scavenges Se from $MoSe_2$. However, the $ScSe_x$ state in the Se 3*d* core level exhibits a *BE* closer to elemental Se (i.e., a reduced oxidation state) than the $ScS_x$ state in the S 2*p* spectrum obtained after depositing Sc on $MoS_2$ in UHV. This suggests the $ScSe_x$ intermetallic exhibits a higher Sc to chalcogen ratio, and therefore a lesser degree of charge transfer from Se to Sc than in $ScS_x$. This trend follows the decreasing Sc–chalcogen electronegativity difference with increasing chalcogen atomic weight. After depositing Sc in HV, only the bulk $MoSe_2$ chemcial states are detected in stark contrast with the Sc–$MoS_2$ system. The *FWHM* of the $MoSe_2$ state in the Se 3*d* core level increases from 0.48 eV after exfoliation to 0.57 eV after Sc is deposited in HV. This suggests that Sc reacts with $MoSe_2$ *in–situ* in HV, presumably via a similar reaction mechanism to that observed *in–situ* after depositing Sc on $MoSe_2$ in UHV. In contrast, the Sc–Se bonds dissociate in the HV ambient due to the highly exothermic formation of Sc–O bonds. In addition, the $BDE_{\text{Sc-O}}$ is ~286 kJ/mol greater than the $BDE_{\text{Sc-Se}}$ corroborating the unfavorable persistence of $ScSe_x$ in the presence of oxidizing gases.[71] Se that dissociates in the scandium oxidation reaction is then free to react with metallic Mo, which is liberated as Sc reduces $MoSe_2$, thereby forming a disordered $MoSe_2$ species. The disordered nature of the re-formed $MoSe_2$ at the interface contributes to the symmetric broadening of the $MoSe_2$ chemical states observed in the corresponding Mo 3*d* and Se 3*d* core levels. The re-formation of transition metal–chalcogen bonds at the contact metal interface could be advantageous in some applications. The strong affinity for oxygen scavenging exhibited by early transition metals such as Sc or Hf may provide a route to forming high-quality, ultra-thin high-κ oxides on TMD surfaces in cases where the TMD metal and chalcogen ions, initially involved in reactions with the deposited early transition metal, readily re-form bonds as the early transition metal-chalcogen bonds dissociate and subsequently form a high-κ oxide. A post-metal oxidation anneal employed in such a process could recrystallize the disordered $MoSe_2$ and improve the interface quality.

The Sc 3*p* core level convolutes the Se 3*d* core level spectra obtained after depositing Sc in UHV and HV (Figure 3.13a). The *BE* and intensity of the Sc 3*p* core level is carefully accounted for based on the intensity ratio and *BE* separation between the Sc 3*p* and Sc 2*p* core levels detected from the reference Sc film (see Chapter 7 for details on fitting the Sc 3*p* core level).

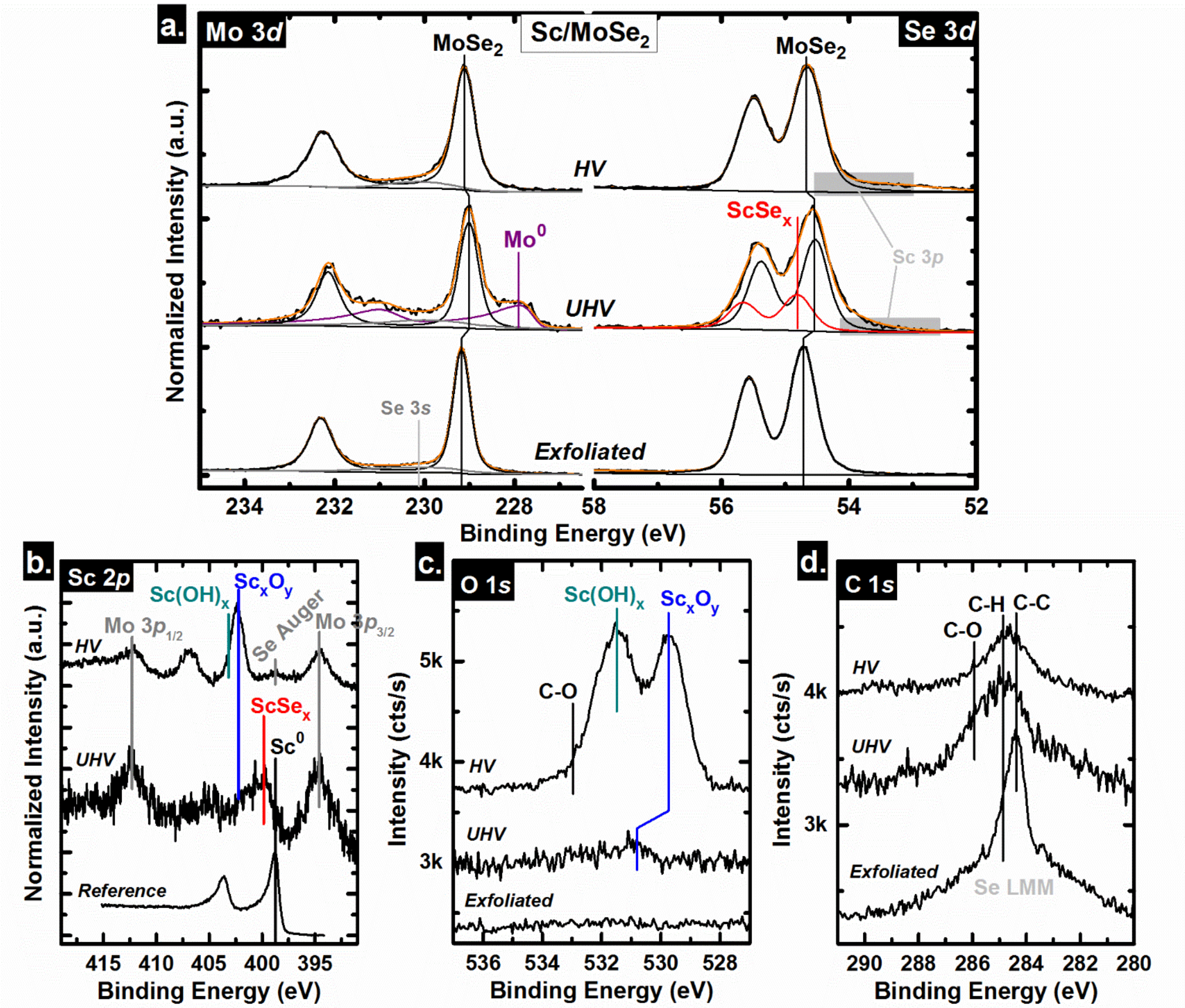

Figure 3.13. a) Mo 3*d*, Se 3*s*, Se 3*d*, Sc 3*p*, b) Sc 2*p*, Mo 3*p*, c) O 1*s*, and d) C 1*s* core level spectra obtained from $MoSe_2$ after exfoliation and subsequent ~1 nm Sc deposition in UHV (*in–situ*) and HV (*ex–situ*). The spectra in b) are normalized to the Sc $2p_{3/2}$ core level.

The Mo 3*p* core level and a Se Auger feature are detected near the Sc 2*p* core level in the corresponding spectra obtained after depositing Sc in UHV and HV (Figure 3.13b). The chemical states detected in the Sc 2*p* core level spectra obtained from $MoSe_2$ after exfoliation and subsequent Sc depositions in UHV and HV are chemically congruent with the states detected in the same core levels obtained from the Sc–$MoS_2$ system and are therefore not discussed further.

### *MoTe₂*

The thermodynamic favorability of reactions between Sc and $MoTe_2$ cannot be directly evaluated at the current time due to a lack of thermodynamic data on scandium telluride compounds. However, the Sc–$MoTe_2$ reaction is likely an exothermic process considering the exothermic nature of the Sc–$MoS_2$ and Sc–$MoSe_2$ reactions and the increasing instability of TMDs with increasing chalcogen atomic mass.[84] In general, reactions involving Sc are more exothermic than another early transition metal, Cr, and it can therefore be assumed that the Sc–$MoTe_2$ reaction is spontaneous like the Cr–$MoTe_2$ reaction. Similar with the exfoliated $MoTe_2$ crystals discussed earlier in this chapter, a small concentration of $TeO_2$ is detected at high *BE* in the Te $3d_{5/2}$ core level obtained from exfoliated $MoTe_2$ (Figure 3.14a). A single chemical state is detected in the corresponding Mo 3*d* core level associated with bulk $MoTe_2$ indicating an absence of $MoO_x$ on the initial surface. After depositing ~1 nm Sc in UHV, additional chemical states are detected in the Te $3d_{5/2}$ and Mo 3*d* core level spectra at *BE*s close to elemental Te (~572.9 eV, see Chapter 8 for more details) and elemental Mo, respectively, which indicates Sc completely reduces $MoTe_2$ near the interface to form metallic Mo and $ScTe_x$. $ScTe_x$ is presumably a metallic species considering the binding energy of the associated Te chemical state is near that of elemental Te. After depositing ~1 nm Sc *ex–situ* in HV, the $ScTe_x$ and metallic Mo that presumably form *in–situ* as Sc is deposited are completely oxidized, which is indicated by the significant concentrations of $TeO_2$ and $MoO_x$ detected at high *BE* in the corresponding Te $3d_{5/2}$ and Mo 3*d* core level spectra (Figure 3.14a). A small, nearly undetectable concentration of metallic Mo persists throughout the processes of depositing Sc in HV and transferring the sample *ex–situ* between the deposition chamber and the UHV cluster tool. It is likely that the residual metallic Mo will oxidize if the air exposure duration during the *ex–situ* transfer had been sufficient for complete oxidation.

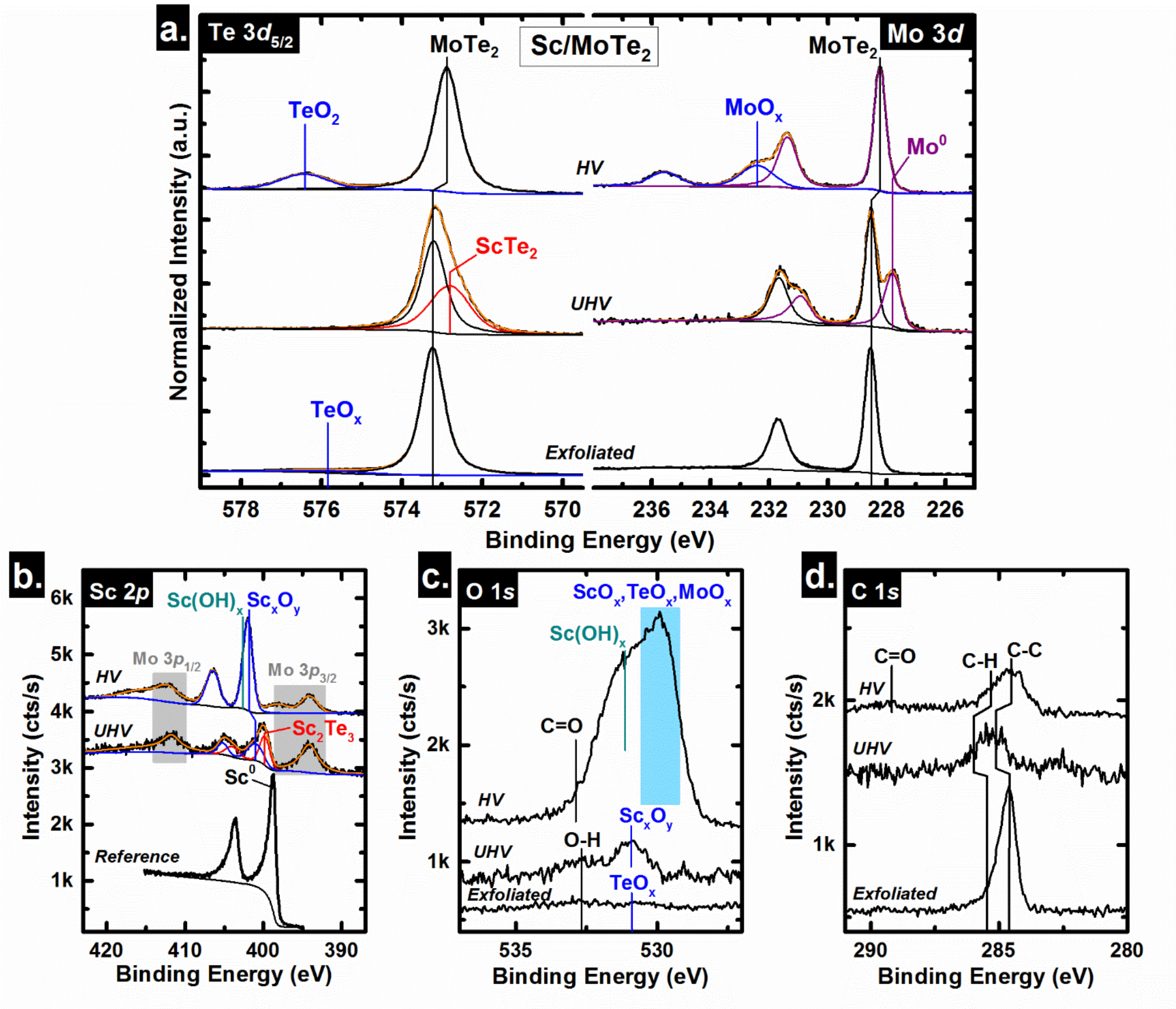

Figure 3.14. a) Te 3$d_{5/2}$, Mo 3*d*, b) Sc 2*p*, Mo 3*p*, c) O 1*s*, and d) C 1*s* core level spectra obtained from MoTe$_2$ after exfoliation and subsequent ~1 nm Sc deposition in UHV (*in–situ*) and HV (*ex–situ*).

Figure 3.14b shows spectra, which include the Sc 2*p* and Mo 3*p* core levels, obtained after depositing ~1 nm Sc on MoTe$_2$ in UHV and HV. The Sc 2*p* core level obtained after depositing Sc in UHV is convoluted by a ScTe$_x$ state at low *BE* and a Sc$_x$O$_y$ state at high *BE*. Interestingly, the $ScTe_x$ chemical state is detected ~1.2 eV higher than metallic Sc (399.77 eV), which is expected considering the *BE* of the corresponding $Te^{x-}$ chemical state is detected near elemental Te. The Sc–Te bond should exhibit ionic character considering the significant electronegativity difference (0.81) and the electron accumulation on the Te anion predicted by DFT.[85] The *BE* shifts of $ScTe_x$ chemical states from elemental Sc and Te that should be detected are not in this work, which is discussed further in Section 3.5.

After exfoliating the $MoTe_2$, a chemical state is detected below 531 eV in the corresponding O 1*s* core level spectrum corroborating the presence of $TeO_x$ on the initial $MoTe_2$ surface (Figure 3.14c). A chemical state associated with adventitious hydroxyl species is also detected at high *BE* in the corresponding O 1*s* core level. The low *BE* chemical state intensity increases after depositing Sc despite an absence of a $TeO_x$ chemical state in the corresponding Te $3d_{5/2}$ core level. Therefore, Sc scavenges oxygen from $TeO_x$ and from the background gases in the UHV cluster tool to form an appreciable concentration of $Sc_xO_y$. The concentrations of transition metal oxide and chalcogen oxide species increases dramatically after depositing Sc *ex–situ* in HV, which is analogous to the chemistry observed in the Sc–$MoS_2$ and Sc–$MoSe_2$ systems.

There are significant differences in the degree of oxidation of Cr and Sc films deposited under HV conditions. Metallic Cr persists following air exposure between the cleanroom reactor and the analysis chamber whereas Sc is completely oxidized as $\Delta G^\circ_{f,Sc2O3}$ (-629.94 kJ/mol)[41] is significantly more negative than $\Delta G^\circ_{f,Cr2O3}$ and $\Delta G^\circ_{f,Cr3O4}$. The $\Delta G^\circ_f$ of all three TMDs investigated in this work and the $\Delta G^\circ_f$ of all associated potential metal chalcogenide reaction products are far more positive relative to that of $\Delta G^\circ_{f,Sc2O3}$. As a result, Sc preferentially oxidizes during deposition under HV conditions rather than reacting with the $MoS_2$ substrate to form reaction products involving Sc (i.e., a scandium chalcogenide). The high concentration of unfilled density of states in the valence *d*-orbital of Sc contribute to its strong affinity to either react with the Mo-based TMDs when deposited under UHV conditions or to oxidize when deposited under HV conditions. Similar to Ti deposition on $MoS_2$,[29] our results show that $Sc_xO_y$, *not* metallic Sc, is likely deposited under HV conditions typical of a cleanroom e-beam tool when the deposition rate is comparable to 0.01 nm/s. Considering the electron affinity of $Sc_2O_3$ (1.96 eV) relative to that of $MoS_2$, $MoSe_2$, and $MoTe_2$ (4.30 eV, 3.80 eV, and 3.75 eV, respectively) one would expect the barrier to conduction across the $Sc_2O_3$ interface to be large unlike the 0.03 eV *SBH* reported by Das et al. between Sc contacts and $MoS_2$.[14] Moreover, $Sc_2O_3$ has also been previously used as a dielectric material in high electron mobility transistors.[13,87,86] Metallic scandium, with a work function of 3.5 eV, would ideally form an Ohmic contact with $MoS_2$, $MoSe_2$, and $MoTe_2$. However, the interface observed between Sc and the three Mo-based TMDs investigated here is not a pristine Sc–TMD or $Sc_2O_3$–TMD interface when Sc is deposited under UHV or HV conditions. The highest performance n-type $MoTe_2$ transistors have recently been demonstrated by utilizing Sc contacts, but a hBN interlayer was required to prevent the detrimental reactions between Sc and $MoTe_2$.[88] The degraded contact performance observed when a $ScTe_x$ intermetallic is present between a Sc contact and $MoTe_2$ is likely due in part to the intermetallic exhibiting a resistivity 2.5× greater than metallic Sc.[89] It is evident that the reaction products formed between Sc and the Mo-based TMDs have a significant impact on the contact resistance exhibited by this junction. The presence of interfacial intermetallics, for instance $MoO_{1.6}S_{1.6}$ in the case of Sc deposited under HV conditions reported here, must be considered when extracting electrical parameters from metallic Sc contacts considering oxidized regions of intermetallic could cause *SBH* inhomogeneity. It is reasonable to expect the impact of interfacial reactions on contact resistance to extend to other contact metal–TMD systems as well, which will be discussed in subsequent chapters.

## 3.5 Discussion

### 3.5.1 Trends in chemical state assignment and reactivity

*Low Work Function Metals: Cr and Sc*

Electronegativity trends can be extended to some chemical states observed in this work. The formation of $CrS_x$ and $ScS_x$ ($CrSe_x$) is associated with the appearance of a chemical state in the S 2*p* (Se 3*d*) core level with a lower *BE* than the S (Se) state in $MoS_2$ ($MoSe_2$). The difference in electronegativity between Mo and S (Mo and Se) is significantly smaller than that between Cr and S or Sc and S (Cr and Se) and therefore one would expect the binding energy of the S (Se) state in $CrS_x$ and $ScS_x$ ($CrSe_x$) compounds to be less than that in $MoS_2$ ($MoSe_2$). This is consistent with the S (Se) chemical states observed at the resulting Cr–$MoS_2$ (Cr–$MoSe_2$) interface formed under both UHV and HV conditions, in addition to the Sc-$MoS_2$ interface formed under UHV conditions. O is significantly more electronegative than S or Se, and therefore one would expect the metal chemical state *BE* in a metal oxide species to be higher than that in a metal sulfide or selenide species. This is consistent with the *BE*s of metal chemical states in various reaction products observed in this study.

The $CrTe_x$ chemical states in the Cr 2*p* and Te $3d_{5/2}$ core levels exhibits *BE*s near the elemental Cr and Te constituents, which is consistent with previous reports of metallic chromium telluride compounds.[76] In metallic species, electrons can move freely between atomic constituents. Therefore, *BE* shifts that would indicate cationic or anionic oxidation states are not observed.

The $ScSe_x$ and $ScTe_x$ chemical states detected in the respective chalcogen core levels after depositing Sc on $MoSe_2$ and $MoTe_2$ in UHV conditions exhibit *BE*s that are near that expected of elemental Se and Te, respectively. It is possible that the peaks/doublets fitted to the Se 3*d* and Te 3$d_{5/2}$ core levels assigned to $ScSe_x$ and $ScTe_x$ are convolutions of an elemental chalcogen state and a scandium chalcogenide state at slightly lower *BE*. This would suggest a lesser degree of charge transfer occurs from Sc to the Se/Te in $ScSe_x$ and $ScTe_x$ than in $MoSe_2$ or $MoTe_2$, which is reasonable considering stable phases of Sc-rich chalcogenides have been synthesized and are stable at RT.[90]

*High Work Function Metals: Au and Ir*

The Au-Te electronegativity difference (0.44) is small compared with the Mo-Te difference (0.06) indicating an increased degree of charge transfer occurs from Te to Au than from Mo to Te. It is therefore reasonable that the chalcogen anion state associated with a $AuTe_x$ species exhibits a *BE* slightly lower than that of elemental Te, unlike the $MoTe_2$ state detected at a slightly higher *BE* from elemental Te as is detected in this work.

Ir forms ternary molybdenum iridium chalcogenide compounds with all of the Mo-based TMDs investigated in this work. The chalcogen and molybdenum chemical states associated with the $Mo_xIr_yS_z$ and $Mo_xIr_ySe_z$ are detected closer to elemental S, Se, and Mo than the $MoS_2$ or $MoSe_2$ states in the same core levels. In addition, the Ir–S and Ir–Se electronegativity differences are less than the Mo–S and Mo–Se electronegativity differences. Therefore, the addition of Ir in the $Mo_xIr_yS_z$ and $Mo_xIr_ySe_z$ compounds slightly oxidizes the the chalcogen anion and reduces the Mo cation states, which manifests as the intermetallic state *BE* shifts towards elemental S, Se, and Mo in the corresponding core levels. In contrast, the Mo and Te states associated with the $Mo_xIr_yTe_z$

compound exhibit *BE* shifts away from elemental Mo and Te. The Ir–Te electronegativity difference (0.1) is slightly larger than that of Mo–Te (0.06). Therefore, the formation of the $Mo_xIr_yTe_z$ compound further reduces the Te anion and oxidizes the Mo cation, which manifests as the *BE* shifts away from elemental Te and Mo observed in this work.

*Reactivity*

Figure 3.15a shows a scatter plot comparing the ratio of the intermetallic chemical state in the chalcogen core level to the total core level intensity with the work functions of the contact metals. Only the chalcogen core level intensities obtained after depositing metals in UHV are plotted in Figure 3.15a because the air exposure after *ex–situ* metal deposition in HV perturbs the interface chemistry beyond the contact metal–TMD reactions. Therefore, any additional chemical variations may not be representative of the true reactivity trends when metals are deposited in HV. The contact metals are related according to Ir > Sc > Cr > Au in order of decreasing reactivity according to the intermetallic concentration formed by each metal averaged across the three TMDs.

While electronegativity comparisons can aid in correlating additional chemical states with reaction products, the thermodynamics of potential reactions can indicate the energetic favorability for certain reactions to occur. The $\Delta G^\circ_f$ of stable intermetallic, metal oxide, and chalcogen oxide compounds in each metal-chalcogen system are plotted as a function of metal work function in Figure 3.15b. The formation of Ir chalcogenide and Au chalcogenide reaction products is thermodynamically unfavorable according to the more positive $\Delta G^\circ_f$ of the stable intermetallics in these systems compared with the $\Delta G^\circ_f$ of the three Mo-based TMDs investigated in this work. The $\Delta G^\circ_{f,Ir2Se3}$ and $\Delta G^\circ_{f,Ir2Te3}$ were not available when this was written. However, the fugacity of a gaseous reactant over different metals can alternatively be used to gauge the energetic favorabilities of reactions with a common reactant. The fugacity represents the effective chemical potential between a metal and a pure gaseous reactant. Fugacity and reaction favorability roughly share a direct relationship. The fugacities of the formation of $Ir_2Se_3$ and $Ir_2Te_3$ in partial pressures of pure Se(*g*) and Te(*g*), respectively, are greater than that of AuSe or AuTe, but smaller than that of $MoSe_2$ or $MoTe_2$. It is therefore reasonable to claim the formation of iridium selenide and iridium telluride are not thermodynamically favorable compared to the persistence of $MoSe_2$ and $MoTe_2$, respectively.[59,84] The unfavorable reactions between Ir and the Mo-based TMDs contradict the significant reactivity observed here (Figure 3.15a). Ir is generally considered a noble transition metal, but its unfilled 5*d*-orbital valence can significantly reduce the energy barrier to reactions in some cases. Ir is the only contact metal investigated in this work with a *d*-orbital valence, which likely enhances orbital overlap with the Mo and therefore reactivity with the Mo-based TMDs. In general, the reactivity between the other three contact metals and the Mo-based TMDs obeys the trends predicted by the relationships between $\Delta G^{\circ}_{\mathrm{f,Mo\text{-}based\ TMD}}$ and $\Delta G^{\circ}_{\mathrm{f,intermetallic}}$. In other words, the reactivity increases with increasingly negative $\Delta G^{\circ}_{\mathrm{f,intermetallic}}$ (Au < Cr < Sc). Overall, the reactivity across the Mo-based TMDs increases with decreasing $BDE_{\mathrm{Mo\text{-}chalcogenide}}$ ($MoS_2 < MoSe_2 < MoTe_2$, in order of increasing reactivity). This trend is related to the increasing TMD instability[91] with decreasing electronegativity difference between metal and chalcogen. The increasing TMD instability can also be related with the decreasing *BE* of the valence *p*-orbital of the chalcogen.[84] When metals are deposited in HV, transition metal and chalcogen oxidation is highly exothermic (except for Se oxidation) and is observed in the Ir, Cr, and Sc systems investigated in this work. The $\Delta G^{\circ}_{\mathrm{f}}$'s of the Mo-based TMDs and the intermetallic reaction products are significantly more positive than that of molybdenum oxide, iridium oxide, chromium oxide, and scandium oxide

(Figure 3.15b). These $\Delta G°_f$ trends are in agreement with the formation of $IrO_x$, $Cr_xO_y$, and $Sc_xO_y$ in addition to other interfacial reaction products when contact metals are deposited under HV conditions.

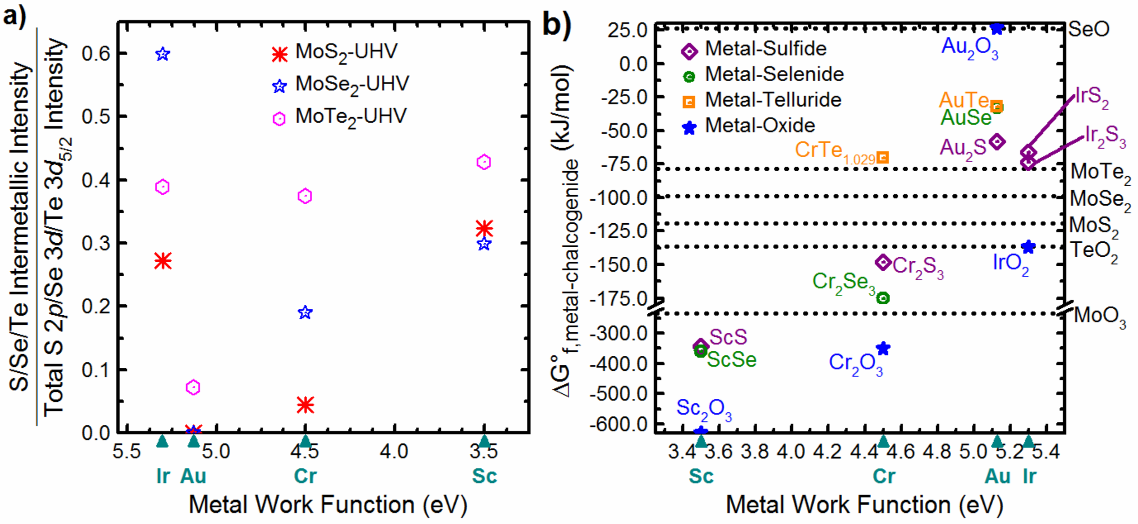

Figure 3.15. a) Reactivity of the metal–TMD systems discussed in this chapter. The reactivity is gauged according to the intensity ratio of the contact metal–chalcogenide (e.g., $ScS_x$) intermetallic chemical state in the corresponding chalcogen core level ($MoS_2$: S 2*p*, $MoSe_2$: Se 3*d*, $MoTe_2$: Te $3d_{5/2}$) to the sum of all chemical states in the same chalcogen core level. These are plotted versus the Ir, Au, Cr, and Sc work functions for metal depositions in UHV (*in–situ*). The 'intensity' refers to the integrated intensity. b) A scatter plot showing the known Gibbs free energy for each metal chalcogenide alloy and relevant metal oxides as a function of metal vacuum work function. The specific compounds are listed on the plot. The dotted lines represent the $\Delta G°_{f,MoS2}$, $\Delta G°_{f,MoSe2}$, $\Delta G°_{f,MoTe2}$, $\Delta G°_{f,MoO3}$, $\Delta G°_{f,TeO2}$, and $\Delta G°_{f,SeO}$ and are shown for comparison.

### 3.5.2 Implications for contact resistance

Through both theoretical calculations and experimental data, the utility of the difference between metal work function and semiconductor electron affinity as a robust tool for predicting *SBH* behavior has been demonstrated previously.[28,92,93] From this, trends in contact resistance can be inferred.[94,95] However, native defects in Mo-based TMDs can cause strong $E_F$ pinning of various contact metals resulting in a discrepancy between the predicted and experimentally derived

*SBH*.[14,19,25,29,88] Therefore, it is difficult to solely use the difference between the metal work function and the TMD electron affinity to predict *SBH*s between contact metals and TMDs until a more comprehensive understanding of the role of defects in metal–TMD $E_F$ pinning is achieved.

The presence of reaction products at the contact metal–TMD interface will also affect the *SBH* and therefore the contact resistance. Deviations from assumed low work function metal-TMD interface chemistries, which have been reported here, and also the relationship between metal deposition chamber ambient and contact resistance[15] are direct indications that interface chemistry and contact resistance are intricately related.[73] Even when a metal–TMD junction is characterized by a vdW interface (e.g., Au–$MoS_2$), the contact resistance can be much higher if the metal is deposited in HV compared with UHV.[15] Given the orders of magnitude greater gas impingement rate in HV compared with UHV, the chamber ambient will directly affect the interfacial chemistry even for higher metal deposition rates typically employed in contact formation.[73]

The band alignment is extracted from all metal–TMD systems investigated in this work assembled by depositing the metal in UHV. The procedure employed to derive the band alignments from XPS measurements is described in Chapter 2. Each of the TMDs exhibits moderate spatial $E_F$ variation, which has been well documented in bulk $MoS_2$ and $WSe_2$ and manifests as a result of significant concentrations of intrinsic defects typically found in bulk TMDs.[25,96] Nonetheless, all of the exfoliated TMDs exhibit a $E_F$ in the upper half of the band gap, which is due in part to the abundant Mo *d*-orbitals predominantly contributing to the DoS in the conduction band edge of Mo-based TMDs. In general, none of the metal–TMD systems discussed in this chapter closely obey the Schottky-Mott rule, which is likely due in part to the significant concentrations of intermetallic species detected at most metal–Mo TMD interfaces investigated in this work. The valence orbital

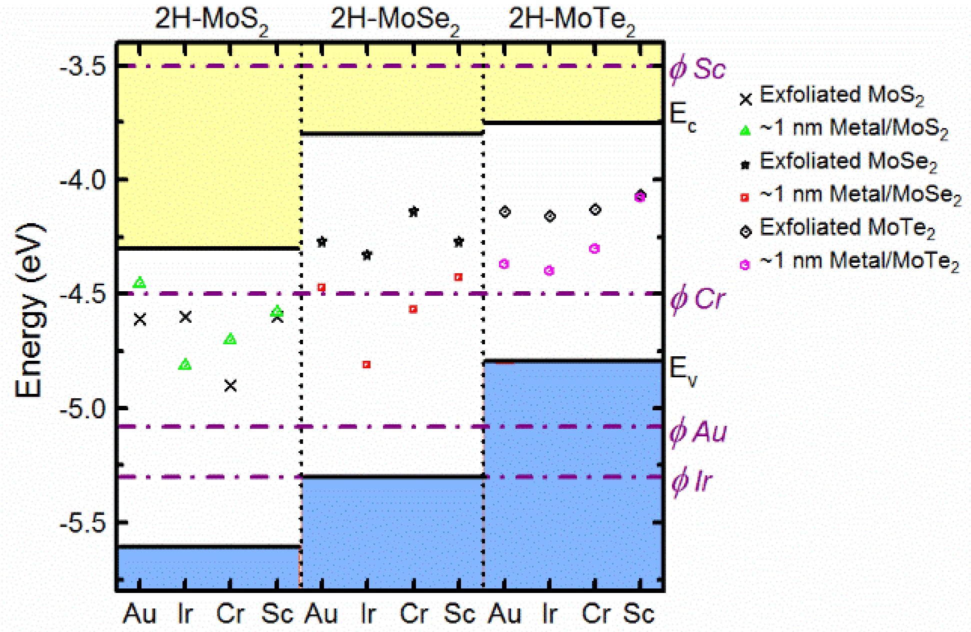

Figure 3.16. The band alignment of metal–TMD systems discussed in this chapter obtained from the initial valence band offset of the exfoliated TMD and the bulk TMD core level shift after depositing ~1 nm metal in UHV, which is ascribed to a $E_F$ shift (see Experimental Details for band diagram construction procedure).

hybridization between the contact metal and TMD constituents also plays a significant role in the band alignment formed between metals and TMDs. Strong $E_F$ pinning near the valence band[19] and near midgap[97] has been reported for a number of metal–Mo TMD systems, which is related to the overlap between valence orbitals of the TMD and the contact metal. The enhanced hybridization that occurs in the Ir–TMD systems discussed in this chapter due to the *d*-orbital valences of Ir and Mo likely causes the largest $E_F$ shift of any contact metal for each Mo-based TMD. In contrast, Au, Cr, and Sc exhibit *s*-orbital valences, which reduces orbital hybridization with Mo. However, a mixture of *s*- and *p*-orbitals make up chalcogen atom valences which enhances orbital hybridization with Cr and Sc and likely contributes to the highly exothermic Cr–chalcogen and Sc–chalcogen reactions. In general, the electron *SBH* decreases with decreasing metal work function (Ir > Cr > Sc, in decreasing order of electron *SBH*) in all three TMDs. Critically, the electron *SBH* of Sc and Ir are far from expected according to the Schottky-Mott rule indicating the intermetallic formed at the Sc–TMD and Ir–TMD interfaces significantly affect the band alignment and contribute to $E_F$ pinning. However, not all intermetallic species will result in an unexpected band alignment. The band alignment detected between Cr and the Mo-based TMDs in this work loosely agrees with the Schottky-Mott rule (with some variation across TMDs), which corresponds with sizeable SBHs in all cases and is therefore detrimental to Cr contact performance. Adventitious carbon is present on all TMD crystals used in this work prior to metal deposition due to the brief period of air exposure included in the experiments after exfoliation and before loading into the deposition chamber for metallization in UHV or HV. Typical device fabrication procedures will involve steps which expose the channel material (e.g., Si, Ge, GaAs, TMDs) to air. As a result, one should expect exfoliated TMDs used in electronic devices to have an appreciable concentration of adsorbates on the surface. Therefore, it is reasonable to assume the interface chemistry between contact metals and Mo-based TMDs as well as the chemistry of the contact metal itself, specifically Au, Ir, Cr, and Sc, will be analogous to the results reported here regardless of the presence or absence of adventitious carbon on the exfoliated TMD surface. The effects of carbon present at the contact metal-TMD interface should be considered in addition to the true chemistry of the interface when evaluating electrical properties of both the contact and the device.

Regardless of the nature of the interface, metals such as Ir, Cr, Sc, and Ti (see Chapter 4) which chemically interact with Mo-based TMDs distort the TMD structure, especially in the monolayer limit.[12,16] A sacrificial TMD layer (or layers) may be necessary in device structures where the integrity of the channel material underneath, and possibly adjacent to, the contact metal must be preserved. Significant reduction in contact resistance has been achieved with a similar destructive mechanism when carbon from underlying graphene diffuses into Ni or Co contacts.[87] However, it has yet to be determined if an analogous mechanism in TMD devices is desirable for lower contact resistance (this is explored in Chapters 6 and 7). Further investigation is necessary to determine the most desirable interface chemistry (vdW gap, interfacial covalent bonding, complete underlying TMD consumption, etc.) and contact architecture (edge, top, mixed, vdW, covalent) for minimized contact resistance and, ideally, Ohmic contacts.

## 3.6 Summary

The interface chemistry between metal contacts (Au, Ir, Cr, and Sc) and the Mo-based TMDs ($MoS_2$, $MoSe_2$, and $MoTe_2$) according to the XPS results discussed in Section 3.4 are displayed graphically in cartoon representations in Figure 3.17 to summarize the reaction products that would typically be found in each system depending on the deposition chamber conditions.

A contact structure in a device stack would commonly employ much thicker metal films than were deposited in this work. Therefore, certain aspects of the contact chemistry may differ from the cartoons displayed in Figure 3.17. For instance, contact metals like Cr that partially oxidize in HV will presumably have a random distribution of $O^{2-}$ and $OH^-$ distributed throughout the contact along with a small concentration of metallic Cr.

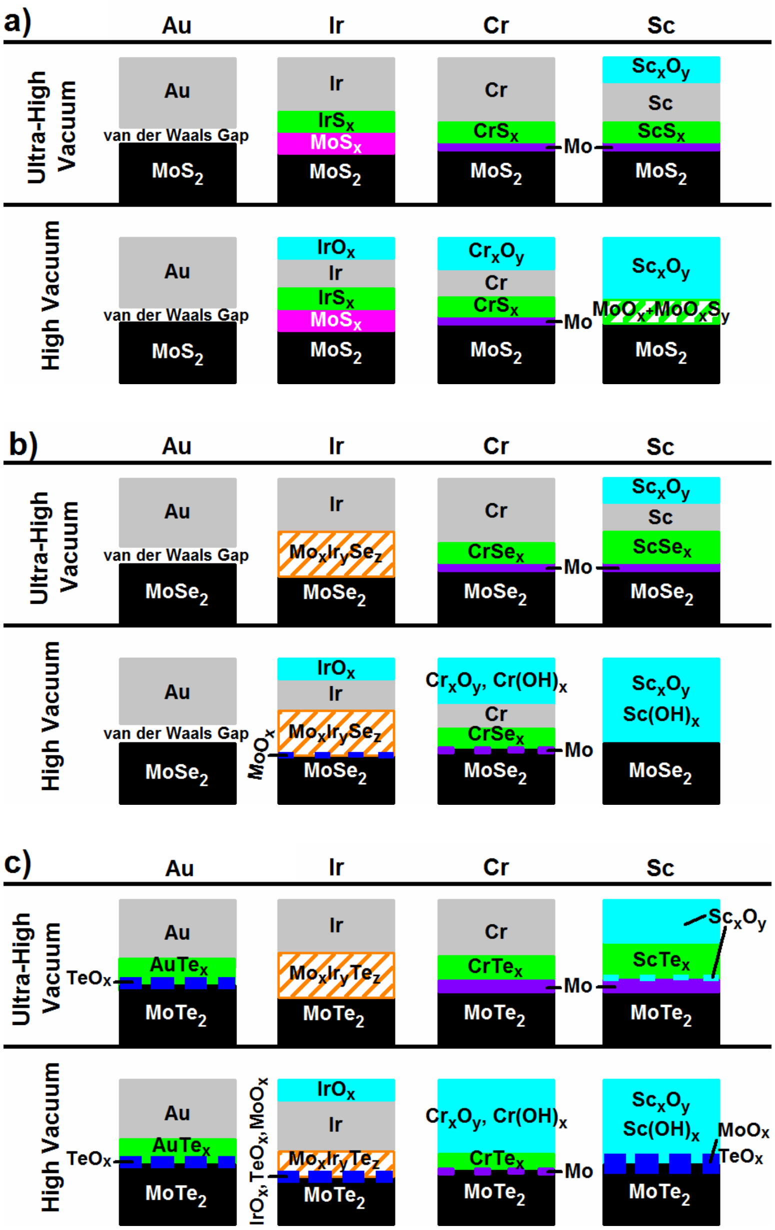

Figure 3.17. Cartoon representations of the interface chemsitry formed between Au, Ir, Cr, and Sc and the TMDs a) $MoS_2$, b) $MoSe_2$, and c) $MoTe_2$ in UHV and HV.

## 3.7 Conclusion

In this work we have determined the dependence of the chemical nature of various interfaces formed between Au, Ir, Cr, and Sc metal contacts on exfoliated $MoS_2$, $MoSe_2$, and $MoTe_2$ on e-beam deposition ambient. Relationships between reaction thermodynamics and the reactivity of each metal–TMD system are established and extended to the corresponding band alignment, which is extracted from XPS measurements. Whether the interface formed is covalent or vdW in nature can depend on a number of different factors including the Gibbs free energy of formation of potential reaction products and the wavefunction overlap between the contact metal and the constituent atoms in the TMD near the interface. The major effect of the reactor ambient on the chemical species that are deposited during metallization is also demonstrated and speculation is given regarding the relationship between interface cleanliness and reactor ambient. Reaction products are detected as a result of Sc, Cr and Ir deposition on most TMDs regardless of deposition chamber ambient, with the exception being the Sc–$MoSe_2$ system. The formation of an Au intermetallic is only observed in the Au–$MoTe_2$ system, which is likely facilitated by the excess Te detected in all $MoTe_2$ crystals investigated in this work considering the reaction between elemental Au(s) and Te(*s*) is exothermic. When deposited under HV conditions, Cr is partially oxidized while Sc is completely oxidized. Despite significant oxidation in both cases, reaction products are still detected at the Cr– and Sc–$MoS_2$ interfaces formed under HV conditions unlike the Cr/Sc–$MoSe_2$ and Cr/Sc–$MoTe_2$ systems due to the increasingly unstable metal chalcogen bond with decreasing electronegativity difference. Our findings shed light on the dependence of interface chemistry and electronic behavior of contacts on a number of different factors, and that the composition of the contact metal at the interface with Mo-based TMDs can vary significantly depending on deposition ambient and contact metal.

## 3.8 References

(1) Franklin, A. D. Nanomaterials in Transistors: From High-Performance to Thin-Film Applications. *Science* **2015,** 349, (6249), 10.

(2) Fiori, G.; Bonaccorso, F.; Iannaccone, G.; Palacios, T.; Neumaier, D.; Seabaugh, A.; Banerjee, S. K.; Colombo, L. Electronics Based on Two-Dimensional Materials. *Nat. Nanotechnol.* **2014,** 9, (10), 768-779.

(3) Cho, S.; Kim, S.; Kim, J. H.; Zhao, J.; Seok, J.; Keum, D. H.; Baik, J.; Choe, D. H.; Chang, K. J.; Suenaga, K.; Kim, S. W.; Lee, Y. H.; Yang, H. Phase Patterning for Ohmic Homojunction Contact in $MoTe_2$. *Science* **2015,** 349, (6248), 625-628.

(4) Chamlagain, B.; Li, Q.; Ghimire, N. J.; Chuang, H.-J.; Perera, M. M.; Tu, H.; Xu, Y.; Pan, M.; Xaio, D.; Yan, J.; Mandrus, D.; Zhou, Z. Mobility Improvement and Temperature Dependence of $MoSe_2$ Field-Effect Transistors on Parylene-C Substrate. *ACS Nano*, **2014**, *8* (5), 5079-5088.

(5) Radisavljevic, B.; Radenovic, A.; Bivio, J.; Giacometti, V.; Kis, A. Single Layer $MoS_2$ Transistors. *Nat. Nanotechnol.* **2011**, *6*, 147-150.

(6) Bao, W.; Cai, X.; Kim, D.; Sridhara, K.; Fuhrer, M. S. High Mobility Ambipolar $MoS_2$ Field-Effect Transistors: Substrate and Dielectric Effects. *Appl. Phys. Lett.* **2013**, *102*, 042104.

(7) Huang, H.; Wang, J.; Hu, W.; Liao, L.; Wang, P.; Wang, X.; Gong, F.; Chen, Y.; Wu, G.; Luo, W. Highly Sensitive Visible to Infrared $MoTe_2$ Photodetectors Enhanced by the Photogating Effect. *Nanotechnology*, **2016**, *27*, 445201.

(8) Galkin, N. G.; Goroshko, D. L.; Sergey, A.; Turchin, T. V.; Self-Organization of $CrSi_2$ Nanoislands on Si(111) and Growth of Monocrystalline Silicon with Buried Multilayers of $CrSi_2$ Nanocrystallites. *J. Nanosci. Nanotechnol.* **2008**, *8,* 557-563.

(9) Fiori, G.; Bonaccorso, F.; Iannaccone, G.; Palacios, T.; Neumaier, D.; Seabaugh, A.; Banerjee, S. K.; Colombo, L. Electronics Based on Two-Dimensional Materials. *Nat. Nanotechnol.* **2014**, *9*, 768-779.

(10) Allain, A.; Kang, J.; Banerjee, K.; Kis, A. Electrical Contacts to Two-Dimensional Materials. *Nat. Mater.* **2015**, *14*, 1195-1205.

(11) Lince, J. R.; Carre, D. J.; Fleischauer, P. D. Schottky-Barrier Formation on a Covalent Semiconductor Without Fermi-Level Pinning: The Metal-$MoS_2$(0001) Interface. *Phys. Rev. B: Condens. Matter Mater. Phys.* **1987**, *36*, 1647-1656.

(12) Kang, J.; Liu, W.; Sarkar, D.; Jena, D.; Banerjee, K. Computational Study of Metal Contacts to Monolayer Transition Metal Dichalcogenide Semiconductors. *Phys. Rev. X* **2014**, *4*, 031005.

(13) Durbin, T. D.; Lince, J. R.; Didziulis, S. V.; Shuh, D. K.; Yarmoff, J. A. Soft X-ray Photoelectron Spectroscopy Study of the Interaction of Cr with $MoS_2$(0001). *Surf. Sci.* **1994**, *302*, 314-328.

(14) Das, S.; Chen, H. Y.; Penumatcha, A. V.; Appenzeller, J. High Performance Multilayer $MoS_2$ Transistors with Scandium Contacts. *Nano Lett.* **2013**, *13*, 100-105.

(15) English, C. D.; Shine, G.; Dorgan, V. E.; Saraswat, K. C.; Pop, E. Improved Contacts to $MoS_2$ Transistors by Ultra-High Vacuum Metal Deposition. *Nano Lett.* **2016**, *16*, 3824-3830.

(16) Luo, B.; Liu, J.; Zhu, S. C.; Yi, L. Chromium is Proposed as an Ideal Metal to Form Contacts with Monolayer $MoS_2$ and $WS_2$. *Mater. Res. Express* **2015**, *2*, 106501.

(17) Popov, I.; Seifert, G.; Tomanek, D. Designing Electrical Contacts to $MoS_2$ Monolayers: A Computational Study. *Phys. Rev. Lett.* **2012**, *108*, 156802.

(18) Michaelson, H. B. The Work Function of the Elements and Its Periodicity. *J. Appl. Phys.* **1977**, *48*, 4729-4733.

(19) Kim, C.; Moon, I.; Lee, D.; Choi, M. S.; Ahmed, F.; Nam, S.; Cho, Y.; Shin, H. J.; Park, S.; Yoo, W. J. Fermi Level Pinning at Electrical Metal Contacts of Monolayer Molybdenum Dichalcogenides. *ACS Nano* **2017**, *11*, 1588–1596.

(20) Gong, C.; Colombo, L.; Wallace, R. M.; Cho, K. The Unusual Mechanism of Partial Fermi Level Pinning at Metal-$MoS_2$ Interfaces. *ACS Nano Lett.* **2014**, *14*, 1714-1720.

(21) Tongay, S.; Suh, J.; Ataca, C.; Fan, W.; Luce, A.; Kang, J. S.; Liu, J.; Ko, C.; Raghunathanan, R.; Zhou, J., et al. Defects Activated Photoluminescence in Two-Dimensional Semiconductors: Interplay Between Bound, Charged, and Free Excitons. *Scientific Reports* **2013**, *3*, 2657.

(22) Amani, M.; Taheri, P.; Addou, R.; Ahn, G. H.; Kiriya, D.; Lien, D.-H.; Ager III, J. W.; Wallace, R. M.; Javey, A. Recombination Kinetics and Effects of Superacid Treatment in Sulfur- and Selenium-based Transition Metal Dichalcogenides. *Nano Lett.* **2016**, *16* (4), 2786-2791.

(23) Zhu, H.; Wang, Q.; Cheng, L.; Addou, R.; Kim, J.; Kim, M. J.; Wallace, R. M. Defects and Surface Structural Stability of $MoTe_2$ Under Vacuum Annealing. *ACS Nano*, **2017**, *11*, 11005-11014.

(24) Guo, Y.; Liu, D.; Robertson, J. 3D Behavior of Schottky Barriers of 2D Transition-Metal Dichalcogenides. *ACS Appl. Mater. Interf.* **2015**, *7*, 25709-25715.

(25) McDonnell, S.; Addou, R.; Buie, C.; Wallace, R. M.; Hinkle, C. L. Defect Dominated Doping and Contact Resistance in $MoS_2$. *ACS Nano* **2014**, *8*, 2880-2888.

(26) Feng, L.; Su, J.; Liu, Z. Effect of Vacancies in Monolayer $MoS_2$ on Electronic Properties of Mo-$MoS_2$ Contacts. *RSC Adv.* **2015**, *5*, 20538-20544.

(27) McGilp, J. F. On Predicting the Chemical Reactivity of Metal-Semiconductor Interfaces. *J. Phys. C: Solid State Phys*. **1984**, *17*, 2249-2254.

(28) Brillson, L. J. Transition in Schottky Barrier Formation with Chemical Reactivity. *Phys. Rev. Lett.* **1978**, *40*, 260-263.

(29) McDonnell, S.; Smyth, C.; Hinkle, C. L.; Wallace, R. M. $MoS_2$-Ti Contact Interface Reactions. *ACS Appl. Mat. Interf.* **2016**, *8*, 8289-8294.

(30) Addou, R.; McDonnell, S.; Barrera, D.; Guo, Z.; Azcatl, A.; Wang, J.; Zhu, H.; Hinkle, C. L.; Quevedo-Lopez, M.; Alshareef, H. N., et al. Impurities and Electronic Property Variations of Natural $MoS_2$ Crystal Surfaces. *ACS Nano* **2015**, *9*, 9124-9133.

(31) Addou, R.; Colombo, L.; Wallace, R. M. Surface Defects on Natural $MoS_2$. *ACS Appl. Mater. Interf.* **2015**, *7*, 11921-11929.

(32) Bulk $MoS_2$ crystals, Ward Science, 2015; https://www.wardsci.com/store/

(33) Bulk $MoS_2$, $MoSe_2$, and $MoTe_2$ crystals, HQ Graphene, 2016; www.hqgraphene.com

(34) ASTM E2108 - 10 Standard Practice for Calibration of the Electron Binding-Energy Scale of an X-Ray Photoelectron Spectrometer, 2000.

(35) Herrera-Gomez, A.; Hegedus, A.; Meissner, P. L. Chemical Depth Profile of Ultrathin Nitrided $SiO_2$ Films. *Appl. Phys. Lett.* **2002**, *81*, 1014-1016.

(36) University of Texas at Dallas Cleanroom http://www.utdallas.edu/research/cleanroom/ (Accessed March 25, 2016).

(37) Horcas, I.; Fernández, R.; Gómez-Rodríguez, J. M.; Colchero, J.; Gómez-Herrero, J.; Baro, A. M. WSXM: A Software for Scanning Probe Microscopy and a Tool for Nanotechnology. *Rev. Sci. Instrum.* **2007**, *78*.

(38) Ellingham Diagram http://web.mit.edu/2.813/www/readings/Ellingham_diagrams.pdf (Accessed November 15, 2015).

(39) Zhou, W.; Zou, X.; Najmaei, S.; Liu, Z.; Shi, Y.; Kong, J.; Lou, J.; Ajayan, P. M.; Yakobson, B. I.; Idrobo, J. Intrinsic Structural Defects in Monolayer Molybdenum Disulphide. *Nano Lett.* **2013**, *13*, 2615-2622.

(40) Luo, Y-R. In *Comprehensive Handbook of Chemical Bond Energies*; CRC Press, Taylor & Francis Group: Boca Raton, FL, 2007.

(41) Selected Values of Chemical Thermodynamic Properties. In *CRC Handbook of Chemistry and Physics 70th Edition*; Weast, R. C.; Lide, D. R.; Astle, M. J.; Beyer, W. H.; CRC Press Inc.: Boca Raton, FL, 1989-1990.

(42) Barton, M. D. The Ag-Au-S System. *Econ. Geol.* **1980**, *75*, 303-316.

(43) Hamasaki, M. Radiation Effects on Thin-Oxide MOS Capacitors Caused by Electron Beam Evaporation of Aluminum. *Solid-State Electron.* **1983**, *26*, 299-303.

(44) Ausman Jr., G. A.; McClean, F. B. Electron-Hole Pair Creation Energy in $SiO_2$. *Appl. Phys. Lett.* **1975**, *26*, 173-175.

(45) Chen, C-H.; Hu, E. L.; Schoenfeld, W. V.; Petroff, P. M. Metallization-Induced Damage in III-V Semiconductors. *J. Vac. Sci. Technol. B.* **1998**, *16*, 3354-3358.

(46) Burek, G. J.; Hwang, Y.; Carter, A. D.; Chobpattana, V.; Law, J. J. M.; Mitchell, W. J.; Thibeault, B.; Stemmer, S.; Rodwell, M. J. W. Influence of Gate Metallization Processes on the Electrical Characteristics of High-κ/$In_{0.53}Ga_{0.47}As$ Interfaces. *J. Vac. Sci. Technol. B.* **2011**, *29*, 040603.

(47) Properties of Inorganic Materials. In *CRC Handbook of Chemistry and Physics 70th Edition*; Weast, R. C.; Lide, D. R.; Astle, M. J.; Beyer, W. H.; CRC Press Inc.: Boca Raton, FL, 1989-1990.

(48) Doniach, S.; Sunjic, M. Many-Electron Singularity in X-ray Photoemission and X-ray Line Spectra from Metals. *J. Phys. C: Solid State Phys.* **1970**, *3*, 285-291.

(49) Hinkle, C. L.; Milojevic, M.; Vogel, E. M.; Wallace, R. M. The Significance of Core-Level Electron Binding Energies on the Proper Analysis of InGaAs Interfacial Bonding. *Appl. Phys. Lett.* **2009**, *95*, 15905.

(50) King, D. E. Oxidation of Gold by Ultraviolet Light and Ozone at 25°C. *J. Vac. Sci. Technol. A.* **1995**, *13*, 1247-1253.

(51) Mathews, J. A.; Watters, L. L. The Carbide of Gold. *Journal of the American Chemical Society*. **1900**, *22*, 108.

(52) Gong, C.; McDonnell, S.; Qin, X.; Azcatl, A.; Dong, H.; Chabal, Y. J.; Cho, K.; Wallace, R. M. Realistic Metal-Graphene Contact Structures. *ACS Nano* **2014**, *8*, 642–649

(53) Ake, O.; Nolang, B.; Osadchii, E. G.; Ohman, L-O,; Rosen, E. In Chemical Thermodynamics of Selenium. Edited by Mompean, F. J.; Perrone, J.; Illemassene, M.

(54) Cakir, D.; Sevik, C.; Peeters, F. M. Engineering Electronic Properties of Metal-$MoSe_2$ Interfaces Using Self-Assembled Monolayers. *J. Materials Chemistry C.* **2014**, *2*, 9842.

(55) Zhang, Y.; Pluchery, O.; Caillard, L.; Lamic-Humblot, A.-F.; Casale, S.; Chabal, Y. J.; Salmeron, M. Sensing the Charge State of Single Gold Nanoparticles via Work Function Measurements. *Nano Lett.,* **2015**, *15*, 51-55.

(56) Bortz, M. L.; Ohuchi, F. S.; Parkinson, B. A. An Investigation of the Growth of Au and Cu on the van der Waals Surfaces of $MoTe_2$ and $WTe_2$. *Surface Science* **1989**, *223*, 285-298.

(57) Zhu, H. Surface and Interface Characterization of 2D Materials: Transition Metal Dichalcogenide and Black Phosphorous. Ph.D. Dissertation, University of Texas at Dallas, TX, 2017.

(58) Wagner, C. D.; Davis, L. E.; Zeller, M. V.; Taylor, J. A.; Raymond, R. M.; Gale, L. H. Empirical Atomic Sensitivity Factors for Quantitative Analysis by Electron Spectroscopy for Chemical Analysis. *Surf. Interface Anal*. **1981**, *3*, 211-225.

(59) Nekrasov, I. A. Geochemistry, Mineralogy, and Genesis of Gold Deposits. Balkema Publishers: Brookfield, VT, 1996, 254-255.

(60) Chemical bonding overview, www.chemhume.co.uk; 2015.

(61) Coelho, P. M.; Komsa, H.-P.; Diaz, H. C.; Ma, Y.; Krasheninnikov, A. V.; Batzill, M. Post-Synthesis Modifications of Two-Dimensional $MoSe_2$ or $MoTe_2$ by Incorporation of Excess Metal Atoms into the Crystal Structure. *ACS Nano*, **2018**, *12*, 3975-3984.

(62) Brush, S. G. In Kinetic Theory Volume 1. The Nature of Gases and of Heat. Pergamon Press LTD: New York, NY, 1965, 135-171.

(63) Biesinger, M. C.; Brown, C.; Mycroft, J. R.; Davidson, R. D.; McIntyre, N. S. X-ray Photoelectron Spectroscopy Studies of Chromium Compounds. *Surf. Interface Anal.* **2004**, *36*, 1550-1563.

(64) Agnostinelli, E.; Battistoni, C.; Fiorani, D.; Mattogno, G.; Nogues, M. An XPS Study of the Electronic Structure of the $Zn_xCd_{1-x}Cr_2X_4$ (X=S, Se) Spinel System. *J. Phys. Chem. Solids.* **1989**, *50*, 269-272.

(65) Westrum, E. F.; Carlson, H. G. Low Temperature Heat Capacities and Thermodynamic Functions of Some Palladium and Platinum Group Chalcogenides. II. Dichalcogenides; $PtS_2$, $PtTe_2$, and $PdTe_2$. *J. Chem. Phys.* **1961**, *35*, 1670-1676.

(66) Hong, J.; Hu, Z.; Probert, M.; Li, K.; Lv, D.; Yang, X.; Gu, L.; Mao, N.; Feng, Q.; Xie, L., et al. Exploring Atomic Defects in Molybdenum Disulphide Monolayers. *Nat. Commun.* **2015**, *6*, 1-8.

(67) Chalamala, B. R.; Wei, Y.; Reuss, R. H.; Aggarwal, S.; Gnade, B. E.; Ramesh, R.; Bernhard, J. M.; Sosa, E. D.; Golden, D. E. Effect of Growth Conditions on Surface Morphology and Photoelectric Work Function Characteristics of Iridium Oxide Thin Films. *Appl. Phys. Lett.* **1999**, *74*, 1394.

(68) Wagner, C. D., *Handbook of X-ray Photoelectron Spectroscopy: a Reference Book of Standard Data for Use in X-ray Photoelectron Spectroscopy*. Physical Electronics Division, Perkin-Elmer Corp.: Eden Prairie, MN, 1979.

(69) Dawson, W. G.; Bullett, D. W. Electronic Structure and Crystallography of $MoTe_2$ and $WTe_2$. *J. Phys. C: Solid State Phys*. **1987**, *20*, 6159.

(70) Choi, J. G.; Thompson, L. T. XPS Study of As-Prepared and Reduced Molybdenum Oxides. *Appl. Surf. Sci.* **1996**, *93*, 143-149.

(71) Waldner, P. Thermodynamic Modeling of the Cr-Fe-S System. *Metall. Mater. Trans. A* **2014**, *45*, 798-814.

(72) Bagus, P.; Staemmler, V.; Woll, C. Exchangelike Effects for Closed-Shell Adsorbates: Interface Dipole and Work Function. *Phys. Rev. Lett.* **2002**, *89*, 096104.

(73) Freedy, K. M.; Giri, A.; Foley, B. M.; Barone, M. R.; Hopkins, P. E.; McDonnell, S. Titanium Contacts to Graphene: Process-Induced Variability in Electronic and Thermal Transport. *Nanotechnology*, **2018**, *29*, 145201.

(74) Kelley, K. K. Contributions to the Data on Theoretical Metallurgy. VIII, The Thermodynamic Properties of Metal Carbides and Nitrides. United States Government Printing Office, Washington, D. C. 1937.

(75) Mohanty, B. C.; Malar, P.; Osipowicz, T.; Murty, B. S.; Varma, S.; Kasiviswanathan, S. Characterization of Silver Selenide Thin Films Grown on Cr-Covered Si Substrates. *Surf. Interface Anal.* **2009**, *41*, 170-178.

(76) Viswanathan, R.; Sai Baba, M.; Raj, D. D. A.; Balasubramanian, R.; Saha, B.; Mathews, C. K. Thermochemistry of Metal-Rich Chromium Telluride and its Role in Fuel-Clad Chemical Interactions. *J. Nuclear Materials*, **1989**, *67*, 94-104.

(77) Mallika, C.; Sreedharan, O. M. Standard Molar Gibbs Energy of Formation of $MoTe_2$ from E.M.F. Measurements. *J. Chem. Thermodynamics* **1988**, *20*, 769-775.

(78) Roy, A.; Guchhait, S.; Pramanik, T.; Hsieh, C.-C.; Rai, A.; Banerjee, S. K. Perpendiular Magnetic Anisotropy and Spin Glass-like Behavior in Molecular Beam Epitaxy Grown Chromium Telluride Thin Films. ACS Nano, 2015, 9 (4), 3772-3779.

(79) Rashba, E. I. Theory of Electrical Spin Injection: Tunnel Contacts as a Solution of the Conductivity Mismatch Problem. *Phys. Rev. B.* **2000**, *62* (24), 267-270.

(80) Reed, T. B. Free Energy of Formation of Binary Compounds: An Atlas of Charts for High Temperature Chemical Calculations. The MIT Press, Cambridge, MA, 1971.

(81) Huang, L.; Li, B.; Zhong, M.; Wei, Z.; Li, J. Tunable Schottky Barrier at $MoSe_2$/Metal Interfaces with a Buffer Layer. *J. Phys. Chem. C.* **2017**, *121*, 9305-9311.

(82) Benoist, L.; Gonbeau, D.; Pfister-Guillouzo, G.; Schmidt, E.; Meunier, G.; Levasseur, A. X-ray Photoelectron Spectroscopy Characterization of Amorphous Molybdenum Oxysulfide Thin Films. *Thin Solid Films.* **1995**, *258*, 110-114.

(83) Merrick, J. A. Bonding in Scandium Monosulfide a NaCl Crystal Type. Ph.D. Dissertation, Iowa State University, IA, 1980.

(84) Doni, E.; Girlanda, R. In Electronic Structure and Electronic Transitions in Layered Materials. Edited by: Grasso, V. Kluwer Academic Publishers: Norwell, MA, 1986.

(85) Li, Y.-X.; Putungan, D. B.; Lin, S.-H. Two-Dimensional $MTe_2$ (M = Co, Fe, Mn, Sc, Ti) Transition Metal Tellurides as Sodium Ion Battery Anode Materials: Density Functional Theory Calculations. *Physics Letters A* **2018**, *382* (38), 2781-2786.

(86) Polyakov, A. Y.; Smirnov, N. B.; Govorkov, A. V.; Danilin, V. N.; Zhukova, T. A.; Luo, B.; Ren, F.; Gila, B. P.; Onstine, A. H.;Abernathy, C. R., et al. Deep Traps in Unpassivated and $Sc_2O_3$–Passivated AlGaN/GaN High Electron Mobility Transistors. *Appl. Phys. Lett.* **2003**, *83*, 2608.

(87) Kim, J.; Mehandru, R.; Luo, B.; Gila, B. P.; Onstine, A. H.; Abernathy, C. R.; Pearton, S. J.; Irokawa, Y. Inversion Behavior in $Sc_2O_3$/GaN Gated Diodes. *Appl. Phys. Lett.* **2002**, *81*, 373-375.

(88) Mlaczko, M. J.; Yu, A. C.; Smyth, C. M.; Chen, V.; Shin, Y. C.; Tsai, Y.-C.; Nishi, Y.; Wallace, R. M.; Pop, E. Contact Engineering High Performance n-Type $MoTe_2$ Transistors. Submitted to *Nano Letters*, **2018**.

(89) Maggard, P. A.; Corbett, J. D. The Synthesis, Structure, and Bonding of $Sc_8Te_3$ and $Y_8Te_3$. Cooperative Matrix and Bonding Effects in the Solid State. *Inorganic chemistry*, **1998**, *37* (4), 814-820.

(90) Maggard, P. A.; Corbett, J. D. $Sc_9Te_2$: A Two-Dimensional Distortion Wave in the Scandium-Richest Telluride. *J. Am. Chem. Soc.* **2000**, *122*, 838-843.

(91) Brainard, W. A. The Thermal Stability and Friction of the Disulfides, Diselenides, and Ditellurides of Molybdenum and Tungsten in Vaccum ($10^{-9}$ to $10^{-6}$ Torr), 1968.

(92) Ayers, P. W.; Anderson, J. S. M.; Bartolotti, L. J. Perturbative Perspectives on the Chemical Reaction Prediction Problem. *Int. J. Quantum Chem.* **2005**, *101*, 520-534.

(93) Sanderson, R. T. In *Chemical Bonds and Bond Energy, 2nd Edition*; Academic Press Inc.: New York, NY, 1976.

(94) King, S. W.; French, M.; Jaehnig, M.; Kuhn, M.; Boyanov, B.; French, B. X-ray Photoelectron Spectroscopy Measurement of the Schottky Barrier at the SiC(N)/Cu Interface. *J. Vac. Sci. Technol. B* **2011**, *29*, 051207.

(95) Lin, Y-J.; Hsu, C-W. Study of Schottky Barrier Heights of Indium-Tin-Oxide on p-GaN Using X-ray Photoelectron Spectroscopy and Current-Voltage Measurements. *J. Elec. Mater.* **2004**, *33*, 1036-1040.

(96) Addou, R.; Wallace, R. M. Surface Analysis of $WSe_2$ Crystals: Spatial and Electronic Variability. *ACS Appl. Mater. Interfaces* **2016**, *8*, 26400–26406.

(97) Lin, Y. F.; Xu, Y.; Wang, S. T.; Li, S. L.; Yamamoto, M.; Aparecido-Ferreira, A.; Li, W. W.; Sun, H. B.; Nakaharai, S.; Jian, W. B.; Ueno, K.; Tsukagoshi, K. Ambipolar $MoTe_2$ Transistors and Their Applications in Logic Circuits. *Adv. Mater.* **2014,** 26, (20), 3263-3269.

# CHAPTER 4

# CHARACTERIZING AND ENGINEERING THE MOS2-TITANIUM CONTACT INTERFACE CHEMISTRY

Authors – Christopher M. Smyth[†], Stephen McDonnell[‡], Pavel Bolshakov[†],

Chadwin D. Young[†], Christopher L. Hinkle[†], and Robert M. Wallace[†]

[†]The Department of Materials Science and Engineering, RL10
The University of Texas at Dallas
800 West Campbell Road
Richardson, Texas, 75080, USA

[‡] The Department of Materials Science and Engineering
University of Virginia
Charlottesville, Virginia, 22904, USA

## 4.1 Preface

The formation of the Ti–$MoS_2$ interface, which is heavily utilized in nanoelectronic device research, is studied by XPS. It is found that if deposition under HV ($\sim 1 \times 10^{-6}$ mbar) as opposed to UHV ($\sim 1 \times 10^{-9}$ mbar) conditions are used, $TiO_2$ forms at the interface rather than Ti when the deposition rate is < 0.01 nm/s. The HV deposition results in an interface free of any detectable reaction between the semiconductor and the deposited contact. In contrast, when metallic titanium is successfully deposited by carrying out depositions in UHV, the titanium reacts with $MoS_2$ forming $Ti_xS_y$ and metallic Mo at the interface. These results have far reaching implications as many prior studies assuming Ti contacts may have actually used $TiO_2$ due to the nature of the deposition tools and the deposition rate employed. Photoresist residues at the contact regions left behind from a typical lithographic patterning process further complicate the metal–$MoS_2$ interface chemistry and contact resistance. Ti contacts deposited in HV (i.e., $TiO_x$ contacts) exhibit rectifying forward bias output characteristics despite the low conduction band offset between $TiO_x$ and $MoS_2$, which is presumably due to the photoresist residue at the interface. $O_2$ plasma is employed to simultaneously remove photoresist residue from the contact regions of $MoS_2$ transistors prior to Ti contact metallization and functionalize the $MoS_2$ surface at the contact regions. The Ti deposited in HV scavenges oxygen from the $MoO_x$ formed on the $MoS_2$ surface during the $O_2$ plasma treatment to form a high-performance, n-type $TiO_x$ contact rather than the hole doping typically associated with a contact employing a high work function $MoO_3$ interlayer. These results demonstrate the benefits of employing an $O_2$ plasma treatment in a $MoS_2$ transistor fabrication process to simultaneously remove photoresist residue from the contact regions and facilitate the formation of an Ohmic-like, n-type $TiO_x$ contact to $MoS_2$.

The content of this chapter is reproduced with permission from ($MoS_2$-Titanium Contact Interface Reactions. ACS Applied Materials and Interfaces. **2016**, 8 (12), 8289-8294). Copyright (2016) American Chemical Society. The content of this chapter has also been reproduced in part with permission from (Contact Engineering for Dual-Gate $MoS_2$ Transistors Using $O_2$ Plasma Exposure. ACS Applied Electronic Materials. **2018**), submitted for publication. Unpublished work copyright (2018) American Chemical Society. In this work, Dr. Stephen McDonnell conceived the experimental plan to study the effects of the deposition chamber environment on the Ti–$MoS_2$ interface chemistry and the experiments were performed by myself. The results were interpreted by Dr. S. McDonnell and myself. The experimental plan to study the $MoS_2$ surface topography and interface chemistry 1) throughout a typical lithographic fabrication process and subsequent $O_2$ plasma treatment and 2) throughout Ti deposition in HV was conceived by myself. The XPS, AFM, and e-beam Ti deposition performed throughout these experiments were performed and the associated results were interpred by myself. P. Bolshakov fabricated the Ti–$MoS_2$ transistors and performed the electrical characterization. All co-authors made valuable contributions throughout the process of preparing the manuscripts.

## 4.2 Introduction

High contact resistance continues to limit the transition metal dichalcogenide (TMD) $MoS_2$ device performance and prevent a true understanding of the transport properties in this material. While some early reports suggested that Ohmic contacts had been achieved using gold[1, 2] and also nickel[2] as the contact metal, Das et al.[3] stated that the apparent linear dependence of the drain current on voltage observed in those studies had misled the authors to the conclusion that the contacts were truly Ohmic. The temperature dependent study by Das et al. showed that a range of metals (Sc, Ti, Ni, and Pt) all exhibited clear Schottky barriers.[3] The authors explained that when a voltage greater than flat-band voltage is used, thermally assisted tunneling adds a component to the current that is not considered by standard thermionic emission theory and can lead to the misconception that the contacts are Ohmic. All elemental metal contacts that have been reported to-date yield low electron Schottky barriers with n-type $MoS_2$,[1-4] a fact that has been explained separately by defect dominated parallel conduction[5] and Fermi level ($E_F$) pinning.[3] The parallel conduction model considers that even if the actual Schottky barrier between the metal and $MoS_2$ follows the Schottky-Mott model, the presence of surface defects that act as low work function contacts can dominate the contact resistance and lead to the extraction of an anomalously low electron Schottky barrier height (*SBH*). This can be true even in cases where the defect concentration is as low as 0.3% areal density.[5] This hypothesis was supported by the work of Kim et al. where the large variability in the characteristics of Ti/Au contacts on $MoS_2$ was attributed to the intrinsic variation in the defect distribution on the $MoS_2$ surface.[6] Nevertheless, the contribution from the defect-free regions of the metal-semiconductor contact is not negligible. Even on highly defective $MoS_2$ the defect-free regions can make up > 95% of the contact area. For n-type $MoS_2$, low work function metals such as Ti and Sc still reportedly allow higher total current than higher work function metals such as Au. This is presumably due to the lower *SBH* in the defect-free regions. Titanium has been used both as a contact metal and as a seed/adhesion layer for a wide range of $MoS_2$ based devices.[6-9] Titanium has also been the focus of theoretical contact studies.[10, 11] The effective electron *SBH* for Ti–$MoS_2$ contacts has been extracted and found to be only 0.05 eV.[3]

The actual chemistry of this interface and the potential variations that could be induced by processing parameters is not yet fully addressed. The interpretation of the electronic properties of

$MoS_2$ based devices has generally assumed an ideally sharp metal–$MoS_2$ interface, where the potential for partial $E_F$ pinning and band realignment due to interface dipole formation has been suggested.[12] However, such an interface likely does not exist given realistic deposition conditions. A recent review by Allain et al.[13] highlighted that density functional theory (DFT) calculations predict Ti will form a covalent bond to the 2D semiconductor surface. The resultant hybridization could then perturb the electronic properties of the $MoS_2$ directly in contact with the metal. The work of McGovern et al.[14] and Lince et al.[15] studying metal interactions with $MoS_2$ crystals showed that many metals, particularly those with low work functions will react with $MoS_2$ causing the liberation of metallic Mo as the sulfur bonds to the deposited metal. In the specific case of titanium, McGovern et al. demonstrated clear reactions between titanium and $MoS_2$ during depositions in ultra-high vacuum (UHV) at a pressure $< 6 \times 10^{-9}$ mbar.[14] However in later work by Lince et al.[15] the authors highlighted their own failure to observe a reactions between Ti and $MoS_2$ was most likely due to the oxidation of Ti during depositions high vacuum (HV) at $1 \times 10^{-7}$ Torr ($1.3 \times 10^{-7}$ mbar). Taken together, these results indicate that the residual gas partial pressure in the deposition chamber may affect the chemical state of Ti deposited by e-beam methods. This could have significant implications on the interpretations of metal-semiconductor interfaces since many commercial e-beam evaporator tools operate in the HV rather than UHV regime. It is possible that this distinction has already manifested itself in conflicting reports. Das et al.[3] extracted *SBH*s on $MoS_2$ of 0.05 eV and 0.15 eV for e-beam deposited “Ti” and Ni contacts, respectively deposited at $\sim 10^{-7}$ mbar pressure.[16] A recent report by English et al.[17] showed that Ti deposited in UHV ($10^{-9}$ mbar) resulted in a higher contact resistance than Ni contacts. Neither of these studies reported any physical characterization of the respective interfaces and differences in the interfacial chemistry for Ti deposited at different pressures, as reported by Lince et al.[15] and McGovern et al.[14], is a possible explanation for the difference between the electrical results of English et al.[17] and those of Das et al.[3]

Deposition conditions aside, a major component that is common to most contact resistance studies involving devices is the use of photoresist during fabrication. Often, a high temperature anneal is used to 'clean' photoresist residue and other contaminants present after device processing from interfaces within a device.[18-21] This is not ideal because reactions at the contact metal–$MoS_2$ interface may take place during such anneals, which can degrade contact performance in some cases. Industry commonly employs a plasma 'descum' step after photoresist development in the lithography processes in order to remove any photoresist residue before further processing.[22] The same concept may be applied to TMDs, such as $MoS_2$, for the same specific purpose.

In this study we show that the direct comparison of *in-situ* interface chemistry studies with reports of device performance may not be representative of the contacts used in devices fabricated under typical *ex-situ* methods. This is because the chemical state of the metal and the metal-semiconductor interface is highly dependent on the metal deposition conditions. Here, the low work function metal titanium is used to demonstrate this dependence since titanium is a commonly used contact metal. The work also investigates the effects of photoresist residue and interface chemistry on the Ti contact performance in back gated $MoS_2$ transistors. A short, low power oxygen ($O_2$) plasma treatment is employed after lithographic patterning of the contact regions and before Ti metallization in HV to etch away the photoresist residue and functionalize the surface to exploit the preferential Ti–O reaction for an electrically superior $TiO_2$ interlayer. Using a 5 second $O_2$ plasma exposure prior to contact metal deposition results in the formation of a high-quality metal–$MoS_2$ contact interface due to the photoresist residue cleaning effect and the reactive formation of $TiO_2$. This process has the potential to be extended to other TMDs and 2D materials to improve the contact metal interface and achieve superior device characteristics.

## 4.3 Experimental Methods

### 4.3.1 Deposition Chamber Ambient Effects on the Ti–$MoS_2$ Interface Chemistry

Geological $MoS_2$ from 2D Semiconductor[23] was cleaned by mechanical exfoliation and the fresh surfaces of the bulk materials were analyzed by monochromatic XPS after both *in-situ* and *ex-situ* metal depositions. *Ex-situ* metal depositions were carried out in a Temescal BJD-1800 e-beam evaporator with elastomer seals producing a HV base pressure of ~$3 \times 10^{-6}$ mbar in the cleanroom facility.[24] The general procedure employed to outgas the Ti source and determine the deposition rate in UHV (cluster tool e-beam) and HV (elastomer-sealed cleanroom deposition tool) are defined in detail in Appendixes A and B. During the outgassing step in this work, the pressure never exceeded $6 \times 10^{-6}$ mbar, and fell to ~$1 \times 10^{-6}$ mbar after outgassing was completed (i.e., the sources were brought to a sub-deposition current). The Ti and Au films were deposited to total thicknesses of 2 nm each (rate $< 0.1$ nm/s) according to a QCM inside the chamber. The *in-situ* depositions were carried out by electron-beam deposition under UHV conditions. The Ti and Au films were deposited to total thicknesses of 2 nm each at rates $< 0.01$ nm/s. To achieve UHV conditions the system is baked to > 120 °C for 96 hours. This procedure reduces in the overall pressure in the chambers as well as reducing the partial pressure of $H_2O$ to below the limit of detection for a residual gas analyzer. In the case of both HV and UHV depositions the sample was at room temperature.

### 4.3.2 $O_2$ Plasma for Photoresist-Free, High-Performance, n-Type Ti–$MoS_2$ Interface

The bulk $MoS_2$ crystals employed in the interface structure and chemistry study of the effects of $O_2$ plasma treatment on photoresist residue and the Ti–$MoS_2$ interface chemistry were each fixed to a cleaved silicon wafer via indium (see Appendix C). Photoresist spin-on and lift-off processes identical to the device fabrication procedure are employed here (see Appendix C) and were performed to simulate the typical concentration of photoresist residue at the Ti–$MoS_2$ interface in the transistors.

Atomic force microscopy (AFM) images were obtained *ex–situ* from $MoS_2$ flakes after exfoliation, development, and descum (see Appendix C) with a Veeco Model 3100 Dimension V Atomic Probe Microscope in non-contact tapping mode. Images were processed using the WSxM software.[25]

The surface chemistry of a bulk, geological $MoS_2$ crystal from 2D Semiconductor[23] was investigated with X-ray photoelectron spectroscopy (XPS) *ex–situ* after exfoliation, development, and descum. The methods employed to outgas the Ti source and determine the deposition rate were identical to those described in Section 4.3.1. After descum and XPS, Ti was deposited *in–situ* in a separate deposition chamber attached to a cluster tool described elsewhere[26] using a deposition rate of 0.1 nm/s. This was done consecutively in two steps to obtain total thickness values of 1 nm and 5 nm, while XPS was performed *in–situ* after each deposition step without breaking vacuum in an analysis chamber attached to the same cluster tool. Before Ti metallization, the deposition chamber, which was initially held at a base pressure of $< 2 \times 10^{-9}$ mbar, was backfilled with air. The flow rate was adjusted to maintain a pressure of $5 \times 10^{-6}$ mbar throughout Ti deposition to simulate the environment commonly found in an elastomer-sealed deposition chamber, which was employed in the device fabrication process performed in this work.

XPS analyses throughout this chapter were performed via a monochromated Al kα X-ray source ($h\nu = 1486.7$ eV) and an Omicron EA125 Hemispherical Analyzer with ± 0.05 eV resolution. High resolution spectra were obtained at a take-off angle of 45°, acceptance angle of 8°, and pass energy of 15 eV. The analyzer was calibrated with polycrystalline Au, Ag, and Cu foils according to ASTM E2108.[27] Spectra were deconvolved with AAnalyzer, a peak fitting software.[28]

## 4.4 Results and Discussion

### 4.4.1 Effects of Pre-Metallization Deposition Chamber Ambient on Ti–$MoS_2$ Interface Chemistry

Figure 4.1 shows a direct comparison of Ti depositions on bulk $MoS_2$ under UHV and HV environments. The 'initial' spectra are an example of the Mo 3*d*, S 2*s*, and S 2*p* core levels observed from a freshly exfoliated surface.[5] To account for sample-to-sample doping variations as well as band bending induced by metal depositions, all core level binding energies (*BE*s) have been referenced to the S $2p_{3/2}$ core level at 162.5 eV.[29] Clearly visible are the Mo $3d_{5/2}$ (229.7 eV), Mo $3d_{3/2}$ (232.8 eV), S 2*s* (226.8 eV), S $2p_{3/2}$ (162.5 eV), and the S $2p_{1/2}$ (163.7 eV) core levels. Care was taken to analyze a sample surface area that displayed no local $E_F$ variations, which can be detected on exfoliated $MoS_2$.[5] The UHV deposition is in qualitative agreement with the result of McGovern et al.[14] From the Mo 3*d* and S 2*p* core levels, it is clear that there are new molybdenum and sulfur states present after the Ti deposition. These can be attributed to the formation of $Ti_xS_y$, metallic molybdenum, and $Mo_xS_y$,[30] similar to that reported for Cr reactions with $MoS_2$.[31] Note that in such an interface, the electrical properties would not be expected to follow the prediction of the Schottky-Mott model for an abrupt Ti–$MoS_2$ interface. Similarly the presence of metallic Mo and $Mo_xS_y$ suggests that this interface would also be quite different from the model discussed by Allain et al.[13] where only covalent bonds between the Ti and top S atoms were assumed and no S–Mo bond scission or metallic Mo formation were considered. The interface chemistry presented here is most likely a good representation of the Ti–$MoS_2$ contact reported by English et al.[17], which resulted in a high contact resistance. In contrast, from the spectra obtained after HV deposition and *ex-situ* characterization, only the signatures of Mo 3*d* and S 2*p* core levels in the $MoS_2$ chemical state exist. Note, that since many devices are fabricated using titanium contacts deposited by e-beam in HV reactors, it is likely that the latter interface more accurately describes the interfaces that are generally reported for devices.

The remarkable difference between these two interfaces can be understood after considering the chemical state of the titanium that has been deposited. Figure 4.2 shows the Ti 2*p* core level after both the UHV and HV depositions, and in both cases the Ti $2p_{3/2}$ and Ti $2p_{1/2}$ core level features are clearly observed. The titanium feature observed after UHV deposition on $MoS_2$ is similar to that expected for metallic titanium (included as dashed data in the figure is a pure metallic Ti control sample spectrum). While both show the Doniac-Sunjic[32] style energy loss tail to the high *BE* side, the loss feature appears to be more intense for the Ti–$MoS_2$ sample. Considering the presence of $Ti_xS_y$ based on the S 2*p* spectra, this higher intensity can be attributed to both the

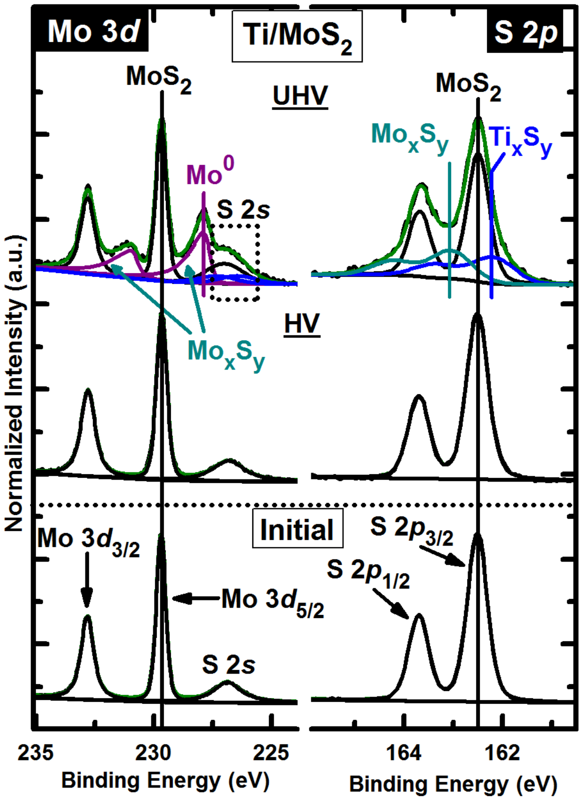

Figure 4.1. Mo 3*d* and S 2*p* core-level spectra for $MoS_2$ cleaned by mechanical exfoliation (Initial), $MoS_2$ after Ti deposition in HV ~3 × $10^{-6}$ mbar, and $MoS_2$ after Ti deposition in UHV ~1 × $10^{-9}$ mbar. No reactions are observed after the HV deposition, however the presence of new chemical states after the UHV deposition suggests reactions between the Ti and the substrate.

Doniac-Sunjic line shape from the metal titanium present and also the $Ti_xS_y$ signature that would be present between 454.1 eV (Ti)[33] and 456.4 eV ($TiS_2$).[34] For the HV deposited sample no metallic Ti is detected. Instead, the spectral feature having a *BE* of 459 eV is consistent with $TiO_2$.[35] One possible explanation for the differing molybdenum and sulfur species at the interface is that the titanium is oxidized before any reactions with the $MoS_2$ can occur, regarding depositions that take place in HV. Considering the base pressure is 3 × $10^{-6}$ mbar in the deposition system, a sizable partial pressure of residual $H_2O$ or $OH^-$ is typically detected in elastomer-sealed vacuum chambers and can be estimated using the kinetic theory of gases to result in an area impingement rate on the

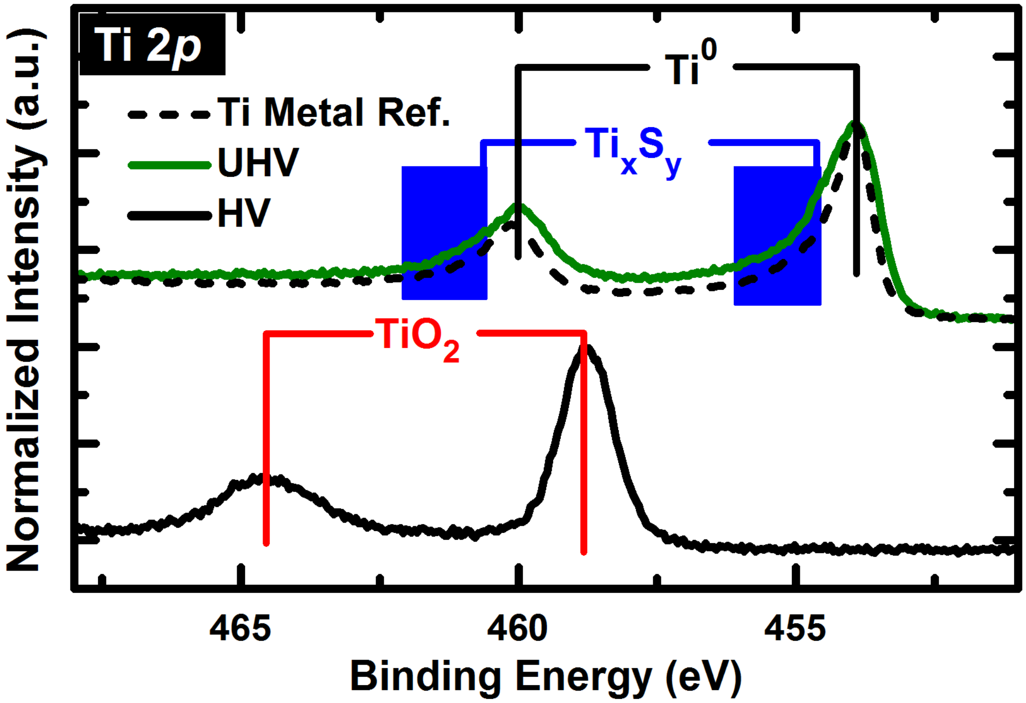

Figure 4.2. Ti 2*p* core-level spectra for Ti deposited in HV (black) ~3 × $10^{-6}$ mbar, Ti deposited in UHV (green) ~1 × $10^{-9}$ mbar and a Ti metal reference (dashed line). From the binding energy positions, the Ti deposited in HV is determined to be $TiO_2$. The Ti deposited in UHV appears to be a combination of Ti metal and $Ti_xS_y$.

order of 5 × $10^{14}$ molecules/cm$^2$ s. With metal deposition rates of < 1 monolayer/minute, it is reasonable to assume that there will be a sufficient supply of oxidizing species on the surface throughout the deposition duration to ensure that any titanium reaching the surface can readily oxidize. Once fully oxidized, it is unlikely that the $TiO_2$ will react with $MoS_2$. Considering the free energy of formation of $TiO_2$ (-890 kJ/mol), $TiS_x$ (-573 to -390 kJ/mol depending on x), and $MoS_2$ (-226 kJ/mol) it is clear that $TiO_2$ is a more stable compound, while $TiS_x$ is still more favorable than $MoS_2$.[36,37] Therefore, it is energetically favorable for Ti to react with $MoS_2$ to form $TiS_x$ under oxygen-deficient conditions. In contrast it is not favorable for reactions to occur at the $TiO_2$-$MoS_2$ interface because the energy of the system is already minimized.

While this explanation may be satisfactory, it cannot be ignored that the HV samples were deposited *ex-situ* (as in a typical device fabrication process) and so the oxidation of the titanium may also have taken place after the deposition rather than during deposition. Two approaches are taken to better understand the oxidation of the Ti and the formation of the markedly different interfaces with $MoS_2$ that occur in HV and UHV. First, the sample with Ti deposited in UHV is exposed to the air so that it can be directly compared to the HV sample that saw a similar air exposure. This directly investigates the impact of post deposition oxidation in air. Second, with freshly exfoliated $MoS_2$ we deposit Ti/Au stacks without breaking vacuum in both HV and UHV. The Au is deposited after the deposition of Ti and is intended to serve as an oxidation barrier to preserve the chemical state of the Ti as it is in the deposition chamber prior to the air exposure.

To determine the role of oxidation in air, the sample obtained by UHV deposition of titanium on $MoS_2$ was exposed to air and allowed to oxidize. Figure 4.3 shows the result of this experiment and it is clear that, while the metallic titanium does indeed oxidize, the interface still shows evidence of metallic Mo and $Ti_xS_y$ (i.e., this is not similar to the abrupt $TiO_2$–$MoS_2$ interface obtained by HV depositions). This strongly suggests that during the titanium depositions under HV (Figure 4.1), the interface reactions are indeed inhibited.

To further test the chemical state of titanium deposited under HV, titanium was deposited on $MoS_2$ and immediately capped in the same HV evaporator with ~2 nm of Au prior to extraction and thus exposing the sample to air. The 2 nm thickness was selected to provide transparency for XPS analysis while functioning as an oxidation barrier. A similar experiment was carried out in UHV. Both samples were exposed to air for 20 minutes after their respective Au deposition.

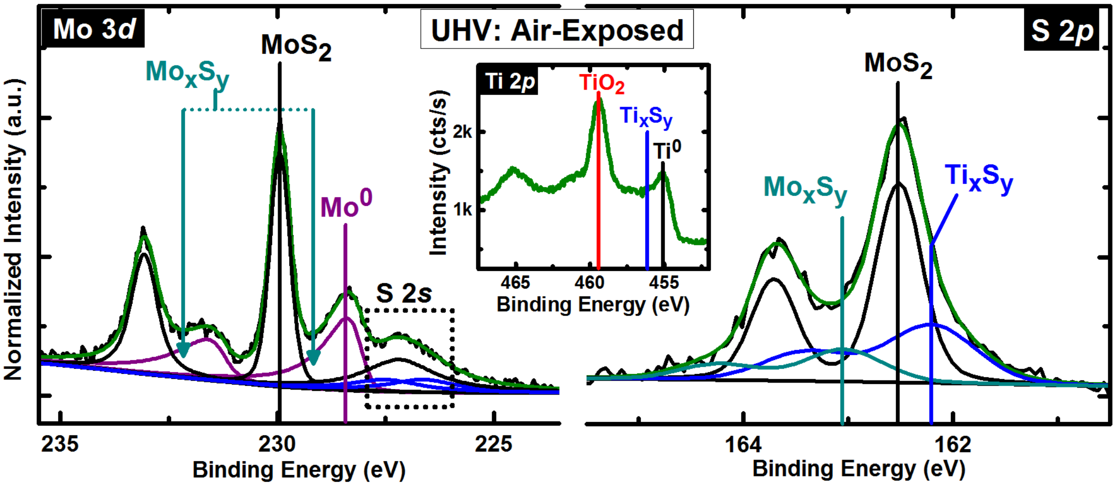

Figure 4.3. Mo 3*d*, S 2*p*, and Ti 2*p* (inset) for UHV Ti–$MoS_2$ exposed to air for 20 minutes. The new high *BE* features in the Ti 2*p* spectra can be attributed to partial oxidation of some of the titanium species, however the presence of $Ti_xS_y$ is still clearly detected in all three core-levels.

Figure 4.4 shows that, in the case of the UHV deposition, the interface remains a mixture of metallic Mo, metallic Ti, $Mo_xS_y$, and $Ti_xS_y$ (Figure 4.3). This demonstrates that the ~2 nm of Au serves as a sufficient barrier against oxidation from the room temperature atmospheric exposure, and, as expected, the Ti reaction with $MoS_2$ to form metallic Mo, metallic Ti, $Mo_xS_y$ and $Ti_xS_y$ bonding is detected. In contrast, for the Au/Ti stack grown in HV and exposed to the air for 20 minutes prior to XPS analysis, the Ti is completely oxidized and no reaction with the $MoS_2$ substrate is detected. This serves as strong evidence that the titanium deposited under HV is actually completely oxidized to form $TiO_2$ during the deposition and nucleation process and that the deposited $TiO_2$ does not react with the underlying $MoS_2$, consistent with the formation energy arguments outlined above. It should be reiterated that, in the literature, titanium has typically been deposited under HV (or at an undisclosed pressure) when fabricating the $MoS_2$ based devices. Therefore, the results here suggest that, other than the intrinsic $MoS_2$ defects,[5, 38,39] the interface between the deposited contact and $MoS_2$ under HV conditions is likely to be spatially abrupt with no detectable reactions between the contact and the $MoS_2$. It is also probable that the contact with $MoS_2$ (and other TMD devices reported) is actually $TiO_2$ and not metallic Ti. The oxidation of Ti on the sample surface by this mechanism should be dependent on the deposition rate as well as the partial pressure of oxidizing species and this will be the focus of future work.

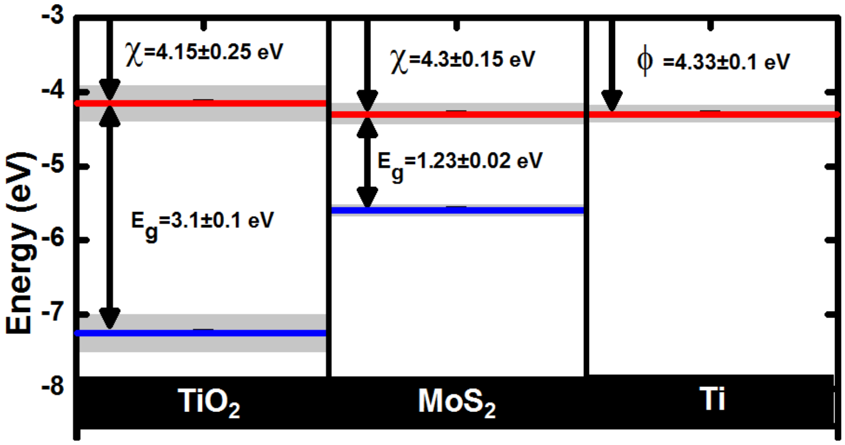

Figure 4.4. Schematic of the band alignments between $TiO_2$, $MoS_2$ and Ti. Within the error for the reported electron affinity values for $TiO_2$ and $MoS_2$, it is clear that $TiO_2$ contacts on $MoS_2$ could be expected to exhibit similar electron Schottky barriers to Ti contacts. The bandgaps and associated errors for $TiO_2$ and $MoS_2$ are taken from Refs. 37-39 and Ref. 22 respectively. The electron affinities/workfunctions and associated errors where applicable for $TiO_2$, Ti and $MoS_2$ and taken from Refs. 38-40, Ref. 41-42, and Ref. 43 respectively.

It is known that thin oxide layers at a metal-semiconductor interface can be used to effectively tune the *SBH* at these interfaces through dipole interactions.[40-43] A mechanism such as this cannot be ruled out as a contributing factor in metal–$MoS_2$ contacts deposited by e-beam methods in the HV regine. In this study however, no evidence of any metallic titanium was found after HV deposition, suggesting that these results are not analogous to the thin oxide interfaces that utilize dipole tuning. Based on the deposition rate and base pressure considerations discussed above, any contact deposited under these conditions would likely be completely oxidized $TiO_2$ and result in no detectable covalent bonding to the $MoS_2$ substrate.

Given that amorphous $TiO_2$ has a bandgap of between 3.0 and 3.5 eV[44,45] it may seem surprising that reasonable device performance is observed for $MoS_2$ based devices fabricated with $TiO_2$ contacts. However, reports on the electron affinity ($\chi$) of $TiO_2$ estimate the value to be between 3.9 and 4.4 eV.[45-47] As such, the observed electron *SBH* with a semiconductor would be expected to be similar to those observed with metallic titanium (workfunction $\phi = 4.3$ eV).[48,49] This results in a low conduction band offset with $MoS_2$ ($\chi = 4.3 \pm 0.15$ eV)[50] and would be consistent with the observed electron *SBH* of 0.05 eV.[3] Figure 4.5 illustrates the band alignment in a $TiO_2$–$MoS_2$ contact as well as the hypothetically abrupt Ti–$MoS_2$ contact. The presence of $TiO_2$ rather than Ti at metal-semiconductor interfaces still has implications. For example, in controlling thermal transport across interfaces, the use of a Ti adhesion layer in metal-semiconductor contacts has drastic effects on the electron and phonon interfacial heat transfer mechanism.[51,52] Due to the low thermal conductivity of disordered $TiO_2$, the presence of $TiO_2$ rather than Ti will increase the thermal resistance.[53] Previous works have shown that the inclusion of disordered thin-film oxides such as $SiO_2$ at metal-semiconductor interfaces can increase the thermal boundary resistance by a factor of 2-3, which quantitatively demonstrates the potential implications of the Ti unintentionally oxidizing during depositions.[54]

### 4.4.2 Exploiting the Preferential Ti–O Reaction for a High–Performance, Photoresist Residue-Free, n-Type $TiO_2$–$MoS_2$ Contact Interface

The work described in Section 4.4.1 explicitly demonstrates Ti is completely oxidized *in–situ* during deposition when metallization occurs in HV (base pressure ~$1 \times 10^{-6}$ mbar) at a deposition rate < 0.1 Å /s. More recent work has demonstrated the ratio of $TiO_x$:Ti within a Ti contact deposited in the HV environment typically found in an elastomer-sealed deposition tool varies from 10% to over 80% depending on the deposition rate and the base pressure of the deposition chamber prior to metallization.[55] Therefore, the concentration of $TiO_x$ within a Ti contact in a device structure will likely contain a mixture of metallic Ti and $TiO_x$. The unusually low deposition rate employed in the work described in the previous section (< 0.1 Å/s) likely facilitates the complete Ti oxidation reported. In a device fabrication process, Ti metallization is typically performed at a deposition rate ~1.0 Å/s. Therefore, it is reasonable to expect an appreciable concentration of metallic Ti within a Ti contact deposited in a typical device fabrication process. The work described in this section demonstrates Ti contact output characteristics in a back-gated $MoS_2$ transistor are converted from rectifying to Ohmic-like when an $O_2$ plasma treatment is employed prior to Ti metallization. XPS and AFM performed in parallel with the device fabrication process and Ti metallization demonstrate the $O_2$ plasma removes photoresist residue and functionalizes the $MoS_2$ surface to achieve a $TiO_x$ interlayer in direct contact with the $MoS_2$.

Figure 4.5 shows the output characteristics measured from $MoS_2$ transistors with Ti contacts excluding (Figure 4.5c) and including (Figure 4.5d, see Figures 4.5 a, b for schematics showing the $O_2$ plasma treatment on the exposed contact areas after development of the photoresist and the final back-gate device structure) the $O_2$ plasma treatment before metallization. The output characteristics of the transistor with Ti/Au contacts[56] excluding the $O_2$ plasma treatment from the fabrication process show non-linearity (Figure 4.5c). With the inclusion of the plasma exposure, the output characteristics become 'Ohmic-like' as shown in Figure 4.5d. The linearity of $I_{DS}$-$V_{DS}$ curves, as well as an overall reduction in device-to-device performance variability, is consistently observed in multiple $MoS_2$ field-effect transistors (FETs) with $O_2$ plasma exposure and Ti/Au contacts.[57] Previous studies that utilize $O_2$ plasma on $MoS_2$ used it either as a functionalization treatment for deposition of uniform, pinhole-free dielectric films or for layer-by-layer etching[58,59]

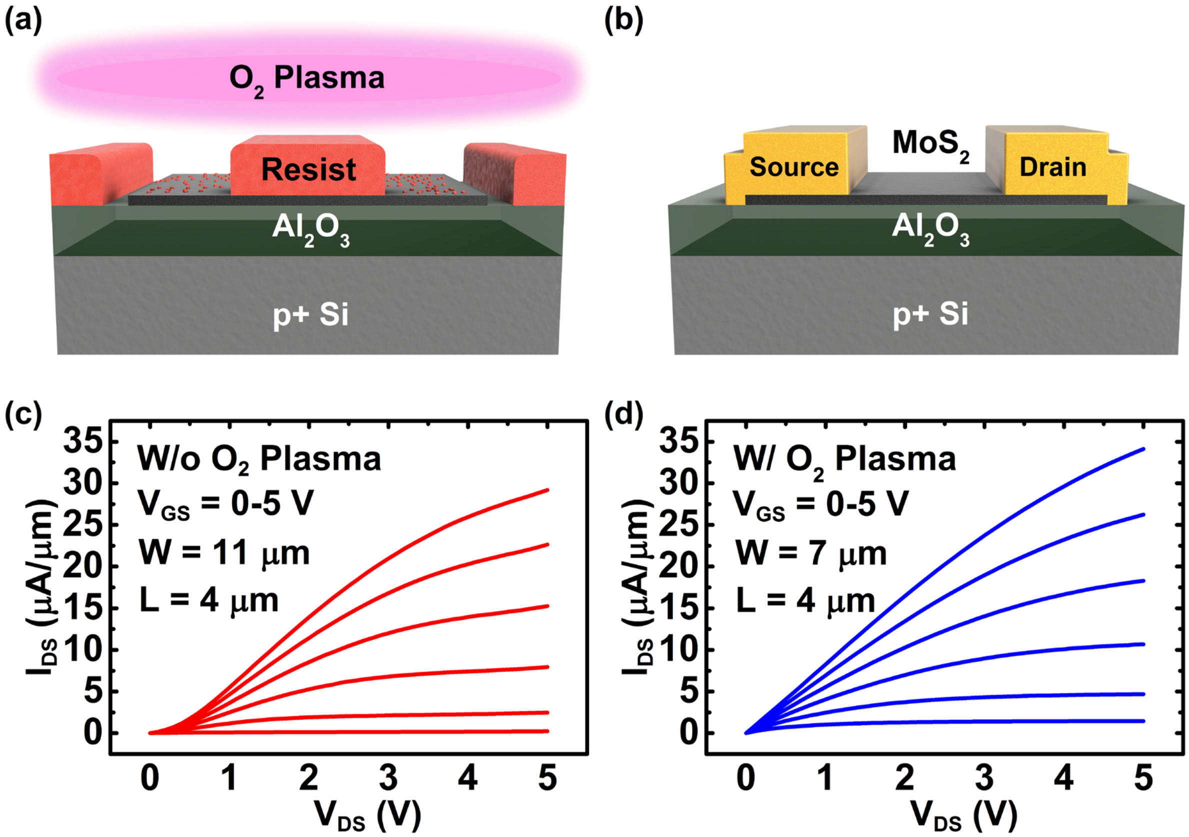

Figure 4.5. a) Graphic illustrating the $O_2$ plasma exposure at the exposed contact areas after development of the photoresist and b) the final back-gate $MoS_2$ FET structure. c) The output characteristics of $MoS_2$ FET without $O_2$ plasma exposure demonstrating non-linear $I_{DS}$-$V_{DS}$ and d) with $O_2$ plasma exposure demonstrating linear $I_{DS}$-$V_{DS}$.

The major side-effect of $O_2$ plasma exposure is the formation of $MoO_x$ byproducts on the $MoS_2$ surface. $MoO_x$ exhibits a high electron affinity and work function (up to ~6.5 eV),[60] leading to formation of a p-type contact ideal for hole injection in $MoS_2$ FETs.[61–63] This would suggest that $O_2$ plasma exposure at the contact areas on $MoS_2$ prior to metal deposition would lead to the formation of p-type contacts, resulting in severe non-linearity in the n-type output characteristics in Figure 4.5d – not less, as observed in this work. Spectroscopic and topographic investigations were performed on $MoS_2$ at all major contact formation steps in the device fabrication process to understand the n-type contact behavior.

Using AFM, the surface topography and phase of few-layer $MoS_2$ flakes after exfoliation, development, and $O_2$ plasma exposure are investigated to ascertain the amount of photoresist residue after development and its removal during $O_2$ plasma. After exfoliation and transfer of $MoS_2$ on to the $Al_2O_3$/Si substrate, the initial surface topography and phase are depicted in Figure 4.6a. A relatively rough surface is detected (root mean square (rms) roughness = 1.43 nm), potentially due to stresses induced during the exfoliation and transfer process. Nonetheless, multiple few-layer $MoS_2$ flakes on the $Al_2O_3$/Si substrate investigated with AFM in this work exhibit similar surface topography to that shown in Figure 4.6a. Following initial AFM, the photolithography process was performed on the $MoS_2$ to form the contact areas. Large islands (up to 20 nm in height and 50 nm in diameter), lower profile wrinkle-like features, and significant increase in rms roughness (6.27 nm) are detected in AFM images after development (Figure 4.6b), which indicates a substantial amount of photoresist residue is left behind after liftoff. This suggests the resist residue will cause discontinuous contact between an adhesion layer often employed in contacts to TMDs, such as Ti,[64–66] and the underlying TMD, which likely convolutes the electrical response of analogous contacts. The AFM images displayed in Figure 4.6c show the $MoS_2$ surface after 5 sec $O_2$ plasma exposure. Large clusters present after development are effectively removed during this step. However, lower profile, wrinkle-like features remain, which could correspond with either small areas of resist residue or patches of $MoO_x$. Nonetheless, the rms roughness after $O_2$ plasma (1.39

nm) is comparable to that of the exfoliated $MoS_2$. This demonstrates that a short $O_2$ plasma step after development is enough to remove a majority of the organic residue prior to metal deposition.

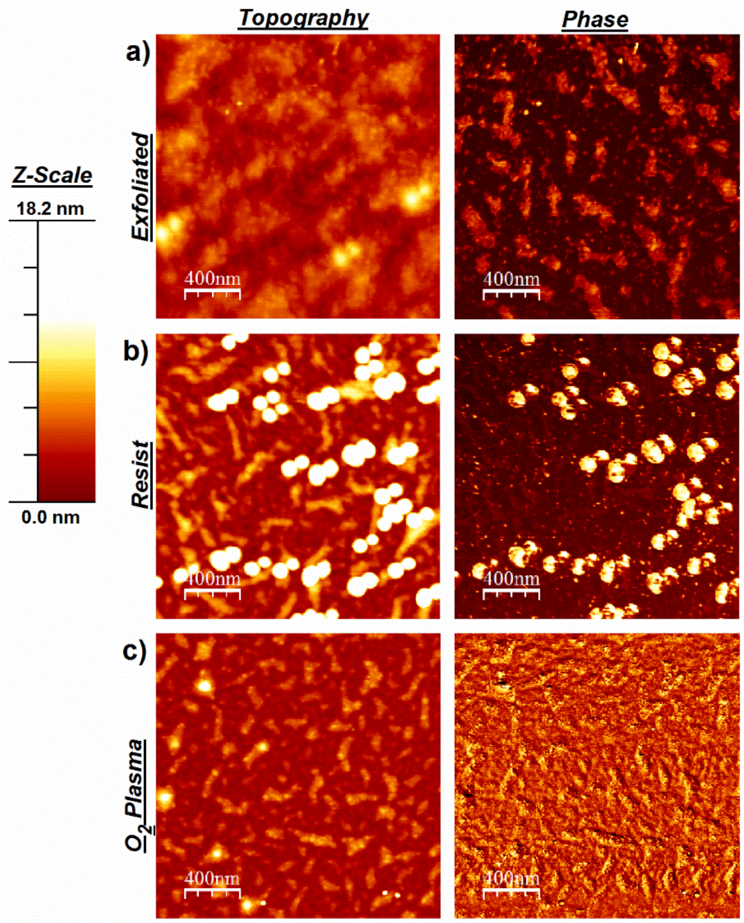

Figure 4.6. AFM topography and phase images obtained from a $MoS_2$ flake after a) exfoliation, b) photolithography processing (photoresist deposition, exposure, development), and c) $O_2$ plasma exposure.

Using XPS, the surface chemistry of two different $MoS_2$ crystals was investigated after exfoliation, development, and Ti deposition in HV (base pressure $5 \times 10^{-6}$ mbar, rate ~1.0 Å /s) to total thicknesses of 1 nm and 5 nm to elucidate the effects of resist residue and $O_2$ plasma on the Ti–$MoS_2$ interface chemistry.[56]

The Mo 3*d* and S 2*p* core level spectra obtained from bulk $MoS_2$ are shown in Figure 4.7a after each of the major processing steps defined above. The Mo $3d_{5/2}$ and $3d_{3/2}$ core levels are detected from exfoliated $MoS_2$ at *BE*s of 229.1 eV and 232.2 eV, respectively, while the S $2p_{3/2}$ and $2p_{1/2}$ core levels are detected at *BE*s of 161.9 eV and 163.1 eV, respectively. Initially, the valence band edge resides 0.9 eV from the $E_F$ (Figure 4.7 c-e). The valence band edge relative to the $E_F$ energy (0 eV in Figure 4.7d) is determined by fitting a linear portion of the lowest *BE* region in the valence band spectrum via linear regression (red lines). A 95% confidence interval is employed in the linear regression, which indicates there is a 95% chance the true value of the valence band edge falls within the associated error bars. The error values displayed in Figure 4.7d reflect the error calculated using the 95% confidence interval when fitting the valence band edge.

After photoresist deposition and development, the $MoS_2$ chemical states shift to higher *BE* by 0.6 eV, which indicates a $E_F$ shift of equal magnitude towards the conduction band ($E_C$) edge. Considering the ~1.4 eV band gap of bulk $MoS_2$, the initial 0.9 eV valence band offset, and 0.6 eV $E_F$ shift after development, the $E_F$ is pinned at the $E_C$ edge by the photoresist residue (Figures 4.7 c-e).[67] The same experiment was performed on a second bulk, geological $MoS_2$ crystal to investigate the consistency of the interface chemistry evolution and $E_F$ pinning across different samples. The $MoS_2$ and Ti chemical states detected from the second crystal throughout the experiment are analogous with the spectra displayed in Figures 4.7 a, b and are therefore not shown here. However, the second exfoliated crystal exhibits a valence band edge 1.3 eV from the $E_F$ and shifts ~0.2 eV after development, which is consistent with $E_F$ pinning at the $E_C$ edge in agreement with the first crystal (Figures 4.7 c-e). This demonstrates photoresist residue pins the $E_F$ at roughly the same energy relative to the band edges regardless of the initial $E_F$ position. Photoresist residue–

induced $E_F$ pinning near the $MoS_2$ $E_C$ edge could explain why it is so difficult to form p-type contacts on $MoS_2$.[68] After the $O_2$ plasma exposure, the $MoS_2$ chemical states in the Mo 3*d* and S 2*p* spectra shift back to the *BE*s etected on exfoliated $MoS_2$. In addition, $O_2$ plasma causes significant oxidation of $MoS_2$ forming $MoO_x$ ($Mo^{6+}$, 232.4 eV in corresponding Mo $3d_{5/2}$ spectrum) and $MoS_xO_y$ (229.6 eV and 162.4 eV in corresponding Mo $3d_{5/2}$ and S $2p_{3/2}$ spectra, respectively). Therefore, the combination of hole injection by $MoO_x$ and organic residue removal causes the $E_F$ shift towards the valence band edge after $O_2$ plasma.

Up to this point, the sample was exposed to air in between each XPS measurement, in the same way the $MoS_2$ flakes were in between lithographic contact formation steps. In contrast, all subsequent Ti deposition steps and corresponding XPS were performed *in–situ* without breaking vacuum to exclude the effects of air exposure on the Ti–$MoS_2$ interface chemistry. If Ti is completely oxidized during the deposition in this work as was reported previously using a much lower deposition rate,[56] then the $MoO_3$ formed during the $O_2$ plasma will remain unperturbed by the Ti deposition. Conversely, if the Ti is only partially oxidized during the deposition in this work, any metallic Ti that does not react with background gases will scavenge oxygen from the $MoO_3$. Therefore, performing the Ti depositions and subsequent XPS *in–situ* is critical to accurately characterizing the interface chemistry evolution during Ti deposition on $O_2$ plasma treated $MoS_2$ in this work.

After depositing 1 nm Ti, $MoO_x$ is detected in a mixture of $Mo^{5+}$, $Mo^{3+}$, and $Mo^{1+}$ oxidation states in the corresponding Mo 3*d* core level spectrum (231.4 eV, 229.5 eV, and 228.9 eV, respectively) indicating a significant amount of $MoO_x$, which is initially present entirely in the $Mo^{6+}$ oxidation state, is reduced by Ti. In addition, 1 nm Ti completely reduces $MoS_xO_y$, forming $TiS_x$ (228.9 eV

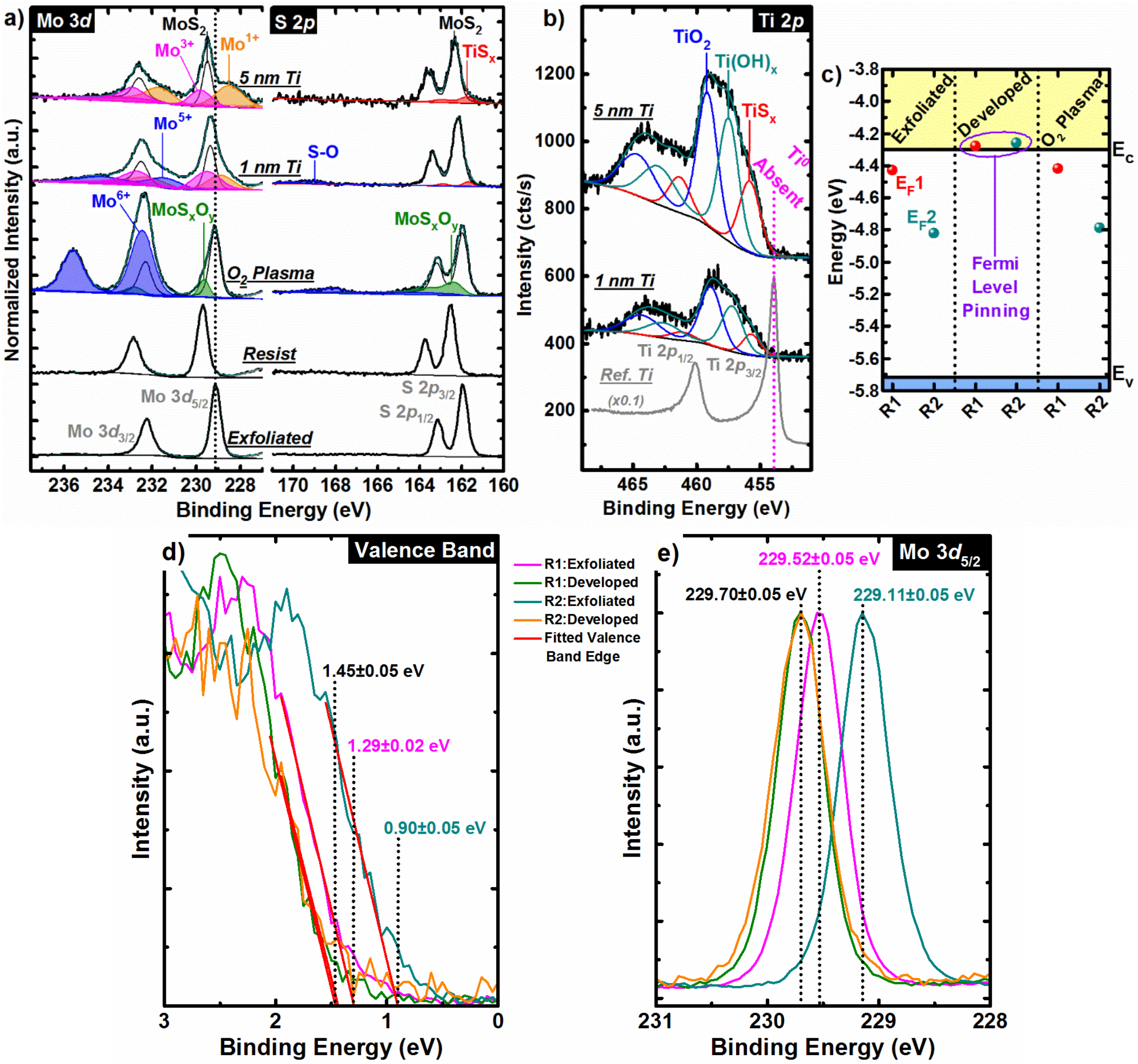

Figure 4.7. XPS core level spectra (a) Mo 3$d$, S 2$p$, and b) Ti 2$p$) obtained from bulk $MoS_2$ after exfoliation, typical photolithographic processing (deposition, exposure, and development), 5 second $O_2$ plasma, 1 nm Ti deposition, and 5 nm Ti deposition. These spectra show $MoO_x$ forms on $MoS_2$ during $O_2$ plasma. Ti deposited during subsequent metallization reduces $MoO_x$ and reacts with $MoS_2$ forming $TiO_x$ and $TiS_x$ at the Ti/$MoS_2$ interface. The spectra in a) and b) were obtained in the same experiment from the same $MoS_2$ crystal. The Ti thicknesses listed reflect the total film thickness. c) Band alignment of two bulk $MoS_2$ crystals after exfoliation and photolithographic processing according to the measured valence band offset and expected bulk $MoS_2$ band gap demonstrating $E_F$ pinning in bulk $MoS_2$ after photolithographic processing. d) Valence band edge and e) Mo 3$d_{5/2}$ core level spectra obtained from two bulk $MoS_2$ crystals after exfoliation and photoresist deposition and development. The intercepts of the fitted (red) lines with the x-axis, denoted by vertical dotted lines in d), correspond with the $MoS_2$ valence band edge relative to the $E_F$ energy (0 eV) within the band gap.

in the corresponding S $2p_{3/2}$ spectrum) as a byproduct. After depositing Ti to a thickness of 5 nm, the $Mo^{5+}$ chemical state falls below the limit of detection and the $Mo^{1+}$ chemical state intensity increases in the corresponding Mo 3*d* spectrum, which indicates $MoO_x$ is reduced further with increasing Ti film thickness. The $MoS_2$ chemical states shift 0.3 eV to higher *BE* after 5 nm Ti deposition compared with that detected after $O_2$ plasma corresponding with a 0.3 eV $E_F$ shift towards the $E_C$ edge.

The Ti 2*p* core level spectra obtained after Ti deposition to total thicknesses of 1 nm and 5 nm are shown in Figure 4.7b. Metallic Ti is below the limit of XPS detection up to a film thickness of 5 nm, which indicates a Ti contact to $O_2$ plasma-treated $MoS_2$ is primarily comprised of Ti–O and Ti–S bonds. As previously mentioned, a high-quality electron contact to $MoS_2$ is achieved by treating the contact regions with $O_2$ plasma and subsequently metallizing with Ti/Au. This indicates Ti reduces $MoO_x$ and forms $TiO_x$ during deposition, which mitigates the hole doping effects of $MoO_x$ and dramatically enhances electron injection into $MoS_2$ via the deliberately formed $TiO_x$ interlayer.

Oxygen (Figure 4.8a) and nitrogen (Figure 4.8b) are below the limit of XPS detection on the exfoliated $MoS_2$ surface, while a chemical state is detected at ~284.0 eV in the associated C 1*s* core level spectrum (Figure 4.8c) indicating the presence of adventitious carbon. After photoresist deposition and development, the concentration of detected organics increase dramatically. The presence of resist residue on $MoS_2$ after development is substantiated by the N=C and O=C bonds detected in the corresponding C 1*s*, O 1*s*, and N 1*s* core level spectra consistent with organic species.[69] In addition to forming $MoO_x$ (~530.3 eV, O 1*s* core level), the $O_2$ plasma treatment removes organic residue according to the decreased intensity of the C=O and C=N chemical states in the corresponding C 1*s*, N 1*s*, and O 1*s* spectra (Figure 4.8). However, chemical states consistent with N–O and C–C bonds (below the limit of XPS detection after development) are detected in the corresponding N 1*s* and C 1*s* core level spectra at *BE*s of 401.3 eV and 284.1 eV, respectively, which is consistent with resist polymer bond scission. Therefore, the $O_2$ plasma does not completely remove the resist residue left behind after development. After Ti deposition, the intensity of chemical states in the corresponding C 1*s*, O 1*s*, and N 1*s* spectra attributed to organic residue decrease more than the expected attenuation of a 1 nm or 5 nm thick Ti overlayer, which suggests Ti also cleans the interface by scavenging residual organics.[70,71]

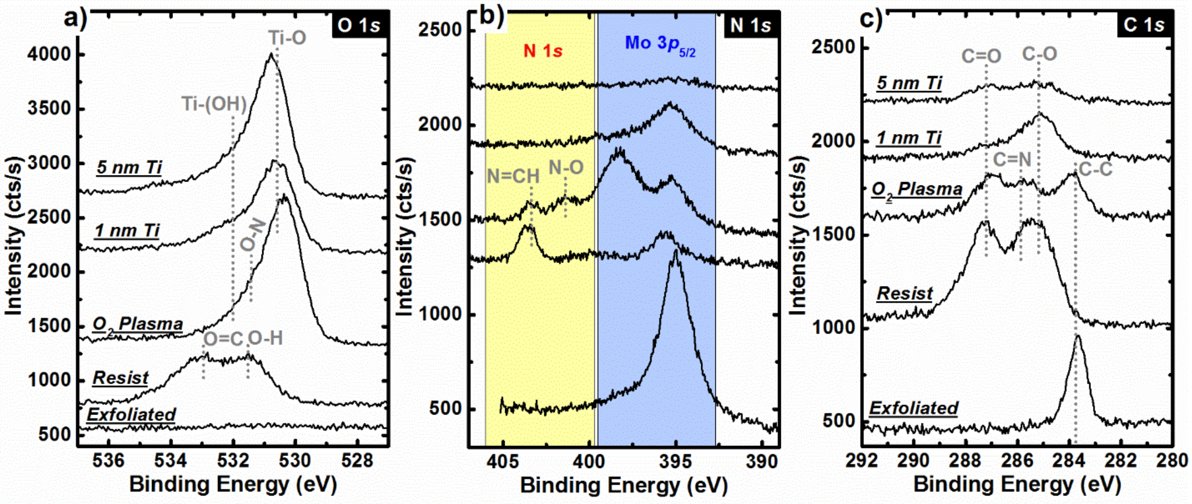

Figure 4.8. a) O 1*s*, b) N 1*s*, and c) C 1*s* core level spectra obtained from $MoS_2$ after exfoliation, photolithographic processing, and Ti deposition. The abundance of organic bonds after development and the cleaning effect by the $O_2$ plasma treatment are evident in the core levels shown here.

The reaction mechanism and corresponding electronic effects proposed here rationalize the ~0.3 eV $E_F$ shift towards the $E_C$ edge detected after 5 nm Ti deposition and the high-performance n-type contact behavior observed in Figure 4.5d. The enhanced carrier injection accompanying the Ti/Au contacts deposited on the $O_2$ plasma treated $MoS_2$ is due to the low $E_C$ offset of the $TiO_x$

layer in direct covalent contact with the $MoS_2$ as has been demonstrated by Kaushik et al. with an atomic layer deposited (ALD) ultrathin $TiO_2$ interfacial layer.[56,72] The removal of organic residue along with the Ti scavanging effect demonstrates the dual purpose of the short $O_2$ plasma exposure prior to contact metal deposition to form high performance n-type contacts on $MoS_2$.

## 4.5 Conclusions

It has been shown that the conditions, under which e-beam deposition of Ti is carried out, play a critical role in the interface formation of Ti on $MoS_2$. While metallic Ti can readily react with $MoS_2$ as confirmed by the experiments carried out in UHV, the oxidation of the Ti that can occur under HV conditions (typical of fabrication deposition tools) prior to any reactions with the substrate can inhibit reactions with the substrate from occurring. Since the oxidation is related to the partial pressure of the oxidizing species in the reactor, this result will likely extend to other substrates and potentially other low work function metals (such as Sc). This work shows that the HV e-beam deposition of Ti actually results in the formation of $TiO_2$ rather than Ti metal at the $MoS_2$ interface. This suggests that many of the previous studies utilizing Ti as a contact or adhesion layer may actually have been employing $TiO_2$ (or a substoichiometric Ti-oxide depending on the deposition rate). Given that the electron affinity of $TiO_2$ is actually quite close to the work function of Ti, the formation of $TiO_2$ rather than Ti in previously reported contact studies would still be consistent with the extracted electron *SBH*s. Our results explain the recent anomalous report of higher than expected contact resistances being observed for Ti contacts deposited under UHV conditions on $MoS_2$. We believe the Ti deposited in that work most likely reacted with the $MoS_2$ forming an interface of metallic Mo, $Mo_xS_y$ and $Ti_xS_y$ that dominated the contact behavior leading to relatively high contact resistance.[17] The work also shows photoresist residue at the contact regions in $MoS_2$ transistors pins the $E_F$ near the $MoS_2$ $E_C$ edge, which convolutes the mechanism behind unexpectedly high Ti contact performance. An $O_2$ plasma clean employed before metallization in a device process flow cleans organic residue from the contact regions and oxidizes the $MoS_2$ surface, which ensures a completely oxidized ~5 nm Ti interlayer and provides a superior contact interface. The removal of organic residue – combined with the formation of a high-performance n-type $TiO_x/MoS_2$ contact interface due to oxygen scavenging by Ti – demonstrates the dual use of $O_2$ plasma exposure and the advantage of a $TiO_x$ contact over the more resistive Ti interface formed in UHV. The results show contaminants left over from the device fabrication processes can significantly degrade contact metal band alignment and $MoS_2$ transistor performance if not properly eliminated. This work has provided an important insight into the true composition of supposedly sharp Ti-semiconductor interfaces and highlights that in the absence of physical characterization, future studies of Ti (and other metal) contacts should include information on the deposition chamber base pressure, deposition rates, and organic residue at critical interfaces so that the true chemical nature of the contact metal interface can be inferred. Such information is particularly important for low work function (high reactivity) metals and the associated contact performance.

## 4.6 References

(1) Radisavljevic, B.; Radenovic, A.; Brivio, J.; Giacometti, V.; Kis, A. Single-Layer $MoS_2$ Transistors. *Nat. Nanotechnol.* **2011**, *6*, 147-150.

(2) Neal, A.; Liu, H.; Gu, J.; Ye, P. In *Metal Contacts to $MoS_2$: A Two-Dimensional Semiconductor*, Device Research Conference (DRC), 2012 70th Annual, **2012**; IEEE: pp 65-66.

(3) Das, S.; Chen, H.-Y.; Penumatcha, A. V.; Appenzeller, J. High Performance Multi-Layer $MoS_2$ Transistors with Scandium Contacts. *Nano Lett.* **2013**, *13*, 100-105.

(4) Liu, H.; Neal, A. T.; Ye, P. D. Channel Length Scaling of $MoS_2$ MOSFETs. *ACS Nano* **2012**, *6*, 8563-8569.

(5) McDonnell, S.; Addou, R.; Buie, C.; Wallace, R. M.; Hinkle, C. L. Defect Dominated Doping and Contact Resistance in $MoS_2$. *ACS Nano* **2014**, *8*, 2880-2888.

(6) Kim, S. Y.; Park, S.; Choi, W. Variability of Electrical Contact Properties in Multilayer $MoS_2$ Thin-Film Transistors. *Appl. Phys. A: Mater. Sci. Process.* **2014**, *117*, 761-766.

(7) Liu, H.; Si, M.; Deng, Y.; Neal, A. T.; Du, Y.; Najmaei, S.; Ajayan, P. M.; Lou, J.; Ye, P. D. Switching Mechanism in Single-Layer Molybdenum Disulfide Transistors: An Insight into Current Flow across Schottky Barriers. *ACS Nano* **2013**, *8*, 1031-1038.

(8) Li, H.-M.; Lee, D.-Y.; Choi, M. S.; Qu, D.; Liu, X.; Ra, C.-H.; Yoo, W. J. Metal-Semiconductor Barrier Modulation for High Photoresponse in Transition Metal Dichalcogenide Field Effect Transistors. *Sci. Rep.* **2014**, *4*, 4041 1-7.

(9) Kwak, J. Y.; Hwang, J.; Calderon, B.; Alsalman, H.; Munoz, N.; Schutter, B.; Spencer, M. G. Electrical Characteristics of Multilayer MoS2 FET's with MoS2/Graphene Heterojunction Contacts. *Nano Lett.* **2014**, *14,* 4511-4516.

(10) Feng, L.-p.; Su, J.; Li, D.-p.; Liu, Z.-t. Tuning the Electronic Properties of Ti–$MoS_2$ Contacts Through Introducing Vacancies in Monolayer $MoS_2$. *Phys. Chem. Chem. Phys.* **2015**, *17*, 6700-6704.

(11) Kang, J.; Sarkar, D.; Liu, W.; Jena, D.; Banerjee, K. *A Computational Study of Metal-Contacts to Beyond-Graphene 2D Semiconductor Materials*, IEEE Int. Electron Devices Meet., Tech. Dig.,2012; pp 17.4.1-17.4.4.

(12) Gong, C.; Colombo, L.; Wallace, R. M.; Cho, K. The Unusual Fermi Level pinning Mechanism at Metal-$MoS_2$ Interfaces. *Nano Lett.* **2014**, *14*, 1714-1720.

(13) Allain, A.; Kang, J.; Banerjee, K.; Kis, A. Electrical Contacts to Two-Dimensional Semiconductors. *Nat. Mater.* **2015**, *14*, 1195-1205.

(14) McGovern, I.; Dietz, E.; Rotermund, H.; Bradshaw, A.; Braun, W.; Radlik, W.; McGilp, J. Soft X-ray Photoemission Spectroscopy of Metal-Molybdenum Bisulphide Interfaces. *Surf. Sci.* **1985**, *152*, 1203-1212.

(15) Lince, J. R.; Carré, D. J.; Fleischauer, P. D. Schottky-Barrier Formation on a Covalent Semiconductor without Fermi-level pinning: The Metal-$MoS_2$ (0001) Interface. *Phys. Rev. B: Condens. Matter Mater. Phys.* **1987**, *36*, 1647.

(16) Appenzeller, J., Private Communication. (2015)

(17) English, C. D.; Shine, G.; Dorgan, V. E.; Saraswat, K. C.; Pop, E. In *Improving Contact Resistance in $MoS_2$ Field Effect Transistors*, Device Research Conference (DRC), 2014 72nd Annual, **2014**; IEEE: pp 193-194.

(18) English, C. D.; Shine, G.; Dorgan, V. E.; Saraswat, K. C.; Pop, E. Improved Contacts to $MoS_2$ Transistors by Ultra-High Vacuum Metal Deposition. *Nano Lett.* **2016**, *16* (6), 3824–3830.

(19) Abraham, M.; Mohney, S. E. Annealed Ag Contacts to $MoS_2$ Field-Effect Transistors. *J. Appl. Phys.* **2017**, *122* (11), 115306.

(20) Pirkle, A.; Chan, J.; Venugopal, A.; Hinojos, D.; Magnuson, C. W.; McDonnell, S.; Colombo, L.; Vogel, E. M.; Ruoff, R. S.; Wallace, R. M. The Effect of Chemical Residues on the Physical and Electrical Properties of Chemical Vapor Deposited Graphene Transferred to $SiO_2$. Appl. Phys. Lett. **2011**, *99*, 122108.

(21) Chan, J.; Venugopal, A.; Prikle, A.; McDonnell, S.; Hinojos, D.; Magnuson, C. W.; Ruoff, R. S.; Colombo, L.; Wallace, R. M.; Vogel, E. M. Reducing Extrinsic Performance-Limiting Factors in Graphene Grown by Chemical Vapor Deposition. ACS Nano **2012**, *6* (4), 3224-3229.

(22) Tiwari, C. S.; Lim, Y. S.; Fulton, R.; Srinivasan, J.; Gisinger, M.; Flynn, P.; Mak, L. H. Characterization of the Descum Process for Various Silicon Substrates Doping. *ECS Trans.* **2013**, *58* (6), 251–259.

(23) Bulk $MoS_2$ crystals, 2D Semiconductors, 2017; http://www.2dsemiconductors.com.

(24) BJD 1800 Temescal e-beam evaporator, 2017; http://www.utdallas.edu/research/cleanroom/

(25) Azcatl, A.; McDonnell, S.; Santosh, K. C.; Peng, X.; Dong, H.; Qin, X.; Addou, R.; Mordi, G. I.; Lu, N.; Kim, J.; et al. $MoS_2$ Functionalization for Ultra-Thin Atomic Layer Deposited Dielectrics. *Appl. Phys. Lett.* **2014**, *104* (11), 111601.

(26) Wallace, R. M. In-Situ Studies of Interfacial Bonding of High-k Dielectrics for CMOS Beyond 22nm. In *ECS Transactions*; **2008**; Vol. 16, pp 255–271.

(27) ASTM E2108-00 Standard Practice for Calibration of the Electron Binding-Energy Scale of an X-Ray Photoelectron Spectrometer, ASTM International, West Conshohocken, PA, 2000,. West Conshohocken, PA 2000, pp E2108-00.

(28) Herrera-Gómez, A.; Hegedus, A.; Meissner, P. L. Chemical Depth Profile of Ultrathin Nitrided $SiO_2$ Films. *Appl. Phys. Lett.* **2002**, *81* (6), 1014–1016.

(29) McDonnell, S.; Brennan, B.; Azcatl, A.; Lu, N.; Dong, H.; Buie, C.; Kim, J.; Hinkle, C. L.; Kim, M. J.; Wallace, R. M. $HfO_2$ on $MoS_2$ by Atomic Layer Deposition: Adsorption Mechanisms and Thickness Scalability. *ACS Nano* **2013**, *7*, 10354-10361.

(30) The $Mo_xS_y$ feature in the S 2*p* spectra is similar to that seen after $He^+$ ion bombardment of $MoS_2$, which was assigned to elemental sulfur.(Ref 28) However, spectral analysis shows that the binding energy position of this feature (~163 eV) is too low to be elemental sulfur (164 eV) and so it has instead been assigned to $Mo_xS_y$. A similar feature must necessarily be present in the Mo 3*d* core-level however this would overlap with the Doniac Sunjic tail of the $Mo^0$ and is therefore not resolved in this study.

(31) Durbin, T. D.; Lince, J. R.; Didziulis, S. V.; Shuh, D. K.; Yarmoff, J. A. Soft-X-ray Photoelectron-Spectroscopy Study of the Interaction of Cr with $MoS_2$(0001). *Surf. Sci.* **1994**, *302*, 314-328.

(32) Doniach, S.; Sunjic, M. Many-Electron Singularity in X-ray Photoemission and X-ray Line Spectra From Metals. *J. Phys. C: Solid State Phys.* **1970**, *3*, 285-291.

(33) Wagner, C. D., *Handbook of X-ray Photoelectron Spectroscopy: a Reference Book of Standard Data for use in X-ray Photoelectron Spectroscopy*. Physical Electronics, Inc., Perkin-Elmer Corp.: 1995.

(34) Fujimori, A.; Suga, S.; Negishi, H.; Inoue, M. X-ray Photoemission and Auger-Electron Spectroscopic Study of the Electronic Structure of Intercalation Compounds $M_x$ $TiS_2$ (M= Mn, Fe, Co, and Ni). *Phys. Rev. B: Condens. Matter Mater. Phys.* **1988**, *38*, 3676-3689.

(35) Longo, R. C.; McDonnell, S.; Dick, D.; Wallace, R.; Chabal, Y. J.; Owen, J. H.; Ballard, J. B.; Randall, J. N.; Cho, K. Selectivity of Metal Oxide Atomic Layer Deposition on Hydrogen Terminated and Oxidized Si (001)-(2× 1) Surface. *J. Vac. Sci. Technol. B* **2014**, *32*, 03D112.1-03D112.6.

(36) *CRC Handbook of Chemistry and Physics*. 70th ed.; West, Robert C., David R. Lide (Eds) CRC Press Inc. Boca Ration, Florida: 1989-1990.

(37) Abendroth, R. P. A *Thermodynamic Study of the Titanium Sulfides*. Ph. D. Thesis, University of Missouri, **1957**.

(38) Addou, R.; Colombo, L.; Wallace, R. M. Surface Defects on Natural $MoS_2$. *ACS Appl. Mater.* I*nterfaces* **2015**, *7*, 11921-11929.

(39) Addou, R.; McDonnell, S.; Barrera, D.; Guo, Z.; Azcatl, A.; Wang, J.; Zhu, H.; Hinkle, C. L.; Quevedo-Lopez, M.; Alshareef, H. N. Impurities and Electronic Property Variations of Natural $MoS_2$ Crystal Surfaces. *ACS Nano* **2015**, *9*, 9124-9133.

(40) Connelly, D.; Faulkner, C.; Grupp, D.; Harris, J. A New Route to Zero-Barrier Metal Source/Drain MOSFETs. *IEEE Trans. Nanotechnol.* **2004**, *3*, 98-104.

(41) Coss, B. E.; Sivasubramani, P.; Brennan, B.; Majhi, P.; Wallace, R. M.; Kim, J. Measurement of Schottky Barrier Height Tuning using Dielectric Dipole Insertion Method at Metal–Semiconductor Interfaces by Photoelectron Spectroscopy and Electrical Characterization Techniques. *J. Vac. Sci. Technol., B* **2013**, *31*, 021202.

(42) Coss, B. E.; Loh, W.-Y.; Floresca, H. C.; Kim, M. J.; Majhi, P.; Wallace, R. M.; Kim, J.; Jammy, R. Dielectric Dipole Mitigated Schottky Barrier Height Tuning Using Atomic Layer Deposited Aluminum Oxide for Contact Resistance Reduction. *Appl. Phys. Lett.* **2011**, *99*, 102108.1-102108.3.

(43) Coss, B. E.; Loh, W.-Y.; Oh, J.; Smith, G.; Smith, C.; Adhikari, H.; Sassman, B.; Parthasarathy, S.; Barnett, J.; Majhi, P. In *CMOS Band-Edge Schottky Barrier Heights using Dielectric-Dipole Mitigated (DDM) Metal/Si for Source/Drain Contact Resistance Reduction*, *IEEE Symp. VLSI Technol., Dig. Tech. Pap*. **2009**; pp 104-105.

(44) Lin, J.-Y. J.; Roy, A. M.; Nainani, A.; Sun, Y.; Saraswat, K. C. Increase in Current Density for Metal Contacts to n-Germanium by Inserting $TiO_2$ Interfacial Layer to Reduce Schottky Barrier Height. *Appl. Phys. Lett.* **2011**, *98*, 092113.1-092113.3.

(45) Hu, S.; Shaner, M. R.; Beardslee, J. A.; Lichterman, M.; Brunschwig, B. S.; Lewis, N. S. Amorphous $TiO_2$ Coatings Stabilize Si, GaAs, and GaP Photoanodes for Efficient Water Oxidation. *Science* **2014**, *344*, 1005-1009.

(46) Robertson, J. Band Offsets of Wide-Band-Gap Oxides and Implications for Future Electronic Devices. *J. Vac. Sci. Technol., B* 2000, *18*, 1785-1791.

(47) Perego, M.; Seguini, G.; Scarel, G.; Fanciulli, M.; Wallrapp, F. Energy Band Alignment at $TiO_2$/Si Interface with Various Interlayers. *J. Appl. Phys.* **2008**, *103*, 3509.1-3509.6.

(48) Michaelson, H. B. The Work Function of the Elements and its Periodicity. *J. Appl. Phys.* **1977**, *48*, 4729-4733.

(49) Eastman, D. Photoelectric Work Functions of Transition, Rare-Earth, and Noble Metals. *Phys. Rev. B: Condens. Matter Mater. Phys.* **1970**, *2*, 1-2.

(50) McDonnell, S.; Azcatl, A.; Addou, R.; Gong, C.; Battaglia, C.; Chuang, S.; Cho, K.; Javey, A.; Wallace, R. M. Hole Contacts on Transition Metal Dichalcogenides: Interface Chemistry and Band Alignments. *ACS Nano* **2014**, *8*, 6265-6272.

(51) Duda, J.; Yang, C.-Y.; Foley, B.; Cheaito, R.; Medlin, D.; Jones, R.; Hopkins, P. Influence of Interfacial Properties on Thermal Transport at Gold: Silicon Contacts. *Appl. Phys. Lett.* **2013**, *102*, 081902.1-081902.5.

(52) Cheaito, R.; Gaskins, J. T.; Caplan, M. E.; Donovan, B. F.; Foley, B. M.; Giri, A.; Duda, J. C.; Szwejkowski, C. J.; Constantin, C.; Brown-Shaklee, H. J. Thermal Boundary Conductance Accumulation and Interfacial Phonon Transmission: Measurements and Theory. *Phys. Rev. B: Condens. Matter Mater. Phys.* **2015**, *91*, 035432.1-035432.12.

(53) Lee, S.-M.; Cahill, D. G.; Allen, T. H. Thermal Conductivity of Sputtered Oxide Films. *Phys. Rev. B: Condens. Matter Mater. Phys.* **1995**, *52*, 253-257.

(54) Hopkins, P. E.; Phinney, L. M.; Serrano, J. R.; Beechem, T. E. Effects of Surface Roughness and Oxide Layer on the Thermal Boundary Conductance at Aluminum/Silicon Interfaces. *Phys. Rev. B: Condens. Matter Mater. Phys.* **2010**, *82*, 085307.1-085307.5.

(55) Freedy, K. M.; Giri, A.; Foley, B. M.; Barone, M. R.; Hopkins, P. E.; McDonnell, S. Titanium Contacts to Graphene: Process-Induced Variability in Electronic and Thermal Transport. *Nanotechnology*, **2018**, *29*, 145201.

(56) McDonnell, S.; Smyth, C.; Hinkle, C. L.; Wallace, R. M. $MoS_2$-Titanium Contact Interface Reactions. *ACS Appl. Mater. Interfaces*, **2016**, *8* (12), 8289-8294.

(57) Bolshakov, P.; Smyth, C. M.; Khosravi, A.; Zhao, P.; Hurley, P. K.; Hinkle, C. L.; Wallace, R. M.; Young, C. D. Contact Engineering for Dual-Gate $MoS_2$ Transistors Using $O_2$ Plasma Exposure. Submitted to ACS Applied Electronic Materials, 2018.

(58) Yang, W.; Sun, Q.-Q.; Geng, Y.; Chen, L.; Zhou, P.; Ding, S.-J.; Zhang, D. W. The Integration of Sub-10 Nm Gate Oxide on MoS2 with Ultra Low Leakage and Enhanced Mobility. *Sci. Rep.* **2015**, *5* (1), 11921.

(59) Zhu, H.; Qin, X.; Cheng, L.; Azcatl, A.; Kim, J.; Wallace, R. M. Remote Plasma Oxidation and Atomic Layer Etching of $MoS_2$. *ACS Appl. Mater. Interfaces* **2016**, *8* (29), 19119–19126.

(60) McDonnell, S.; Azcatl, A.; Addou, R.; Gong, C.; Battaglia, C.; Chuang, S.; Cho, K.; Javey, A.; Wallace, R. M. Hole Contacts on Transition Metal Dichalcogenides: Interface Chemistry and Band Alignments. *ACS Nano* **2014**, *8* (6), 6265–6272.

(61) Battaglia, C.; Yin, X.; Zheng, M.; Sharp, I. D.; Chen, T.; McDonnell, S.; Azcatl, A.; Carraro, C.; Ma, B.; Maboudian, R.; et al. Hole Selective $MoO_x$ Contact for Silicon Solar Cells. *Nano Lett.* **2014**, *14* (2), 967–971.

(62) Chuang, S.; Battaglia, C.; Azcatl, A.; McDonnell, S.; Kang, J. S.; Yin, X.; Tosun, M.; Kapadia, R.; Fang, H.; Wallace, R. M.; et al. $MoS_2$ P-Type Transistors and Diodes Enabled by High Work Function $MoO_x$ Contacts. *Nano Lett.* **2014**, *14* (3), 1337–1342.

(63) Santosh, K. C.; Longo, R. C.; Addou, R.; Wallace, R. M.; Cho, K. Electronic Properties of $MoS_2/MoO_x$ Interfaces: Implications in Tunnel Field Effect Transistors and Hole Contacts. *Sci. Rep.* **2016**, *6* (1), 33562.

(64) Liu, H.; Si, M.; Deng, Y.; Neal, A. T.; Du, Y.; Najmaei, S.; Ajayan, P. M.; Lou, J.; Ye, P. D. Switching Mechanism in Single-Layer Molybdenum Disulfide Transistors: An Insight into Current Flow across Schottky Barriers. *ACS Nano* **2014**, *8* (1), 1031–1038.

(65) Li, H. M.; Lee, D. Y.; Choi, M. S.; Qu, D.; Liu, X.; Ra, C. H.; Yoo, W. J. Metal-Semiconductor Barrier Modulation for High Photoresponse in Transition Metal Dichalcogenide Field Effect Transistors. *Sci. Rep.* **2014**, *4* (1), 4041.

(66) Kim, S. Y.; Park, S.; Choi, W. Variability of Electrical Contact Properties in Multilayer $MoS_2$ Thin-Film Transistors. *Appl. Phys. A* **2014**, *117* (2), 761–766.

(67) Addou, R.; McDonnell, S.; Barrera, D.; Guo, Z.; Azcatl, A.; Wang, J.; Zhu, H.; Hinkle, C. L.; Quevedo-Lopez, M.; Alshareef, H. N.; et al. Impurities and Electronic Property Variations of Natural $MoS_2$ Crystal Surfaces. *ACS Nano* **2015**, *9* (9), 9124–9133.

(68) Kim, C.; Moon, I.; Lee, D.; Choi, M. S.; Ahmed, F.; Nam, S.; Cho, Y.; Shin, H.-J.; Park, S.; Yoo, W. J. Fermi Level Pinning at Electrical Metal Contacts of Monolayer Molybdenum Dichalcogenides. *ACS Nano* **2017**, *11* (2), 1588–1596.

(69) Introduction to DNQ-Novolac Resists - Henderson Research Group https://sites.google.com/site/hendersonresearchgroup/helpful-primers-introductions/intro-to-dnq-novolac-resists. (Accessed October 3, 2018)

(70) Joiner, C. A.; Roy, T.; Hesabi, Z. R.; Chakrabarti, B.; Vogel, E. M. Cleaning Graphene with a Titanium Sacrificial Layer. *Appl. Phys. Lett.* **2014**, *104*, 223109.

(71) Venugopal, A. Effect of Contacts, Graphene Type and Underlying Substrate on the Transport Properties of Graphene. Ph.D. Dissertation, University of Texas at Dallas, TX, 2012.

(72) Kaushik, N.; Karmakar, D.; Nipane, A.; Karande, S.; Lodha, S. Interfacial N-Doping Using an Ultrathin $TiO_2$ Layer for Contact Resistance Reduction in $MoS_2$. *ACS Appl. Mater. Interfaces* **2016**, *8* (1), 256–263.

# CHAPTER 5

# EFFECTS OF DEPOSITION CONDITIONS ON THE INTERFACE CHEMISTRY BETWEEN CONTACT METALS AND TUNGSTEN CHALCOGENIDES

Authors – Christopher M. Smyth[†], Rafik Addou[†], Stephen McDonnell[‡],
Christopher L. Hinkle[†], and Robert M. Wallace[†]

[†]The Department of Materials Science and Engineering, RL10
The University of Texas at Dallas
800 West Campbell Road
Richardson, Texas, 75080, USA

[‡] The Department of Materials Science and Engineering
University of Virginia
Charlottesville, Virginia, 22904, USA

## 5.1 Preface

Contact metals (Au, Ir, Cr, and Sc) are deposited on bulk $WS_2$, $WSe_2$, and $WTe_2$ under UHV ($< 2 \times 10^{-9}$ mbar) and HV ($< 5 \times 10^{-6}$ mbar) conditions and subsequently characterized with XPS to elucidate the effects of reactor base pressure on resulting interface chemistry, contact chemistry, and band alignment. The reactivity of the contact metals with the W-based TMDs follows the Sc > Ir > Cr > Au relationship in decending order. Au forms a vdW interface with $WS_2$ and $WSe_2$ regardless of deposition chamber ambient, but the significant Te excess in $WTe_2$ facilitates the formation of the $AuTe_x$ intermetallic at the Au–$WTe_2$ interface which contrasts thermodynamic predictions. Ir, Cr, and Sc form a covalent interface with all W-based TMDs by reducing the TMD to form interfacial metal chalcogenide intermetallics. When Cr and Sc are deposited under HV conditions, significant oxygen incorporation is observed. Tungsten oxychalcogenide forms at the Cr–TMD interfaces and the majority of the deposited Cr is converted to $Cr_xO_y$ and $Cr(OH)_x$ *in–situ*. Sc is completely oxidized when deposited in HV. Regardless of the contact metal, $WO_x$ forms during deposition under HV conditions which may positively affect hole transport. None of the metals deposited in UHV obey the Schottky-Mott rule; the $E_F$ is moderately pinned near the conduction band edge of $WS_2$ and near the middle of the band gap in $WSe_2$. Ir deposition results in the largest $E_F$ shifts and the smallest hole Schottky barriers in $WS_2$ and $WSe_2$, while Cr and Sc form the smallest electron SBHs with $WS_2$ and $WSe_2$, respectively. The reaction products detected at the interfaces and the defects in the TMDs contribute to anomalous band alignment. These results reveal the *true* interface chemistry formed between metals and W-based TMDs under UHV and HV conditions and demonstrate the impact on the $E_F$ position following contact formation on the W-based TMDs.

Part of the text and figures in this chapter have been repurposed from ($WSe_2$-Contact Metal Interface Chemistry and Band Alignment under High Vacuum and Ultra High Vacuum Deposition Conditions. 2D Materials. 2017, 4, 025084) according to the CC BY license. The authors are Christopher M. Smyth (UTD), Rafik Addou (UTD), Stephen McDonnell (UVA), Christopher L. Hinkle (ND), and Robert M. Wallace (UTD). Dr. S. McDonnell and Dr. R. M. Wallace are acknowledged for conceiving the experimental plan. The experiments were performed and the data was analyzed and interpreted by myself. Dr. R. Addou obtained the STM images. All co-authors provided valuable inputs when preparing the manuscript.

## 5.2 Introduction

As the scaling of Si–based electronic devices approaches its limit, alternative materials to Si are under investigation to permit extension of Moore's law scaling. Two dimensional materials, specifically transition metal dichalcogenides (TMDs, e.g., $MoS_2$, $WSe_2$), with atomic scale thickness, tunable bandgap (~0.7-2.2 eV), and comparable mobilities with existing Si metal-oxide-semiconductor (MOS) channels, have emerged as strong candidates to complement current Si-based device technology.[1,2] TMDs are, in principle, ideal for the design of ultrashort channel field effect transistors (FETs) due to these novel properties which stem from their layered nature and set TMDs apart from Si, Ge, and III–V semiconductor materials.

Whereas $MoS_2$ has been widely studied as a potential channel material in TMD-based FETs,[3-7] studies focused on W-based FETs are less prevalent. The electrical behavior of various contact metals on TMDs will vary significantly depending on the TMD, for instance the transition metal sulfides favors n–type conduction,[8,9] while $WSe_2$ favors p–type conduction[10] and $WTe_2$ is a semimetal.[11] To date, reasonable performance has been achieved in $WSe_2$-($WS_2$)-based FETs with measured $I_{ON}/I_{OFF}$ ratio $>10^8$ ($>10^7$) and mobility ($\mu$) of $2.1 \times 10^3$ (~50) $cm^2/V^{-1}$ $s^{-1}$. However, the parasitic effects of contact resistance must be accounted for as substantial differences can arise between measured $\mu$ (e.g., 100 $cm^2/V^{-1}$ $s^{-1}$) and intrinsic $\mu$ (e.g., 500 $cm^2/V^{-1}$ $s^{-1}$) in TMD-based devices if contact resistance effects are overlooked.[12-14] Although $WTe_2$ is not useful in transistor applications, it shows promise as an atomically thin interconnect material[11] and a spin torque switch for magnetic technologies.[15] The interface chemistry between contact metals and $WTe_2$ is just as important as in TMD-based transistors because inversion symmetry is only broken in the monolayer form of $WTe_2$ and efficient spin polarized current injection in a spin torque device requires a high enough contact resistance to preserve spin orientation but low enough to permit sufficient current injection. Substantial reactions with a metal contact could consume an entire $WTe_2$ monolayer, which would be catastrophic to its functionality in both a spin torque device and as an interconnect layer.

Contact resistance (0.2 kΩ µm)[16] in TMD-based devices is an order of magnitude greater than what has been achieved in Si–based devices (0.01 kΩ–µm) to date.[10,17,18] Ion implantation is commonly employed to reduce contact resistance in Si-based devices. Analogous doping schemes involving surface charge transfer[19,20] or substitution[21] have been developed for TMDs, although doping effects degrade in air for many of these strategies. Alternative methods have been employed recently in TMD–based devices for reduced contact resistance and include but are not limited to a $WO_x$ hole injection layer,[22] metallic edge contacts,[16,23] vacuum annealing,[24] and metallic 2D top contacts.[14,25] Contact resistances from 0.2–2 kΩ µm have been achieved in $WS_2$- and $WSe_2$-based FETs employing the strategies listed above. Perhaps the most promising advance is represented by the performance enhancement achieved via $WO_x$ hole injection layer as other strategies require processes such as large scale phase transformation or manually stacking exfoliated 2D materials for device structures are not commercially viable. Top contacts to TMDs offer a direct route to commercially viable device structures. Therefore, the contact metal must be carefully selected based on its work function to achieve the desired carrier injection into the TMD channel. Theoretically, carrier injection in an electronic device depends upon the SBH, or the difference between the metal work function and the electron affinity of the TMD (in the case of an electron SBH) or $E_{ion}$ (in the case of a hole SBH).

However, many factors play a role in the chemical and electrical nature of the interface between W-based TMDs and metal contacts, including the difference between contact material work function and the electron affinity of the TMD (see Schottky–Mott model)[26] as well as the *d*–orbital interaction between the contact metal and W in W-based TMDs.[13,27,28] Reaction products which form at the contact metal–TMD interface provide additional, often compositionally dependent, electronic states, which can reside in the TMD band gap and contribute to the complex mechanism of FLP. In addition, gap states, and therefore FLP, are associated with the substantial concentration of defects common in geological and synthetic TMDs.[29-32] Kang et al. predicts covalent bonding and "Ohmic interfaces" between $WSe_2$ and Pd, W, and Ti.[27] However, experimentally determined n-type and ambipolar transport in $WSe_2$ FETs employing In and Ti as contact materials, respectively, disagree with DFT predictions regarding analogous device architectures.[13,19,27] Theoretical calculations predict the shortest bond length, lowest potential barrier, and highest density of states at the $E_F$ between Cr and $WS_2$, but do not consider the perturbative effects of surface defects or adsorbates.[33] DFT models predicting the electronic properties and nature of the chemical bonding at various metal–TMD interfaces limit material systems to a pure metal, defect free TMD, and a pristine metal–TMD interface due to computational limitations, which is, of course, far from reality.[10,27,33]

Our recent work clearly demonstrates the dependence of contact composition and contact–$MoS_2$ interface chemistry on deposition chamber ambient, as reactions were observed between Ir, Cr, and Sc when deposited on $MoS_2$ under either high vacuum (HV, $5 \times 10^{-6}$ mbar – typical of cleanroom tools encountered in device fabrication) or lower pressure ultrahigh vacuum (UHV, $1 \times 10^{-9}$ mbar) conditions.[34] Furthermore, significant oxidation of Cr and Sc were observed when deposited under HV conditions. McDonnell et al. found that both the contact metal composition and the contact–$MoS_2$ interface chemistry differs drastically when Ti is deposited under UHV conditions compared with HV conditions.[35] Interface chemistry presumably plays a significant role in contact performance as significant improvements in contact resistance has been realized in $MoS_2$-based FETs via UHV contact deposition.[4] It is therefore not appropriate to rely solely on the presence of pristine interfaces between contact metals and W-based TMDs or a compositionally pure metallic contact, as is done in modeling. As a result, more realistic contact metal–TMD interface models, which consider the defective nature of TMDs and availability of background gas molecules at the TMD surface during metal deposition, in tandem with carefully designed experiments are essential to determine the optimal contact material and deposition conditions for superior TMD–based device performance.

To elucidate a more complete understanding of the true chemical and electronic interaction between contact metal and W-based TMDs, its dependence on deposition chamber ambient is explored for contact metals with vacuum work functions ranging from 3.5 to 5.3 eV, specifically Ir, Au, Cr, and Sc.[3,36,37] As noted previously, Cr is also often employed as an “adhesion layer” for contacts in device fabrication.[34] XPS is employed to evaluate the contact composition, metal–(bulk)W-based TMD interface chemistry, and $E_F$ shift resulting from metal deposition under different deposition chamber conditions. The potential implications of experimentally determined interface chemistry on the band alignment between metal contacts and W-based TMDs and transport across the interface are discussed.

## 5.3 Methods

*Metal Deposition under UHV and HV Conditions and Interface Characterization.* All $WS_2$, $WSe_2$, and $WTe_2$ samples originated from the same bulk crystals purchased from HQ Graphene.[38] The procedures employed for sample preparation, mounting, metal source outgassing, determining metal deposition rates (0.3–0.6 nm/min depending on the metal), metal deposition under both HV and UHV conditions, and subsequent XPS analysis are identical to that employed for an analogous investigation of interface chemistry between Au, Ir, Cr, and Sc and bulk $MoS_2$ described in Appendix A. Exfoliation is performed under laboratory ambient conditions, as is typical in device fabrication. Under UHV conditions, metals were deposited via electron beam in a chamber, base pressure $\sim 1 \times 10^{-9}$ mbar, attached to a UHV cluster tool described in detail elsewhere.[39] Following metal deposition, samples were transferred to a separate chamber, without breaking vacuum through a UHV transfer tube held at $1 \times 10^{-10}$ mbar, where XPS was performed. Under HV conditions, metals were deposited in an elastomer–sealed Temescal BJD–1800 e–beam evaporator with base pressure $\sim 1 \times 10^{-6}$ mbar in the cleanroom facility.[40] Samples were then transferred *ex–situ* as quickly as possible to the analysis chamber under UHV conditions for all XPS characterization (~5 min air exposure between removal from cleanroom deposition tool and loading into UHV cluster tool). All Au, Ir, Cr, and Sc films were deposited on the TMDs with a target thickness of 1 nm.

The method by which the Au 4*f*, Ir 4*f*, Cr 2*p*, and Sc 2*p* core level reference spectra were obtained is described in Appendix B. The W metal reference was obtained by sputtering 50 nm of W under an $N_2$ flow of 30 sccm onto a Si(111) wafer cleaned in a 100:1 HF bath. The base pressure of the interconnected sputtering chamber is ~$2 \times 10^{-9}$ mbar. Prior to transferring the sample into the sputtering chamber for W deposition, the W target was outgassed for 1 hour with identical parameters as those employed during deposition. Following outgassing, the chamber was pumped to a pressure of $2 \times 10^{-9}$ mbar before moving the sample inside from UHV transfer tube. The sputtering tool is employed solely for the purpose of obtaining the W reference spectrum, and is attached to the same UHV cluster tool as was mentioned earlier. Prior to obtaining the W 4*f* reference spectrum, the W film obtained by sputter deposition was bombarded with $Ar^+$ ions accelerated under 5 kV and 25 mA for a total of 30 minutes to ensure a clean, oxide-free surface. The reference W 4*f* spectrum was obtained *in–situ* via XPS under UHV conditions immediately following $Ar^+$ ion treatment. The corresponding O 1*s* and C 1*s* core level spectra were also obtained to confirm a clean W film within the photoelectron sampling depth.

*Growing, Damaging, and Characterizing amorphous $WO_3$ and $WO_x$ Films.* HeI photons (21.2 eV) are employed in the UPS measurements performed in this work. An amorphous $WO_3$ (a-$WO_3$) film was grown by reactively sputtering tungsten with a power of 100 W under a combined flow of 10 sccm Ar and 10 sccm $O_2$ onto a $SiO_2$/Si substrate at room temperature. Oxygen deficient, amorphous $WO_x$ (a-$WO_x$) was prepared from a-$WO_3$ by exposing the film to 100 W Ar plasma (10 sccm Ar flow). The a-$WO_3$ and a-$WO_x$ films were characterized with UPS and XPS *in-situ* under UHV conditions immediately following growth and Ar plasma exposure without breaking vacuum.

*XPS Instrumentation, Parameters, and Data Analysis.* XPS characterization of the exfoliated TMDs and the TMDs following metal deposition was performed via a monochromated Al Kα source and Omicron EA125 hemispherical analyzer with ±0.05 eV resolution. In addition, a takeoff angle of 45°, acceptance angle of 8°, and pass energy of 15 eV were employed during spectral acquisition. The analyzer was calibrated with Au, Ag, and Cu foils according to ASTM E1208.[41] Spectra were deconvolved using AAnalyzer,[42] a curve fitting software.

## 5.4 Results and Discussion

We first consider the effects of reactor ambient upon interface chemistry between contact metals (Au, Ir, Cr, and Sc) and W-based TMDs ($WS_2$, $WSe_2$ and $WTe_2$) via detailed analysis of appropriate core level spectra obtained by XPS prior to and following metal deposition under UHV and HV conditions. In addition, we employ thermodynamics to justify the chemical states observed in core level spectra.

All $\Delta G^\circ_f$ values are reported per chalcogen or oxygen anion. All electronegativities are reported according to the Pauling electronegativity scale. Interfaces at which the metal does not interact chemically with the TMD will be referred to as vdW interfaces. Interfaces at which reactions between deposited metal and TMD are detected will be referred to as covalent interfaces. The binding energies of all reaction products detected in the tungsten (W 4*f*) and chalcogen (S 2*p*, Se 3*d*, or Te $3d_{5/2}$) core level spectra can be found in Table 5.1. See Section 5.3 for details on photoelectron core level spectra acquisition.

Table 5.1. Binding energies of chemical states detected in W $4f_{7/2}$, S $2p_{3/2}$, Se $3d_{5/2}$, and Te $3d_{5/2}$ core level spectra from $WS_2$, $WSe_2$, and $WTe_2$ after exfoliation and subsequent metal deposition in UHV (*in–situ*) or HV (*ex–situ).*

| Metals | TMD | Core Level | Exfoliated (UHV) | UHV | HV |
|---|---|---|---|---|---|
| Au | $WS_2$ | W $4f_{7/2}$ | 33.18 ($WS_2$) | 33.00 ($WS_2$) | 33.08 ($WS_2$) |
| | | S $2p_{3/2}$ | 162.78 ($WS_2$) | 162.61 ($WS_2$) | 162.72 ($WS_2$) |
| | $WSe_2$ | W $4f_{7/2}$ | 32.85 ($WSe_2$) | 32.58 ($WSe_2$) | 32.64 ($WSe_2$)<br>35.08 ($WO_2$) |
| | | Se $3d_{5/2}$ | 55.08 ($WSe_2$) | 54.83 ($WSe_2$) | 54.88 ($WSe_2$) |
| | $WTe_2$ | W $4f_{7/2}$ | 31.44 ($WTe_2$)<br>35.34 ($WO_x$) | 31.45 ($WTe_2$)<br>35.38 ($WO_x$) | 31.49 ($WTe_2$)<br>35.43 ($WO_x$) |
| | | Te $3d_{5/2}$ | 572.63 ($WTe_2$)<br>576.57 ($TeO_2$) | 572.63 ($WTe_2$)<br>572.93 ($AuTe_x$)<br>576.43 ($TeO_2$) | 572.66 ($WTe_2$)<br>572.98 ($AuTe_x$)<br>576.41 ($TeO_2$) |
| Ir | $WS_2$ | W $4f_{7/2}$ | 33.30 ($WS_2$) | 32.62 ($W_xIr_yS_z$)<br>33.73 ($WS_2$) | 31.82 ($W_xIr_yS_z$)<br>32.40 ($WS_2$)<br>32.84 ($WO_x$) |
| | | S $2p_{3/2}$ | 162.93 ($WS_2$) | 162.37 ($WS_2$)<br>162.75 ($W_xIr_yS_z$) | 162.02 ($WS_2$)<br>162.30 ($W_xIr_yS_z$)<br>166.36 ($SO^{x-}$) |
| | $WSe_2$ | W $4f_{7/2}$ | 32.78 ($WSe_2$) | 32.05 ($WSe_z$)<br>32.29 ($WSe_2$) | 31.83 ($WSe_z$)<br>32.22 ($WSe_2$)<br>35.09 ($WO_x$) |
| | | Se $3d_{5/2}$ | 55.04 ($WSe_2$) | 54.50 ($WSe_2$)<br>54.73 ($WSe_x$)<br>55.43 ($IrSe_2$) | 54.44 ($WSe_2$)<br>54.57 ($WSe_x$)<br>54.69 ($IrSe_x$) |
| | $WTe_2$ | W $4f_{7/2}$ | 31.44 ($WTe_2$)<br>35.51 ($WO_x$) | 31.46 ($WTe_2$)<br>31.91 ($W_xIr_yTe_z$) | 31.47 ($WTe_2$)<br>31.89 ($W_xIr_yTe_z$)<br>35.10 ($WO_x$) |
| | | Te $3d_{5/2}$ | 572.61 ($WTe_2$)<br>576.65 ($TeO_2$) | 572.59 ($WTe_2$)<br>573.16 ($W_xIr_yTe_z$) | 572.66 ($WTe_2$)<br>573.28 ($W_xIr_yTe_z$)<br>575.72 ($TeO_2$) |
| Cr | $WS_2$ | W $4f_{7/2}$ | 33.07 ($WS_2$) | 31.63 ($W^0$*)<br>32.87 ($WS_x$)<br>33.03 ($WS_2$) | 31.30 ($W^0$)<br>32.91 ($WS_x$)<br>33.07 ($WS_2$) |
| | | S $2p_{3/2}$ | 161.86 ($MoS_2$) | 162.41 ($CrS_x$,$WS_x$)<br>162.61 ($WS_2$) | 162.54 ($CrS_x$,$WS_x$)<br>162.65 ($WS_2$) |
| | $WSe_2$ | W $4f_{7/2}$ | 32.81 ($WSe_2$) | 31.32 ($W^0$)<br>32.40 ($WSe_2$) | 31.14 ($W^0$)<br>32.38 ($WO_xSe_y$)<br>32.58 ($WSe_2$)<br>35.15 ($WO_x$) |
| | | Se $3d_{5/2}$ | 55.05 ($WSe_2$) | 54.35 ($Cr_xSe_y$)<br>54.65 ($WSe_2$) | 54.05 ($Cr_xSe_y$)<br>54.58 ($WO_xSe_y$)<br>54.84 ($WSe_2$) |
| | $WTe_2$ | W $4f_{7/2}$ | 31.51 ($WTe_2$)<br>35.53 ($WO_x$) | 31.12 ($W^0$*)<br>31.48 ($WTe_2$)<br>35.54 ($WO_x$) | 31.42 ($WTe_2$)<br>35.43 ($WO_x$) |
| | | Te $3d_{5/2}$ | 572.70 ($WTe_2$)<br>576.54 ($TeO_2$) | 572.68 ($WTe_2$)<br>573.10 ($W_xCr_yTe_z$) | 572.62 ($WTe_2$)<br>575.96 ($TeO_2$) |
| Sc | $WS_2$ | W $4f_{7/2}$ | 33.22 ($WS_2$) | 31.63 ($WS_x$)<br>32.89 ($WS_2$) | 33.11 ($WS_2$)<br>33.51 ($WO_x$) |

| | | | | | |
|---|---|---|---|---|---|
| | | S 2$p_{3/2}$ | 162.83 ($WS_2$) | 161.94 ($ScS_x$)<br>162.62 ($WS_2$)<br>162.42 ($WS_x$) | 162.76 ($WS_2$) |
| | $WSe_2$ | W 4$f_{7/2}$ | 32.86 ($WSe_2$) | 227.69 ($Mo^0$)<br>229.00 ($MoSe_2$) | 229.10 ($MoSe_2$) |
| | | Se 3$d_{5/2}$ | 55.09 ($WSe_2$) | 54.47 ($MoSe_2$)<br>54.76 ($ScSe_x$) | 54.20 ($MoSe_2$) |
| | $WTe_2$ | W 4$f_{7/2}$ | 31.40 ($WTe_2$)<br>35.55 ($WO_x$) | 31.21 ($W^0$)<br>31.43 ($WTe_2$)<br>35.22 ($WO_x$) | 31.47 ($WTe_2$)<br>31.83 ($W_xSc_yTe_z$)<br>35.66 ($WO_x$) |
| | | Te 3$d_{5/2}$ | 572.60 ($WTe_2$)<br>576.54 ($TeO_2$) | 572.66 ($WTe_x$)<br>572.92 ($W_xSc_yTe_z$) | 572.64 ($WTe_2$)<br>575.96 ($TeO_2$) |
| *van der Waals interface Metal/TMD* | | | | | |
| *Covalent interface Metal/TMD* | | | | | |

### 5.4.1 Van der Waals Au–$WS_2$ and $WSe_2$ Interfaces and Covalent Au–$WTe_2$ Interface

*$WS_2$*

Reactions between Au and $WS_2$ are thermodynamically unfavorable considering the $\Delta G°_{f,Au2S}$ = -58.1 kJ/mol[43] is far more positive than the $\Delta G°_{f,WS2}$ (-164.9 kJ/mol).[44] The $WS_2$ chemical states in the S 2*p* and W 4*f* core levels obtained after exfoliation are separated by 129.60 eV, which is held constant throughout this chapter when fitting the bulk $WS_2$ chemical states detected in the W 4*f* and S 2*p* core levels after metal deposition. Using the integrated intensities of the S 2*p* and W 4*f* core levels obtained from exfoliated $WS_2$ corrected with the appropriate ASFs, the S:W ratio is ~2.0:1 in agreement with the expected stoichiometry. The concentrations of transition metal oxide and chalcogen oxide species on the $WS_2$ surface before Au deposition are below the limit of XPS detection, which is expected considering the high stability of $WS_2$ in air compared with the other W-based TMDs (see Section 5.4.6). Any reaction products that form at the Au–$WS_2$ interface in UHV or HV are below the limit of XPS detection (Figure 5.1a), which indicates Au forms a vdW interface with $WS_2$ at RT. However, a small concentration of $WO_x$ is detected after depositing Au in HV, which is consistent with the energetically favorable reaction between oxygen in the atmosphere and the dangling bonds at the $WS_2$ domain edges according to previously reported DFT calculations.[45] The shift to lower BE exhibited by the $WS_2$ core levels after depositing Au in UHV and HV is consistent with the expected upward band bending induced by depositing a high work function metal (relative to the semiconductor $E_F$) on $WS_2$. The band alignment obtained after depositing Au in UHV and HV in addition to the implications of $WO_x$ forming at the metal–$WS_2$ interface in HV on the band alignment will be discussed in more detail in Section 5.4.6.

The BEs of the Au $4f_{7/2}$ core level obtained from Au films deposited on $WS_2$ under UHV and HV conditions are ~0.25 eV higher than that of the Au reference (83.75 eV, Figure 5.1b). This suggests that the Au deposited under either UHV or HV conditions exhibits a smaller work function than expected of bulk, polycrystalline Au, consistent with the size-dependent work function of Au nanoparticles on a Si(111) substrate.[48] It is possible that BE shifts from bulk Au core levels exhibited by the Au films deposited on $WS_2$ in UHV and HV indicates additional non-metallic Au chemical states are detected corresponding with reactions between Au and $WS_2$. However, when the Au 4*f* core level spectra obtained following Au deposition under UHV and HV conditions are shifted 0.25 eV to lower BE and normalized with the reference Au 4*f* core level spectrum (Figure 5.2), the spectra are identical in line shape and FWHM indicating the Au films deposited on $WS_2$ are comprised of metallic Au.

Considering the attenuation of the W 4*f* and S 2*p* core levels following Au deposition under UHV conditions, the thickness of the Au film is estimated to be 6 Å. This represents an estimate of the average film thickness. However, images obtained *ex–situ* by AFM following Au deposition on all W-based TMDs discussed in this chapter under UHV and HV conditions demonstrate VW type Au growth regardless of deposition chamber ambient (Figure 5.3). These results are consistent

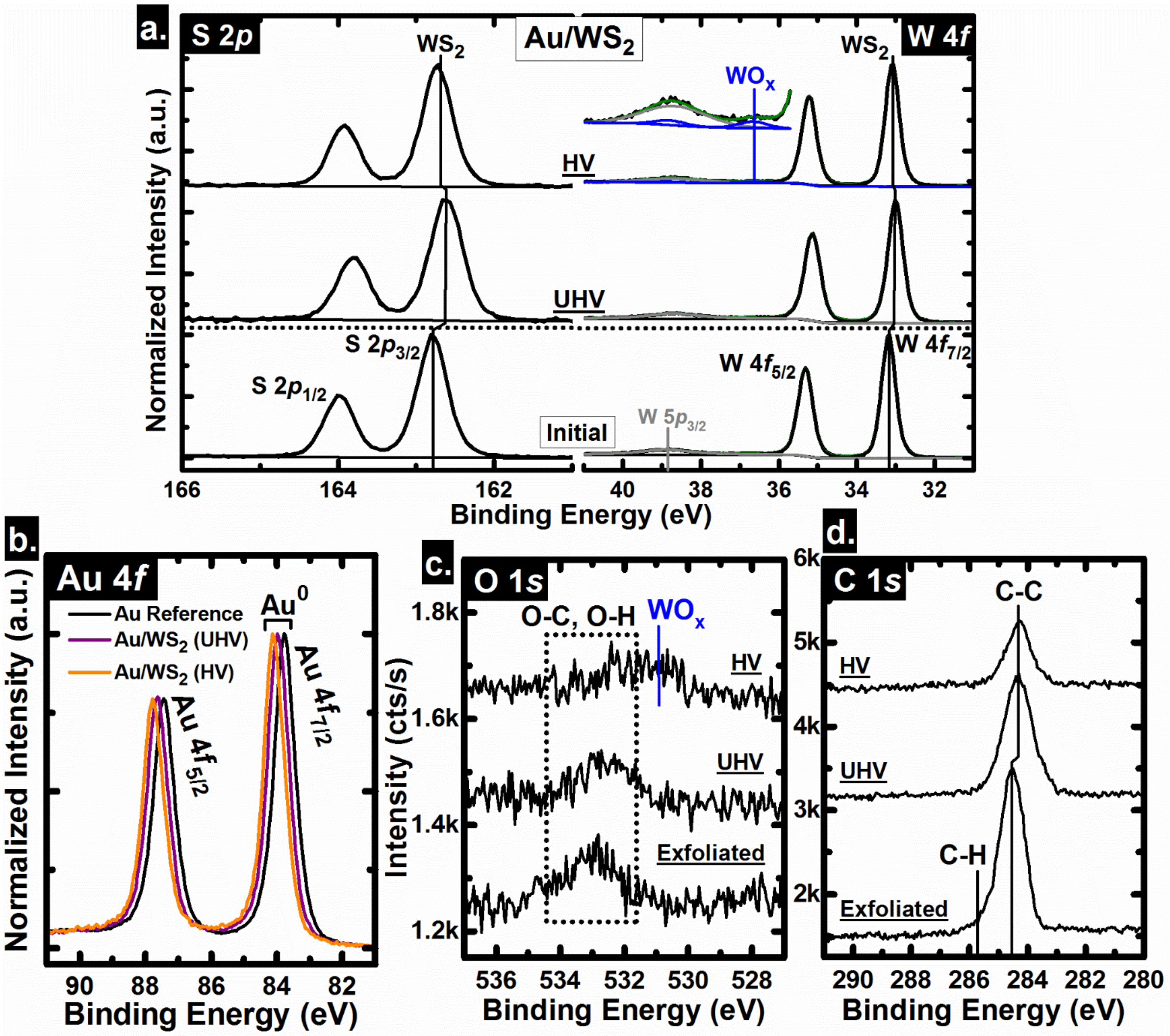

Figure 5.1. XPS spectra of the a) S 2*p*, W 4*f*, W 5$p_{3/2}$, c) O 1*s* and d) C 1*s* core level spectra obtained from $WS_2$ after exfoliation and subsequently depositing Au under UHV and HV conditions. b) XPS spectra of the Au 4*f* core level obtained from an Au reference and following Au deposition on $WS_2$ under UHV and HV conditions.

with a similar study alternatively employing STM to investigate Au growth on $WSe_2$.[47] Therefore, the estimate of Au thickness based upon the attenuation of the bulk $WS_2$ chemical states is not representative of the Au film morphology in the initial stages of growth on $WS_2$, specifically the height and diameter of Au clusters. The significant difference in RMS roughness of the Au–$WS_2$ surface formed in HV likely manifests as a result of depositing a thinner Au film in HV compared with UHV according to the 0.5× lower integrated intensity of the corresponding ‘HV’ Au 4*f* core level.

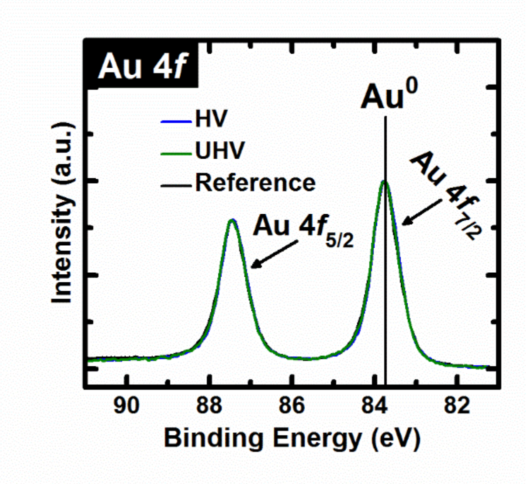

Figure 5.2. Au 4*f* core level spectra, obtained following Au deposition under UHV and HV conditions, shifted 0.25 eV to lower BE and normalized with the reference Au 4*f* core level spectrum.

The O 1*s* and C 1*s* core level spectra obtained from WS$_2$ after exfoliation and subsequent Au depositions in UHV and HV are displayed in Figures 5.1 c, d. Adventitious oxygen and carbon based species are detected on the exfoliated WS$_2$ surface before depositing Au in the forms of C–C, C–H, and O–H bonds, which adsorb on the WS$_2$ surface after exfoliation during the brief duration of air-exposure prior to loading into the UHV cluster tool for XPS and subsequent metallization. C–C and O–H species are detected after depositing Au in UHV and HV. Similar oxygen- and carbon-based adventitious species are detected on all exfoliated TMDs investigated in this chapter. Therefore, only chemical states detected in the O 1*s* and/or C 1*s* core levels that reflect oxygen- and/or carbon-based species other than the adventitious species detected in the Au–WS$_2$ system will be addressed throughout the remainder of this chapter. A chemical state is detected below 531.0 eV in the O 1*s* core level obtained after depositing Au in HV. This BE is

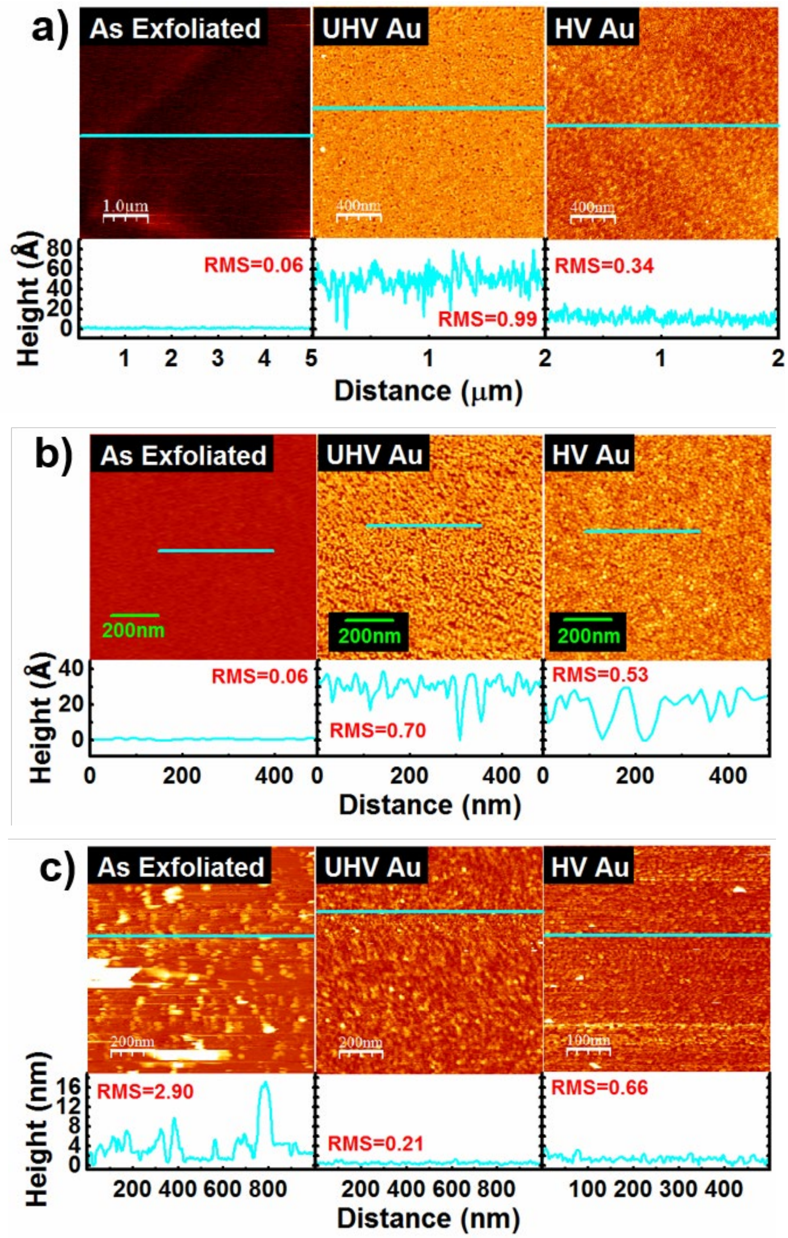

Figure 5.3. AFM images obtained *ex–situ* from a) $WS_2$, b) $WSe_2$, and c) $WTe_2$ after exfoliation and subsequent Au deposition in UHV and HV with corresponding line profiles below each image. The light blue line superimposed on each image represent the location each line profile was obtained from. The RMS roughness values are displayed in red. The topography of the exfoliated W-based TMDs displayed in a), b), and c) are consistent with all of the W-based TMDs before all other metal depositions performed in this work. Therefore, the AFM images obtained from the exfoliated W-based TMDs before Ir, Cr, and Sc depositions discussed later in this chapter are not displayed in the corresponding figures.

consistent with the oxygen chemical state in a transition metal oxide compound and indicates the formation of $WO_x$ either *in–situ* during Au deposition in the elastomer-sealed deposition tool or during the *ex–situ* transfer from the cleanroom deposition tool to the UHV cluster tool. The $WS_2$ crystal employed in this work exhibited a mirror like surface indicative of a small aerial density of domain edges where oxidation is most energetically favorable, which validates the $WO_x$ concentration near the limit of XPS detection after depositing Au in HV.

There are no carbon-related chemical states detected in any of the W 4*f*, Se 3*d*, Au 4*f*, Ir 4*f*, Cr 2*p*, or corresponding C 1*s* core level spectra which would suggest the formation of metal–carbon bonds of any kind. However, a typical procedure employed to fabricate TMD-based devices will involve exposing the channel material to air prior to patterning and metal deposition. Therefore, it is reasonable to assume the interface between metal and TMD channel will contain carbon, which could impact contact resistance.

### *WSe₂*

Reactions between Au and $WSe_2$ are not thermodynamically favorable. The persistence of $WSe_2$ is far more energetically favorable than the reduction of $WSe_2$ by Au to form AuSe as $\Delta G^\circ_{f,WSe2}$ = -132.0 kJ/mol, whereas the $\Delta G^\circ_{f,AuSe}$ = -31.99 kJ/mol.[48] The same presumably applies for other gold selenide stoichiometries. Figure 5.4a displays the Se 3*d*, W 4*f*, and W $5p_{3/2}$ core level spectra obtained from bulk $WSe_2$ following exfoliation and subsequent Au deposition under UHV and HV conditions.

Following exfoliation, the Se $3d_{5/2}$ and W $4f_{7/2}$ core levels are detected at binding energies of 55.08 and 32.85 eV, respectively, corresponding with a peak separation of 22.23 eV, typical of exfoliated, bulk $WSe_2$.[32,49] Following Au deposition under UHV conditions, no new chemical states are detected in either the Se 3*d* or W 4*f* core levels. This indicates Au forms a vdW interface

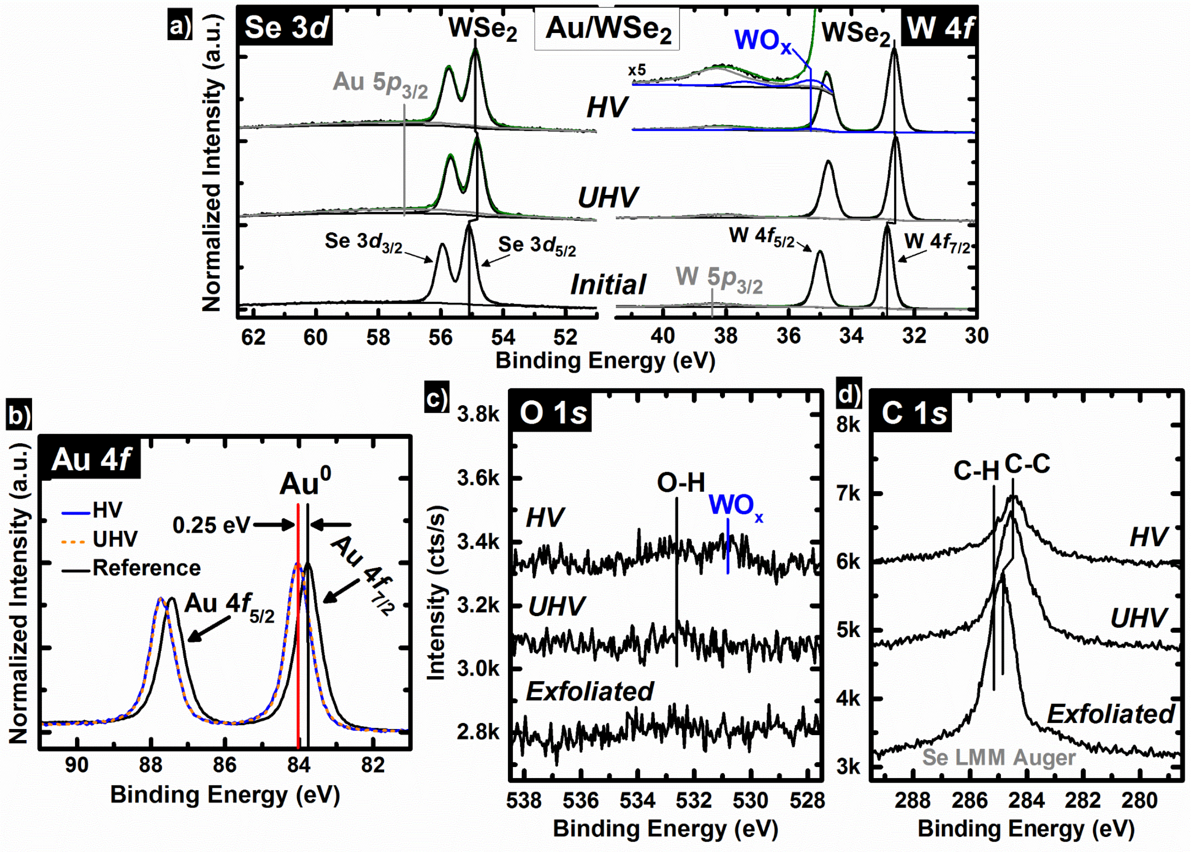

Figure 5.4. XPS spectra of the a) Se 3*d*, W 4*f*, W 5$p_{3/2}$, c) O 1*s*, and d) C 1*s* core level spectra obtained from as–exfoliated WSe$_2$ and following Au deposition under UHV and HV conditions. b) XPS spectra of the Au 4*f* core level obtained from an Au reference and following Au deposition on WSe$_2$ under UHV and HV conditions. The inset in a) displays the W 4*f* core level spectrum obtained following Au deposition under HV conditions between binding energies of 41 and 34 eV with intensity multiplied by five to clearly show the WO$_x$ chemical state.

with WSe$_2$, which has been predicted by DFT and verified in previous experiments.[10,26,50] Au deposition on WSe$_2$ under HV conditions also results in a vdW interface. In contrast with Au deposition under UHV conditions, the formation of WO$_x$ via WSe$_2$ oxidation is observed, evidenced by the additional chemical state appearing at a BE of 35.25 eV in the corresponding W 4*f* core level spectrum. WSe$_2$ oxidation is thermodynamically favorable in the presence of gaseous oxidizing species typically present in the atmosphere (e.g., $OH^-$, $H_2O$, $CO^-$, $CO_2$) as $\Delta G^\circ_{f,WO2}$ = -267.0 kJ/mol and $\Delta G^\circ_{f,WO3}$ = -254.7 kJ/mol, respectively.[51] Recently, DFT calculations predicted a particularly low kinetic energy barrier to oxygen adsorption on $WSe_2$ as a passivation mechanism under ambient conditions.[45] Addou et al. experimentally observed oxidation of $WSe_2$ domain edges, which are the most reactive sites within a $WSe_2$ domain.[28,52] Despite mild $WSe_2$ oxidation following Au deposition under HV conditions, the Se:W ratio remains virtually identical with that detected prior to and following Au deposition under UHV conditions (2.1:1). (The method employed in calculating stoichiometries reported here is discussed in further detail in the Experimental Details, Chapter 2.) The formation of $WO_x$ rather than $WO_xSe_y$ would result in complete loss of Se from $WSe_2$ and corresponding complete oxidation of $W^{x+}$ formed from $WSe_2$ reduction. Any Se–Se or Se– O bonds resulting from the liberation of Se from $WSe_2$ via oxidation is below the limit of detection due to the significant difference between atomic sensitivity factors of the W 4*f* and Se 3*d* core levels (W 4*f* >> Se 3*d*, see Experimental Details). $WO_xSe_y$ formation would be evidenced by the appearance of chemical states in the W 4*f*, Se 3*d*, and O 1*s* core level spectra in addition to chemical states associated with bulk $WSe_2$ and $WO_x$ (see Cr–$WSe_2$ formed under HV conditions). A change in $WSe_2$ stoichiometry resulting from $WO_x$ formation via Au deposition under HV conditions is not expected and, if it occurs in this case, is below the detection limit of XPS.

After depositing Au in UHV and HV, the Au 4*f* core level is detected at ~0.25 eV higher BE from the reference Au 4*f* core level similar with that detected from the $WS_2$ samples after Au deposition. Corresponding AFM images indicate Au also exhibits VW growth on $WSe_2$ (Figure 5.3b) according to the significant increase in RMS roughness from 0.07 nm after exfoliation to 0.70 nm and 0.53 nm after depositing Au on $WSe_2$ in UHV and HV, respectively. Therefore, the deviation of the work function of the Au nanoclusters that grow on the $WSe_2$ surface from that of bulk Au likely manifests as the BE shift exhibited by the corresponding Au 4*f* core levels. Significant SBH lowering has been reported when high work function metal nanoparticles (e.g., Au, Pt) are present at the interface between a semiconductor and another substantially lower work function metal contact (e.g., Ti).[53-55] Therefore, the charge transfer mechanism between an incomplete coverage Au film (effectively Au nanoparticles) and $WSe_2$ could be analogously employed in conjunction with a substantially lower work function electrode metal (e.g., Ti, Sc) as a SBH lowering technique for electron contacts on $WS_2$- and $WSe_2$-based devices.

In contrast with the exfoliated $WS_2$ crystal, adventitious oxygen based species are below the limit of detection on the exfoliated $WSe_2$ crystal (Figure 5.4c). A chemical state is detected below 531.0 eV in the O 1*s* core level obtained after depositing Au in HV corroborating the formation of $WO_x$ during deposition in the elastomer-sealed deposition tool according to the high BE chemical state detected in the corresponding W 4*f* core level.

### *WTe₂*

Reactions between Au and $WTe_2$ are thermodynamically unfavorable. However, elemental Au(s) and Te(s) react exothermically. Before Au deposition, the exfoliated $WTe_2$ crystal exhibits a Te:W ratio of ~2.4:1 indicating a Te rich stoichiometry consistent with bulk $WTe_2$ crystals characterized by XPS previously.[56] Te-rich $WTe_2$ has been reported after exfoliating bulk crystals many times indicating the Te excess detected in the crystals employed in this work is likely distributed throughout the bulk. The $WTe_2$ investigated in this work exhibits the stable 1T' phase of the binary W-Te system where the Te:W ratio is ideally 2:1. The W and Te core levels exhibited by 1T'-

$WTe_2$ are asymmetric with tails to higher BE consistent with core-hole screening due to its semimetallic electronic structure (Figure 5.5a).[57,58] The $WTe_2$ chemical states in the W 4*f* and Te $3d_{5/2}$ core levels are separated by 541.19 eV after exfoliation, which is maintained throughout this work when fitting the bulk $WTe_2$ chemcial states. In addition, chemical states are detected at high BE in the Te $3d_{5/2}$ and W 4*f* core levels obtained from exfoliated $WTe_2$ consistent with $TeO_x$ and $WO_x$, respectively. Significant $WTe_2$ oxidation in ambient conditions has been documented previously.[59] Previously reported DFT calculations indicate reactions between $WTe_2$ and $O_2$ is energetically favorable.[56] However, the same DFT calculations indicate $WTe_2$ oxidation in air is a defect-mediated process due to the relatively inert nature of the defect-free basal plane of $WTe_2$. The defective nature of the $WTe_2$ in this work presumably facilitates spontaneous W and Te oxidation in air before loading the sample into the UHV cluster tool for metallization. After depositing Au in UHV and HV, a third chemical state is detected in the corresponding Te $3d_{5/2}$ core level at 572.95 eV indicating the formation of $AuTe_x$ via reactions between Au and $WTe_2$. The $AuTe_x$ chemical state is detected at high BE from the bulk TMD chemical state in the Te $3d_{5/2}$ core level unlike the $AuTe_x$ state detected at the Au–$MoTe_2$ interface. The bulk $WTe_2$ chemical states exhibit BEs consistent with elemental W and Te, which is expected considering the semimetallic nature of $WTe_2$. Therefore, charge transfer from Au to Te upon the formation of $AuTe_x$ manifests as an appreciable shift of the associated $Te^{x-}$ chemical state to higher BE. The Te-Mo electronegativity difference is larger than the Te-Au electronegativity difference by 0.12, which indicates the BE shift of the 2H-$MoTe_2$ chemical state should be larger than the $AuTe_x$ chemical state in the Te core levels consistent with the XPS results obtained in this work. The concentration of $WO_x$ and $TeO_x$ detected on $WTe_2$ after depositing Au in HV is ~3× larger than that detected on the exfoliated $WTe_2$ surface (after correcting for the photoelectron attenuation caused by the deposited Au film). This could be due to a higher defect density on the exfoliated $WTe_2$ surface resulting in a higher concentration of $WO_x$ and $TeO_x$ before depositing Au in HV compared with the $WTe_2$ surface before depositing Au in UHV. The additional ~5 minutes of air exposure that the $WTe_2$ was subjected to after depositing Au in HV could also cause a higher concentration of surface oxides to form compared with the $WTe_2$ crystal immediately loaded into the UHV cluster tool. Unfortunately, XPS was not performed on exfoliated $WTe_2$ prior to depositing Au in HV. Therefore, the concentration of $WO_x$ and $TeO_x$ on the $WTe_2$ crystals detected after depositing Au in UHV and HV cannot be accurately compared.

The Au 4*f* core levels obtained after depositing Au on $WTe_2$ in UHV and HV are dominated by a chemical state exhibiting an asymmetric line shape consistent with core-hole screening in metallic species, which corresponds with metallic Au (Au–Au bonding). The metallic Au chemical states detected after Au deposition in UHV and HV are shifted ~0.25 eV to higher BE, which is similar with the Au 4*f* core level spectra obtained after deposting Au on $MoSe_2$, $MoTe_2$, $WS_2$, and $WSe_2$. The Au nanoparticle size-dependent work function argument provided earlier as a hypothesis to explain this phenomenon likely manifests in each of the aforementioned Au–TMD systems as the unexpectedly high metallic Au chemical state BE in the corresponding Au 4*f* core levels. An additional chemical state is detected at high BE in the Au 4*f* core level spectra obtained after depositing Au on $WTe_2$ in UHV and HV conditions corroborating the formation of Au–Te bonds. In addition to adventitious carbon and oxygen based species, the significant concentration of $WO_x$ and $TeO_x$ detected in the Te $3d_{5/2}$ and W 4*f* core levels is corroborated by the chemical state detected at ~530.7 eV in the O 1*s* core level spectrum obtained from exfoliated $WTe_2$ (Figure

5.5c). Au–O bonds that may form at the Au–$WTe_2$ interface are below the limit of XPS detection.

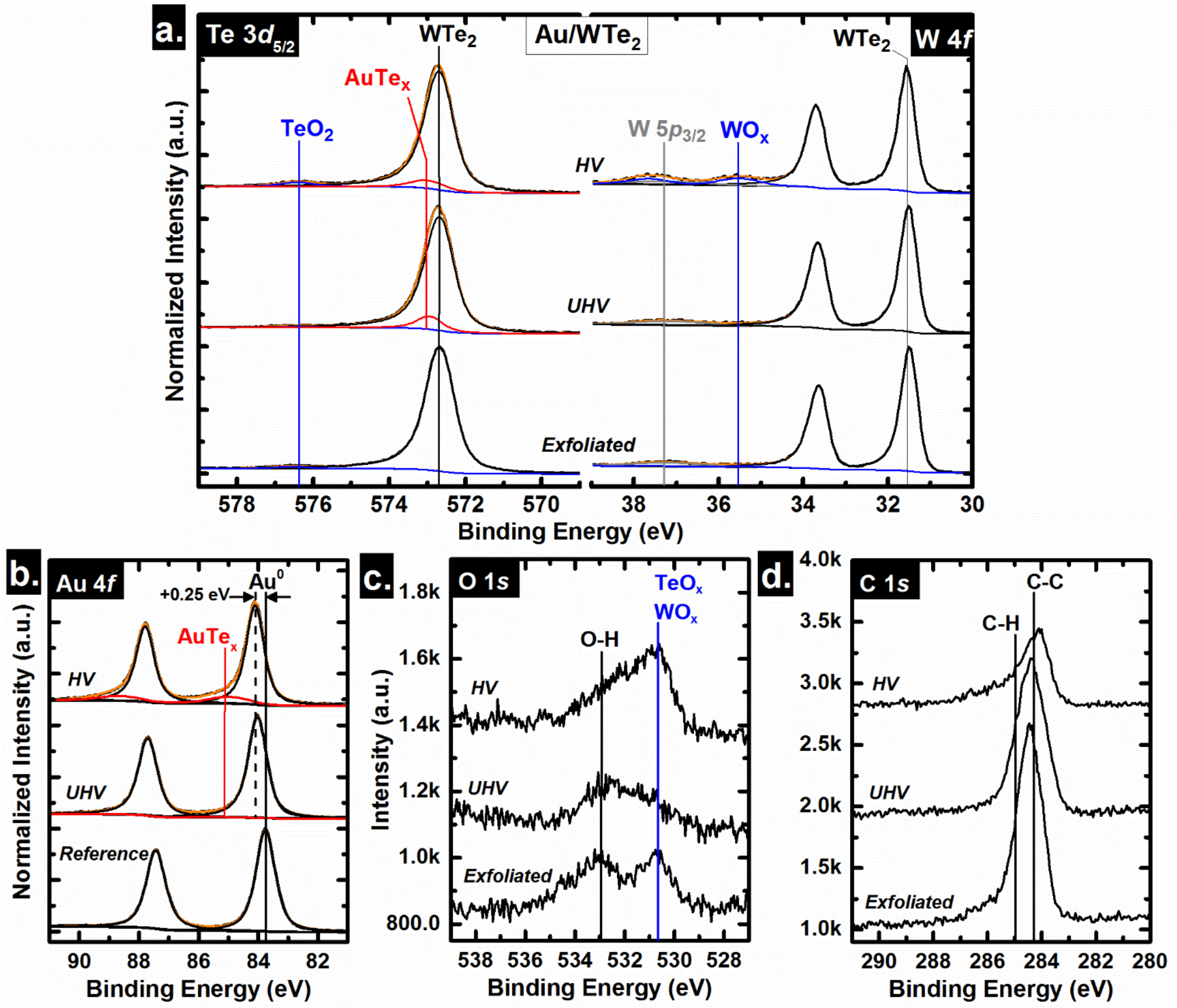

Figure 5.5. XPS spectra of the a) Te $3d_{5/2}$, W 4*f*, W $5p_{3/2}$, c) O 1*s*, and d) C 1*s* core level spectra obtained from $WTe_2$ after exfoliation and subsequent Au depositions in UHV and HV. b) XPS spectra of the Au 4*f* core level obtained from an Au reference and following Au deposition on $WTe_2$ under UHV and HV conditions.

A reaction in which Au scavenges oxygen from $WO_x$ or $TeO_x$ is unlikely considering the sizeable BDEs of the Te–O and W–O bonds ($BDE_{Te\text{-}O}$ =391 kJ/mol, $BDE_{W\text{-}O}$ = 653 kJ/mol).[60]

The oxidized surface of exfoliated $WTe_2$ exhibits a much higher RMS roughness (2.60 nm) than the exfoliated surfaces of $WS_2$ and $WSe_2$ (0.06 nm in both cases), which is likely related to the significant concentrations of surface oxides detected on $WTe_2$ that are below the limit of XPS detection on exfoliated $WS_2$ and $WSe_2$. The RMS roughness decreases by roughly a factor of 10 after depositing Au on $WTe_2$ in UHV and HV, which contrasts the factor of 10 increase in RMS roughness detected after depositing Au on $WS_2$ and $WSe_2$. Nonetheless, the surfaces of the W-based TMDs exhibit similar RMS roughnesses after Au is deposited regardless of the deposition chamber ambient prior to metallization. The AFM images obtained after exfoliation and subsequent metallization in this work reflect different regions depending on the experimental step. Therefore, the much smoother $WTe_2$ surface detected after depositing Au could be a product of obtaining the AFM image from an initially much smoother, less oxidized region of the $WTe_2$ surface than the 'Exfoliated' image in Figure 5.3c reflects. Aerial variation in $TeO_x$ and $WO_x$ concentrations on $WTe_2$ is expected considering the well-documented aerial variations in defect density across bulk TMD surfaces regardless of the TMD origin (geologic or synthetic).[29-32]

### 5.4.2 Covalent Ir–$WS_2$, Ir–$WSe_2$ and Ir–$WTe_2$ Interfaces

*$WS_2$*

The interface chemistry detected at the Ir–$WS_2$ interface formed in UHV and HV is analogous with the chemistry detected at Ir–$MoS_2$ interface. Additional chemical states are detected at high (low) BE in the S 2*p* (W 4*f*) core levels obtained after depositing Ir on $WS_2$ in UHV and HV (Figure 5.6a) indicating Ir reacts with $WS_2$ to form $WS_x$ and $IrS_x$. The broad chemical state detected at high BE in the S 2*p* core level obtained after depositing Ir on $WS_2$ in UHV and HV is presumably convoluted by the $IrS_x$ and $WS_x$ chemical states. It is also possible that Ir reacts with $WS_2$ to form a ternary $W_xIr_yS_z$ intermetallic, in which case the high BE doublet detected in the S 2*p* core level spectra corresponds with a single intermetallic chemical state. A third chemical state is detected in the W 4*f* core level after depositing Ir in HV at a BE consistent with the $W^{2+}$ chemical state previously detected in $WO_2$, which indicates an appreciable concentration of tungsten oxide forms during Ir deposition in HV.[61] $WO_2$ formation is more exothermic than $MoO_3$ by ~100 kJ/mol,[51] which rationalizes the formation of tungsten oxide detected after depositing Ir on $WS_2$ in HV and the contrasting absence of molybdenum oxide after depositing Ir on $MoS_2$ in HV. The $WS_2$ chemcial states shift ~0.68 eV to lower BE after depositing Ir in UHV, which is qualitatively consistent with the upward band bending expected in a semiconductor when contacted by a transition metal with a high work function relative to the $E_F$ of the semiconductor, as is the case in the Ir–$WS_2$ system (Ir work function = 5.3 eV, see Section 5.6.4 for detailed band alignment discussion).[36] Ir forms a highly uniform film on $WS_2$ regardless of the deposition chamber ambient prior to metallization according to the negligible increase in RMS roughness from 0.06 nm after exfoliating $WS_2$ to 0.09 nm after depositing Ir in UHV and HV (Figure 5.7a). The Ir film thickness deposited in UHV is ~2 nm according to the attenuation of the $WS_2$ chemical states in the S 2*p* and W 4*f* core levels. The appreciable concentration of $WO_x$ detected at the Ir–$WS_2$ interface after depositing Ir in HV despite the highly uniform, pinhole-free structure and predominantly metallic Ir composition of the Ir film indicates tungsten oxidation occurs *in–situ* during metallization in the elastomer-sealed deposition tool. Reactions between Ir and $WS_2$ are not thermodynamically favorable ($\Delta G^\circ_{f,IrSx}$ = -58.1 – -73.6 kJ/mol[62] > $\Delta G^\circ_{f,WS2}$ = -164.9 kJ/mol).[44] However, W exhibits a d-orbital valence similar to Mo. Therefore, defects (e.g., sulfur vacancies) in the $WS_2$ could facilitate reactions with Ir via enhanced *d*-orbital overlap between W and Ir.

The chemical states detected in the Ir 4*f* core level obtained after depositing Ir on $WS_2$ in UHV and HV (Figure 5.6b) are analogous with the chemical states detected in the Ir 4*f* core level spectra obtained after depositing Ir on $MoS_2$ and will therefore not be discussed in detail.

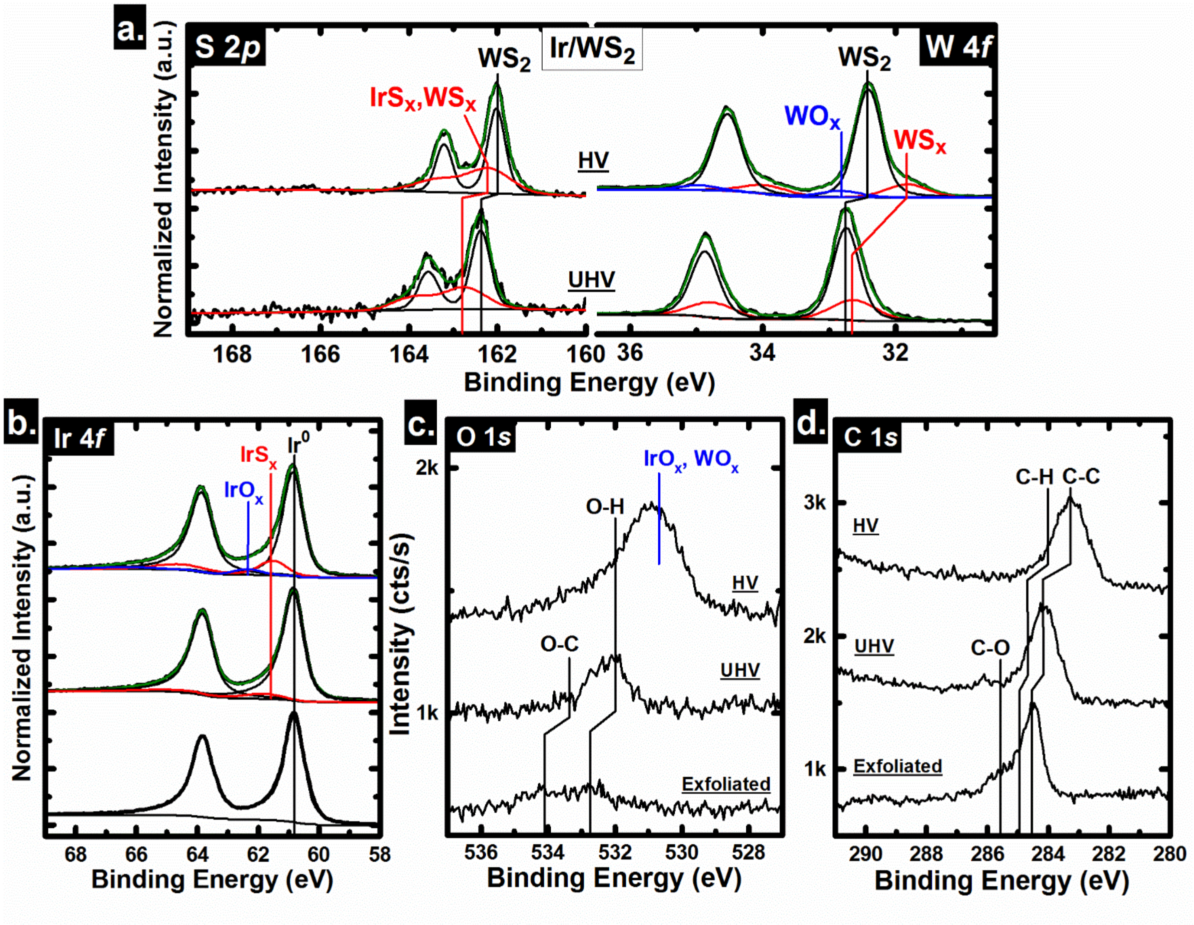

Figure 5.6. XPS spectra of the a) S 2*p*, W 4*f*, c) O 1*s*, and d) C 1*s* core level spectra obtained from as–exfoliated WS$_2$ and following Ir deposition under UHV and HV conditions. b) XPS spectra of the Ir 4*f* core level obtained from an Ir reference and following Ir deposition on WS$_2$ under UHV and HV conditions.

O–C bonds are detected on WS$_2$ after exfoliation and subsequent Ir deposition in UHV in addition to the adventitious species discussed in Section 5.4.1.1 (Figures 5.6 c, d), which could originate from the carbon tape holding the WS$_2$ to the sample plate throughout the experiment. After depositing Ir on WS$_2$ in HV, the intensities of the transition metal oxide chemical states (BE < 531.0 eV) in the corresponding O 1*s* core level increases significantly due to the formation of WO$_x$ and IrO$_x$. The BE of the 'C–C' chemical state in the C 1*s* core level shifts below 284.0 eV after depositing Ir in HV, which would typically indicate the presence of a metal–carbon bond. However, there are no chemical states in the Ir or W core levels detected at a lower BE from that of metallic W (W–W bonding) or Ir (Ir–Ir bonding). Therefore, the unexpectedly low BE of the 'C–C' chemical state after depositing Ir in HV is likely due to the upward band bending effects induced by the high work function transition metal, Ir.

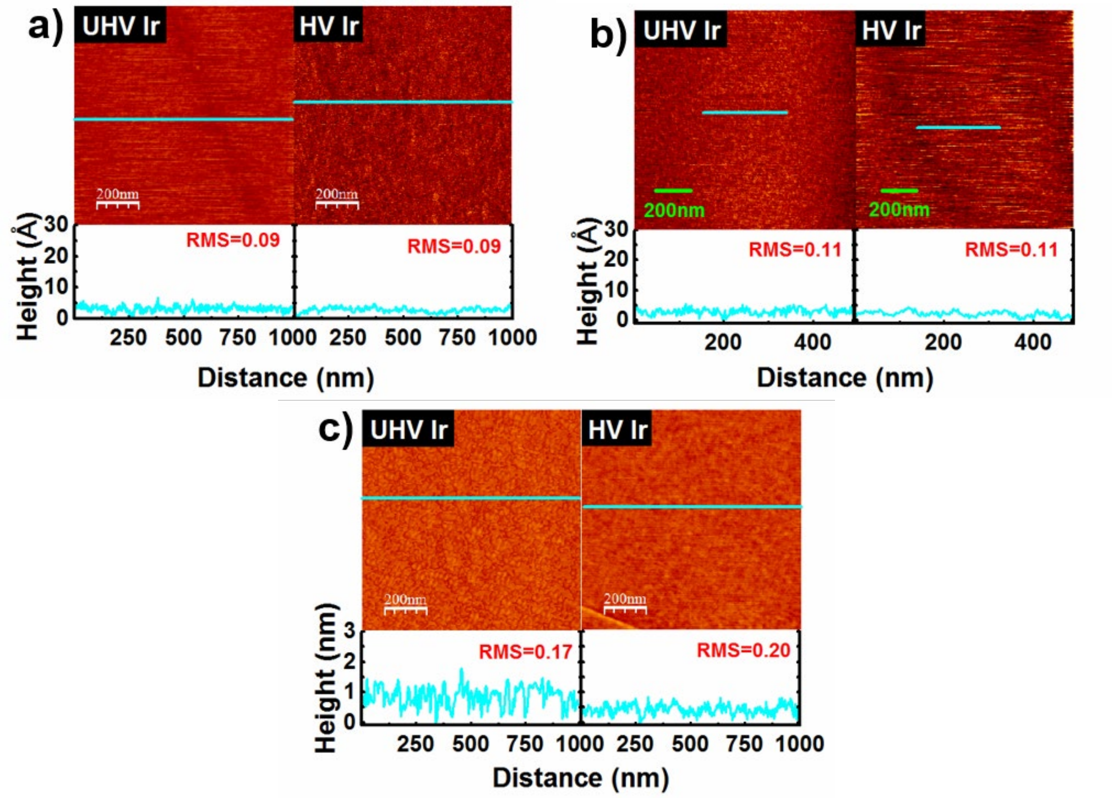

Figure 5.7. AFM images obtained *ex–situ* from a) $WS_2$, b) $WSe_2$, and c) $WTe_2$ after depositing Ir in UHV and HV with corresponding line profiles displayed below each image. The light blue line superimposed over each image represents the location each line profile was obtained from. The RMS roughness values are displayed in red.

*WSe₂*

Figure 5.8a shows the Se 3*d* and W 4*f* core level spectra obtained following Ir deposition under UHV and HV conditions. Ir reacts with $WSe_2$ to form sub-stoichiometric tungsten selenide ($WSe_x$, x<2) and an IrSe$_x$ intermetallic by scavenging Se from WSe$_2$, regardless of the deposition chamber ambient prior to metallization.

The interface chemistry detected in the Ir–WSe$_2$ system after metallization in UHV and HV is similar to the interface chemistry detected in the Ir–WS$_2$ system discussed above. Following deposition under UHV conditions, the bulk WSe$_2$ chemical states detected in the W 4$f_{7/2}$ and Se 3$d_{5/2}$ core level spectra at binding energies of 32.29 and 54.50 eV, respectively, have shifted 0.49 eV to lower binding energy from as–exfoliated WSe$_2$. This indicates Ir induces a E$_F$ shift towards

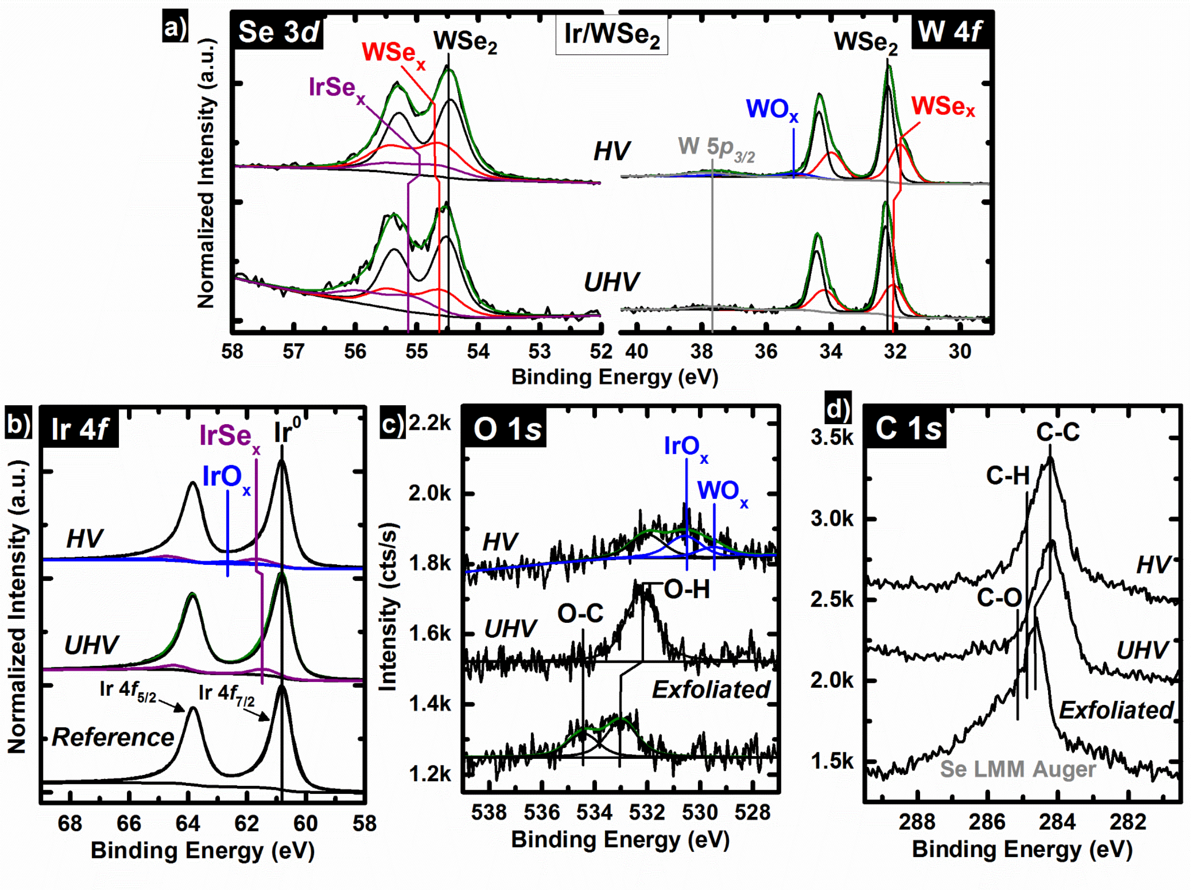

Figure 5.8. XPS spectra of the a) Se 3*d*, W 4*f*, W 5$p_{3/2}$, c) O 1*s*, and d) C 1*s* core level spectra obtained from as–exfoliated WSe$_2$ and following Ir deposition under UHV and HV conditions. b) XPS spectra of the Ir 4*f* core level obtained from an Ir reference and following Ir deposition under UHV and HV conditions.

the valence band maximum (VBM) of $WSe_2$, which is expected as the $E_F$ of Ir (Ir work function= 5.3 eV)[36] should reside deep in the band gap of $WSe_2$. The chemical state detected at high BE in the Se 3*d* core level spectrum obtained following Ir deposition under UHV and HV conditions indicates the formation of $IrSe_x$ at the Ir–$WSe_2$ interface under either base pressure. The $IrSe_x$ and $WSe_x$ chemical states in the Se 3*d*, W 4*f*, and Ir 4*f* core level spectra exhibit binding energies which are seemingly dependent upon the deposition chamber ambient. This could be related to the difference in Ir film thickness achieved under UHV and HV as well as slight differences in reaction product stoichiometry. Reduction of $WSe_2$ to form sub-stoichiometric $WSe_x$ would result in a simultaneous reduction and oxidation of the $W^{4+}$ and $Se^{2-}$ chemical states in $WSe_2$, respectively, which agrees with the additional chemical states detected in the W 4*f* and Se 3*d* core level spectra at binding energies of 32.05 and 54.73 eV, respectively (Figure 5.8a).

Figure 5.8b displays the Ir 4*f* core level spectra obtained from an Ir reference film (see Chapter 2 for more details) and following Ir deposition on $WSe_2$ under UHV and HV conditions. Both peaks comprising the reference Ir 4*f* doublet exhibit a significant degree of asymmetry, consistent with core–hole screening commonly observed in metallic species.[61] The intense asymmetric doublet detected with Ir $4f_{7/2}$ core level at a binding energy of 60.78 eV following Ir deposition under UHV and HV conditions indicates that metallic Ir (Ir–Ir bonding) comprises the majority of the deposited film. However, a chemical state in addition to metallic Ir is detected in the Ir 4*f* core level spectra following Ir deposition under UHV and HV conditions with a binding energy of 61.40 and 61.67 eV, respectively, indicating the formation of a small concentration of $IrSe_x$. Unique to Ir deposition under HV conditions, a third chemical state is detected at high binding energy (62.59 eV) from the $IrSe_x$ state, indicating the formation of a small concentration of $IrO_x$.

Figures 5.8 c, d display the O 1*s* and C 1*s* core level spectra obtained from as–exfoliated $WSe_2$ and following Ir deposition under UHV and HV conditions. The evolution of the chemical states in the O 1*s* and C 1*s* core levels throughout $WSe_2$ exfoliation and subsequent Ir deposition in UHV and HV are analogous with the evolution of the oxygen- and carbon-based species detected in the Ir–$WS_2$ system. The $IrO_x$ and WO chemical states detected in the O 1*s* core level after depositing Ir on $WSe_2$ in HV are individually distinguishable in contrast with the broad feature detected at low BE in the O 1*s* core level obtained after depositing Ir on $WS_2$ in HV. Reduction of $WSe_2$ by Ir results in available W atoms free to react with residual oxidizing species. The electronegativity of Ir (2.20) is less than that of W (2.36),[63] which indicates iridium oxide should exhibit a chemical state in the O 1*s* core level spectrum with a lower BE than an analogous tungsten oxide species, consistent with the chemical states detected in the Ir–$WSe_2$ system here. Formation of $IrO_x$ and $WO_x$ in the presence of excess oxidizing gases is thermodynamically favorable as the $\Delta G^\circ_{f,Ir2Se3}$ and $\Delta G^\circ_{f,WSe2}$ are considerably more positive than that of $IrO_2$ and $WO_2$ or $WO_3$.[34]

Thickness estimations using the attenuation of the total intensities of the Se 3*d* and W 4*f* core level spectra suggest that the thickness of the Ir film deposited under UHV conditions is 2.0 and 2.5 nm thick, respectively. This indicates Se diffusion into Ir in addition to Ir–Se interfacial bonding rather than Ir–Se bonding solely across the Ir–$WSe_2$ interface, similar to previous reports of sulfur out–diffusion when Ir is deposited on $MoS_2$.[34] AFM images indicate Ir grows uniformly on $WSe_2$ regardless of deposition chamber ambient (Figure 5.7b) considering the negligible increase in RMS roughness (0.05 nm) after depositing Ir compared with the exfoliated $WSe_2$ surface. It is therefore reasonable to directly compare W 4*f* and Se 3*d* chemical state attenuation following Ir deposition under either base pressure to evaluate the Ir film thickness even at a thickness less than

2 nm. Intermetallic species comprised of the contact metal and chalcogenide at the metal–$WSe_2$ interface, such as $IrSe_x$ in this case, may permit control of interface resistivity, similar to various silicides employed in MOSFET and CMOS technology.[64] Furthermore, the highly effective wetting capability of Ir on $WS_2$, $WSe_2$, $MoS_2$,[34] and $MoSe_2$ could be utilized in employing Ir as an adhesion layer for hole contacts. However, the electronic structure of the particular iridium chalcogenide compound(s) formed at the contact/TMD interface should be carefully considered. The chalcogen:Ir stoichiometry can affect the electrical behavior and therefore the associated transport properties of such compounds.[65] Full coverage films are not obtained in the case of Cr, which is commonly employed as an adhesion layer in contacts to TMDs, at a target thickness of less than 5 nm (see Section 5.4.3 for details regarding the morphology of Cr films on W-based TMDs). An inhomogeneous contact–channel interface in regard to the metal which is in direct contact with the underlying channel material could result in spatially varying interface chemistry and associated transport properties. Employing Ir, which forms a uniform film under either UHV or HV conditions at a target film thickness of ~1 nm, as an adhesion layer would eliminate the potential for inhomogeneous interface chemistry and therefore may result in an electrically superior contact on a number of different TMDs.

*$WTe_2$*

The thermodynamic favorability of reactions between Ir and $WTe_2$ cannot be gauged due to the unknown $\Delta G^\circ_{f,IrTe}$. However, the fugacity of IrTe is less negative than that of $WTe_2$, which suggests reactions between Ir and Te are less thermodynamically favorable than the persistence of $WTe_2$ (see Chapter 3 for the relationship between the fugacity and the favorability of a reaction).[66]

The Te $3d_{5/2}$, W $4f$, W $5p_{3/2}$, Ir $4f$, O $1s$, and C $1s$ core levels obtained after $WTe_2$ exfoliation and subsequent Ir deposition in UHV and HV are shown in Figure 5.9.

Ir reacts aggressively with $WTe_2$ regardless of the deposition chamber ambient prior to Ir deposition. Additional chemical states are detected at high BE in the Te $3d_{5/2}$ and W $4f$ core levels after depositing Ir in UHV and HV indicating the formation of a ternary $W_xIr_yTe_z$ compound. The $W_xIr_yTe_z$ chemical states exhibit symmetric peak shapes unlike the asymmetric shape of the metallic $WTe_2$ chemical states indicating Ir covalently bonds with $WTe_2$ to form the $W_xIr_yTe_z$ reaction product. After Ir is deposited in UHV, the $WO_x$ and $TeO_x$ detected on the exfoliated $WTe_2$ surface fall below the limit of XPS detection. It is unlikely the Ir scavenges oxygen from $WO_x$ or $TeO_x$ considering the substantial BDEs of the Te–O and W–O bonds as well as the thermodynamically unfavorable reactions between Ir and tungsten oxide or tellurium oxide (see Section 5.4.6 for more details). Therefore, the Ir film thickness deposited in UHV is sufficient to attenuate the photoelectrons originating from the $WO_x$ and $TeO_x$ species below the limit of XPS detection. After depositing Ir in HV, a third chemical state is detected in the Te $3d_{5/2}$ and W $4f$ core levels at high BE from the $W_xIr_yTe_z$ chemical state indicating the presence of $TeO_x$ and $WO_x$. The ratio of the integrated intensity of the $TeO_x$ chemical state to the total integrated intensity of the Te $3d_{5/2}$ core level detected after depositing Ir in HV (0.18) is much higher than that detected on the exfoliated $WTe_2$ (0.03). Therefore, the reaction that occurs between Ir and $WTe_2$ lowers the energetic and/or kinetic barrier to Te oxidation. It is possible that the high concentration of $TeO_x$ detected after depositing Ir in HV forms during the *ex–situ* transfer step from the elastomer sealed deposition tool to the UHV cluster tool. The effects of the *ex–situ* transfer step employed in this work when characterizing the interface chemistry between metals deposited in HV and TMDs is addressed in Chapter 7 for the Sc–$WSe_2$ system.

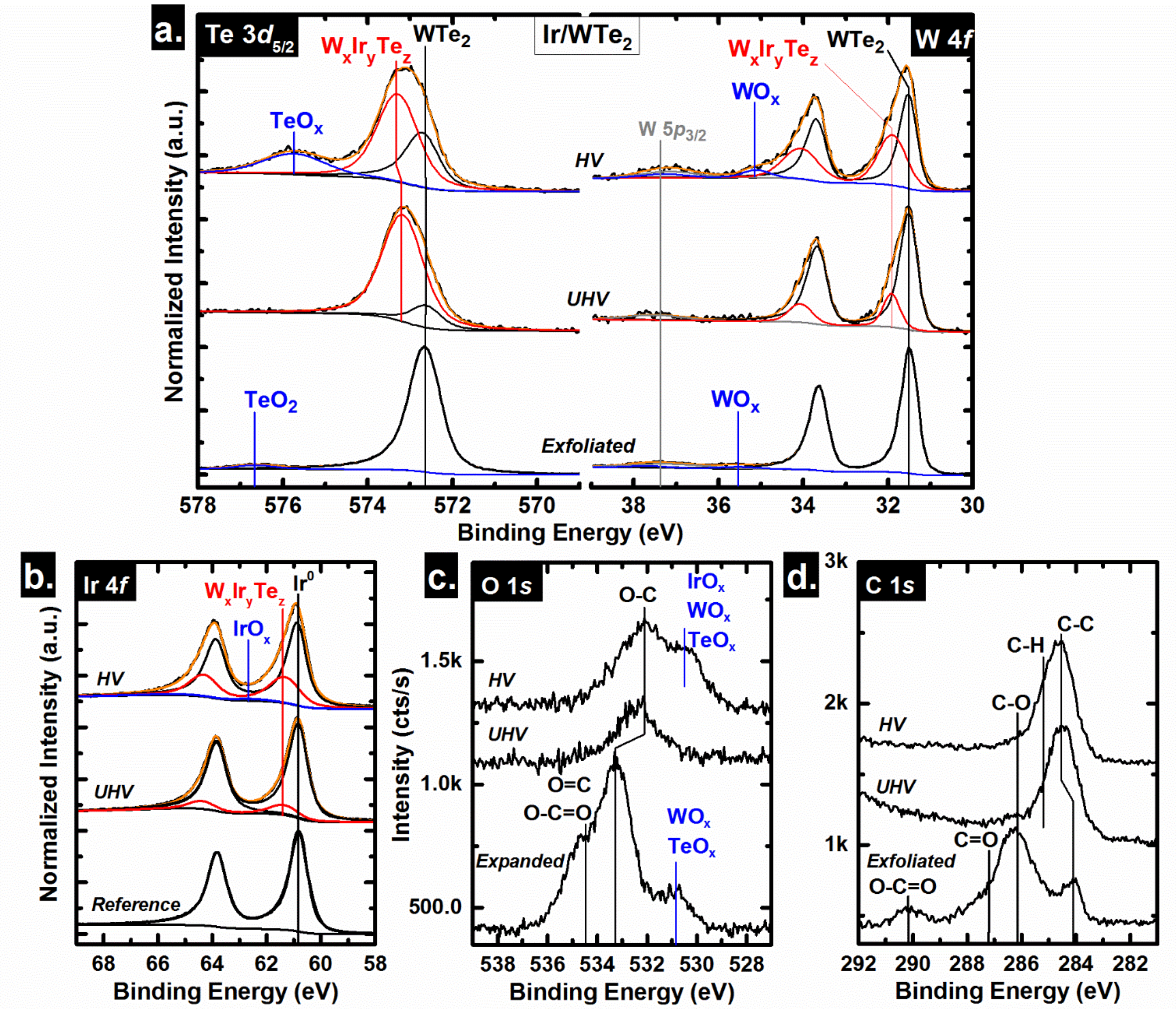

Figure 5.9. XPS spectra of the a) Te $3d_{5/2}$ W $4f$, W $5p_{3/2}$, c) O $1s$, and d) C $1s$ core level spectra obtained from $WTe_2$ after exfoliation and subsequent Ir deposition in UHV and HV. b) Ir $4f$ core level obtained from an Ir reference film and after depositing Ir on $WTe_2$ in UHV and HV.

The chemical states detected in the Ir 4*f* core level spectra obtained after depositing Ir on $WTe_2$ in UHV and HV are analogous with the chemical states detected in the Ir 4*f* core level spectra obtained after depositing Ir on $WS_2$ and $WSe_2$ and are therefore not discussed in detail here.

A significant concentration of C=O and O–C=O bonds are detected in the O 1*s* and C 1*s* core levels obtained from the exfoliated $WTe_2$ in addition to the oxygen- and carbon-based adventitious species discussed previously (Figures 5.9 c, d). The organic C=O and O–C=O species most likely originate from the carbon tape used to fix bulk TMDs to a 4” Si wafer in this work. The C=O and O–C=O chemical states are below the limit of XPS detection after depositing Ir in UHV. It is unlikely that the Ir reduces the C=O based organic species due to the absence of a chemical state above 62.0 eV in the corresponding Ir 4*f* core level that would indicate the presence of $IrO_x$. It is possible that carbon tape makes up a small portion of the region probed after exfoliating $WTe_2$, while the carbon tape is absent from the region probed after depositing Ir in UHV.

The RMS roughness of the $WTe_2$ surface after depositing Ir in UHV (0.17 nm) and HV (0.20 nm) is higher than that of the Ir–$WS_2$ and Ir–$WSe_2$ surfaces by roughly a factor of 10 (Figure 5.7c), which is reasonable considering the RMS roughness of the exfoliated $WTe_2$ surface is higher than that of the exfoliated, oxide-free $WS_2$ and $WSe_2$ surfaces by more than a factor of 100. Nonetheless, the RMS roughness of the $WTe_2$ surface after depositing Ir is ~3× higher than the $WTe_2$ surface after depositing Au, which indicates Ir grows on $WTe_2$ via the FM mechanism. FM growth typically manifests from an energetically favorable adatom–substrate interaction, which is consistent with the abundance of reaction products that are detected at the Ir–$WTe_2$ interface.

### 5.4.3 Substantial Oxidation of the Low Work Function Metal Cr and Associated Reaction Products Formed with W-Based TMDs in HV

*$WS_2$*

Cr is commonly employed as an adhesion layer in contacts to TMDs. The interface chemistry between a TMD and an adhesion layer will play a significant role in the band alignment and contact performance even in cases where the adhesion layer is 1-2 nm thick. Reactions between Cr and $WS_2$ are thermodynamically unfavorable considering the $\Delta G°_{f,Cr2S3}$ is slightly more positive than the $\Delta G°_{f,WS2}$ (Figure 5.19b). The evolution of the S 2*p* and W 4*f* core levels throughout $WS_2$ exfoliation and subsequent Cr depositions in UHV and HV are displayed in Figure 5.10a. The chemistry detected at the Cr–$WS_2$ interface is independent of the deposition chamber ambient prior to metallization. Additional chemical states are detected in the S 2*p* (~162.5 eV) and W 4*f* (~32.9 eV) core levels at low BE from the bulk $WS_2$ chemical states that indicate the formation of reaction products, which are either separate $CrS_x$ and $WS_x$ species or a single ternary $W_xCr_yS_z$ compound (Figure 5.10a). A sulfur-deficient $WS_x$ state that would form in the S 2*p* core level if sulfur was scavenged from $WS_2$ by Cr would exhibit a BE closer to elemental sulfur (i.e., at higher BE) than the $WS_2$ state, which is not the case here. The chemical state exhibited by a ternary $W_xCr_yS_z$ compound in the S 2*p* core level could reasonably exhibit a higher oxidation state than the $WS_2$ chemical state due to the enhanced degree of charge transfer induced by the reaction between Cr and $WS_2$. A third chemical state with an asymmetric line shape is detected in the W 4*f* core level spectra obtained after depositing Cr in UHV and HV. After depositing Cr in UHV, the BE of the asymmetric chemical state in the corresponding W 4*f* core level spectrum is ~0.3 eV higher from the expected BE of metallic W indicating the reduction reaction is incomplete. In a separate study (see Chapter 7 for details), the BE of the $WSe_x$ chemical state in the W 4*f* core level approaches that of metallic W as more Sc is deposited indicating a minimum metal thickness is required to completely reduce the interfacing $WSe_2$. It is therefore reasonable that the amount of Cr deposited on $WS_2$ in UHV in this work is insufficient to completely reduce the interfacing $WS_2$. After depositing Cr on $WS_2$ in HV, the BE of the asymmetric chemical state in the corresponding W 4*f* core level spectrum is in close agreement with the expected BE of metallic W indicating the interfacing $WS_2$ is completely reduced. The reaction between Cr and $WS_2$ is presumably a defect mediated process considering the thermodynamics of the system indicate an unfavorable reaction at RT. Previous reports based on STM[67] and inductively coupled plasma mass spectrometry indicate defect densities in bulk $WS_2$ crystals are comparable with $MoS_2$ (typical aerial defect density ~$10^{12}$ $cm^{-2}$). It is therefore reasonable to suspect the defect density on the $WS_2$ surface is high enough to facilitate reactions comparable with the concentration of intermetallic species detected here at the Cr–$WS_2$ interface.

$WO_x$ is below the limit of XPS detection after depositing Cr in HV, which suggests the Cr forms a full coverage film on $WS_2$ and is an effective oxygen diffusion barrier.

The chemical states detected in the Cr $2p_{3/2}$ core level after depositing Cr on $WS_2$ in UHV and HV (Figure 5.10b) are analogous with the chemical states detected in the Cr $2p_{3/2}$ core level after depositing Cr on $MoS_2$ in UHV and HV and are therefore not discussed in detail here.

After depositing Cr on $WS_2$ in UHV, a chemical state in addition to the expected carbon-based adventitious species is detected in the corresponding C 1*s* core level at ~283.4 eV indicating the formation of a transition metal carbide. There are no chemical states detected in the corresponding W 4*f* core level that would indicate W–C bonds, which indicates chromium carbide is the most likely compound. The intensity of the carbidic chemical state in the C 1*s* core level indicates the corresponding chemical state in the Cr $2p_{3/2}$ core level should be above the limit of detection considering the photoionization cross section of the Cr $2p_{3/2}$ core level is roughly an order of magnitude higher than that of the C 1*s* core level.[68] A previous XPS study of chromium carbide compounds reports the $Cr_xC_y$ chemical state at a BE ~5 eV lower from the metallic Cr chemical

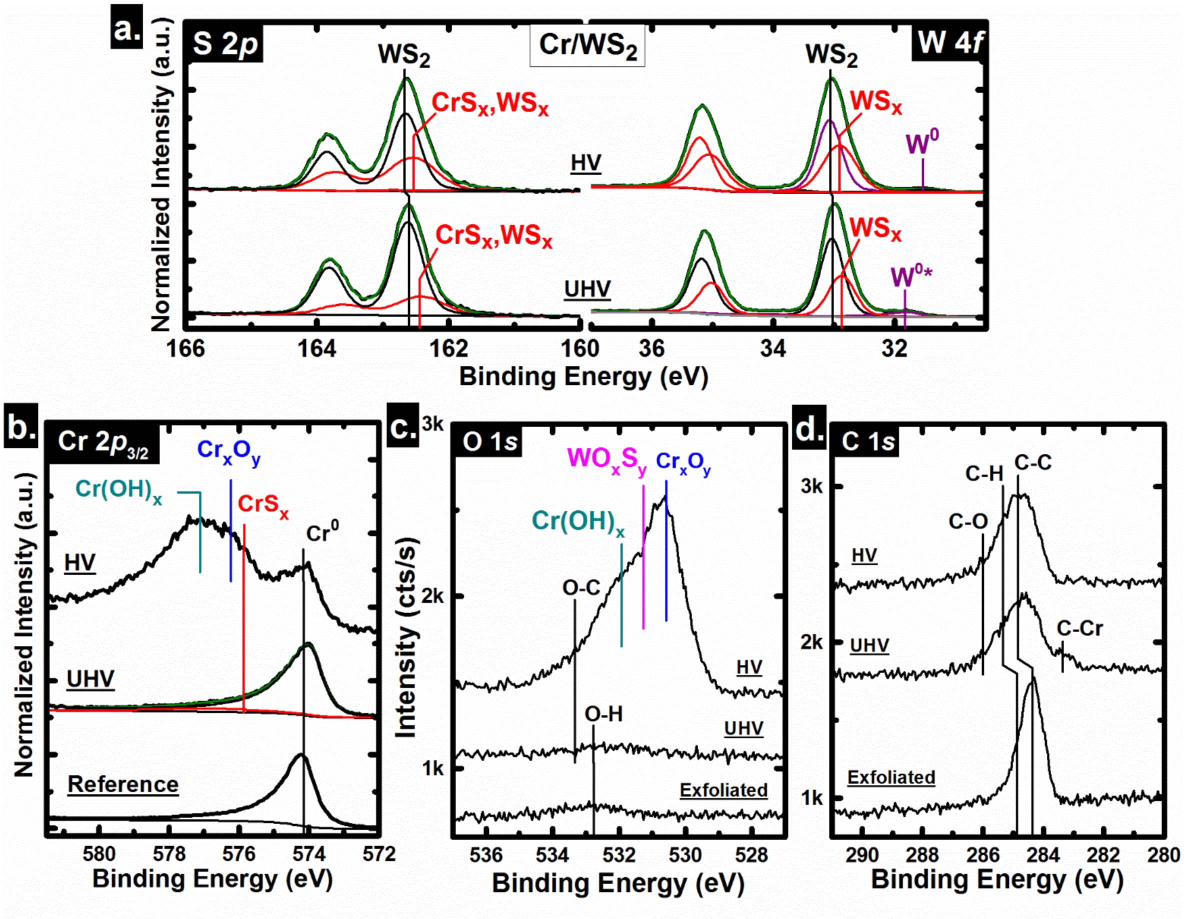

Figure 5.10. XPS spectra of the a) S 2*p*, W 4*f*, b) Cr 2$p_{3/2}$, c) O 1*s*, and d) C 1*s* core level spectra obtained from $WS_2$ after exfoliation and subsequent Cr deposition in UHV and HV. The Cr 2$p_{3/2}$ core level spectra are normalized to the metallic Cr peak.

state in the Cr core levels,[69] which is outside the Cr 2*p* window obtained in this work. Interestingly, the carbidic chemical state in the C 1*s* core level is below the limit of XPS detection after depositing Cr on $WS_2$ in HV. It is unclear why the Cr–C bond is detected in the Cr–$WS_2$ system after Cr is deposited in UHV, but not on any other TMDs investigated in this work after depositing Cr. Nonetheless, the formation of chromium carbide is an exothermic process ($-71.5$ kJ/mol $< \Delta G^{\circ}_{f,CrxCy} < -54.4$ kJ/mol)[60] and likely forms at the contacts in a TMD-based device due to reactions between Cr and organic photoresist residues left behind by lithographic patterning.

Similar to the topography of Cr films on $MoS_2$, Cr grows via a VW mechanism on $WS_2$ when deposited in UHV despite substantial reactions detected at the Cr–$WS_2$ interface. When Cr is deposited in UHV and AFM images are subsequently obtained *ex–situ*, the Cr surface exhibits a RMS roughness roughly 3× higher than the RMS roughness of the $WS_2$ surface after depositing Cr in HV (Figure 5.11a). The rate of formation of Cr–Cr and Cr–S bonds are presumably comparable considering the VW type growth mechanism indicates the adatom–adatom interaction is energetically favored over adatom–substrate interaction, yet significant reactions are detected at the interface by XPS.[70] In this case, the adatom is Cr. The predominant mixture of $Cr_xO_y$ and $Cr(OH)_x$ deposited in HV wets the $WS_2$ surface more effectively than the metallic Cr that is deposited in UHV, resulting in the smoother surface observed in AFM images obtained after depositing Cr on $WS_2$ in HV. If Cr is deposited in HV, a full coverage Cr 'adhesion layer' is likely achievable at lower film thicknesses than if Cr is deposited in UHV according to the AFM images obtained in this work. However, the significant concentrations of $Cr_xO_y$ and $Cr(OH)_x$ detected in the Cr film deposted in HV in this work indicate a comparable chemistry will be found in a Cr adhesion layer deposited in HV. Therefore, Cr contacts should be deposited in the highest vacuum available to minimize the concentration of oxygen and hydroxide incorporated into the Cr film. In a device fabrication process where the Cr contact layer is deposited in HV, the effects of a significant concentration of chromium oxide and hydroxide within the contact should be considered when interpreting contact performance.

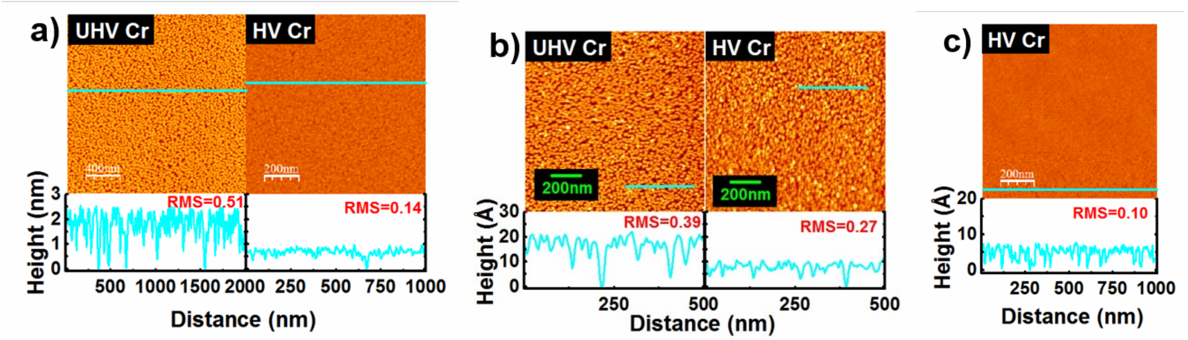

Figure 5.11. AFM images obtained *ex–situ* from a) $WS_2$ and b) $WSe_2$ after depositing Cr in UHV and HV and c) $WTe_2$ after depositing Cr in HV. Line profiles are displayed below each image and the light blue line superimposed over each image represents the location each line profile was obtained from. The RMS roughness values are displayed in red. The AFM images obtained from $WTe_2$ after depositing Cr in UHV show only background noise and are not representative of the true topography of the Cr–$WTe_2$ surface. Therefore, only the AFM images obtained after depositing Cr on $WTe_2$ in HV are shown here.

### *$WSe_2$*

The Se 3*d*, W 4*f*, and W 5$p_{3/2}$ core level spectra obtained following Cr deposition on $WSe_2$ under both UHV and HV conditions are displayed in Figure 5.12a.

Bulk $WSe_2$ is detected in the W 4$f_{7/2}$ (32.40 [UHV] and 32.58 eV [HV]) and Se 3$d_{5/2}$ (54.65 [UHV] and 54.84 eV [HV]) core level spectra obtained following Cr deposition under both UHV and HV conditions despite reactions between Cr and $WSe_2$ in both cases. An asymmetric doublet is detected in the W 4*f* core level spectra following Cr deposition under UHV and HV conditions at BEs of 31.24 and 31.14 eV, respectively, indicating the formation of metallic W (W–W bonding). The BEs and degrees of asymmetry of both the metallic W chemical state in the W 4$f_{7/2}$ and W 4$f_{5/2}$ core levels are in close agreement with those detected from a W reference. In addition, Se scavenging by Cr results in the formation of $CrSe_x$ regardless of deposition chamber base pressure, evidenced by the chemical states detected in the Se 3*d* core level spectra at BEs of 54.35 (UHV) and 54.05 eV (HV). It is important to note that $CrSe_2$ is a member of the TMD family of layered

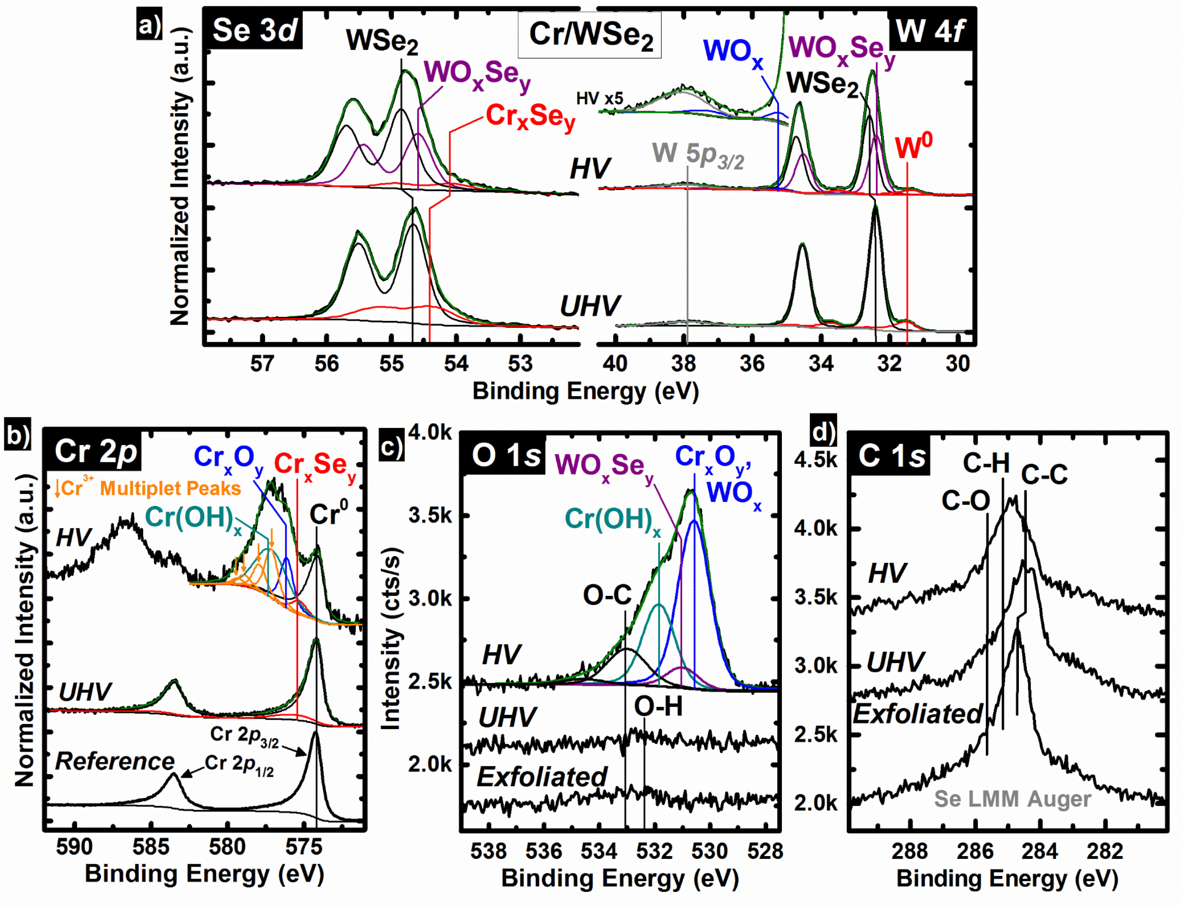

Figure 5.12. XPS spectra of the a) Se 3*d*, W 4*f*, W 5*p*$_{3/2}$, b) O 1*s*, and d) C 1*s* core level spectra obtained from as–exfoliated WSe$_2$ and following Cr deposition on WSe$_2$ under UHV and HV conditions. b) XPS spectra of the Ir 4*f* core level obtained from an Ir reference and following Ir deposition on WSe$_2$ under UHV and HV conditions. The HV W 4*f* core level spectrum and associated fit data between 35 and 40 eV binding energy has been magnified (intensity ×5) to clearly display the WO$_x$ chemical state.

materials with metallic transport properties and therefore CrSe$_x$ formation could be advantageous for charge transport across the interface.[71] Complete reduction of WSe$_2$ by Cr to form metallic W and CrSe$_x$ at the interface is thermodynamically favorable as the $\Delta G°_{f,Cr2Se3}$ (-175.1 kJ/mol)[72] is more negative compared with the $\Delta G°_{f,WSe2}$. However, when Cr is deposited under HV conditions, intermediate WSe$_x$ (x<2) that presumably forms as Cr scavenges Se is not stable in an atmosphere containing an excess of oxidizing gases (i.e., under HV or in air). As a result, reduced tungsten selenide ($WSe_x$) oxidizes to form $WO_xSe_y$, as indicated by the chemical states detected in the W 4*f* and Se 3*d* core level spectra following Cr deposition under HV conditions at BEs of 32.38 eV and 54.58 eV, respectively. A decrease in BE of the $WO_xSe_y$ chemical state from that of bulk $WSe_2$ in the W 4*f* core level spectrum indicates a decrease in W oxidation state from $WSe_2$ ($W^{4+}$) to $WO_xSe_y$ ($W^{3+}$). It may be intuitive to expect an increase in W oxidation state resulting from oxidation of $WSe_x$ because O is significantly more electronegative than Se.[63] Cr reacting with Se atoms from $WSe_2$ will result in a reduced W oxidation state from $W^{4+}$ in $WSe_2$. In the event that each Se atom involved in the formation of $CrSe_x$ is not replaced by an oxygen atom during the formation of $WO_xSe_y$, it would be possible for W to undergo a net decrease in oxidation state from $W^{4+}$ in $WSe_2$ to $W^{3+}$ in $WO_xSe_y$. Cr exhibits a significantly smaller electronegativity (1.66)[63] than W. This suggests the $Se^{2-}$ chemical state in a $CrSe_x$ compound would appear at lower BE from an analogous $WO_xSe_y$ compound, which is consistent with the chemical states reported here. In addition, a nearly undetectable concentration of metallic W is converted to $WO_x$, evidenced by the chemical state at high BE (35.15 eV) in the W 4*f* core level spectrum obtained following Cr deposition under HV conditions. As was mentioned earlier, the formation of $WO_x$ is highly thermodynamically favorable.

There are substantial differences in Cr 2*p* core level spectra for different reactor base pressures. The Cr 2*p* core level spectra obtained from a Cr reference and following Cr deposition on $WSe_2$ under UHV and HV conditions are displayed in Figure 5.12b. The reference Cr $2p_{3/2}$ and Cr $2p_{1/2}$ core levels (see the Experimental Details, Chapter 2 for details regarding the Cr reference) exhibit BEs of 574.10 eV and 583.41 eV, respectively, FWHMs of 0.92 and 1.45 eV, respectively, and significant degrees of asymmetry.[73] Following Cr deposition on $WSe_2$ under UHV conditions, metallic Cr (Cr–Cr bonding) and $CrSe_x$ are detected at BEs of 574.05 eV and 575.74 eV,[74] respectively. We only fit the Cr $2p_{3/2}$ core level spectrum obtained following Cr deposition under HV conditions due to parameter constraints in the fitting software. A much smaller concentration of metallic Cr is detected following Cr deposition under HV conditions coinciding with the formation of a substantial concentration of both $Cr_xO_y$ and $Cr(OH)_3$ as evidenced by the chemical states detected at 575.99 and 577.21 eV, respectively, in the HV Cr $2p$ core level spectrum.[71,75,76] The four peaks which appear at higher BE from the $Cr_xO_y$ chemical state in the Cr $2p_{3/2}$ core level spectrum (each denoted by a downward pointing arrow) arise from multiplet splitting common in transition metal ions with unpaired *d*-electrons.[75] Multiplet splitting observed in the $2p$ core levels of various first row transition metal ions ($Cr^{3+}$ in $Cr_xO_y$ in this case) is predicted theoretically[77] and the origins of which are discussed in further detail elsewhere.[71,75] Peaks originating from multiplet splitting similarly convolute the the Cr $2p_{3/2}$ core levels obtained after depositing Cr on the TMDs discussed throughout Chapters 3 and 5 in HV. The binding energies of the chemical states associated with $Cr_xO_y$ and $Cr(OH)_3$ are in much closer agreement with those of reference samples[75] when the four multiplet peaks are included in fitting the Cr $2p$ spectrum obtained following Cr deposition under HV conditions compared with BEs of the same chemical states when the multiplet peaks are omitted. In addition, the stoichiometry of $Cr_xO_y$ is reasonably close to $Cr_2O_3$, the most stable oxide of chromium, when multiplet peaks are included in fitting the HV Cr $2p$ core level spectrum. If multiplet peaks are omitted from the HV Cr $2p$ spectrum, the stoichiometry of the chromium hydroxide species is far from $Cr(OH)_3$, which is the most stable hydroxide of chromium. $Cr(OH)_3$ is localized to the outermost surface as is evident when comparing normalized O 1*s* core level spectra obtained at two different take off angles (Figure 5.13).

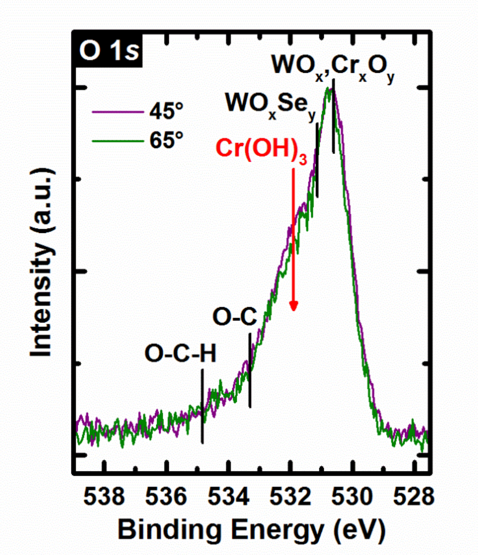

Figure 5.13. O 1*s* core level spectrum obtained following Cr deposition under HV conditions at two different photoelectron take off angles (45°, 65°).

The binding energy of the $Cr(OH)_3$ chemical states in the O 1*s* and Cr $2p_{3/2}$ core level spectra are consistent with previous XPS analysis of a $Cr(OH)_3$ reference sample and its formation has been observed in other transition metals via passivation upon air exposure.[75] The conversion of Cr to $Cr_xO_y$ is highly thermodynamically favorable as $\Delta G°_{f,Cr2O3}$ = -353 kJ/mol and $\Delta G°_{f,Cr3O4}$ = -383 kJ/mol.[51] Unlike Sc, which completely oxidizes under HV conditions and following brief air exposure,[34] Cr oxidation is not as thermodynamically favorable. This permits preservation of $CrSe_x$ at the Cr–$WSe_2$ interface despite substantial oxidation of remaining metallic Cr. The location of $CrSe_x$ at the interface formed with $WSe_2$ under HV conditions beneath metallic Cr, $Cr_xO_y$, and $Cr(OH)_3$ serves as a kinetic barrier to oxidation.

Figure 5.12c displays the O 1*s* core level spectra obtained from exfoliated $WSe_2$ as well as $WSe_2$ following Cr deposition under UHV and HV conditions. The evolution of the oxygen chemical states after $WSe_2$ exfoliation and subsequent Cr deposition in UHV is analogous with that detected in the Cr–$MoS_2$ system discussed in Chapter 3 and is therefore not discussed in detail here.

Following Cr deposition under HV conditions, a significant concentration of oxygen-based species are detected, including O–C–H (534.46 eV), O–C (532.95 eV), and $WO_xSe_y$ (531.1 eV), similar to the BE previously reported from an analogous tungsten oxychalcogenide ($WO_xS_y$) chemical state in the O 1*s* core level spectrum.[34] A chemical state is also detected at 531.85 eV corresponding with the formation of $Cr(OH)_3$ according to the intensities of the related chemical states corrected with ASFs, which is in reasonably close agreement with previous XPS analysis of a bulk $Cr(OH)_3$ sample.[75] The most intense chemical state detected at 530.58 eV in the HV O 1*s* core level spectrum consists of a convolution of $Cr_xO_y$ and $WO_x$ chemical states. Transition metal oxide species can exhibit a range of BEs between 528.0 and 531.0 eV depending on both the transition metal and its oxidation state.[76]

The evolution of the carbon chemical states after exfoliating $WSe_2$ and subsequently depositing Cr in UHV and HV are analogous with the Cr–$MoS_2$ system and will therefore not be discussed in detail here. The concentration of Cr–C bonds is below the limit of XPS detection after depositing Cr on $WSe_2$, but cannot be confidently ruled out due to the presence of Cr–C bonds at the Cr–$WS_2$ interface.

The Cr surface formed on $WSe_2$ in UHV exhibits a RMS roughness (0.39 nm) that is significantly higher than that detected from the Cr film deposited on $WSe_2$ in HV (Figure 5.11b), which is consistent with that observed in AFM images obtained from the Cr–$WS_2$ system. This corroborates the RMS roughness of the Cr film is minimized by performing the deposition in HV.

### *$WTe_2$*

The Cr–$WTe_2$ reaction is thermodynamically unfavorable if the reaction results in the formation of a $CrTe_{1.029}$ compound (Figure 5.21b). Before depositing Cr in UHV, the exfoliated $WTe_2$

exhibits a Te:W ratio of ~2.8:1 indicating a substantial Te excess. The concentrations of $WO_x$ and $TeO_x$ (according to the intensities of the associated chemical states relative to the total integrated intensity of the corresponding W 4*f* and Te 3$d_{5/2}$ core levels) detected on the exfoliated $WTe_2$ surface are ~10× higher than on the exfoliated $WTe_2$ surfaces before depositing Au and Ir in UHV (Figure 5.14a). This is seemingly correlated with the ~1.2× higher Te:W ratio detected in the $WTe_2$ crystal before depositing Cr in UHV compared with the exfoliated $WTe_2$ crystals before depositing Au or Ir in UHV. The extreme Te excess and increased degree of surface oxidation detected here indicates a lower quality $WTe_2$ crystal, which could enhance reactions with a contact metal. Reactions between Cr and $WTe_2$ result in the formation of $CrTe_x$ and metallic W according to the chemical states detected at high BE in the Te 3$d_{5/2}$ core level and at low BE in the W 4*f* core level, respectively (Figure 5.14a). The low BE chemical state detected in the W 4*f* core level after depositing Cr in UHV exhibits an asymmetric line shape and a BE in good agreement with the W reference film. It is likely that the concentration of $CrTe_x$ formed at the Cr–$WTe_2$ interface in UHV is enhanced by the Te excess in the $WTe_2$ employed here, but the metallic W detected in the corresponding W 4*f* core level indicates Cr also scavenges Te from $WTe_2$ to form $CrTe_x$. After depositing Cr in UHV, $TeO_x$ is below the limit of XPS detection, while an appreciable concentration of $WO_x$ is detected. The Te–O BDE is roughly half that of the W–O BDE. Therefore, Cr preferentially scavenges oxygen from Te when deposited in UHV and leaves an appreciable concenrtration of $WO_x$ at the Cr–$WTe_2$ interface. An appreciable concentration of $WO_x$ should be expected at the interface between various metals and W-based TMDs, especially when the contact metal is deposited in HV. The implications of $WO_x$ at the metal–TMD interface on the band alignment and contact performance will be discussed in greater detail in Section 5.4.5. Only $WTe_2$

chemical states are detected in the Te $3d_{5/2}$ and W $4f$ core levels after depositing Cr in HV. The persistence of Cr–Te bonds in the presence of excess oxidizing gases typically found in an elastomer-sealed deposition tool is thermodynamically unfavorable. The Cr–Te bonds that presumably form *in–situ* during Cr deposition in HV dissociate in favor of more stable Cr–O and Cr–(OH) bonds. The liberated $Te^{x-}$ is then free to react with metallic W from the initial Cr–$WTe_2$ reaction and form disordered $WTe_2$ at the interface. The disordered $WTe_2$ likely causes the ~0.1 eV broadening exhibited by the Te $3d_{5/2}$ core level (gaussian = 0.64, lorentzian = 0.51) obtained after depositing Cr in HV compared with the FWHM of the Te $3d_{5/2}$ core level obtained from the exfoliated $WTe_2$ (gaussian = 0.52, lorentzian = 0.51). The procedure employed in calculating the FWHM of a peak fitted to an XPS spectrum is provided in the Experimental Details (Chapter 2). The Te $3d_{5/2}$ core level spectra obtained after depositing Cr in UHV and HV is convoluted by the Cr $2p_{3/2}$ core level (Figure 5.14b). A normalized Cr $2p_{3/2}$ reference spectrum from a metallic Cr film is superimposed over the Te $3d_{5/2}$ core level spectrum obtained after exfoliating $WTe_2$ for comparison. Significant concentrations of $CrTe_x$ and $Cr_xO_y$ are detected after depositing Cr in UHV as evidenced by the two chemical states detected at high BE from the asymmetrically shaped metallic Cr chemical state in the corresponding Cr $2p_{3/2}$ core level. After depositing Cr on other Mo- and W-based TMDs in UHV, the $Cr_xO_y$ concentration is near the limit of XPS detection. The significant concentration of $Cr_xO_y$ detected at the Cr–$WTe_2$ interface indicates Cr readily scavenges oxygen from preexisting oxides on the $WTe_2$ surface. The broad feature detected at high BE in the Cr $2p_{3/2}$ core level obtained after depositing Cr in HV is convoluted by $Cr_xO_y$, $Cr(OH)_x$, and $Cr^{3+}$ multiplet splitting peaks. Any $CrTe_x$ remaining at the interface after depositing Cr in HV and the reansferring the sample *ex–situ* from the elastomer-sealed deposition tool to the UHV cluster tool is unresolvable from the convoluted Te 3$d_{5/2}$/Cr 2$p_{3/2}$ spectrum. The free energies of formation of chromium oxide and chromium hydroxide species are far more negative than the known free energy of formation of $CrTe_{1.029}$ indicating the intermetallic compound is unstable in air. However, depositing a much thicker Cr film in HV may preserve the $CrTe_x$ intermetallic at the Cr–$WTe_2$ interface.

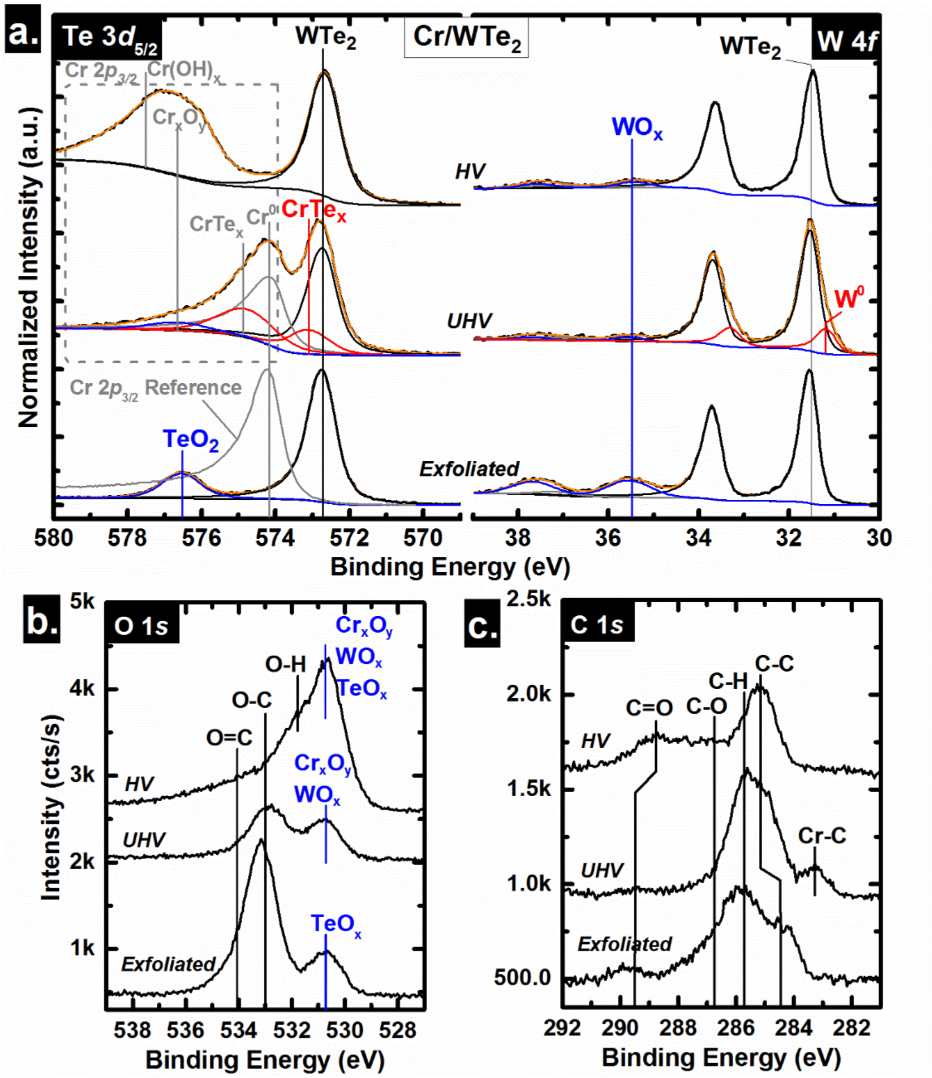

Figure 5.14. XPS spectra of the a) Te 3$d_{5/2}$, W 4$f$, Cr 2$p_{3/2}$, b) O 1$s$, and c) C 1$s$ core level spectra obtained from $WTe_2$ after exfoliation and subsequent Cr deposition in UHV and HV. The spectra in a) are normalized to the Te 3$d_{5/2}$ core level.

A significant concentration of O=C and O–C bonds are detected after exfoliating $WTe_2$ (in addition to the previously described adventitious species) and likely originate from the carbon tape holding the $WTe_2$ to the Si substrate in this experiment (Figures 5.14 c, d). A significant concentration of Cr–C bonds is detected after depositing Cr in UHV, which could originate from reactions between Cr and the carbon tape or from reactions between Cr and the adventitious carbon on the $WTe_2$ surface. The organic O=C and O–C bonds persist after depositing Cr in UHV and are detected in higher concentrations in the O 1*s* and C 1*s* core levels after depositing Cr in HV. Interestingly, Cr–C bonds are below the limit of XPS detection after depositing Cr in HV, which could be due to Cr–C bond dissociation in favor of more energetically stable chromium oxide and hydroxide species.

The RMS roughness of the $WTe_2$ surface after depositing Cr in HV (0.10 nm) is comparable with the RMS roughnesses of the Cr–$WS_2$ and Cr–$WSe_2$ samples fabricated in HV. Therefore, Cr films deposited in HV will exhibit lower RMS roughness values regardless of the TMD substrate due to the significant concentration of oxygen that reacts with Cr during deposition (Figure 5.11c).

### 5.4.4 Sc

*$WS_2$*

The Sc–$WS_2$ reaction is highly exothermic considering the $\Delta G^{\circ}_{f,WS2}$ is more positive than the $\Delta G^{\circ}_{f,ScS}$ by > 180 kJ/mol (Figure 5.21b). W–O bonds detected initially on the $WS_2$ surface after exfoliation are below the limit of XPS detection after depositing Sc in UHV. Sc reacts aggressively with $WS_2$ when deposited in UHV (Figure 5.15a). The chemical states detected at high BE in the corresponding S 2*p* core level and low BE in the corresponding W 4*f* core level indicate the presence of a sulfur-deficient $WS_x$ species that forms as Sc scavenges sulfur from $WS_2$. The formation of $ScS_x$ during Sc deposition in UHV is corroborated by the chemical state detected at low BE from the $WS_2$ chemical state in the corresponding S 2*p* core level. The Sc-S electronegativity difference is 0.2 greater than the W-S electronegativity difference, which suggests a greater degree of charge transfer occurs from Sc to S than from W to S. Therefore, the $ScS_x$ chemical state in the S 2*p* core level should exhibit a greater BE shift from elemental S than the $WS_x$ chemical state as is detected in this work. The $WS_x$ chemical state detected in the W 4*f* core level after depositing Sc in UHV exhibits a BE ~0.4 eV higher than the expected BE of metallic W, which indicates Sc does not completely reduce the $WS_2$ at the interface. In all other Sc–TMD systems discussed in Chapters 3 and 5, Sc completely reduces the TMD. $WS_2$ is the most thermodynamically stable of the six Mo- and W-based TMDs investigated in this work, which indicates the Sc–$WS_2$ reaction is the least thermodynamically favorable of the six Sc–TMD reactions considered. After depositing Sc in HV, the $WS_x$ and $ScS_x$ reaction products that were detected after depositing Sc in UHV are below the limit of XPS detection. The sulfur that is scavenged from $WS_2$ by Sc *in–situ* during deposition in HV is presumably liberated as Sc reacts with background gases in the deposition chamber to form more energetically stable Sc–O bonds (see Chapter 7 for details regarding a relevant experiment). The $S^{2-}$ radicals are then free to react with the $WS_x$ that presumably forms *in–situ* during Sc deposition in HV and form disordered $WS_2$ at the interface. The $WS_2$ chemical states detected in the S $2p_{3/2}$ and W $4f_{7/2}$ core levels after depositing Sc in HV are broadened symmetrically by ~0.1 eV like the bulk TMD chemical states detected after depositing Cr on $WTe_2$ in HV, which likely manifests from the disordered $WS_2$ at the interface. An additional chemical state is detected at high BE in the W 4*f* core level after depositing Sc in HV, which indicates the formation of $WO_x$.

The Sc 2*p* core level obtained from a Sc reference film and from $WS_2$ after depositing Sc in UHV and HV are shown in Figure 5.15b. The chemical states detected in the Sc 2*p* core level after depositing Sc in UHV and HV are analogous with the chemical states detected in the Sc 2*p* core level spectra obtained from the Sc–$MoS_2$ system and are therefore not discussed further.

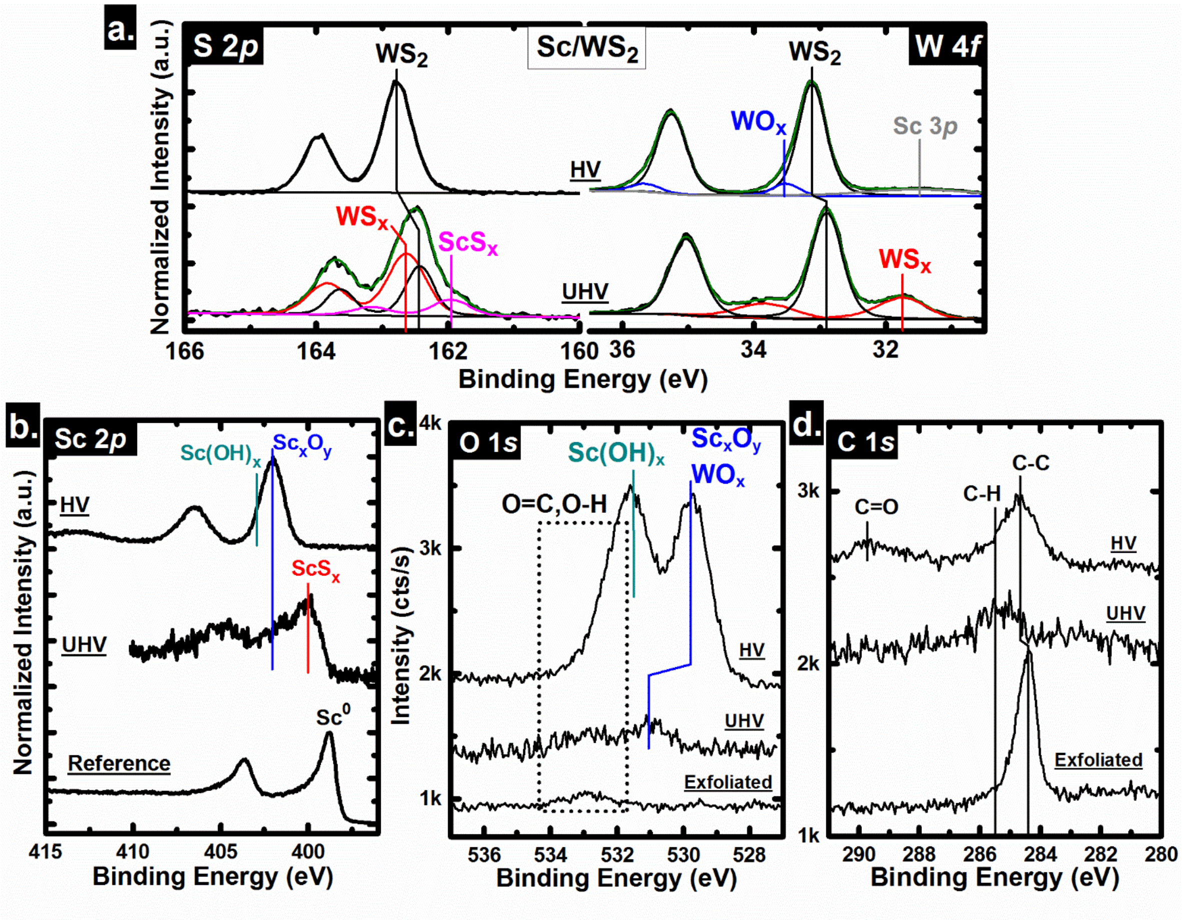

Figure 5.15. XPS spectra of the a) S 2*p*, W 4*f*, Sc 3*p*, b) Sc 2*p*, c) O 1*s*, and d) C 1*s* core levels obtained from $WS_2$ after exfoliation and subsequent Sc deposition in UHV and HV. The spectra in a) and c) are normalized to the S $2p_{3/2}$, W $4f_{7/2}$, and Sc $2p_{3/2}$ core levels, respectively. The Sc 3*p* core level is present at low BE from the W 4*f* core level obtained after depositing Sc in UHV, but is outside the spectrum window and therefore does not appear in a).

The evolution of the chemical states in the O 1*s* and C 1*s* core level spectra throughout $WS_2$ exfoliation and subsequent Sc depositions in UHV and HV are analogous with that detected in the

Sc–MoS$_2$ system. However, O=C bonds are detected after depositing Sc on WS$_2$ in HV (Figure 5.15d), which likely originate from the carbon tape employed to hold the WS$_2$ to the Si substrate in this work.

The Sc films deposited on WS$_2$ in UHV and HV exhibit RMS roughnesses similar to that of the exfoliated WS$_2$ surface. The highly uniform nature of the 1-2 nm Sc films on WS$_2$ regardless of the deposition chamber ambient prior to Sc deposition indicates a FM-type growth mechanism likely facilitated by the energetically favorable formation of Sc–S bonds compared with the formation of Sc–Sc bonds.

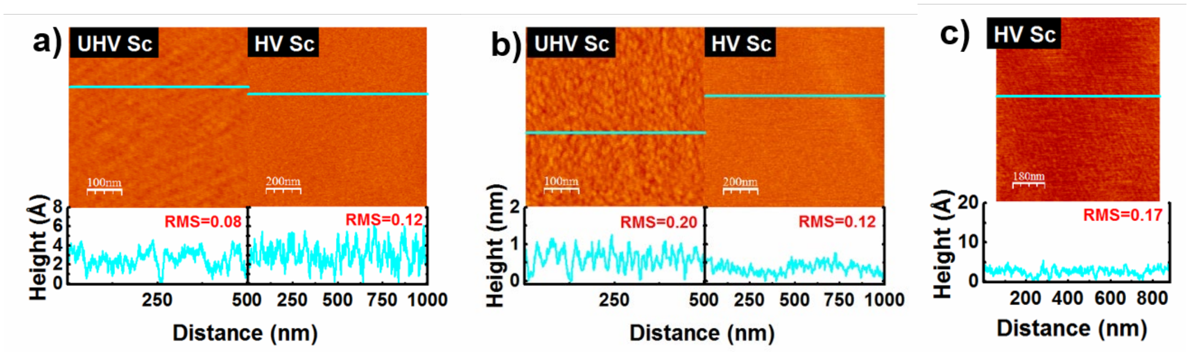

Figure 5.16. AFM images obtained *ex–situ* from a) WS$_2$ and b) WSe$_2$ after depositing Sc in UHV and HV and c) WTe$_2$ after depositing Sc in HV. Corresponding line profiles are displayed below each image and the light blue line superimposed over each image represents the location each line profile was obtained from. The RMS roughness values are displayed in red. The AFM images obtained from WTe$_2$ after depositing Sc in UHV only show background noise and are therefore not shown here.

*WSe$_2$*

Reactions between Sc and WSe$_2$ are highly exothermic (Figure 5.21b). The interface chemistry detected after depositing Sc on WSe$_2$ in UHV and HV (Figure 5.17) is analogous with the chemistry detected in the Sc–MoS$_2$ system and will therefore not be discussed further.

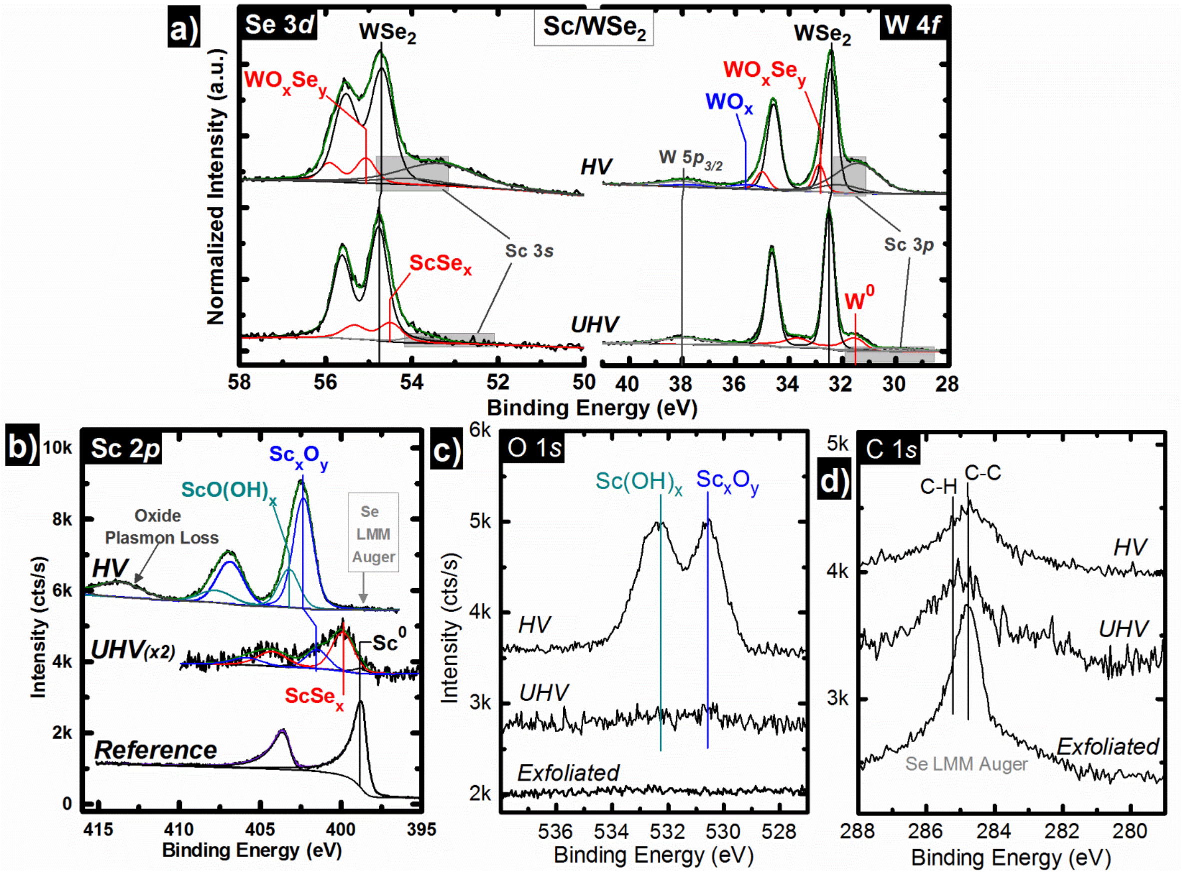

Figure 5.17. XPS spectra of the a) Se 3*d*, Sc 3*s*, Sc 3*p*, W 4*f*, W 5$p_{3/2}$, b) Sc 2*p*, c) O 1*s*, and d) C 1*s* core level spectra obtained from WSe$_2$ after exfoliation and subsequent Sc deposition in UHV and HV. The Sc 2*p* reference spectrum is also displayed for comparison in b). The spectra in a) and c) are normalized to the Se 3$d_{5/2}$, W 4$f_{7/2}$, and Sc 2$p_{3/2}$ core levels, respectively.

### *WTe*$_2$

Any $\Delta G^\circ_f$ to the scandium telluride binary system is unknown. However, the thermodynamic favorability of the Sc–WTe$_2$ reaction can be inferred from the highly exothermic nature of the Sc–WS$_2$ and Sc–WSe$_2$ reactions. Significant concentrations of WO$_x$ and TeO$_x$ are detected on the exfoliated WTe$_2$ surface in agreement with other WTe$_2$ crystals employed in this work. The chemical states detected after depositing Sc on WTe$_2$ in UHV and HV (Figures 5.18 a, b) are analogous with the chemical states detected in the Sc–MoTe$_2$ system. Organic species (O–C and

O–C=O bonds), which likely originate from the carbon tape used to fix the $WTe_2$ to a Si substrate in this work, are detected after exfoliating the $WTe_2$ and subsequently depositing Sc in UHV and HV (Figures 5.18 c, d). Sc–C bonds are below the limit of XPS detection but cannot be confidently ruled out (see Chapter 7 for evidence of a spontaneous reaction between Sc and adventitious carbon on the $WSe_2$ surface).

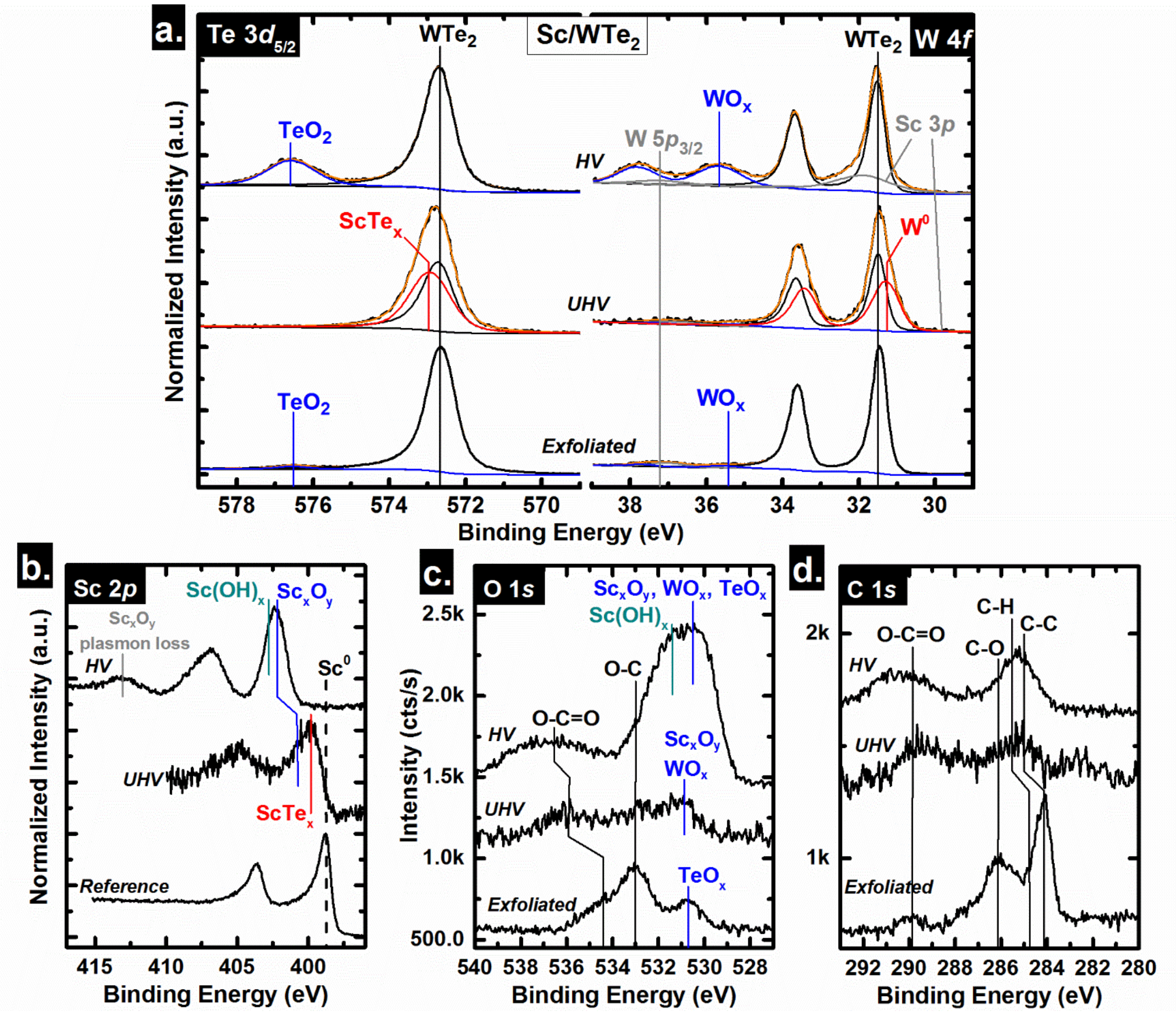

Figure 5.18. XPS spectra of the a) Te $3d_{5/2}$, W 4*f*, W $5p_{3/2}$, Sc 3*p*, b) Sc 2*p*, c) O 1*s*, and d) C 1*s* core level spectra obtained from $WTe_2$ after exfoliation and subsequent Sc deposition in UHV and HV. The normalized reference Sc 2*p* spectrum is also shown in b) for comparison.

The RMS roughness of the Sc film deposited on $WTe_2$ in HV (0.17 nm, Figure 5.16c) is comparable with the surface topography of the Sc–$WS_2$ and Sc–$WSe_2$ samples regardless of the deposition chamber ambient prior to Sc deposition.

### 5.4.5 Implications of $WO_x$ at the interface between contact metals and W-based TMDs

$WO_x$ is detected at all interfaces formed between W–based TMDs and contact metals deposited in HV investigated in this work excluding the Cr–$WS_2$ interface. It is therefore necessary to consider the effects of $WO_x$ at the metal–TMD interface on band alignment as a typical device fabrication process will involve contact metallization under HV conditions. The $WO_x$ chemical state detected in th W 4*f* core level spectra at high BE after exfoliating and subsequently depositing Au, Ir, Cr, or Sc on $WSe_2$ and $WTe_2$ exhibits a BE between the $W^{6+}$ and $W^{4+}$ chemical states indicating the presence of a $W^{5+}$ state.[78] The high BE chemical state detected in the W 4f core level spectra obtained from $WS_2$ after depositing contact metals in UHV or HV exhibits a BE between the previously reported $WO_2$ and $W_2O_3$ chemical states indicating the presence of a lower W oxidation state than in the $WO_x$ formed on $WSe_2$ and $WTe_2$. $WS_2$ is more thermodynamically stable than $WSe_2$ and $WTe_2$, which suggests $WS_2$ is more resistant to oxidation in the presence of atmospheric gases and therefore rationalizes the lower O:W ratio in the $WO_x$ detected in the metal–$WS_2$ systems. The $WO_x$ detected in the $WSe_2$ and $WTe_2$ systems after depositing metals in HV exhibits an O:W ratio between 2.6:1 and 2.7:1. Preferential $WSe_2$ domain edge oxidation in the presence of excess oxidizing species has been predicted by DFT calculations and recently experimentally verified with STM and STS.[79] The same work theoretically predicted and experimentally verified metallic behavior at oxidized $WSe_2$ domain edges. XPS obtained from $WSe_2$ grown by CVD with oxidized edges indicates an O:W ratio between 2.6:1 and 2.7:1, consistent with oxygen deficient

$WO_3$ studied elsewhere[79] and also with $WO_x$ detected in the $WSe_2$ and $WTe_2$ systems in this work. A number of different oxygen deficient $WO_3$ compounds are expected to be metallic even considering the error associated with stoichiometry calculation by XPS (±0.2).[79,80]

Figure 5.19a displays the expected band alignment between amorphous $WO_3$ (a-$WO_3$), oxygen deficient a-$WO_3$ (a-$WO_x$, $x<3$) and the W-based TMDs. The absolute energies of the TMD band edges are derived from previous work by Addou et al.,[10] Keyshar et al.,[81] and Zhang et al.,[82] while the band structure of a-$WO_3$ and a-$WO_x$ are derived from UPS and XPS measurements of a-$WO_3$ and a-$WO_x$ films (see Experimental Details, Section 5.3 for information regarding the synthesis and characterization of a-$WO_3$ and a-$WO_x$ films). Photoelectron spectroscopy has demonstrated, both previously[83] and in this work, the formation of shallow occupied gap states (Figure 5.19d) and a concomitant $E_F$ shift towards the conduction band edge (Figure 5.19a) upon the formation of oxygen vacancies in $WO_3$. This results in metallic n-type conduction in a-$WO_x$, the structure and electronic properties of which are likely analogous with $WO_x$ detected on $WSe_2$ and $WTe_2$ following metal deposition under HV conditions. The band gap of the a-$WO_3$ film is defined by the difference between the onset of the plasmon loss at higher BE from the O 1*s* core level and the BE of the tungsten oxide chemical state in the O 1*s* core level (graphically represented in Figure 5.19b). This technique is applicable to tungsten oxides as the density of states near the VBM are comprised primarily of O 2*p* states, while the W 5*d* states in a stoichiometric film are unoccupied.[84] We find that the surface of a-$WO_3$ exhibits an $E_{ion}$ ($E_F$) of 9.77 eV (6.90 eV) according to UPS and XPS. Subjecting the a-$WO_3$ film to $Ar^+$ sputtering to generate oxygen vacancies causes the $E_F$ to shift 0.20 eV towards the conduction band. In addition, the sputtering induces the formation of additional chemical states at low BE from the $WO_3$ chemical state in the W 4*f* core level spectrum

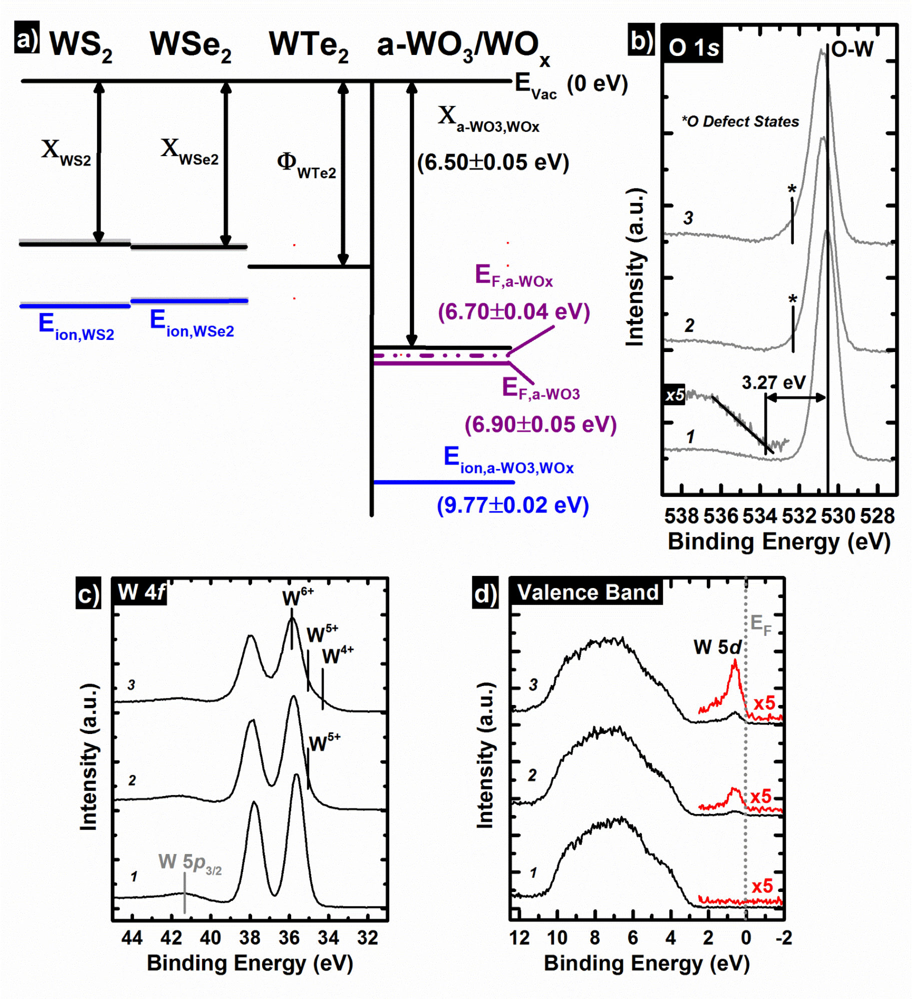

Figure 5.19. a) Expected band alignment between $WS_2$, $WSe_2$, $WTe_2$ and both amorphous $WO_3$ (a-$WO_3$) and a-$WO_x$ ($x<3$). The electron affinity ($\chi$) of $WS_2$ and $WSe_2$ are 4.0 eV and 4.05 eV, respectively, and the ionization energy ($E_{ion}$) of $WS_2$ and $WSe_2$ are 5.5 eV and 5.35 eV, respectively. The work function of metallic 1T' $WTe_2$ is 4.55 eV. Grey regions represent the ±0.05 eV error margins reported in conjunction with respective energies. b) O 1*s*, c) W 4*f*, and d) valence band spectra obtained from 1) reactively sputtered a-$WO_3$ and 2) following 2 minutes and 3) 8 minutes of total exposure of the a-$WO_3$ film to Ar plasma *in-situ*. The appearance of occupied W 5*d* chemical states near the conduction band edge via the generation of oxygen vacancies by plasma exposure are clearly resolvable in the corresponding valence band spectra and are reflected in the concomitant FL shift. The intensity of the valence band spectra between binding energies of 2.5 and -2 eV have been multiplied by five to clearly show the increasing occupation of the W 5*d* core level following exposure of a-$WO_3$ to Ar plasma for 2 and 8 minutes, respectively.

corresponding with lower W oxidation states (e.g., 5+, 4+) and at high BE from the WO$_3$ chemical state in the O 1*s* core level corresponding with oxygen ‘defect states’ (denoted by *). Migas et al. predicts degenerate n-type doping of WO$_x$ (2.63<x<2.92) via an increasingly large E$_F$ shift into the conduction band with decreased O:W ratio from WO$_3$.[85] This is consistent with previously

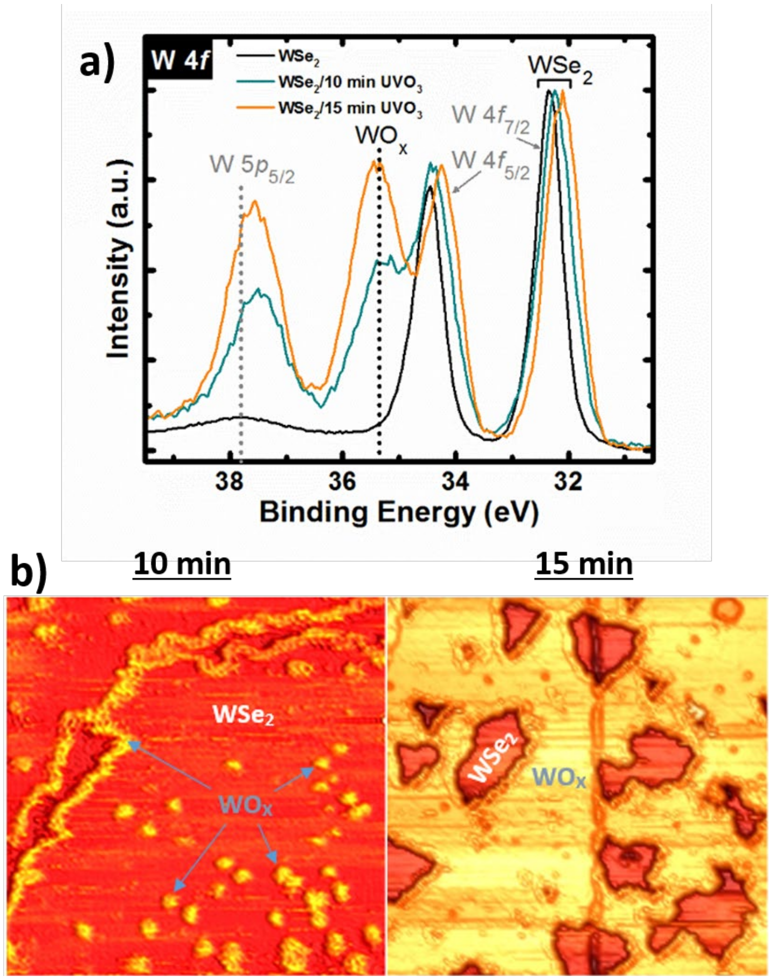

Figure 5.20. a) W 4*f* core level spectra obtained from a pristine WSe$_2$ film, a WSe$_2$ film after 10 min UV-O$_3$ treatment, and a WSe$_2$ film after 15 min UV-O$_3$ treatment showing the durect relationship between increasing WO$_x$ concentration and increasing p-type core level shift. b) STM images obtained from the WSe$_2$ films treated with UV-O$_3$ for 10 min and 15 min showing the significant increase in WO$_x$ coverage with increasing time of UV-O$_3$ treatment. The WSe$_2$ films were grown by MOCVD according to a procedure outlined in Ref. 90. The STM images are provided courtesy of Dr. R. Addou.

observed oxygen vacancy-induced n-type doping in tungsten oxide.[64] However, we do not observe a $E_F$ shift into the conduction band as Migas et al. predicts, only towards it. The W 5*d* orbital becomes populated with electrons as oxygen vacancies and corresponding lower oxidation states $W^{x+}$ (x=5, 4, …, 0) are generated. After $Ar^+$ sputtering the a-$WO_x$ film, an additional feature is detected near the $E_F$ in the corresponding valence band spectra (spectra 2 and 3 in Figure 5.19d), which corresponds with partial filling of the W 5*d* orbital and demonstrates the potential for metallic transport in oxygen deficient tungsten oxide.[86]

The vacuum work functions of a-$WO_3$ and a-$WO_x$ extracted in this work agree with a previous report[22] and indicate their potential as Ohmic hole contacts in TMD-based devices. In addition, the degree of p-type $E_F$ shift in $WSe_2$ can be controlled from < 0.1 eV to > 0.25 eV by varying the $WO_x$ coverage on the TMD surface (Figure 5.20). This hole doping strategy may be successfully applied to $WS_2$, however additional experiments are necessary. This work highlights the potential for enhanced hole transport in semiconducting W-based TMD devices by hole injection (also applicable with other TMDs) by inserting $WO_x$ at the contact–TMD interface. In addition, predominant hole transport in $WSe_2$ devices could be a product of the interface chemistry formed between contact metal and TMD under HV conditions.

### 5.4.6 Reactivity Trends between Metal Contacts and W-Based TMDs

The reactivity of each metal (Ir, Au, Cr, Sc)–TMD ($WS_2$, $WSe_2$, $WTe_2$) interface formed in UHV is plotted versus the contact metal work function in Figure 5.21a. The reactivity of the interface is gauged according to the ratio of the sum of the intensities of the metal (Ir, Au, Cr, Sc) chalcogenide intermetallic chemical state and the reduced TMD (e.g., $WSe_x$) chemical state in the associated chalcogen core level to the total integrated intensity of the chalcogen core level. In general, the reactivity varies significantly between Ir, Au, Cr, and Sc. However, the reactivity of a single metal varies little across the three W-based TMDs in the cases of Ir, Cr, and Sc. The reactivity across the four contact metals investigated here follows Sc > Ir > Cr > Au in decreasing order. In other words, Sc exhibits the highest reactivity by forming the highest concentration of scandium chalcogenide intermetallic with all three W-based TMDs out of the four contact metals investigated. The highly reactive nature of Sc is predicted by thermodynamics. Sc–TMD reactions are far more exothermic than the potential reactions in any other metal–TMD system investigated in this work (Figure 5.21b). Ir exhibits a much higher reactivity than thermodynamics predicts. The defective nature of bulk TMDs (e.g., excess chalcogen in the tellurides, chalcogen vacancies in the sulfides and selenides) likely facilitates orbital hybridization between the Ir and W *d*-orbital valences due to the associated absence of screening potentials (e.g., chalcogen atoms). In general, the W-based TMDs are more thermodynamically stable than the Mo-based TMDs, which manifests as a lower degree of reactivity between metals and the W-based TMDs. In both the W- and Mo-based TMDs, the tellurides are the most reactive followed by the selenides and the sulfides, which are the least reactive. This work shows that the thermodynamics of contact metal–TMD systems can roughly predict the interface chemistry formed between a metal and a TMD when the metal is deposited in UHV. The appreciable concentration of background gases in an elastomer-sealed deposition tool complicates the thermodynamics of the system and makes it more difficult to accurately predict which compounds will be stable in the presence of oxidizing gases and which compounds will oxidize.

Reactions between early transition metals, which generally exhibit low ionization energy valences due to the unfilled *d*-orbital, and TMDs are more accurately predicted by the thermodynamics of the metal–TMD system. More complicated DFT calculations reported to date do not take into account the role of surface adsorbates or defects in the TMD on the thermodynamics and kinetics of metal–TMD reactions. This work shows the interface chemistry can vary significantly depending on the concentration of defects on the TMD surface, which can cause associated variations in contact performance (see Chapters 6 and 7). Furthermore early transition metals can scavenge oxygen from the surface of more unstable TMDs (e.g., tellurides). The benefit or detriment of interfacial oxide, carbide, or intermetallic species to the contact performance is largely determined by the electronic structure of the reaction product. Therefore, the work described here and also in Chapter 3 is critical to engineering higher performance, more consistent contacts to

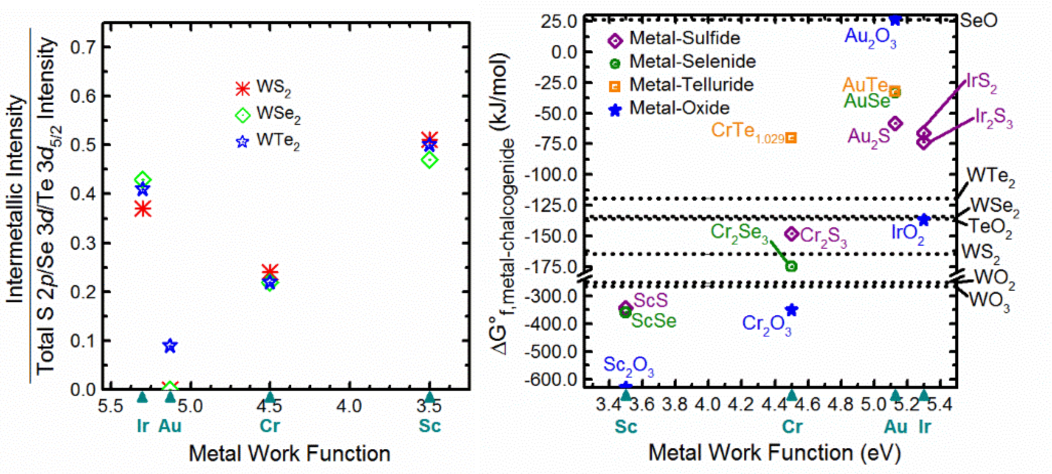

Figure 5.21. a) Reactivity of the metal–TMD systems discussed in this chapter. The reactivity is gauged according to the intensity ratio of the contact metal–chacogenide (e.g., $ScS_x$ ) intermetallic chemical state in the corresponding chalcogen core level ($WS_2$: S 2*p*, $WSe_2$: Se 3*d*, $WTe_2$: Te $3d_{5/2}$) to the sum of all chemical states in the same chalcogen core level. These are plotted versus the Ir, Au, Cr, and Sc work functions for metal depositions in UHV (*in–situ*). The 'intensity' refers to the integrated intensity. b) A scatter plot showing the known Gibbs free energy for each metal chalcogenide alloy and relevant metal oxides as a function of metal vacuum work function. The specific compounds are listed on the plot. The dotted lines represent the $\Delta G^\circ_{f,WS2}$, $\Delta G^\circ_{f,WSe2}$, $\Delta G^\circ_{f,WTe2}$, $\Delta G^\circ_{f,WO2}$, $\Delta G^\circ_{f,WO3}$, $\Delta G^\circ_{f,TeO2}$, and $\Delta G^\circ_{f,SeO}$ and are shown for comparison.

TMDs and necessitates a greater understanding of the interface chemistry across the numerous combinations of contact metal and TMD that could be useful in future technology.

### 5.4.7 Effects of Interface and Contact Chemistry on the Band Alignment between Metals and W-Based TMDs

Theories attempting to explain the FLP mechanism between a three–dimensional semiconductor and metal include, but are not limited to, the formation of gap states by decaying metal wavefunction into the semiconductor[87,88] and also by defects and/or disorder at the metal/semiconductor interface.[89] Regardless of the mechanism, the formation of interface gap states play a critical role in FLP between metal and semiconductor.[37] McDonnell et al. found that defects present in $MoS_2$ provide preferential conduction pathways across the metal–$MoS_2$ interface.[31] It is therefore possible that the defective nature of TMDs plays a critical role in FL realignment upon metallization of a TMD. In addition, strong orbital hybridization of the transition metal in the TMD and contact metal near the metal–TMD interface has been predicted by DFT.[13,37] This facilitates charge redistribution across the interface and therefore influences the position of the pinned FL relative to the underlying bulk TMD. The Mo *d*–orbital contributes the majority of density of states near the conduction band minimum of $MoS_2$,[37] hence the tendency for FLP near the $MoS_2$ as strongest *d*–orbital overlap occurs there. Analogous FLP may occur in W-based TMDs near the VBM as the W *d*–orbital contributes the majority of the density of states near the VBM.[13] Figure 5.22 displays the $E_F$ position of exfoliated W-based TMDs and $E_F$ shifts induced by metal depositions under UHV conditions in band diagram form. The $WTe_2$ employed in this work exhibits the metallic 1T' phase. Therefore, the work function of 1T'-$WTe_2$ according to DFT calculations[82] is displayed in Figure 5.22 for reference, but the $E_F$ alignment between the contact metals and $WTe_2$ will not be discussed. The $E_F$ position prior to metal deposition is determined by linearly extrapolating the low BE tail of the valence band spectrum to the baseline noise level via linear regression (see Experimental Details, Chapter 2 for more details). The separation between a core level and the $E_F$ in a compound will remain constant assuming constant chemistry and structure (e.g., bulk TMD unaffected by reactions at the interface). Therefore, the $E_F$ shift induced by depositing a metal is determined by quantifying the corresponding BE shift exhibited by the bulk TMD chemical state in the chalcogen core level. A $E_F$ shift towards the VBM will be denoted as positive.

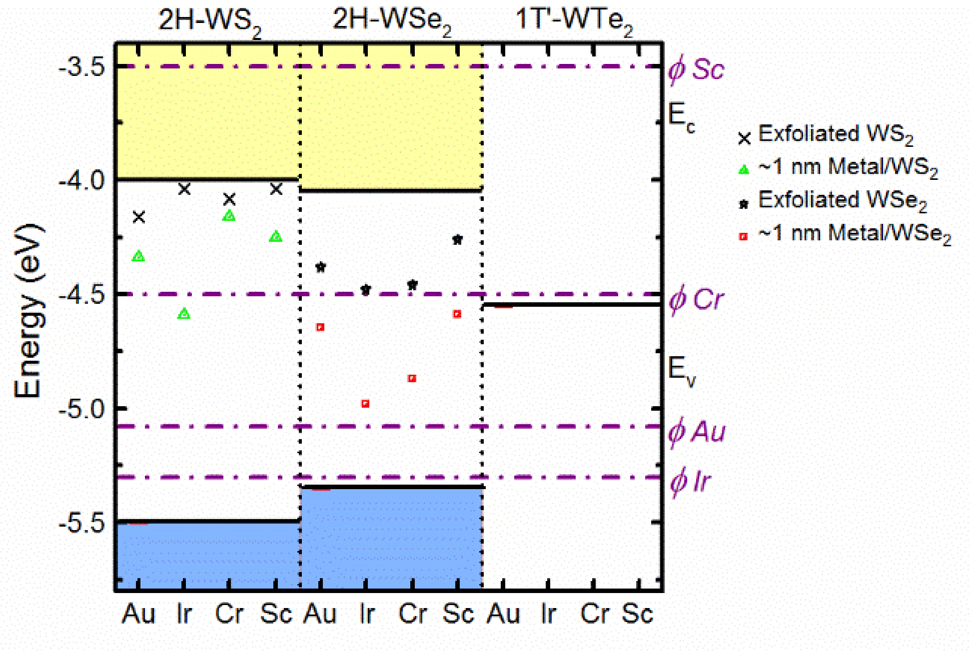

Figure 5.22. The band alignment of metal–TMD systems discussed in this chapter obtained from the initial valence band offset of the exfoliated TMD and the bulk TMD core level shift after depositing ~1 nm metal in UHV, which is ascribed to a EF shift (see Experimental Details for band diagram construction procedure).

Moderate $E_F$ variations are detected across the exfoliated $WS_2$ (4.10±0.06 eV) and $WSe_2$ (4.37±0.11 eV) crystals, which is expected considering the defective nature of bulk TMDs and the spatial $E_F$ variation across bulk $WSe_2$ crystals (both geologic and synthetic origins) reported previously.[32] The $E_F$ shifts observed after metal depositions on $WS_2$ and $WSe_2$ deviate significantly from the expected band alignment according to the Schottky-Mott rule. The largest positive $E_F$ shift and the smallest hole SBH detected from $WS_2$ and $WSe_2$ are achieved when Ir is deposited. Charge transfer is enhanced between Ir and W due to the shared *d*-orbital valences, which contrasts the *s*- and *p*-orbital valences of Au, Cr, and Sc. In addition, the unexpectedly large hole SBH detected in the Ir–$WS_2$ and Ir–$WSe_2$ systems is likely due in part to the ternary intermetallic that forms at both interfaces.

The smallest electron SBH is formed when Cr is deposited on $WS_2$ in UHV (0.16±0.10 eV) and when Sc on $WSe_2$ in UHV (0.54±0.10 eV). The metallic W detected at the interfaces formed between the W-based TMDs and the low work function metals, Cr and Sc, presumably has little effect on the resulting band alignment. A systematic $E_F$ shift towards an absolute value of ~4.6 eV (the work function of polycrystalline W)[36] that would indicate appreciable electrostatic effects associated with the metallic W reaction product is not detected when Cr and Sc are deposited. The $CrSe_x$ intermetallic at the Cr–$WSe_2$ interface could cause the associated band alignment detected in this work considering $CrSe_2$ exhibits a work function of ~5.2 eV.[90] The low electron SBH detected after depositing Cr on $WS_2$ in UHV is far from the low hole SBH expected between $CrS_2$ (work function ~5.6 eV)[90] and $WS_2$, which indicates the $CrS_x$ intermetallic that forms at the Cr–$WS_2$ interface is sulfur deficient and exhibits a work function closer to metallic Cr. Carefully choosing the processing conditions to tune the stoichiometry of the $CrS_x$ and $CrSe_x$ species that form at the Cr–$WS_2$ and Cr–$WSe_2$ interfaces, respectively, in UHV may lead to more efficient spin polarized carrier injection in sulfide or selenide based magnetic devices considering $Cr_2Se_3$ and $Cr_2S_3$ exhibit significant magnetoresistance.[91,92]

Although $Cr_xO_y$ is below the limit of XPS detection when Cr is deposited in UHV, the electronic structure of chromium oxide varies substantially with composition[90,93,94] and therefore is likely to appreciably affect the $E_F$ position when Cr is deposited under HV conditions. Recently, n-type conduction has been reported for Cr contacts (HV) to multi-layer $WSe_2$-based devices in contrast with the band alignment obtained in this work when Cr is deposited on $WSe_2$ in UHV.[95] Therefore, the electronic structure of the intermetallic that forms in each metal–TMD system where reactions are detected has a significant effect on the resulting electrostatics. This highlights the need to understand the role of the interface on contact performance in TMD-based devices.

Less severe band bending induced by Au deposition under either UHV or HV conditions is consistent with VW-type Au growth on $WSe_2$, which results in Au clusters with significantly smaller work functions than expected of bulk, polycrystalline Au. Au nanoparticles on the order of 5 nm in diameter suspended on a Si(111) substrate can exhibit a work function as small as 3.4 eV, with the work function approaching that of bulk Au as particle size increases.[46] It is also possible that orbital hybridization near the interface accompanied by charge redistribution results in FLP and therefore an anomalously low Au work function. The 0.53 eV electron SBH measured in this work is in relatively close agreement with previous DFT predictions of electron SBH for Au contacts to monolayer (0.58 eV) and bilayer (0.66 eV) $WSe_2$.[10] Nonetheless, this highlights the complex nature of $E_F$ realignment even at a vdW interface.

In general, the electron SBHs detected in the metal–$WS_2$ systems are significantly smaller than in the metal–$WSe_2$ systems, which qualitatively agrees with the metal–$MoS_2$ and metal–$MoSe_2$ band alignments discussed in Chapter 3. Therefore, $E_F$ pinning will occur near the conduction band edge of transition metal sulfides and near the middle of the band gap in transition metal selenides. Historically, low electron SBH contacts are more commonly reported than hole contacts in transition metal sulfide devices,[3,8] while $E_F$ pinning near the middle of the $MoSe_2$ band gap is predicted by DFT.[96] The gap states associated with chalcogen vacancies common in bulk TMDs contribute significantly to the $E_F$ pinning energy relative to the band edges and will convolute the effects of interface reactions on the band alignment. In general, defects are not localized to a TMD surface. Therefore, defects will always be present near the metal–TMD interface as long as there is at least one TMD layer unaffected by contact metal-induced reactions. Reactions that consume all of the TMD underneath the contact metal in single or few layer TMD devices may eliminate the $E_F$ pinning effects of defect induced gap states.

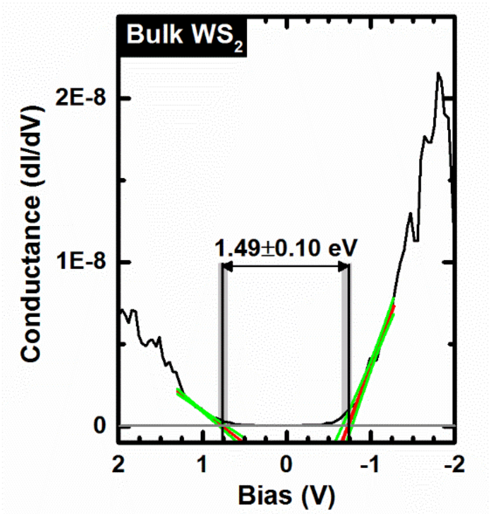

Figure 5.23. Scanning tunneling spectroscopy obtained from bulk $WS_2$ after exfoliation explicitly showing a band gap of ~1.5 eV in agreement with previous literature reports. The spectrum is an average of 20 individual sweeps. The grey regions around the vertical lines denoting the band edges reflect the 95th percentile uncertainty in the fit. The red lines reflect the best fits of the scanning tunneling spectrum at the band edges, while the green lines reflect the upper and lower bounds of the 95th percentile error associated with the best fit lines. The STS displayed here are provided courtesy of Mr. C. R. Cormier and Dr. R. Addou.

It is important to reiterate that experiments discussed here were performed on bulk TMD crystals. However, single or few layer TMDs are most commonly employed as the channel material in device structures. The band structure of single and few layer TMDs (and therefore the band alignment formed with various contact metals) can be quite different from that of the bulk analog due to quantum confinement. Single layer (bilayer, bulk) $WSe_2$ exhibits a band gap of 2.2 (1.8, 1.3) ±0.1 eV, while bulk (monolayer, bilayer) $WS_2$ exhibits a band gap of 1.5 (1.9, 1.7 according to PEEM) ±0.1 eV according to STS (Figure 5.23).[79] Angle resolved photoemission spectroscopy indicates the VBM of monolayer (bilayer, bulk) $WSe_2$ resides 1.8 (1.5, 1.1) eV from the $E_F$.[97] Error in photoemission measurements manifests in both the resolution of the spectrometer and also the method by which the VBM is extracted, typically on the order of ±0.03-0.04 eV.[98] P.-C. Yeh et al.[97] report a spectrometer resolution of ±0.1 eV but none associated with the VBM extraction method employed. Therefore, an error of ±0.13-0.14 eV associated with the ARPES derived VBM according to $WSe_2$ layer number is suspected. Together, these STM and ARPES measurements suggest a relatively unperturbed conduction band minimum (~0.3 eV offset from $E_F$) and increasingly large $E_{ion}$ and therefore bandgap with decreasing number of $WSe_2$ layers. The magnitude of the electron SBH between the same contact metals deposited under analogous conditions as were studied in this work and single or few layer $WSe_2$ are therefore expected to be similar to those reported here. However, associated hole Schottky barriers are likely to be much greater in magnitude in the mono, bi-, and tri-layer cases due to substantial increase in associated $E_{ion}$.

Another report indicates the electronic structure variation with increasing number of $WS_2$ layers differs from the ARPES study of $WSe_2$. PEEM measurements obtained from mono, bi-, and tri-layer $WS_2$ grown on $SiO_2$ show the conduction band minimum shifts away from the vacuum level by ~0.3 eV, while the VBM shifts towards the vacuum level by < 0.1 eV from mono to tri-layer $WS_2$.[81] Therefore, the hole SBHs extracted from the metal–$WS_2$ stacks by XPS in this work are expected to be similar with the same contact metals on single or few layer $WS_2$. However, reactions at the metal–TMD interface that consume all of the underlying TMD can be considered as a pseudo edge contact. Superior contact performance achieved in an edge contact architecture compared with a top contact architecture has been theoretically predicted[27] and experimentally demonstrated.[23] Therefore, the number of TMD layers consumed by the contact metal and the chemistry at the metal–TMD interface should be understood in detail when engineering bulk contacts in TMD devices and when interpreting the electrical performance of the contacts. The relationship between processing conditions, interface chemistry, and contact performance in the Pd–$WSe_2$ system is considered in detail in Chapter 6.

DFT predicts a direct proportionality between metal–TMD *d*–orbital overlap and the electronic transport across the interface.[13,27,28] Parameters such as interatomic distance and bond energy between contact metal and chalcogen are proposed as predictive factors for chemical and electrical properties of various metal–TMD interfaces. However, additional compounds arising from reactions in the vicinity of the interface will perturb orbital overlap further, resulting in different chemical and electrical interface properties. The $E_F$ shifts reported here provide evidence that interfacial reaction products in addition to the inherently defective nature of TMDs contribute to anomalous $E_F$ positions detected for various contact metals on $WS_2$ and $WSe_2$, and therefore must be understood in greater detail to engineer Ohmic bulk metal contacts.

## 5.5 Summary

The interface chemistry between metal contacts (Au, Ir, Cr, and Sc) and the W-based TMDs ($WS_2$, $WSe_2$, and $WTe_2$) according to the XPS results discussed in Section 5.4 are displayed graphically in cartoon representations in Figure 5.24 to summarize the reaction products that would typically be found in each system depending on the deposition chamber conditions.

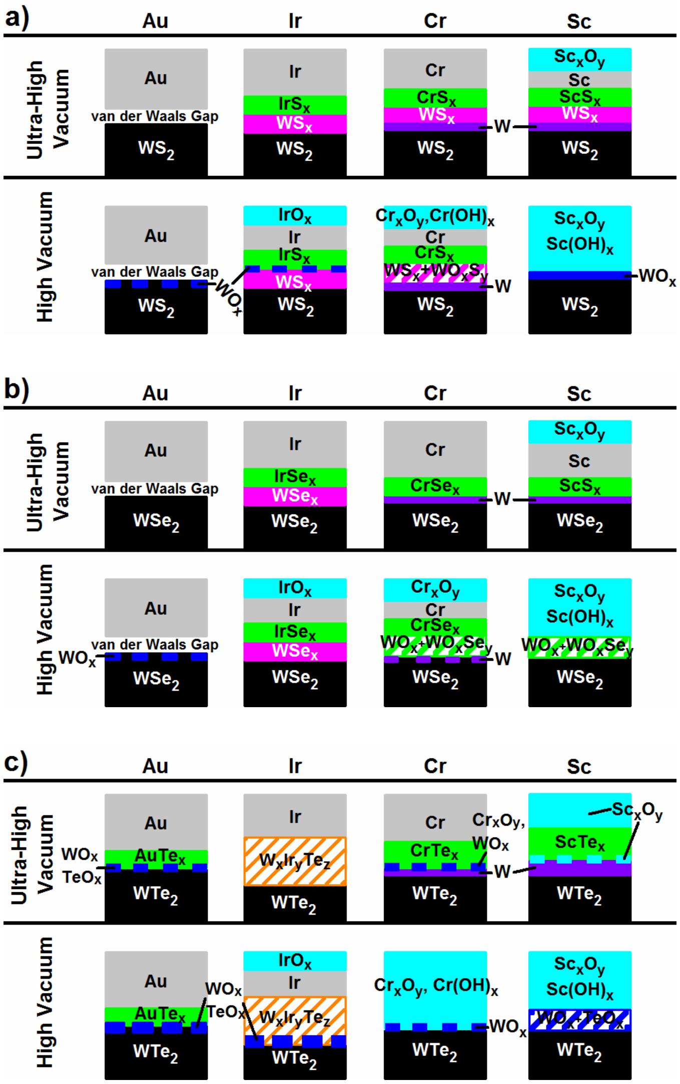

Figure 5.24. Cartoon representations of the interface chemsitry formed between Au, Ir, Cr, and Sc and the TMDs a) $WS_2$, b) $WSe_2$, and c) $WTe_2$ in UHV and HV.

A contact structure in a device stack would commonly employ much thicker metal films than were deposited in this work. Therefore, certain aspects of the contact chemistry may differ from the cartoons displayed in Figure 5.24. For instance, contact metals like Cr that partially oxidize in HV will presumably have a random distribution of $O^{2-}$ and $OH^-$ distributed throughout the contact along with a small concentration of metallic Cr. The concentration of metal oxide species that form as a result of the deposited contact metal scavenging oxygen from the TMD surface will vary depending on the concentration of oxygen-based species on the TMD surface prior to metallization. In addition, carbidic species are not shown in any of the cartoons, but should be expected in a device structure that contains organic residues from the fabrication process where a highly reactive contact metal (Cr, Ti, Sc) is employed.

## 5.6 Conclusions

This work elucidates variation in interface chemistry and contact metal chemistry with deposition chamber ambient for Au, Ir, Cr, and Sc deposited on bulk $WS_2$, $WSe_2$, and $WTe_2$. When the more reactive metals Cr and Sc are employed, thermodynamics reliably predicts favorable metal–TMD, metal–background gas, and metal–carbon reactions. Cr and Sc readily scavenge chalcogen atoms from the TMD, generally resulting in the formation of a chromium or scandium chalcogenide and metallic W at the interface in UHV. Cr and Sc are nearly 100% oxidized *in–situ* when deposited in HV due to reactions with the appreciable concentration of background gases in an elastomer-sealed deposition tool, which likely implicates contact performance. When the reportedly noble, high work function metals Au and Ir are deposited, reaction thermodynamics predict the formation of inert interfaces that are covalent in reality according to this work. Defects typically found on the order of $10^{12}$ cm$^{-2}$ in bulk TMDs likely facilitate intermetallic formation at interfaces that should be inert according to thermodynamics. The highly Te rich nature of the $WTe_2$ crystals employed in this work (Te:W ratio ~2.8:1) likely permits reactions between the excess Te and the high work function metals Au and Ir. Despite the 2:1 chalcogen:W ratio detected in the $WS_2$ and $WSe_2$ crystals employed here, the significant concentration of chalcogen vacancies in the TMDs likely facilitates *d*-orbital overlap between Ir and W resulting in the theoretically unfavorable reactions that are detected in the Ir–$WS_2$ and Ir–$WSe_2$ systems. Thermodynamics accurately predicts the vdW interfaces that are detected in the Au–$WS_2$ and Au–$WSe_2$ systems. $WO_x$ forms at the metal–$WSe_2$ interface under HV conditions regardless of the contact metal and likely improves hole transport due to the extremely high electron affinity and conductive nature of sub-stoichiometric tungsten oxide. Interfacial intermetallics likely generate gap states, contributing to FLP and unexpected SBHs in all metal–TMD systems. The $E_F$ is moderately pinned near the conduction band edge in $WS_2$ across all metals, while the $E_F$ is moderately pinned near the middle of the $WSe_2$ band gap. Ir causes the largest $E_F$ shift and the smallest hole SBH on both $WS_2$ and $WSe_2$, while Cr and Sc form the smallest electron SBHs on $WS_2$ and $WSe_2$, respectively. These results highlight the complex nature of the interface chemistry between metals and W-based TMDs, its dependence upon deposition chamber base pressure, and the implications it can have on band alignment.

## 5.7 References

(1) Schwierz, F. Graphene and Beyond: Two-Dimensional Materials for Transistor Applications. 2015, Micro- and Nanotechnology Sensors, Systems, and Applications VII Proc. 9467 94670W

(2) McDonnell, S.; Wallace, R. M. Atomically-Thin Films for Device Applications based upon 2D TMDS Materials. *Thin Solid Films*, **2016**, *616*, 482-501.

(3) Das S.; Chen, H. Y.; Penumatcha, A. V.; Appenzeller, J. High Performance Multilayer $MoS_2$ Transistors with Scandium Contacts. *Nano Lett.* **2013**, *13*, 100-105.

(4) English, C. D.; Shine, G.; Dorgan, V. E.; Saraswat, K. C.; Pop, E. Improved Contacts to $MoS_2$ Transistors by Ultra-High Vacuum Metal Deposition. *Nano Lett.* **2016**, *16*, 3824-3830.

(5) Radisavljevic, B.; Radenovic, A.; Bivio, J.; Giacometti, V.; Kis, A. Single Layer $MoS_2$ Transistors. *Nat. Nanotechnol.* **2011**, *6*, 147-150.

(6) Bao, W.; Cai, X.; Kim, D.; Sridhara, K.; Fuhrer, M. S. High Mobility Ambipolar $MoS_2$ Field-Effect Transistors: Substrate and Dielectric Effects. *Appl. Phys. Lett.* **2013**, *102*, 042104.

(7) McDonnell, S.; Addou, R.; Hinkle, C. L.; Wallace, R. M. Physico–Chemical Characterization of $MoS_2$/Metal and $MoS_2$/oxide interfaces, in: 2D Materials for Nanoelectronics, Eds. Houssa, M.; Dimoulas, A.; Molle, A. (Boca Raton, FL: CRC Press).

(8) Kim, C.; Moon, I.; Lee, D.; Choi, M. S.; Ahmed, F.; Nam, S.; Cho, Y.; Shin, H. J.; Park, S.; Yoo, W. J. Fermi Level Pinning at Electrical Metal Contacts of Monolayer Molybdenum Dichalcogenides. *ACS Nano* **2017**, *11*, 1588–1596.

(9) Yue, Y.; Chen, J.; Zhang, Y.; Ding, S.; Zhao, F.; Wang, Y.; Zhang, D.; Li, R.; Dong, H.; Hu, W.; Feng, Y.; Feng, W. Two-Dimensional High-Quality Monolayered Triangular $WS_2$ Flakes for Field-Effect Transistors. ACS Appl. Mater. Interfaces. 2018, 10, 22435-22444.

(10) Wang, Y.; Yang, R. X.; Quhe, R.; Zhong, H.; Cong, L.; Ye, M.; Ni, Z.; Song, Z.; Yang, J.; Shi, J.; Li, J.; Lu, J. Does p-type Ohmic Contact Exist in $WSe_2$-Metal Interfaces? *Nanoscale*, **2016**, *8*, 1179-1191.

(11) Mleczko, M. J.; Xu, R. L.; Okabe, K.; Kuo, H.-H.; Fisher, I. R.; Philip Wong, H.-S.; Nishi, Y.; Pop, E. High Current Density and Low Thermal Conductivity of Atomically Thin Semimetallic $WTe_2$. *ACS Nano*, **2016**, *10*, 7507-7514.

(12) Podzorov, V.; Gershenson, M. E.; Kloc, Ch.; Zeis, R.; Bucher, E. High-Mobility Field-Effect Transistors based on Transition Metal Dichalcogendes. *Appl. Phys. Lett.* **2004**, *84* (17), 3301-3303.

(13) Liu, W.; Kang, J.; Sarkar, D.; Khatami, Y.; Jena, D.; Banerjee, K. Role of Metal Contacts in Designing High-Performance Monolayer n-Type $WSe_2$ Field Effect Transistors. *Nano Lett.* **2013**, *13*, 1983-1990.

(14) Chuang, H.-J.; Chamlagain, B.; Koehler, M.; Perera, M. M.; Yan, J.; Mandrus, D.; Tomanek, D.; Zhou, Z. Low-Resistance 2D/2D Ohmic Contacts: A Universal Approach to High-Performance $WSe_2$, $MoS_2$, and $MoSe_2$ Transistors. *Nano Lett.*, **2016**, *16* (3), 1896-1902.

(15) MacNeill, D.; Stiehl, G. M.; Guimaraes, M. H. D.; Buhrman, R. A.; Park, J.; Ralph, D. C. Control of Spin-Orbit Torques through Crystal Symmetry in $WTe_2$/Ferromagnet Bilayers. *Nature Physics*, **2017**, *13*, 300-305.

(16) Ma, Y.; Liu, B.; Zhang, A.; Chen, L.; Fathi, M.; Shen, C.; Abbas, A. N.; Ge, M.; Mecklenburf, M.; Zhou, C. Reversible Semiconducting-to-Metallic Phase Transition in Chemical Vapor Deposition Grown Monolayer $WSe_2$ and Applications for Devices. *ACS Nano*, **2015**, *9* (7), 7383-7391.

(17) Lin, Y.-C. Nanoscale Contact Engineering for Si/Silicide Nanowire Devices. Ph. D. Dissertation, University of California Los Angeles, CA, 2012.

(18) Agrawal, A.; Lin, J.; Barth, M.; White, R.; Zheng, B.; Chopra, S.; Gupta, S.; Wang, K.; Gelatos, J.; Mohney, S. E.; Datta, S. Fermi Level Depinning and Contact Resistivity Reduction using a Reduced Titania Interlayer in n-Silicon Metal-Insulator-Semiconductor Ohmic Contacts. *Appl. Phys. Lett.*, **2014**, *104*, 112101.

(19) Fang, H.; Chuang, S.; Chang, T. C.; Take, K.; Takahashi, T.; Javey, A. High-Performance Single Layered $WSe_2$ p-FETs with Chemically Doped Contacts. *Nano Lett.*, **2012**, *12* (7), 3788-3792.

(20) Du, Y.; Liu, H.; Neal, A. T.; Si, M.; Ye, P. D.Molecular Doping of Multilayer $MoS_2$ Field-Effect Transistors: Reduction in Sheet and Contact Resistance. *IEEE Electron Device Lett.*, **2013**, *34* (10), 1328-1330.

(21) Yang, L. Majumdar, K.; Liu, H.; Du, Y.; Hatzistergos, M.; Hung, P. Y.; Tieckelmann, R.; Tsai, W.; Hobbs, C.; Ye, P. D. Chloride Molecular Doping Technique on 2D Materials: $WS_2$ and $MoS_2$. *Nano Lett.*, **2014**, *14* (11), 6275-6280.

(22) Yamamoto, M., Nakahara, S., Ueno, K., Tsukagoshi, K. Self-Limiting Oxides on $WSe_2$ as Controlled Surface Acceptors and Low-Resistance Hole Contacts. *Nano Lett.*, **2016**, *16* (4), 2720-2727.

(23) Cho, S.; Kim, S.; Kim, J. H.; Zhao, J.; Seok, J.; Keum, D. H.; Baik, J.; Choe, D.-H.; Chang, K. J.; Suenaga, K.; Kim, S. W.; Lee, Y. H.; Yang, H. Phase Patterning for Ohmic Homojunction Contact in $MoTe_2$. *Science*, **2015**, *349* (6248), 625-628.

(24) Baugher, B. W. H.; Churchill, H. O. H.; Yang, Y.; Jarillo-Herrero, P. Intrinsic Electronic Transport Properties of High-Quality Monolayer and Bilayer $MoS_2$. *Nano Lett.*, **2013**, *13* (9), 4212-4216.

(25) Chuang, H.-J.; Tan, X.; Ghimire, N. J.; Perera, M. M.; Chamlagain, B.; Cheng, M. M.-C.; Mandrus, D.; Tomanek, D.; Zhou, Z. High Mobility $WSe_2$ p- and n-type Field-Effect Transistors Contacted by Highly Doped Graphene for Low-Resistance Contacts. *Nano Lett.*, **2014**, *14*, 3594-3601.

(26) Sze, S. M., Ng, K. K., Physics of Semiconductor Devices (Wiley, New York, 1981), 363-373.

(27) Kang, J.; Liu, W.; Sarkar, D.; Jena, D.; Banerjee, K. Computational Study of Metal Contacts to Monolayer Transition-Metal Dichalcogenide Semiconductors. *Phys. Rev. X.* **2014**, *4*, 031005.

(28) Popov, I.; Seifert, G.; Tomanek, D. Designing Electrical Contacts to $MoS_2$ Monolayers: A Computational Study. *Phys. Rev. Lett.* **2012**, *108*, 156802.

(29) Addou, R.; Colombo, L.; Wallace, R. M. Surface Defects on Natural $MoS_2$. *ACS Appl. Mater. Interfaces,* **2015**, *7*, 11921-11929.

(30) Addou, R. McDonnell, S.; Barrera, D.; Guo, Z.; Azcatl, A.; Wang, J.; Zhu, H.; Hinkle, C. L.; Quevedo-Lopez, M.; Alshareef, H. N.; Colombo, L.; Hsu, J. W. P.; Wallace, R. M. Impurities and Electronic Property Variations of Natural $MoS_2$ Crystal Surfaces. *ACS Nano,* **2015**, *9*, 9124-9133.

(31) McDonnell, S.; Addou, R.; Buie, C.; Wallace, R. M.; Hinkle, C. L. Defect-Dominated Doping and Contact Resistance in $MoS_2$. *ACS Nano,* **2014**, *8,* 2880-2888.

(32) Addou, R.; Wallace, R. M. Surface Analysis of $WSe_2$ Crystals: Spatial and Electronic Variability. *ACS Appl. Mater. Interfaces,* **2016**, *8* (39), 26400-26406.

(33) Luo, B.; Liu, J.; Zhu, S. C.; Yi, L. Chromium is Proposed as an Ideal Metal to Form Contacts with Monolayer $MoS_2$ and $WS_2$. *Mater. Res. Express*, **2015**, *2*, 106501.

(34) Smyth, C. M.; Addou, R.; McDonnell, S.; Hinkle, C. M.; Wallace, R. M. Contact Metal-$MoS_2$ Interfacial Reactions and Potential Implications on $MoS_2$-Based Device Performance. *J. Phys. Chem. C.* **2016**, *120* (27), 14719-14729.

(35) McDonnell, S.; Smyth, C. M.; Hinkle, C. L.; Wallace, R. M. $MoS_2$-Titanium Contact Interface Reactions. *ACS Appl. Mater. Interfaces,* **2016**, *8*, 8289-8294.

(36) Michaelson, H. B. The Work Function of the Elements and its Periodicity. *J. Appl. Phys.* **1977**, *48*, 4729-4733.

(37) Gong, C.; Colombo, L.; Wallace, R. M.; Cho, K. The Unusual Mechanism of Partial Fermi Level Pinning at Metal-$MoS_2$ Interfaces. *Nano Lett.* **2014**, *14*, 1714-1720.

(38) $WS_2$, $WSe_2$, and $WTe_2$ bulk crystals, HQ Graphene, 2017; www.hqgraphene.com

(39) Wallace, R. M. In *Physics and Technology of High-K Gate Dielectrics 6*; Kar, S.; Landheer, D.; Houssa, M.; Misra, D.; VanElshocht, S.; Iwai, H.; The Electrochemical Society: Pennington, NJ, 2008; Ch. 6, pp 255-271.

(40) BJD 1800 Temescal e-beam evaporator, 2017; http://www.utdallas.edu/research/cleanroom

(41) ASTM E2108-10 Standard Practice for Calibration of the Electron Binding Energy Scale of an X-Ray Photoelectron Spectrometer, 2000.

(42) Herrera-Gomez, A.; Hegedus, A.; Meissner, P. L. Chemical Depth Profile of Ultrathin Nitrided $SiO_2$ Films. *Appl. Phys. Lett.,* **2002**, *81*, 1014–1016.

(43) Selected Values of Chemical Thermodynamic Properties. In *CRC Handbook of Chemistry and Physics 70th Edition*; Weast, R. C.; Lide, D. R.; Astle, M. J.; Beyer, W. H.; CRC Press Inc.: Boca Raton, FL, 1989-1990.

(44) Nekrasov, I. A. Geochemistry, Mineralogy, and Genesis of Gold Deposits. Balkema Publishers: Brookfield, VT, 1996, 254-255.

(45) Longo, R. C.; Addou, R.; Santosh, KC.; Noh, J.-Y.; Smyth, C. M.; Barrera, D.; Zhang, C.; Hsu, J. W. P.; Wallace, R. M.; Cho, K. Intrinsic air stability mechanisms of two-dimensional transition metal dichalcogenide surfaces: basal versus edge oxidation. *2D Materials*, **2017**, *4*, 025050.

(46) Zhang, Y.; Pluchery, O.; Caillard, L.; Lamic-Humblot, A.-F.; Casale, S.; Chabal, Y. J.; Salmeron, M. Sensing the Charge State of Single Gold Nanoparticles via Work Function Measurements. *Nano Lett.,* **2015**, *15*, 51-55.

(47) Rettenberger, A.; Bruker, P.; Metzler, M.; Mugele, F.; Matthes, Th. W.; Bohmisch, M.; Boneberg, J.; Friemelt, K.; Leiderer, P. STM Investigation of the island Growth of Gold on $WS_2$ and $WSe_2$. *Surf. Sci.,* **1998**, *402-404*, 409-412.

(48) Ake, O.; Nolang, B.; Osadchii, E. G.; Ohman, L-O,; Rosen, E. In Chemical Thermodynamics of Selenium. Edited by Mompean, F. J.; Perrone, J.; Illemassene, M.

(49) McDonnell, S.; Azcatl, A.; Addou, R.; Gong, C.; Battaglia, C.; Chuang, S.; Cho, K.; Javey, A.; Wallace, R. M. Hole Contacts on Transition Metal Dichalcogenides: Interface Chemistry and Band Alignments. *ACS Nano,* **2014**, *8 (6)*, 6265-6272.

(50) Klein, A.; Pettenjofer, C.; Jaegermann, W.; Lux-Steiner, M.; Bucher, E. A Photoemission Study of Barrier and Transport Properties of the Interfaces of Au and Cu with $WSe_2$(0001) Surfaces. *Surf. Sci.* **1994**, *321*, 19-31.

(51) Selected Values of Chemical Thermodynamic Properties. In *CRC Handbook of Chemistry and Physics 70th Edition*; Weast, R. C.; Lide, D. R.; Astle, M. J.; Beyer, W. H.; CRC Press Inc.: FL, 1989-1990.

(52) Park, J. H.; Vishwanath, S.; Liu, X.; Zhou, H.; Eichfeld, S. M.; Fullerton-Shirley, S. K.; Robinson, J. A.; Feenstra, W. M.; Furdyna, J.; Jena, D.; Xing, H. G.; Kummel, A. C. Scanning Tunneling Microscopy and Spectroscopy of Air Exposure Effects on Molecular Beam Epitaxy Grown $WSe_2$ Monolayers and Bilayers. *ACS Nano*, **2016**, *10*, 4258-4267.

(53) Lee. S.-K.; Zetterling, C.-M.; Ostling, M.; Aberg, I.; Manusson, M. H.; Deppert, K.; Wernersson, L.-E.; Samuelson, L.; Litwin, A. Reduction of the Schottky Barrier Height on Silicon Carbide using Au Nano-Particles. *Solid-State Electron.*, **2002**, *46*, 1433-1440.

(54) Baskar Reddy, M.; Ashok Kumar, A.; Janardhanam, V.; Rajagopal Reddy, V.; Narasimha Reddy, P. Current-Voltage-Temperature (I-V-T) Characteristics of Pd/Au Schottky Contacts on n-InP(111). *Current Applied Physics*, **2009**, *9*, 972-977.

(55) Zheng, H.; Mahajan, B. K.; Su, S. C.; Mukherjee, S.; Gangopadhyay, K.; Gangopadhyay, S. Barrier Modification of Metal-Contact on Silicon by Sub-2 nm Platinum Nanoparticles and Thin Dielectrics. *Sci. Rep.* **2016**, *6*, 25234.

(56) Zhu, H. Surface and Interface Characterization of 2D Materials: Transition Metal Dichalcogenide and Black Phosphorous. Ph.D. Dissertation, University of Texas at Dallas, TX, 2017.

(57) Augustin, J.; Eyert, V.; Böker, T.; Frentrup, W.; Dwelk, H.; Janowitz, C.; Manzke, R. Electronic band structure of the layered compound Td-WTe2. *Phys. Rev. B,* **2000**, *62*, 10812–10823.

(58) Doniach, S.; Sunjic, M. Many-Electron Singularity in X-ray Photoemission and X-ray Line Spectra from Metals. *J. Phys. C: Solid State Phys.* **1970**, *3*, 285-291.

(59) Walsh, L. A.; Yue, R.; Wang, Q.; Barton, A. T.; Addou, R.; Smyth, C. M.; Zhu, H.; Kim, J.; Colombo, L.; Kim, M. J. $WTe_2$ Thin Films Grown by Beam-Interrupted Molecular Beam Epitaxy. *2D Materials*, **2017**, *4*, 025044.

(60) Luo, Y-R. In *Comprehensive Handbook of Chemical Bond Energies*; CRC Press, Taylor & Francis Group: Boca Raton, FL, 2007.

(61) Meyer, J.; Kroger, M.; Hamwi, S.; Gnam, F.; Riedl, T.; Kowalsky, W.; Kahn, A. Charge Generation Layers Comprising Transition Metal-Oxide/Organic Interfaces: Electronic Structure and Charge Generation Mechanism. *Appl. Phys. Lett.* **2010**, *96*, 193302.

(62) Westrum, E. F.; Carlson, H. G. Low Temperature Heat Capacities and Thermodynamic Functions of Some Palladium and Platinum Group Chalcogenides. II. Dichalcogenides; $PtS_2$, $PtTe_2$, and $PdTe_2$. *J. Chem. Phys.* **1961**, *35*, 1670-1676.

(63) Chemical bonding overview, www.chemhume.co.uk; 2015.

(64) Zhang, A.-L.; Smith, U. Self-Aligned Silicides for Ohmic Contacts in Complementary Metal-Oxide-Semiconductor Technology: $TiSi_2$, $CoSe_2$, and NiSi. *J. Vac. Sci. Tech. A.*, **2004**, *22*(4), 1361-1370.

(65) Morsli, M.; Bonnet, A.; Tregouet, Y.; Conan, A.; Jobic, S.; Brec, R. Electronic Properties and Band Structure of $IrSe_2$. *Appl. Surf. Sci.*, **1991**, *50*, 500-504.

(66) Wagner, C. D.; Davis, L. E.; Zeller, M. V.; Taylor, J. A.; Raymond, R. M.; Gale, L. H. Empirical Atomic Sensitivity Factors for Quantitative Analysis by Electron Spectroscopy for Chemical Analysis. *Surf. Interface Anal*. **1981**, *3*, 211-225.

(67) Amani, M.; Taheri, P.; Addou, R.; Ahn, G. H.; Kiriya, D.; Lien, D.-H.; Ager III, J. W.; Wallace, R. M.; Javey, A. Recombination Kinetics and Effects of Superacid Treatment in Sulfur- and Selenium-based Transition Metal Dichalcogenides. *Nano Lett.* **2016**, *16* (4), 2786-2791.

(68) Scofield, J. H. Theoretical Photoionization Cross Sections from 1 to 1500 keV. Lawrence Livermore Laboratory, **1973**, UCRL-51326.

(69) Detroye, M.; Reniers, F.; Buess-Herman, C.; Vereecken, J. AES-XPS study of chromium carbides and chromium iron carbides. *Appl. Surf. Sci.,* **1999**, *144-145*, 78-82.

(70) Yue, R.; Nie, Y.; Walsh, L. A.; Addou, R.; Liang, C.; Lu, N.; Barton, A. T.; Zhu, H.; Che, Z.; Barrera, D.; Cheng, L.; Cha, P.-R.; Chabal, Y. J.; Hsu, J. W. P.; Kim, J.; Kim, M. J.; Colombo, L.; Wallace, R. M.; Cho, K.; Hinkle, C. L. Nucleation and growth of $WSe_2$: Enabling Large Grain Transition Metal Dichalcogenides. *2D Materials*, **2017**, *4*, 045019.

(71) Lebegue, S.; Bjorkman, T.; Klintenberg, K.; Nieminen, R. M.; Eriksson, O. Two-Dimensional Materials from Data Filtering and *Ab Initio* Calculations. *Phys. Rev. X.*, **2013**, *3*, 031002.

(72) Mohanty, B. C.; Malar, P.; Osipowicz, T.; Murty, B. S.; Varma, S.; Kasiviswanathan, S. Characterization of Silver Selenide Thin Films Grown on Cr-Covered Si Substrates. *Surf. Interface Anal.* **2009**, *41*, 170-178.

(73) Chen, C-H.; Hu, E. L.; Schoenfeld, W. V.; Petroff, P. M. Metallization-Induced Damage in III-V Semiconductors. *J. Vac. Sci. Technol. B.* **1998**, *16*, 3354-3358.

(74) Boscher, N. D.; Carmalt, C. J.; Prieto, A. G.; Pankhurst, Q. A.; Palgrave, R. G.; Parkin, I. P. Synthesis and Characterisation of Chromium Oxyselenide ($Cr_2Se_{0.7}O_{2.3}$) Formed from Chemical Vapour Synthesis: A New Antiferromagnet. *Eur. J. Inorg. Chem.*, **2007**, *29*, 4579-4582.

(75) Biesinger, M. C., Payne, B. P., Grosvenor, A. P., Lau, L. W. M., Gerson, A. R., Smart, R. St. C. Resolving Surface Chemical States in XPS Analysis of First Row Transition Metals, Oxides and Hydroxides: Cr, Mn, Fe, Co and Ni. *Appl. Surf. Sci.*, **2011**, *257*, 2717-2730.

(76) Wagner, C. D. Handbook of X-Ray Photoelectron Spectroscopy: a Reference book of Standard Data for Use in X-ray Photoelectron Spectroscopy; Physical Electronics Division, Perkin-Elmer Corp.: Eden Prarie, MN, 1979.

(77) Gupta, R. P., Sen, S. K. Calculation of Multiplet Structure of Core *p*-Vacancy Levels. II. *Phys. Rev. B*, **1975**, *12* (1), 15-19.

(78) Katrib, A.; Hemming, F.; Wehrer, P.; Hilaire, L.; Maire, G. The Multi-Surface Structure and Catalytic Properties of Partially Reduced $WO_3$, $WO_2$ and WC+$O_2$ or W+$O_2$ as Characterized by XPS. *J. Electron Spectrosc. Relat. Phenom.* **1995**, *76*, 195-200.

(79) Addou, R.; Smyth, C. M.; Noh, J.; Lin, Y-C.; Robertson, J. A.; Cho, K.; Wallace, R. M. One Dimensional Metallic Edges in Atomically Thin $WSe_2$ Induced by Air Exposure, *2D Material*s, **2017**, *5*, 025017.

(80) Heda, N. L.; Ahuja, U. Electronic Properties and Compton Scattering Studies of Monoclinic Tungsten Dioxide. *Radiation Physical and Chemistry*. **2015**, *106*, 33-39.

(81) Keyshar, K.; Berg, M.; Zhang, X.; Vajtai, R.; Gupta, G.; Chan, C. K.; Beechem, T. E.; Ajayan, P. M.; Mohite, A. D.; Ohta, T. Experimental Determination of the Ionization Energies of $MoSe_2$, $WS_2$, and $MoS_2$ on $SiO_2$ Using Photoemission Electron Microscopy. *ACS Nano*, **2017**, *11* (8), 8223-8230.

(82) Zhang, C.; Gong, C.; Nie, Y.; Min, K.-A.; Liang, C.; Oh, Y. J.; Zhang, H.; Wang, W.; Hong, S.; Colombo, L.; Wallace, R. M.; Cho, K. Systematic Study of Electronic Structure and Band Alignment of Monolayer Transition Metal Dichalcogenides in van der Waals Heterostructures. *2D Materials*, **2016**, *4*, 015026.

(83) Fleisch, T. H.; Mains, G. J. An XPS Study of the UV Reduction and Photochromism of $MoO_3$ and $WO_3$. *J. Chem. Phys.*, **1982**, *76*, 780.

(84) Greiner, M. T.; Lu, Z.-H. Thin-Film Metal Oxides in Organic Semiconductor Devices: Their Electronic Structures, Work Functions and Interfaces. *NPG Asia Materials*, **2013**, e55.

(85) Migas, D. B.; Shaposhnikov, V. L.; Borisenko, V. E. Tungsten Oxides. II. The Metallic Nature of Magnéli Phases. *J. Appl. Phys.* **2010**, *108*, 093714.

(86) Lin, Y.-C.; Jariwala, B.; Bersch, B. M.; Xu, K.; Nie, Y.; Wang, B.; Eichfeld, S. M.; Zhang, X.; Choudhury, T. H.; Pan, Y.; Addou, R.; Smyth, C. M.; Li, J.; Zhang, K.; Haque, M. A.; Folsch, S.; Feenstra, R. M.; Wallace, R. M.; Cho, K.; Fullerton-Shirley, S. K.; Redwing, J. M.; Robinson, J. A. Realizing Large-Scale, Electronic-Grade Two-Dimensional Semiconductors. *ACS Nano*, **2018**, *12* (2), 965-975.

(87) Heine, V. Theory of Surface States. *Phys. Rev. Lett.*, **1965**, *138*, A1689.

(88) Louie, S. G.; Cohen, M. L. Self-Consistent Pseudopotential Calculation for a Metal-Semiconductor Interface. *Phys. Rev. Lett.,* **1975**, *35*, 866-869.

(89) Hasegawa, H.; Sawada, T. On the Electrical Properties of Compound Semiconductor Interfaces in Metal/Insulator/Semiconductor Structures and the Possible Origin of Interface States. *Thin Solid Films,* **1983**, *103*, 119-140.

(90) Rasmussen, F. A.; Thygesen, K. S. Computational 2D Materials Database: Electronic Structure of Transition-Metal Dichalcogenides and Oxides. *J. Phys. Chem. C.,* **2015**, *119*, 13169-13183.

(91) Maignan, A.; Breard, Y.; Guilmeau, E.; Gascoin, F. Transport, Thermoelectric, and Magnetic Properties of a Dense $Cr_2S_3$ Ceramic. *J. Appl. Phys.* **2012**, *112*, 013716.

(92) Adachi, Y.; Izaki, K.; Koike, K.; Morita, H.; Kaneko, T.; Kimura, H.; Inoue, A. Electrical Resistivity and Magnetic Property for $Cr_2Se_3$ and its Te-Substitution System. *Journal of Magnetism and Magnetic Materials*, **2007**, *310*, 1849-1850.

(93) Rodriguez, J. A.; Chaturvedi, S.; Kuhn, M.; van Ek, J.; Diebold, U.; Robbert, P. S.; Geisler, H.; Ventrice Jr., C. A. $H_2S$ Adsorption on Chromium, Chromia, and Gold/Chromia Surfaces: Photoemission Studies. *J. Chem. Phys.* **1997**, *107*, 9146-9156.

(94) Dillmann, B.; Rohr, F.; Seiferth, O.; Klivenyi, G.; Bender, M.; Homann, K.; Yakovkin, I. N.; Ehrlich, D.; Baumer, M.; Kuhlenbeck, H.; Feund, H.-J. Adsorption on a Polar Oxide Surface: $O_2$, $C_2H_4$, and Na on $Cr_2O_3$(0001)/Cr(110). *Faraday Discuss.,* **1996**, *105*, 295-315.

(95) Liu, C. Yan, X.; Zhang, E.; Song, X.; Sun, Q.; Ding, S.; Bao, W.; Xiu, F.; Zhou, P.; Zhang, D. W. Various and Tunable Transport Properties of $WSe_2$ Transistor Formed by Metal Contacts. *Small*, **2017**, 1604319.

(96) Huang, L.; Tao, L.; Li, Y.; Dong, H.; Wei, Z.; Li, J. Role of Defects in Enhanced Fermi Level Pinning at Interfaces Between Metals and Transition Metal Dichalcogenides. *Phys. Rev. B.* **2014**, *96*, 205303.

(97) Yeh, P.-C.; Jin, W.; Zaki, N.; Zhang, D.; Liou, J. T.; Sadowski, J. T.; Al-Mahboob, A.; Dadap, J. I.; Herman, I. P.; Sutter, P.; Osgood Jr., R. M. Layer-Dependent Electronic Structure of an Atomically Heavy Two-Dimensional Dichalcogenide. *Phys. Rev. B.*, **2015**, 041407(R).

(98) Chambers, S. A.; Droubay, T.; Kaspar, T. C.; Gutowski, M. Experimental Determination of Valence Band Maxima for $SrTiO_3$, $TiO_2$, and SrO and the Associated Valence Band Offsets with Si(001). *J. Vac. Sci. Technol. B,* **2014**, *22*, 2205.

# CHAPTER 6

# ENGINEERING THE WSE2–PALLADIUM INTERFACE CHEMISTRY FOR FIELD-EFFECT TRANSISTORS WITH HIGH PERFORMANCE HOLE CONTACTS

Authors – Christopher M. Smyth[†], Lee A. Walsh[‡], Pavel Bolshakov[†], Massimo Catalano[†§], Rafik Addou[†], Luhua Wang[†], Jiyoung Kim[†], Moon J. Kim[†], Chadwin D. Young[†], Christopher L. Hinkle[†], and Robert M. Wallace[†]

[†]The Department of Materials Science and Engineering, RL10
The University of Texas at Dallas
800 West Campbell Road
Richardson, Texas, 75080, USA

[‡]Tyndall National Institute
University College Cork
Lee Maltings, Prospect Row
Cork, Ireland

[§]CNR IMM, Institute for Microelectronics and Microsystems
Via Monteroni, I-73100
Lecce, Italy

## 6.1 Preface

Palladium has been widely employed as a hole contact to $WSe_2$ and has enabled, at times, the highest $WSe_2$ transistor performance. However, there are orders of magnitude variation across the literature in Pd–$WSe_2$ contact resistance and $I_{ON}/I_{OFF}$ ratios with no true understanding of how to consistently achieve high–performance contacts. In this work, $WSe_2$ transistors with impressive $I_{ON}/I_{OFF}$ ratios of $10^6$ and Pd–$WSe_2$ Schottky diodes with near–zero variability are demonstrated utilizing Ohmic–like Pd contacts through deliberate control of the interface chemistry. The increased concentration of a $PdSe_x$ intermetallic is correlated with an Ohmic band alignment and concomitant defect passivation, which further reduces the contact resistance, variability, and barrier height inhomogeneity. The lowest contact resistance occurs when a 60 minute post metallization anneal at 400 °C in forming gas (FG) is performed. X-ray photoelectron spectroscopy indicates this FG anneal produces 3× the concentration of $PdSe_x$ and an Ohmic band alignment, in contrast to that detected after annealing in ultra–high vacuum, during which a 0.2 eV hole Schottky barrier forms. Raman spectroscopy and scanning transmission electron microscopy highlight the necessity of the fabrication step to achieve high–performance contacts as no $PdSe_x$ forms and $WSe_2$ is unperturbed by room temperature Pd deposition. However, at least one $WSe_2$ layer is consumed by the necessary interface reactions that form $PdSe_x$ requiring strategic exploitation of a sacrificial $WSe_2$ layer during device fabrication. The interface chemistry and structural properties are correlated with Pd–$WSe_2$ diode and transistor performance and the recommended processing steps are provided to enable reliable high–performance contact formation.

The content of this chapter is adapted with permission from (Engineering the Pd–$WSe_2$ Interface for FETs with High–Performance Hole Contacts). Reproduced with permission from ACS Applied

Nano Materials, submitted for publication. Unpublished work copyright 2018, American Chemical Society. In this work, Dr. L. A. Walsh played an integral part in data interpretation and experimental design. P. Bolshakov fabricated the FETs, performed device measurements, and assisted in interpreting the electrical characteristics of the FETs under the supervision of Prof. C. D. Young. Dr. M. Catalano obtained the TEM and EDS at UTD and assisted in image and spectra interpretation under the supervision of Prof. M. J. Kim. L. Wang milled lamella from select Si–Pd–$WSe_2$–$SiO_2$–Si samples and trained me on the FIB instrument under the supervision of Prof. M. J. Kim. The Raman spectra were obtained by myself under the supervision of Prof. J. Kim. Dr. R. Addou and the rest of the authors provided inputs while preparing the manuscript. Mr. Andrew C. Yu (MIT) and Dr. Michal. J. Mleczko (Intel) are acknowledged for useful discussions regarding the analytical Schottky barrier fitting procedure, the Landauer theory behind the model, and the MATLAB code used for fitting under the supervision of Prof. Eric Pop (Stanford).

## 6.2 Introduction

In 3D semiconductor based devices, the continuous engineering of commercially viable contacts utilizes a detailed understanding of relationships between processing conditions (e.g., deposition chamber ambient, post metallization annealing ambient), interface chemistry, and contact performance.[1] Transition metal silicides[2] in the case of Si, or salicides in the case of compound 3D semiconductors (e.g., InGaAs),[3,4] have long been the industry standard contacts in conventional CMOS technology. These materials exhibit phase and stoichiometry dependent electronic properties, which are tunable with carefully designed processing conditions. Analogous chalcogen–based intermetallic species may be available for engineering superior contacts in TMD–based devices. However, processing condition–contact performance relationships in TMDs remain largely unexplored to date. State–of–the–art contact resistance to TMDs ($R_c$ = 0.2 kΩ-μm) remains a few times greater than target values established in the most recent International Technology Roadmap for Semiconductors (ITRS).[5] A large parasitic contact resistance is also problematic because it can convolute the intrinsic properties (e.g., mobility) of a TMD device.[6,7] A variety of new strategies have been employed[8–13] to lower TMD contact resistance, but direct deposition of bulk metals in top contact architectures are the easiest to implement in a full field effect transistor (FET) process flow and are preferred for future technologies.

Pd contacts are widely employed in $WSe_2$ FETs as they have been used to demonstrate the best FET properties with Ohmic–like p-type behavior and $I_{ON}/I_{OFF}$ ratios $>10^8$, which is orders of magnitude better performance than analogous devices with other metals.[5,13–18] However, reported $R_c$ (ranging from $10^{-1}$–$10^5$ kΩ-μm) and transistor $I_{ON}/I_{OFF}$ ratios ($10^4$–$10^9$) vary widely across $WSe_2$ devices with Pd contacts reported in the literature.[5,15,16,19–22] Pd is expected to be a good p-type contact to $WSe_2$ because of its (vacuum) work function and relative alignment to the $WSe_2$ valence band edge. However, choosing a contact metal based solely upon a low predicted Schottky barrier according to the Schottky–Mott rule[23] often results in unexpected contact performance.[13,24,25] In reality, defects within the TMD,[26–28] thermodynamically favorable reactions, and metal oxidation during deposition have been shown to result in variable contact performance.[29-31] In addition, metal–TMD reactions, often enhanced at elevated temperatures, disrupt the layered TMD structure in the contact regions of a mono or few layer TMD–based device. The number of layers consumed by interface reactions, and therefore resulting changes in the density of states within the underlying TMD, should be considered when interpreting variations in contact performance.[32] This necessitates a more comprehensive understanding of the interface chemistry–contact performance relationship in metal–TMD systems.

In this work, we determine the effects of deposition ambient and post metallization annealing conditions on the interface chemistry and band alignment with *in–situ* photoemission–based experiments. In addition, the number of $WSe_2$ layers consumed by reactions with the contact metal are evaluated with Raman spectroscopy, scanning transmission electron microscopy (STEM), and energy dispersive X–ray spectroscopy (EDS). Finally, we evaluate the electrical performance of optimized high work function Pd contacts to $WSe_2$ using Schottky diode and field effect transistor (FET) structures. Recommendations based on these findings are provided to enable the best performance Pd–$WSe_2$ contacts, which are confirmed through our outstanding FET performance metrics.

## 6.3 Experimental Details

*Metal Deposition, Post–Metallization Annealing, and* in–situ *Characterization.*

a) Single Deposition Step Under UHV or HV Conditions: All $WSe_2$ samples throughout this work were obtained from the same bulk $WSe_2$ crystal (HQ Graphene).[33] Prior to deposition under UHV or HV conditions, $WSe_2$ and Pd metal source were prepared and metal deposition rates and reference metal core level spectra were obtained identical to that employed in similar work described elsewhere.[29,30] The reference Pd 3*d* core level spectrum was obtained *in–situ* from a 50 nm Pd film evaporated on Si at RT in UHV. A standard Scotch Tape© method was employed *ex–situ*. The surface chemistry was probed with XPS both after exfoliation and subsequent metal deposition under UHV conditions (base pressure $<2 \times 10^{-9}$ mbar).

b) Step–wise Deposition and Post–Metallization Annealing: After outgassing the metal source and determining the deposition rate, Pd was deposited in steps on separate bulk $WSe_2$ crystals under UHV conditions to target thicknesses of 1, 2, 10, 20, 30, and 50 Å. Each sample was then annealed in UHV or FG (10% $H_2$, 90% $N_2$; 1 mbar) at 200 °C, 300 °C, and 400 °C. The surface chemistry was probed with XPS after exfoliation and each subsequent deposition and annealing step. The secondary electron (SE) cutoff was also probed with XPS throughout metal deposition steps and post metallization annealing to track the work function. The procedure employed to construct band diagrams from XPS measurements and details of the cluster tool in which deposition and analysis were performed is also described in Chapter 2.[34,35]

*XPS Instrumentation, Parameters, and Data Analysis.* XPS characterization was performed via a monochromated Al Kα source and Omicron EA125 hemispherical analyzer with ±0.05 eV resolution. In addition, a takeoff angle of 45°, acceptance angle of 8°, and pass energy of 15 eV were employed during high resolution spectral acquisition. The analyzer was calibrated with polycrystalline Au, Ag, and Cu foils according to ASTM E1208.[36] Spectra were deconvolved using AAnalyzer,[37] a curve fitting software. The stoichiometry of bulk $WSe_2$ and any other reaction products referred to in the text below were calculated using appropriate relative sensitivity factors for the W 4*f*, Se 3*d*, and Pd 3*d* core levels (2.959, 0.722, and 4.642, respectively, with all three reflecting both spin orbit split peaks in each of the aforementioned core levels).[38]

*Quantifying Layer Number Consumption: Sample Fabrication and Characterization.* $WSe_2$ flakes were exfoliated onto a $SiO_2$(270 nm)/Si substrate and annealed *in–situ* at 300 °C in Ar (base pressure $<2 \times 10^{-8}$ mbar, backfilled with Ar to $10^0$ mbar) to remove tape residue. Numerous 1 to 5 layer (i.e., 1L to 5L) flakes were then identified with optical microscopy, atomic force microscopy

(AFM) and Raman spectroscopy (see Section 6.4.1 for details). Topographic images were obtained *ex–situ* from bare $WSe_2$ flakes after exfoliating onto 270 nm $SiO_2$ substrates and annealing in $N_2$ at 300 °C for 1 hr to remove resist residue. A Veeco Model 3100 Dimension V Atomic Probe Microscope[39] was employed in non–contact tapping mode. Images were processed and line profiles were obtained with the WSxM software.[40]

Special care was taken to ensure 5 nm thick Pd films subsequently deposited at RT under UHV conditions were full coverage and pinhole–free (see Appendix E for details). Pd films were deposited under UHV conditions onto exfoliated highly oriented pyrolytic graphite (HOPG), a 2D material with a van der Waals surface similar to $WSe_2$. Pd films were identified as pinhole free at a thickness preventing carbon detection by low energy ion scattering spectroscopy (LEISS). Si was deposited under UHV conditions onto full coverage Pd–HOPG substrates also prepared under UHV conditions without breaking vacuum. A Si film was identified as pinhole free at a thickness preventing Pd detection by LEISS. Spectra were obtained *in–situ* immediately following metal or Si deposition without breaking vacuum.

Separate samples were annealed after metallization *in–situ* in UHV or FG at 300 °C for 1 hr. Immediately following metal deposition and, in the case of two of three samples, post metallization annealing, a full coverage 10 nm thick Si film was deposited *in–situ* as a capping layer to protect Pd–$WSe_2$ samples from oxidation upon air exposure during *ex–situ* Raman spectroscopy. After capping with Si, the samples were removed from vacuum and Raman spectroscopy was performed on the same flakes as were probed after exfoliation. Any annealing steps were performed prior to Si capping to prevent potentially erroneous results due to intermixing between Si and underlying Pd at elevated temperatures.

A laser power density of 0.49 mW/μm$^2$ and detector with 0.2 cm$^{-1}$ resolution were employed in obtaining all Raman spectra shown in the main text. Exposure times of 1 s (5 s) with 10 (5) total accumulations were employed in obtaining Raman spectra from exfoliated $WSe_2$ flakes after thermal cleaning (and subsequent *in–situ* metallization and, in the case of two of three samples, post metallization annealing). These parameters were carefully determined to prevent laser induced damage to $WSe_2$ (see Section 6.4.1 for a discussion of the Raman measurement parameters and their impact on $WSe_2$).

Raman spectra were deconvolved with the peak fitting software AAnalyzer to obtain vibrational mode shifts. Peak shapes were defined by a combination of Gaussian and Lorentzian functions. The Lorentzian contribution was held constant for each set of spectra representing a certain number of $WSe_2$ layers from a given sample.

*High Resolution STEM and EDS.* Si/Pd/$WSe_2$/$SiO_2$ samples fabricated for interrogation via Raman spectroscopy were cross sectioned for high resolution STEM in an aberration corrected JEM-ARM200F instrument operated at 200 kV. STEM cross–sectional samples were prepared in a FIB microscope (FEI Nova 200 Dual Beam), images were obtained by annular bright field and high angle annular dark field (HAADF), and EDS experiments performed in an Aztec Energy Advanced Microanalysis System according to the procedure outlined in detail elsewhere.[35]

*Device Fabrication and Measurements.*

a) $Al_2O_3$ was first deposited (~27 nm) at 250 ºC onto a p++ Si wafer and was followed by a 400 °C anneal under FG to reduce charge traps. The $Al_2O_3$ layer serves as the 'substrate' for exfoliated $WSe_2$ flakes. Al was then deposited as the backside contact by electron beam evaporation. Using photolithography, source/drain contacts were defined and Pd/Au (20/150 nm) contacts were then deposited under UHV by electron beam evaporation. Finally a lift–off process was performed. The devices were electrically characterized under ambient temperature and pressure in a Cascade Probe Station using a Keithley 4200 Semiconductor Characterization System.

b) Schottky Diodes: A bulk $WSe_2$ crystal with mirror–like surface (low surface defect density) was exfoliated and loaded into a UHV cluster tool. 60 nm Pd followed by 100 nm Au were deposited in UHV to form periodic arrays of circular Au/Pd contact pads (diameters = 50, 100, 200 μm) across the $WSe_2$. Forward and reverse bias I–V curves were obtained by sweeping from 0 to 2 V and 0 to -2 V (0.01 V step), respectively, to avoid hysteresis effects. Measurements were obtained after metallization and anneals in FG (1 mbar) at 200 °C, 300 °C, and 400 °C. C–V measurements were obtained from the same diodes (in parallel with I–V measurements) at frequencies of 100 kHz, 500 kHz, and 1MHz.

## 6.4 Results and Discussion

### 6.4.1 Effects of Processing Conditions on Pd–$WSe_2$ Interface Chemistry and Structure

*van der Waals Interface at Room Temperature According to Chemistry and Structure*

The impingement rate of residual gas molecules under high vacuum (HV) conditions ($<2 \times 10^{-6}$ mbar) is orders of magnitude greater than that found under ultra–high vacuum (UHV) conditions ($<2 \times 10^{-9}$ mbar) according to the kinetic theory of gases. Such rates are further enhanced by species liberated through desorption of heated surfaces, which may be employed in a metal contact deposition process. A HV deposition ambient is often utilized for device contact fabrication. Significant interface chemistry differences with the deposition ambient have been demonstrated previously for other metal–TMD systems.[29–31]

The chemistry at the Pd–$WSe_2$ interface is reflected in Figure 6.1 as a function of ambient pressure in the deposition chamber (see Section 6.3 for details). When deposited at room temperature (RT), reaction products are not detected at the Pd–$WSe_2$ interface regardless of chamber pressure. The chemical states detected in the corresponding Se 3*d*, W 4*f*, and Pd 3*d* core level spectra reflect bulk $WSe_2$ and metallic Pd, respectively (Figure 6.1a). The $WSe_2$ chemical states in the W 4*f* and Se 3*d* core level spectra shift to lower binding energy (BE) after Pd deposition under either UHV or HV conditions indicating the Fermi level ($E_F$) shifts towards the valence band edge. This is consistent with upward band bending in $WSe_2$ due to the high work function of Pd relative to the $E_F$ of $WSe_2$. Reactions between Pd and $WSe_2$ are not thermodynamically favorable at RT as the Gibbs Free Energy of Formation $\Delta G^{\circ}_{f,Pd4Se}$ at 25 °C (-60.67 kJ/mol, which is similar to that of $Pd_2Se$ and PdSe)[41] is slightly more positive than that of $WSe_2$ ($\Delta G^{\circ}_{f,WSe2}$ = -67.44 kJ/mol).[42.43]

The two spin orbit split branches of the Pd 3*d* core level spectrum detected following Pd deposition on $WSe_2$ in UHV exhibit larger full widths at half maximum (FWHM) than that of the metal Pd 3*d* reference spectrum (Figure 6.1b). However, the BE of the Pd $3d_{5/2}$ core level obtained following deposition under UHV and HV conditions ($Pd^0$: 334.96 eV) agrees well with that of the Pd reference film obtained in this work (334.93 eV). Furthermore, Pd 3*d* core level peak shapes similar to those obtained after Pd deposition at RT in this work have been observed previously in photoemission studies of Pd films on $MoS_2$[44] and isolated Pd clusters on various substrates.[45] It is also noted that any oxygen based species present on the 'initial' exfoliated $WSe_2$ samples employed in this work are below the limit of XPS detection (Figure 6.1c). The Pd $3p_{3/2}$ and O 1*s* core levels, when carefully deconvolved, indicates that oxygen is below the limit of detection after Pd deposition in UHV (Figure 6.1c). Both the reference metal Pd film and the Pd deposited on

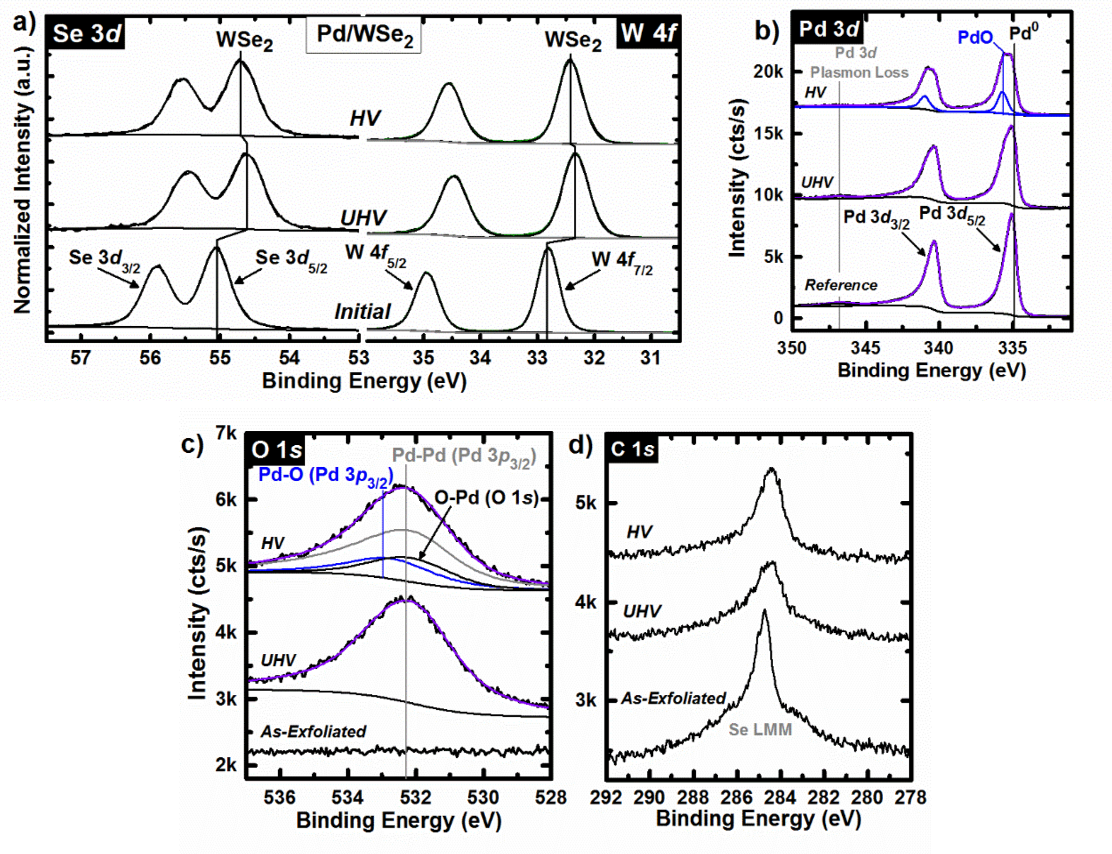

Figure 6.1. a) Se 3*d*, W 4*f*, b) Pd 3*d*, c) O 1*s* and d) C 1*s* core level spectra obtained by XPS from exfoliated $WSe_2$ (Initial) and following Pd deposition under UHV and HV conditions.

$WSe_2$ in UHV exhibit asymmetric line shapes consistent with core hole screening in metallic species.[46] However, the two spin orbit split peaks in the 'UHV' Pd 3*d* spectrum are slightly more asymmetric than that of the reference Pd film, which is assumed to be an inherent feature of the Pd islands comprising the film deposited on $WSe_2$ and not due to Pd–O formation. Therefore, only metallic Pd is detected when Pd is deposited on $WSe_2$ at RT in UHV in contrast to the pronounced Pd–C chemical state detected in the Pd 3*d* core level spectrum from the Pd–graphite interface.[47] In contrast, when Pd is deposited under HV conditions, an additional chemical state is detected at higher BE from metallic Pd (Figure 6.1 b,c). This corresponds with the formation of PdO, which likely occurs during air exposure before X–ray photoelectron spectroscopy (XPS) analysis (PdO formation is exothermic, $\Delta G^{\circ}_{f,PdO}$ = -136 kJ/mol).[48]

Oxygen is below the limit of XPS detection on exfoliated $WSe_2$. The broad peak detected in the same region as the O 1*s* core level after Pd deposition in UHV corresponds with the Pd $3p_{3/2}$ core level. The Pd $3p_{3/2}$ and O 1*s* core levels are deconvolved by applying fitting parameters obtained from the reference Pd $3p_{3/2}$ and Pd $3d_{5/2}$ core level spectra (Pd $3p_{3/2}$ full width at half maximum and double lorentzian factor = 2.85 eV and 1.6, respectively; separation between Pd $3p_{3/2}$ and Pd $3d_{5/2}$ core levels = 197.00 eV). Any additional chemical states necessary to obtain an accurate fit ($\chi^2 \leq 0.001$) of the raw data are attributed to the O 1*s* core level. Applying the reference fit parameters to the peak in the 'UHV' spectrum in Figure 6.1a yields an accurate fit of the raw data, which indicates oxygen is below the limit of XPS detection (<0.1 at. %) after Pd deposition in UHV. When deconvoluting the 'HV' spectrum in Figure 6.1a, two chemical states with 0.72 eV separation and 0.34 area ratio (Pd–O:Pd–Pd ratio, obtained from the two chemical states fit to the corresponding Pd 3*d* spectrum) are employed to fit the Pd $3p_{3/2}$ contribution to the overall spectrum. An additional peak is included to obtain an accurate fit of the raw data, which is assigned to the O–Pd chemical state in the O 1*s* core level.

Pd does not react with any adventitious species residing on the $WSe_2$ surface at RT regardless of reactor base pressure (Figure 6.1d). The spectra shown in Figure 6.1c are convoluted by the C 1*s* core level (narrow peak) and a broad Se LMM Auger peak. Adventitious carbon is detected on all exfoliated $WSe_2$ samples throughout this work at a BE of ~284.6 eV. In all cases, adventitious carbon is detected after Pd deposition, presumably at the Pd–$WSe_2$ interface. The adventitious carbon chemical state shifts 0.4 eV to lower BE upon Pd deposition, which is consistent with the corresponding BE shifts exhibited by the bulk $WSe_2$ chemical states and can therefore be attributed to upward band bending induced by the Pd. The chemical state in the C 1*s* core level associated with C–Pd bonds at Pd/graphene and Pd/graphite interfaces is detected at 284.0 eV,[47] which is more than 0.2 eV lower than the BE of the C 1*s* chemical state detected in this work after Pd deposition on $WSe_2$ substantiating our argument that Pd does not react with adventitious carbon on $WSe_2$. Therefore, the C 1*s* core level will not be discussed for the remainder of the chapter.

*Thermally Induced Intermetallic Formation under Vacuum Conditions*

Although performing a single deposition step under UHV and HV conditions offers a useful differentiation in interface chemistry with vacuum conditions, Pd grows as islands on $WSe_2$ and therefore may result in a band alignment inconsistent with that of a thick, continuous Pd contact to $WSe_2$ typically employed for a device. In addition, post metallization annealing often drives interface reactions and concomitant $E_F$ shifts. Therefore, the interface chemistry and band alignment between Pd and $WSe_2$ was tracked by *in–situ* XPS throughout stepwise Pd deposition and post metallization annealing under UHV conditions (1 hr at each temperature, see Experimental Details).

Figure 6.2a displays the evolution of the Se 3*d* and W 4*f* core level spectra throughout stepwise Pd deposition and post metallization annealing under UHV conditions. Figure 6.2b displays the evolution of integrated intensities (including both spin–orbit split peaks and corrected by atomic sensitivity factors, see Experimental Details) of chemical states related to the Pd–$WSe_2$ interaction in the Se 3*d*, W 4*f*, and Pd 3*d* core level spectra throughout stepwise Pd deposition and post metallization annealing under UHV conditions. In addition, the Pd 3*d* core level spectra obtained throughout the experiment is shown in Figure 6.2c. The chemical states in the Se 3*d* and W 4*f* core levels are initially detected from exfoliated $WSe_2$ at binding energies of 55.05 and 32.80 eV, respectively, and remain the only detectable W and Se chemical states throughout Pd deposition. The absence of detectable reaction products at RT (e.g., Pd–Se bond formation) agrees with thermodynamic predictions but contrasts with the (ideal) covalent Pd–$WSe_2$ interface in a top contact configuration predicted by Kang et al. using augmented density functional theory methods that employ defect–free interfaces where Pd–Se bonding is prominent even at 0 K.[49]

No additional chemical states are detected in any core levels following the 200 °C anneal consistent with the formation of reaction products. Expanded Se 3*d* and W 4*f* core level spectra obtained following each anneal are displayed adjacent to Figure 6.2a accentuating minute changes with increased annealing temperature. Annealing at 300 °C under UHV conditions causes Pd to reduce the underlying $WSe_2$ resulting in the formation of $PdSe_x$ (54.42 eV, Se $3d_{5/2}$) and $WSe_x$ (55.11 eV, Se $3d_{5/2}$; 31.99 eV, W $4f_{7/2}$; Figure 6.2a). This is similar to the reducing behavior observed for Pd deposited on $Bi_2Se_3$, another Se–based layered material.[50] $PdSe_x$ exhibits a $Se^{2-}$ chemical state with lower BE than that of bulk $WSe_2$ due to the greater electronegativity difference between Pd and Se (0.35) compared with that between W and Se (0.19).[51] This results in a greater ionic character associated with the Pd–Se bond compared with the W–Se bond in $WSe_2$. $PdSe_x$ and $WSe_x$ chemical states detected in the Se 3*d* and W 4*f* core level spectra intensify following the 400 °C anneal (Figures 6.2 a, b). In addition, chemical states associated with $WSe_x$ exhibit BE shifts (Se $3d_{5/2}$: +0.29 eV, W $4f_{7/2}$: -0.15 eV) consistent with a decreased oxidation state, suggesting that $WSe_x$ reduction is enhanced at higher annealing temperatures. A small concentration of $WO_x$ forms during the 400 °C anneal. $WO_x$ is detected in the W 4*f* core level after annealing at 400 °C as evidenced by the appearance of a high BE state at 35.69 eV. The Pd film undergoes mild

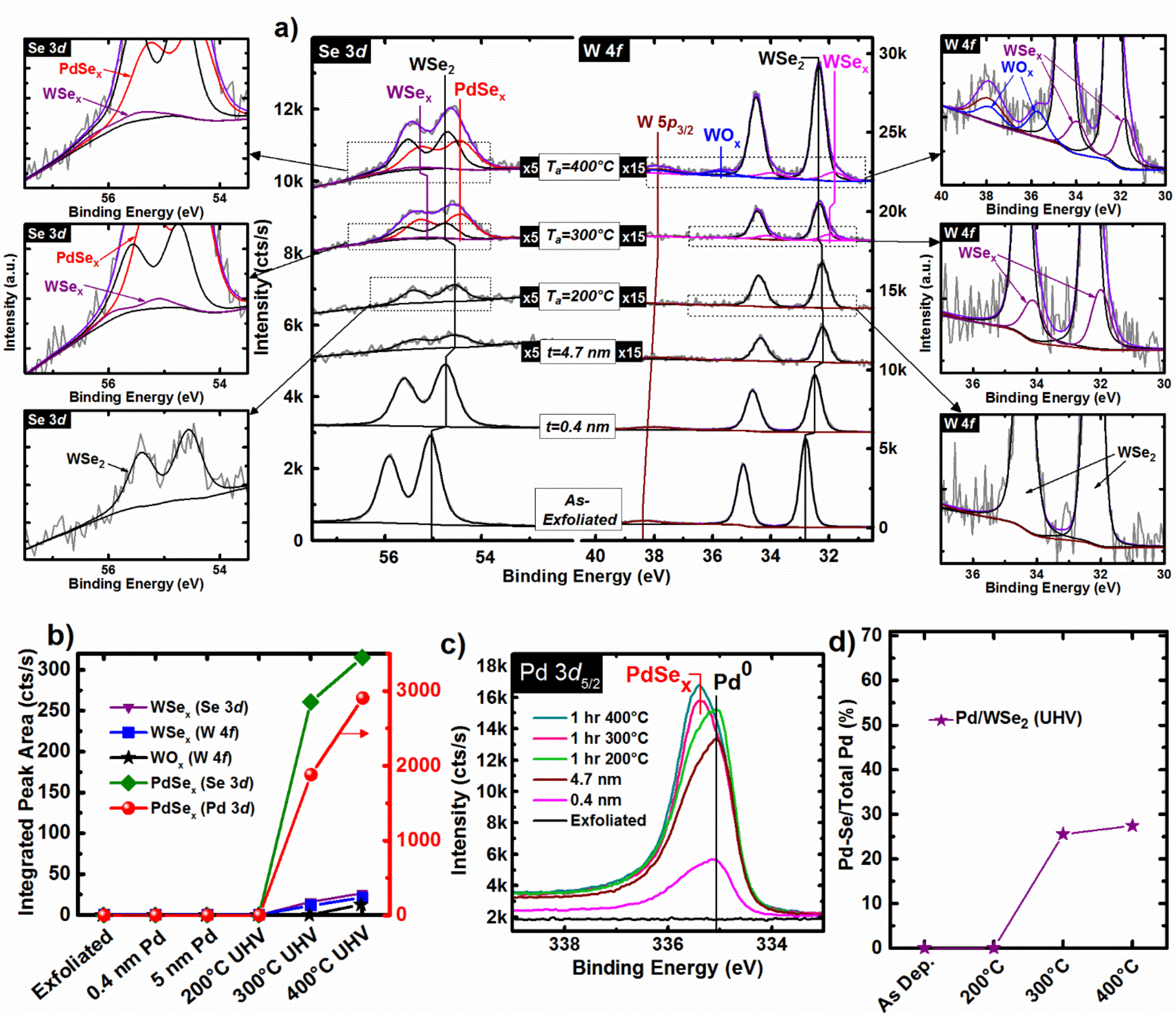

Figure 6.2. a) Deconvoluted Se 3*d*, W 4*f*, and W 5$p_{3/2}$ core level spectra obtained throughout Pd deposition on WSe$_2$ and post metallization annealing in UHV. The inset plots at right and left display magnified Se 3*d* and W 4*f* core level spectra obtained following each anneal. Residuals associated with the peak fits are 0.001 % (not shown for clarity). b) Integrated intensities of chemical states in the Se 3*d*, W 4*f*, and Pd 3*d* core level spectra associated with various reaction products as well as the c) Pd 3*d* core level spectra obtained throughout Pd deposition on WSe$_2$ and post metallization annealing under UHV. It is explicitly noted that the integrated peak areas shown in b) represent only the areas of the respective chemical state fitted to each denoted core level spectrum. The red line (spheres) in b) is plotted vs the right y-axis while all other data points are plotted vs the left y-axis. d) Interfacial reactivity gauged by the ratio of the intensity of the chemical state in the Pd 3*d* core level corresponding with PdSe$_x$ to the total intensity of the respective core level after depositing at RT and subsequent *in-situ* annealing in UHV showing the onset of PdSe$_x$ formation at 300 °C and 28% Pd to PdSe$_x$ conversion at 400 °C.

agglomeration at 400 °C, possibly leaving regions of extremely thin Pd or even exposed $WSe_x$ or $WSe_2$. $WO_x$ formation could occur in these regions from reactions with background gases in the chamber considering the pressure increases to ~$10^{-7}$ mbar during the first 10 minutes of the anneal, then decreases quickly into UHV.

The BE of the chemical state consistently detected in the Pd $3d_{5/2}$ core level (334.91 eV) agrees well with the Pd reference (334.94 eV) indicating the deposited film is composed solely of metallic Pd throughout RT deposition and after annealing at 200 °C in UHV. A chemical state in addition to metallic Pd is detected in the Pd 3*d* core level after 300 °C anneal at a BE of 335.49 eV corresponding with the formation of $PdSe_x$.[52] The $PdSe_x$ chemical state binding energies in the Pd 3*d* and Se 3*d* core levels do not appreciably change following the 400 °C anneal but do increase in intensity. In addition, the intensity ratio between the $PdSe_x$ and the metallic Pd chemical states in the Pd 3*d* core level increases from 0.34 to 0.40 (Figure 6.2d) upon annealing at 400 °C corroborating an increasing $PdSe_x$ concentration with increased annealing temperature. The BE of the $PdSe_x$ chemical state in the Pd 3*d* core level spectra obtained after annealing at 300 °C and 400 °C is 0.22 eV lower than that of the PdO chemical state detected following Pd deposition under HV conditions, which rules out the formation of PdO at elevated temperatures in UHV (Figure 6.3).

The normalized O 1*s* core level spectra obtained after RT Pd deposition and *in–situ* annealing under UHV conditions are shown in Figure 6.3. The Pd $3p_{3/2}$ core level convolutes the O 1*s* core level spectrum. There are no resolvable peaks below 531.0 eV that would suggest the formation of Pd–O or W–O bonds throughout the experiment. However, the intensity of the $WO_x$ chemical state in the W 4*f* core level spectrum obtained after 400 °C UHV anneal (Figure 6.3) suggests the intensity of the associated oxygen chemical state should be comparable with the noise detected in the corresponding O 1*s* core level spectrum.

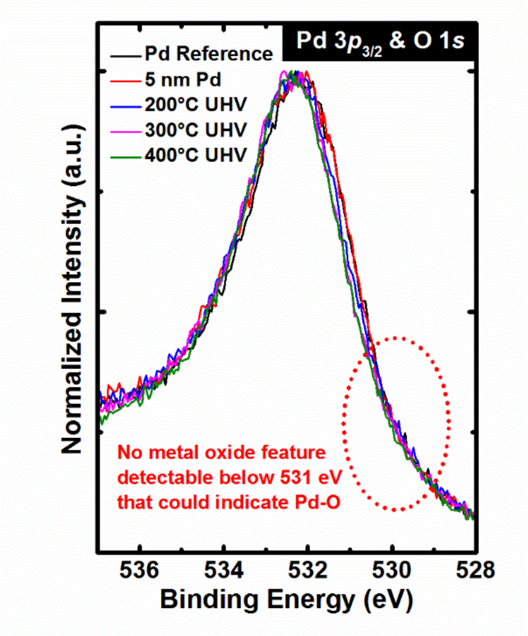

Figure 6.3. O 1*s* core level spectra convoluted by the Pd 3$p_{3/2}$ core level spectra obtained after ~5 nm Pd deposition on $WSe_2$ and post metallization annealing in UHV.

$PdSe_x$ formation at 300 °C in UHV is reasonable considering the $\Delta G°_{f,WSe2}$ and $\Delta G°_{f,Pd4Se}$ variation with temperature. $\Delta G°_{f,Pd4Se}$ ($\Delta G°_{f,WSe2}$) becomes increasingly negative (positive) as temperature increases. At 300 °C, $\Delta G°_{f,Pd4Se}$ and $\Delta G°_{f,WSe2}$ (-62.34 kJ/mol[41] and -63.62 kJ/mol,[42] respectively) are within the ±3.2 kJ/mol uncertainty of each other associated with the uncertainty in the temperature set point of the heater employed for annealing (±25 °C). In addition, reactions are more favorable at surface and edge defects commonly found in TMDs.[26-28] Furthermore, there are a number of stable phases in the palladium selenide binary system across a wide range of compositions stable down to room temperature.[52] It is known, however, that stable alloys of Pd–W are not expected to form at the temperatures examined here (T < 500 °C).[53] Therefore, Pd–Se formation at or above 300 °C in UHV is thermodynamically favorable either in the top or edge contact configuration. Finally, based on these results, it is noted that the DFT predictions[49] indicating Pd–Se bond formation at temperatures well below room temperature suggest that further refinements of the interaction potentials and methods (such as including the impact of defects) are needed for better agreement with experimental contact metal reaction studies.

It is important to note that any reactions between metal and $WSe_2$ could manifest due to $WSe_2$ instability at the annealing temperatures employed in this work.[54,55] Reactions between metal and TMD are likely far more favorable at defect sites within the vicinity of the TMD surface than across a defect–free van der Waals plane. Separate bulk $WSe_2$ samples were consecutively annealed at 200 °C, 300 °C, 400 °C, and 450 °C for one hour each under UHV or FG conditions obtaining XPS *in–situ* after each annealing step to investigate its thermal stability at annealing temperatures employed in this work (Figure 6.4).

Both exfoliated $WSe_2$ samples exhibit sharp, symmetric doublets in the Se 3*d* and W 4*f* core level spectra consistent with a lack of $E_F$ variation across either XPS sampling area (Figure 6.4a). The FWHM and binding energies of the bulk $WSe_2$ chemical states and also the valence band edge (Figure 6.4b) remain constant at all annealing temperatures and ambients, which indicates chemical stability. A small concentration of oxygen is detected on the sample annealed in UHV (Figure 6.4c), which likely corresponds with $WO_x$ according to the BE at ~530.2 eV consistent with a transition metal oxide. However, this does not cause a discrepancy in the $E_F$ between the two samples as the valence band edges detected from each sample throughout annealing align quite closely. Adventitious carbon is detected on both exfoliated $WSe_2$ samples, which is consistent with all bulk $WSe_2$ samples employed throughout this work (Figure 6.4d). The concentration of carbon decreases slightly while annealing at 200 °C and is completely desorbed while annealing at 300

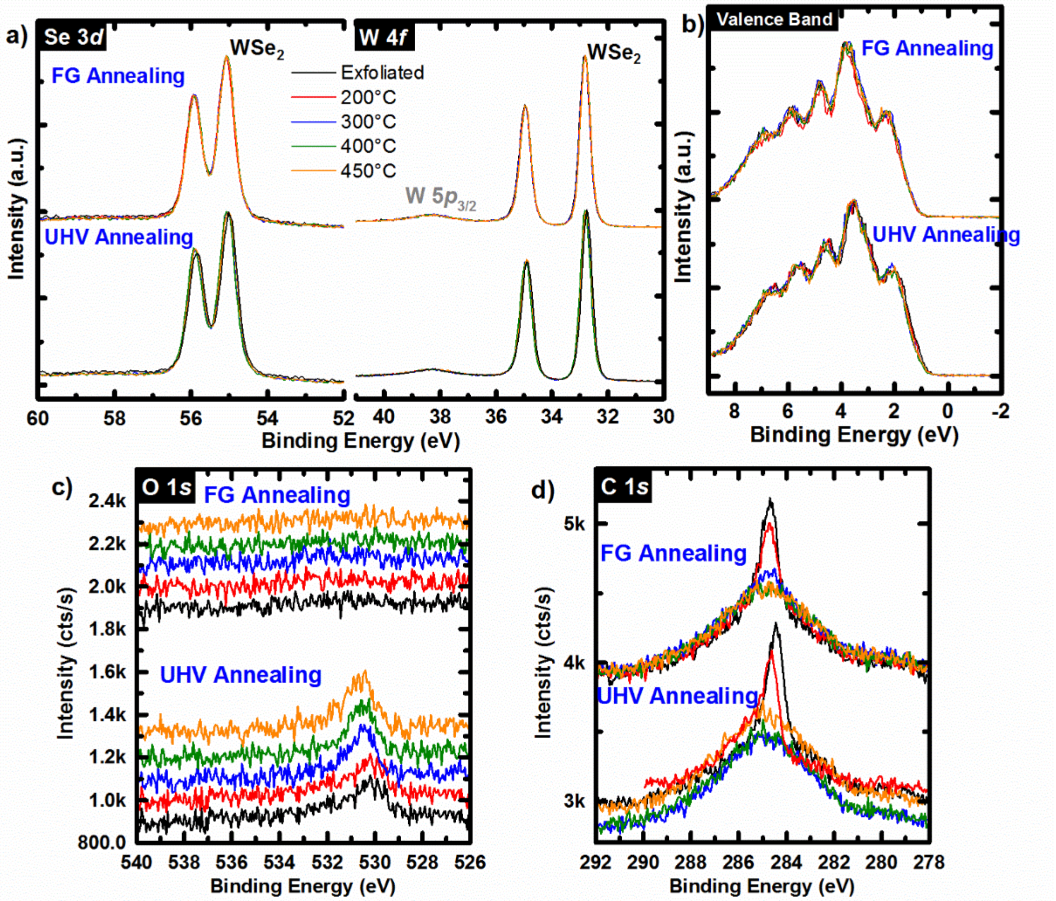

Figure 6.4. a) Se 3*d*, W 4*f*, b) valence band, c) O 1*s*, and d) C 1*s* core level spectra obtained throughout annealing bulk $WSe_2$ under UHV or FG conditions. Colors represent the anneal temperature.

°C regardless of annealing ambient. In addition, the Se:W ratio remains constant throughout annealing (Table 6.1). This provides strong evidence that bulk $WSe_2$ employed here is chemically stable throughout the thermal budget imparted during the annealing experiments.

Table 6.1. Se:W ratio calculated from core level spectra obtained from exfoliated, bulk $WSe_2$ prior to and throughout *in-situ* annealing under UHV ($< 2 \times 10^{-9}$ mbar) and forming gas (90% $N_2$/10% $H_2$; 1 mbar) conditions.

| | Stoichiometry (Se:W) | |
|---|---|---|
| | **UHV** | **FG** |
| **Exfoliated** | 2.01 | 1.99 |
| **200°C** | 2.01 | 2.07 |
| **300°C** | 1.99 | 2.06 |
| **400°C** | 2.00 | 2.04 |
| **450°C** | 2.00 | 2.01 |

*Enhanced Reactions and Defect Passivation by FG Anneal*

Post metallization annealing is often performed in various gases (e.g., $H_2$, $N_2$+$H_2$) and is well–established in conventional device fabrication technologies (e.g., Si, Ge, III–V, etc.) for interface passivation. Forming gas (FG, 90% $N_2$:10% $H_2$) is more reductive than UHV conditions and can also enable defect passivation by hydrogen, which can penetrate to various interfaces within a TMD–based device.[56] Since Pd is a powerful $H_2$ catalyst,[57,58] the effects of annealing a Pd contact in FG is of particular interest as it may facilitate hydrogen transport to the Pd–$WSe_2$ interface and affect interface chemistry.

Annealing the Pd–$WSe_2$ structure in FG (1 mbar, 1 hr at each temperature) results in a markedly different interface, both chemically and electrically, compared to UHV. Annealing at 200 °C in FG drives Pd to reduce $WSe_2$ and form substoichiometric $WSe_x$ ($x \approx 1.1$, Se $3d_{5/2}$: 55.27 eV, W $4f_{7/2}$: 31.99 eV, Figure 6.5a) as well as $PdSe_x$, which is detected as the chemical state that appears in the corresponding Pd 3*d* core level spectrum (Se $3d_{5/2}$: 53.86 eV, Figure 6.5b). The $WSe_x$ chemical state in the W 4*f* (Se 3*d*) core level shifts -0.19 eV (-0.13 eV) towards elemental W (away from elemental Se) after the 400 °C FG anneal consistent with a decreased (increased) oxidation state. In addition, the concentration of $PdSe_x$ increases with increasing temperature in FG as seen

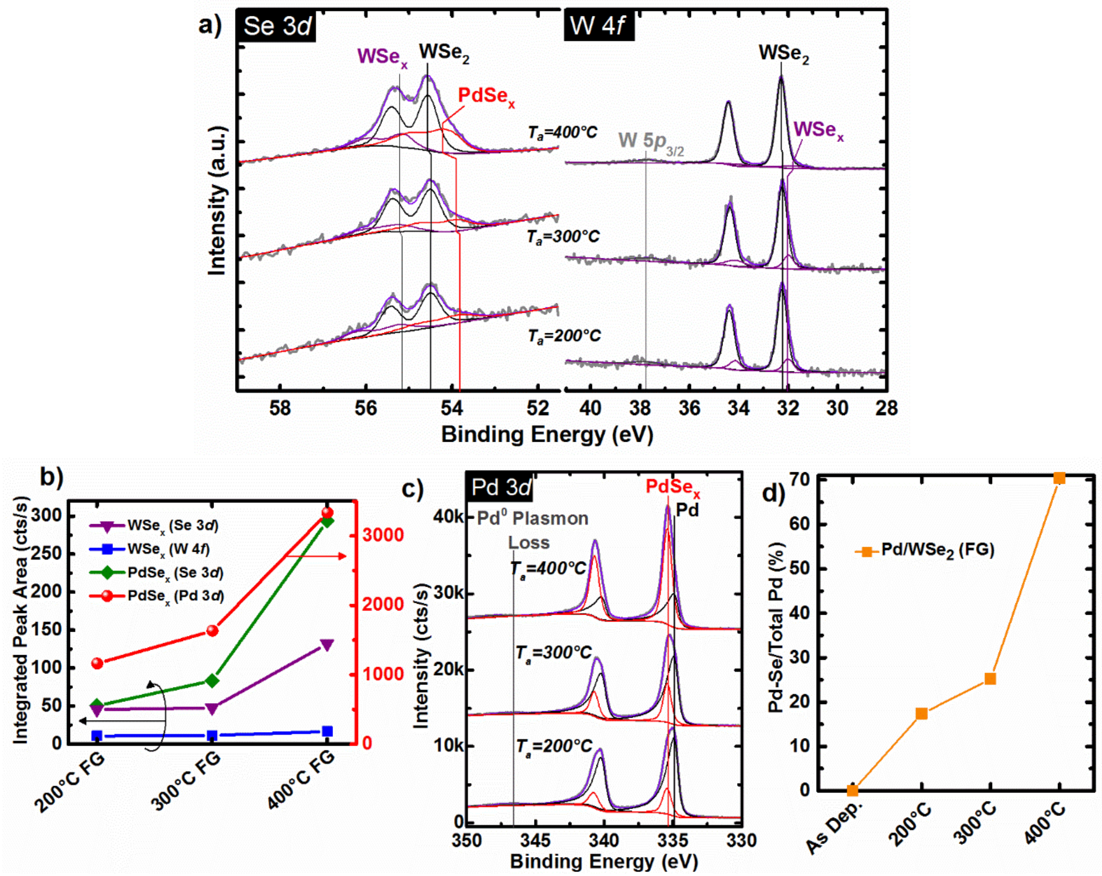

Figure 6.5. a) Deconvoluted Se 3*d*, W 4*f*, and W 5$p_{3/2}$ core level spectra obtained after annealing a ~50 Å Pd–WSe$_2$ structure in forming gas (1 mbar) for 1 hr at 200 °C, 300 °C, and 400 °C, respectively. b) Integrated intensities (including both spin orbit split branches in each core level) of chemical states in Se 3*d*, W 4*f*, and Pd 3*d* core level spectra associated with various reaction products as well as the c) Pd 3*d* core level spectra obtained after annealing a ~50 Å Pd–WSe$_2$ structure under ambient pressure forming gas at 200 °C, 300 °C, and 400 °C, respectively, for 1 hr each. It is explicitly noted that the integrated peak areas shown in b) represent only the areas of the respective chemical state fitted to each denoted core level spectrum. d) Interfacial reactivity gauged by the ratio of the intensity of the chemical state in Pd 3*d* core level corresponding with PdSe$_x$ to the total intensity of the respective core level after depositing at RT and subsequent *in-situ* annealing in FG showing the onset of PdSe$_x$ formation at 200 °C and 70% Pd to PdSe$_x$ conversion at 400 °C.

in the increase of intensity ratio between the PdSe$_x$ and WSe$_2$ chemical states in the corresponding Se 3*d* core level spectra (0.3±0.1 after 200 °C FG anneal to 0.6±0.1 after 400 °C FG anneal, Figure 6.5a). Furthermore, the PdSe$_x$ concentration increases from 17.4% of the total Pd 3*d* intensity after

200 °C FG anneal to 70.4% of the total Pd 3*d* intensity after 400 °C FG anneal (Figure 6.5 c,d). The $WSe_x$:$WSe_2$ concentration ratio does not change after the annealing steps.

The concentration of $PdSe_x$ relative to metallic Pd after annealing at 400 °C in FG (70.4%) is far greater than that detected after the 400 °C UHV anneal (27.5%) despite nearly identical final Pd film thicknesses on each sample according to the attenuation of the $WSe_2$ chemical state in the Se 3*d* core level. Metallic W remains below the limit of detection, suggesting that $WSe_x$ is stable in FG despite enhanced $PdSe_x$ formation at 300 °C and 400 °C. It is already clear that annealing ambient can significantly affect the resulting interface chemistry. When the anneal is performed in FG, Pd readily dissociates $H_2$[58] and supplies atomic hydrogen (H*) to the interface with $WSe_2$. The energy associated with breaking the H–H bond (bond dissociation energy, $BDE_{H\text{-}H}$ = 432.1 kJ/mol; see Table 6.2 for for all relevant BDE values)[59] is much greater than that of the W–Se bond (418.1 kJ/mol).[60]

Table 6.2. Bond dissociation energies of relevant bonds in the Pd–$WSe_2$ system in FG.

| | **kJ/mol** | **kcal/mol** | **eV** |
|---|---|---|---|
| **H-H**[58] | 432.1 | 103.27 | 4.48 |
| **W-Se**[59] | 418.1 | 99.92 | 4.33 |
| **H-Se**[61] | 310.7 | 74.26 | 3.22 |
| **H-(SeH)**[61] | 330.1 | 78.89 | 3.42 |
| **$H-(Se^+)$**[58] | 306.0 | 73.14 | 3.17 |
| **$H-(Se^-)$**[58] | 331.0 | 79.11 | 3.43 |
| **H-Pd(diatomic)**[58] | 234.0±25.0 | 55.93±5.98 | 2.43±0.26 |
| **H-Pd(polycrystalline)**[58] | 59 | 14.10 | 0.61 |
| **H-Pd(111)**[58] | 253.0 | 60.47 | 2.62 |
| **$H_2$-Pd(111)**[58] | 87.0 | 20.79 | 0.90 |
| **Pd-Pd**[58] | 136.0 | 32.50 | 1.41 |
| **$H-(W^+)$**[58] | 222.5 | 53.18 | 2.31 |

| | | | |
|---|---|---|---|
| **H-W(100)**[58] | 283.0 | 67.64 | 2.93 |
| **H-W(110)**[58] | 285.0 | 68.12 | 2.95 |
| **H-W(111)**[58] | 294.0 | 70.27 | 3.05 |
| **H-W(211)**[58] | 289.0 | 69.07 | 3.00 |
| **$H_2$-W(polycrystalline)**[58] | 134.0 | 32.03 | 1.39 |
| **$H_2$-W(100)**[58] | 156.0 | 37.28 | 1.62 |
| **$H_2$-W(110)**[58] | 136.8 | 32.70 | 1.42 |
| **$H_2$-W(111)**[58] | 153.0 | 36.57 | 1.59 |
| **$H_2$-W(211)**[58] | 146.0 | 34.89 | 1.51 |
| **Pd-Se** | Not known | | |

Therefore, W–Se and Pd–H bond scission with corresponding Se–H and W–H bond formation is energetically favorable during the FG anneals. H*, which has been reported to act as an amphoteric passivant in chalcogen based systems,[62] passivates the resulting dangling bonds in $WSe_2$ thereby stabilizing the structure. Additional energy released by $H_2$ splitting throughout the anneal breaks Se–H bonds facilitating the exothermic reaction with Pd to form $PdSe_x$ and resulting in an intimate contact with $WSe_2$.

The significant differences in Pd–$WSe_2$ interface chemistry observed between samples annealed in UHV or FG translate to differences in band alignment and contact performance, which will be discussed in greater detail later.

### *Thermally Induced Structural and Chemical Perturbation in Pd–$WSe_2$*

The results discussed thus far were obtained from bulk $WSe_2$ crystals whereas typical TMD–based devices are comprised of mono to few layer films. Therefore, it is of great interest to investigate the number of $WSe_2$ layers affected by interface reactions as controlling this may offer another route to tunable contact properties.

The effects of metal–TMD interactions on the vibrational and electronic properties of TMDs has previously been investigated with Raman spectroscopy.[63–65] In one report, the partial coverage of monolayer $MoS_2$ with deposited Pd films resulted in a complex convolution of the $E^1_{2g}$ and $A_{1g}$ vibrational modes due to spatially varying strain across the TMD.[64] Here, Raman spectroscopy is similarly employed to investigate the effects of interfacial perturbations on the characteristic vibrational modes of exfoliated mono and few layer $WSe_2$ flakes. However, special care was taken to ensure full coverage of the deposited Pd films (see Appendix E for details). By carefully determining necessary thicknesses of Pd and Si for full coverage films, the spectral variations are reliably presumed to reflect only the effects of metal–$WSe_2$ reactions.

Laser interrogation can impart significant damage (e.g., roughness) upon TMD surfaces.[65,66] The parameters employed here in obtaining Raman spectra from $WSe_2$ were carefully chosen according to control experiments to avoid damaging $WSe_2$ and interpret spectral changes originating from chemical or physical Pd–$WSe_2$ interactions rather than laser induced intermixing. Various combinations of laser power density (0.49 and 3.32 mW/$\mu m^2$), exposure time (1, 2, 3, 4, 5, and 10 s), and number of spectral accumulations (5, 10, and 20) were tested on the exfoliated $WSe_2$ surface. The surface topography and spatial variation in composition (phase) of exfoliated few layer $WSe_2$ flakes is investigated prior to and following Raman spectroscopy, specifically in the vicinity of regions probed by the Raman laser. Figures 6.6 a–f show the corresponding topographical and phase images obtained by AFM. Regions probed by Raman laser are circled in green. The parameters associated with each probed location are listed in Table 6.3 according to the number assigned to each location.

Bright spots appear on all $WSe_2$ terraces in each topographical image displayed and likely reflect the roughness of the underlying $SiO_2$ as the flakes investigated are single or few layer in thickness. In Figure 6.6a, the topography of the probed $WSe_2$ flake is unaffected by laser interrogation during Raman spectroscopy, whereas significant topographical and/or phase contrast is observed in the vicinity of all other probed regions in the associated AFM images (Figures 6.6 b–f). This indicates a laser power density of 0.49 $mA/\mu m^2$, exposure time of either 5 or 10 seconds, and accumulating 5 spectra will preserve the structural and, presumably, the chemical integrity of exfoliated $WSe_2$. Therefore, we also assume that the same set of parameters will provide an adequate spectral resolution from $WSe_2$ buried under 5 nm Pd and 10 nm Si cap as evidenced by the Raman spectra shown in the main text. All other parameter combinations result in damaged $WSe_2$ as is evidenced by the various unusual features observed within the circled regions of Figures 6.6 b–f after performing Raman spectroscopy. Therefore, spectra acquired from $WSe_2$ flakes after 5 nm Pd deposition, post metallization annealing, and finally a 10 nm Si cap were obtained with 0.49 $mW/\mu m^2$ power density, 5 s exposure, and 5 accumulations to avoid such spurious damage effects. The Raman spectra collected from 1L $WSe_2$ employing the parameters associated with b(8) in Table 6.3 (blue curve) as well as a spectrum from a separate 1L $WSe_2$ flake employing 0.49 $mW/\mu m^2$, 10 accumulations, and 1 s exposure time (black curve) are normalized according to the 2LA(M) mode and shown in Figure 6.7a. Both the $E^1_{2g}/A_{1g}$ and 2LA(M) peaks obtained with parameter set 8 (blue) are redshifted by 1.5 $cm^{-1}$ from the spectrum which was obtained without damaging $WSe_2$ (black). The software controlling the Raman spectrometer employed in this work sums each accumulation consecutively throughout the measurement. It is therefore possible that the redshift observed here when laser power density of 3.32 $mW/\mu m^2$ is employed manifests

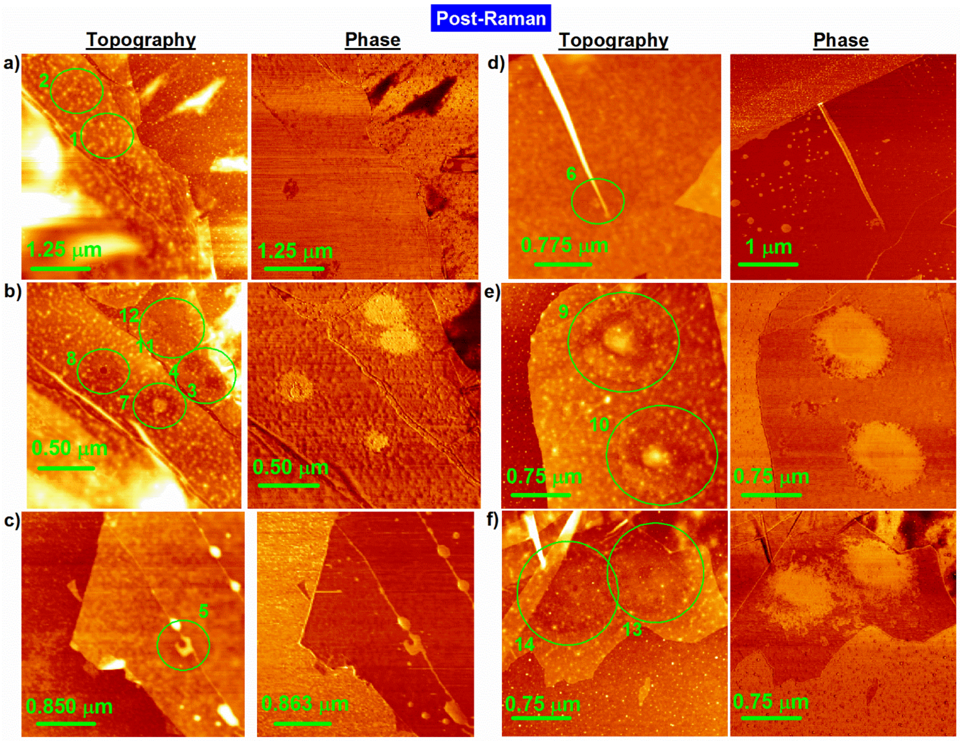

Figure 6.6. AFM topography and phase images obtained from exfoliated $WSe_2$ flakes after performing Raman spectroscopy employing a number of different parameter combinations. Each combination of parameters employed are listed according to probed location in Table 6.3.

initially as a result of Joule heating. This is consistent with a shift to lower wavenumber (higher frequency) expected of Raman active vibrational modes with increased temperature. The Joule heating induced by laser irradiation therefore provides enough energy to damage $WSe_2$ in some cases (i.e., Se loss and concomitant $WO_x$ formation) and even completely evaporate $WSe_2$ in the case of region 8 (Figures 6.7 a, b). Despite completely evaporating $WSe_2$ directly probed by the 3.32 $mW/\mu m^2$ laser in region 8, a Raman spectrum is still obtained. However, this is likely a result of $WSe_2$ evaporation occurring incrementally over the course of each accumulation, providing an appreciable signal to noise during the first few exposures. Therefore, even in severe cases where $WSe_2$ is completely desorbed as it appears in region 8, a Raman spectrum with reasonable signal to noise can still be obtained and other methods must be employed to test for laser induced damage.

Table 6.3. Parameters employed in performing Raman spectroscopy according to probed location in each AFM image in Figure 6.6.

| Image(spot) | Power Density (mW/$\mu$m$^2$) | Exposure Time (s) | Accumulations | Damage |
|---|---|---|---|---|
| a1 | 0.49 | 5 | 5 | no |
| a2 | 0.49 | 10 | 5 | no |
| b3 | 0.49 | 3 | 10 | yes |
| b4 | 0.49 | 5 | 10 | yes |
| b7 | 3.32 | 1 | 5 | yes |
| b8 | 3.32 | 2 | 5 | yes |
| b11 | 3.32 | 1 | 10 | yes |
| b12 | 3.32 | 2 | 10 | yes |
| c5 | 0.49 | 10 | 10 | yes |
| d6 | 0.49 | 4 | 20 | yes |
| e9 | 3.32 | 5 | 5 | yes |
| e10 | 3.32 | 10 | 5 | yes |
| f13 | 3.32 | 5 | 10 | yes |
| f14 | 3.32 | 10 | 10 | yes |

Using the layer number–dependent 2LA(M) shifts and passive laser parameters determined from the calibration experiments just described, the number of $WSe_2$ layers consumed by the interface reactions are quantified by Raman spectroscopy. The first order vibrational modes of some TMDs exhibit layer number dependent Raman shifts (e.g., $MoS_2$, $WS_2$).[67,68] However, these modes are degenerate in $WSe_2$[68,69] and do not exhibit any discernible systematic shift or intensity dependence with layer number. This degeneracy can only be broken if uniaxial strain (i.e., along either the arm–chair or zig–zag directions) is applied to mono or few–layer $WSe_2$.[70] Therefore, the second order longitudinal acoustic mode at the M point in the Brillouin zone [2LA(M)] has been employed here to track the number of layers present in $WSe_2$ flakes. The 2LA(M) mode is detectable with resonant excitation conditions, which occur in $WSe_2$ when a 532 nm laser is utilized,[70] so a He–Ne laser ($\lambda$=532 nm) is employed in this work to access the $E^1_{2g}$, $A_{1g}$, and 2LA(M) modes. The

2LA(M) mode exhibits 2.5, 0.5, 0.5, and 0.3 cm$^{-1}$ red shifts from 1L (261.3 cm$^{-1}$) to 2L, 2L to 3L, 3L to 4L, and 4L to 5L WSe$_2$ (Figure 6.8a inset), respectively, permitting accurate layer number identification for mono and few layer flakes.

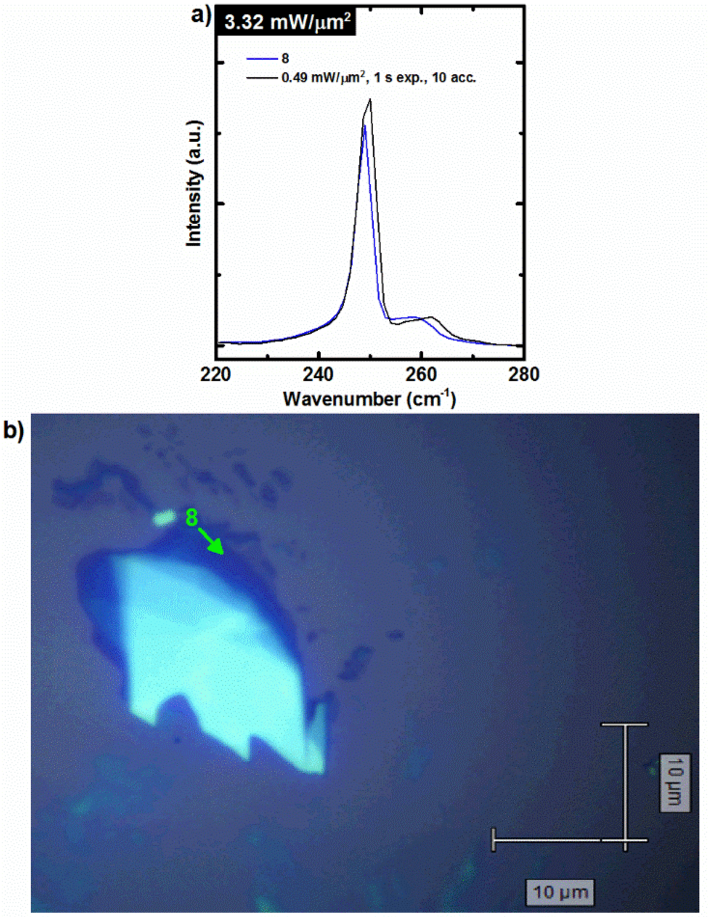

Figure 6.7. a) Raman spectra obtained from mono layer WSe$_2$ flakes with parameters according to b(8) in Table 6.3 (blue curve) and also with 0.49 mW/μm$^2$, 1 s exposure, and 10 accumulations (black curve). The spectra are normalized to the 2LA(M) mode. b) Optical microscope image of an exfoliated WSe$_2$ flake on SiO$_2$ substrate showing completely evaporated WSe$_2$ in region 8 (Figure 6.7b) as indicated by the circular feature at the end of the green arrow exhibiting a contrast nearly identical to the substrate.

Prospective single and few layer WSe$_2$ flakes were exfoliated onto SiO$_2$ substrates and initially screened according to optical contrast. 1L, 2L, and 3L WSe$_2$ flakes were then selected based on flake height according to AFM and the characteristic wavenumber of the 2LA(M) mode. The AFM images and line profiles obtained from the selected 1L, 2L, and 3L flakes after exfoliation and thermal cleaning (see Experimental Details) are displayed in Figure 6.8.

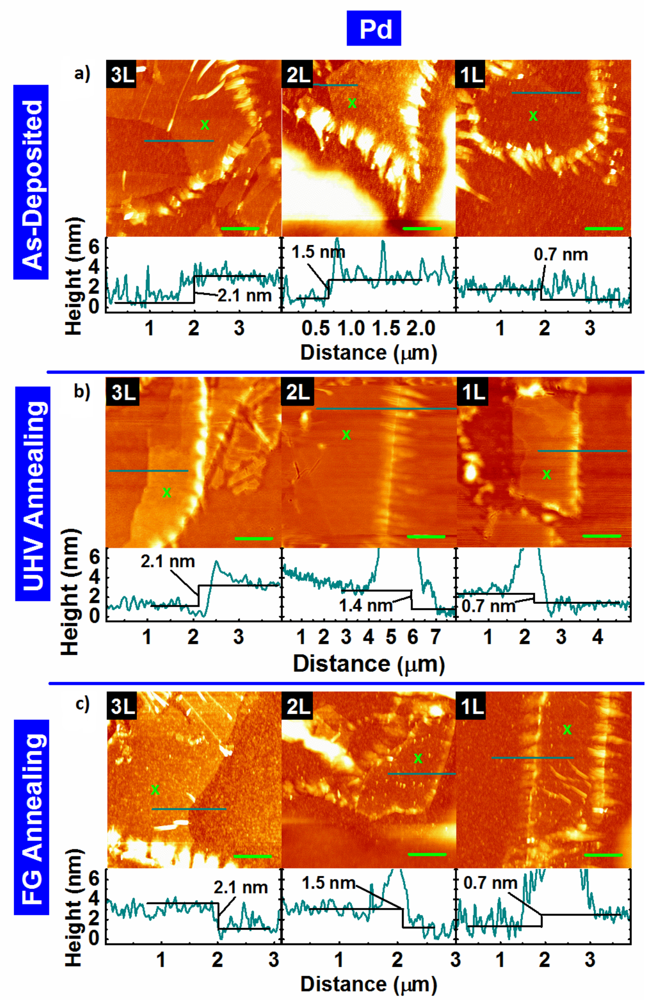

Figure 6.8. AFM topography images and associated line profiles of $WSe_2$ flakes after exfoliation and annealing. The green scale bar in each image represents 2 μm. The green 'x' marked on each image denotes the region on each $WSe_2$ flake probed by Raman spectroscopy. The blue line in each image denotes the cut represented by the line profile below each image.

The Raman spectra obtained from the same flakes after depositing 5 nm Pd/10 nm Si are shown in Figures 6.9 b–d. Raman spectra obtained from 1L, 2L, and 3L $WSe_2$ following Pd deposition under UHV conditions at RT (Figure 6.9) are expected to reflect an absence of interface reactions characteristic of a vdW interface as indicated by XPS. Phonon mode splitting, due to inhomogeneous Pd growth or interface bonding–induced non–uniform strain[64] in $WSe_2$ layers, is not observed in any of the spectra following Pd deposition at RT (Figure 6.9c). More importantly, the 2LA(M) shift detected from the 1L, 2L, and 3L flakes is much less than the ±0.2 $cm^{-1}$ error of the spectrometer following Pd deposition at RT, indicating unperturbed $WSe_2$. However, the intensity of the $E^1_{2g}/A_{1g}$ peak decreases slightly relative to that of the 2LA(M) peak following RT Pd deposition. The $A_{1g}$ mode is expected to be 8× the intensity of the $E^1_{2g}$ mode. Therefore, it is reasonable to conclude that, although RT Pd deposition does not result in detectable reactions with $WSe_2$, the full coverage film dampens the out of plane vibrations resulting in decreased $A_{1g}$ intensity relative to the 2LA(M) peak.

Annealing Pd/1L $WSe_2$ under UHV conditions at 300 °C results in partial quenching of the $E^1_{2g}/A_{1g}$ modes and complete quenching of the 2LA(M) modes suggesting partial layer consumption due to the interface reactions (Figure 6.9d). Therefore, the anneal transforms the predominantly top Pd contact configuration at RT into a pseudo–edge contact, which is predicted to exhibit superior electrical performance compared with a top Pd–$WSe_2$ contact.[49] A weak feature detected around the initial $E^1_{2g}/A_{1g}$ peak position after annealing indicates only traces of the 1L 2H–$WSe_2$ structure persist. The $E^1_{2g}/A_{1g}$ peaks detected from both 2L and 3L $WSe_2$ after annealing at 300 °C under UHV conditions exhibit asymmetric broadening to lower wavenumber consistent with a direct proportionality between the concentration of defects in $WSe_2$ and the magnitude of $E^1_{2g}$ blue shift.[70] In addition, the 2LA(M) peak exhibits an apparent 0.7 $cm^{-1}$ redshift and noticeable broadening in the cases of both 2L and 3L $WSe_2$ after 300 °C UHV anneal, suggesting the consumption of one layer according to the expected 0.5±0.2 $cm^{-1}$ 2LA(M) red shift transitioning from 3L to 2L $WSe_2$. However, a 0.7 $cm^{-1}$ red shift is significantly less than that expected of a

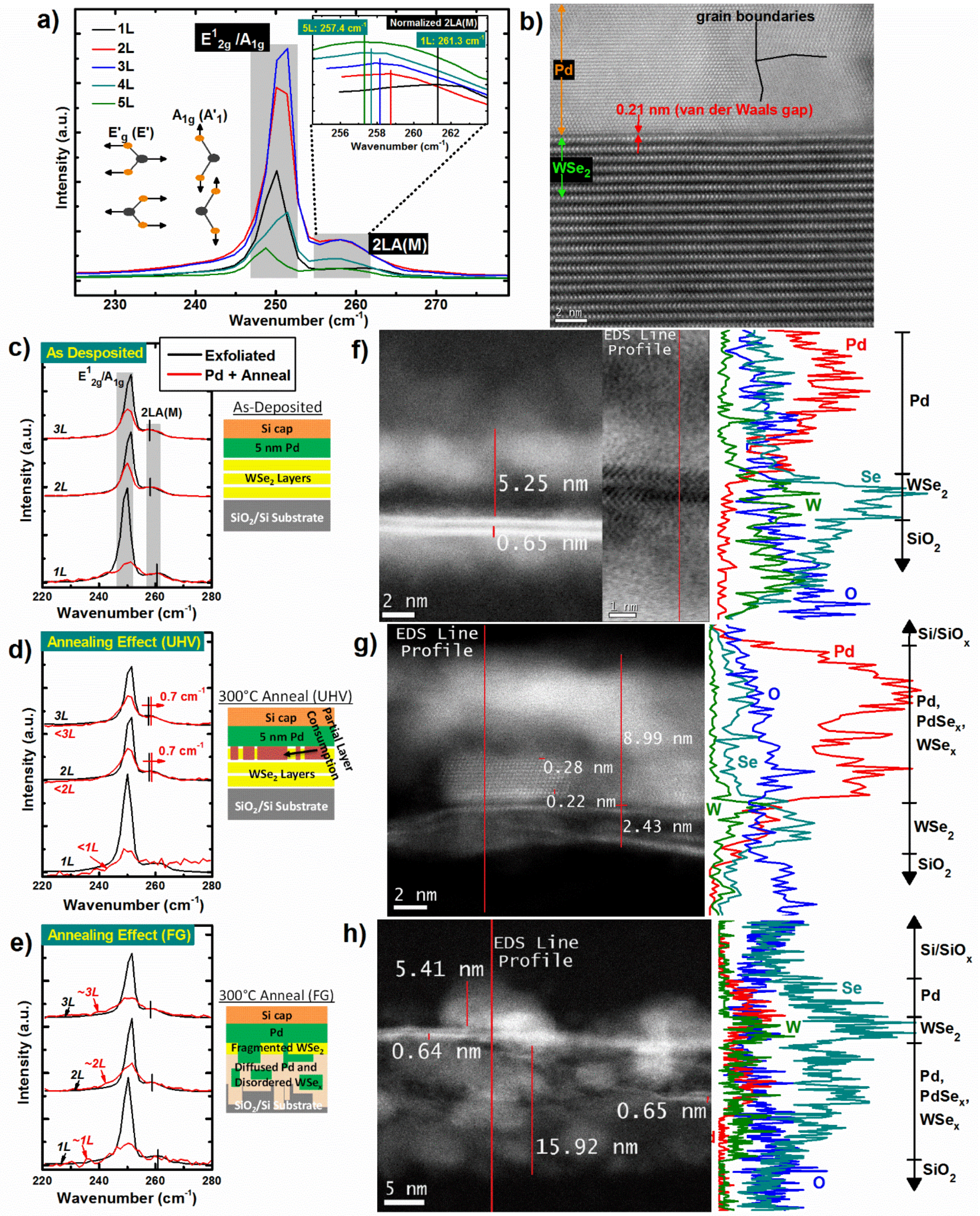

Figure 6.9. a) Characteristic layer number dependent shifts of $E^1_{2g}$ , $A^1_g$, and 2LA(M) vibrational modes of $WSe_2$ from one layer (1L) to 5 layers (5L) thick. b) Cross section TEM image highlighting the van der Waals gap formed between Pd and bulk $WSe_2$ at RT. Raman spectra obtained from 1L, 2L, and 3L $WSe_2$ prior to (black) and following (red) c) 5 nm Pd deposition under UHV conditions and subsequent annealing in d) UHV or e) FG at 300 °C. f-h) TEM images and EDS spectra obtained from FIB cross sections of the same 2-3L $WSe_2$ from c-e). Schematics of Pd/$WSe_2$ interface chemistry according to Raman Spectra are displayed adjacent to associated plots.

transition from 2L to 1L $WSe_2$. This suggests layer consumption is incomplete during the 300 °C UHV anneal, which manifests as broadening from a convolution of multiple peaks in the spectrum around 260 $cm^{-1}$ (Figure 6.9d).

In contrast, after annealing at 300 °C in FG, neither the $E^1_{2g}/A_{1g}$ nor 2LA(M) modes detected from any of the 1L, 2L, or 3L $WSe_2$ flakes exhibit appreciable shifts (Figure 6.9e). Additionally, these modes remain above the limit of detection even in the case of 1L $WSe_2$ and exhibit significant broadening in all cases indicating reactions with Pd induced by FG anneal. The broadened but detectable $E^1_{2g}/A_{1g}$ and 2LA(M) modes even in the case of 1L $WSe_2$ suggests there are regions in which the original 2H structure of $WSe_2$ is preserved adjacent to the disordered regions. These results corroborate XPS–indicated persistence of $WSe_x$ throughout post metallization annealing in FG.

After probing with Raman spectroscopy, lamella were milled from the same $WSe_2$ flakes with a focused ion beam (FIB). Each interface was interrogated by high resolution STEM and EDS (Figures 6.9 f–h) and corroborate the interpretation of the Raman spectra discussed above before and after Pd deposition and post metallization anneal. The STEM image and corresponding EDS profile obtained from a 2L $WSe_2$ flake after Pd deposition at RT (Figure 6.9f) confirm the vdW nature of the Pd–$WSe_2$ interface (Figure 6.9b) as Se and W are below the limit of EDS detection throughout the Pd film. In addition, the two $WSe_2$ layers are represented by parallel regions of bright contrast ~0.7 Å thick with a darker contrast region between them corresponding to the interlayer vdW gap. A narrow region of bright contrast in direct contact with the top $WSe_2$ layer corresponds with a wetting layer of Pd as indicated by the EDS spectrum in Figure 6.9f. The oxygen concentration is on the order of the noise level in EDS spectra (<0.1 at. %) within the Pd–

$WSe_2$ region for all lamella discussed here (Figure 6.9 f–h). Any crystalline structure within the Pd film deposited at RT is not evident in the TEM image shown in Figure 6.9f, but a thicker Pd film (~20 nm) deposited at RT on $WSe_2$ exhibits polycrystallinity (Figure 6.9b). The 5 nm Pd film deposited on $WSe_2$ flakes could be below the critical thickness for Pd crystallization at RT on $WSe_2$.

The 3L $WSe_2$ and deposited Pd film are altered structurally while annealing under UHV conditions (Figure 6.9g) compared with the ordered nature observed only after RT deposition. The EDS spectrum in Figure 6.9g shows Se outdiffusion into the Pd, which corroborates $PdSe_x$ formation at the expense of the underlying $WSe_2$, which is consistent with the XPS and Raman data. There is also a thin region of W–rich $WSe_x$ localized to the Pd–$WSe_2$ interface corresponding to the $WSe_x$ that forms while annealing under UHV conditions (observed in the XPS spectra). Se outdiffusion and $WSe_2$ fragmentation indicated by STEM and EDS agree well with the disordering of the 1L $WSe_2$, observed in the corresponding Raman spectra. Interestingly, Pd undergoes partial crystallization at 300 °C in UHV. The $\{111\}$ plane of the nanocrystal, visible in Figure 6.9g, interfaces with the underlying $WSe_x$ as evidenced by the 0.22 nm interatomic distance and 0.28 nm interplanar distance, which are consistent with the $\langle 110 \rangle$ family of directions and $\{111\}$ family of planes in face–centered cubic Pd ($a = 0.39$ nm), respectively.[71] The statistical distribution of different Pd nanocrystal facets in direct contact with $WSe_2$ could significantly affect the contact performance and band alignment as $\Phi_{Pd}$ varies by up to 0.4 eV depending on the crystallographic orientation.[72]

STEM images and EDS spectra obtained from 2L $WSe_2$ after post metallization FG annealing at 300 °C show an extremely disordered Pd–$WSe_2$ structure (Figure 6.9h), similar to post metallization annealing under UHV conditions. Interestingly, EDS indicates Pd diffuses through $WSe_2$ and up to 16 nm into the underlying $SiO_2$ (region of patchy bright contrast below $WSe_2$). Previous reports have demonstrated the highly favorable nature of Pd diffusion into $SiO_2$ even at moderate annealing temperatures such as those employed here.[73] In addition, Se and W are detected by EDS throughout the Pd/$SiO_2$ layer formed under $WSe_2$ suggesting Se and W are carried into the $SiO_2$ substrate with the Pd diffusion front. Both layers of the structure towards the right of the STEM image in Figure 6.9g are ~7 Å thick and a region of dark contrast between the layers is resolvable, which indicates a vdW gap is present. This suggests the kinetics of Pd diffusion through $WSe_2$ and into the underlying $SiO_2$ enables the movement of whole $WSe_2$ fragments into the substrate. Only Se diffuses upwards into the Pd clusters remaining on top of the $WSe_2$. Despite fragmentation, the 2L structure of remaining $WSe_2$ fragments is preserved during post metallization annealing in FG in agreement with the corresponding Raman spectra.

These results clearly show post metallization annealing can perturb not only the interface chemistry but also the structure of Pd–$WSe_2$, with more significant disordering at elevated temperature under FG conditions in which Pd not only disrupts the $WSe_2$ but also the $SiO_2$ substrate (Figure 6.9 c-h). In addition, a pseudo edge contact is formed during the post metallization anneal which enhances hole injection efficiency (discussed in the next Section). These results are consistent with predictions of Pd–Se covalent bonds and a lower carrier injection barrier in the edge contact configuration.[49]

Understanding how many TMD layers are affected by reactions at the metal–TMD interface could offer an additional robust approach to improve contact performance in TMD–based devices. In a device where the contact metal consumes at least one TMD layer, the intermetallic formed likely remains in lateral contact with the adjacent TMD channel. Therefore, any TMD layers in the contact region consumed by reactions at the metal–TMD interface should be considered pseudo edge contacts, while simultaneously in top contact with underlying, unperturbed layers. Therefore, it may be possible to tune charge injection by deliberately choosing the number of TMD layers in the contact region of a TMD–based device according to the number of 'sacrificial' layers consumed by reactions and the resulting band structure of preserved layers. Competing contributions from lateral injection from the channel to the intermetallic and vertical injection from the underlying unperturbed TMD to the intermetallic must be considered when designing a representative device.[74,75]

### 6.4.2 Band Alignment and Electrical Performance in Pd–$WSe_2$ Stacks and Transistors

Figure 6.10a displays the absolute binding energies of the $WSe_2$ chemical state in the Se $3d_{5/2}$ core level spectra detected from bulk $WSe_2$ after exfoliation and subsequent stepwise metal deposition and post metallization annealing.[76]

Exfoliated $WSe_2$ prior to Pd deposition exhibits a $E_F$ = 0.58 eV from the valence band edge considering the initial $\Delta_{VB}$ offset and work function (0.58±0.07 eV and 4.82±0.06 eV, respectively; Figure 6.10d). The bulk $WSe_2$ chemical states shift to lower BE throughout Pd deposition. A total shift of -0.59 eV is detected after 4.7 nm Pd is deposited (Figure 6.10a), which corresponds with substantial upward band bending and a $E_F$ position within the VB. Therefore, XPS indicates that a Pd contact deposited on $WSe_2$ under UHV conditions should exhibit Ohmic hole behavior, which agrees well with device performance reported previously[14] and obtained in this work. The $E_F$ position does not change during the 200 °C UHV anneal consistent with an absence of reaction products detected by XPS. A cumulative +0.19 eV $E_F$ shift is detected after anneals at 300 °C and

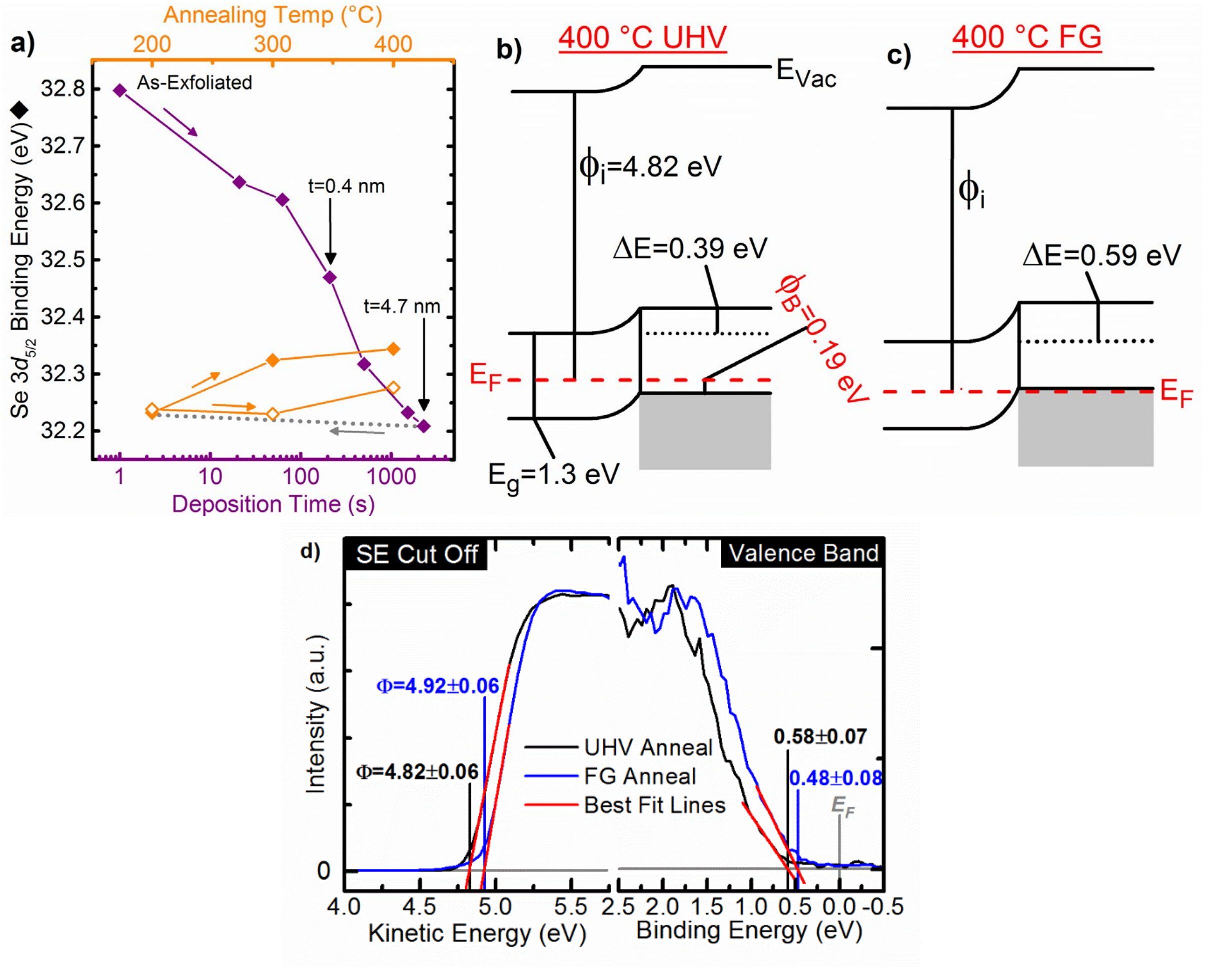

Figure 6.10. a) Binding energies of the bulk $WSe_2$ chemical state in the Se 3*d* core level spectra throughout stepwise Pd deposition and post metallization annealing under either UHV or FG conditions. The Se 3$d_{5/2}$ binding energy shifted to virtually the same value after the final Pd deposition step on each sample. Therefore, only the data obtained from the 'UHV annealed' sample prior to annealing is shown (purple). The Se 3$d_{5/2}$ binding energy detected on the UHV (FG) annealed sample are represented by the closed (open) diamonds. b, c) Corresponding band diagrams obtained from d) initial $WSe_2$ work function and valence band edge offset in conjunction with core level shifts throughout annealing, which show the hole Schottky barrier formed by the UHV anneals and Ohmic hole band alignment formed by the FG anneals. d) Secondary electron cutoff and valence band edge spectra obtained from both 'exfoliated' $WSe_2$ samples prior to metal deposition. The red lines show linear fits obtained by regression.

400 °C under UHV conditions, which is associated with the formation of a 0.19 eV hole Schottky barrier (Figure 6.10b) and corresponds with a subsequent increase in concentration of $PdSe_x$ and $WSe_x$ (Figure 6.2c). The increase in concentration of $PdSe_x$ and of Se vacancies in $WSe_x$[77] likely

contributes to the formation of a hole Schottky barrier, but the most important effect of the 400 °C UHV anneal is the formation of Pd–Se bonds and corresponding enhanced contact performance. Prior to Pd deposition and FG anneals, $WSe_2$ exhibits a $E_F = 0.48\pm0.08$ eV above the valence band edge (Figure 6.10 a,d). Impurities typically detected in $WSe_2$ (even in synthetic crystals) can act as unintentional dopants, which likely causes the spatial $E_F$ variation observed across the exfoliated $WSe_2$ samples investigated here.[78] The $E_F$ remains unperturbed after annealing at 300 °C in FG but exhibits a minor +0.06 eV shift after 400 °C FG anneal. Therefore, the $E_F$ remains within the VB after 400 °C FG anneal in contrast to the hole Schottky barrier created by annealing Pd–$WSe_2$ at 300 °C under UHV conditions (Figure 6.10c). Interestingly, annealing in FG converts Pd to $PdSe_x$ in a much greater concentration compared with that under UHV conditions regardless of annealing temperature (Figure 6.3c). Because of this, the $E_F$ remains within the VB throughout annealing in FG unlike under UHV conditions. Therefore, hydrogen, which likely diffuses throughout the Pd–$WSe_2$ interfacial region while annealing in FG, seems to play a significant role in passivating defects (e.g., $WSe_x$) generated by the reactions. In addition, certain species of $PdSe_x$ (e.g., $Pd_4Se$, $Pd_7Se_4$) exhibit metallic conductivity ($\sigma\approx10^4$–$10^5$ $(\Omega\text{-cm})^{-1}$). The combination of maximizing $PdSe_x$ concentration and passivating defects at the Pd–$WSe_2$ interface by performing the anneal in FG is critical to forming consistent high–performance Pd hole contacts to $WSe_2$.

To corroborate the XPS–derived band alignments discussed above with electrical behavior of representative devices, bulk $WSe_2$ Schottky diodes and back gated few layer (7–10 nm thick flakes) $WSe_2$ transistors were fabricated with Pd contacts and subjected to anneals in either FG or UHV at 200 °C, 300°C, and 400 °C for 1 hr each. Their electrical performance was evaluated throughout the experiment. It is important to note that the $WSe_2$ FETs were fabricated on an $Al_2O_3$

substrate deposited on Si by atomic layer deposition unlike the Si/Pd/$WSe_2$/$SiO_2$/Si samples fabricated for analysis by Raman spectroscopy and TEM.

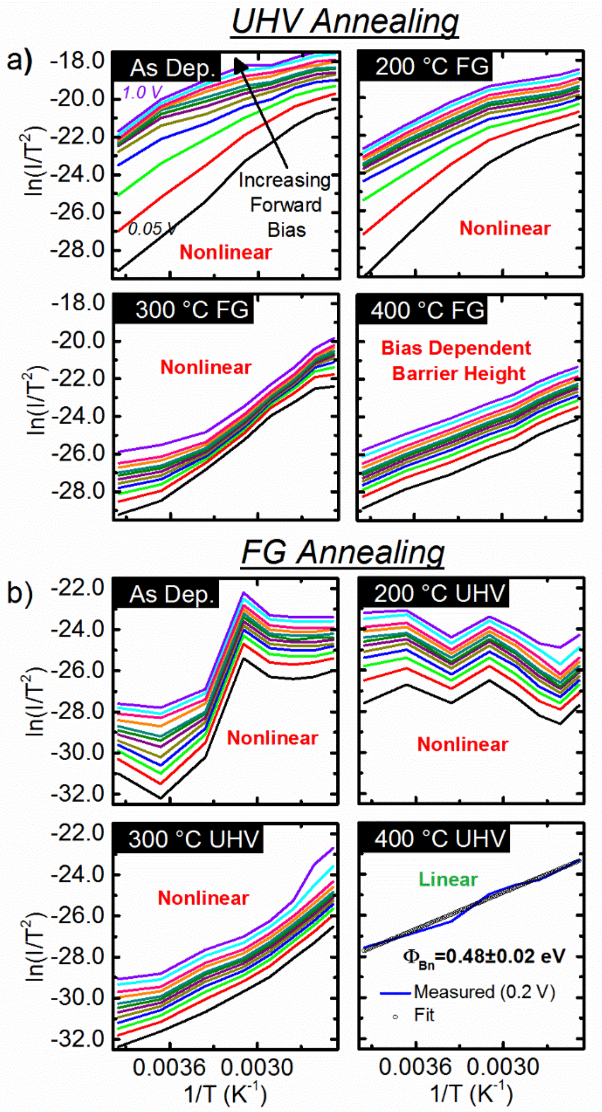

Figure 6.11. Arrhenius plots obtained from temperature dependent I-V measurements of Pd–bulk $WSe_2$ Schottky diodes after fabrication and subsequent post metallization annealing in either UHV or FG. These plots show the nonlinear behavior in all cases but one (400 °C FG) demonstrating the need for an alternative method for accurate Schottky barrier height extraction.

An Arrhenius plot ($\ln(I/T^2)$ vs 1/T) of I–V data from a Schottky diode can be employed to extract the Schottky barrier height in the forward bias region for V>>kT/q, provided the transformed data can be accurately fit by linear regression. Nonlinear temperature dependence is observed for all samples regardless of annealing temperature except after the 400 °C FG anneal (Figure 6.11), in which case the barrier height is significantly underestimated and other mechanisms, such as tunneling or a spatially inhomogeneous barrier height, must be considered to accurately extract the Schottky barrier height. After post metallization annealing at 400 °C in UHV, linear behavior is observed at 0.2 V forward bias and an electron Schottky barrier of 0.48 eV is extracted from the slope of the best fit line (Figure 6.11b). This barrier height is much smaller than the 'homogeneous' barrier height extracted using the inhomogeneous barrier height model, likely because the thermionic emission model considers a uniform barrier height. Therefore, the thermionic emission model will underestimate the barrier height in devices with an inhomogenenous barrier height. Therefore, thermionic emission does not accurately describe the conduction mechanism for all annealing conditions investigated here.

TMDs can exhibit high defect densities that dominate the electrical behavior of a metal–TMD junction.[27] Therefore, a Schottky barrier model[79] that accounts for the effects of an unknown aerial density ($\rho_p$) of circular low Schottky barrier regions with radius $r_p$ surrounded by non–defective regions with a different electron Schottky barrier height (SBH, $\Phi_{B0}$) was employed to extract $\Phi_{B0}$, $\rho_p$, the modified Richardson constant (A**), series resistance ($R_s$), and difference in Schottky barrier height between defective and non–defective regions ($\Delta$) according to annealing conditions. Equation 6.1 was fitted to the measured forward bias I-V data in Figure 6.12a via nonlinear regression (see Appendix F for details).

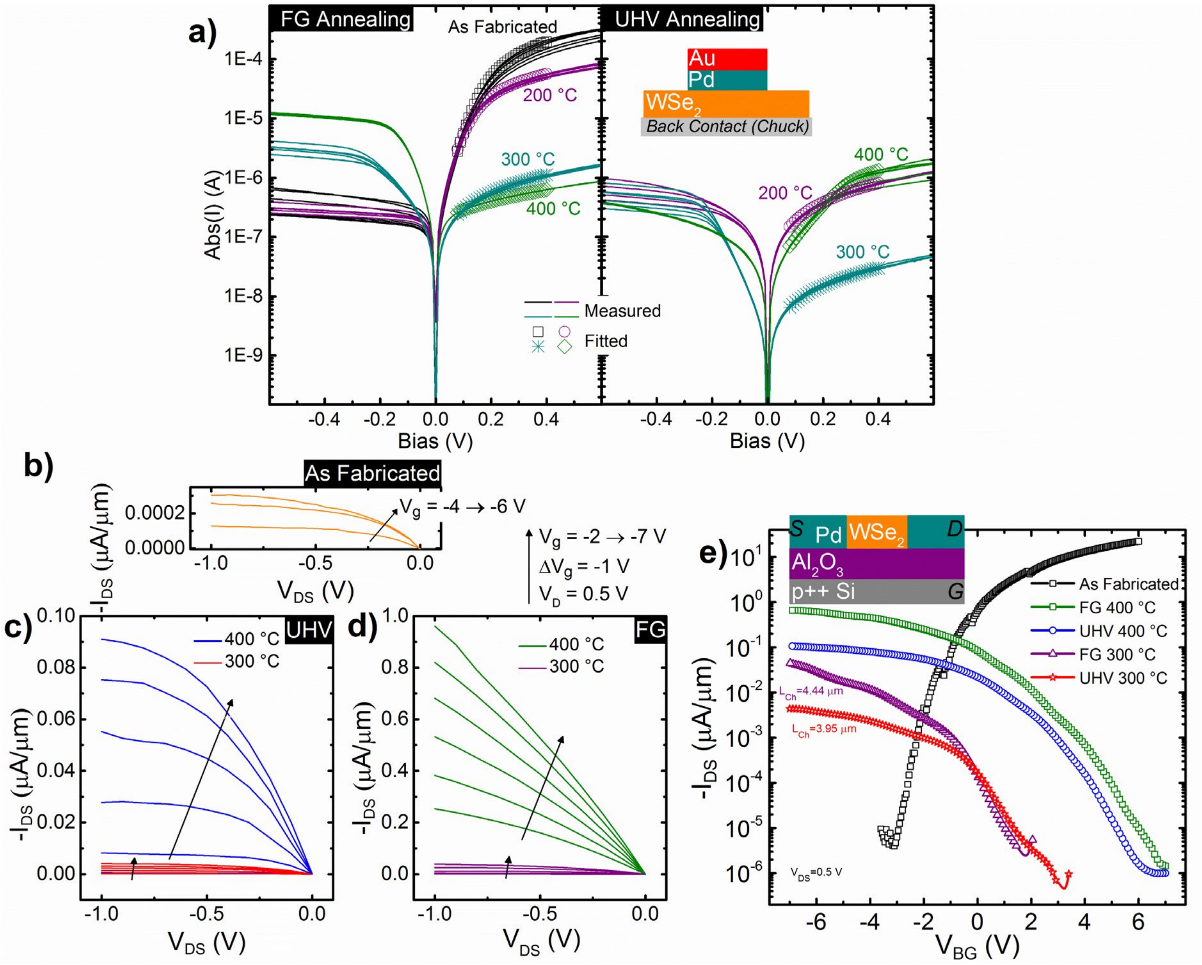

Figure 6.12. a) I-V curves obtained from Pd–WSe$_2$ Schottky diodes after metallization and annealing in UHV or FG (lines) with nonlinear regression fits (symbols) obtained using an inhomogeneous Schottky barrier height model. Reverse bias $I_{DS}$-$V_{DS}$ of Pd contacts to back gated WSe$_2$ devices after b) fabrication and annealing at 200 °C (not shown), 300 °C, and 400 °C in c) UHV and d) FG. e) $I_{DS}$-$V_{BG}$ of the same devices showing dramatic improvements in the hole conduction after annealing.

$$I_{total} = AA^{**}T^2 e^{\frac{-\Phi_{B0}}{kT}} \left[ e^{\frac{q\left(V_{applied}-R_S I_{total}\right)}{kT}} - 1 \right] \left[ 1 + \rho_p \frac{\pi kT \left(r_p^2\Delta\right)^{\frac{1}{3}} \eta^{\frac{2}{3}}}{3q\left(V_{bb}\right)^{\frac{2}{3}}} \exp\left( \frac{-q\phi_{B0}}{kT} + \frac{3q\left(r_p^2\Delta\right)^{\frac{1}{3}}\left(V_{bb}\right)^{\frac{1}{3}}}{kT\eta^{\frac{1}{3}}} \right) \right]$$

Equation 6.1

where

$$V_{bb} = \phi_{b0} - V_{b0} - V_{applied} + R_s I_{total}$$

Equation 6.2

and

$$\eta = \frac{\varepsilon_s \varepsilon_0}{q(N_a - N_d)}$$

Equation 6.3

The model also considers the area of the diode (A), the temperature (T), the applied bias ($V_{applied}$), the band bending of the barrier in the non–defective regions ($V_{b0}$), the bulk $WSe_2$ dielectric constant ($\varepsilon_s$), and the unintentional doping density of the $WSe_2$ ($N_a$-$N_d$). $WSe_2$ doping densities of $1.30 \times 10^{17} \pm 0.35 \times 10^{17}$ $cm^{-3}$ and $1.19 \times 10^{17} \pm 0.39 \times 10^{17}$ $cm^{-3}$ for the samples annealed in UHV and FG, respectively, were determined by the $1/C_2$ vs V method (Figure 6.13). This method involves measuring the capacitance of the Schottky diodes in reverse bias and extracting the slope (m) of the $1/C^2$ vs V plot, which is then inserted into Equation 6.3 to solve for $N_D$-$N_A$,

$$m = \frac{2}{q\varepsilon_S\varepsilon_0(N_D - N_A)}$$

Equation 6.4

where q is the charge of an electron, $\varepsilon_S$ is the $WSe_2$ dielectric constant (7.2),[80] $\varepsilon_0$ is the vacuum permittivity and $N_D$-$N_A$ is the unintentional doping density of the $WSe_2$.

This method requires the data plotted as $1/C^2$ vs V to exhibit slope and intercept independent of frequency,[81] which is demonstrated in Figure 6.13a for three different Schottky diodes. The $WSe_2$ doping density varies spatially from $1.00 \times 10^{17}$ $cm^{-3}$ to $2.02 \times 10^{17}$ $cm^{-3}$, as expected according to previous work,[27,78] according to the range of slopes fitted in the $1/C^2$ vs V plot for a number of diodes and two different synthetic $WSe_2$ crystals (Figure 6.13).

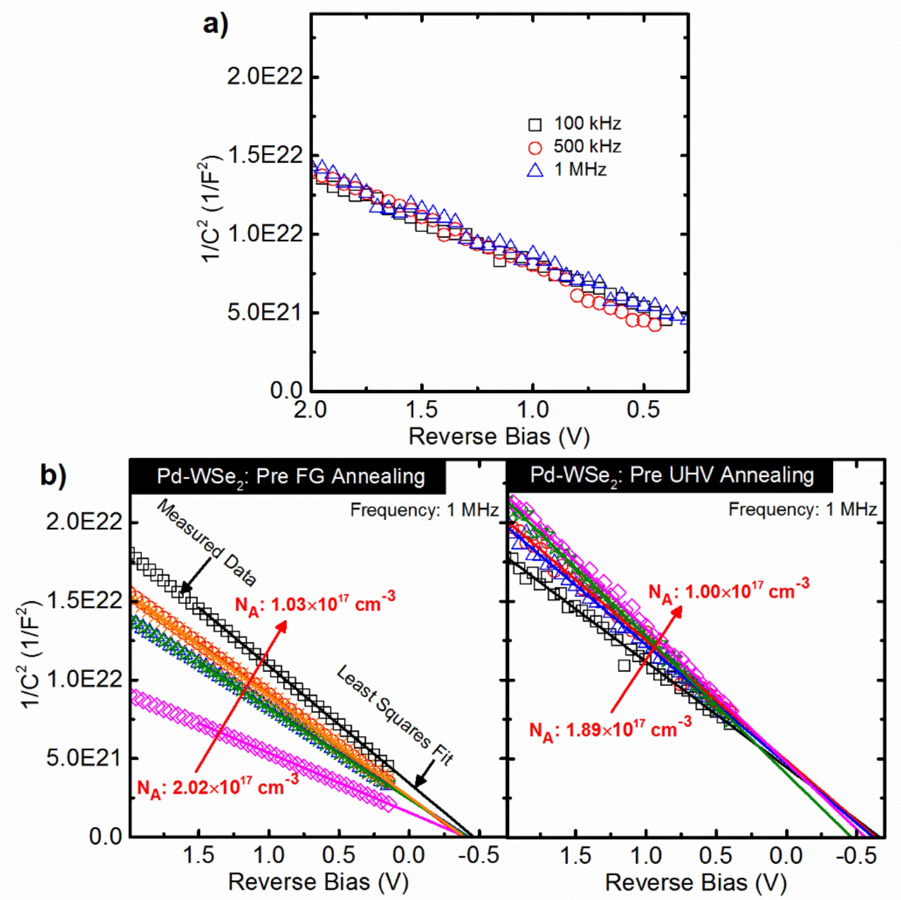

Figure 6.13. $1/C^2$ vs V plots and fitted lines measured from a) a Pd–$WSe_2$ Schottky diode demonstrating a frequency independent slope and b) from many Pd–$WSe_2$ Schottky diodes prior to subsequent anneals in UHV or FG (measured at 1 MHz), which demonstrate a spatially varying $WSe_2$ doping density across a single $WSe_2$ crystal and from crystal to crystal.

SBH extracted after fabrication and annealing in UHV or FG are listed in Table 6.4. The $r_p$ was fixed at 1.5 nm according to a previous detailed STM study of defects in $WSe_2$.[78] A close fit of the forward bias I–V data is obtained in all cases ($R^2 > 0.99$), yielding a relatively low $R_s \approx 80 \pm 16$ Ω, reasonable $A^{**} \approx 10 \pm 2$ A/cm$^{-2}$ K$^{-2}$, $\Phi_{B0} = 1.29 \pm 0.05$ eV, $\Delta = 1.10 \pm 0.05$ eV and $\rho_p = 3.6 \times 10^{12} \pm 3.1 \times 10^{12}$ cm$^{-2}$ prior to annealing in UHV or FG are extracted from the two respective samples (Table 6.4, Figure 6.15, $R_s$ and $A^{**}$ are averaged from six diodes on each sample). The extracted $\Phi_{B0}$ and $\rho_p$ are in good agreement with the XPS–derived band alignment (electron

Schottky barrier height of 0.01 ± 0.10 eV) and previous STM–derived aerial defect density ($10^{12}$ $cm^{-2}$).[78] The $\rho_p$ is relatively high (compared to defect densities in more mature semiconductors) but below the XPS detection limit (0.1 at. %), which explains why additional chemical states corresponding with the low SBH regions are not detected in W 4*f* and Se 3*d* core levels prior to annealing. The effective Richardson constant previously extracted from an Au–$WSe_2$ Schottky diode (27.6 $A/cm^{-2}$ $K^{-2}$), which corresponds to a hole effective mass of $0.23m_0$,[82] is larger than the A** obtained here employing a hole effective mass of $0.33m_0$.

The 400 °C UHV anneal suppresses (enhances) the reverse (forward) bias current (Figure 6.12a), corresponding with an increased hole SBH ($\Phi_{B0}$ = 1.07 ± 0.02 eV), which is in close agreement with the XPS–derived appreciable hole Schottky barrier formed by the UHV anneal (XPS: electron Schottky barrier height of 0.19 eV).

Table 6.4. Electron and hole Schottky barrier heights and the corresponding $WSe_2$ band gap extracted from Pd–$WSe_2$ Schottky diodes and FETs after fabrication and subsequent annealing in either UHV or FG.

| **Schottky Diode** | | **UHV** | | | **FG** | | |
|---|---|---|---|---|---|---|---|
| | *As Fab.* | *200 °C* | *300 °C* | *400 °C* | *200 °C* | *300 °C* | *400 °C* |
| **Φn (eV)** | 1.29 | 1.29 | 1.27 | 1.07 | 1.29 | 1.29 | 1.29 |
| **Φp (eV)** | 0.01 | 0.01 | 0.03 | 0.23 | 0.01 | 0.01 | 0.01 |
| **Band Gap (eV)** | 1.3 | 1.3 | 1.3 | 1.3 | 1.3 | N/A | 1.3 |
| **FET** | | **UHV** | | | **FG** | | |
| | *As Fab.* | *200 °C* | *300 °C* | *400 °C* | *200 °C* | *300 °C* | *400 °C* |
| **Φn (eV)** | 0.73 | 0.99 | 1.02 | 1.05 | 0.99 | N/A | 1.33 |
| **Φp (eV)** | 0.65 | 0.5 | 0.43 | 0.34 | 0.44 | N/A | 0.06 |
| **Band Gap (eV)** | 1.38 | 1.49 | 1.45 | 1.39 | 1.43 | N/A | 1.39 |

After the 400 °C FG anneal, the reverse (forward) bias current is increased (suppressed) by 100×, which corresponds with a $\Phi_{B0} = 1.29 \pm 0.01$ eV and corroborates the XPS–derived Ohmic band alignment ($E_F$ resides within the valence band). Furthermore, the 400 °C FG anneal effectively eliminates the diode–to–diode I–V variability and reduces the $\rho_p$ to $2.0 \times 10^7$ cm$^{-2}$, facilitating the dramatic improvement in hole conduction, contact performance consistency, and defect passivation achievable through enhanced $PdSe_x$ formation and H* radicals provided by the FG anneal.

It is difficult to accurately extract electron and hole SBH from the transfer characteristics of ambipolar ultra–thin body FETs. Employing a thermionic emission model, which neglects tunneling, is of questionable validity considering tunneling current is appreciable in devices where the depletion width is defined by the channel thickness, as is the case in few layer TMD FETs.[83] Therefore, in this work we employ an analytical Schottky barrier height model based on Landauer theory to extract both the electron and hole SBH from the transfer characteristics of back gated $WSe_2$ FETs before and after annealing (method and equations described in Appendix G).[83] This model accounts for both thermionic and tunneling contributions to the total current density and therefore the band alignment can be accurately extracted from the measured $I_{DS}$ in the subthreshold region, where conduction depends on the Schottky barriers at the contacts and scattering in the channel is negligible. The SBH extracted from Pd–$WSe_2$ FETs after fabrication and subsequent annealing in either UHV or FG are listed in Table 6.4 and the corresponding fits obtained using the analytic Schottky barrier model are displayed in Figure 6.14. The fits of the subthreshold regions of the $I_{DS}$–$V_{BG}$ curves are performed independently on each carrier branch from the point of minimum current. In–plane carrier effective masses $m_e^*=0.33m_0$ and $m_h^*=0.46m_0$ are employed in the model.[84] The transfer characteristics of the device after 300 °C FG anneal are omitted because of a measurement error. Nonetheless, the devices annealed in FG underwent consecutive anneals at 200 °C, 300 °C, and 400 °C and therefore the 400 °C FG anneal $I_{DS}$–$V_{BG}$ transfer characteristics can be directly compared to those obtained from a separate device after 400 °C UHV anneal.

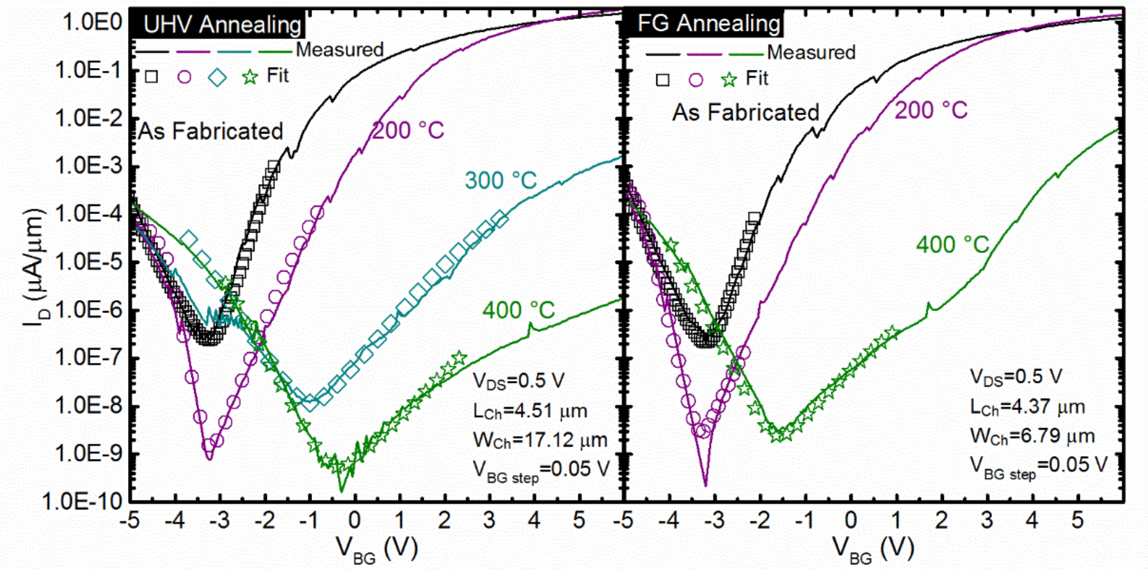

Figure 6.14. Measured $I_{DS}$-$V_{BG}$ transfer curves from Pd–$WSe_2$ back gated FETs after fabrication and subsequent post metallization annealing in either UHV or FG.

Prior to annealing, the $E_F$ is pinned near the middle of the bandgap in contrast with the as–fabricated band alignments extracted from Pd–bulk $WSe_2$ discussed earlier (Figure 6.15). Photoresist residue in the contact regions, which is not present in samples fabricated on bulk $WSe_2$, could play a role in pinning the $E_F$ near midgap in as–fabricated FETs, which would explain the near–midgap $E_F$ position.

According to the analytic Schottky barrier model, the 400 °C FG (UHV) anneal decreases the hole Schottky barrier to 0.10 eV (0.23 eV), corresponding with a significant increase in reverse bias $I_{DS}$ by ~$10^4$ (~$10^3$) (Figure 6.12 b–d). Regardless of annealing ambient, increasing the annealing

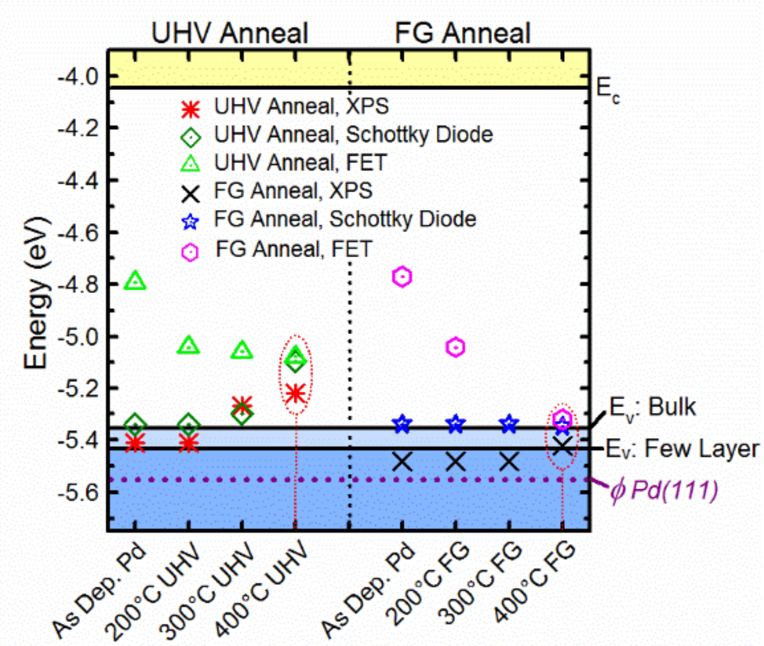

Figure 6.15. Pd–$WSe_2$ band alignment determined by XPS (UHV *, FG ×), Schottky diodes (UHV ◇, FG ★), and FETs (UHV △, FG ⬢) after fabrication and throughout post metallization annealing showing the appreciable hole Schottky barrier formed by the 400 °C UHV anneal and the Ohmic hole band alignment formed by the 400 °C FG anneal in the case of all barrier height extraction techniques.

temperature from 300 °C to 400 °C results in an off state $V_G$ shift of 4–5 V and the saturation current increases by ~$10^2$ (Figure 6.12e), which is consistent with hole–dominant conduction that is enhanced as the annealing temperature increases. The 400 °C FG anneal produces $I_{DS}$–$V_{DS}$ that are linear beyond $V_{DS}$ = -1 V (at $V_{DS}$ = -5 V, $I_{DS,sat}$ = ~5 μA/μm) unlike devices annealed under UHV, which reach saturation around $V_{DS}$ = -1 V. Critically, annealing to 400 °C in FG results in an Ohmic band alignment according to the analytic Schottky barrier model as well as a 10× increase in $I_{ON}/I_{OFF}$ ratio compared with the 0.23 eV hole Schottky barrier and $I_{ON}/I_{OFF}$ achieved at 400 °C under UHV. This confirms an Ohmic hole band alignment is formed by annealing in FG and indicates contact performance greatly improves with increasing $PdSe_x$ concentration. Therefore, Pd–$WSe_2$ contacts annealed under FG conditions will exhibit superior performance compared to UHV annealed or as–deposited Pd–$WSe_2$ contacts (Figures 6.12 and 6.15). Furthermore, annealing in FG at 400 °C decreases the $I_{OFF}$ by $10^2$ compared with the $I_{OFF}$ prior to annealing (Figure 6.14). Interfacial defects passivated by H* during the FG anneal could play a significant role in reducing the $I_{OFF}$. This highlights FG annealing as a critical step to superior Pd–$WSe_2$ contact performance.

Based on the physical and electrical characterization, the $E_F$ shifts according to XPS, Schottky diodes, and FET transfer characteristics, it is clear that a post metallization anneal at 400 °C in FG results in an Ohmic Pd hole contact to $WSe_2$ with reduced performance variability. Furthermore, the $I_{ON}/I_{OFF}$ ratio achieved by annealing Pd–$WSe_2$ transistors in FG ($4 \times 10^6$) is more than an order of magnitude greater than that achieved by annealing under UHV ($1 \times 10^5$). This correlates to an enhanced $PdSe_x$ formation after annealing at 400 °C in FG. The relative concentration ratio of $PdSe_x$:Pd is 2.3 for the FG anneal compared with just 0.7 after annealing at 400 °C in UHV. This work demonstrates Pd–$WSe_2$ interface engineering for high performance Ohmic hole contacts, an applicable strategy in many metal–TMD systems, and represents significant progress towards achieving low power electronics benchmarks.[14]

## 6.5 Conclusions

This work demonstrates Ohmic Pd hole contacts to $WSe_2$ by deliberately forming a $PdSe_x$ interfacial intermetallic and passivating pre–existing defects with hydrogen through post metallization annealing at 400 °C in FG. Furthermore, $PdSe_x$ formation in FG corresponds with a 0.6 eV reduction in hole SBH, $I_{ON}$ increase of $10^4$, and an $I_{OFF}$ decrease by $10^2$ compared with as–fabricated Pd–$WSe_2$ transistors. These metrics highlight the need for the 60 minute 400 °C FG anneal to achieve high performance Pd contacts and suggests hydrogen plays an integral part in defect passivation. XPS indicates ~3× higher $PdSe_x$ concentration and Ohmic band alignment form as a result of the 400 °C FG anneal compared with the $PdSe_x$ concentration and 0.2 eV hole Schottky barrier that form during 400 °C UHV anneal. Raman spectroscopy and STEM corroborate the van der Waals interface formed with $WSe_2$ during RT Pd deposition, representing the first reported experimental observation by STEM of the often theorized van der Waals gap between a non–reactive metal and TMD, and explicitly show a much greater degree of intermixing after FG annealing than after UHV annealing. A sacrificial $WSe_2$ layer in addition to the 400 °C FG anneal is needed to accommodate the $PdSe_x$ formation critical to achieve the high performance Pd contacts to $WSe_2$ demonstrated here. This work shows that a carefully chosen combination of characterization techniques can be leveraged to engineer superior performance in any metal–semiconductor based device beyond the Pd–$WSe_2$ system discussed here. A more comprehensive understanding of the relationships between processing conditions, contact chemistry, and device performance would significantly advance TMD–based technology.

## 6.6 References

(1) Abraham, M.; Mohney, S. E. Annealed Ag Contacts to $MoS_2$ Field-Effect Transistors. *J. Appl. Phys.* **2017**, *122*, 115306.

(2) Wu, Y.; Xiang, J.; Yang, C.; Lu, W.; Lieber, C. M. Single-Crystal Metallic Nanowires and Metal/semiconductor Nanowire Heterostructures. *Nature* **2004**, *430*, 61–65.

(3) Lin, J. C.; Yu, S. Y.; Mohney, S. E. Characterization of Low-Resistance Ohmic Contacts to N- and P-Type InGaAs. *J. Appl. Phys.* **2016**, *114*, 044504.

(4) Walsh, L. A.; Hughes, G.; Weiland, C.; Woicik, J. C.; Lee, R. T. P.; Loh, W. Y.; Lysaght, P.; Hobbs, C. Ni-(In,Ga)As Alloy Formation Investigated by Hard-X-Ray Photoelectron Spectroscopy and X-Ray Absorption Spectroscopy. *Phys. Rev. Appl.* **2014**, *2*, 064010.

(5) Allain, A.; Kang, J.; Banerjee, K.; Kis, A. Electrical Contacts to Two-Dimensional Semiconductors. *Nat. Mater.* **2015**, *14*, 1195–1205.

(6) Prakash, A.; Appenzeller, J. Bandgap Extraction and Device Analysis of Ionic Liquid Gated $WSe_2$ Schottky Barrier Transistors. *ACS Nano* **2017**, *11*, 1626–1632.

(7) Appenzeller, J.; Zhang, F.; Das, S.; Knoch, J. Transition Metal Dichalcogenide Schottky Barrier Transistors: A Device Analysis and Material Comparison. In *2D Materials for Nanoelectronics*; Houssa, M.; Dimoulas, A.; Molle, A., Ed.; Taylor & Francis: New York, 2016; pp. 207–240.

(8) McDonnell, S.; Azcatl, A.; Addou, R.; Gong, C.; Battaglia, C.; Chuang, S.; Cho, K.; Javey, A.; Wallace, R. M. Hole Contacts on Transition Metal Dichalcogenides: Interface Chemistry and Band Alignments. *ACS Nano* **2014**, *8*, 6265–6272.

(9) Chuang, H. J.; Chamlagain, B.; Koehler, M.; Perera, M. M.; Yan, J.; Mandrus, D.; Tománek, D.; Zhou, Z. Low-Resistance 2D/2D Ohmic Contacts: A Universal Approach to High-Performance $WSe_2$, $MoS_2$, and $MoSe_2$ Transistors. *Nano Lett.* **2016**, *16*, 1896–1902.

(10) Cho, S.; Kim, S.; Kim, J. H.; Zhao, J.; Seok, J.; Keum, D. H.; Baik, J.; Choe, D.; Chang, K. J.; Suenaga, K.; et al. Phase Patterning for Ohmic Homojunction Contact in $MoTe_2$. *Science* **2015**, *349*, 625-628.

(11) Kappera, R.; Voiry, D.; Yalcin, S. E.; Branch, B.; Gupta, G.; Mohite, A. D.; Chhowalla, M. Phase-Engineered Low-Resistance Contacts for Ultrathin $MoS_2$ Transistors. *Nat. Mater.* **2014**, *13*, 1128–1134.

(12) Sung, J. H.; Heo, H.; Si, S.; Kim, Y. H.; Noh, H. R.; Song, K.; Kim, J.; Lee, C.-S.; Seo, S.-Y.; Kim, D.-H.; et al. Coplanar Semiconductor–metal Circuitry Defined on Few-Layer $MoTe_2$ via Polymorphic Heteroepitaxy. *Nat. Nanotechnol.* **2017**, *12*, 1064-1070.

(13) Liu, W.; Kang, J.; Sarkar, D.; Khatami, Y.; Jena, D.; Banerjee, K. Role of Metal Contacts in Designing High-Performance Monolayer N-Type $WSe_2$ Field Effect Transistors. *Nano Lett.* **2013**, *13*, 1983–1990.

(14) Fang, H.; Chuang, S.; Chang, T. C.; Takei, K.; Takahashi, T.; Javey, A. High-Performance Single Layered $WSe_2$ P-FETs with Chemically Doped Contacts. *Nano Lett.* **2012**, *12*, 3788–3792.

(15) Allain, A.; Kis, A. Electron and Hole Mobilities in Single-Layer $WSe_2$. *ACS Nano* **2014**, *8*, 7180–7185.

(16) Tosun, M.; Chuang, S.; Fang, H.; Sachid, A. B.; Hettick, M.; Lin, Y. High-Gain Inverters Based on $WSe_2$ Complementary Field-Effect Transistors. *ACS Nano* **2014**, *8*, 4948–4953.

(17) Das, S.; Appenzeller, J. $WSe_2$ Field Effect Transistors with Enhanced Ambipolar Characteristics $WSe_2$ Field Effect Transistors with Enhanced Ambipolar Characteristics. *Appl. Phys. Lett.* **2013**, *103*, 103501.

(18) Liu, B.; Ma, Y.; Zhang, A.; Chen, L.; Abbas, A. N.; Liu, Y.; Shen, C.; Wan, H.; Zhou, C. High-Performance $WSe_2$ Field-Effect Transistors via Controlled Formation of In-Plane Heterojunctions. *ACS Nano* **2016**, *10*, 5153–5160.

(19) Xu, S.; Wu, Z.; Lu, H.; Han, Y.; Long, G.; Chen, X.; Han, T.; Ye, W.; Wu, Y.; Lin, J.; et al. Universal Low-Temperature Ohmic Contacts for Quantum Transport in Transition Metal Dichalcogenides. *2D Mater.* **2016**, *3*, 21007.

(20) Lin, Y.-C.; Jariwala, B.; Bersch, B. M.; Xu, K.; Nie, Y.; Wang, B.; Eichfeld, S. M.; Zhang, X.; Choudhury, T. H.; Pan, Y.; et al. Realizing Large-Scale, Electronic-Grade Two-Dimensional Semiconductors. *ACS Nano* **2018**, *12*, 965-975.

(21) Zhao, P.; Kiriya, D.; Azcatl, A.; Zhang, C.; Tosun, M.; Liu, Y.; Hettick, M.; Kang, J. S.; Mcdonnell, S.; et al. Air Stable P‑Doping of $WSe_2$ by Covalent Functionalization. *ACS Nano* **2014**, *8*, 10808–10814.

(22) Wang, S.; Zhao, W.; Giustiniano, F.; Eda, G. Effect of Oxygen and Ozone on P-Type Doping of Ultra-Thin $WSe_2$ and $MoSe_2$ Field Effect Transistors. *Phys. Chem. Chem. Phys.* **2016**, *18*, 4304–4309.

(23) Schottky, W. Halbleitertheorie Der Sperrschicht. *Physik* **1938**, *26*, 843.

(24) Das, S.; Chen, H. Y.; Penumatcha, A. V.; Appenzeller, J. High Performance Multilayer $MoS_2$ Transistors with Scandium Contacts. *Nano Lett.* **2013**, *13*, 100–105.

(25) Kim, C.; Moon, I.; Lee, D.; Choi, M. S.; Ahmed, F.; Nam, S.; Cho, Y.; Shin, H. J.; Park, S.; Yoo, W. J. Fermi Level Pinning at Electrical Metal Contacts of Monolayer Molybdenum Dichalcogenides. *ACS Nano* **2017**, *11*, 1588–1596.

(26) Addou, R.; McDonnell, S.; Barrera, D.; Guo, Z.; Azcatl, A.; Wang, J.; Zhu, H.; Hinkle, C. L.; Quevedo-Lopez, M.; Alshareef, H. N.; et al. Impurities and Electronic Property Variations of Natural $MoS_2$ Crystal Surfaces. *ACS Nano* **2015**, *9*, 9124–9133.

(27) McDonnell, S.; Addou, R.; Buie, C.; Wallace, R. M.; Hinkle, C. L. Defect Dominated Doping and Contact Resistance in $MoS_2$. *ACS Nano* **2014**, *8*, 2880–2888.

(28) Park, J. H.; Vishwanath, S.; Liu, X.; Zhou, H.; Eichfeld, S. M.; Fullerton-Shirey, S. K.; Robinson, J. A.; Feenstra, R. M.; Furdyna, J.; Jena, D.; et al. Scanning Tunneling Microscopy and Spectroscopy of Air Exposure Effects on Molecular Beam Epitaxy Grown $WSe_2$ Monolayers and Bilayers. *ACS Nano* **2016**, *10*, 4258–4267.

(29) Smyth, C. M.; Addou, R.; McDonnell, S.; Hinkle, C. L.; Wallace, R. M. Contact Metal-$MoS_2$ Interfacial Reactions and Potential Implications on $MoS_2$-Based Device Performance. *J. Phys. Chem. C* **2016**, *120*, 14719–14729.

(30) Smyth, C. M.; Addou, R.; McDonnell, S.; Hinkle, C. L.; Wallace, R. M. $WSe_2$-Contact Metal Interface Chemistry and Band Alignment under High Vacuum and Ultra High Vacuum Deposition Conditions. *2D Mater.* **2017**, *4*, 025084.

(31) McDonnell, S.; Smyth, C.; Hinkle, C. L.; Wallace, R. M. $MoS_2$-Titanium Contact Interface Reactions. *ACS Appl. Mater. Interfaces* **2016**, *8*, 8289–8294.

(32) English, C. D.; Shine, G.; Dorgan, V. E.; Saraswat, K. C.; Pop, E. Improved Contacts to $MoS_2$ Transistors by Ultra-High Vacuum Metal Deposition. *Nano Lett.* **2016**, *16*, 3824–3830.

(33) Bulk $WSe_2$ crystals, HQ Graphene, 2017; www.hqgraphene.com.

(34) Wallace, R. M. In-Situ Studies of Interfacial Bonding of High-K Dielectrics for CMOS Beyond 22 nm. *ECS Trans.* **2008**, *16*, 255–271.

(35) Wallace, R. M. In-Situ Studies on 2D Materials. *ECS Trans.* **2014**, *64*, 109–116.

(36) ASTM E2108-10 Standard Practice for Calibration of the Electron Binding-Energy Scale of an X-Ray Photoelectron Spectrometer, **2000**.

(37) Herrera-Gómez, A.; Hegedus, A.; Meissner, P. L. Chemical Depth Profile of Ultrathin Nitrided $SiO_2$ Films. *Appl. Phys. Lett.* **2002**, *81*, 1014–1016.

(38) Moulder, J. F.; Stickle, W. F.; Sobol, P. E.; Bomben, K. D. *Handbook of X-Ray Photoelectron Spectroscopy*; Chastain, J., Ed.; Eden Prairie, **1992**.

(39) BJD 1800 Temescal e-beam evaporator, University of Texas at Dallas Cleanroom, 2016; http://www.utdallas.edu/research/cleanroom/.

(40) Horcas, I.; Fernández, R.; Gómez-Rodríguez, J. M.; Colchero, J.; Gómez-Herrero, J.; Baro, A. M. WSXM: A Software for Scanning Probe Microscopy and a Tool for Nanotechnology. *Rev. Sci. Instrum.* **2007**, *78*.

(41) Mountain, B. W.; Wood, S. A. Chemical Controls on the Solubility, Transport, and Deposition of Platinum and Palladium in Hydrothermal Solutions: A Thermodynamic Approach. *Econ. Geol.* **1988**, *83*, 492–510.

(42) Ake, O.; Nolang, B.; Osadchii, E. G.; Ohman, L-O.; Rosen, E. *Chemical Thermodynamics of Selenium* ed Mompean, F. J. et al. **2005** (Amsterdam, The Netherlands, Elsevier B. V.)

(43) $\Delta G^{\circ}_{f}$ referred to in this work are given per anionic constituent within each relevant compound.

(44) Dong, H.; Gong, C.; Addou, R.; McDonnell, S.; Azcatl, A.; Qin, X.; Wang, W.; Wang, W.-H.; Hinkle, C. L.; Wallace, R. M. Schottky Barrier Height of Pd/$MoS_2$ Contact by Large Area Photoemission Spectroscopy. *ACS Appl. Mater. Interfaces* **2017**, *9*, 38977-38983.

(45) Voogt, E. H.; Mens, A. J. M.; Gijzeman, O. L. J.; Geus, J. W. XPS Analysis of Palladium Oxide Layers and Particles. *Surf. Sci.* **1996**, *350*, 21–31.

(46) Doniach, S.; Sunjic, M. Many-Electron Singularity in X-ray Photoemission and X-ray Line Spectra from Metals. *J. Phys. C: Solid State Phys.* **1970**, *3*, 285-291.

(47) Gong, C.; McDonnell, S.; Qin, X.; Azcatl, A.; Dong, H.; Chabal, Y. J.; Cho, K.; Wallace, R. M. Realistic Metal-Graphene Contact Structures. *ACS Nano* **2014**, *8*, 642–649.

(48) R. C. Weast, D. R. Lide, M. J. Astle, W. H. B. Selected Values of Chemical Thermodynamic Properties. In *CRC Handbook of Chemistry and Physics*; CRC Press: Boca Raton, FL, **1995**.

(49) Kang, J.; Liu, W.; Sarkar, D.; Jena, D.; Banerjee, K. Computational Study of Metal Contacts to Monolayer Transition-Metal Dichalcogenide Semiconductors. *Phys. Rev. X* **2014**, *4*, 031005.

(50) Walsh, L. A.; Smyth, C. M.; Barton, A. T.; Wang, Q.; Che, Z.; Yue, R.; Kim, J.; Kim, M. J.; Wallace, R. M.; Hinkle, C. L. Interface Chemistry of Contact Metals and Ferromagnets on the Topological Insulator $Bi_2Se_3$. *J. Phys. Chem. C* **2017**, *121*, 23551-23563.

(51) Pauling, L. The Nature of the Chemical Bond. *J. Am. Chem. Soc.* **1931**, *53* (4), 1367-1400.

(52) Kukunuri, S.; Austeria, P. M.; Sampath, S. Electrically Conducting Palladium Selenide ($Pd_4Se$, $Pd_{17}Se_{15}$, $Pd_7Se_4$) Phases: Synthesis and Activity towards Hydrogen Evolution Reaction. *Chem. Commun.* **2016**, *52*, 206–209.

(53) Naidu, S. V. N.; Rao, P. R. The Pd-W (Palladium-Tungsten) System. In *Monograph Series on Alloy Phase Diagrams: Phase Diagrams of Binary Tungsten Alloys*; Nagender, S. V. N.; Rao, P. R., Ed.; India Institute of Metals, Calcutta, **1991**.

(54) Nan, H.; Wang, Z.; Wang, W.; Liang, Z.; Lu, Y.; Chen, Q.; He, D.; Tan, P.; Miao, F.; Wang, X.; et al. Strong Photoluminescence Enhancement of $MoS_2$ through Defect Engineering and Oxygen Bonding. *ACS Nano* **2014**, *8*, 5738–5745.

(55) Tongay, S.; Suh, J.; Ataca, C.; Fan, W.; Luce, A.; Kang, J. S.; Liu, J.; Ko, C.; Raghunathanan, R.; Zhou, J.; et al. Defects Activated Photoluminescence in Two-Dimensional Semiconductors: Interplay between Bound, Charged and Free Excitons. *Sci. Rep.* **2013**, *3*, 2657.

(56) Zhao, P.; Azcatl, A.; Bolshakov, P.; Moon, J.; Hinkle, C. L.; Hurley, P. K.; Wallace, R. M.; Young, C. D. Effects of Annealing on Top-Gated $MoS_2$ Transistors with $HfO_2$ Dielectric. *J. Vac. Sci. Technol. B, Nanotechnol. Microelectron. Mater. Process. Meas. Phenom.* **2017**, *35*, 01A118.

(57) Kim, J.; Chung, Y. M.; Kang, S. M.; Choi, C. H.; Kim, B. Y.; Kwon, Y. T.; Kim, T. J.; Oh, S. H.; Lee, C. S. Palladium Nanocatalysts Immobilized on Functionalized Resin for the Direct Synthesis of Hydrogen Peroxide from Hydrogen and Oxygen. *ACS Catal.* **2012**, *2*, 1042–1048.

(58) Pentland, N.; Bockris, J. O'M.; Sheldon, E. Hydrogen Evolution Reaction on Copper, Gold, Molybdenum, Palladium, Rhodium, and Iron. *J. Electrochem. Soc.* **1957**, *104*, 182-194.

(59) Luo, Y-R. In *Comprehensive Handbook of Chemical Bond Energies*; CRC Press, Taylor & Francis Group: Boca Raton, FL, **2007**.

(60) Sevy, A.; Huffaker, R. F.; Morse, M. D. Bond Dissociation Energies of Tungsten Molecules: WC, WSi, WS, WSe, and WCl. *J. Phys. Chem. A.* **2017**, *121*, 9446-9457.

(61) Gibson, S. T.; Greene, J. P.; Berkowitz, J. A Photoionization Study of HSe and $H_2Se$. *J. Chem. Phys.* **1986**, *85*, 4815.

(61) Amani, M.; Lien, D.; Kiriya, D.; Xiao, J.; Azcatl, A.; Noh, J.; Madhvapathy, S. R.; Addou, R.; KC, S.; Dubey, M.; et al. Near-Unity Photoluminescence Quantum Yield in $MoS_2$. *Science* **2015**, *350*, 1065–1068.

(62) Chen, C.-H.; Wu, C.-L.; Pu, J.; Chiu, M.-H.; Kumar, P.; Takenobu, T.; Li, L.-J. Hole Mobility Enhancement and P-Doping in Monolayer $WSe_2$ by Gold Decoration. *2D Mater.* **2014**, *1*, 034001.

(63) Gong, C.; Huang, C.; Miller, J.; Cheng, L.; Hao, Y.; Cobden, D.; Kim, J.; Ruoff, R. S.; Wallace, R. M.; Cho, K.; et al. Metal Contacts on Physical Vapor Deposited Monolayer $MoS_2$. *ACS Nano* **2013**, *7*, 11350–11357.

(64) Yuan, H.; Cheng, G.; You, L.; Li, H.; Zhu, H.; Li, W.; Kopanski, J. J.; Obeng, Y. S.; Hight Walker, A. R.; Gundlach, D. J.; et al. Influence of Metal-$MoS_2$ Interface on $MoS_2$ Transistor Performance: Comparison of Ag and Ti Contacts. *ACS Appl. Mater. Interfaces* **2015**, *7*, 1180–1187.

(65) Tran Khac, B. C.; Jeon, K. J.; Choi, S. T.; Kim, Y. S.; Delrio, F. W.; Chung, K. H. Laser-Induced Particle Adsorption on Atomically Thin $MoS_2$. *ACS Appl. Mater. Interfaces* **2016**, *8*, 2974–2984.

(66) Parkin, W. M.; Balan, A.; Liang, L.; Das, P. M.; Lamparski, M.; Naylor, C. H.; Rodríguez-Manzo, J. A.; Johnson, A. T. C.; Meunier, V.; Drndić, M. Raman Shifts in Electron-Irradiated Monolayer $MoS_2$. *ACS Nano* **2016**, *10*, 4134–4142.

(67) Zhao, W.; Ghorannevis, Z.; Amara, K. K.; Pang, J. R.; Toh, M.; Zhang, X.; Kloc, C.; Tan, P. H.; Eda, G. Lattice Dynamics in Mono- and Few-Layer Sheets of $WS_2$ and $WSe_2$. *Nanoscale* **2013**, *5*, 9677.

(68) O'Brien, M.; McEvoy, N.; Hanlon, D.; Hallam, T.; Coleman, J. N.; Duesberg, G. S. Mapping of Low-Frequency Raman Modes in CVD-Grown Transition Metal Dichalcogenides: Layer Number, Stacking Orientation and Resonant Effects. *Sci. Rep.* **2016**, *6*, 19476.

(69) Sahin, H.; Tongay, S.; Horzum, S.; Fan, W.; Zhou, J.; Li, J.; Wu, J.; Peeters, F. M. Anomalous Raman Spectra and Thickness-Dependent Electronic Properties of $WSe_2$. *Phys. Rev. B - Condens. Matter Mater. Phys.* **2013**, *87*, 165409.

(70) Shi, W.; Lin, M.-L.; Tan, Q.-H.; Qiao, X.-F.; Zhang, J.; Tan, P.-H. Raman and Photoluminescence Spectra of Two-Dimensional Nanocrystallites of Monolayer $WS_2$ and $WSe_2$. *2D Mater.* **2016**, *3*, 025016.

(71) Dutta, B N; Dayal, B. Lattice Constants and Thermal Expansion of Palladium and Tungsten up to 878°C by X-Ray Method. *Phys. Status Solidi(b)* **1963**, *3*, 2253–2259.

(72) Michaelson, H. B. The Work Function of the Elements and Its Periodicity. *J. Appl. Phys.* **1977**, *48*, 4729–4733.

(73) Schleich, B.; Schmeisser, D.; Göpel, W. Structure and Reactivity of the System $Si/SiO_2/Pd$: A Combined XPS, UPS and HREELS Study. *Surf. Sci.* **1987**, *191*, 367–384.

(74) Wang, Y.; Yang, R. X.; Quhe, R.; Zhong, H.; Cong, L.; Ye, M.; Ni, Z.; Song, Z.; Yang, J.; Shi, J.; et al. Does P-Type Ohmic Contact Exist in $WSe_2$–metal Interfaces? *Nanoscale* **2016**, *8*, 1179–1191.

(75) Somvanshi, D.; Kallatt, S.; Venkatesh, C.; Nair, S.; Gupta, G.; Anthony, J. K.; Karmakar, D.; Majumdar, K. Nature of Carrier Injection in metal/2D Semiconductor Interface and Its Implications for the Limits of Contact Resistance. *Phys. Rev. B* **2017**, *96*, 025423.

(76) The separation between the $WSe_2$ chemical state in the Se 3*d* and W 4*f* core level spectra were held constant in all fits and therefore the $WSe_2$ state in the W 4*f* core level spectra is omitted from Figure 6.10a.

(77) Huang, B.; Yoon, M.; Sumpter, B. G.; Wei, S. H.; Liu, F. Alloy Engineering of Defect Properties in Semiconductors: Suppression of Deep Levels in Transition-Metal Dichalcogenides. *Phys. Rev. Lett.* **2015**, *115*, 126806.

(78) Addou, R.; Wallace, R. M. Surface Analysis of $WSe_2$ Crystals: Spatial and Electronic Variability. *ACS Appl. Mater. Interfaces* **2016**, *8*, 26400–26406.

(79) Tung, R. T. Electron Transport of Inhomogeneous Schottky Barriers. *Appl. Phys. Lett.* **1991**, *58* (24), 2821-2823.

(80) Kim, K.; Larentis, S.; Fallahazad, B.; Lee, K.; Xue, J.; Dillen, D. C.; Corbet, C. M.; Tutuc, E. Band Alignment in $WSe_2$–Graphene Heterostructures. *ACS Nano*, **2015**, *9* (4), 4527-4532.

(81) D. K. Schroder, Semiconductor Material and Device Characterization, 3rd Ed., John Wiley & Sons, Inc., NJ, USA 2006.

(82) Klein, A.; Pettenkofer, C.; Jaegermann, W.; Lux-Steiner, M.; Bucher, E. A Photoemission Study of Barrier and Transport Properties of the Interfaces of Au and Cu with $WSe_2$(0001) Surfaces. *Surf. Sci.*, **1994**, *321*, 19-31.

(83) Penumatcha, A. V. Salazar, R. B.; Appenzeller, J. Analysing Black Phosphorous Transistors Using an Analytic Schottky Barrier MOSFET Model. *Nat. Commun.* **2015**, *6*, 8948.

(84) Liu, W.; Cao, W.; Kang, J.; Banerjee, K. High–Performance Field–Effect–Transistors on Monolayer $WSe_2$. *ECS Trans.* **2013**, *58* (7), 281-285.

# CHAPTER 7

# ENGINEERING THE INTERFACE CHEMISTRY FOR N-TYPE SCANDIUM CONTACTS TO HIGH–PERFORMANCE WSE$_2$ DEVICES

Authors – Christopher M. Smyth[†], Lee A. Walsh[‡], Pavel Bolshakov[†], Massimo Catalano[†§], Michael Schmidt[‡], Brendan Sheehan[‡], Rafik Addou[†], Luhua Wang[†], Jiyoung Kim[†], Moon J. Kim[†], Chadwin D. Young[†], Christopher L. Hinkle[†], and Robert M. Wallace[†]

[†]The Department of Materials Science and Engineering, RL10
The University of Texas at Dallas
800 West Campbell Road
Richardson, Texas, 75080, USA

[‡]Tyndall National Institute
University College Cork
Lee Maltings, Prospect Row
Cork, Ireland

[§]CNR IMM, Institute for Microelectronics and Microsystems
Via Monteroni, I-73100
Lecce, Italy

## 7.1 Preface

Sc has been employed as an electron contact to a number of two–dimensional (2D) materials (e.g., $MoS_2$, black phosphorous) and has enabled, at times, the lowest electron contact resistance. However, the extremely reactive nature of Sc leads to stringent processing requirements and metastable device performance with no true understanding of how to achieve consistent, high–performance Sc contacts. In this work, $WSe_2$ transistors with impressive subthreshold slope (109 mV/dec) and $I_{ON}/I_{OFF}$ ($10^6$) are demonstrated without post metallization processing by depositing Sc contacts in ultra–high vacuum at room temperature (RT). The lowest electron Schottky barrier height (SBH) is achieved by mildly oxidizing the $WSe_2$ *in–situ* before metallization, which minimizes reactions between Sc and $WSe_2$. Post metallization anneals in reducing environments (ultra–high vacuum, forming gas) degrade the $I_{ON}/I_{OFF}$ by $\sim 10^3$ and increase the subthreshold slope by a factor of 10. X–ray photoelectron spectroscopy indicates the anneals increase the electron SBH by 0.4-0.5 eV and correspondingly convert 100% of the deposited Sc contacts to selenium–based intermetallic or highly resistive scandium oxide. Raman spectroscopy and scanning transmission electron microscopy highlight the highly exothermic reactions between Sc and $WSe_2$ consume at least one layer upon deposition at RT and at least three layers after the 400 °C anneals in either ultra–high vacuum or forming gas, necessitating multiple sacrificial $WSe_2$ layers during fabrication. Scanning tunneling microscopy/spectroscopy elucidate the enhanced local density of states below the $WSe_2$ Fermi level around individual Sc atoms in the $WSe_2$ lattice, which directly connects the scandium selenide intermetallic with the unexpectedly large electron SBH measured from the transistor transfer characteristics. The interface chemistry and structural properties are correlated with Sc–$WSe_2$ transistor and diode performance. The recommended combination of processing conditions and steps is provided to facilitate consistent Sc contacts to any 2D material. In this work, Dr. L. A. Walsh played an integral part in data interpretation and experimental design. P. Bolshakov fabricated the FETs, performed device measurements, and assisted in interpreting the electrical characteristics of the FETs under the supervision of Prof. C. D. Young. Dr. M. Catalano obtained the TEM and EDS at UTD and assisted in image and spectra interpretation under the supervision of Prof. M. J. Kim. Dr. M. Schmidt and Dr. B. Sheehan milled lamella from Pd–Sc–$WSe_2$ Schottky diodes and performed TEM at Tyndall Nat'l. Inst. I am extremely grateful for their generous allocation of equipment time and expertise. L. Wang milled lamella from select Si–Sc–$WSe_2$–$SiO_2$–Si samples and trained me on the FIB instrument under the supervision of Prof. M. J. Kim. The Raman spectra were obtained by myself under the supervision of Prof. J. Kim. The Schottky diodes were fabricated and characterized electrically by myself under the supervision of Drs. C. L. Hinkle and R. M. Wallace. Dr. R. Addou and the rest of the authors provided inputs while preparing the manuscript. Andrew C. Yu (MIT) and Dr. Michal. J. Mleczko (Intel) are acknowledged for useful discussions regarding the analytical Schottky barrier fitting procedure, the Landauer theory behind the model, and the MATLAB code used for fitting under the supervision of Prof. Eric Pop (Stanford U.).

### 7.2 Introduction

Continuous engineering of contacts compatible with state of the art semiconductor technology relies upon a detailed understanding of the critical relationships between processing conditions, interface chemistry and structure, and contact performance.[1] Silicides[2] and salicides[3,4] exhibit a broad spectrum of composition–dependent contact resistances ($R_c$) and have long been employed as standard, low resistance contacts in traditional (Si, Ge) and compound (e.g., InGaAs) semiconductor–based CMOS technologies. Similar interface engineering has only recently been explored to improve Pd contacts to $WSe_2$,[5] a semiconducting member of the transition metal dichalcogenide (TMD) family of two–dimensional (2D) materials, and is a promising, versatile strategy to engineer high performance contacts comparable with Si technology ($R_c \approx 50$ Ω-cm).[6] High defect concentrations ($> 10^{18}$ $cm^{-3}$),[7-9] metal–TMD and metal–ambient gas reaction products,[10-12] and spurious electrostatic effects[13,14] often manifest as strong $E_F$ pinning[15] and/or large parasitic $R_c$, which can convolute the intrinsic properties (e.g., mobility) of a TMD–based device.[16,17] A number of strategies have been employed to reduce $R_c$ to TMDs, with varying degrees of success.[18-23] However, many are incompatible with typical back–end–of–line process flows and direct metallization in top contacted devices is preferred. Impressive electron contact performance in $MoS_2$ and black phosphorous (BP) devices has been demonstrated with Sc contacts.[24-26] However, Sc has yet to be explored as a contact metal in $WSe_2$–based devices. Furthermore, the highly reactive nature of Sc lends to processing difficulties and metastable device performance.[25,26] Sc spontaneously forms scandium oxide, a high–κ dielectric with a 5–6 eV band gap,[27] even in ultra–high vacuum (UHV) conditions[10] and when a capping layer is employed to limit spurious air–exposure induced effects.[25] The electrical properties of scandium oxide depend largely on the defect concentration, which can vary significantly depending on the processing conditions.[10,25,27] Therefore, engineering high performance Sc contacts to $WSe_2$ require a detailed understanding of the relationship between processing conditions, interface chemistry, and Sc contact performance.

$WSe_2$ is also a promising alternative 2D switch in state–of–the–art magnetoresistive random–access memory technology due to the giant spin splitting in the valence band (456 meV),[28] moderate hole mobility,[15] and low switching power. Spin–torque transfer based on the spin–valley Hall effect in $WSe_2$ has emerged as a preferred magnetic bit–writing method in analogous devices[29] but relies on a single $WSe_2$ layer, which can experience catastrophic damage during processing. Before the technology can be integrated in commercial applications, the effects of common back–end–of–line processing conditions on the integrity of the $WSe_2$ monolayer must be quantified.

In this work, we establish relationships between processing conditions (deposition chamber ambient, post metallization annealing temperature and ambient), interface chemistry, and band alignment in the Sc–$WSe_2$ system with *in–situ* XPS experiments. The number of $WSe_2$ layers consumed by reactions with Sc after fabrication, 300 °C post metallization anneals, and as a function of time between fabrication and characterization are quantified with Raman spectroscopy, scanning tunneling electron microscopy (STEM), and energy dispersive X-ray spectroscopy (EDS). Scanning tunneling microscopy/spectroscopy (STM/STS) elucidate the effects of Sc atoms on the local density of $WSe_2$ surface states, providing insight into the extracted band alignment. We demonstrate moderate $E_F$ depinning in metal–$WSe_2$ systems by deliberate growth of a $Sc_xO_y$ depinning layer at the contact–$WSe_2$ interface. Finally, we evaluate the electrical performance of UHV–deposited Sc contacts to $WSe_2$ field effect transistors (FETs) as a function of post metallization annealing conditions. Recommendations are provided to preserve the high performance Sc electron contacts to $WSe_2$ and to alleviate $E_F$ pinning in metal–$WSe_2$ systems, which are based upon the impressive FET performance metrics and band alignment control demonstrated here.

## 7.3 Experimental Details

*Metal Deposition, Post–Metallization Annealing, and* in-situ *Characterization.*

a) Single Deposition Step Under UHV or HV Conditions: All $WSe_2$ samples throughout this work were obtained from synthetic, bulk $WSe_2$ crystals grown by HQ Graphene.[30] Prior to deposition under UHV (base/deposition pressure $< 2 \times 10^{-9}/7 \times 10^{-9}$ mbar) or HV (base/deposition pressure $< 2 \times 10^{-9}/5 \times 10^{-6}$ mbar) conditions, the bulk $WSe_2$ and Sc source were prepared and the metal deposition rates and reference metal core level spectra were obtained identical to that employed in similar work described in Appendixes A and B.[10,11] The Sc deposition in HV was performed in the same deposition chamber as the depositions performed in UHV. The deposition in HV was performed by first ramping the filament current up to the deposition current under UHV conditions, then backfilling the chamber with air to a pressure of $5 \times 10^{-6}$ mbar, and finally opening the shutters to start the deposition. This method permits *in–situ* characterization by XPS after Sc deposition in HV unlike when the deposition is performed *ex–situ*. The reference Sc 2*p* core level spectrum was obtained *in–situ* from a 50 nm thick Sc film evaporated onto HOPG at RT in UHV. The surface chemistry was probed with XPS after exfoliation and *in–situ* after subsequent metal depositions.

b) Step–wise Deposition and Post–Metallization Annealing: The metal source was outgassed, deposition rate was determined, Sc was stepwise deposited, and subsequent post metallization anneals were performed using the same procedures as were employed in analogous experiments of the Pd–$WSe_2$ system (see Section 6.3). The stoichiometry of bulk $WSe_2$ and any other reaction products referred to in the main text were calculated using appropriate relative sensitivity factors for the W 4*f*, Se 3*d*, and Sc 2*p* core levels (2.959, 0.722, and 1.678, respectively, with all three reflecting both spin orbit split peaks in each of the aforementioned core levels).[31] These relative sensitivity factors apply to the particular XPS instrument employed in this study. Dividing the integrated intensity of core level spectra corresponding with the elements in a compound by these sensitivity factors permits estimation of stoichiometry and overall elemental concentration. Stoichiometry ratios calculated employing the above described method are accompanied by a ±0.2 error. The cluster tool in which deposition and analysis were performed is described in Chapter 2.[32,33]

*XPS Instrumentation, Parameters, and Data Analysis.* XPS characterization was performed via a monochromated Al Kα source and Omicron EA125 hemispherical analyzer with ±0.05 eV resolution. In addition, a takeoff angle of 45°, acceptance angle of 8°, and pass energy of 15 eV were employed during high-resolution spectral acquisition. The analyzer was calibrated with polycrystalline Au, Ag, and Cu foils according to ASTM E1208.[34] Spectra were deconvolved using AAnalyzer,[35] a curve fitting software.

*Quantifying Layer Number Consumption: Sample Fabrication and Characterization.* The Si/Sc/$WSe_2$/$SiO_2$/Si flakes were prepared and characterized using the same procedure as was employed in preparing the Si/Pd/$WSe_2$/$SiO_2$/Si samples described in Chapter 6 (see Section 6.2). Special care was taken to ensure full coverage 5 nm thick Sc films were deposited on the $WSe_2$ flakes and (see Appendix E). Separate samples were annealed after metallization *in–situ* in UHV or FG at 300 °C for 1 hr. Immediately following metal deposition and post metallization annealing (where applicable), a full coverage 10 nm thick Si capping layer was deposited *in–situ* to protect Sc–$WSe_2$ samples from spurious air–exposure induced chemical reactions during *ex–situ* Raman spectroscopy. The anneals were performed before depositing the Si cap to prevent intermixing between Si and the underlying Sc–$WSe_2$ heterostructure at elevated temperatures.

The laser parameters employed in the Raman spectroscopy performed in this chapter are identical to those employed in the work discussed in Chapter 6. These parameters were carefully tuned to prevent laser induced damage to $WSe_2$ (see Section 6.4.1.4).

Raman spectra were deconvolved with the peak fitting software AAnalyzer to rigorously determine Raman shifts. Peak shapes were defined by a combination of Gaussian and Lorentzian functions. The Lorentzian contribution was held constant for each set of spectra representing a certain number of $WSe_2$ layers from a given sample.

*High Resolution STEM and EDS.*

a) Lamella were milled from the $Si/Sc/WSe_2/SiO_2$ samples fabricated for characterization by Raman spectroscopy using a FIB microscope (FEI Nova 200 Dual Beam). High resolution STEM was performed in an aberration corrected JEM-ARM200F instrument operated at 200 kV. Images were obtained using annular bright field and high angle annular dark field (HAADF) modes. EDS experiments were performed in an Aztec Energy Advanced Microanalysis System according to the procedure outlined in detail elsewhere.[33]

b) A lamella from a 65 nm Pd/3 nm $Sc/WSe_2$ diode treated with AH (see below for details) was cross sectioned using an FEI Dual Beam Helios Nanolab 600i SEM/FIB microscope. High resolution annular bright field TEM images were obtained with a JEOL 2100 operated at 200 kV.

*Device Fabrication.*

a) Back-gated field effect transistors were fabricated and characterized using the same procedures and instruments as were employed in the work described in Chapter 6 (see Section 6.3). However 20 nm Sc/50 nm Pd/150 nm Au contacts were employed in this work (unless otherwise defined).

b) Schottky Diodes: A bulk $WSe_2$ crystal with mirror-like surface (lowest possible surface defect density) was exfoliated and loaded into a UHV cluster tool.[32,33] Select samples were treated with AH *in–situ* prior to metallization. Sc/65 nm Pd contacts (see Section 7.4.3 for Sc thickness details) were deposited in UHV followed by 100 nm Au deposited *ex–situ* in an elastomer sealed Temescal BJD–1800[36] (base pressure $< 5 \times 10^{-6}$ mbar) to form periodic arrays of circular Sc/Pd/Au contact pads (diameters = 50, 100, 200 μm) across the $WSe_2$. Forward and reverse bias I-V curves were obtained by sweeping from 0 to 2 V and 0 to -2 V (0.01 V step), respectively, to avoid hysteresis effects. Measurements were obtained after metallization and subsequent anneals in FG (1 mbar) at 200 °C, 300 °C, and 400 °C.

*Atomic Hydrogen Treatment.* A hydrogen atom beam source (HABS 40, MBE Komponenten, Germany) with tungsten filament was operated at a filament temperature of 1500 °C and a constant $H_2$ flow (99.9999% purity) maintained at a partial pressure of $5 \times 10^{-6}$ mbar using a precision leak valve. The bulk $WSe_2$ samples were maintained at a substrate temperature of 300 °C throughout the treatment, which was performed for 45 minutes. After the treatment and cooling to RT, the surface chemistry was checked with XPS. Contacts were then deposited *in–situ*.

*Scanning Tunneling Microscopy and Spectroscopy.* A bulk $WSe_2$ crystal was exfoliated and loaded into a UHV cluster tool described in Section 2.1.[33] The STM/STS images and spectra were acquired at RT in the constant current mode using an etched tungsten tip. Imaging under positive (negative) bias probes filled (empty) surface states within a few eV of the $E_F$. The conductance (*dI/dV* versus V) curves obtained in this work are each differentiated averages of 20 curves obtained sequentially at a single location. STM images are processed in the WSxM software.[31]

## 7.4 Results and Discussion

### 7.4.1 Effects of Processing Conditions on the Sc–$WSe_2$ Interface Chemistry and Structure

*Highly Exothermic Reactions between Sc, $WSe_2$, and Background Gases in Vacuum*

The metal–semiconductor interface chemistry can vary significantly with the deposition chamber base pressure and the deposition rate.[10-12,37] According to the kinetic theory of gases, the impingement rate of background gases on the substrate during deposition in high vacuum (HV) is sufficiently high for continuous metal oxidation on the substrate surface. In addition, the reaction products formed between highly reactive metals, such as Sc, and TMDs also undergo exothermic reactions with the background ambient, complicating the interface chemistry further.

Sc aggressively reacts with $WSe_2$ when deposited at room temperature (RT) regardless of the deposition chamber base pressure. Figure 7.1a shows the Se 3*d* and W 4*f* core level spectra obtained from exfoliated, bulk $WSe_2$ after depositing ~1 nm Sc at RT in UHV or HV. When deposited in UHV, Sc completely reduces $WSe_2$ to form metallic W and $ScSe_x$. The presence of metallic W is confirmed by the binding energy of the asymmetrically shaped low binding energy (BE) chemical state in the corresponding W 4*f* core level spectrum (W $4f_{7/2}$ BE = 31.30 eV), which is in close agreement with that of a metallic W reference (see Appendix B for details regarding the metallic W reference). The $ScSe_x$ chemical state in the Se 3*d* core level spectrum is detected at lower BE from the $WSe_2$ chemical state, which is expected considering the electronegativity of Sc (1.36) is much less than that of W (2.36).[38]

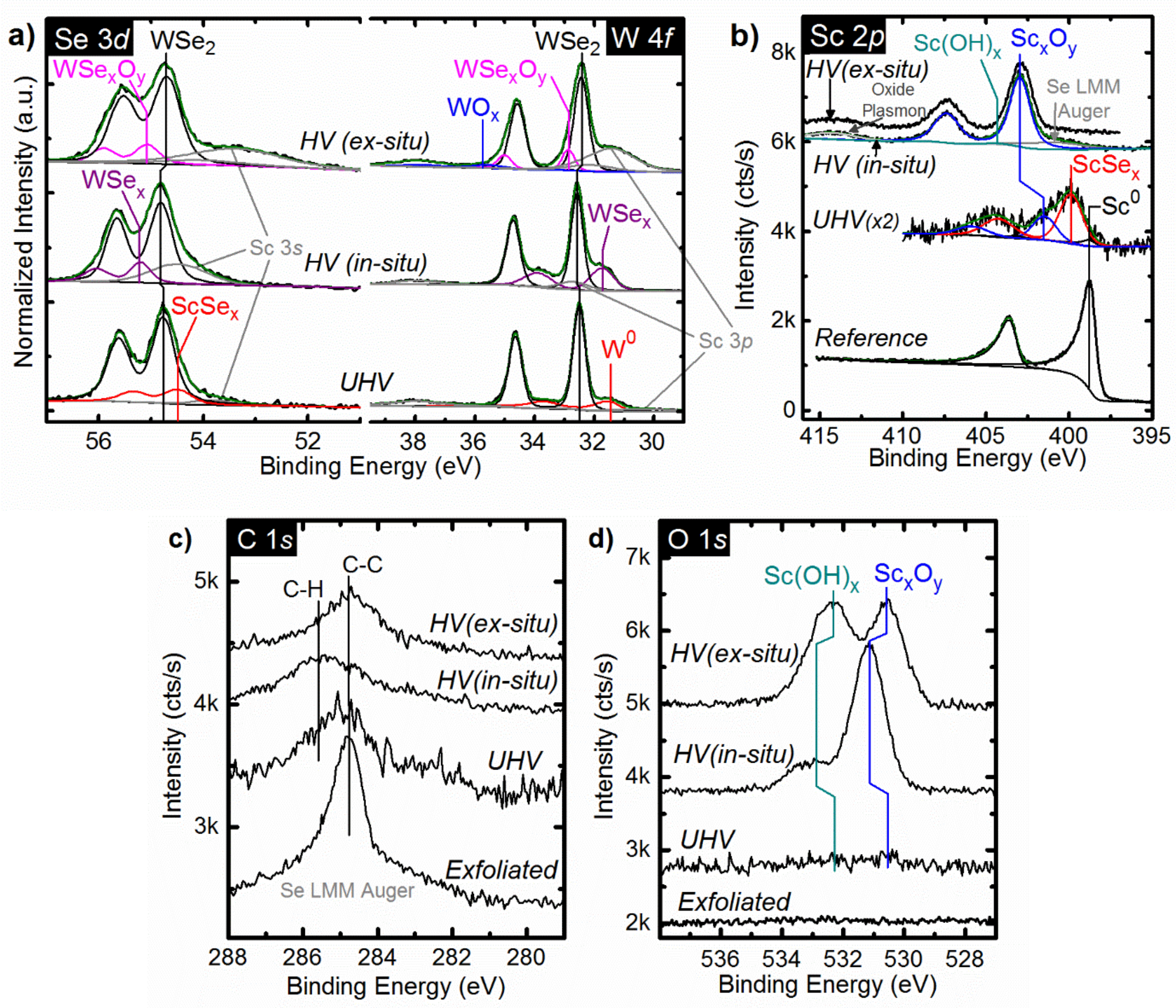

Figure 7.1. a) Se 3*d*, W 4*f*, b) Sc 2*p*, c) C 1*s*, and d) O 1*s* core level spectra obtained *in–situ* after Sc deposition in UHV and HV on bulk WSe$_2$ (base pressure < 2 × $10^{-9}$ mbar in each case, see Section 7.3 for details on the deposition in HV). Significant reactions occur between Sc, WSe$_2$, and background gases in the chamber, which completely convert Sc and ScSe$_x$ to Sc$_x$O$_y$ when the deposition is performed in HV.

The work discussed in Chapters 3, 4, and 5 investigating the interface chemistry between transition metals and TMDs have shown that early transition metals typically oxidize *in–situ* when deposited in HV.[10-12] However, the HV deposition was performed *ex–situ* from the post metallization XPS in Chapters 4 and 5.[10,11] In this experimental design, it is difficult to explicitly determine whether the observed oxidation occurs *in–situ* during metallization or while transferring the sample between the elastomer-sealed deposition tool and the UHV cluster tool. In this work, the HV Sc deposition was performed in the same chamber as the UHV deposition, but the chamber was backfilled with air to $5 \times 10^{-6}$ mbar before the deposition to simulate the conditions typically found in an elastomer sealed deposition tool. This experimental design eliminates any spurious air–exposure induced changes in interface chemistry, elucidating the true chemistry in the Sc–$WSe_2$ system formed in HV. Sc was also deposited *ex–situ* in an elastomer–sealed deposition chamber and transferred to the UHV cluster tool for XPS to compare the Sc–$WSe_2$ interface chemistry formed in HV with and without air exposure between deposition and XPS.

Sc reduces $WSe_2$ when deposited in HV with and without the air–exposure step between Sc deposition and XPS. When Sc deposition and subsequent XPS are performed *in–situ*, the presence of substoichiometric $WSe_x$ is evidenced by the chemical states detected at 55.19 eV (31.73 eV) in the Se 3*d* (W 4*f*) core level spectrum. When the HV Sc deposition and subsequent XPS are performed *ex–situ*, the $WSe_x$ that presumably forms as Sc is deposited is oxidized, as evidenced by the appearance of $WSe_xO_y$ and $WO_x$ chemical states at higher binding energy from the bulk $WSe_2$ chemical state in the W 4*f* core level (Figure 7.1a). However, in a typical contact structure where a thicker Sc film and inert capping metal are employed, $WSe_xO_y$ and $WO_x$ are likely absent from the interface.

The additional grey peaks at low BE relative to the Se 3*d* and W 4*f* core levels correspond with the Sc 3*s* and Sc 3*p* core levels, respectively. The binding energy and area of these peaks were carefully calibrated according to a Sc reference film to maximize the accuracy of the fit. The Sc $2p_{3/2}$-Sc 3*s* and Sc $2p_{3/2}$-Sc $3p_{3/2}$ core level BE separations (348.40 eV and 370.22 eV, respectively) obtained from the Sc reference sample are employed when fitting all W 4*f* and Se 3*d* core level spectra obtained from Sc–$WSe_2$ structures. The Sc 3*s*:Sc 2*p* and Sc 3*p*:Sc 2*p* intensity ratios (0.07 and 0.10, respectively) obtained from the Sc reference have been employed to determine the intensity of the chemical states detected in the Sc 3*s* and Sc 3*p* core level spectra relative to the intensity of the chemical states in the corresponding Sc 2*p* core level spectra throughout this work. When deposited in UHV, the majority of the ~1 nm Sc film reacts to form either $ScSe_x$ or $Sc_xO_y$ (Figure 7.1b). In contrast, all of the Sc deposited in HV is oxidized (including or excluding air–exposure between deposition and XPS) to form a film with O:Sc ratio of 1.43 (slightly oxygen deficient $Sc_2O_3$). Therefore, a Sc contact deposited in HV will completely oxidize *in–situ*, likely implicating contact performance considering $Sc_2O_3$ has been employed as a high–κ dielectric.[39] Complete Sc oxidation *in–situ* in HV is reasonable considering Sc–O bond formation is highly exothermic ($\Delta G^{\circ}_{f,Sc2O3}$=-630 kJ/mol)[40] compared with the persistence of Sc–Se bonds ($\Delta G^{\circ}_{f,ScSe}$=-360 kJ/mol).[40] The presence of $Sc_xO_y$ and $Sc(OH)_x$ are corroborated by the chemical states detected in the corresponding O 1*s* core level (Figure 7.1d).

Figures 7.1 c, d show the C 1*s* and O 1*s* core level spectra obtained after Sc is deposited on exfoliated, bulk $WSe_2$ in UHV and HV (*in-situ* and *ex-situ*). In each case, the base pressure of the deposition chamber is $< 2 \times 10^{-9}$ mbar. $Sc_xO_y$ and $Sc(OH)_x$ are detected regardless of background pressure due to the highly exothermic reactions between scandium and oxygen.[41] Reactions between Sc and adventitious carbon, which is detected on the exfoliated $WSe_2$ surface at ~284.4 eV (Figure 7.1c), or nitrogen in the background ambient are below the limit of detection. However, when a thicker Sc film is deposited on $WSe_2$ in UHV, there is evidence for the formation of ScC and/or ScN according to XPS, which is discussed in greater detail later in this chapter.

### *Complete Sc Oxidation at Elevated Temperatures in UHV*

A complete understanding of the relationship between processing conditions, interface chemistry, and contact performance is critical to engineering the Sc–$WSe_2$ interface for high–performance electron transport. Post metallization annealing can drive additional reactions and concomitant $E_F$ shifts depending on the temperature and ambient conditions. Therefore, the interface chemistry and band alignment between Sc and $WSe_2$ were tracked *in–situ* throughout stepwise Sc deposition in UHV and post metallization annealing (see Section 7.3 for experimental details).

Figure 7.2a displays the W 4*f* and Se 3*d* core level spectra obtained from bulk $WSe_2$ after exfoliation, stepwise Sc depositions, and subsequent UHV anneals. After depositing ~0.9 nm Sc, chemical states in addition to those of bulk $WSe_2$ are detected in the corresponding Se 3*d* (W 4*f*) core level spectrum at 54.14 eV and 55.06 eV (31.78 eV) indicating the formation of $ScSe_x$ ($WSe_x$) as Sc reduces the $WSe_2$ near the interface (Figures 7.2 b, c). The binding energy of the '$WSe_x$' chemical states exhibit increasing binding energy shifts towards that of metallic W (~31.2 eV) and elemental Se (~55.5 eV) during additional Sc depositions. After depositing ~1.5 nm Sc, a chemical state with asymmetric line shape (typical of transition metals)[42] consistent with metallic W is detected at 31.15 eV in the corresponding W 4*f* core level, which suggests the $WSe_2$ nearest the interface is completely reduced by Sc. The intensity of the metallic W chemical state increases up to an effective Sc film thickness of 3.2 nm is deposited (Figure 7.2a), which suggests spontaneous

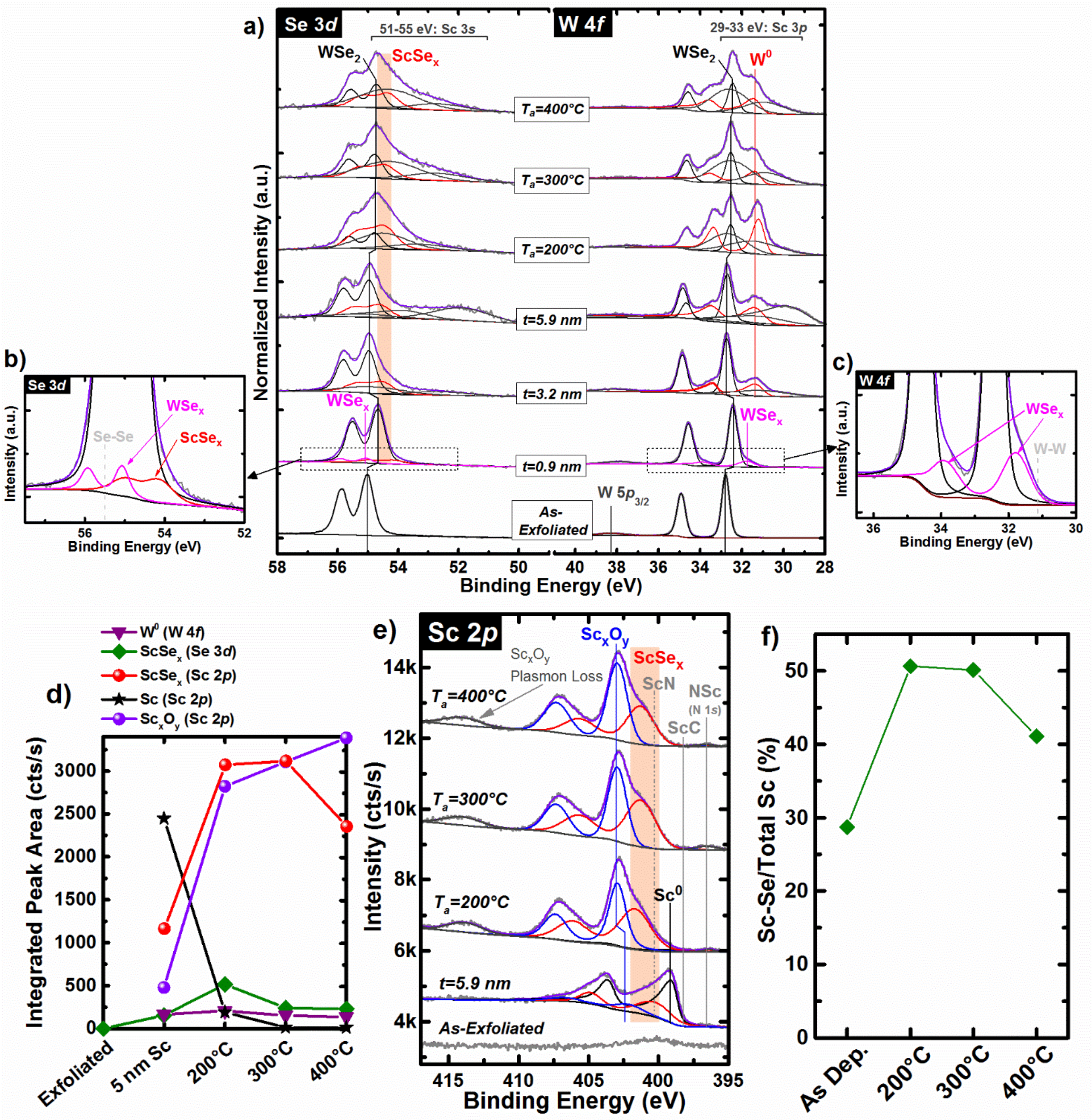

Figure 7.2. a) Se 3$d$, W 4$f$, and W 5$p_{3/2}$ core level spectra obtained from bulk $WSe_2$ throughout stepwise Sc deposition and subsequent *in-situ* annealing (all under UHV conditions) with b) and c) associated zoomed in regions of each core level after 0.9 nm Sc deposition. d) Integrated intensities of chemical states in Se 3$d$, W 4$f$, and Sc 2$p$ core level spectra associated with various reaction products as well as the e) Sc 2$p$, core level spectra obtained from bulk $WSe_2$ after exfoliation, depositing ~5.9 nm Sc in UHV, and subsequent *in-situ* UHV anneals. f) Percentage of the deposited Sc film converted to $ScSe_x$ after room temperature deposition and subsequent UHV anneals, which depicts the aggressive reactions between Sc and $WSe_2$ at room temperature and moderate intermetallic stability during 200 °C and 300 °C UHV anneals.

reactions between Sc and $WSe_2$ continue throughout the first ~3 nm Sc deposition. Once the Sc–$WSe_2$ reaction saturates, the concentration of metallic Sc gradually increases during subsequent depositions beyond a total film thickness of 3.2 nm The intensities of the $ScSe_x$ and metallic W chemical states exhibit negligible intensity increases during subsequent Sc depositions up to a total Sc film thickness of ~5.9 nm. The target Sc film thickness was 5 nm, but deviations from the calibrated deposition rate can manifest as a result of using Sc pellets as the source material instead of a solid Sc slug. In addition, calculating the Sc film thickness from core level attenuation requires the density of the attenuating film, which is difficult to estimate in this particular case considering the complex chemistry, which is discussed below.

Figure 7.2d displays the evolution of integrated intensities of chemical states associated with $WSe_x$, $ScSe_x$, $Sc_xO_y$, and metallic Sc formed after depositing ~5.9 nm Sc on $WSe_2$ and subsequent UHV anneals. The integrated intensities displayed include both spin orbit split peaks in each of the Sc 2*p*, Se 3*d*, and W 4*f* core levels and are corrected by the appropriate atomic sensitivity factors unique to the detector employed (see Section 7.3). The 200 °C UHV anneal drives Sc to react with additional $WSe_2$, which is evidenced by increases in the intensities of the $ScSe_x$ and metallic W chemical states in the corresponding Se 3*d* and W 4*f* core level spectra (Figures 7.2 a, d). However, the concentration of $ScSe_x$ decreases incrementally during the 300 °C and 400 °C UHV anneals, which indicates Sc–Se bonds are dissociated in favor of Sc–O bonds as is predicted by thermodynamics (Figure 7.2 d-f).[40] In addition, the concentration of metallic W decreases slightly during the 300 °C and 400 °C UHV anneals, which suggests metallic W bonds with the $Se^{2+}$ ions from reduced $ScSe_x$ (Figures 7.2 a, d).

Figure 7.2e shows the Sc 2*p* core level spectrum obtained after depositing 5.9 nm Sc and after each subsequent UHV anneal. 28.7% of the 5.9 nm Sc film is converted to $ScSe_x$ (Sc 2*p* BE = 400.27 eV) at RT, while the other 71.3% of the film is comprised of a mixture of metallic Sc (398.89 eV), $Sc_xO_y$ (402.16 eV), ScC (397.98 eV), and ScN (400.66 eV). ScC and ScN are near the limit of XPS detection, which is why they are difficult to see in Figure 7.2e. The presence of ScC and ScN in the same Sc–$WSe_2$ system is validated in the discussion below.

During the 200 °C and 300 °C UHV anneals, all of the deposited metallic Sc either reacts with the underlying $WSe_2$ to form $ScSe_x$ and metallic W or with the outer ambient to form $Sc_xO_y$ as evidenced by the dramatic intensification of the $ScSe_x$ and $Sc_xO_y$ chemical states in the corresponding Sc 2*p* core level spectrum (Figure 7.2e). 17.9% of the $ScSe_x$ formed during the 300 °C UHV anneal is converted to $Sc_xO_y$ during the 400 °C anneal (Figures 7.2 d, e), which is thermodynamically favorable.[40] Extending the duration or increasing the temperature of the UHV anneal would presumably increase the relative $Sc_xO_y$ concentration within the film.

Adventitious carbon is detected on both $WSe_2$ surfaces in the form of adventitious ($sp^3$) carbon (~284.8 eV) due to the brief air exposure after exfoliation and before loading into the UHV cluster tool for Sc deposition and anneals (Figure 7.3a). The broad feature convoluting the C 1*s* core level in Figure 7.3a corresponds with a Se loss feature typically detected from $WSe_2$.[43] The C 1*s* core level and Se loss feature attenuate throughout initial Sc depositions, as expected, up to a total film thickness of ~1.5 nm without the appearance of additional chemical states. After depositing 3.2 nm Sc, a carbidic chemical state is detected at ~281.6 eV in the corresponding C 1*s* core level spectra (Figure 7.3a), which indicates the formation of a transition metal carbide. This chemical state persists throughout subsequent Sc depositions.

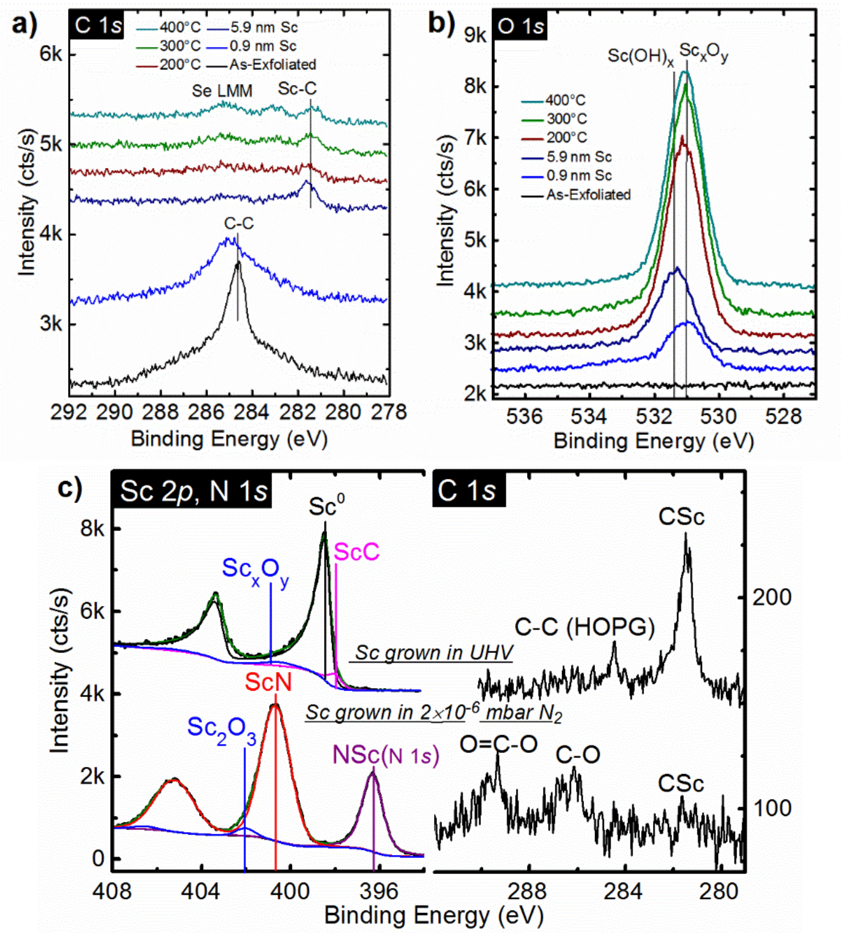

Figure 7.3. Evolution of the a) C 1*s* and b) O 1*s* core level spectra throughout stepwise Sc deposition under UHV conditions at RT and subsequent *in–situ* post metallization annealing under UHV conditions. c) Sc 2*p*, N 1*s*, and C 1*s* core level spectra obtained from a Sc film deposited on HOPG in UHV (top) and in a $N_2$ partial pressure of $2 \times 10^{-6}$ mbar showing Sc–C and Sc–N bond formation is favorable when C and/or N are present.

The formation of the Sc–C bond is exothermic at RT ($\Delta G°_{f,ScC}$=-164 kJ/mol),[44] which suggests ScC is present during initial deposition steps, but below the limit of XPS detection until a total of 3.2 nm Sc is deposited. It is also possible that Sc–C forms *in–situ* as Sc scavenges C from background gases (e.g., CO, $CO_2$) under UHV and is therefore surface-localized. The intensities and BEs of the low BE chemical states in the Sc 2*p* and C 1*s* core level spectra remain virtually constant throughout annealing under UHV conditions, which suggests the ScC is stable during the UHV anneals.

Let us also consider a different assignment to the low binding energy chemical state detected in the Sc 2*p* window after Sc depositions between 3.2 nm and 5.9 nm total film thicknesses. The chemical state may also correspond with the formation of ScN, which could occur via background gases in the deposition chamber. XPS results reported previously obtained from ScN films report associated chemical states at binding energies of 400.2 and 396.1 eV in the Sc $2p_{3/2}$ and N 1*s* core levels, respectively, which closely agree with the chemical states detected from reference ScN films grown in this work (Figure 7.3c).[45,46] It is reasonable to conclude that the low BE state detected in the same window as the Sc 2*p* core level spectrum after 3.2 nm Sc deposition (~396.5 eV, Figure 7.2e) indicates the presence of ScN in the Sc films deposited on $WSe_2$ in this work. We therefore deduce that both ScC and ScN are detected within the deposited Sc films in this work. The presence of ScN and ScC throughout a Sc contact could implicate the band structure and therefore its electrical performance, but such a study is outside the scope of this work.

Sc readily oxidizes *in–situ* throughout deposition at RT as evidenced by the increasing intensity of the corresponding O 1*s* core level spectra (Figure 7.3b). The spectra also exhibit a slight asymmetry to higher binding energy, which can be ascribed to a combination of hydroxyl incorporation and oxygen vacancies that are found naturally in the amorphous Sc film at RT.[47]

The UHV anneals dehydrate $Sc(OH)_x$ and convert it to $Sc_xO_y$ as evidenced by the less pronounced degree of asymmetry in the O 1*s* spectra anneal shown in Figure 7.3b. However, the concentrations of $Sc(OH)_x$ and $Sc_xO_y$ do not change (according to XPS) during the 300 °C or 400 °C anneals considering the shapes of the corresponding O 1*s* core levels remain virtually constant.

Interestingly, $ScSe_x$ formed underneath $Sc_xO_y$ is stable even at elevated temperatures, which is surprising considering $ScSe_x$ is below the limit of detection when Sc is deposited under HV conditions. This suggests the 2-3 nm thick $Sc_2O_3$ presumably formed on top of the $ScSe_x$ intermetallic layer is a good oxygen diffusion barrier at or below 400 °C in a UHV ambient.

### *Intermetallic Reduction via Forming Gas Annealing*

A dramatic increase in intermetallic concentration at the metal–$WSe_2$ interface can be achieved by performing the post metallization anneal in forming gas (FG) rather than UHV.[5] In addition, annealing a TMD device in a partial pressure of $H_2$ has been shown to passivate defects and improve performance.[48,49] Therefore, we investigated the effects of FG anneals on the Sc–$WSe_2$ interface chemistry and band alignment. Prior to performing the FG anneals, stepwise Sc deposition at RT on bulk $WSe_2$ results in the same Sc film thickness, interface chemistry, and $E_F$ position (Figure 7.4a) as were detected prior to the UHV anneals (Figure 7.2).

During the 200 °C FG anneal, the metallic W chemical state in the corresponding W 4*f* core level shifts +0.30 eV, while the $ScSe_x$ chemical states in the Se 3*d* and Sc 2*p* core levels shift -0.35 eV and +1.26 eV, respectively, indicating the formation of a ternary $W_xSc_ySe_z$ compound (Figures 7.4 a-c). $W_xSc_ySe_z$ formation during post metallization annealing is evidenced by the +0.1 and -0.34 eV BE shifts of corresponding low BE states in W 4*f* and Se 3*d* core level spectra, which indicates oxidation of metallic W to $W^{1+}$ and a greater degree of charge transfer from $Se^{2-}$ to its positively charged constituents ($Sc^{x+}$ and $W^{1+}$). In addition, the low BE state in the W 4*f* core level spectrum exhibits a symmetric after annealing at 200°C compared with the metallic W doublet detected before annealing corroborating the oxidation of metallic W. The anneal also dissociates Sc–Se bonds as evidenced by the small concentration of elemental Se detected at 55.30 eV in the

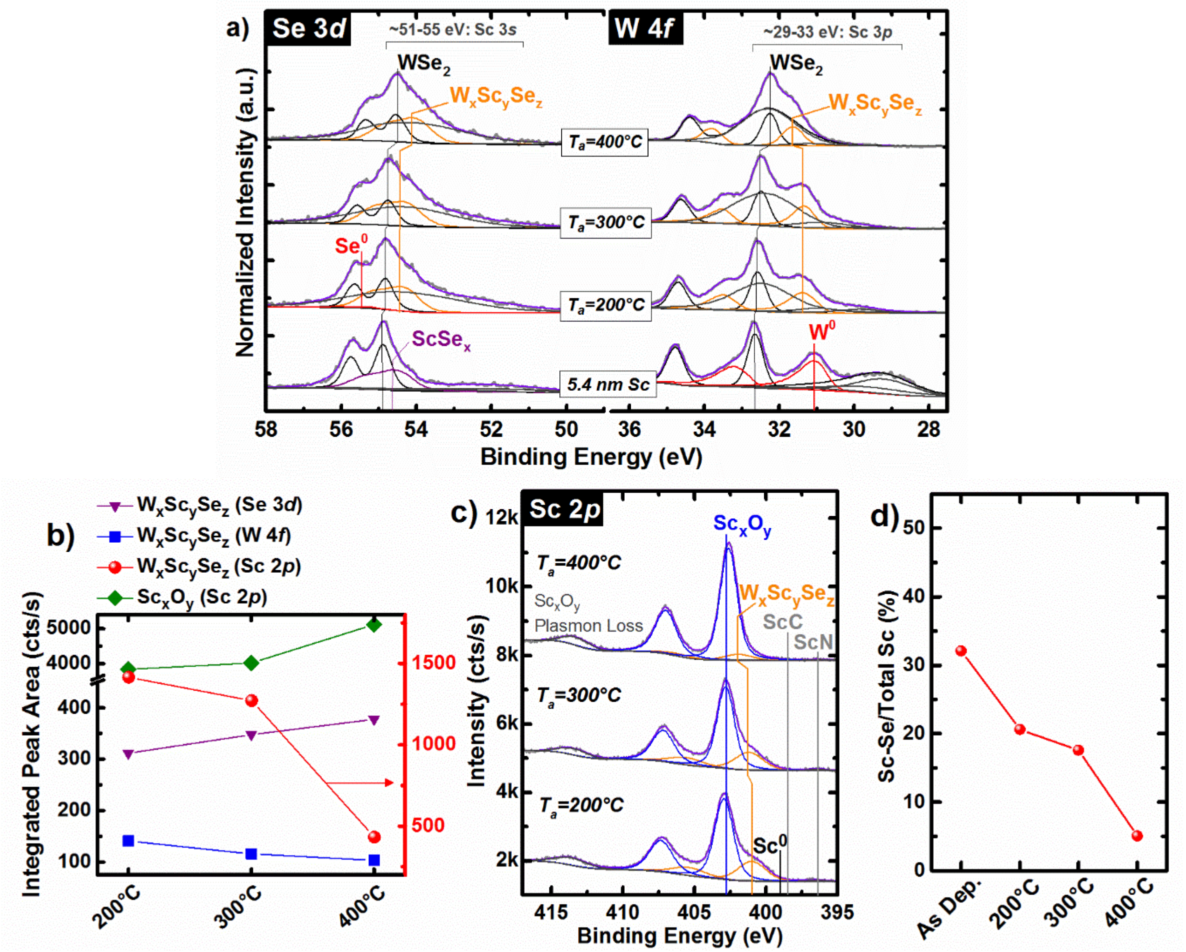

Figure 7.4. a) Se 3*d*, W 4*f*, and W $5p_{3/2}$ core level spectra obtained from bulk $WSe_2$ throughout stepwise Sc deposition under UHV conditions and subsequent *in-situ* annealing under FG ambient. b) Integrated intensities of the $W_xSc_ySe_z$ intermetallic and $Sc_xO_y$ chemical states in the Se 3*d*, W 4*f*, and Sc 2*p* core level spectra. c) Sc 2*p* core level spectra obtained from bulk $WSe_2$ after Sc deposition at room temperature and subsequent *in–situ* FG anneals. d) Percentage of the deposited Sc film converted to ScSe intermetallic after deposition at RT and subsequent FG anneals showing aggressive reactions at RT and increasing Sc–Se dissociation with increasing FG anneal temperature.

corresponding Se 3*d* core level. Once W–Se bonds form, Sc–Se bond scission is more favorable considering the relevant bond dissociation energies ($BDE_{Sc\text{-}Se}$ = 385 kJ/mol, $BDE_{W\text{-}Se}$ = 418 kJ/mol).[50,51] After the 400 °C FG anneal, the $W_xSc_ySe_z$ chemical states in the W 4*f* (Se 3*d*) core level shifts +0.42 eV (-0.34 eV) relative to that detected after the 200 °C FG anneal (Figure 7.4a), which is consistent with a decreased concentration of Sc within the $W_xSc_ySe_z$ compound and a corresponding increased oxidation state of the associated $W^{x+}$ component (Figure 7.4a). Thermodynamics indicates an additional anneal performed either for a longer period or at a higher temperature could completely dissociate Sc from $W_xSc_ySe_z$, potentially implicating contact performance.

The 200 °C FG anneal converts nearly all of the deposited Sc into either $W_xSc_ySe_z$ or $Sc_xO_y$ (Figure 7.4b). The chemical state corresponding with Sc–Se bonds in the Sc 2*p* core level exhibits a four-fold intensity increase during the 200 °C FG anneal, which corroborates the formation of $W_xSc_ySe_z$. The intensity of the $W_xSc_ySe_z$ chemical state in the Sc 2*p* core level decrease in intensity by 10% and 70% during the 300 °C and 400 °C FG anneals, respectively (Figures 7.4 b, c), in contrast with the relatively stable intermetallic concentration throughout the UHV anneals. The ScN and ScC chemical states detected after the 200 °C FG anneal fall below the limit of XPS detection after the 400 °C FG anneal. This suggests the partial pressure of $H_2$ in the FG ambient dissociates Sc–C and Sc–N bonds, which is an energetically favorable process (the energy liberated when an H–H bond is broken is greater than the $BDE_{ScC}$ and $BDE_{ScN}$).[50]

A low binding energy chemical state is detected at ~281.6 eV in the C 1*s* core level spectra detected after ~5.7 nm Sc deposition at RT, which is ascribed to the formation of ScC (Figure 7.5a). Unlike the UHV anneals, ScC is reduced by the FG anneals to a concentration below the limit of XPS detection, which is indicated by an absence of detectable carbidic chemical state in the C 1*s* core level spectrum obtained after the 400 °C FG anneal (Figure 7.5a).

A chemical state is detected at ~533.0 eV in addition to the $Sc_xO_y$ chemical state at ~530.8 eV in

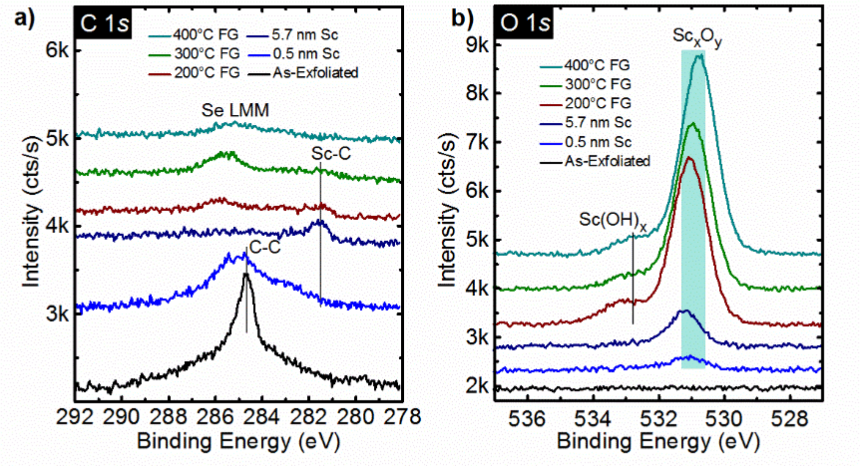

Figure 7.5. Evolution of the a) C 1*s* and b) O 1*s* core level spectra throughout stepwise Sc deposition under UHV conditions at RT and subsequent *in–situ* post metallization annealing under a) UHV and b) FG conditions.

the O 1*s* core level obtained after the 200 °C FG anneal (Figure 7.5b), which could indicate the formation of $Sc(OH)_x$ as a result of hydrogen incorporation into the oxygen-deficient $Sc_xO_y$ film. The $Sc(OH)_x$ state is detected at a much higher BE after the FG anneals compared with that detected after the UHV anneals, which could manifest from a more hydrogen-rich scandium oxide film formed during the anneals in a hydrogen partial pressure.

This work indicates a Sc contact to $WSe_2$ will completely oxidize when the post metallization anneal is performed in FG, provided the anneal is performed at a high enough temperature or for a long enough time. Complete Sc–Se, Sc–C, and Sc–N bond dissociation in the presence of oxygen–containing species (i.e., the background gases in a vacuum chamber) are energetically favorable considering either the thermodynamics (see earlier Sections for relevant $\Delta G°_f$) or the kinetics ($BDE_{Sc\text{-}O} > BDE_{Sc\text{-}N} > BDE_{Sc\text{-}C} > BDE_{Sc\text{-}Se} > BDE_{Sc\text{-}Sc}$)[50] of the system. The effects of the increased $Sc_xO_y$ concentration on the band alignment and performance of the Sc contact to $WSe_2$ will be discussed in detail later.

### *Multiple $WSe_2$ Layers Consumed by Thermally Exacerbated Reactions with Sc*

The experiments discussed above were performed on bulk $WSe_2$, which provides an appropriate platform to characterize effects of certain post metallization anneals on the metal–TMD interface chemistry and band alignment. However, FETs are typically fabricated with single and few layer TMDs. In addition, edge contacts exhibit superior performance compared to top contact analogs according to DFT calculations[52,53] and experimental demonstrations.[53,54] The true structure of the contact (edge versus top) will be affected by reactions at the metal–TMD interface. For example, a true top contact is formed when an inert metal–TMD interface is formed (e.g., Au–$WSe_2$),[11] while a pseudo–edge contact is formed when all of the TMD underneath the contact is consumed in reactions with the deposited metal.[5] The broken inversion symmetry in $WSe_2$ films with $D_{3h}$ symmetry is critical to the unique giant spin orbit splitting in the valence band in the absence of an out–of–plane electric field.[28] It is therefore of interest to quantify the number of $WSe_2$ layers affected by reactions with Sc.

Variations in structural and electronic properties of single and few layer TMDs due to interactions with a deposited metal have been investigated previously.[55-57] For example, depositing an incomplete coverage metal film on $MoS_2$ resulted in a complex vibrational response due to metal–induced spatially varying strain across the TMD.[56] In this work, Raman spectroscopy is employed to quantify the number of layers consumed by reactions with Sc via a characteristic, layer number–dependent vibrational mode exhibited by $WSe_2$. Special care was taken to ensure a full coverage Sc film was deposited (Appendix E). In addition, a 10 nm thick Si capping layer was deposited *in–situ* after the Sc deposition and the subsequent anneal (where applicable) to prevent any spurious, air–exposure induced changes in the Raman spectra obtained *ex–situ* (Appendix E).[5] Therefore, any structural changes manifesting in the Raman spectra are attributed to Sc–$WSe_2$ reactions. It is important to note here the Raman measurements were obtained within 24 hours of Sc/Si deposition and the subsequent anneal.

The first ($1^{st}$) order in-plane ($E^1_{2g}$) and out-of-plane ($A_{1g}$) vibrational modes of sulfur- and tellurium-based TMDs are easily distinguishable and exhibit layer number dependent Raman shifts.[58] However, the $E^1_{2g}$ and $A_{1g}$ modes are degenerate in the case of $WSe_2$ and do not exhibit any discernible characteristic shifts or changes in intensity with layer number.[59] The layer number dependent Raman shifts exhibited by the second ($2^{nd}$) order longitudinal acoustic mode at the M point in the Brillouin zone [2LA(M)] from single layer to five layer $WSe_2$ [2.5 $cm^{-1}$, 0.5 $cm^{-1}$, 0.5 $cm^{-1}$, and 0.3 $cm^{-1}$ red shifts increasing from one layer (1L, 261.3 $cm^{-1}$) to 2L, 2L to 3L, 3L to 4L, and 4L to 5L $WSe_2$] are demonstrated and discussed in Section 6.4.1.4.[5] Therefore, the number of $WSe_2$ layers remaining after the Sc deposition and subsequent anneal can be accurately determined by tracking the Raman shift of the 2LA(M) mode. A $\lambda$=532 nm laser is employed here to access the 2LA(M) mode via resonant excitation conditions.[60] The laser power density (0.49 mA/$\mu m^2$), number of sweeps (5), and exposure time per sweep (5 seconds) employed in this work were carefully selected according to control experiments performed previously (Section 6.4.1.4)[5] to prevent laser-induced $WSe_2$ damage. Therefore, spectral changes were confidently interpreted as indicators of chemical or physical interactions between Sc and $WSe_2$ rather than laser–induced intermixing.

Prospective single and few layer $WSe_2$ flakes were exfoliated onto $SiO_2$ substrates and initially screened according to optical contrast. 1L, 2L, 3L, and 5L (where applicable) $WSe_2$ flakes were then selected based on flake height according to AFM and the characteristic wavenumber of the

2LA(M) mode. The AFM images and line profiles obtained from the selected 1L, 2L, 3L, and 5L flakes after exfoliation and thermal cleaning (see Section 7.3) are displayed in Figure 7.6.

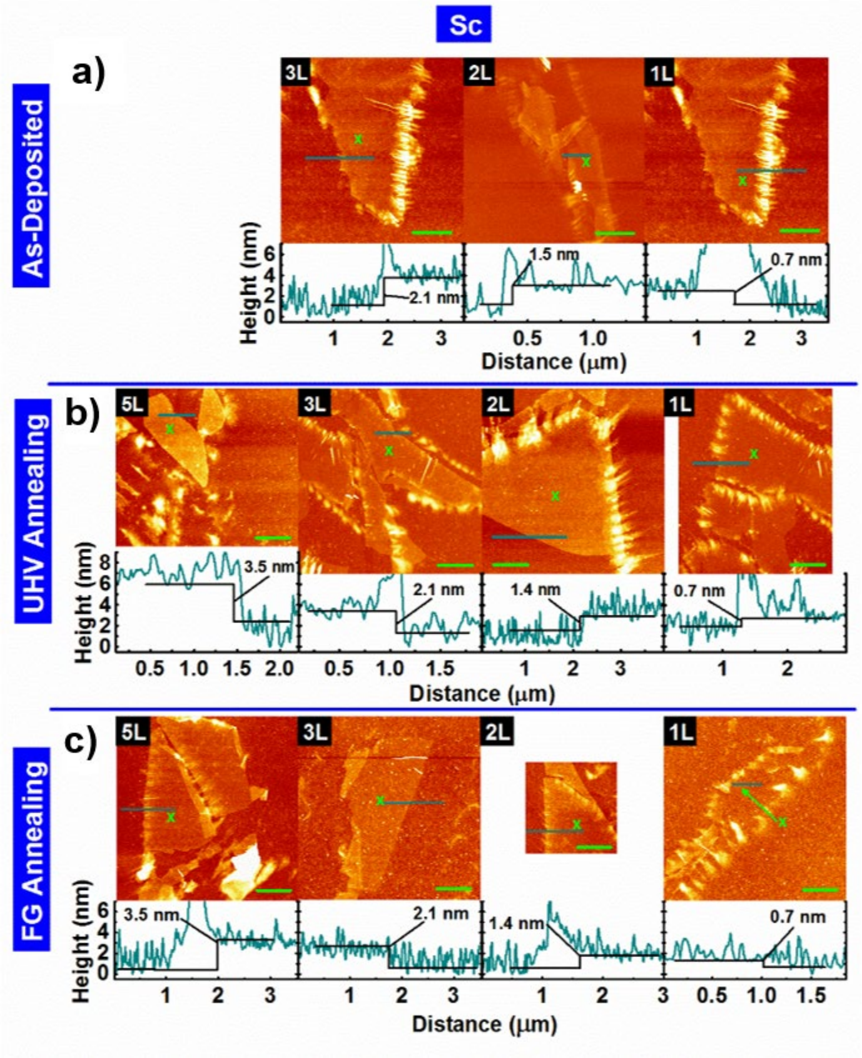

Figure 7.6. AFM topography images and associated line profiles of $WSe_2$ flakes after post-exfoliation annealing. The bright green scale bar in each image represents 2 μm.

Figures 7.7 a–c display the Raman spectra obtained from exfoliated 1L, 2L, and 3L $WSe_2$ flakes before and after depositing 5 nm Sc at RT and subsequent 300 °C UHV or FG anneals. Depositing 5 nm Sc at RT completely quenches the 1st and 2nd order modes of the 1L $WSe_2$ flake, which indicates 1L $WSe_2$ is consumed by reactions with Sc at RT (Figure 7.7a). The 1.0 and 1.1 $cm^{-1}$ red shifts and slight symmetric broadening exhibited by the 2LA(M) mode detected from the 2L and 3L $WSe_2$ flakes, respectively, after depositing 5 nm Sc at RT suggest the interfacing reaction products cause stiffening (softening) of the $A_{1g}$ ($E^1_{2g}$) mode of the underlying $WSe_2$.[56,61]

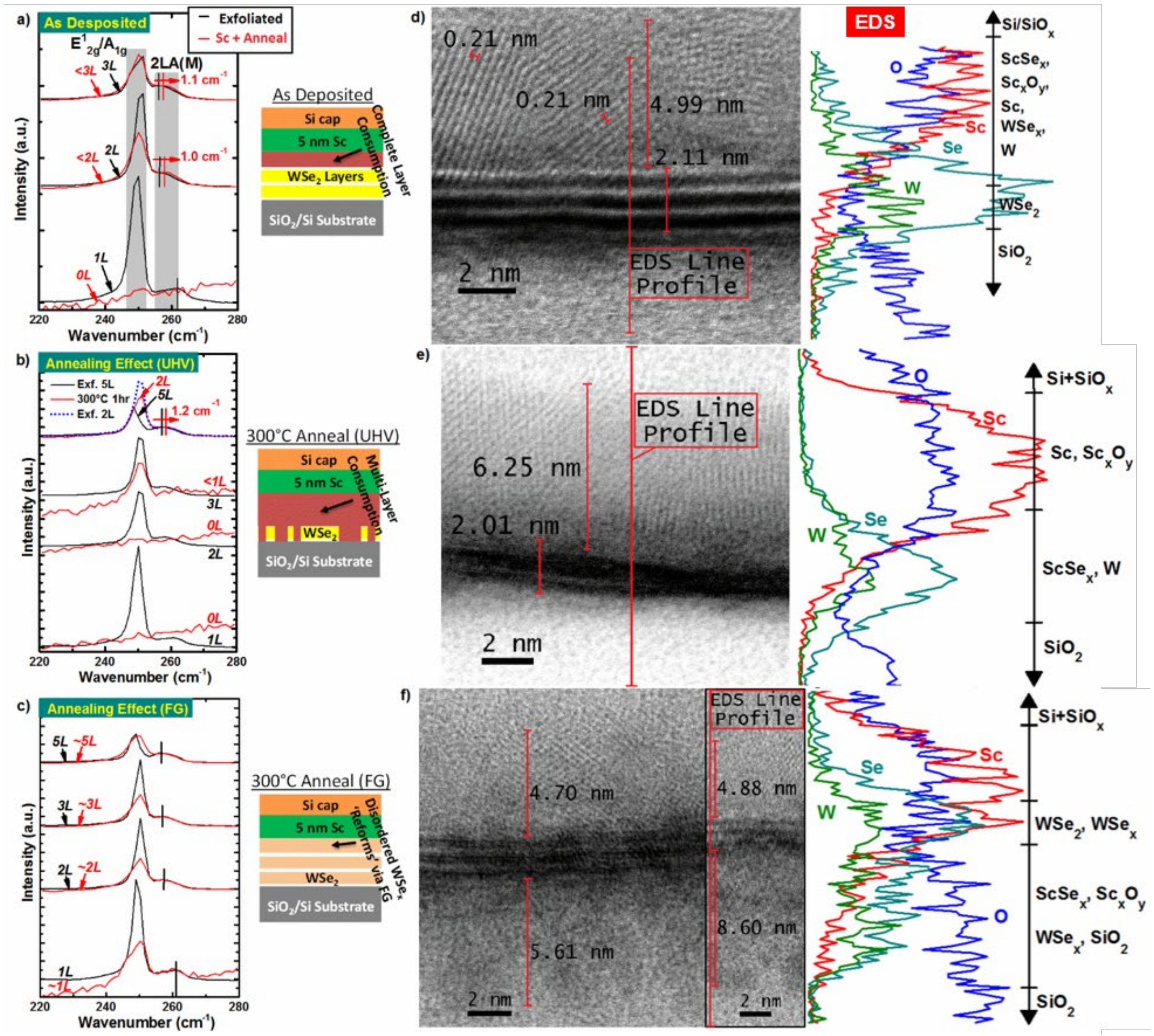

Figure 7.7. Raman spectra displaying peaks corresponding with the $E^1_{2g}$ , $A_{1g}$, and 2LA(M) vibrational modes of $WSe_2$ obtained from 1L, 2L, 3L, and 5L (where applicable) flakes prior to and following a) 5 nm Sc deposition under UHV conditions and subsequent post metallization anneal at 300°C in b) UHV or c) forming gas. All spectra are normalized to the 2LA(M) peak unless vibrational modes are below the limit of detection. d-f) Cross section TEM images and associated EDS spectra obtained from the same 3L $WSe_2$ flakes investigated by Raman spectroscopy.

After the 300 °C UHV anneal, the 1st and 2nd order vibrational modes of the 1L and 2L $WSe_2$ flakes are completely quenched, while the 1st order modes exhibited by the 3L flake are near the limit of detection (Figure 7.7b). This suggests at least two and possibly three $WSe_2$ layers are consumed by reactions catalyzed during the 300 °C UHV anneal. To more explicitly quantify the number of layers consumed during the anneal, the vibrational modes of a 5L $WSe_2$ flake were also probed throughout the experiment (Figure 7.7c). After the anneal, the corresponding 2LA(M) mode exhibits a 1.2 $cm^{-1}$ blue shift, which is consistent with a transition from 5L to 2L $WSe_2$.[5] The spectrum obtained from exfoliated 2L $WSe_2$ (dotted line) is normalized to the 5L $WSe_2$ spectra to clearly show the similarity between the spectrum of pristine 2L $WSe_2$ and 5L $WSe_2$ after Sc deposition and subsequent 300 °C UHV anneal. Therefore, we confidently conclude that three $WSe_2$ layers are consumed by reactions with Sc during the 300 °C UHV anneal.

Interestingly, 1L $WSe_2$ exhibits 1st and 2nd order modes above the limit of detection after the 300 °C FG anneal despite significant reactions detected by XPS in this work. In addition, asymmetric broadening towards lower wavenumber is detected in the 1st order modes of all $WSe_2$ flakes after the FG anneal. This behavior indicates $Se^{x+}$ (liberated by Sc–Se bond scission) reacts with metallic W to form defective $WSe_x$ clusters and is consistent with the Raman spectrum obtained from a $WSe_2$ film lacking long range order.[61]

Roughly nine months after characterizing the 10 nm Si/5 nm Sc/3L $WSe_2$/270 nm $SiO_2$/Si samples with Raman spectroscopy, lamella were milled from the samples and imaged by TEM in annular bright field mode. The corresponding TEM images are shown in Figures 7.7 d-f. Prior to the anneals, nanocrystalline grains with lattice spacing of 0.21 nm are observed in the Sc film, which is consistent with the Sc{111} family of planes.[62] A significant concentration of oxygen is detected by EDS throughout the Sc film (Figures 7.7 d-f). However, the lattice spacing of the grains observed in Figure 7.7d is not consistent with that of $Sc_2O_3$ (0.31 nm),[63] which indicates the oxygen is dispersed in amorphous regions of the film between grains. Se and W diffusion into the Sc film is observed in the corresponding EDS (Figure 7.7d). The three ~0.7 nm thick stripes of dark contrast coincide with high–Z W atoms and therefore indicate the presence of three $WSe_2$ layers (Figure 7.7d). The top most $WSe_2$ layer in Figure 7.7d appears to have retained its planar structure in some regions, which contradicts the Raman spectra discussed above.

In a parallel study, a 65 nm Pd/10 nm Sc/bulk $WSe_2$ sample was fabricated at RT in UHV. After storing the sample in ambient conditions for two weeks, a lamella was cross sectioned by FIB and characterized by TEM. A corresponding TEM image is shown in Figure 7.8. A 3-5 nm thick disordered region between the $WSe_2$ bulk and the lighter contrast Sc film suggests 4-7 $WSe_2$ layers are perturbed by reactions with Sc in this particular sample, which experienced a comparable thermal schedule with the sample reflected in Figure 7.7d. The time between fabrication and TEM characterization between the two samples differs by ~8.5 months, which likely plays a key role in the dramatically different interface structures observed. A previous study investigating Sc contact performance in BP FETs found a ~9 nm thick $Sc_xO_y$ layer had formed at the Sc–BP interface after capping the device with $Al_2O_3$ and storing it in a nitrogen glovebox for one month.[25] A similar phenomenon is likely observed in this work. The top most $WSe_2$ layer in Figure 7.7d could be an amorphous $WSe_x$ layer assembled as the Sc film converts to $Sc_xO_y$ over time. The interface structure shown in Figure 7.8 likely provides a more accurate depiction of that obtained during Sc deposition in UHV. In addition, the Sc–Se dissociation and subsequent Sc–O formation reaction is presumably a very slow, but exothermic process at RT even in an oxygen deficient ambient[25] if a thick (> 10 nm) oxygen diffusion barrier is employed.

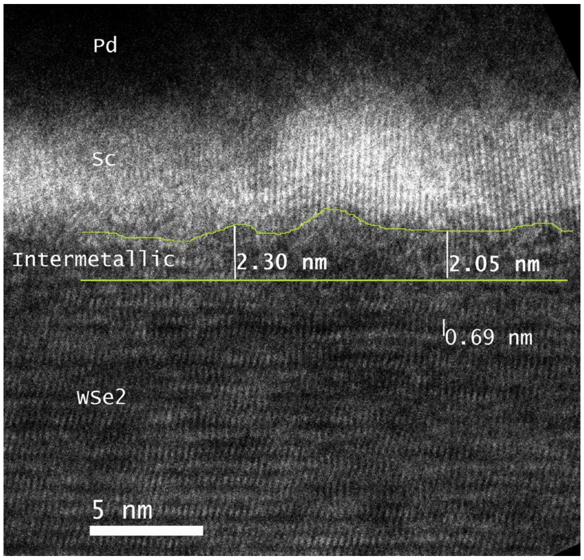

Figure 7.8. Cross section TEM image of the Sc–bulk $WSe_2$ interface obtained roughly two weeks after 10 nm Sc/65 nm Pd deposition in UHV showing 2.0–2.5 nm of $WSe_2$ is consumed by reactions at the Sc–$WSe_2$ interface in contrast with the TEM images in Figure 7.7, which were obtained roughly one year after sample fabrication.

The thickness of the dark contrast region observed after the 300 °C UHV anneal (~2.0 nm, Figure 7.7e) is consistent with that expected of pristine 3L $WSe_2$. However, individual layers are no longer distinguishable, which suggests significant intermixing occurs between $WSe_2$ and Sc and corroborates three $WSe_2$ layers are consumed by reactions during the 300 °C UHV anneal. An amorphous region is observed between the disordered $WSe_2$ and the polycrystalline Sc film, which likely corresponds with the $ScSe_x$ intermetallic detected by XPS after the same anneal. EDS indicates Se and W diffuse ~3 nm up into the Sc film and down into the $SiO_2$ substrate. The 0.30 nm lattice spacing exhibited by the nanocrystallites in the Sc film after the anneal (Figure 7.7e) indicates the dramatic increase in scandium oxide detected by XPS after the same anneal corresponds with the formation of a polycrystalline $Sc_2O_3$ film.

After the 300 °C FG anneal, local atomic structure and interlayer van der Waals gaps are resolvable in the corresponding TEM image (Figure 7.7f). EDS indicates Se and W diffuse 2-3 nm into the Sc film, while Sc, Se, and W diffuse up to 5 nm into the underlying $SiO_2$ (dark regions below the $WSe_2$). Metal diffusion into the underlying dielectric in back-gated devices could implicate the device performance (e.g., gate modulation, increased off current). The $WSe_2$ film is comprised of disordered regions with limited atomic order adjacent regions of 3L $WSe_2$ with clearly resolvable van der Waals gaps between each layer. These observations corroborate our hypothesis, based on the corresponding XPS and Raman results; W–Se bonds re-form via Sc–Se bond dissociation throughout the FG anneals.

In a device where the contact metal consumes at least one TMD layer, the resulting intermetallic likely remains in intimate lateral contact with the adjacent channel. Therefore, any TMD layers in the contact region consumed by reactions at the metal–TMD interface should be considered pseudo-edge contacts, which may exhibit superior performance to the top contact analog. In addition, understanding changes in the band structure of few layer TMDs associated with interface reaction-induced layer number thinning is critical to engineering superior performance in a wide variety of TMD devices. For instance, maintaining an odd number of layers in the channel of a $WSe_2$ spin valve is critical to device operation.

### 7.4.2 Band Alignment and Electrical Performance of the Sc Contact to $WSe_2$

The band alignments discussed in the following Section and depicted in Figure 7.9 are constructed according to the initial valence band offset and secondary electron cutoff of the exfoliated $WSe_2$ samples employed in this work and the subsequent bulk $WSe_2$ chemical state shifts detected throughout Sc deposition and subsequent anneals. A detailed description of the method is provided in Chapter 2. The $E_F$ shifts towards the conduction (valence) band edge will be referred to in the following discussion as positive (negative). Figure 7.9a displays the absolute binding energies of the $WSe_2$ chemical state in the Se $3d_{5/2}$ core level spectra detected from $WSe_2$ after exfoliation and subsequent stepwise Sc deposition and post metallization annealing.[64]

After exfoliation, the $E_F$ is detected 0.95 ± 0.10 eV from the $WSe_2$ valence band edge according to the initial valence band offset and secondary electron cutoff (0.95 ± 0.03 eV, 4.36 ± 0.03 eV, respectively; Figure 7.9d). The bulk $WSe_2$ chemical states initially shift to lower BE during the first two Sc depositions. In contrast, the $E_F$ shifts towards higher BE beyond an effective Sc film thickness of 5 Å. The $WSe_x$ and $ScSe_x$ formed during initial Sc depositions likely shift the $E_F$ towards the valence band, while the metallic Sc that accumulates in latter depositions shift the $E_F$ towards the conduction band. Depositing ~5.7 nm Sc at RT in UHV shifts the $WSe_2$ chemical states -0.09 eV (Figure 7.9a) from the binding energies detected after exfoliation, which corresponds with the formation of a 0.44 ± 0.10 eV electron Schottky barrier. The appreciable Schottky barrier detected here is far from the expected Ohmic electron band alignment expected between Sc and $WSe_2$ considering the low metal work function (3.5 eV).[65] It is possible the metallic W, formed as a product of the Sc–$WSe_2$ reaction, dominates the band alignment in an unannealed Sc contact to $WSe_2$ (polycrystalline W work function ≈ 4.5 eV).[65]

As the UHV anneal temperature increases, the $E_F$ shift towards lower binding energy increases in magnitude, exhibiting a total -0.26 eV shift after the 400 °C UHV anneal. The $E_F$ shift corresponds with an increased electron Schottky barrier height to 0.70 ± 0.10 eV (Figure 7.9b).

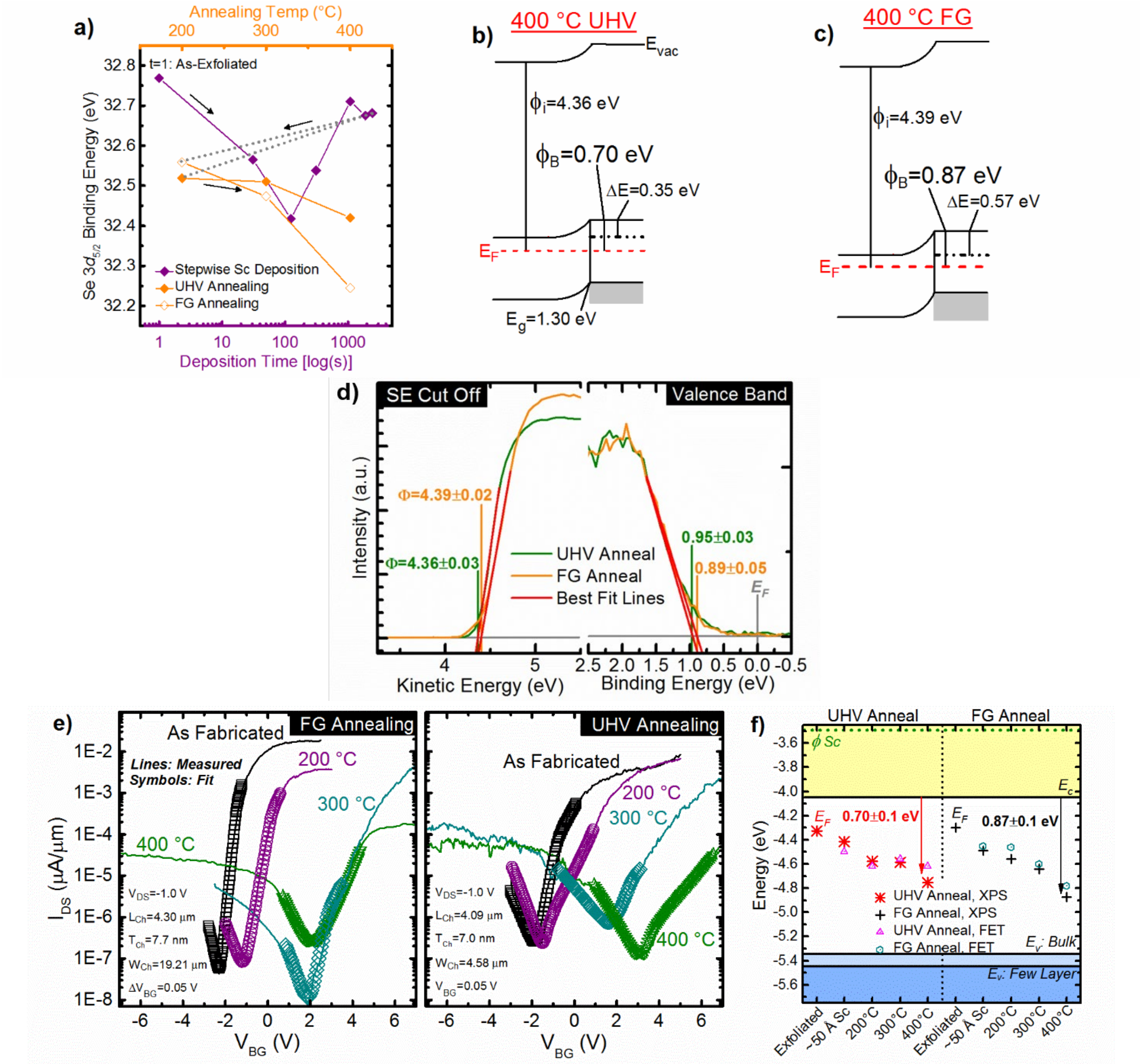

Figure 7.9. a) Binding energies of the bulk $WSe_2$ chemical state in the Se 3*d* core level spectra throughout stepwise Sc deposition and post metallization annealing in either UHV ◆ or FG ◇ conditions. The binding energy shifts throughout room temperature Sc deposition are similar for both samples, which is why the data points obtained from the 'FG anneal' sample prior to the anneals are displayed in a). Band alignments after the samples are annealed in b) UHV and c) FG at 400 °C, which are derived from XPS measurements. d) Secondary electron cutoff and valence band edge spectra obtained from exfoliated $WSe_2$. The red lines show fits of linear regions obtained by regression (95% confidence interval). The symbols in e) correspond with fits of the $I_{DS}$–$V_{BG}$ obtained with an analytical Schottky barrier model to extract the electron and hole Schottky barrier heights throughout the anneals. f) Band alignment between Sc and $WSe_2$ after contact deposition and post metallization anneals according to XPS in a) and the analytical fits of the $I_{DS}$–$V_{BG}$ curves in e). The ambipolar FET characteristics obtained after FG and UHV anneals corroborate the midgap band alignment indicated by XPS.

A separate bulk $WSe_2$ crystal was employed to characterize the effects of FG anneals on the interface chemistry and band alignment between Sc and $WSe_2$. Prior to Sc deposition and the subsequent FG anneals, the exfoliated $WSe_2$ exhibits a $E_F$ 0.89 ± 0.10 eV above the valence band edge (Figures 7.9 c, d). The electron Schottky barrier height detected after depositing ~5 nm Sc and prior to the FG anneals (0.43 eV) is close to that detected before the UHV anneals. Throughout FG annealing, the magnitude of the $E_F$ shift towards the valence band increases until after the 400 °C FG anneal, the electron Schottky barrier height increases to 0.87 ± 0.10 eV (Figures 7.9 a, c). Similar with the sample annealed in UHV, a significant electron Schottky barrier is achieved via the FG anneals and could manifest as a result of the abundance of reaction products detected at the Sc–$WSe_2$ interface.

$E_F$ pinning occurs due to gap states in the semiconductor that can be generated by defects,[9] interface reactions, or a deliberately placed re-pinning layer.[66] An appreciable concentration of oxygen deficient $Sc_xO_y$ in the Sc film could generate gap states in the underlying $WSe_2$, producing the near-midgap alignment detected after the 400 °C anneals. When annealing is performed in UHV, the chemistry, and therefore the electrostatics of the junction, are also convoluted by $ScSe_x$. The Ohmic hole band alignment reported recently between Pd and $WSe_2$ after a 400 °C FG anneal was facilitated by passivating defects at the interface with atomic hydrogen in the FG ambient.[5] However, the beneficial effects of hydrogen-induced defect passivation on the Sc contact to $WSe_2$ are either negligible compared with the interface chemistry effects or require hydrogen radicals, which are not readily catalyzed from $H_2$ by Sc as they are in Pd.

To corroborate the XPS-derived near-midgap band alignment with the electrical performance of Sc contacts to $WSe_2$, back-gated, few-layer $WSe_2$ FETs were fabricated on an $Al_2O_3/Si$ substrate with 20 nm Sc/50 nm Pd/100 nm Au contacts. It is difficult to accurately extract Schottky barrier heights from ultra-thin body transistors in which the depletion width is defined by the thickness of the region under the contacts, such as in few layer TMD FETs. Therefore, an analytical Schottky barrier model based on Landauer transport theory[14] was employed here to extract electron and hole Schottky barrier heights from the measured $I_{DS}$-$V_{BG}$ characteristics of our few layer $WSe_2$ FETs with Sc contacts. The model, which has been employed in recent works,[14,15,25,26] accounts for thermionic emission and the appreciable tunneling contribution to the total current due to the ultra-thin body of the devices. The physics upon which the analytical model is based and the fitting procedure are described in Appendix G. After fabrication, the Sc–$WSe_2$ FETs exhibit impressive $I_{ON}/I_{OFF}$ ratios on the order of $10^6$, subthreshold slope (SS) of 109 mV/dec (among the best reported to date),[16] and electron Schottky barriers of 0.4-0.45 eV (Figure 7.9e), which are in good agreement with the corresponding XPS-derived 0.36-0.44 eV electron Schottky barrier height (Figure 7.9f). Analogous $WSe_2$ FETs with Pd contacts exhibit a larger 0.73 eV electron Schottky barrier height, which is likely attributed to photoresist residue induced $E_F$ pinning.[5] Sc mitigates $E_F$ pinning effects related to photoresist residue in as-fabricated devices by reacting with the $WSe_2$ at RT and 'cleaning' resist residue from the interface. Reactions between Sc and common resist polymers are favorable considering Sc–C, Sc–N, and Sc–O bonds are all detected in a resist-free Sc–$WSe_2$ system, as discussed earlier.

The 400 °C UHV and FG anneals convert 94.9% and 59.9% of the Sc film to $Sc_xO_y$, respectively. According to the analytical Schottky barrier model, the UHV and FG anneals increase the electron Schottky barrier height to 0.70 eV and 0.87 eV, respectively (Figures 7.9 e, f). The additional 0.17 eV $E_F$ shift towards the valence band detected after the FG anneals could be related to the much higher $Sc_xO_y$ concentration within the deposited film, considering the charge neutrality level of $Sc_2O_3$ (~5.3 eV)[67] aligns closely with the $WSe_2$ valence band edge. In addition, the $I_{ON}/I_{OFF}$ ratio decreases by ~$10^3$ and the SS increases by approximately a factor of 10 after the UHV and FG anneals. High performance Sc electron contacts to BP have recently been demonstrated.[25,26] One study correlates significant improvements in n-type device performance with the formation of a $Sc_xO_y$ layer between the Sc contact and BP over one month in ambient conditions.[26] $Sc_xO_y$ formed in the presence of hydroxide molecules (e.g., gettered from air), such as the $Sc_xO_y$ that formed over time at the Sc–BP interface, contains a significant concentration of hydrogen (Figure 7.1d), which presumably affects the conductivity. The anneals performed in this work dehydrogenate the $Sc_xO_y$ in the Sc films on $WSe_2$[27] resulting in the degraded performance measured with increasing anneal temperature. Therefore, post metallization anneals in a reducing environment (e.g., UHV or FG) should be avoided to prevent device performance degradation, maximize the gate modulation, minimize the turn-on voltage, and maintain a low electron Schottky barrier when Sc contacts are employed.

### 7.4.3 Controlling the Contact Polarity by Inserting an $Sc_xO_y$ Interlayer

$E_F$ depinning at the contacts in devices based on 2D materials has been achieved by inserting a tunnel barrier[15,68] or 're-pinning' layer[66] between the contact and the channel. $Sc_xO_y$ has only recently been explored, albeit unintentionally, as an interlayer to control contact performance.[26] In this work, $WSe_2$ was treated with AH to etch the surface, which promotes surface oxidation *in–situ* in UHV. The formation of $WO_x$ as a result of atomic hydrogen is evidenced by the two chemical states detected at higher binding energy from the $WSe_2$ chemical state in the corresponding W 4*f* core level spectrum (Figure 7.10a), consistent with the $W^{5+}$ and $W^{4+}$ (different bonding environment from $W^{4+}$ in $WSe_2$) oxidation states.[69] A chemical state is detected in the corresponding O 1*s* core level spectrum (Figure 7.10a) at ~530.8 eV, which is consistent with that of a transtion metal oxide.[70] Pd/Sc contacts were then deposited *in-situ,* in UHV, at RT, and through a shadow mask to reactively form a $Sc_xO_y$ interlayer between the metal and the $WSe_2$. Sc scavenges oxygen from $WO_x$ during the UHV deposition, forming an interfacial $Sc_xO_y$ layer. A 3 nm Sc film was deposited on one sample to form an interlayer entirely comprised of intermetallics and $Sc_xO_y$ and therefore facilitate hole dominant conduction via the Pd layer. 15 nm Sc was deposited on another AH-treated sample to form a substantial metallic Sc layer between the $Sc_xO_y$ interlayer and the Pd capping layer, which facilitates electron dominant conduction.

The forward bias currents measured from the 65 nm Pd/3 nm Sc/$WSe_2$ diodes between 25 °C and 110 °C were transformed according to Equation 7.1[71]

$$\frac{I}{1-e^{\frac{qV}{kT}}}$$

Equation 7.1

where I, q, V, k, and T represent the measured current, electron charge, applied bias, Boltzmann's constant, and temperature, and the linear region in each curve between 0.15 V and 0.35 V was fitted using linear regression. The Richardson constant (33.9 $A/cm^{-2}\ K^{-2}$, $m_e$*=0.33),[72] Schottky barrier height (0.85 eV), and an ideality factor (1.00, averaged from 5 diodes) are calculated from the slope and intercept of the best fit line to the I–V curve obtained at 110 °C (Figures 7.10 b-d).[71] An ideality factor of 1.00 indicates the barrier height is homogeneous across the interface. This suggests the atomic hydrogen treatment coupled with the $Sc_xO_y$ interlayer eliminate defects at the interface unlike the highly inhomogeneous barrier formed between Pd and $WSe_2$ at RT.[5] However, the $E_F$ resides much closer to midgap when the $Sc_xO_y$ interlayer is included between Pd and $WSe_2$

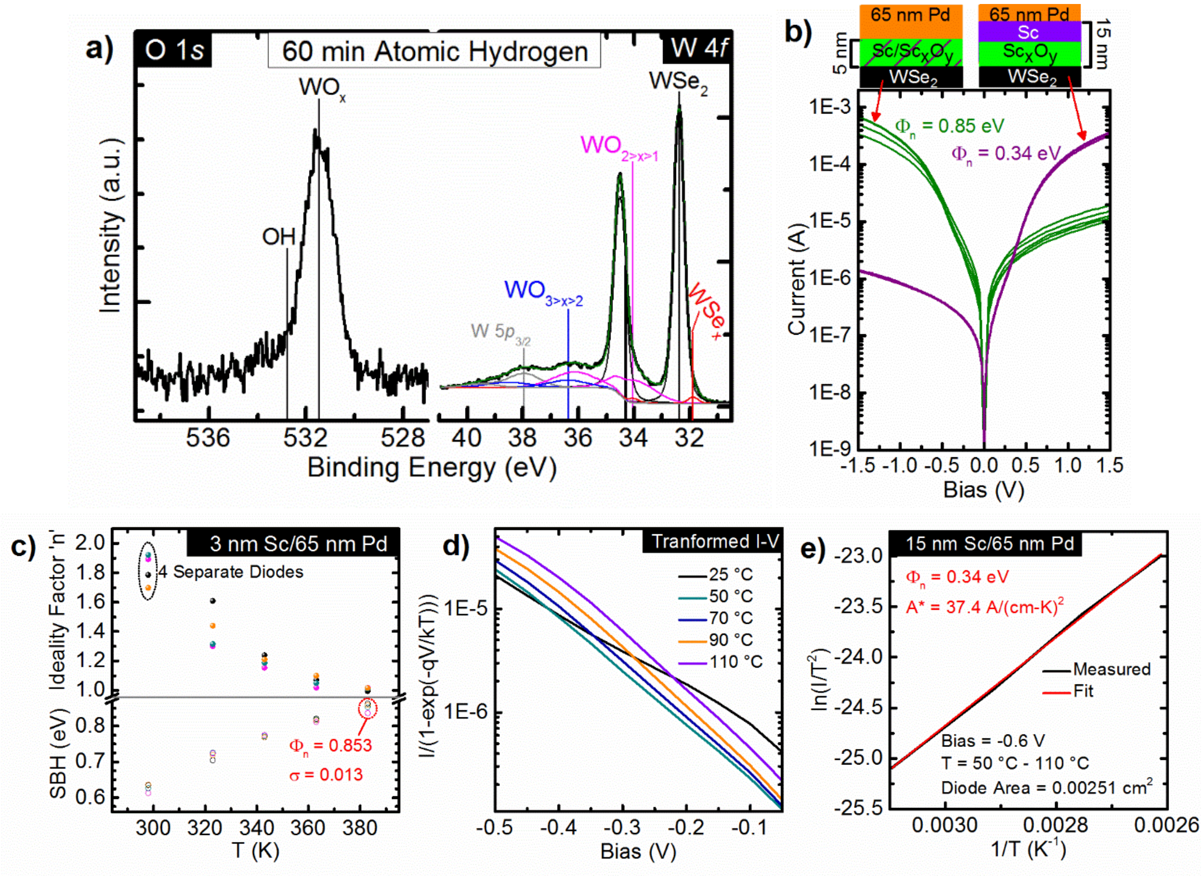

Figure 7.10. a) O 1*s* and W 4*f* core level spectra obtained *in-situ* from bulk $WSe_2$ after 60 minute AH treatment. b) I-V characteristics obtained from Pd–Sc–$WSe_2$ Schottky diodes deliberately treated with AH before metallization to form an interlayer. c) The ideality factor and electron Schottky barrier height obtained from linear fits of d) transformed, temperature dependent I–V characteristics of four Pd/15 nm Sc/$WSe_2$ Schottky diodes. e) The Arrhenius plot and associated linear fit obtained from a Pd/5 nm Sc/$WSe_2$ Schottky diode at V = -0.6 over a temperature range of 50 °C to 110 °C.

compared with the Ohmic hole band alignment exhibited by Pd contacts to $WSe_2$ at RT.[5] Some metallic Sc is likely present within the interlayer and contributes to the near–midgap alignment measured here. An Arrhenius plot of the temperature dependent I-V curves obtained from the 3 nm Sc/65 nm Pd/$WSe_2$ Schottky diodes exhibited significant nonlinearity and would have therefore yielded an unreliable Schottky barrier height. $WSe_2$ Schottky diodes were fabricated with a $Sc_xO_y$ layer at the Sc contact interface by depositing the first few nm of Sc *in–situ* in HV and continuing the Sc deposition in UHV to obtain a Sc/$Sc_xO_y$/$WSe_2$ diode structure. However, the $Sc_xO_y$ deposition rate was underestimated and the diodes exhibited rectifying ambipolar I-V characteristics (not shown here), which corroborates the detriment of a thick $Sc_xO_y$ layer at the Sc contact interface.

The transformed temperature dependent I-V curves obtained from the 65 nm Pd/15 nm Sc/$WSe_2$ Schottky diodes yield ideality factors > 3 in all cases, which indicates the corresponding Schottky barrier heights will be unreliable. However, an Arrhenius plot of the reverse bias I-V characteristics of the 65 nm Pd/15 nm Sc/$WSe_2$ Schottky diodes yields a linear pattern, from which a 0.34 eV electron Schottky barrier is extracted. The 0.34 eV electron Schottky barrier obtained with the 15 nm Sc layer deposited onto the atomic hydrogen-treated $WSe_2$ is 0.51 eV smaller than the diodes where only 3 nm Sc was deposited (Figures 7.10 b, e) and ~0.1 eV less than Sc–$WSe_2$ FETs after metallization at RT. The contact structures, fabrication and processing details, and Schottky barrier heights of all devices from this work are summarized in Table 7.1. Therefore, electron dominant conduction is facilitated by the low work function metallic Sc layer that accumulates on top of the interfacial $Sc_xO_y$. More effective $E_F$ depinning may be achievable with scandium oxide by tuning the $Sc_xO_y$ layer to minimize the thickness and maximize the tunneling current or by directly depositing the $Sc_xO_y$ rather than depositing metallic Sc on oxidized $WSe_2$.

Table 7.1. Schottky diode and FET contact structure, fabrication details, and electron Schottky barrier height after processing.

| Sc Thickness | Pd Thickness | Anneal Temperature | Anneal Ambient | Atomic Hydrogen Treatment | Electron Schottky Barrier Height |
|---|---|---|---|---|---|
| 20 nm | 50 nm | N/A | N/A | N/A | 0.44 eV |
| 20 nm | 50 nm | 400 °C | UHV | N/A | 0.70 eV |
| 20 nm | 50 nm | 400 °C | 95% $N_2$, 5% $H_2$ | N/A | 0.87 eV |
| 3 nm | 65 nm | N/A | N/A | 45 min | 0.85 eV |
| 15 nm | 65 nm | N/A | N/A | 45 min | 0.34 eV |

The electron Schottky barrier formed between Sc and $WSe_2$ can be reduced by limiting the intermetallic concentration (i.e., minimizing intermetallic-induced gap states). The contact structure, fabrication and processing details, and employing an optimized, oxygen deficient $Sc_xO_y$ interlayer will minimize reactions with $WSe_2$ and also provide greater $E_F$ control when other contact metals are employed in conjuction with the interlayer.

### 7.4.4 Local Density of States around Sc Atoms/Clusters on $WSe_2$: STM and STS

The Sc–$WSe_2$ diodes and FETs discussed above exhibit appreciable 0.4–0.45 eV electron Schottky barriers at RT, which is unexpected considering the work function of Sc (~3.5 eV) is smaller than the electron affinity of $WSe_2$ (~4.1 eV).[9,73] Scanning tunneling microscopy (STM) and spectroscopy (STS) elucidate the surface topography and local density of states (LDOS). Therefore, STM and STS can provide insight into changes in the electronic structure of the $WSe_2$ surface induced by Sc in the earliest stages of metallization (i.e., after depositing a < 3 Å Sc film). The exfoliated $WSe_2$ surface before metallization is atomically flat with a random distribution of atomic scale defects across the surface, similar to previously published STM images from bulk $WSe_2$.[9] The upper and lower STM images in Figure 7.11a were obtained *in–situ* under positive and negative tip bias, respectively, from exfoliated, bulk $WSe_2$ after depositing ~1 Å Sc in UHV at RT. Sc atoms/clusters appear as small bright spots surrounded by large dark regions under forward bias, while they appear as large bright patches and ~2 nm diameter rings under reverse bias. The dark contrast exhibited by Sc regions in positive bias indicate an associated high resistance tunneling barrier and therefore fewer occupied LDOS. Sc oxidation occurs in UHV and therefore could contribute to the suppressed LDOS around Sc when 'filled' states are probed.

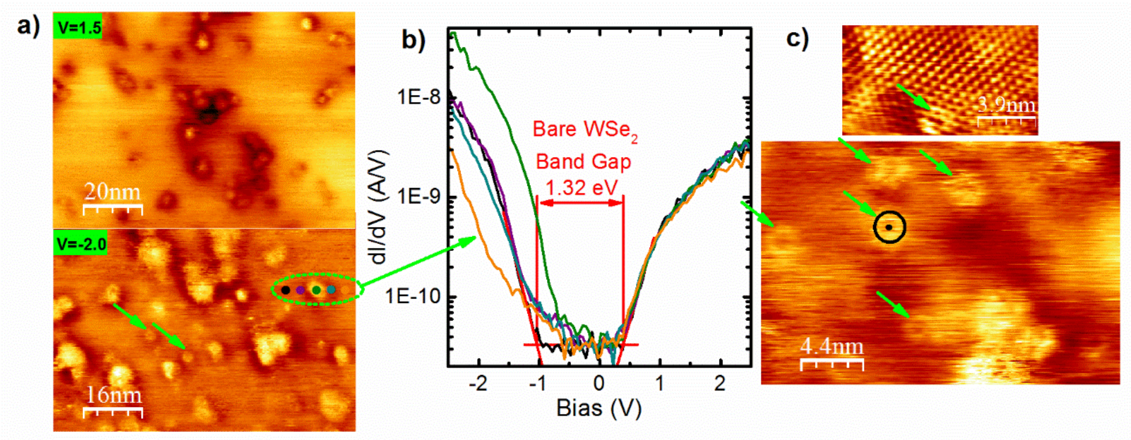

Figure 7.11. a) STM images obtained from $WSe_2$ after a ~1 Å Sc film was deposited in UHV with the upper (lower) image obtained at 1.5 V and 0.5 A (-1.8 V and 0.8 A). b) STS conductance spectra obtained from points spanning a ~3 nm diameter Sc cluster and the surrounding $WSe_2$ showing the significant increase in LDOS below the $WSe_2$ $E_F$ when the tip probes directly over the Sc cluster. Each spectrum is a differentiated average of 20 sweeps over the same spot. c) High resolution STM images obtained from the same 1 Å Sc–$WSe_2$ sample showing atomic resolution in a region of bare $WSe_2$, rings of bright contrast reflecting charge redistribution around single Sc atoms (some indicated by green arrows), and larger Sc clusters.

Five STS were obtained in an array spanning a Sc cluster and the surrounding $WSe_2$ (dots in Figure 7.11a, lower image). The bare $WSe_2$ exhibits a band gap of 1.32 ± 0.05 eV, which is consistent with previous STM studies of bulk $WSe_2$ (Figure 7.11b).[9] The $E_F$ is detected 0.33 ± 0.05 eV from the valence band edge, which is consistent with the XPS-derived band alignment of exfoliated $WSe_2$ in this work. As the tip approaches the Sc cluster, the reverse bias conductance and density of gap states below the $E_F$ increase and reach a maximum when the tip is positioned directly over it. The enhanced density of states in the valence band observed over Sc clusters is qualitatively consistent with the $E_F$ shift away from the conduction band detected by XPS after depositing Sc on $WSe_2$.

In high resolution reverse bias images (Figure 7.11c), individual Sc atoms and the associated Sc–Se bonds are inferred from numerous ~2 nm diameter rings of bright contrast (pointed out by arrows). These regions exhibit central symmetry, which suggests a one dimensional feature (i.e., a single atom) is present at the center. Similar features were observed via STM around isolated Mo atoms at interstitial sites in the $MoTe_2$ lattice.[73] The ring of bright contrast observed in reverse bias images manifests as a result of charge transfer from Sc to the surrounding Se atoms, similar to the charge redistribution associated with mirror twin boundaries in TMDs. Therefore, the formation of Sc–Se bonds and the associated enhanced density of states below the $WSe_2$ $E_F$ contribute significantly to the unexpectedly high electron Schottky barrier formed between the Sc contact and $WSe_2$.

## 7.5 Discussion

The physical characterization, $E_F$ shifts according to XPS, and electrical characteristics of Schottky diodes and FETs indicate the $WSe_2$ FETs exhibit the lowest electron Schottky barrier height, the highest $I_{ON}/I_{OFF}$ ratio (~$10^6$), and the steepest SS (109 mV/dec) when the intermetallic concentration at the Sc–$WSe_2$ interface is minimized and the concentration of metallic Sc within the contact is maximized. In this work, the lowest electron Schottky barrier between Sc and $WSe_2$ (0.34 eV) is achieved by oxidizing the $WSe_2$ surface prior to Sc deposition, which both limits the Sc–$WSe_2$ reaction and avoids the deleterious post metallization anneals. Inserting an inert, oxygen-free tunneling layer (e.g., hBN)[15] between Sc and $WSe_2$ would more effectively prevent the Sc–$WSe_2$ reactions and decrease oxygen concentration in the Sc layer compared to the reactively formed $Sc_xO_y$ interlayer employed in this work, likely resulting in the highest performance Sc contact to $WSe_2$. Sc immediately consumes one $WSe_2$ layer at RT and at least three layers during the post metallization anneals. This work establishes relationships between the Sc–$WSe_2$ interface chemistry, structure, and band alignment associated with specific pre- and post-metallization processing steps, which are integral to engineering consistent, high-performance Sc contacts to any TMD. Critically, we demonstrate high performance n-type $WSe_2$ FETs with Sc contacts and establish processing conditions (both to employ and to avoid) for consistent, high-performance n-type Sc contacts.

## 7.6 Conclusions

This work demonstrates high-performance n-type $WSe_2$ FETs with impressive $I_{ON}/I_{OFF}$ ($10^6$) and SS (109 mV/dec), which is achieved without any post metallization processing and by depositing the Sc contacts in UHV. Mildly oxidizing the $WSe_2$ surface at the contact regions before metallization reduces the electron SBH formed between Sc and $WSe_2$ at RT by 0.1 eV as a direct result of the minimized concentration of scandium selenide at the interface. The largest electron Schottky barrier heights of 0.7 eV and 0.87 eV (400 °C UHV and FG, respectively) worst SS (~1 V/dec), and lowest $I_{ON}/I_{OFF}$ ratios (~$10^3$) are measured when post metallization anneals are employed. XPS indicates the anneals increase the electron SBH by 0.4-0.5 eV and completely oxidize the Sc contact, which cause the aforementioned degraded device performance. STM and STS explicitly relate the unexpectedly large electron SBH observed between Sc and $WSe_2$ throughout this work with an enhanced LDOS below the $WSe_2$ $E_F$ in the presence of Sc–Se bonds, which necessitates processing conditions that limit the Sc–$WSe_2$ reaction. The significant reactions between Sc and $WSe_2$ are corroborated by Raman spectroscopy and STEM, which indicate 1L $WSe_2$ is consumed at RT and at least three $WSe_2$ layers are consumed during the anneals. The processing condition-dependent number of $WSe_2$ layers consumed by Sc is a critical benchmark for future device architectures based on $WSe_2$, especially those relying on the giant spin-Hall effect that occurs in $WSe_2$ with $D_{3h}$ symmetry. This work shows a detailed understanding of the relationships between processing conditions, interface chemistry, and contact performance can be leveraged in any metal–TMD system to consistently achieve the highest device performance.

### 7.7 References

(1) Abraham, M.; Mohney, S. E. Annealed Ag Contacts to $MoS_2$ Field-Effect Transistors. *J. Appl. Phys.* **2017**, *122*, 115306.

(2) Wu, Y.; Xiang, J.; Yang, C.; Lu, W.; Lieber, C. M. Single-Crystal Metallic Nanowires and Metal/semiconductor Nanowire Heterostructures. *Nature* **2004**, *430*, 61–65.

(3) Lin, J. C.; Yu, S. Y.; Mohney, S. E. Characterization of Low-Resistance Ohmic Contacts to N- and P-Type InGaAs. *J. Appl. Phys.* **2016**, *114*, 044504.

(4) Walsh, L. A.; Hughes, G.; Weiland, C.; Woicik, J. C.; Lee, R. T. P.; Loh, W. Y.; Lysaght, P.; Hobbs, C. Ni-(In,Ga)As Alloy Formation Investigated by Hard-X-Ray Photoelectron Spectroscopy and X-Ray Absorption Spectroscopy. *Phys. Rev. Appl.* **2014**, *2*, 064010.

(5) Smyth, C. M.; Walsh, L. A.; Bolshakov, P.; Catalano, M.; Addou, R.; Wang, L.; Kim, J.; Kim, M. J.; Young, C. D.; Hinkle, C. L.; Wallace, R. M. Engineering the Pd-$WSe_2$ Interface Chemistry for FETs with High Performance Hole Contacts. Under review, *ACS Appl. Nano Materials*, **2018**.

(6) Allain, A.; Kang, J.; Banerjee, K.; Kis, A. Electrical Contacts to Two-Dimensional Semiconductors. *Nat. Mater.* **2015**, *14*, 1195–1205.

(7) Addou, R.; McDonnell, S.; Barrera, D.; Guo, Z.; Azcatl, A.; Wang, J.; Zhu, H.; Hinkle, C. L.; Quevedo-Lopez, M.; Alshareef, H. N.; et al. Impurities and Electronic Property Variations of Natural $MoS_2$ Crystal Surfaces. *ACS Nano* **2015**, *9*, 9124–9133.

(8) McDonnell, S.; Addou, R.; Buie, C.; Wallace, R. M.; Hinkle, C. L. Defect Dominated Doping and Contact Resistance in $MoS_2$. *ACS Nano* **2014**, *8*, 2880–2888.

(9) Addou, R.; Wallace, R. M. Surface Analysis of $WSe_2$ Crystals: Spatial and Electronic Variability. *ACS Appl. Mater. Interfaces* **2016**, *8*, 26400–26406.

(10) Smyth, C. M.; Addou, R.; McDonnell, S.; Hinkle, C. L.; Wallace, R. M. Contact Metal-$MoS_2$ Interfacial Reactions and Potential Implications on $MoS_2$-Based Device Performance. *J. Phys. Chem. C* **2016**, *120*, 14719–14729.

(11) Smyth, C. M.; Addou, R.; McDonnell, S.; Hinkle, C. L.; Wallace, R. M. $WSe_2$-Contact Metal Interface Chemistry and Band Alignment under High Vacuum and Ultra High Vacuum Deposition Conditions. *2D Mater.* **2017**, *4*, 025084.

(12) McDonnell, S.; Smyth, C.; Hinkle, C. L.; Wallace, R. M. $MoS_2$-Titanium Contact Interface Reactions. *ACS Appl. Mater. Interfaces* **2016**, *8*, 8289–8294.

(13) Joo, M.-K.; Moon, B. H.; Ji, H.; Han, G. H.; Kim, H.; Lee, G.; Lim, S. C.; Suh, D.; Lee, Y. H. Electron Excess Doping and Effective Schottky Barrier Reduction on the $MoS_2$/h-BN Heterostructure. *ACS Nano*, **2016**, *16* (10), 6383-6389.

(14) Penumatcha, A. V. Salazar, R. B.; Appenzeller, J. Analysing Black Phosphorous Transistors Using an Analytic Schottky Barrier MOSFET Model. *Nat. Commun.* **2015**, *6*, 8948.

(15) Mleczko, M. J.; Yu, A. C.; Smyth, C. M.; Shin, Y. C.; Chen, V.; Tsai, Y.-C.; Nishi, Y.; Wallace, R. M.; Pop, E. Contact Engineering High Performance n-Type $MoTe_2$ Transistors. Submitted to *Nano Lett.*, **2018**.

(16) Prakash, A.; Appenzeller, J. Bandgap Extraction and Device Analysis of Ionic Liquid Gated $WSe_2$ Schottky Barrier Transistors. *ACS Nano* **2017**, *11*, 1626–1632.

(17) Appenzeller, J.; Zhang, F.; Das, S.; Knoch, J. Transition Metal Dichalcogenide Schottky Barrier Transistors: A Device Analysis and Material Comparison. In *2D Materials for Nanoelectronics*; Houssa, M.; Dimoulas, A.; Molle, A., Ed.; Taylor & Francis: New York, 2016; pp. 207–240.

(18) McDonnell, S.; Azcatl, A.; Addou, R.; Gong, C.; Battaglia, C.; Chuang, S.; Cho, K.; Javey, A.; Wallace, R. M. Hole Contacts on Transition Metal Dichalcogenides: Interface Chemistry and Band Alignments. *ACS Nano* **2014**, *8*, 6265–6272.

(19) Chuang, H. J.; Chamlagain, B.; Koehler, M.; Perera, M. M.; Yan, J.; Mandrus, D.; Tománek, D.; Zhou, Z. Low-Resistance 2D/2D Ohmic Contacts: A Universal Approach to High-Performance $WSe_2$, $MoS_2$, and $MoSe_2$ Transistors. *Nano Lett.* **2016**, *16*, 1896–1902.

(20) Cho, S.; Kim, S.; Kim, J. H.; Zhao, J.; Seok, J.; Keum, D. H.; Baik, J.; Choe, D.; Chang, K. J.; Suenaga, K.; et al. Phase Patterning for Ohmic Homojunction Contact in $MoTe_2$. *Science* **2015**, *349*, 625-628.

(21) Kappera, R.; Voiry, D.; Yalcin, S. E.; Branch, B.; Gupta, G.; Mohite, A. D.; Chhowalla, M. Phase-Engineered Low-Resistance Contacts for Ultrathin $MoS_2$ Transistors. *Nat. Mater.* **2014**, *13*, 1128–1134.

(22) Sung, J. H.; Heo, H.; Si, S.; Kim, Y. H.; Noh, H. R.; Song, K.; Kim, J.; Lee, C.-S.; Seo, S.-Y.; Kim, D.-H.; et al. Coplanar Semiconductor–metal Circuitry Defined on Few-Layer $MoTe_2$ via Polymorphic Heteroepitaxy. *Nat. Nanotechnol.* **2017**, *12*, 1064-1070.

(23) Liu, W.; Kang, J.; Sarkar, D.; Khatami, Y.; Jena, D.; Banerjee, K. Role of Metal Contacts in Designing High-Performance Monolayer N-Type $WSe_2$ Field Effect Transistors. *Nano Lett.* **2013**, *13*, 1983–1990.

(24) Das, S.; Chen, H. Y.; Penumatcha, A. V.; Appenzeller, J. High Performance Multilayer $MoS_2$ Transistors with Scandium Contacts. *Nano Lett.* **2013**, *13*, 100–105.

(25) Wang, C.-H.; Incorvia, J. A. C.; McClellan, C. J.; Yu, A. C.; Mleczko, M. J.; Pop, E.; Philip Wong, H.-S. Unipolar n-Type Black Phosphorous Transistors with Low Work Function Contacts. *Nano Lett.*, **2018**, *18*, 2822-2827.

(26) Li, L.; Engel, M.; Farmer, D. B.; Han, S.-J.; Philip Wong, H.-S. High-Performance p-Type Black Phosphorous Transistor with Scandium Contact. *ACS Nano*, **2016**, *10*, 4672-4677.

(27) Liu, A.; Liu, G.; Zhu, H.; Song, H.; Shin, B.; Fortunato, E.; Martins, R.; Shan, F. Water-Induced Scandium Oxide Dielectric for Low-Operating Voltage n- and p-Type Metal-Oxide Thin-Film Transistors. *Adv. Funct. Mater.*, **2015**, *25*, 7180-7188.

(28) Zhu, Z. Y.; Cheng, Y. C.; Schwingenschlogl, U. Giant Spin-Orbit-Induced Spin Splitting in Two-Dimensional Transition-Metal Dichalcogenide Semiconductors. *Phys. Rev. B.* **2011**, *84*, 153402.

(29) Shao, Q.; Yu, G.; Lan, Y.-W.; Shi, Y.; Li, M.-Y.; Zheng, C.; Zhu, X.; Li, L.-J.; Amiri, P. K.; Wang, K. L. Strong Rashba-Edelstein Effect-Induced Spin-Orbit Torques in Monolayer Transition Metal Dichalcogenide/Ferromagnet Bilayers. *Nano Lett.* **2016**, *16* (12), 7514-7520.

(30) Bulk $WSe_2$ crystals, HQ Graphene, 2017; www.hqgraphene.com.

(31) Horcas, I.; Fernández, R.; Gómez-Rodríguez, J. M.; Colchero, J.; Gómez-Herrero, J.; Baro, A. M. WSXM: A Software for Scanning Probe Microscopy and a Tool for Nanotechnology. *Rev. Sci. Instrum.* **2007**, *78*.

(32) Wallace, R. M. In-Situ Studies of Interfacial Bonding of High-K Dielectrics for CMOS Beyond 22 nm. *ECS Trans.* **2008**, *16*, 255–271.

(33) Wallace, R. M. In-Situ Studies on 2D Materials. *ECS Trans.* **2014**, *64*, 109–116.

(34) ASTM E2108-10 Standard Practice for Calibration of the Electron Binding-Energy Scale of an X-Ray Photoelectron Spectrometer, **2000**.

(35) Herrera-Gómez, A.; Hegedus, A.; Meissner, P. L. Chemical Depth Profile of Ultrathin Nitrided $SiO_2$ Films. *Appl. Phys. Lett.* **2002**, *81*, 1014–1016.

(36) BJD 1800 Temescal e-beam evaporator, University of Texas at Dallas Cleanroom, 2017; http://www.utdallas.edu/research/cleanroom/

(37) Freedy, K. M.; Giri, A.; Foley, B. M.; Barone, M. R.; Hopkins, P. E.; McDonnell, S. Titanium Contacts to Graphene: Process-Induced Variability in Electronic and Thermal Transport. *Nanotechnology*, **2018**, *29*, 145201.

(38) Chemical bonding overview, www.chemhume.co.uk; 2015.

(39) Gila, B. P.; Johnson, J. W.; Mehandru, R.; Luo, B.; Onstine, A. H.; Allums, K. K.; Krishnamoorthy, V.; Bates, S.; Abernathy, C. R.; Ren, F.; Pearton, S. J. Gadolinium Oxide and Scandium Oxide: Gate Dielectrics for GaN MOSFETs. Phys. Stat. Sol. 2001, 188 (1), 239-242.

(40) R. C. Weast, D. R. Lide, M. J. Astle, W. H. B. Selected Values of Chemical Thermodynamic Properties. In *CRC Handbook of Chemistry and Physics*; CRC Press: Boca Raton, FL, **1995**.

(41) Wagner, C. D.; Davis, L. E.; Zeller, M. V.; Taylor, J. A.; Raymond, R. H.; Gale, L. H. Empirical Atomic Sensitivity Factors for Quantitative Analysis by Electron Spectroscopy for Chemical Analysis. *Surf. Interface Anal.* **1981**, *3*, 211–225.

(42) Doniach, S.; Sunjic, M. Many-Electron Singularity in X-ray Photoemission and X-ray Line Spectra from Metals. *J. Phys. C: Solid State Phys.* **1970**, *3*, 285-291.

(43) Weightman, P.; Roberts, E. D.; Johnson, C. E. $L_{2,3}$MM Auger Processes in Selenium. J. Phys. C: Solid State Phys., 1975, 8, 550-566.

(44) Sidorko, V. R.; Goncharuk, L. V.; Gordiychuk, O. V.; Antonchenko, R. V. Thermodynamic Properties of Scandium Carbides. *J. Alloys and Compounds*, **1995**, *228*, 159-163.

(45) Porte, L. Stoichiometric ScN and Nitrogen Deficient Scandium Nitride Layers Studied by Photoelectron Spectroscopy. *J. Phys. C Solid State Phys.* **2000**, *18*, 6701–6709.

(46) King, S. W.; Davis, R. F.; Nemanich, R. J. Gas Source Molecular Beam Epitaxy of Scandium Nitride on Silicon Carbide and Gallium Nitride Surfaces. *J. Vac. Sci. Technol. A Vacuum, Surfaces, Film.* **2014**, *32*, 61504.

(47) Biesinger, M. C.; Lau, L. W. M.; Gerson, A. R.; Smart, R. S. C. Resolving Surface Chemical States in XPS Analysis of First Row Transition Metals, Oxides and Hydroxides: Sc, Ti, V, Cu and Zn. *Appl. Surf. Sci.* **2010**, *257*, 887–898.

(48) Zhao, P.; Azcatl, A.; Bolshakov, P.; Moon, J.; Hinkle, C. L.; Hurley, P. K.; Wallace, R. M.; Young, C. D. Effects of Annealing on Top-Gated $MoS_2$ Transistors with $HfO_2$ Dielectric. *J. Vac. Sci. Technol. B, Nanotechnol. Microelectron. Mater. Process. Meas. Phenom.* **2017**, *35*, 01A118.

(49) Amani, M.; Lien, D.; Kiriya, D.; Xiao, J.; Azcatl, A.; Noh, J.; Madhvapathy, S. R.; Addou, R.; KC, S.; Dubey, M.; et al. Near-Unity Photoluminescence Quantum Yield in $MoS_2$. *Science* **2015**, *350*, 1065–1068.

(50) Luo, Y-R. In *Comprehensive Handbook of Chemical Bond Energies*; CRC Press, Taylor & Francis Group: Boca Raton, FL, **2007**.

(51) Sevy, A.; Huffaker, R. F.; Morse, M. D. Bond Dissociation Energies of Tungsten Molecules: WC, WSi, WS, WSe, and WCl. *J. Phys. Chem. A.* **2017**, *121*, 9446-9457.

(52) Kang, J.; Liu, W.; Sarkar, D.; Jena, D.; Banerjee, K. Computational Study of Metal Contacts to Monolayer Transition-Metal Dichalcogenide Semiconductors. *Phys. Rev. X* **2014**, *4*, 031005.

(53) Liu, W.; Kang, J.; Cao, W.; Sarkar, D.; Khatami, Y.; Jena, D.; Banerjee, K. High-Performance Few-Layer-$MoS_2$ Field-Effect-Transistor with Record Low Contact-Resistance. DOI: 10.1109/IEDM.2013.6724660.

(54) Kappera, R.; Voiry, D.; Yalcin, S. E.; Branch, B.; Gupta, G.; Mohite, A. D.; Chhowalla, M. Phase-Engineered Low-Resistance Contacts for Ultrathin $MoS_2$ Transistors. Nat. Mater., 2014, 13, 1128-1134.

(55) Chen, C.-H.; Wu, C.-L.; Pu, J.; Chiu, M.-H.; Kumar, P.; Takenobu, T.; Li, L.-J. Hole Mobility Enhancement and P-Doping in Monolayer $WSe_2$ by Gold Decoration. *2D Mater.* **2014**, *1*, 034001.

(56) Gong, C.; Huang, C.; Miller, J.; Cheng, L.; Hao, Y.; Cobden, D.; Kim, J.; Ruoff, R. S.; Wallace, R. M.; Cho, K.; et al. Metal Contacts on Physical Vapor Deposited Monolayer $MoS_2$. *ACS Nano* **2013**, *7*, 11350–11357.

(57) Yuan, H.; Cheng, G.; You, L.; Li, H.; Zhu, H.; Li, W.; Kopanski, J. J.; Obeng, Y. S.; Hight Walker, A. R.; Gundlach, D. J.; et al. Influence of Metal-$MoS_2$ Interface on $MoS_2$ Transistor Performance: Comparison of Ag and Ti Contacts. *ACS Appl. Mater. Interfaces* **2015**, *7*, 1180–1187.

(58) Tan, Q.-H.; Zhang, X.; Luo, X.-D.; Zhang, J.; Tan, P.-H. Layer-Number Dependent High-Frequency Vibration Modes in Few-Layer Transition Metal Dichalcogenides Induced by Interlayer Couplings. J. Semicond., 2017, 38, 031006.

(59) Zhao, W.; Ghorannevis, Z.; Amara, K. K.; Pang, J. R.; Toh, M.; Zhang, X.; Kloc, C.; Tan, P. H.; Eda, G. Lattice Dynamics in Mono- and Few-Layer Sheets of $WS_2$ and $WSe_2$. *Nanoscale* **2013**, *5*, 9677.

(60) Sahin, H.; Tongay, S.; Horzum, S.; Fan, W.; Zhou, J.; Li, J.; Wu, J.; Peeters, F. M. Anomalous Raman Spectra and Thickness-Dependent Electronic Properties of $WSe_2$. *Phys. Rev. B - Condens. Matter Mater. Phys.* **2013**, *87*, 165409.

(61) Shi, W.; Lin, M.-L.; Tan, Q.-H.; Qiao, X.-F.; Zhang, J.; Tan, P.-H. Raman and Photoluminescence Spectra of Two-Dimensional Nanocrystallites of Monolayer $WS_2$ and $WSe_2$. *2D Mater.* **2016**, *3*, 25016.

(62) Spedding, F H; Daane, A H; Herrmann, K. W. The Crystal Structures and Lattice Parameters of High-Purity Scandium, Yttrium, and the Rare Earth Metals. *Acta Crystallogr.* **1596**, *9*, 559.

(63) Feijoo, P. C.; del Prado, A.; Toledano-Luque, M.; San Andres, E.; Lucia, M. L. Scandium Oxide Deposited by High-Pressure Sputtering for Memory Devices: Physical and Interfacial Properties. *Appl. Phys. Lett.*, **2010**, *107*, 084505.

(64) The separation between the $WSe_2$ chemical states in the Se $3d_{5/2}$ and W $4f_{7/2}$ core level spectra were held constant throughout Sc deposition and post metallization annealing. Therefore, the binding energies of the $WSe_2$ chemical state in the W $4f_{7/2}$ core level spectra are omitted from Figure 7.9a.

(65) Michaelson, H. B. The Work Function of the Elements and Its Periodicity. *J. Appl. Phys.* **1977**, *48*, 4729-4733.

(66) Chen, J.-R.; Odenthal, P. M.; Swartz, A. G.; Floyd, G. C.; Wen, H.; Luo, K. Y.; Kawakami, R. K. Control of Schottky Barriers in Single Layer $MoS_2$ Transistors with Ferromagnetic Contacts. *Nano Lett.*, **2013**, *13*, 3106-3110.

(67) Scandium oxide charge neutrality level

(68) Coss, B. E.; Smith, C.; Loh, W.-Y.; Majhi, P.; Wallace, R. M.; Kim, J.; Jammy, R. Contact Resistance Reduction to FinFET Source/Drain Using Novel Dipole Schottky Barrier Height Modulation Method. DOI: 10.1109/LED.2011.2148091.

(69) Katrib, A.; Hemming, F.; Wehrer, P.; Hilaire, L.; Maire, G. *J. Electron Spectrosc. Relat. Phenom.* **1995**, *76*, 195-200.

(70) Wagner, C. D. *Handbook of X-Ray Photoelectron Spectroscopy: A Reference Book of Standard Data for Use in X-Ray Photoelectron Spectroscopy*; Perkin Elmer: Eden Prarie, 1979.

(71) D. K. Schroder, Semiconductor Material and Device Characterization, 3rd ed., John Wiley & Sons, Inc., NJ, USA 2006.

(72) Liu, W.; Cao, W.; Kang, J.; Banerjee, K. High–Performance Field–Effect–Transistors on Monolayer $WSe_2$. *ECS Trans.* **2013**, *58* (7), 281-285.

(73) Coelho, P. M.; Komsa, H.-P.; Diaz, H. C.; Ma, Y.; Krasheninnikov, A. V.; Batzill, M. Post-Synthesis Modifications of Two-Dimensional $MoSe_2$ or $MoTe_2$ by Incorporation of Excess Metal Atoms into the Crystal Structure. *ACS Nano*, **2018**, *12*, 3975-3984.

# CHAPTER 8

# INTERFACE REACTION AND FERMI LEVEL PINNING MECHANISMS BETWEEN PALLADIUM CONTACTS AND TELLURIUM FILMS GROWN BY MOLECULAR BEAM EPITAXY

Authors – Christopher M. Smyth, Guanyu Zhou, Adam T. Barton,

Robert M. Wallace, and Christopher L. Hinkle

The Department of Materials Science and Engineering, RL10
The University of Texas at Dallas
800 West Campbell Road
Richardson, Texas, 75080, USA

## 8.1 Preface

Palladium has been widely employed as the electrode metal in Te-based electronic devices and has enabled the highest Te transistor performance. Theoretical calculations predict strong Fermi level pinning near the Te valence band between Te and metal contacts spanning a wide work function range, which likely explains the predominant p-type conduction in Te transistors reported to date. However, the effects of the tellurium oxide that spontaneously forms in air on the band alignment at the contacts has not yet been explored. In this work, X-ray and ultraviolet photoelectron spectra (XPS and UPS, respectively) together show 0.4 nm and 1.5 nm thick native surface oxide films depin the Fermi level between metallic Pd contacts and Te films, which suggests the depinning effect occurs independent of the native oxide thickness. An atomic hydrogen treatment completely removes the native oxide from the Te surface. Removing the native oxide from Te facilitates strong Fermi level pinning between Pd and Te according to XPS and UPS, corroborating the depinning effect when the native oxide is present at the Pd–Te interface. A palladium telluride intermetallic is detected at the Pd–Te interface independent of the presence or absence of the native surface oxide. However, the concentration of $PdTe_x$ is 40% higher when the oxide is removed from the Te surface before Pd metallization, which corroborates the enhanced Fermi level pinning effect when the native oxide is removed. The reflection high energy electron diffraction (RHEED) pattern observed *in–situ* after the Te growth is initially streaky, which indicates a wire textured film relative to the HOPG substrate. However, the oxidation in air causes a surface reconstruction from atomically flat to multi-stepped according to the intra-streak modulated intensity that manifests in the corresponding RHEED patterns. This work shows an atomic hydrogen treatment effectively removes the native oxide from the Te surface. Critically, a controlled nanometer scale $TeO_x$ metal–

Te interlayer is a promising route to Fermi level depinning in contact metal–Te systems and will therefore facilitate the realization of electron contacts to Te for back end of line-compatible complementary logic circuits.

In this work, Dr. G. Zhou grew the Te films and prepared the HOPG substrates and helped interpret RHEED patterns. A. Barton helped obtain and interpret RHEED patterns. The Pd depositions, *in–situ* photoelectron spectroscopy (XPS and UPS), and atomic hydrogen treatment were performed by myself. Prof. C. L. Hinkle first suggested the study and both he and Prof. R. M. Wallace advised on the details of the experimental design. The text below was prepared by myself.

## 8.2 Introduction

Heterogeneous integration of high performance semiconducting materials using back end of line-compatible growth and processing conditions would greatly impact semiconductor technology and applications. Typically, achieving the exceptional crystal quality necessary for high speed, low power electronics requires growth temperatures far exceeding the thermal budget constraints required to preserve the integrity of circuitry assembled in front end of line processing. Tellurium has recently emerged as an ideal semiconductor candidate for device processing under a stringent thermal budget due to the extraordinary room temperature hole mobility and remarkable crystal quality demonstrated at growth temperatures ≤ 120 °C on a diverse array of substrates (single crystal, amorphous, polymer).[1,2] Similar with 2D semiconducting chalcogenides, Te exhibits a thickness dependent electronic structure with a 0.33 eV direct band gap in the bulk form that transitions to a 0.92 eV indirect band gap in a 2D monolayer.[3,4] Tellurium grows in unique 1D helical chains with threefold screw axis symmetry characterized by intrachain covalent bonding and interchain van der Waals bonding.[1] Te-based transistors reported to date have predominantly exhibited p-type conduction, which is largely due to the high work function metal Pd most commonly employed as the electrode material.[1,2,5,6] In fact, electrons transporting both parallel and perpendicular to the 1D Te chains are ligher than holes in bulk Te[7] indicating an electron mobility comparable with (and perhaps superior to) the reported hole mobilities (700-3000 $cm^2/V$ s)[1,2,5] should be achievable in the bulk form. Therefore, low electron Schottky barrier metal contacts are essential to realizing n-type Te devices.

Unfortunately, the spontaneous formation of a native oxide on Te in air[8] and the low melting (vaporization) temperature of Te in ambient conditions (in vacuum)[9] represent difficult-to-accommodate engineering challenges. A monumental effort that began early in the development of semiconductor technology dedicated to controlling the chemical and structural properties of the native oxide(s) in all technologically relevant semiconductors (silicon and its analogs,[10-13] III-V,[14-16] and 2D material[17-20]) continues today and should be extended to novel materials, such as Te. Crystalline $TeO_2$ is a wide gap semiconductor, but this work suggests the native Te surface oxide is amorphous. The effects of the native oxide on contact performance and, perhaps most importantly, contact polarity are not known. Thin 1-2 nm transition metal oxide layers have been successfully implemented in 3D[21,22] and 2D[23,24] semiconductor-based devices to simultaneously reduce contact resistance and alleviate Fermi level pinning. However, this technique requires precise control over the oxide thickness and coverage to maximize the tunneling current and minimize the contact resistance.

Recent reports have demonstrated the interface chemistry formed between metal contacts and transition metal dichalcogenides (TMD) varies significantly depending on the contact metal,[25-27] the TMD,[25-27] the quality of the TMD,[28,29] the deposition chamber ambient,[25-27] and post metallization processing conditions.[30] Similar to the continued contact resistance reduction achieved in silicide contact technology, processing-induced metal–TMD interface chemistry variations result in corresponding changes in band alignment and contact performance.[30,31] It is therefore critical to understand the interface chemistry formed between metal contacts and Te and the effects of the native oxide structure on the interface chemistry.

In this work, X-ray and ultraviolet photoelectron spectroscopy (XPS and UPS, respectively) are employed to demonstrate the formation of a palladium telluride intermetallic between Pd contacts and MBE-grown ~10 nm wire-textured Te films regardless of the thickness of the $TeO_x$ surface layer that forms in air when the sample is transferred from the growth system to the UVH cluster tool for characterization and metallization. The native oxide, which is amorphous, increases rapidly in thickness from 0.4 nm after 10 minutes in air to 1.5 nm after just 24 hours in air and induces a surface reconstruction within each domain from an atomically flat to a multi-stepped surface according to reflection high energy electron diffraction (RHEED). Atomic hydrogen completely removes the native oxide formed in air and facilitates a 40% increase in palladium telluride concentration at the corresponding oxygen-free Pd–Te interface. Depositing ~3 nm Pd on Te films exposed to air induces a work function shift from 4.64 eV to ~5.6 eV as expected of metallic Pd.[32] Critically, the work function shifts lower to 4.30 eV after depositing ~3 nm Pd on an atomic hydrogen-treated (i.e., oxide-free) Te film. This work indicates the native tellurium oxide can be advantageously engineered for Fermi level depinning between metal contacts and Te thereby providing a robust, back end of line-compatible process for complementary metal-oxide-semiconductor technology based on Te.

## 8.3 Experimental Details

*Te Growth.* The molecular beam epitaxy (MBE) growth process was carried out in a VG Semicon V80H MBE system with a base pressure of $1 \times 10^{-10}$ mbar, which increases to $3 \times 10^{-10}$ mbar during deposition. A cracker source (MBE-Komponenten) was employed to deposit Te (Alfa Aesar, 99.9999%) with base, valve, and cracker temperatures of 300 °C, 390 °C, and 440 °C, respectively. The highly oriented pyrolytic graphite (HOPG) substrates were mechanically exfoliated and, after loading into UHV, degassed *in–situ* at 600 °C for 60 minutes then cooled to -70 °C for the growth. The cryogenic growth temperature was reached by radiatively cooling the substrate via a liquid nitrogen-filled cryo shroud over ~12 hours. After the 1.5 hour growth (effective target thicknes ~10 nm), the samples were held in the growth chamber for 48 hours to slowly warm up, after which the RHEED pattern transitioned from diffuse to streaky indicating a transition from an amorphous film to a polycrystalline, wire-textured film.

*Air Exposure and Pd Deposition.* The Te growth was performed in a separate UHV cluster tool from the Pd metallization and associated characterization. All Te/HOPG samples described throughout this work were fabricated in the same growth. The duration of air exposure for each sample was controlled by monitoring the time between removing the samples from the growth chamber and loading the samples into the UHV cluster tool for metallization and characterization (10 minutes or 24 hours). The UHV cluster tool in which metallization and characterization are performed is described in detail elsewhere.[33,34]

The processes employed to outgas the metal Pd source and determine the deposition rate (~0.01 Å/s) were identical to the procedures described in Appendix A, respectively. Pd was deposited at room temperature on the Te samples to target thicknesses of 0.3 nm, 0.6 nm, 1 nm, and 3 nm respectively. The deposition rate determined at the beginning of the experiment was used to determine all deposition times, which led to slight variations in the measured Pd thickness compared with the target Pd film thickness. XPS and RHEED were performed *in–situ* after each deposition step.

*Atomic Hydrogen Treatment.* An MBE Komponenten Hydrogen Atom Beam Source (HABS 40) with tungsten filament was operated at a filament temperature of 1500 °C and a constant $H_2$ flow (99.9999% purity) adjusted *in–operando* to maintain a chamber pressure of $5 \times 10^{-6}$ mbar using a precision leak valve. The Te/HOPG sample was held at room temperature throughout the 45 minute atomic hydrogen (AH) treatment.

*RHEED*. After loading the samples into UHV, AH treatment (where applicable), and subsequent Pd deposition steps, RHEED was obtained *in–situ* with a Staib RHEED-15[35] system operated at 15 kV and 1.42 A. Images were obtained using image digitization/stabilization software from KSA.[36]

*Photoelectron Spectroscopy.* Core level spectra were obtained using a monochromated Al Kα source and an Omicron EA125 hemispherical analyzer with resolution of ±0.05 eV. The orientation between the sample surface normal and the detector was 45°, the acceptance angle was set to 8°, and a pass energy of 15 eV was used when acquiring high resolution spectra. The work function of the detector was calibrated with sputter-cleaned Au, Ag, and Cu foils according to ASTM E2108.[37] Core level spectra were deconvolved using AAnalyzer, a curve fitting software.[38] UPS was carried out using the same hemispherical analyzer as was employed in XPS measurements. HeI photons (hν = 21.2 eV) were employed as the incident beam, which were generated by striking a plasma in a differentially pumped glass capillary tube connected to the analysis chamber. A constant flow of ultra-high purity He (99.9999%) was maintained throughout the experiment using a precision leak valve. The plasma was maintained throughout spectral aquisition at 90 mA, 150 V, capillary tube pressure of $1.6 \times 10^{-1}$ mbar, and analysis chamber pressure of ~$2.0 \times 10^{-7}$ mbar. UPS spectra were acquired using a pass energy of 2 eV. A -9.82 eV bias was applied to all samples during UPS measurements to access the secondary electron cutoff. The work function was calibrated by shifting the UPS spectrum from a sputter-cleaned Au foil such that the secondary electron cutoff matched the expected polycrystalline Au work function of 5.13 eV and the inflection point of the low BE tail in the valence band spectrum crossed 0 eV binding energy (BE).[32] The same shift was applied to all subsequently acquired UPS spectra throughout this work. The work function was determined by extrapolating the steepest linear region of the secondary electron cutoff to its intercept with the baseline noise level via linear regression in Origin Pro Version 9.

## 8.4 Results and Discussion

Tellurium oxidation occurs spontaneously in air ($\Delta G^\circ_{f,TeO2}$ = -135.1 kJ/mol) and is observed on the initial surface of all Te films analyzed in this work, which is evidenced by the high BE chemical state detected in the corresponding Te $3d_{5/2}$ core level spectra (~576.1 eV, Figure 8.1).[39] All standard Gibbs free energies of formation provided in this work are reported per anion (e.g., $O^{2-}$, $Te^{2-}$). Previous work reports the native oxide thickness increases rapidly within the first few hours of exposing a Te film to air and saturates at a thickness of 1.5 nm after roughly six days in air.[40] The thickness of the native $TeO_x$ at the exposed channel, in the case of a back-gated tellurium transistor, or at the metal contact–Te interface will have significant implications on performance. In Figures 8.1 a, b, the Te $3d_{5/2}$ core levels obtained from Te films (grown by MBE on HOPG) after exposing samples to air for 10 minutes and 24 hours and subsequently depositing Pd in UHV up to a total thickness of ~3 nm are shown at left. The native $TeO_2$ grows to an effective thickness of 0.4 nm after 10 minutes in air and increases in thickness to 1.5 nm after 24 hours in air according to Equation 8.1

$$d = \lambda cos\theta ln\left(1 + \frac{\rho_M}{\rho_{ox}}\frac{I_{ox}}{I_M}\right)$$

Equation 8.1

where $d$ represents the tellurium oxide thickness, $\lambda$ represents the IMFP of photoelectrons from the Te film traveling through the $TeO_2$, $\rho_M$ (6.24 $g/cm^3$)[41] and $\rho_{ox}$ (5.67 $g/cm^3$)[41] represent the densities of the Te and the $TeO_2$, and $I_M$ and $I_{ox}$ represent the integrated intensities of the Te and $TeO_2$ (or $TeO_x$ in some cases) chemical states detected by XPS in a tellurium core level. Pd undergoes an exothermic reaction with tellurium to form $PdTe_x$ regardless of the native oxide thickness ($\Delta G^\circ_{f,PdTe}$ = -94.7 kJ/mol, $\Delta G^\circ_{f,PdTe2}$ = -34.7 kJ/mol).[42] The chemical state detected at high Be from the Te–Te chemical state and at low BE from the Te–O chemical state in the Te $3d_{5/2}$ core level spectra obtained after depositing Pd on the Te films exposed to air is associated with the formation of Te–Pd bonds at the interface (Figures 8.1 a, b). The Pd–Te reaction detected in this work is consistent with significant charge transfer predicted between Pd and Te in a previous DFT study, in which the binding energy per Te atom (3.36 eV) is the highest of any metal investigated in the study (Sc, Au, Cu, Ni, Ag, and Pt).[43] According to Mulliken population analysis, the 4*d* and 5*s* orbitals of Pd hybridize in the vicinity of Te resulting in three unpaired electrons in Pd that are free to bond with Te. The concentration of $PdTe_x$ formed at the interface seems to be independent of the native oxide thickness according to the similar $PdTe_x$ chemical state intensity in the Te $3d_{5/2}$ core levels obtained after depositing 3 nm Pd on the Te samples exposed to air for 10 minutes and

24 hours. After depositing ~3 nm Pd, the intensity of the $TeO_2$ chemical state around 576.1 eV decreases to near the limit of XPS detection and another chemical state at slightly lower BE is detected in the corresponding Te $3d_{5/2}$ core level indicating Pd also reduces $TeO_2$ to form Pd–O. The formation of PdO ($\Delta G°_{f,PdO}$ = -136.0 kJ/mol)[39] is more exothermic than the Pd–Te reaction. However, the Te–O bond dissociation energy (391.0 kJ/mol)[44] is much higher compared with that of the Te–Te bond (257.6 kJ/mol),[44] which presumably limits the Pd–$TeO_2$ reaction at the interface.

The $TeO_2$ that forms on the Te surface during 10 minutes in air is completely removed by exposing the oxidized surface to AH for 45 minutes. The $TeO_2$ chemical state detected in the Te $3d_{5/2}$ core level after exposing the Te film to air for 10 minuntes is below the limit of XPS detection in the Te $3d_{5/2}$ core level obtained after the AH treatment (Figure 8.1c). The potential energy associated with a hydrogen radical (H*, 217.5 kJ/mol)[44] is less than the energy required to break a Te–O bond. However, Te–O bond scission is energetically favorable under the continuous flux of H* during the AH treatment. Interestingly, Te–Te bond scission requires less energy than Te–O bond scission, which suggests the AH treatment may also slowly etch the Te film. However, there are no obvious indications of such a phenomenon in the results shown here. Additional experiments are required to definitively confirm or refute Te etching by AH. The concentration of $PdTe_x$

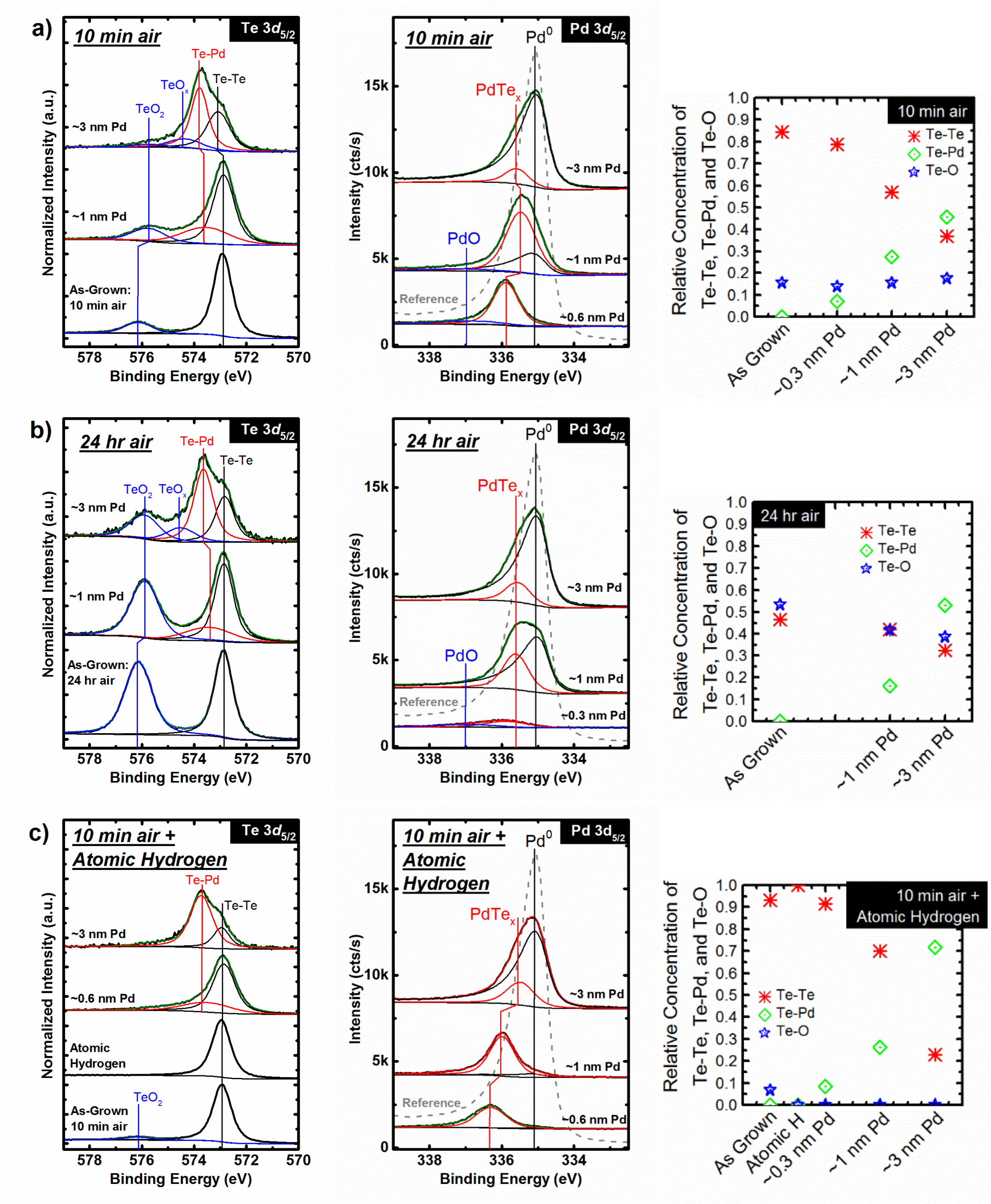

Figure 8.1. Te $3d_{5/2}$ and Pd $3d_{5/2}$ core levels obtained after depositing Pd on Te films grown on HOPG after exposing the films to air for a) 10 minutes and b) 24 hours and also c) after exposing the sample to air for 10 minutes and subsequently performing atomic hydrogen *in–situ*. The scatter plots shown at right reflect the relative intensities of the chemical states detected in the Te $3d_{5/2}$ core level throughout each experiment.

detected at the $TeO_2$-free Pd–Te interface is ~40% higher than the $PdTe_x$ concentration detected after depositing an equivalent Pd film on oxidized Te films, which is expected considering an oxygen free Te surface offers more Te sites for Pd to react with than an oxidized Te surface.

The Pd $3d_{5/2}$ core levels obtained in parallel with the Te $3d_{5/2}$ core levels discussed above are also displayed in Figure 8.1. The Pd $3d_{5/2}$ core levels obtained after initial Pd depostions (0.3 nm and 0.6 nm) on the Te films exposed to air for 10 minutes and 24 hours (Figures 8.1 a, b) are comprised mostly of the symmetric Pd–Te chemical state (335.9 eV) as well as the low intensity Pd–O chemical state (337.0 eV). The Pd–Te chemical state shifts to lower BE as additional Pd is deposited indicating the $PdTe_x$ becomes more Pd rich with increasing effective Pd thickness. The Pd–O chemical state falls below the limit of XPS detection after ~1 nm Pd is deposited corroborating the hypothesis that the PdO is isolated to the Pd–Te interface and only forms when Pd scavenges oxygen from $TeO_2$. After depositing ~3 nm Pd, the Pd $3d_{5/2}$ core level is dominated by the metallic Pd chemical state (334.9 eV) with asymmetric tail to higher BE, which is in close agreement with the Pd reference film (grey dashed spectrum in each Pd $3d_{5/2}$ plot in Figure 8.1, see Appendix B for details on synthesis and characterization of the reference film). The Pd $3d_{5/2}$ core level obtained from the Te film after AH treatment and subsequently depositing ~1 nm Pd is dominated by the symmetric Pd–Te chemical state detected at 336.0 eV (Figure 8.1c), which corroborates the much higher $PdTe_x$ concentration formed in the absence of the native surface $TeO_2$.

Pd–C bonds are below the limit of XPS detection throughout the experiment. A single chemical state with an asymmetric tail to higher BE is detected at 284.3 eV in all C 1*s* core level spectra obtained throughout this experiment corresponding with the $sp^2$ C–C bonding in the HOPG substrate. This indicates adventitious carbon-based species are absent from all Te samples throughout this work. It is therefore unlikely that transition metal carbide species would form at the interface between Te and any transition metal unless an additional process (e.g., lithography) deposited carbonaceous species on the surface prior to metallization.

It is useful to understand the band alignment between Pd and Te as a function of the native oxide thickness (0-1.5 nm). UPS was performed in parallel with XPS and RHEED throughout the *in–situ* experiments to track the work function of the samples as a function of air exposure time, AH treatment (where applicable), and stepwise Pd metallization. Figure 8.2 shows the corresponding work function measurements from each sample.

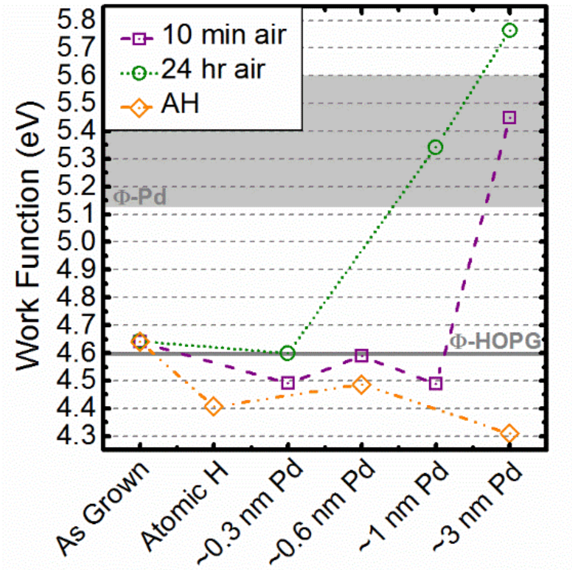

Figure 8.2. Work function according to UPS of Te films after growth, AH treatment (where applicable), and subsequent Pd depositions up to total thicknesses of ~3 nm.

The Te films exposed to air for 10 minutes and 24 hours exhibit a work function of 4.64 eV, which suggests the work function shift saturates after a monolayer of oxygen chemisorbs onto the Te. Removing the native oxide from the Te surface via the AH treatment coincides with a work function decrease to 4.41 eV. Surface oxidation generally causes an increase in the work function due to the formation of dipoles between the chemisorbed oxygen atoms and the covalently bound substrate atoms.[45,46] After depositing Pd to total film thicknesses of ~0.3 nm and ~0.6 nm, the work function of the Te samples with surface oxide decreases slightly to 4.59 eV, while the work function of the AH treated sample increases to 4.49 eV. The minor work function fluctuations detected after initial Pd depositions likely manifests in part from the island-like growth of Pd (growth mechanisms discussed below). After ~3 nm Pd is deposited on the Te films with surface oxide, the work function increases dramatically to 5.45 eV (10 minutes air exposure) and 5.76 eV (24 hours air exposure). These work function values are reasonably close to the expected work functions of polycrystalline Pd (5.12 eV) and the (111) surface of Pd (5.60 eV), which corroborates the accumulation of metallic Pd with increasing Pd thickness indicated by XPS (Figures 8.1 a, b). In stark contrast, the work function shifts lower to 4.31 eV after depositing ~3 nm Pd on the AH-treated Te film.

Thin 1-2 nm transition metal oxide interlayers have been successfully employed in various semiconductor devices at the metal contact–semiconductor interface to simultaneously reduce the contact resistance and depin the Fermi level. $TeO_2$ is a wide band gap (bulk: 3.32 eV, monolayer 3.70 eV)[47] semiconductor that could reasonably serve as a Fermi level depinning layer between a contact metal and a semiconductor. The significant work function increase detected here after depositing ~3 nm Pd on Te films with a native surface oxide and contrasting work function decrease when the native surface oxide is removed indicates the native $TeO_2$ depins the Fermi level between Pd and Te. The significant increase in $PdTe_x$ that forms at the Pd–Te interface when the Te is treated with atomic hydrogen before metallization could also affect the work function considering other palladium chalcogenide materials exhibit work function values between 3.7 and 4.7 eV.[48,49] There are a number of stable palladium telluride alloys at room temperature and their electronic structure could vary with stoichiometry.[50]

Figure 8.3 displays the RHEED images obtained from the Te films after air exposure, AH treatment (where applicable), and subsequent ~0.3 nm Pd deposition. A streaky diffraction pattern with modulated intensity along each streak is observed after exposing the samples to air. The streak spacing agrees qualitatively with the RHEED pattern obtained *in–situ* from the Te films immediately after the growth and subsequent warm up 'anneal' (Figure 8.4a), which indicates the lattice constant of the Te beneath the surface oxide is preserved. However, the diffraction pattern is much weaker and more diffuse after the samples are exposed to air indicating the oxide that forms on the surface interferes with the diffraction from the underlying Te. In addition, the intra-streak modulated intensity in the RHEED patterns shown here are not observed in RHEED images obtained *in–situ* after the MBE growth and warm up 'anneal'. A transition from continuous streaks to modulated streaks in the RHEED pattern indicates a transition from an atomically flat surface to a multi-stepped surface.[51] It is possible that the modulated intensity, streaky RHEED pattern manifests from the surface oxidation considering Te films grown at different temperatures and therefore with markedly different surface morphologies exhibit identical streaky RHEED patterns with no intra-streak intensity modulation. After performing AH to remove the surface oxide, the RHEED pattern remains streaky with a modulated intra-streak intensity. However, the modulated streaky pattern is more intense and well defined than the RHEED patterns obtained from the oxidized Te films, which suggests the Te surface undergoes a reconstruction when exposed to air and removing the native oxide via AH enhances the diffraction from the restructured surface.

Additional experiments are needed to precisely determine the restructuring mechanism and the modified surface structure.

Depositing ~0.3 nm Pd causes significant changes to the RHEED pattern of each sample. A sharp, spotty RHEED pattern is obtained from the Te film exposed to air for 24 hours after the first Pd deposition (Figure 8.3b). The RHEED pattern obtained from the 10 minute air-exposed Te film after the first Pd deposition is also spotty, but is much more diffuse and less intense than the pattern observed from the 24 hour air-exposed Te film. The spotty diffraction pattern observed after depositing ~0.3 nm Pd on the oxidized Te films indicates Pd exhibits 3D, island-like growth on the oxidized Te surface. When the surface oxide is removed by AH and the first Pd deposition is performed, there are no discernible features detected in the corresponding RHEED pattern. Therefore, the oxide-free Te surface provides a high energy surface favorable for strong interactions between the substrate atoms and Pd and a resulting layer-by-layer growth, while the thick surface oxide on the 24 hour air-exposed sample provides a low energy surface that is more favorable for 3D island-like Pd growth. Concentric rings are observed in the RHEED patterns obtained from all samples after depositing ~3 nm Pd (Figure 8.4) indicating that the initial growth mechanism differs depending on the initial Te surface chemistry, but the film morphology eventually coalesces into a randomly oriented polycrystalline film beyond a critical Pd thickness (< 3 nm).

Significant Fermi level pinning is predicted between contact metals spanning a wide work function range and Te. Even the extremely low work function metal Sc (3.5 eV) is predicted to exhibit a 0.34 eV electron Schottky barrier with monolayer Te (0.92 eV band gap).[43] However, the aforementioned theoretical study does not consider the effects of a native oxide at the metal–Te

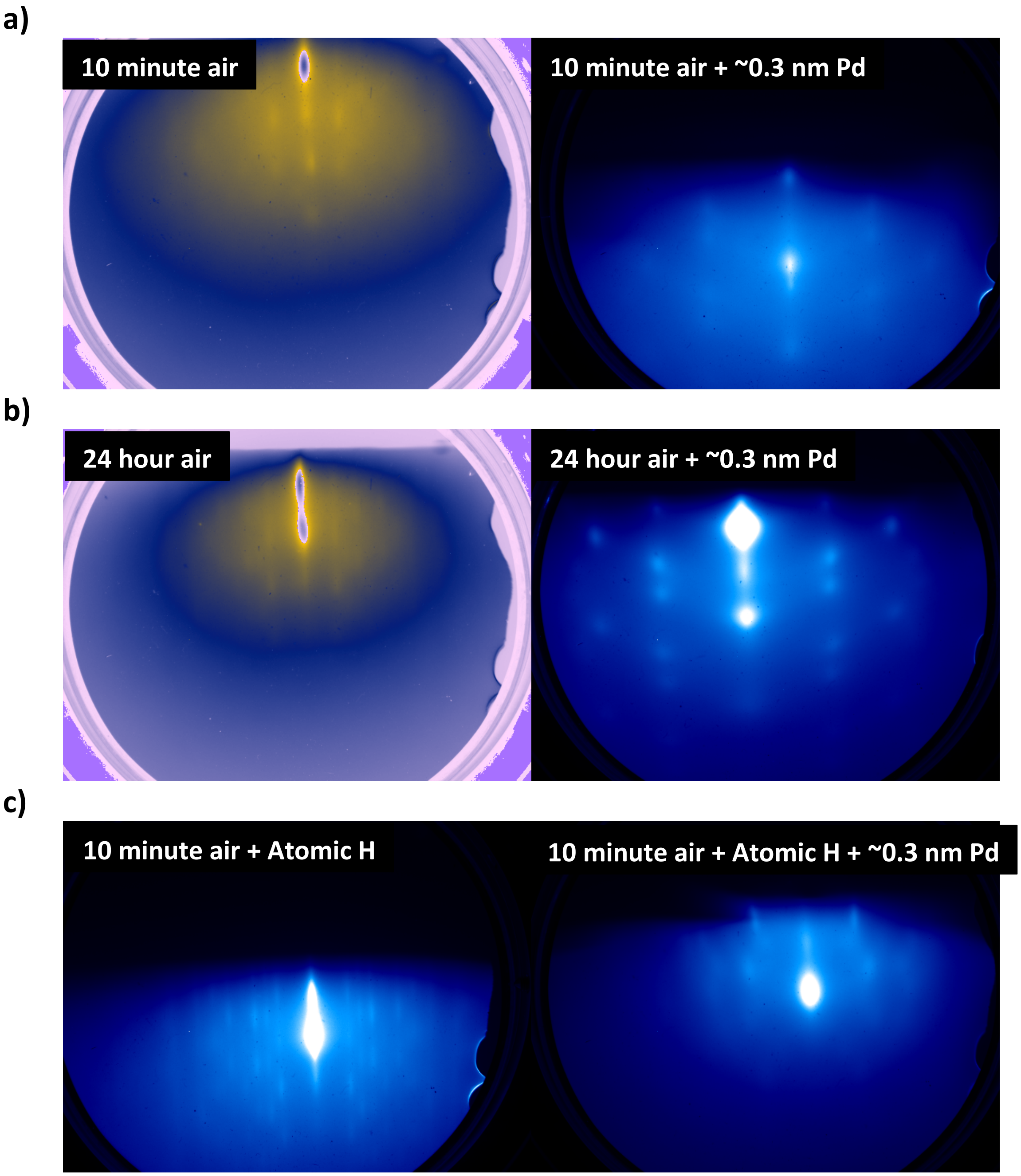

Figure 8.3. Reflection high energy electron diffraction images obtained from Te films grown on HOPG after exposing the samples to air for 10 minutes, 24 hours, and 10 minutes followed by AH treatment (left). The diffraction patterns on the right were obtained from the same samples after depositing ~0.3 nm Pd in UHV showing different growth mechanisms depending on the concentration of $TeO_x$ on the initial surface.

interface on the band alignment or the current injection. The significant Fermi level depinning observed in this work between metallic Pd contacts and Te indicates the Fermi level between other metals and Te can be reliably depinned by tuning the $TeO_2$ thickness and coverage at the contact regions in a Te device enabling the formation of electron contacts. The orientationally dependent transport between metal contacts and Te is similar with metal–TMD systems in that theory predicts superior contact performance to Te is achievable in the edge contact configuration (i.e., metal atoms are covalently bound to the terminal Te atoms of each 1D Te chain).[43] It is likely that the dangling bonds at the Te chain ends facilitate higher reactivity than on the interchain van der waals surfaces, but the relationship between Te domain orientation and reactivity has not yet been studied. It is possible that the oxidation only occurs at Te chain terminations as a result of the enhanced reactivity at the corresponding dangling bonds, which would rationalize the formation of the palladium telluride intermetallic even on a Te film with an effective oxide thickness of 1.5 nm.

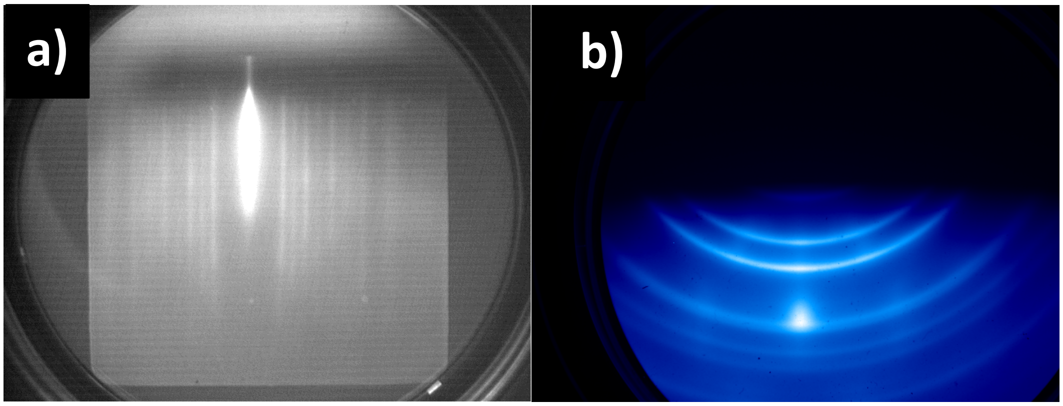

Figure 8.4. RHEED patterns obtained a) *in–situ* from the Te film after growth at -70 °C and subsequent warm up ‘anneal’. b) RHEED pattern obtained after depositing ~3 nm Pd on the AH-treated Te film, which is representative of the RHEED patterns obtained from the other samples after depositing ~3 nm Pd.

## 8.5 Conclusions

This work demonstrates AH effectively removes the native surface oxide from MBE grown Te films that forms spontaneously in air. Depositing the widely employed contact metal Pd on Te films grown by MBE results in the formation of a palladium telluride intermetallic regardless of the presence or absence of the native surface oxide. The concentration of $PdTe_x$ that forms between Pd and oxide-free Te is 40% higher than that detected after depositing Pd on Te films with a native surface oxide. The work function of the Te film (4.64 eV after air-exposure) decreases to 4.41 eV after removing the surface oxide via AH and unexpectedly decreases further to 4.30 eV after subsequently depositing ~3 nm Pd *in–situ*, which indicates the $PdTe_x$ that forms at the interface pins the Fermi level. Critically, when ~3 nm Pd is deposited on the Te films with a native surface oxide, the work function shifts to ~5.6 eV as expected of metallic Pd. Therefore, a controlled thickness of the native tellurium oxide that forms on Te in air could offer a robust, back end of line-compatible route to Fermi level depinning between metal contacts and Te and facilitate the formation of electron contacts to Te for Te-based CMOS logic.

## 8.6 References

(1) Zhou, G.; Addou, R.; Wang, Q.; Honari, S.; Cormier, C. R.; Cheng, L.; Yue, R.; Smyth, C. M.; Laturia, A.; Kim, J.; Vandenberghe, W. G.; Kim, M. J.; Wallace, R. M.; Hinkle, C. L. High-Mobility Helical Tellurium Field-Effect Transistors Enabled by Transfer-Free, Low-Temperature Direct Growth. *Adv. Mater.*, **2018**, *30* (36), 1803109.

(2) Wang, Y.; Qiu, G.; Wang, R.; Huang, S.; Wang, Q.; Liu, Y.; Du, Y.; Goddard, W. A.; Kim, M. J.; Xu, X.; Ye, P. D.; Wu, W. Field-Effect Transistors made from Solution-Grown Two-Dimensional Tellurene. *Nature Electronics*, **2018**, *1*, 228-236.

(3) Huang, X.; Guan, J.; Lin, Z.; Liu, B.; Xing, S.; Wang, W.; Guo, J. Epitaxial Growth and Band Structure of Te Film on Graphene. *Nano Lett.*, **2017**, *17*, 4619-4623.

(4) Liu, Y.; Wu, W.; Goddard, W. A. Tellurium: Fast Electrical and Atomic Transport along the Weak Interaction Direction. *J. Am. Chem. Soc.*, **2018**, *140*, 550-553.

(5) Qui, G.; Wang, Y.; Nie, Y.; Zheng, Y.; Cho, K.; Wu, W.; Ye, P. D. Quantum Transport and Band Structure Evolution under High Magnetic Field in Few-Layer Tellurene. *Nano Lett.*, **2018**, *18*, 5760-5767.

(6) Amani, M.; Tan, C.; Zhang, G.; Zhao, C.; Bullock, J.; Song, X.; Kim, H.; Shrestha, V. R.; Gao, Y.; Crozier, K. B.; Scott, M.; Javey, A. Solution-Synthesized High-Mobility Tellurium Nanoflakes for Short-Wave Infrared Photodetectors. *ACS Nano*, **2018**, *12*, 7253-7263.

(7) Peng, H.; Kioussis, N. Elemental Tellurium as a Chiral p-Type Thermoelectric Material. *Phys. Rev. B*, **2014**, *89*, 195206.

(8) Lee, W.-Y.; Geiss, R. H. Degradation of Thin Tellurium Films. *J. Appl. Phys.*, 1983, *54*, 1351.

(9) Thin film reference data, Oxford Vacuum Science Ltd, 2018; http://www.oxford-vacuum.com/background/thin_film/reference_data.pdf.

(10) Morita, M.; Ohmi, T. Characterization and Control of Native Oxide on Silicon. *Jpn. J. Appl. Phys.*, 1994, *33*, 370.

(11) Ohwaki, T.; Takeda, M.; Takai, Y. Characterization of Silicon Native Oxide Formed in SC-1, $H_2O_2$, and Wet Ozone Processes. *Jpn. J. Appl. Phys.*, **1997**, *36*, 5507.

(12) Sahari, S. K.; Murakami, H.; Fujioka, T.; Bando, T.; Ohta, A.; Makihara, K.; Higashi, S.; Miyazaki, S. Native Oxidation Growth on Ge(111) and (100) Surfaces. *Jpn. J. Appl. Phys.*, **2011**, *50*, 04DA12.

(13) Muller, D. A.; Sorsch, T.; Moccio, S.; Baumann, F. H.; Evans-Lutterodt, K.; Timp, G. The Electronic Structure at the Atomic Scale of Ultrathin Gate Oxides. *Nature*, **1999**, *399*, 758-761.

(14) Hinkle, C. L.; Sonnet, A. M.; Vogel, E. M.; McDonnell, S.; Hughes, G. J.; Milojevic, M.; Lee, B.; Aguirre-Tostado, F. S.; Choi, K. J.; Kim, H. C.; Kim, J.; Wallace, R. M. GaAs Interfacial Self-Cleaning by Atomic Layer Deposition. *Appl. Phys. Lett.*, **2008**, *92*, 071901.

(15) Qin, X.; Wang, W.-E.; Droopad, R.; Rodder, M. S.; Wallace, R. M. A Crystalline Oxide Passivation on $In_{0.53}Ga_{0.47}As$ (100). *J. Appl. Phys.*, **2017**, *121*, 125302.

(16) O'Connor, E.; Brennan, B.; Djara, V.; Cherkaoui, K.; Monaghan, S.; Newcomb, S. B.; Contreras, R.; Milojevic, M.; Hughes, G.; Pemble, M. E.; Wallace, R. M.; Hurley, P. K. A Systematic Study of $(NH_4)_2S$ Passivation (22%, 10%, 5%, or 1%) on the Interface Properties of the $Al_2O_3/In_{0.53}Ga_{0.47}As/InP$ System for n-Type and p-Type $In_{0.53}Ga_{0.47}As$ Epitaxial Layers. *J. Appl. Phys.*, **2011**, *109*, 024101.

(17) Azcatl, A.; McDonnell, S.; KC, S.; Peng, X.; Dong, H.; Qin, X.; Addou, R.; Mordi, G. I.; Lu, N.; Kim, J.; Kim, M. J.; Cho, K.; Wallace, R. M. $MoS_2$ Functionalization for Ultra-Thin Atomic Layer Deposited Dielectrics. *Appl. Phys. Lett.*, **2014**, *104*, 111601.

(18) Addou, R.; Smyth, C. M.; Noh, J.-Y.; Lin, Y.-C.; Pan, Y.; Eichfeld, S. M.; Folsch, S.; Robinson, J. A.; Cho, K.; Feenstra, R. M.; Wallace, R. M. One Dimensional Metallic Edges in Atomically Thin $WSe_2$ Induced by Air Exposure. *2D Mater.*, **2018**, *5* (2), 025017.

(19) Yamamoto, M.; Nakaharai, S.; Ueno, K.; Tsukagoshi, K. Self-Limiting Oxides on $WSe_2$ as Controlled Surface Acceptors and Low-Resistance Hole Contacts. *Nano Lett.*, **2016**, *16* (4), 2720-2727.

(20) Mleczko, M. J.; Zhang, C.; Lee, H. R.; Kuo, H.-H.; Magyari-Kope, B.; Moore, R. G.; Shen, Z.-X.; Fisher, I. R.; Hishi, Y.; Pop, E. $HfSe_2$ and $ZrSe_2$: Two-Dimensional Semiconductors with Native High-k Oxides. *Science Advances*, **2017**, *3* (8), e1700481.

(21) Agrawal, A.; Lin, J.; Barth, M.; White, R.; Zheng, B.; Chopra, S.; Gupta, S.; Wang, K.; Gelatos, J.; Mohney, S. E.; Datta, S. Fermi Level Depinning and Contact Resistivity Reduction using a Reduced Titania Interlayer in n–Silicon Metal–Insulator–Semiconductor Ohmic Contacts. *Appl. Phys. Lett.*, **2014**, *104*, 112101.

(22) Lee, J. S.; Bishop, S. R.; Kaufman-Osborn, T.; Chagarov, E.; Kummel, A. C. Monolayer Passivation of Ge(100) Surface via Nitridation and Oxidation. *ECS Trans.*, **2010**, *33* (6). 447-454.

(23) Kaushik, N.; Karmakar, D.; Nipane, A.; Karande, S.; Lodha, S. Interfacial n-Doping Using an Ultrathin $TiO_2$ Layer for Contact Resistance Reduction in $MoS_2$. *ACS Appl. Mater. Interfaces*, **2016**, *8*, 256-263.

(24) Chen, J.-R.; Odenthal, P. M.; Swartz, A. G.; Floyd, G. C.; Wen, H.; Luo, K. Y.; Kawakami, R. K. Control of Schottky Barriers in Single Layer $MoS_2$ Transistors with Ferromagnetic Contacts. *Nano Lett.*, **2013**, *13*, 3106-3110.

(25) Smyth, C. M.; Addou, R.; McDonnell, S.; Hinkle, C. L.; Wallace, R. M. Contact Metal-$MoS_2$ Interfacial Reactions and Potential Implications on $MoS_2$-Based Device Performance. *J. Phys. Chem. C,* **2016**, *120*, 14719–14729.

(26) Smyth, C. M.; Addou, R.; McDonnell, S.; Hinkle, C. L.; Wallace, R. M. $WSe_2$-Contact Metal Interface Chemistry and Band Alignment under High Vacuum and Ultra High Vacuum Deposition Conditions. *2D Mater.,* **2017**, *4*, 025084.

(27) McDonnell, S.; Smyth, C.; Hinkle, C. L.; Wallace, R. M. $MoS_2$-Titanium Contact Interface Reactions. *ACS Appl. Mater. Interfaces,* **2016**, *8*, 8289–8294.

(28) McDonnell, S.; Addou, R.; Buie, C.; Wallace, R. M.; Hinkle, C. L. Defect Dominated Doping and Contact Resistance in $MoS_2$. *ACS Nano,* **2014**, *8*, 2880–2888.

(29) Addou, R.; McDonnell, S.; Barrera, D.; Guo, Z.; Azcatl, A.; Wang, J.; Zhu, H.; Hinkle, C. L.; Quevedo-Lopez, M.; Alshareef, H. N.; et al. Impurities and Electronic Property Variations of Natural $MoS_2$ Crystal Surfaces. *ACS Nano,* **2015**, *9*, 9124–9133.

(30) Smyth, C. M.; Walsh, L. A.; Bolshakov, P.; Catalano, M.; Addou, R.; Wang, L.; Kim, J.; Kim, M. J.; Young, C. D.; Hinkle, C. L.; Wallace, R. M. Engineering the Pd–$WSe_2$ Interface Chemistry for FETs with High Performance Hole Contacts. Under Review, *ACS Applied Nano Materials*, **2018**.

(31) English, C. D.; Shine, G.; Dorgan, V. E.; Saraswat, K. C.; Pop, E. Improved Contacts to $MoS_2$ Transistors by Ultra-High Vacuum Metal Deposition. *Nano Lett.,* **2016**, *16*, 3824–3830.

(32) Michaelson, H. B. The Work Function of the Elements and Its Periodicity. *J. Appl. Phys.,* **1977**, *48*, 4729–4733.

(33) Wallace, R. M. In-Situ Studies of Interfacial Bonding of High-K Dielectrics for CMOS Beyond 22 nm. *ECS Trans.,* **2008**, *16*, 255–271.

(34) Wallace, R. M. In-Situ Studies on 2D Materials. *ECS Trans.,* **2014**, *64*, 109–116.

(35) 15 keV RHEED source, Staib Instruments, 2018; https://www.staibinstruments.com/rheed-15/

(36) KSA 400 software for *in–situ* RHEED, k-Space Associates Inc., 2018; http://www.k-Space.com

(37) ASTM E2108-10 Standard Practice for Calibration of the Electron Binding-Energy Scale of an X-Ray Photoelectron Spectrometer, **2000**.

(38) Herrera-Gómez, A.; Hegedus, A.; Meissner, P. L. Chemical Depth Profile of Ultrathin Nitrided $SiO_2$ Films. *Appl. Phys. Lett.,* **2002**, *81*, 1014–1016.

(39) Selected Values of Chemical Thermodynamic Properties. In *CRC Handbook of Chemistry and Physics 76th Edition*; Weast, R. C.; Lide, D. R.; Astle, M. J.; Beyer, W. H.; CRC Press Inc.: FL, **1995**.

(40) Lee, W.-Y.; Geiss, R. H. Degradation of Thin Tellurium Films. *J. Appl. Phys.*, **1983**, *54*, 1351.

(41) Physical Constants of Inorganic Compounds. In *CRC Handbook of Chemistry and Physics 76th Edition*; Weast, R. C.; Lide, D. R.; Astle, M. J.; Beyer, W. H.; CRC Press Inc.: FL, **1995**.

(42) Nekrasov, I. A. Geochemistry, Mineralogy, and Genesis of Gold Deposits. Balkema Publishers: Brookfield, VT, 1996, 254-255.

(43) Yan, J.; Zhang, X.; Pan, Y.; Li, J.; Shi, B.; Liu, S.; Yang, J.; Zhang, H.; Ye, M.; Quhe, R.; Wang, Y.; Yang, J.; Pan, F.; Lu, J. Monolayer Tellurene–Metal Contacts. *J. Mater. Chem. C*, **2018**, *6*, 6153.

(44) Luo, Y-R. In *Comprehensive Handbook of Chemical Bond Energies*; CRC Press, Taylor & Francis Group: Boca Raton, FL, **2007**.

(45) Ogawa, S.; Takakuwa, Y. Temperature Dependence of Oxidation-Induced Changes of Work Function on Si(001) 2 × 1 Surface Studied by Real-Time Ultraviolet Photoelectron Spectroscopy. *Jpn. J. Appl. Phys.*, **2005**, *44* (33), L1048-L1051.

(46) Maeno, Y.; Yamamoto, M.; Naito, S.; Mabuchi, M.; Hashino, T. Change in the Work Function of Zirconium by Oxidation at High Temperatures and Low Oxygen Pressures. *J. Chem. Soc. Faraday Trans.*, **1991**, *87* (9), 1399-1403.

(47) Guo, S.; Zhu, Z.; Hu, X.; Zhou, W.; Song, X.; Zhang, S.; Zhang, K.; Zeng, H. Ultrathin Tellurium Dioxide: Emerging Direct Bandgap Semiconductor with High-Mobility Transport Anisotropy. *Nanoscale*, **2018**, *10*, 8397.

(48) Barawi, M.; Ferrer, I. J.; Ares, J. R.; Sánchez, C. Hydrogen Evolution Using Palladium Sulfide (PdS) Nanocorals as Photoanodes in Aqueous Solution. *ACS Appl. Mater. Interfaces*, **2014**, *6*, 20544-20549.

(49) Kukunuri, S.; Austeria, P. M.; Sampath, S. Electrically Conducting Palladium Selenide ($Pd_4Se$, $Pd_{17}Se_{15}$, $Pd_7Se_4$) Phases: Synthesis and Activity towards Hydrogen Evolution Reaction. *Chem. Commun.,* **2016**, *52*, 206–209.

(50) Gossé, S.; Guéneau, C. Thermodynamic Assessment of the Palladium–Tellurium (Pd–Te) System. *Intermetallics*, **2011**, *19*, 621.629.

(51) Hasegawa, S. Reflection High-Energy Electron Diffraction. In *Characterization of Materials*; Kaufmann, E. N. Ed.; John Wiley & Sons, 2012.

# CHAPTER 9

# CONCLUSIONS AND FUTURE WORK

In this work, relationships between processing conditions, interface chemistry and structure, band alignment, and electrical performance of metal contacts to TMDs and Te are explored. In Chapters 3, 4, and 5, XPS is employed to determine the effects of the deposition environment on the interface chemistry and band alignment between metals and the Mo- and W-based TMDs. In general, Au forms a vdW interface with all S- and Se-based TMDs investigated, but reacts with the Te-based TMDs. The excess Te detected in the $MoTe_2$ and $WTe_2$ crystals facilitates reactions with Au that would otherwise be thermodynamically unfavorable. Intermetallic reaction products are detected in all other metal–TMD systems investigated in this work regardless of the deposition environment. The more reactive metals Ti and Sc completely oxidize *in–situ* when deposited in HV. $WO_x$ is detected at the interface formed between all metals and W-based TMDs in HV and likely implicates contact performance in W-based TMD devices. None of the metal–TMD systems obey the Schottky-Mott rule. In general, the Fermi level is pinned in the upper half of the band gap (near the conduction band) between metals and S-based TMDs and in the lower half of the band gap (near the valence band) between metals and Se-based TMDs.

The work in Chapter 4 also considers the effect of photoresist residue and a pre-metallization $O_2$ plasma clean on the interface chemistry and performance of Ti contacts to $MoS_2$. The versatile $O_2$ plasma treatment removes the photoresist residue and oxidizes the $MoS_2$. Ti reduces the $MoO_x$ and $MoO_xS_y$ formed during the plasma resulting in a mixed $TiO_x$/$TiS_x$ contact with Ohmic-like linear output characteristics and a low 0.08 eV electron SBH with $MoS_2$ in contrast with the rectifying contact behavior measured when the $O_2$ plasma treatment is omitted. In future work, a facile process will be developed to clean organic residue from the $MoS_2$ surface without altering the structure or chemistry, which may alleviate Fermi level pinning induced by resist residue and enable processing (e.g., doping, etching) on a pristine $MoS_2$ surface.

In Chapter 6, the increased concentration of a $PdSe_x$ intermetallic is correlated with an Ohmic band alignment and concomitant defect passivation, which further reduces the contact resistance, variability, and barrier height inhomogeneity of Pd contacts to $WSe_2$. The lowest contact resistance occurs when a 60 minute post metallization anneal at 400 °C in FG is performed. In contrast, the work in Chapter 7 demonstrates the highest performance $WSe_2$ transistors with Sc contacts are achieved without post-metallization processing by depositing the Sc contacts in UHV at RT. Device performance is dramatically degraded after post-metallization anneals in reducing environments (UHV, FG), which occurs due to the dramatic change in contact chemistry. STM and STS elucidate the enhanced local DoS below the $WSe_2$ Fermi level around individual Sc atoms in the $WSe_2$ lattice, which directly connects the unexpectedly large electron SBH to the $ScSe_x$ intermetallic. The opposing trends in Pd and Sc contact performance versus the intermetallic concentration at the $WSe_2$ interface necessitates choosing processing conditions based on a detailed understanding of the metal–TMD chemistry–performance relationship.

The work in Chapter 8 focused on the Pd contact to Te, a novel 1D high-mobility semiconductor. Reactions are detected by XPS between MBE-grown Te and Pd. A $PdTe_x$ intermetallic forms at the Pd–Te interface at RT despite the presence of a native surface oxide. An atomic hydrogen treatment completely removes the native oxide from the Te surface. Work function measurements show the native tellurium oxide depins the Fermi level between Pd and Te, therefore offering a promising route to contact engineering in Te devices. It is critical to validate the Fermi level depinning effect of the native tellurium oxide interlayer by extracting SBHs between different contact metals and Te in future work.

# APPENDIX A

# METAL DEPOSITION PROCEDURE

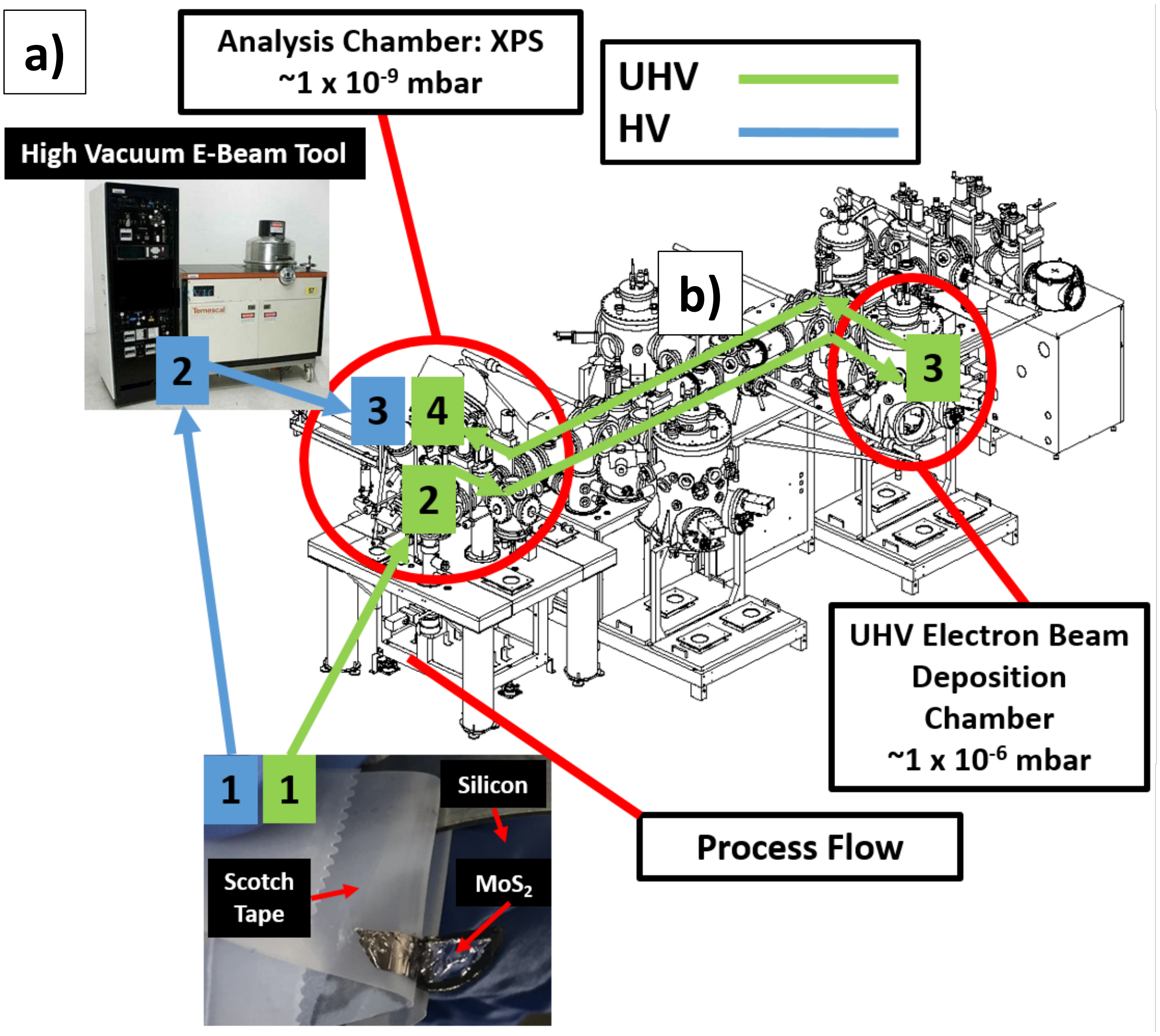

Figure A.1. Diagram of the UHV cluster tool used for metal depositions in UHV (Chapters 3-7) and HV (Chapter 7) and *in–situ* XPS characterization, and images of the cleanroom e-beam reactor used for *ex–situ* metal depositions in HV. Step-by-step experimental procedure visually displaying the process flow utilized for in–situ deposition in UHV or HV via the backfill method (green path) compared with *ex–situ* deposition in HV (blue path).

*In-situ* metal depositions were carried out by electron beam using pellet metal source material and graphite crucible liners from Kurt J. Lesker. The deposition chamber base pressure was < 5 × 10-

$^{9}$ mbar before all metal depositions performed by e-beam in the UHV cluster tool (Figure 2.1a). Bulk TMD crystals were mechanically exfoliated and immediately loaded into the UHV cluster tool for initial surface characterization by XPS (Figure A.1). Before transferring the sample from the analysis chamber to the deposition chamber, metal sources were outgassed at a higher current than was used for deposition (i.e., outgassing current). Once the pressure in the chamber reached steady state at the outgassing current (indicating sufficient outgassing, typically after 2-4 hours), the current was decreased to that used for deposition (i.e., the deposition current). At the deposition current, the deposition rate was determined by monitoring the total thickness of metal deposited over a duration with a quartz crystal microbalance (QCM). The deposition rate typically decreased over time. Therefore, rate was logged roughly every five minutes over the course of a 30-60 minute deposition to more accurately calculate the deposition time required for a desired thickness. The configuration of the e-beam deposition chamber (Figure A.2a) does not permit the use of the QCM to monitor the deposited metal thickness during the deposition. After determining the deposition rate, the current was turned off and the sample was moved from the UHV transfer tube into the deposition chamber. All samples were rotated during metal deposition (Figure A.2a). With the shutter closed, the current was increased to the outgassing current, held for four minutes, decreased to the deposition current, and held for one minute to mimic the conditions used to obtain the deposition rate. The shutter was subsequently opened and deposition proceeded for a duration calculated according to the corresponding deposition rate to yield the desired film thickness (Figure A.2b). After the calculated deposition time elapsed, the shutter was closed, the current turned off, and the sample moved to the analysis chamber for XPS via UHV transfer tube where the sample surface and interface chemistry were characterized using XPS (Figure A.1).

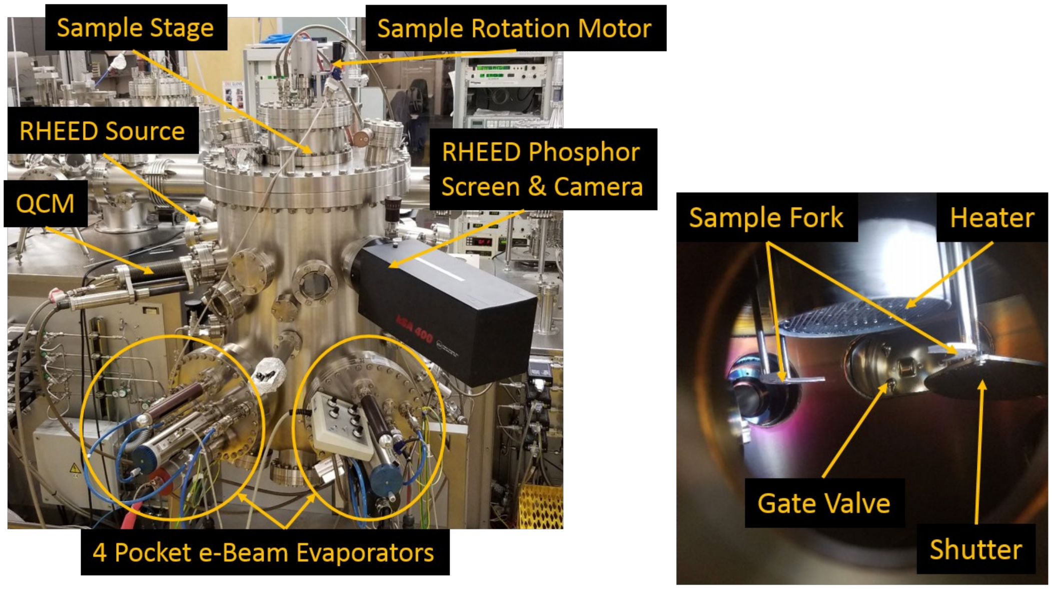

Figure A.2. a) The electron beam deposition chamber used throughout the work described in this dissertation for metal depositions *in–situ* in UHV and HV (using the backfill technique) with all relevant hardware labeled. b) View inside the e-beam deposition chamber displayed in a) showing the sample fork, the shutter, the gate valve, and the heater.

*Ex-situ* metal depositions were carried out under HV conditions in an elastomer-sealed Temescal BJD-1800 e-beam evaporator, base pressure ~$1 \times 10^{-6}$ mbar, in the cleanroom facility (Ref. 36, Chapter 3). After exfoliating a bulk TMD crystal and immediately loading into the cleanroom deposition tool (Figure A.1), the sources were outgassed (with shutter closed) at a current higher than that used for the deposition. During outgassing, the pressure in the chamber never exceeded $6 \times 10^{-6}$ mbar. After the outgassing step and subsequently ramping the current down (i.e., to a sub-deposition current but > 0 A), the chamber pressure was dependent upon the outgassed metal, falling to ~$4 \times 10^{-6}$ mbar in the cases of Au and Ir and ~$1 \times 10^{-6}$ mbar in the cases of Cr and Sc. With the shutter open, the current was carefully ramped up until the QCM indicated metal evaporation was occurring. Deposition continued until the desired film thickness was achieved. Samples were removed from the cleanroom deposition tool and inserted into the cluster tool under

UHV for XPS analysis as quickly as possible to limit any spurious contamination due to air exposure. The total time of transfer from the cleanroom deposition tool to the UHV cluster tool (Figure A.1) was ~15 min.

Samples used for deposition under HV conditions were not characterized in their exfoliated condition because this would increase air exposure time. Although the exfoliated TMD crystals are not characterized before metal deposition in the elastomer-sealed cleanroom deposition tool, the sample surfaces are assumed to be chemically congruent with the bulk crystals characterized before metal deposition in UHV as they originate from the same TMD crystals.

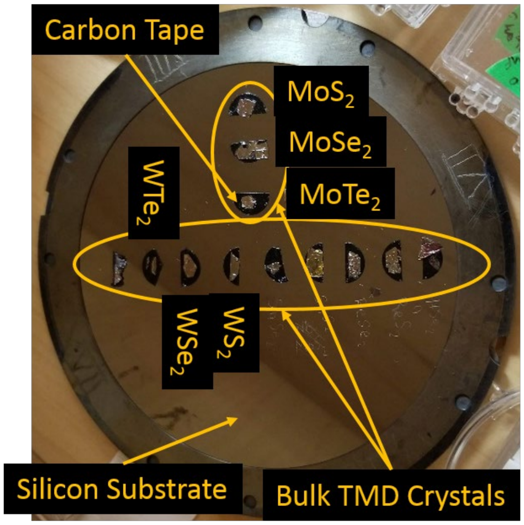

Figure A.3. Bulk TMDs mounted to a 4” silicon wafer by carbon tape, which was used for the interface chemistry studies in Chapters 3 and 5.

# APPENDIX B

# PREPARING AND CHARACTERIZING METAL REFERENCE FILMS AND FOILS

In cases where metal reference foils were not available, films were deposited using the e-beam deposition in the PVD chamber attached to the seven chamber UHV cluster tool (Figure 2.1a). Deposition rates employed in depositing metal reference films were determined separately from the deposition rates employed in interface chemistry studies in which 1-5 nm films were deposited. Metal reference films were deposited at ~1 Å/s to ensure oxygen-free films (especially in the case of the more reactive metals Ti, Cr, and Sc). Before depositing a metal reference film, a 12 $mm^2$ bulk HOPG substrate (Figure B.1) was mechanically exfoliated and immediately loaded into the seven-chamber UHV cluster tool (Figure 2.1a).

Figure B.1. Typical exfoliated HOPG substrate on which metal reference films were deposited.

All metal reference films (Ti, Ir, Cr, Sc, Pd) were deposited in UHV to total thicknesses of ~25 nm to ensure the substrate material was not detectable. A 50 nm Au film was required to completely bury the HOPG substrate and fill in pinholes across the Au film. After deposition, reference films were immediately transferred without breaking vacuum from the e-beam reactor to the analysis chamber for XPS via the UHV transfer tube held at $\sim 1 \times 10^{-9}$ mbar.

Mo and W sources were not available in the e-beam deposition chamber attached to the UHV cluster tool (Figure 2.1a) used in this study. Instead, polycrystalline Mo and W foils (~1 $cm^2$, 99.99% pure) were used to obtain the Mo 3*d* and W 4*f* reference spectra. The foils were ultrasonicated in methanol, acetone, and 2-propanol (in that order) for 10 minutes each and dried under $N_2$ gas before loading into the UHV cluster tool. In the analysis chamber (Figure 2.1a), the foils were sputtered with $Ar^+$ ions (2 keV, 25 mA, rastered over 1 $cm^2$) for 45 min to remove any surface contaminants. Immediately following the sputter cleaning (i.e., as soon as the Ar flow was shut off and the chamber pressure fell to $< 5 \times 10^{-9}$ mbar), the foils were characterized by XPS in the same chamber. The O 1*s* and C 1*s* core level spectra and a survey scan were obtained from each foil in addition to the Mo 3*d* and W 4*f* core levels to confirm the absence of adventitious contaminants on the surface.

# APPENDIX C

# SAMPLE PREPARATION AND PHOTOLITHOGRAPHY PROCESS: STUDYING THE EFFECTS OF PHOTORESIST RESIDUE ON THE TI–MOS$_2$ INTERFACE CHEMISTRY

Bulk MoS$_2$ crystals were employed in the AFM/XPS study of the effects of O$_2$ plasma on photoresist residue and the chemistry and performance of Ti contacts to MoS$_2$ (Chapter 4). The MoS$_2$ crystals were each fixed to a cleaved silicon wafer to make the uneven bulk MoS$_2$ compatible with a conventional lithography process. The MoS$_2$ crystals were fixed to silicon and the lithography process was performed according to the following steps:

1. Exfoliate the backside of the bulk MoS$_2$ crystal
2. Deposit 40 nm Cr/100 nm Au onto the backside via e-beam (Temescal BJD-1800), base pressure $< 5 \times 10^{-6}$ mbar
3. Clean the cleaved silicon wafer by ultrasonicating in methanol, 2-propanol, and acetone for 10 minutes each
4. Completely cover the polished surface of the cleaved silicon wafer with indium foil and heat the wafer/foil stack on a hot plate to 250 °C, well above the melting point of indium
5. After the indium foil melts, place the Cr/Au side of the bulk MoS$_2$ crystal onto the liquid indium and apply pressure. Let sit on the hot plate for 60 seconds
6. Remove the MoS$_2$/silicon sample from the hot plate and let cool
7. Exfoliate the top MoS$_2$ surface
8. Apply a generous amount of AZ nLOF 2020 negative photoresist so that the MoS$_2$ is covered. Remove all bubbles from the surface of the photoresist
9. Spin on the resist at 3000 rpm for 60 seconds
10. Bake the sample at 110 °C for 2 minutes

11. Develop the photoresist by submerging the $MoS_2$/silicon sample in 100 mL of the AZ 200 MIF developer solution for 15 minutes at room temperature

12. Remove the sample from the developer solution, rinse with deionized water, and dry with $N_2$

13. Subject the sample to $O_2$ plasma in the Trion Sirius-T2 RIE Etcher (base pressure < 5 mTorr, 200 mTorr $O_2$, 5 second $O_2$ gas flow stabilization, 5 second $O_2$ plasma, 50 W)

14. Load the sample into the UHV cluster tool described elsewhere for metallization and *in–situ* XPS

15. Outgas the Ti source according to the procedure described in Appendix A. Without ramping down the e-beam current, transfer in the $MoS_2$/silicon sample and backfill the chamber with air to $5 \times 10^{-6}$ mbar

16. Use procedure described in Appendix A to determine the Ti deposition rate

16. Deposit Ti to total thicknesses of 1 nm, 2 nm, and 5 nm while performing XPS *in–situ* after each metal deposition

# APPENDIX D

# PHOTOLITHOGRAPHY PROCESS FOR BACK-GATED FIELD EFFECT TRANSISTOR FABRICATION

Individual transistors were fabricated using a similar photolithography process to the outlined process in Appendix C. However, the substrate preparation and contact metallization processes differ from the indium adhesive technique and the step-wise metallization processes defined in Appendix C. $Al_2O_3$ (~27 nm for optical contrast and rapid $MoS_2$ flake identification) was deposited by ALD at 250 $^oC$ onto a p++ Si wafer with a native oxide for back gate isolation. On the opposite side of the Si wafer, Al was deposited for a backside wafer contact followed by a 400 $^oC$ forming gas anneal to reduce charge traps. The ALD $Al_2O_3$ on the p++ Si then serves as the 'substrate' and the $Al_2O_3$ serves as a back gate oxide for exfoliated multi-layer $MoS_2$ flakes. Using photolithography (same photoresist, spin-on, and post spin-on bake as listed in Appendix C), source/drain contacts are defined on the transferred flake (~4-8 nm thickness) followed by a 5 sec $O_2$ plasma exposure (“descum”) at 50 W and 200 mTorr (base pressure <5 mTorr) to remove photoresist residue prior to contact metal deposition on geological $MoS_2$. Immediately after, Ti/Au (10 nm/140 nm) is deposited using e-beam evaporation (Temescal BJD-1800) in high vacuum (base pressure $< 5 \times 10^{-6}$ mbar) followed by a lift-off process to produce $p^{++}Si/Al_2O_3/MoS_2/Ti/Au$ back gate structures. Electrical back gate measurements are then performed.

In Chapters 6 and 7, the $WSe_2$ devices were fabricated using the aforementioned procedures to prepare the substrate, back contact, isolate $WSe_2$ flakes, define source/drain contacts, and perform lift-off. The contacts were deposited in the seven chamber UHV cluster tool described in Chapter 2 (metal thicknesses defined in the respective chapters). Back gate electrical measurements were performed immediately after the lift-off process. Post-fabrication anneals and back gate electrical measurements were performed in succession as quickly as possible (all anneals and measurements completed within 72 hours of metallization) after lift-off and initial electrical measurements to limit the effects of air exposure on the device performance. The annealing conditions and duration are defined in the respective chapters.

# APPENDIX E

## FULL-COVERAGE, PINHOLE FREE METAL-ON-GRAPHITE AND SILICON-ON-METAL FILMS

Special care was taken to ensure full coverage Pd, Sc, and Si films were deposited on $WSe_2$ in the $Si/Pd/WSe_2/SiO_2/Si$ and $Si/Sc/WSe_2/SiO_2/Si$ samples (Chapters 6 and 7). $He^+$ ion–based low energy ion scattering spectroscopy (LEISS) was employed to check the surface composition of the films, where a full coverage film would be indicated by an absence of detectable substrate atoms by LEISS. Spectra were obtained *in–situ* immediately following Pd, Sc, or Si deposition without breaking vacuum. Figures E.1 a, b display the LEISS spectra obtained from Pd and Sc films deposited on HOPG, respectively, and Si films subsequently deposited on full coverage Pd and Sc, respectively.

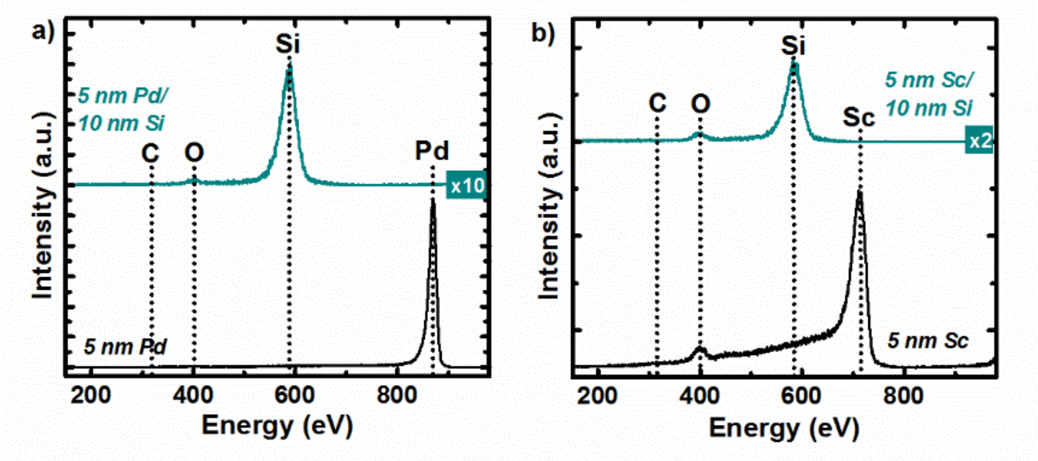

Figure E.1. LEISS spectra obtained from a full coverage a) Pd and b) Sc film on HOPG and full coverage Si film on a) Pd and b) Sc.

After depositing 5 nm Pd or 5 nm Sc on HOPG, carbon is below the limit of detection by LEISS indicating the films are full coverage at this thickness. After subsequently depositing 10 nm Si on the 5 nm Pd or 5 nm Sc film, Pd and Sc are below the limit of LEISS detection indicating a full coverage Si film. *In–situ* surface oxidation of the amorphous Si films deposited by e-beam in UHV is reasonable considering the $\Delta G^{\circ}_{SiO2}$ = -428.4 kJ/mol (Ref. 41, Chapter 3). Therefore, oxygen detected by LEISS after depositing Si is attributed to surface oxidation rather than an incomplete Si film or oxygen incorporated throughout the Si film during deposition.

# APPENDIX F

# FITTING SCHOTTKY DIODE I-V CURVES WITH NONLINEAR REGRESSION

The I-V curves measured from Pd–$WSe_2$ Schottky diodes are fitted with an inhomogeneous Schottky barrier model defined by Equations 6.1-6.3. The initial band alignment of the exfoliated, bulk $WSe_2$ is obtained from the valence band offset measured by XPS (see Section 6.4.2). The built in lsqcurvefit function in MATLAB was employed in the nonlinear regression fitting procedure. The function tolerance, max iterations, optimality tolerance, step tolerance, and max function evaluations were set at 1 x $10^{-400}$, 50000, 1 x $10^{-400}$, 1 x $10^{-400}$, and 50000, respectively. The code is provided below:

```
%function [K] = PatchyIVFit()
%clear all; close all;
A=0.00251;
q=1.602E-19;
eta=(8.854E-14*7.2)/(q*1.19E17);
k=1.3806E-23;
T=298;
Vb=0.58; %update this according to the particular WSe2 crystal
options=optimoptions(@lsqcurvefit,'FunctionTolerance',1E-
400,'MaxIterations',50000,'OptimalityTolerance',1E-400,'StepTolerance',1E-
400,'MaxFunctionEvaluations',50000,'Algorithm','trust-region-reflective')
lb=[1.1 100 1E10 0.2E-7 0.8];
ub=[1.25 300 1E14 5E-7 1.1];
%As Deposited
x0=[1.25 100 3E12 1.5E-7 1.1]; %update initial variable guesses according to
the I-V curve
xdata=[]; %applied bias
ydata=[]; %measured current corresponding with xdata
%Below is a form of the inhomogeneous barrier equation that considers the
SBH, rho, Rs, SBH standard deviation of the defective areas, and A**
%F=@(x,xdata)[abs(A*x(1)*T^2.*(1/exp((q.*x(2))./(k.*T))).*(exp((q.*(xdata-
(x(3).*ydata)))./(k.*T))-1).*...
%    (1+((8*pi.*x(4).*x(5).^2.*eta.^(1/3))./(9.*((x(2)-Vb)-
(xdata+(x(3).*ydata))).^(1/3)))).*...
%    exp(((q.*x(5))).^2.*((x(2)-Vb)-
(xdata+(x(3).*ydata))).^(2/3))./(2*(k*T)^2.*eta.^(2/3))))-ydata)];
%Below is a form of inhomogeneous barrier equation from Ref. (83) in Chapter
6 that considers the A**, homogeneous SBH, SBH of the defective areas, and Rs
F=@(x,xdata)[(A*10*T^2.*(1/exp((q.*x(1))./(k.*T))).*(exp((q.*(xdata+x(2).*yda
ta))./(k.*T))-1).*...
```

```
   (1+x(3).*((k.*T.*pi.*(x(4).^2.*x(5)).^(1/3).*eta.^(2/3))./(3.*q.*((((x(1)-
Vb)-(xdata+x(2).*ydata)).^(2/3)))).*...
    exp(-((q.*x(1))./(k.*T))+((3.*q.*(x(4).^2.*x(5)).^(1/3).*(((x(1)-Vb)-
(xdata+x(2).*ydata)).^(1/3)))./((k*T).*eta.^(1/3)))))))];
format short e
x=lsqcurvefit(F,x0,xdata,ydata,lb,ub,options)
V1=[xdata F(x,xdata)];
plot(xdata,ydata,'ro',xdata,abs(F(x,xdata)),'r-')
xlabel('Bias (V)')
ylabel('I (A)')
xlswrite('3_2_1_AsDepFit',V1)
```

# APPENDIX G

# LANDAUER PHYSICS-BASED SCHOTTKY BARRIER HEIGHT EXTRACTION FROM CONTACTS TO ULTRA-SHALLOW CHANNEL SEMICONDUCTORS

The depletion width $\lambda$ in an ultra–thin body device (e.g., in a few–layer TMD transistor) is defined by the body thickness rather than the doping density in the semiconductor, that is, $\lambda = \sqrt{\frac{\varepsilon_{\mathrm{ch}}}{\varepsilon_{\mathrm{ox}}} t_{\mathrm{ch}} t_{\mathrm{ox}}}$ where $\varepsilon_{\mathrm{ch}}$, $\varepsilon_{\mathrm{ox}}$, $t_{\mathrm{ch}}$, and $t_{\mathrm{ox}}$ represent the dielectric constant of the channel (7.2), the dielectric constant of the gate oxide (9.8), the thickness of the channel (defined in the relevant chapters, device–to–device variation), and the thickness of the oxide (28 nm). Tunneling contributes significantly to the total current due to the body thickness–defined Schottky barrier widths and therefore the reverse current will never be completely thermionic. The current in the 'off state' (i.e., subthreshold region) can be defined as a sum of the tunneling and thermionic hole and electron currents in different operating modes of the device, which are depicted in Figure G.1. Width-normalized hole and electron contributions to current are defined herein as:

$$I_{\mathrm{D,p}} = \frac{2q}{h}\int_{-\infty}^{E_{\mathrm{V}}} T_{\mathrm{V}}(E) M_{\mathrm{V}}(E)[f_{\mathrm{D}}(E) - f_{\mathrm{D}}(E - qV_{\mathrm{DS}})]d\mathrm{E} \qquad \text{Equation G.1}$$

$$I_{\mathrm{D,n}} = -\frac{2q}{h}\int_{E_{\mathrm{C}}}^{+\infty} T_{\mathrm{C}}(E) M_{\mathrm{C}}(E)[f_{\mathrm{D}}(E) - f_{\mathrm{D}}(E - qV_{\mathrm{DS}})]d\mathrm{E} \qquad \text{Equation G.2}$$

Calculated relative to conduction and valence band edges, $E_{\mathrm{C}}$ and $E_{\mathrm{V}}$, $f_{\mathrm{D}}(E)$ denotes the Fermi dirac distribution, and $M(E)$ are electron/hole modes in conduction/valence bands. Mode values are denoted by:

$$M_{\mathrm{V}}(E) = \frac{g_{\mathrm{v}}}{\pi\hbar}\sqrt{2m_h^*[E_{\mathrm{V}}(V_{\mathrm{GS}}) - E]},\ E_{\mathrm{V}}(V_{\mathrm{GS}}) > E \qquad \text{Equation G.3}$$

$$M_C(E)=\frac{g_v}{\pi\hbar}\sqrt{2m_e^*[E-E_C(V_{GS})]},\ E>E_C(V_{GS})$$ Equation G.4

Where $g_v$ is the valley degeneracy (6 in the case of 2H phase TMDs), $m_e^*$ and $m_h^*$ are carrier effective masses (0.33m$_0$ and 0.49m$_0$), and $E_C(V_{GS})$ and $E_V(V_{GS})$ are the gate-bias dependent band positions in the channel. The Wentzel – Kramers – Brillouin (WKB) approximation is used to calculate the tunneling probability through the source and drain ($T_S$ and $T_D$) separately. The total transmission through the device is defined as $T(E)=\frac{T_S T_D}{1-R_S R_D}$, where $T_{S(D)}$ and $R_{S(D)}=1-T_{S(D)}$ are transmission and reflection through source (drain) barriers. Assuming a triangular tunnel barrier at the source and drain in the WKB approximation, the transmission is given by

$$T_{S(D),WKB}=\exp\left(-\int_0^{\lambda}\kappa(E)dx\right)$$ Equation G.5

Where $\kappa_V(E)=\frac{1}{\hbar}\sqrt{2m_h^*[E-E_V(x)]}$ and $\kappa_C(E)=\frac{1}{\hbar}\sqrt{2m_e^*[E_C(x)-E]}$ define complex carrier momentum along the valence and conduction bands. Therefore, both thermionic and tunneling injection of electrons and holes are considered across subthreshold sweeps.

Simultaneous fits of $\Phi_n$ and $\Phi_p$ were performed on ~5 μm long (exact lengths defined within each chapter), back–gated WSe$_2$ FETs on 28 nm ALD Al$_2$O$_3$/Si substrates, at low drain bias $V_{DS}$ = 0.5 V. The bands are approximated with a parabolic shape. $\Phi_n$ and $\Phi_p$ ranges are defined in a MATLAB fitting code built upon the analytical model defined above. The code calculates the $I_{hole}$ and $I_{electron}$ based on all combination of $\Phi_n$ and $\Phi_p$ within the defined ranges. The $I_{DS}$–$V_{BG}$, which is summed from the $I_{hole}$ and $I_{electron}$, that best fits the measured data indicates the corresponding $\Phi_n$ and $\Phi_p$.

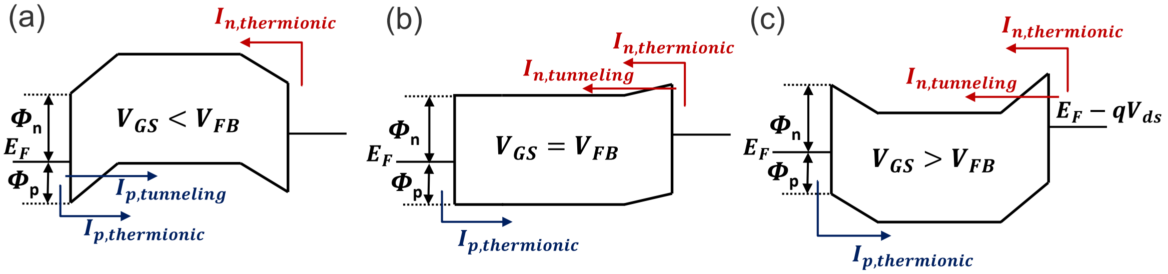

Figure G.1. Band alignment of an ambipolar Schottky barrier FET a) below, b) at, and c) above flatband biasing in gate voltage with principal mechanisms of carrier injection and true barrier heights $\Phi_n$, $\Phi_p$ demarcated for a contact Fermi level pinned deep within the band gap.

# APPENDIX H

## REMOTE FORMING GAS PLASMA FOR FACILE PHOTORESIST RESIDUE REMOVAL

The remote forming gas plasma employed in this work is generated by a Litmas remote plasma source (Litmas PRS) in a Picosun PEALD chamber (Figure H.1a). The Litmas PRS includes a cylindrical inductive plasma source with an RF power operating range between 1500 W and 3000 W. The forming gas flow rate is controlled by a leak valve connected to the cylinder in which the plasma is generated and also by the regulator on the gas cylinder. The forming gas flow rate is

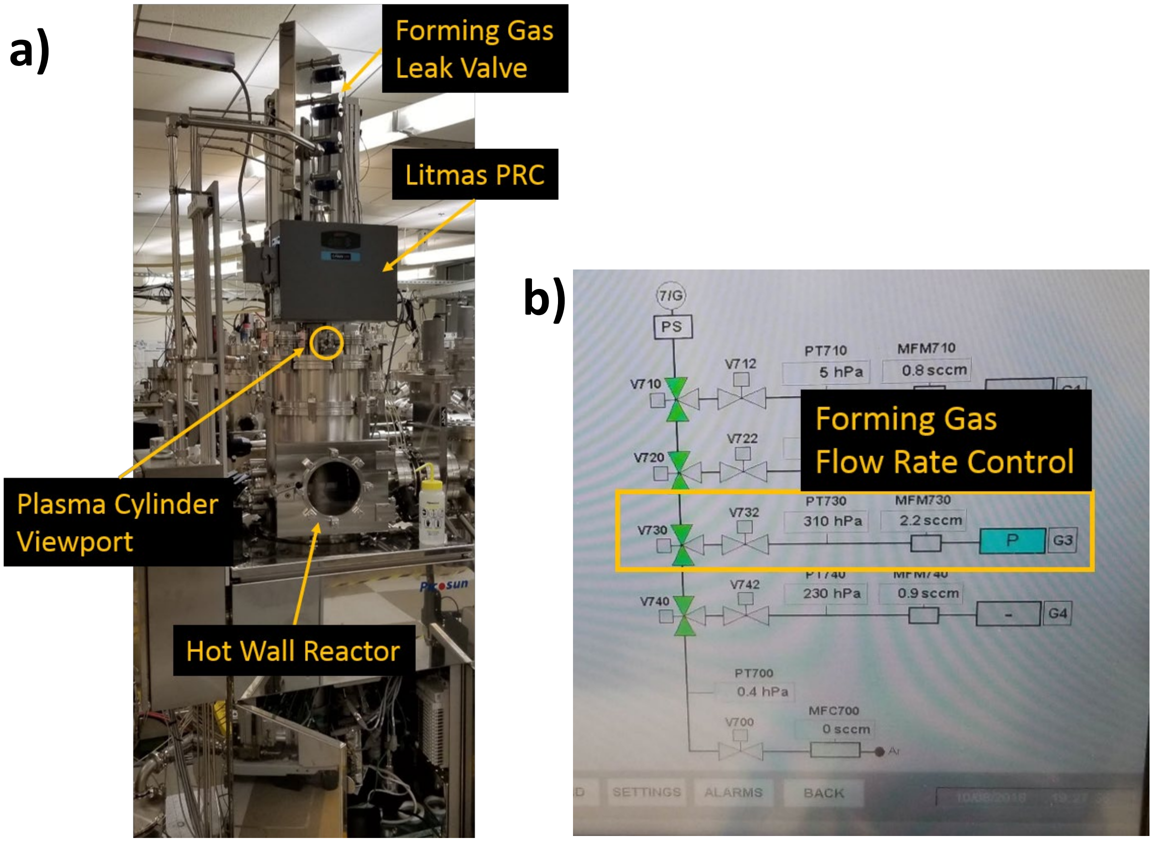

Figure H.1. a) Litmas remote plasma source integrated onto the Picosun PEALD system. b) Screen shot of the “PI Chart” screen in the Picosun PEALD graphic user interface where the remote plasma gas flow rate is controlled.

defined by the G3 and V732 valves in the graphic user interface used to control the Picosun PEALD tool (Figure H.1b). The gas flow can be regulated with and without the plasma ignited according to the procedure described in another dissertation from a previous PhD student advised by Prof. R. M. Wallace (Ref. 57, Chapter 3).

Preliminary investigations have been performed regarding the effectiveness of a remotely generated FG plasma to clean organic residue from $MoS_2$ without imparting damage. The remote plasma recipes attempted thus far are listed in Table H.1. Details related to the process and hardware used for the remote plasma processes are provided in Appendix H.

Table H.1. Remote forming gas plasma recipes attempted to clean resist residue from $MoS_2$ while preserving the chemical and structural integrity.

| | 1. 90% $N_2$/10% $H_2$ | 2. 90% $N_2$/10% $H_2$ | 3. 90% Ar/10% $H_2$ |
|---|---|---|---|
| **Forming gas flow rate (sccm)** | 125 | 125 | 130 |
| **Carrier gas, Flow Rate (sccm)** | 150 | 150 | 150 |
| **Substrate Temperature (°C)** | 150 | 100 | 100 |
| **Power (W)** | 1500 | 1500 | 500, 1000, 2000 |
| **Stabilization Time (sec)** | 90 | 90 | 90 |
| **Treatment Time (min)** | 5 (4×) | 5 (4×) | 5 (1×, 500 W, no effect)<br>5 (1×, 1000 W, no effect)<br>30 (5×, 2000 W) |
| **Characterization** | XPS (not shown) | XPS, AFM | XPS |

Recipe 1 was ineffective because the photoresist decomposes at 150 °C. In recipe 2, the substrate temperature was decreased to 100 °C at which the developed photoresist was stable for at least two hours according to XPS measurements and optical images (not shown here). A 20 minute treatment using recipe 2 removed most of the organic residue, but incorporated nitrogen and oxygen into the $MoS_2$ lattice resulting in a hole doping effect (Figures H.3 a-c). According to AFM images, the process randomly etched the surface, which is undesirable (Figure H.2). Although recipe 2 successfully removed photoresist residue, it is only a useful process if hole contacts to $MoS_2$ are desired and the device structure can accommodate the uneven etching.

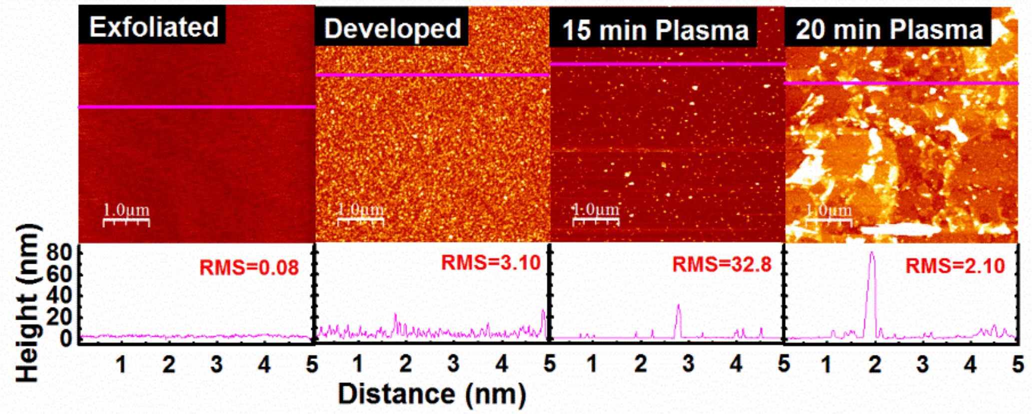

Figure H.2. AFM images from bulk $MoS_2$ after exfoliation, photolithography (see Appendix C), 15 min remote FG (90% $N_2$/10% $H_2$) plasma, and 20 min remote FG plasma.

To avoid the nitridation reaction induced by the $N_2$-based FG plasma, an Ar-based forming gas was employed in recipe 3. When recipe 3 was operated at a low power (500 W, 1000 W), changes in surface chemistry were below the XPS detection limit (data not shown here). At a power of 2000 W, recipe 3 slowly removed organic residue without damaging the $MoS_2$ surface (Figure H.4). After 90 minutes total treatment time, the Ar-based remote plasma completely ashed the organic residue leaving only C–C bonds (Figure H.4c). The surface chemistry was unaffected by additional treatments using recipe 3 beyond 90 minutes total treatment time. Future work will focus on fine-tuning the Ar-based remote FG plasma to completely remove all organics without compromising the structure or chemistry of the $MoS_2$ surface. The effects of the recipe on the line edge roughness and dimensions of lithographically patterned features will be evaluated. Finally, the contact performance of an organic residue-free metal–$MoS_2$ interface in a device will be evaluated and compared with devices contaminated by organic residues.

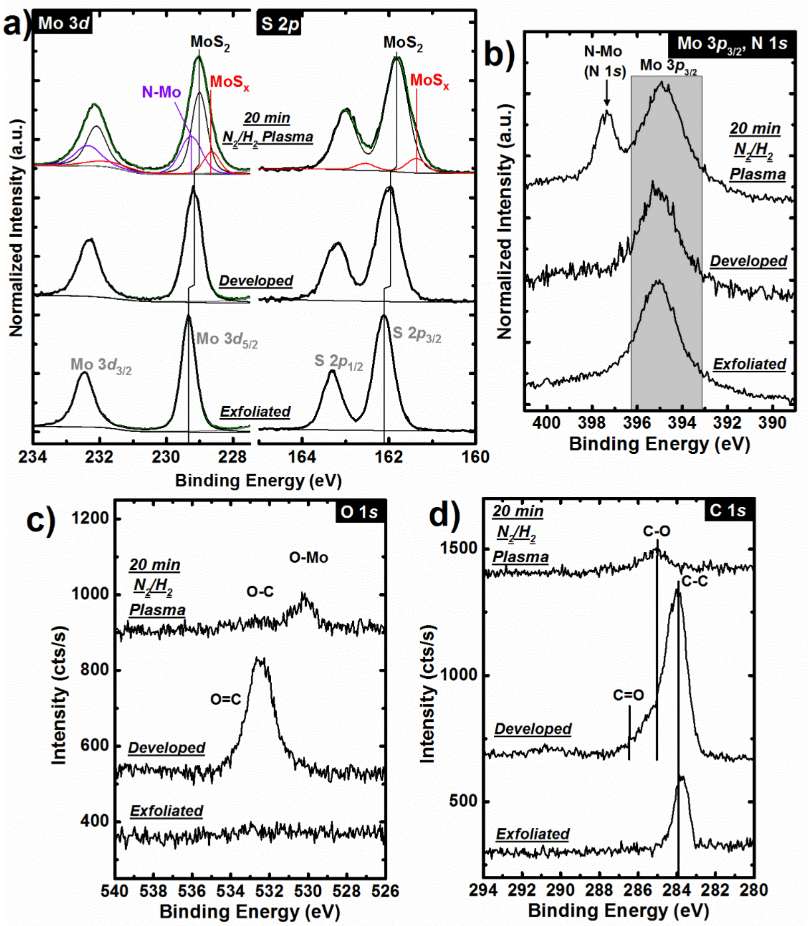

Figure H.3. a) Mo 3*d*, S 2*p*, b) Mo 3$p_{3/2}$, N 1*s*, c) O 1*s*, and d) C 1*s* spectra obtained from bulk MoS$_2$ after exfoliation, photolithography, and 20 min remote FG (90% N$_2$/10% H$_2$) plasma.

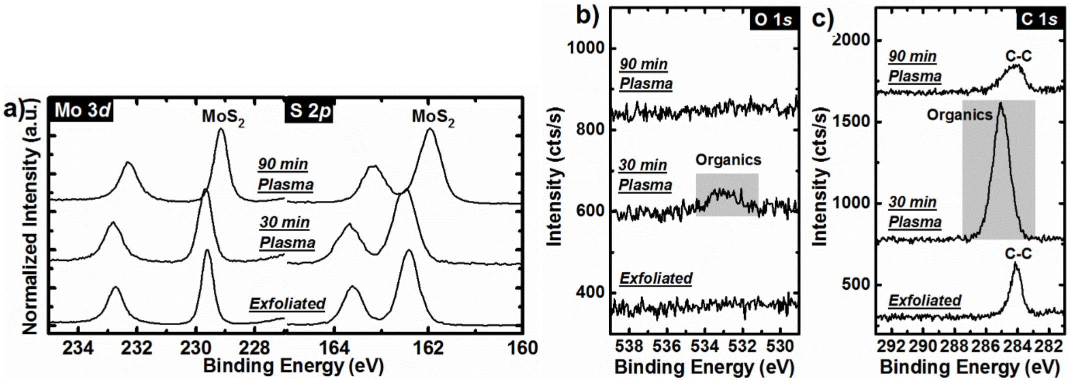

Figure H.4. a) Mo 3*d*, S 2*p*, b) O 1*s*, and c) C 1*s* core level spectra obtained from bulk MoS$_2$ after exfoliation, photolithographic processing and development (spectra not shown), and sequential remote plasma treatments employing a FG (90% Ar, 10% H$_2$) ambient.

# BIOGRAPHICAL SKETCH

Christopher Smyth grew up in Apopka, FL, where he developed a love of warm weather and all things related to the ocean. He received a BS in Materials Science and Engineering from the Georgia Institute of Technology in 2014, where he researched alternative materials for dye sensitized solar cells. In 2015, he enrolled as a graduate research assistant in the PhD program of Materials Science and Engineering at The University of Texas at Dallas under the supervision of Professors Robert M. Wallace and Christopher L. Hinkle. His PhD research has focused on characterizing and engineering the interface between metal contacts and novel materials, such as low dimensional chalcogenides and topological insulators, towards improving contact performance for next generation electronics. He has received multiple conference and academic awards including the best presentation at the 2016 Semiconductor Interface Specialists Conference. He is particularly interested in novel materials synthesis, unique doping schemes, and precision metrology for beyond-CMOS computing.

# CURRICULUM VITAE

**Christopher Smyth** (US Citizen) smyth.chris7@gmail.com

## OBJECTIVE STATEMENT

To obtain a full time position in research and development of critical surfaces, processes, or materials growth as an integral part of a collaborative effort to solve unique engineering challenges for next generation technologies.

## EDUCATION

**University of Texas at Dallas**, Richardson, TX (USA) GPA: 3.77
*Doctor of Philosophy in Materials Science and Engineering (successfully defended thesis)*
Jan. 2015 – Dec. 2018
Thesis: Characterizing and Engineering the Metal Contact Interface in 1D and 2D Chalcogenide Systems

**Georgia Institute of Technology**, Atlanta, GA (USA)
*Bachelor of Science in Materials Science and Engineering* Dec. 2014

## TECHNICAL SKILLS

- Photoelectron & Ion Scattering Spectroscopies (XPS, UPS, ISS)
- X-ray Diffraction (XRD)
- Scanning Probe Microscopy (AFM, STM)
- Scanning Electron Microscopy, Focused Ion Beam Milling (SEM, FIB)
- Physical Vapor Deposition/Thin Film Deposition (PVD, e-Beam, Sputtering, thermal evaporation)
- Atomic Layer Deposition (ALD; thermal, plasma enhanced)
- Infrared Spectroscopy (Raman)
- Electrical Device Characterization (Schottky Diode, Transistor)
- Ultra-high vacuum (UHV) and related advanced material characterization equipment maintenance and modification
- Software: MATLAB, Origin, AAnalyzer, WSxM, Python, MS Office

## ACADEMIC RESEARCH EXPERIENCE

**Graduate Research Assistant, University of Texas at Dallas** Jan. 2015 – Present
Advisors: Profs. Robert M. Wallace, Ph.D. & Christopher L. Hinkle, Ph.D.

- Eliminated device to device variability and enhanced $I_{ON}/I_{OFF}$ ratio and $I_{DS}$ by $10^2$ and $10^5$, respectively, in $WSe_2$ Schottky diodes and transistors with Pd contacts by establishing a post metallization forming gas (FG) anneal as a critical processing step to consistent, high-performance contacts. Extracted an ideal Ohmic hole band alignment after the FG anneals in contrast with an undesirable 0.2 eV hole Schottky barrier after the UHV anneals by fitting I-V curves from diodes and transistors using unique analytical transport models. XPS was employed to corroborate the aforementioned differences in device performance with a 3× increase in $PdSe_x$ intermetallic concentration and a $10^5\times$ decrease in interfacial defect density when the anneals are performed in FG. I designed and performed the experiments, interpreted the results, and performed the analytical fitting of electrical data using MATLAB

- Demonstrated high performance n-type $WSe_2$ transistors with Sc contacts with $10^6$ $I_{ON}/I_{OFF}$ and SS ≈ 100 mV/dec. Observed significantly degraded device performance after the 400 °C anneals in UHV or FG, specifically a $10^2$ decrease in $I_{ON}/I_{OFF}$, an order of magnitude increase in SS, and ~0.3 eV increase in electron Schottky barrier. Employed XPS to correlate the degraded device performance with significant oxidation in the Sc contact. This work establishes post metallization anneals are disadvantageous to Sc contact performance in general. I designed and performed the experiments and interpreted the results
- For the first time, employed the layer number-dependent Raman shift of a 2nd order vibrational mode of $WSe_2$ to quantify the number of $WSe_2$ layers consumed by reactions with the contact metal during post metallization anneals, which is critical information when designing $WSe_2$ memory devices that operate based on spin polarized current. I conceived the novel idea, performed the experiments, and interpreted the results
- Related metal deposition conditions (UHV vs HV) with metal-TMD interface chemistry and band alignment for 44 different contact metal-TMD systems using XPS, also correlated reactivity with morphology of the deposited metal using scanning probe microscopy (AFM). I performed the experiments and interpreted the results
- ALD half cycle study of low temperature $Al_2O_3$ deposition on methyl ammonium lead bromide ($MAPbBr_3$) perovskite; also qualified preexisting thermal ALD processes for $Al_2O_3$ deposition on Si.
- Facile cleaning of photoresist residue from two-dimensional TMDs using direct and remote $O_2$ and forming gas plasma recipes for enhanced metal contact performance in TMD transistors
- Team oriented research: collaborated with 7 university/institution collaborators from 3 countries across 3 different funding centers throughout my graduate research
- Conceived and wrote one multi-year research proposal and one proposal for synchrotron experiments

**Undergraduate Research Assistant, Georgia Institute of Technology** Apr. 2012 – Dec. 2014
Advisor: Prof. Eric M. Vogel, Ph.D.

- Studied effects of different $TiO_2$-based dye sensitized solar cell architectures on quantum efficiency; varied $TiO_2$ morphology (nanoparticle, nanotube, nanorod), electrode material (Pt film, graphene), and substrate materials

## HONORS AND AWARDS

| | |
|---|---|
| Best Poster Presentation – NEW LIMITS Annual Review | Aug. 14, 2018 |
| Stella Kim Memorial Fellow | Fall 2017, Spring & Summer 2018 |
| Ed Nicollian Best Presentation Award, Semiconductor Interface Specialists Conference (SISC) | Dec. 2016 |

## CONFERENCE PRESENTATIONS – 7 total peer reviewed conference presentations

**C. M. Smyth** *et al.*, "Contacts to $MoTe_2$ and $MoSe_2$: Effects of Processing Conditions," 48th IEEE Semiconductor Interface Specialists Conference (SISC), San Diego, CA (2017).

**C. M. Smyth** *et al.*, "Effects of Processing Conditions on Metal-TMD Interface Chemistry and Band Alignment," 59th Electronic Materials Conference (EMC), South Bend, IN (2017).

**C. M. Smyth** *et al.*, "Contacts on $WSe_2$: Interface Chemistry and Band Alignment," 47th IEEE Semiconductor Interface Specialists Conference (SISC), San Diego, CA (2016).

**C. M. Smyth** *et al.*, "Reactivity and Wettability of PVD Metals on 2D Transition Metal Dichalcogenides," 62nd AVS International Symposium, San Jose, CA (2015).

## SELECTED PUBLICATIONS – 15 total accepted or submitted peer reviewed articles to date

**C. M. Smyth** *et al.,* "Engineering the Pd–$WSe_2$ Interface Chemistry for High Performance Field Effect Transistors with Ohmic Hole Contacts" *ACS Appl. Nano Materials*, **2018**, Under Review.

**C. M. Smyth** *et al.*, "Engineering the Interface Chemistry for n-Type Sc Contacts to $WSe_2$-Based Devices" *2D Materials*, **2018**, Submitted.

**C. M. Smyth** *et al.*, "$WSe_2$–Contact Metal Interface Chemistry and Band Alignment under High Vacuum and Ultra–High Vacuum Deposition Conditions" *2D Materials*, **2017**, *2D Materials*, **2017**, *4* (2), 025084.

**C. M. Smyth** *et al.*, "Contact Metal-$MoS_2$ Interfacial Reactions and Potential Implications on $MoS_2$-based Device Performance" *J. Phys. Chem. C*, **2016**, *120* (27), 14719-14729.

Bolshakov, P.; **Smyth, C. M.** *et al.,* "Contact Engineering for Dual-Gate $MoS_2$ Transistors Using $O_2$ Plasma Exposure" *ACS Appl. Mater. Interfaces*, **2018**, Submitted.

R. Addou, **C. M. Smyth** *et al.*, "One Dimensional Metallic Edges in Atomically Thin $WSe_2$" *2D Materials*, **2018**, *5* (2), 025017.

## PROFESSIONAL AFFILIATIONS

SRC Graduate Researcher: LEAST and nCORE programs

| | |
|---|---|
| Head Student Representative, Graduate Materials Science Department UTDallas | Aug. 2017 – June 2018 |
| MRS-University of Texas at Dallas Chapter | Jan. 2015 – present |
| Lambda Chi Alpha National Fraternity | Aug. 2012 – Dec. 2014 |